A multi-wavelength study on the low-mass stellar populations of the southern high-mass star-forming regions RCW 34 and NGC 2626

RJ Czanik

orcid.org 0000-0001-7037-3812

Thesis submitted in fulfilment of the requirements for the degree *Doctor of Philosophy in Space Physics* at the North-West University

Promoter: Prof DJ van der Walt

Graduation July 2019

20175132

ACKNOWLEDGEMENTS

First and foremost, I want to thank my promoter, Prof. Johan van der Walt for the opportunity to complete my doctorate under his supervision. Prof, you did not just serve as my mentor in my post-graduate training but truly taught me how to be a scientist; how to critically evaluate any problem, including my own work. Thank you for all the opportunities that you granted me, and letting me attend numerous international conferences during my post-graduate career. Ek moet daarby sê dat Prof baie diep spore in my loopbaan getrap het, wysheid wat ek vir baie jare nog sal volg, baie dankie.

I also want to thank my loving wife, Joret for the support, love, and understanding throughout the course of this research project - I could not have done this without you. You were my muse in difficult times, nurtured my motivation when I did not want to continue and most importantly the liters and liters of coffee you brought me in the late nights. To my parents, Benti and Marietjie I want to give a very special thank you, this extensive piece of work was only possible by the love, support, and sacrifices that you made for me. You, my dear parents, exposed me to such wonderful things as science, creativity and discovering the world around me — you shaped me into the man I am today, I will always be thankful towards you and love you very dearly. None of this would have been possible without you my loving wife and parents, you three mean the world to me. I also want to thank all of my family and friends for their support.

I want to thank my examiners for their time in reviewing my work. I also want to thank Jacqui Heilgendorff for proofreading this thesis.

Everyone at the Centre for Space Research, thank you for the wonderful years that I have spent in Potchefstroom during my studying career, it was a wonderful part of my life. For financial support during this project, I have to thank the Centre for Space Research, North-West University, and the National Research Foundation.

ABSTRACT

The physical processes of how stars form is well understood and documented. However, the finer details of how high-mass stars ($M > 8$ M$_\odot$) form is not yet fully known. High-mass stars are usually associated with class II 6.7-GHz methanol masers and are always accompanied by lower-mass stars, all forming part of the same cluster. The high extinction caused by the dust in the molecular clouds from which these young open clusters form serves as an observational obstacle in the optical. Two high-mass star-forming regions located in Vela, RCW 34 and NGC 2626, are part of the few clusters that are detectable in the optical and are the focus of this thesis.

A deep near-infrared (*NIR*) imaging study was performed on RCW 34 and NGC 2626, using the 1.4-m Infrared survey facility (*IRSF*) telescope in Sutherland. A total exposure time of about 3 hours was obtained of a $15.9' \times 15.9'$ and a $7.9' \times 7.9'$ field around RCW 34 and NGC 2626, respectively. From the Near-infrared (*NIR*) photometry, using the Linear regression with errors and scatter (*LinES*) optimisation method, a custom extinction law was derived for RCW 34. The same regression method was used for NGC 2626 and is equivalent to the general extinction law used for the Galactic plane. An extinction map of each region was built using the extinctions measured for each field star behind the two star-forming regions, using the *NICEST* interpolation method. The *NIR* photometry showed that there are 593 and 39 sources with excess *NIR*-emission in RCW 34 and NGC 2626, respectively. The excess emission sources in RCW 34 showed that the cluster is larger than stated in the literature, and it spans the entire $15.9' \times 15.9'$ field. Excess emission sources in NGC 2626 confirmed the extent of the cluster and the remnant molecular cloud, as documented in the literature.

Optical photometry from the VST/OmegaCAM Photometric Hα survey of the Southern Galactic plane (*VPHAS+*) survey was obtained for RCW 34 and NGC 2626. For each cluster the sources with Hydrogen Balmer-alpha line (Hα) emission were identified based on the amount of (r'–$H\alpha$) colour excess emitted from the source. The optical $r'/(r'–i')$ colour-magnitude diagrams were used to determine the mass and age of cluster members that showed excess *NIR*- or Hα-emission.

Spectroscopy was performed with Southern African large telescope (*SALT*) on stars with a high likelihood of being Hα-emission sources based on the excess emission in their *NIR*-colours and optical colours. A total of 92 candidates were identified in RCW 34 and 24 in NGC 2626. Of the candidates in each region, 18 and 11 showed Hα-emission lines in RCW 34 and NGC 2626, respectively. The *SALT* candidates were selected based on the amount of (R_s–$H\alpha$) and (H–K_s) colour excess they showed in the SuperCOSMOS sky survey (*SuperCOSMOS*) and *IRSF* photometric systems. The stars with an Hα-emission line were identified as T Tauri stars. Most of the Hα-emission line profiles were noisy, those with the best signal-to-noise profiles were used to determine what the emission source of the Hα-emission line is. Combining the *SALT* observations with the *VPHAS+* photometry showed that sources with an Hα-emission line identified with *SALT* do not show ($r' - H$) colour excess. This eliminated the possible use of *VPHAS+* photometry in the identification of sources with Hα-emission. The *SALT* spectra of the star driving the Herbig-Haro object (HH-132) and the methanol maser in NGC 2626 were used to classify the star as a late O or early B star. This may be the first time that optical spectra of a star that caused a maser have been observed in literature. The spectra shows that this young high-mass star is on the main sequence.

Keywords: HII regions, star formation, RCW 34, NGC 2626, open clusters, pre-main sequence stars, HH-132, High-mass star-forming regions, T Tauri stars, near-infrared photometry, IRSF, optical photometry, SALT, optical spectroscopy

OPSOMMING

Die fisiese prosesse van hoe stervorming plaasvind word deeglik verstaan en is goed gedokumenteer. Die fyner werkinge van hoe hoë-massa sterre ($M > 8$ M$_\odot$) vorm word nog nie ten volle begryp nie. Hoë-massa sterre word gewoonlik met klas-II 6.7-GHz metanol masers geassosieer en gaan gepaard met laer-massa sterre wat almal deel van dieselfde sterretros vorm. Hoë uitdowing in die molekulêre wolke waaruit hierdie jong oop sterretrosse vorm, maak optiese studies uitdagend. Twee hoë-massa stervormingsgebiede in Vela, RCW 34 en NGC 2626, is deel van die enkeles wat in die optiese gesien kan word en is die fokus van hierdie proefskrif.

'n Diep naby-infrarooi (*NIR*) fotometriese studie is op RCW 34 en NGC 2626 met die 1.4-m *IRSF* teleskoop in Sutherland uitgevoer. 'n Totale blootstellingstyd van ongeveer 3 ure is van 'n $15.9' \times 15.9'$ en 'n $7.9' \times 7.9'$ veld onderskeidelik rondom RCW 34 en NGC 2626 verkry. Uit die NIR-fotometrie is 'n spesifieke uitdowingswet vir RCW 34 afgelei deur die *LinES* lineêre-regressie metode van Ascenso *et al* (2012) te gebruik. Vir NGC 2626 is die algemene uitdowingswet vir die Galaktiese Vlak van Rieke & Lebofsky (1985) gebruik, want dit is as geldig bepaal. 'n Uitdowingskaart van elke gebied is met die *NICEST*-interpolasiemetode van Lombardi *et al* (2011) gebou, deur die uitdowing van agtergrondsterre agter elke stervormingsgebied te gebruik. Die *NIR*-fotometrie het onderskeidelik 593 en 39 sterre met oormatige NIR-emissie in RCW 34 en NGC 2626 geïdentifiseer. Oormatige emissie-bronne in RCW 34 wys dat die sterretros groter is as wat 'n vorige studie deur Bik *et al* (2010) bevind het; Dit strek oor die volle $15.9' \times 15.9'$ veld. Oormatige emissie-bronne in NGC 2626 bevestig dat die sterretros so groot is soos wat vorige studies deur Mueller & Graham (2000) en Sharma *et al* (2016) bevind het.

Optiese fotometrie is vanaf die *VPHAS+* opname vir RCW en NGC 2626 verkry. Vir elke sterretros is die bronne vir oormatige Hα-emissie getoets op grond van die hoeveelheid oormatige emissie in die (r'–$H\alpha$) kleur van elke bron, geïdentifiseer. Die optiese (r'/r'–i') kleur-magnitude diagramme is gebruik om die massa en ouderdom van troslede wat oormatige *NIR*- en Hα-emissie toon, te bepaal.

Spektroskopie is met *SALT* op 92 sterre in RCW 34 en 24 sterre in NGC 2626 uitgevoer, waaruit onderskeidelik 18 en 11 met 'n Hα-emissie lyn geïdentifiseer is. Die *SALT*-kanditaatsterre is volgens die hoeveelheid oormatige (R_s–$H\alpha$) en (H–K_s) kleur wat hulle in die *SuperCOSMOS*- opname en *IRSF*-data gewys het, gekies. Die sterre wat 'n Hα-emissie lyn getoon het, is as T Tauri tipe sterre geïdentifiseer. Meeste van die waargenome sterre met 'n Hα-emissie lyn het 'n geruis in hul spektra getoon, maar die enkeles wat 'n duidelike profiel getoon het is gebruik om te bepaal wat die emissiebron van die Hα-emissielyn is. Met die kombinering van die *SALT*-waarnemings en die *VPHAS+* fotometriese data is gevind dat die *SALT*-bronne wat 'n Hα-emissie lyn toon nie oormatige emissie in die ($r' - H\alpha$) kleur het nie. Hierdie bevinding het alle sterre wat as Hα-emissie- bronne met die *VPHAS+* data geïdentifiseer is, geëlimineer. Die *SALT*-spektra van die ster wat die Herbig-Haro objek (HH-132) en die metanol maser in NGC 2626 dryf is gebruik om die ster as 'n laat O- of vroë B-tipe ster te klassifiseer. Dit mag die eerste keer wees wat optiese spektra van 'n aktiverende ster vir 'n maser in die literatuur waargeneem is. Die spektra het getoon dat hierdie jong hoë-massa ster al op die hoofreeksfase is.

Sleutel woords: HII gebiede, ster vorming, RCW 34, NGC 2626, oop stertrosse, voor hooftak sterre, HH-132, Hoë-massa ster-vormings gebiede, T Tauri sterre, naby-infrarooi ster-vormings gebiede, IRSF, optiese fotometrie, SALT, optiese spektroskopie

Contents

List of Tables

List of Figures

List of physical constants

Quantity	Symbol	Magnitude	Units
Speed of Light	c_0	2.99792458×10^{8}	$\mathrm{m.s^{-1}}$
Mass of the Sun	$\mathrm{M}_\odot$	1.9885×10^{30}	kg
Radius of the Sun	$R_\odot$	6.95508×10^{8}	m
Parsec	pc	3.086×10^{16}	m
Planck's constant	h	6.62607×10^{-34}	$\mathrm{m^2kg.s^{-1}}$
Gravitational constant	G	6.67406×10^{-11}	$\mathrm{m^3.kg^{-1}.s^{-2}}$
pi	π	3.141592653	
Mass of Hydrogen atom	m_H	1.6727×10^{-27}	kg
Boltzmann constant	k	1.3806×10^{-23}	$\mathrm{m^2.kg.s^{-2}.K^{-1}}$
Astronomical Unit	AU	1.49610^{11}	m

CHAPTER 1: INTRODUCTION

1.1 A global view of star formation and the contextual framework for studying star-forming regions

The only source of information we have about stellar systems outside of our own is electromagnetic emission given off in some radiative process. We can only perceive a small part of the electromagnetic spectrum with our eyes in the form of visible light. However, we can study the full spectrum of electromagnetic radiation by using measurements from electronic detectors. Most of the light that can be seen with the naked eye on a clear night, looking up at the sky, comes from stars in the Milky Way. The origin, evolution, and ending fate of the stars in the Milky Way are well understood and documented today in many textbooks, for example, Kippenhahn *et al* (2012) or Stahler & Palla (2005). This process is cyclic, starting with the birth of each star from the densest parts of the Interstellar medium (ISM) inside a molecular cloud. A star's life span is as long as the structural balance between the gravitational pull of its mass, and the expansive forces caused by the nuclear fusion of primarily hydrogen, helium, and some heavier elements in its core. When the star's hydrogen fuel supply becomes depleted, it will expand to become a giant star with a helium-burning core, and burn hydrogen in an outer layer. During the helium burning phase the core temperature will rise significantly, causing the star to become structurally unstable. The star will start to throw off some of its outer layers into the ISM. The severity of the expulsion of matter and the duration of the giant phase depends on the star's mass. Once the star reaches the end of the giant phase, it will very violently throw off its outer layers into the ISM, enrich it with elements heavier than hydrogen, and form part of the next generation of stars.

Some stages in the stellar evolutionary process are not fully understood and are under scientific investigation. One specific topic is the formation of high-mass stars. The physical processes involved in the formation of a star with a mass higher than $M_* > 8\ M_\odot$ are still unclear. When high-mass stars form there are always low-mass cluster members in the directly surrounding environment — this will also be the subject of this thesis. This thesis will focus on how some of the global properties of high-mass star-forming regions can be determined by studying the lower-mass stellar populations which are accordingly associated.

A high-mass star-forming region has a single or multiple young OB star(s) which produce HII regions. During the early stages of the lifetimes of these objects they are usually embedded in the parental molecular cloud, which makes observational studies challenging. These high-mass stars have short life spans (3-10 Myr) so it is rare that they are seen outside of the embedding material or away from nebulous regions. HII regions are very often associated with environments that host multiple epochs of star formation, for example, the Orion nebula cluster (see Alves & Bouy 2012), the Pipe Nebula (see Alves *et al* 2008), NGC 2264 (see Teixeira *et al* 2012), and NGC 3603 (see Di Cecco *et al* 2014) amongst others. It is important to study complex environments that have multiple phases of star formation, and understand them better, for the following reasons:

- Not a single instance has been recorded of a high-mass star that formed on its own — they always form as part of a cluster. Moreover, there are very few high-mass stars that are considered to be alone. For 342 clusters in a 2 kpc radius around the Sun, only 12.4% of O stars are single in their specific clusters, and 4.2% do not have any B stars directly associated in their clusters (see Kharchenko *et al* 2012, Schmeja *et al* 2014, and Dib *et al* 2017). If the formation of lower-mass stars is better understood in the context of a high-mass star-forming region, then high-mass star formation can be better understood in a larger environmental picture.

- To gain understanding of the relationship that high-mass and lower-mass stars have on each other in terms of their formation. Thorough studies will give a much clearer picture of their complex, inter-connected relationship. For example, such studies could investigate whether the presence of a very young high-mass star triggers the formation and influence the dynamical evolution of the lower-mass members in a young cluster.

- To investigate in which order the formation of high- and low-mass stars occurs in an environment of competitive accretion? Do a few low-mass protostars attract each other and merge? Or, alternatively, does a high-mass star form, and some of the matter that is attached to the high-mass clump start to group together and form splintered off, lower-mass stars?

- High-mass stars also have strong stellar winds that will perturb the embedding material and may be the triggering mechanism for the formation of lower-mass stars from dense molecular cloud. A high-mass star's life usually ends in a violent supernova explosion. If it is in — or close to — a molecular cloud this event is thought to be one of the major causes of perturbing the molecular cloud and triggering the formation of lower-mass stars. To tell whether the high-mass star dies in a supernova explosion and this triggers the onset of the next epoch of star formation — or if it disrupts the formation of lower-mass stars — a detailed analysis of the region is needed.

- Understanding the formation of high-mass stars is important on a Galactic scale. High-mass stars are the main sources of ultra-violet radiation in the Galaxy, causing the dispersion of ionised gas in the ISM. At the end of their lives they are the primary distributors of heavier metals into the ISM. The evolution of high-mass stars in the environment of the Galactic disk also plays a major role in the evolution and distribution of the ISM in the Galactic plane. By better understanding, the formation and evolution of this environment, the larger picture of galaxy evolution is better understood.

1.1.1 The biggest unanswered questions in star cluster formation theory

The subject of the formation of open clusters is still under strong investigation, because there are some gaps in the theoretical models that can only be solved with observational data. The questions that are still unanswered are (1) what determines the star-formation rate of a new cluster, (2) how does the dynamics of the gas in the molecular cloud influence clustering and (3) what influences the IMF (see Krumholz 2014 and Joshi 2016). The clusters involving high-mass star formation are of particular interest, because the gaps in high-mass star-formation theory can only be answered by better studying these regions (see Battersby *et al* 2017). The only environment where the formation of clusters which include both high-mass and low-mass stars can be studied is the Milky Way galaxy. The Galactic plane is the only environment where there is enough molecular gas where star formation can occur and is located close enough that a definite distinction can be made between low-mass cluster members. It is not an easy task to get high precision measurements in the equatorial plane of the Milky Way, because of the limitations of the instruments, and the distances to these star-forming regions. There are not many star-forming regions and open clusters which are located within a few kpc of the Sun and can be studied in detail. Star-forming regions that are further from the Sun — especially on the other side of the Galactic centre — are nearly impossible to detect (see Schmeja *et al* 2014).

A compact or ultra-compact HII region is a nebulous region of ionised hydrogen gas that is mainly embedded in dense molecular gas. Sometimes they are on the outskirts of the molecular clouds and are indicators of the presence of a young OB star. HII regions usually have an association with young low-mass stars and there may be an ongoing process of star formation in its direct vicinity. HII regions serve as signposts of young embedded high-mass stars and indicators of regions which may have active star formation. There are less than 200 HII regions that are visible in the optical, and these are not as deeply embedded as the vast majority, which are only detectable in the infrared (see Kharchenko *et al* 2012). Each HII region is produced by and associated with young OB stars, and on the odd occasion with a single O or B star. By studying the clusters of lower-mass stars associated with these high-mass star-forming regions, a general understanding about cluster formation is gained. This will

also help in gaining a better understanding of cluster formation, and fundamental questions about star formation can be better answered. The first of these fundamental questions is: *how are the young stars in a cluster spatially arranged in relation to each other, and the gas from which they formed*? In high-mass star-forming regions, an OB star ionizes the gas around itself, creating a compact HII region and disperses all of its embedding gas. The stars and the gas from which they formed are distributed non-homogeneous relative to the molecular cloud. The stellar surface density of stars that form in regions close to the Sun are very inhomogeneous according to Kharchenko *et al* (2013), and the stellar surface density varies drastically across each star-forming region. This inhomogeneous distribution makes the task of understanding the order in which star formation occurred, and how the cluster evolved, dynamically difficult.

Another fundamental question that could be better answered through deeper understanding of of cluster formation is: *What is the true spatial extent of a young star cluster and how do you distinguish between young cluster members and the surrounding field stars?* This may seem like a trivial problem, but it is complex and difficult to answer. By knowing exactly which stars are cluster members and which ones are not, the total mass, star-forming efficiency, dynamical evolution, and other properties of the cluster can be determined. Tied to this is the question of the *time evolution of stellar clustering*, or how many cluster members will break free from the cluster's gravitational bond. It is very difficult to determine how a star cluster has dynamically evolved. It is just as difficult to predict which cluster members will remain gravitationally bound to each other after many of the young members have broken free from the cluster (see Fujii & Portegies Zwart 2016). The decline of the number of stars that are gravitationally bound together or the functional decline ($\mathrm{d}N/\mathrm{d}\tau \propto \tau^{\gamma}$) — which measures how the cluster members disassociate from the cluster, is also still under investigation (see Joshi 2016). Which factors play the largest roll in the disassociation between cluster members is not known yet. What determines if a star remains part of the cluster, or breaks free, is still an open question.

The *mass function for open clusters* is a power-law given by Krumholz (2014) in the form of $\mathrm{d}N/\mathrm{d}M = M^{-\beta}$, where $\beta = 2$ for most of the range of masses in open clusters. The evolved mass function for open clusters and its underlying cause have not received so much attention as the initial mass function. The evolved mass function is the mass distribution of a matured open cluster, after a substantial period has passed since all of the cluster members have reached the main sequence (see Luhman *et al* 1998). The Initial Mass Function (IMF) is a theoretical construct that was conceptualised by Salpeter (1955) for the distribution of stellar masses at birth, which can be better understood from studying stars that form at the same instance (see Kroupa 2001 and Maschberger 2013). An open cluster's mass distribution changes over a long period from the IMF to the evolved mass function, because some cluster members break free while others reach the end of their lifetimes. Young open clusters are a good environment with which the IMF can be tested, because these stellar populations formed at the same period, so the distribution of their masses should resemble the IMF. The relation between the dense core mass function (CMF) and the evolution of IMF is not understood yet (see Goodwin *et al* 2008). The CMF is the distribution of masses for dense starless cores; it differs significantly from the IMF. The evolution of the mass distribution of the dense starless cores to the IMF at stellar birth is not yet understood. From the mass distribution of young stars in an open cluster, it is possible to relate the stellar mass distribution to the CMF, for example the detailed study by Drass *et al* (2016) of the Orion nebula cluster.

Distinguishing between single stellar systems and binary systems is very challenging for some mass ranges in regions with high stellar population densities. The effects of unresolved binaries on the mass distribution that is derived from a young cluster was shown by Kroupa (2001) as significant for K and M stars. There are not as many binary systems for K and M stars as there are for higher mass stars, however, a large number of K and M stars that do have binary companions affect the estimated mass distribution. It is not just binary systems, but multiple stellar systems that may not be photometrically resolved; it is possible to find triple, quadruple or even more stellar systems that form together (see Chapman *et al* 1992 and Pineda *et al* 2011). To resolve multiple systems in a field

is very difficult, because the cluster is observed from a single angle. Without precise parallax solutions for star-forming regions close to the Sun, it is not possible to resolve the correct projection resolution. It is only possible to resolve multiple systems by using time-based photometric and spectroscopic techniques.

1.2 This Thesis

In this research project, an attempt is made in gaining some insight into the star-formation history and properties of two individual high-mass star-forming regions. This is done by performing an observational study on low-mass cluster members that are associated with high-mass star-forming regions. By using the observational data of single low-mass cluster members and the synthesis of the observed data from different wavelength regimes into one dataset, some insight about the clutser can be gained. This can be done by viewing the low-mass population of stars as an ensemble and determining a few important properties such as the age, metallicity, and spectral type of a few stars in each cluster.

1.2.1 Rationale for this research project

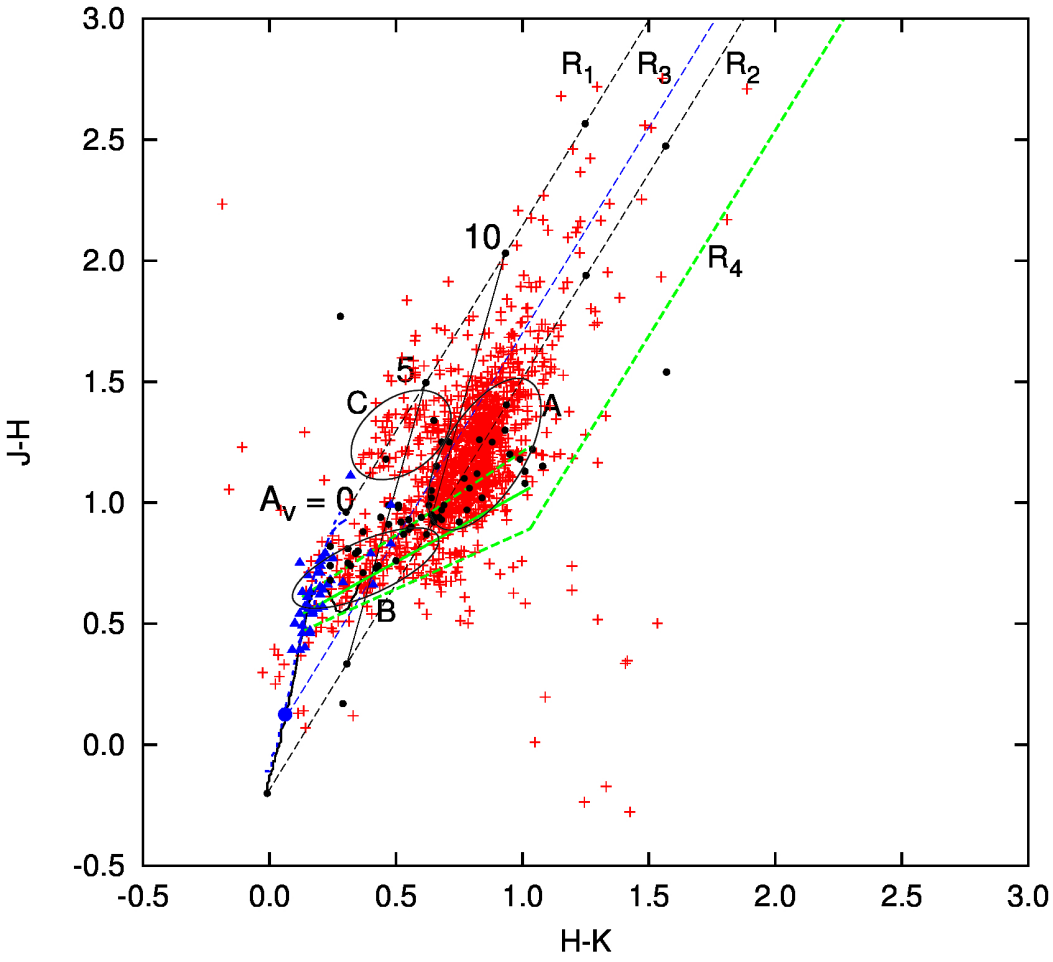

Figure 1.1: Colour-colour diagram of cluster members associated with RCW 34 which were suspected to be CTTs, taken from van der Walt *et al* (2012).

This thesis is a continuation of two previous studies on the southern high-mass star-forming region RCW 34, with the addition of the high-mass star-forming region NGC 2626. The first study on RCW 34 was done by de Villiers (2009), and was a deep *NIR* study focused on the low-mass cluster members associated with the high-mass star-forming region. It was discovered that hundreds of low-mass members ($\sim$ 800 out of 1283, or 62%) showed excess emission in their *NIR* broadband colours, which clustered together around the classical T Tauri locus on a *NIR* colour-colour diagram. This

excess emission is typical of what one would expect from embedded classical T Tauri stars (CTTs). However, having hundreds of them clustering around the classical T Tauri locus, or just the T Tauri locus, is not known in the literature. The diagram used in this study is shown in Figure 1.1. A CTTs is a pre-main sequence star that is accompanied by an accretion disk and has an age of younger than 3 Myr. A CTTs has a characteristic Hα-emission line with an equivalent width of 10Å. A T Tauri that is evolved more than 3 Myr, is called a weak-line T Tauri. A Weak T Tauri star (WTTs) has an age between 3-10 Myr and its primary fuel source is not yet hydrogen burning, but the accretion disk is not as prominent as before. A WTTs has a Hα-emission line with an equivalent width less than 10Å.

Figure 1.1 was taken from the paper by van der Walt *et al* (2012) to illustrate the results from the study by de Villiers (2009). The main sequence from Koornneef (1983) was taken and transformed to the *2MASS* photometric system. Further, the T Tauri locus from Meyer *et al* (1997) is plotted with a 1σ upper and lower limit. There are also four bracketing reddening lines: R1 and R2 are at the outer limits of the main sequence respectively, and R3 is the reddening line for an F0 star which is the upper limit for T Tauri stars. R4 is the limit for reddened CTTs. Three groups of stars were identified in the paper by van der Walt *et al* (2012) and are also shown in the Figure 1.1. The first group is A which are the $\sim$ 800 stars suspected to be reddened CTTs. The second group, group B fall between the upper and lower limits of the CTT locus, indicating that they are CTTs. The third group — group C — is in the position where one would find reddened WTTs — the cluster members that are closer to the main sequence than the CTTs.

The type of grouping on a colour-colour diagram as shown in Figure 1.1 is not very common for the low-mass members that are associated with other high-mass star-forming regions, especially with $\sim 63\%$ of the cluster in group A. Most of the low-mass stars found in a high-mass star-forming region are found closer to the main sequence. For example, those in the Taurus-Auriga region (see Kenyon *et al* 2008), there were single cluster members that appeared in the region of group A. The Orion Nebula Cluster (ONC) (see Dahm & Simon 2005) had quite a few cluster members in this area, but not such a high percentage as RCW 34 and then IC 348 (see Barentsen *et al* 2011) also only had a few in the position of group A. The cases for the ONC and IC 348 are thoroughly discussed and shown in the paper by van der Walt *et al* (2012). There are also other star-forming regions like NGC 1333 (see Lada *et al* 1996), L1630 (see Li *et al* 1997), NGC 2316 (see Teixeira *et al* 2004), and the Horsehead Nebula (see Bowler *et al* 2009) that have very low surface densities CTTs if compared with the results from de Villiers (2009).

The spatial clustering of the stars in region A in Figure 1.1 was tested by de Villiers (2009) using a two-point correlation function. The two-point correlation function showed similar traits than that for the Taurus-Auriga, and upper Sco star-forming regions as found by Kraus & Hillenbrand (2008), suggesting that Group A also spatially clusters together. This spatial clustering extended 1.7 pc at the distance of RCW 34, which is 2.5 kpc. With the results of previous studies suggesting that there are roughly 800 CTTs and the proof of clustering from the two-point correlation function, the cluster associated with RCW 34 needed further investigation. Thus an optical study was performed by Czanik (2013) on RCW 34 as an attempt to get a better understanding of this young cluster, and to establish if the findings by de Villiers (2009) could be confirmed in an independent investigation.

The optical photometric study was on the same ($7.7' \times 7.7'$) field on which the *NIR* study was performed. Results from the photometry showed only 78 sources that matched between the V, R, and I bands over a slightly larger $8' \times 8'$ field. The data that was used for the photometric observations were not obtained with the goal to study faint low-mass cluster members, meaning the sensitivity was not near what one would require when studying faint embedded stellar sources. Additionally, a spectroscopic investigation was conducted on some of the brightest sources in the cluster, and those that showed the highest levels of excess emission in the $(H - K_s)$ colours. Two sets of observations were used. The first dataset was observed in 2002 on 28 of the brightest sources in the cluster, and the second dataset consists of 31 stars that were chosen based on the excess in their *NIR* colours and

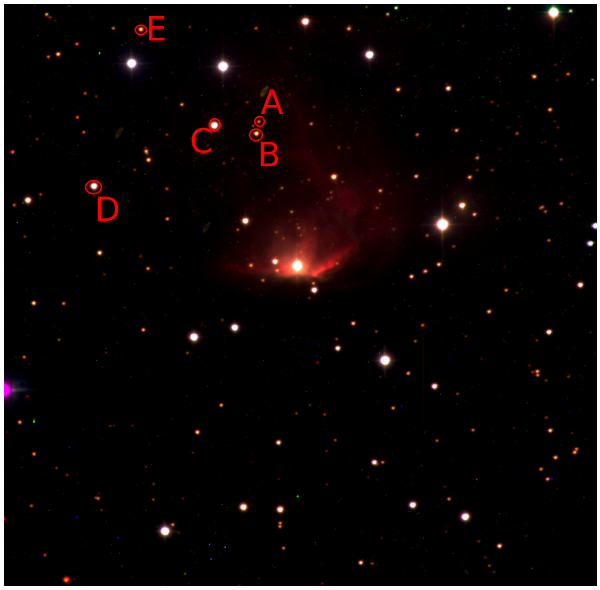

(a) The 5 sources that showed Hα-emission from the optical study by Czanik (2013).

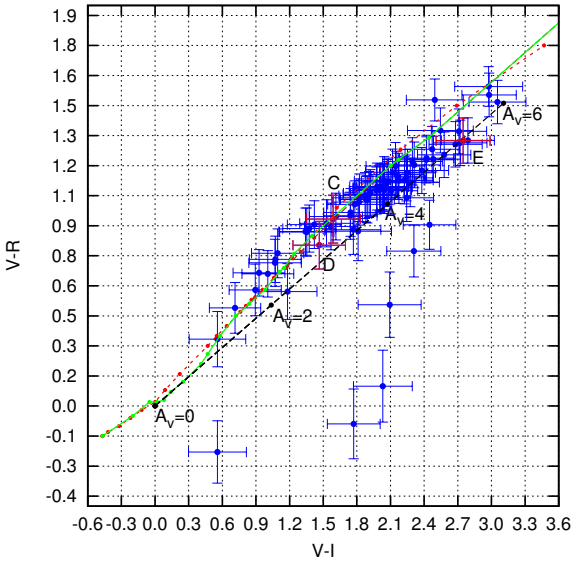

(b) Of the 5 sources that showed Hα-emission only 3 matched in the VRI and did not nessicarily show excess blue emission in their broad band colours.

Figure 1.2: Optical data from the study by Czanik (2013).

the J-band magnitude. Out of the spectroscopic datasets, only five stars showed Hα-emission, which most probably originates from a circumstellar disk found around CTTs. Moreover, of these five stars, only a single one showed a Li-absorption line which is found in CTTs that are younger than 3 Myr. This low number of sources suggested that either the sensitivity of the equipment from the optical study was not high enough to confirm the results of the *NIR* study, or that the results of the *NIR* study were incorrect. Finding inconsistencies like this in scientific research is important, because it shows systematic or interpretive errors, which would imply a new investigation into the specific subject.

A very important realisation was made during the execution of the project for this thesis, namely: an error was made in the study by de Villiers (2009). The mistake was made when the transformation was done from the instrumental *IRSF* magnitude system to the *2MASS* magnitude system. The standard transformation equations from the *IRSF* to *2MASS* system would not work, because the measurements were made from a set of images stacked from observations that were done at various air masses, implying that standard star calibration was not possible. A set of transformation equations from the instrumental colours/magnitudes to the *2MASS* system was derived using 40 of the brightest sources on the image. The transformation equations that were used by de Villiers (2009) and then in the paper that followed from that research by van der Walt *et al* (2012) were:

$$J_{2MASS} = J_{IRSF} + 0.1175 \times (J - H)_{IRSF} - 4.2318 \tag{1.1}$$

$$H_{2MASS} = H_{IRSF} - 0.0761 \times (H - K)_{IRSF} - 4.0974 \tag{1.2}$$

$$K_{2MASS} = K_{IRSF} + 0.024 \times (H - K)_{IRSF} - 5.0834 \tag{1.3}$$

Equations 1.1, 1.2, and 1.3 would work fine if one were to transform the respective magnitudes on that specific colour-magnitude diagram, for example equation 1.1 would be used for a $J/(J - H)$ diagram, but not for the purpose of a colour-colour diagram as shown in Figure 1.1. The reason for this is there would be extra colour-terms in the transformation equations, creating a bias and giving incorrect results.

From equations (1.1), (1.2), and (1.3) follows that:

$$\begin{aligned}(J-H)_{2MASS} &= (J_{IRSF} + 0.1175 \times (J-H)_{IRSF} - 4.2318) \\ &\quad - (H_{IRSF} - 0.0761 \times (H-K)_{IRSF} - 4.0974) \\ (J-H)_{2MASS} &= (J-H)_{IRSF} + 0.1175 \times (J-H)_{IRSF} + 0.0761 \times (H-K)_{IRSF} - 0.1344 \\ \Rightarrow (J-H)_{2MASS} &= 1.1175(J-H)_{IRSF} + 0.0761(H-K)_{IRSF} - 0.1344\end{aligned}$$

And:

$$\begin{aligned}(H-K)_{2MASS} &= (H_{IRSF} - 0.0761 \times (H-K)_{IRSF} - 4.0974) \\ &\quad - (K_{IRSF} + 0.024 \times (H-K)_{IRSF} - 5.0834) \\ (H-K)_{2MASS} &= (H_{IRSF} - K_{IRSF}) - 0.1001 \times (H-K)_{IRSF} + 0.9860 \\ \Rightarrow (H-K)_{2MASS} &= 0.8999(H-K)_{IRSF} + 0.9860\end{aligned}$$

The extra $(H-K)_{IRSF}$ term in the $(J-H)_{2MASS}$ equation affects where the stars lie in Figure 1.1. Equations (1.1), (1.2) and (1.3) were also used in such a manner that a magnitude with a colour correcting term is needed to calculate a colour transformation. It would have been much simpler if a direct colour transformation were rather used, something in the form of $(H-K)_{2MASS} = c1 \times (H-K)_{IRSF} + c2$. This also makes more sense, because this type of equation implicitly only transforms the qualities that one wants to measure, a colour transformation is done by using the colour only. The error implies that one can not accept the measurements and results from Figure 1.1.

This thesis will take a new approach to a multi-wavelength study on RCW 34, and also NGC 2626 (which is not well documented in the literature). The unanswered questions in star-formation theory have been outlined in section 1.1, and an attempt will be made to address some of them by finding results that address the following questions:

- Would a new deep *NIR* and optical study on RCW 34 deliver such a low turn-up of T Tauris as the optical study by Czanik (2013)?

- How would a deep *NIR* $(J-H)/(H-K_s)$ colour-colour diagram of RCW 34 look, if the colour transformations were done correctly?

- How many cluster members in RCW 34 or NGC 2626 show Hα-emission lines? Does any of them have the characteristic Li-absorption line that is seen in young CTTs?

- What would the visual extinction towards embedded cluster members that show excess emission be? Can extinction maps of each region be constructed?

- How do RCW 34 and NGC 2626 compare to each other as high-mass star-forming regions that are in different parts of the Milky Way? Is there a structural relationship between the high-mass and low-mass stars? Is there an apparent hierarchical structure in the cluster and are there commonalities in their properties?

- What is the full extent of the cluster in RCW 34 when analysed on a larger scale, for example on a field that is 16×16 arcmin^2, instead of the smaller 7.7×7.7 arcmin^2 field, that was studied in the previous project? The two-point correlation function from de Villiers (2009) did not show to where the cluster extends, thus it may be larger than the field studied in the previous study.

- What is the metallicity, age, accretion rate, and current evolutionary stage for some cluster members? By knowing these properties for individual cluster members can these parameters tell us something about each cluster?

- Is it possible to determine what the evolutionary relationship between the low- and high-mass stars for each cluster is?

1.2.2 Background on the environments around RCW 34 and NGC 2626

1.2.2.1 *RCW 34*

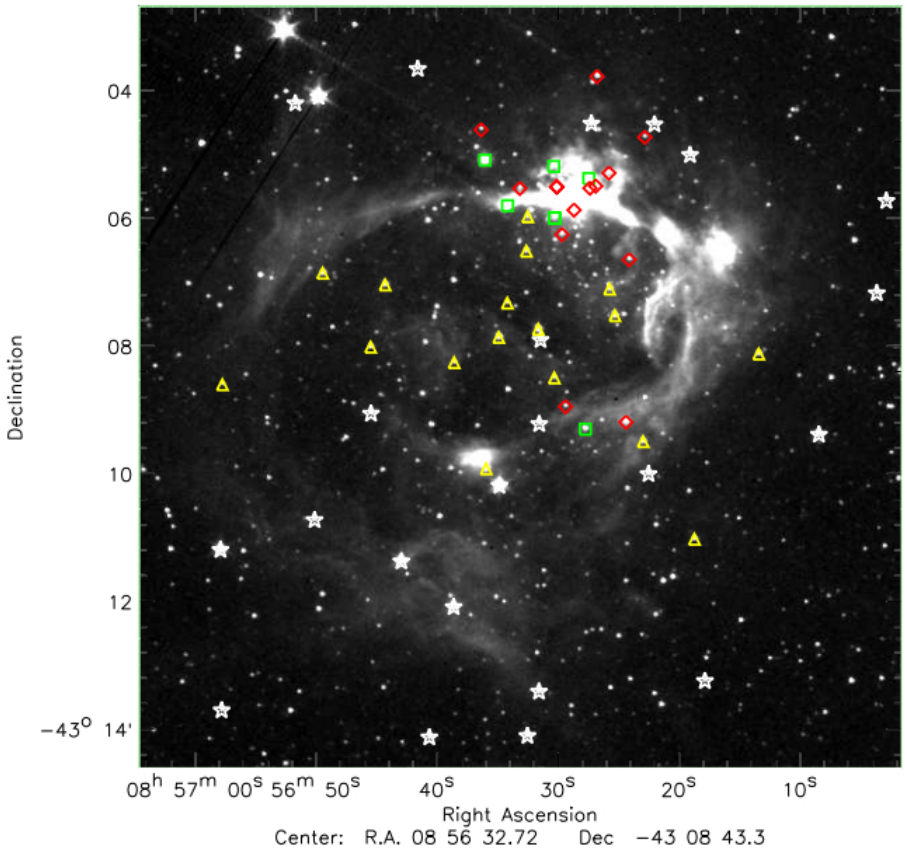

Figure 1.3: A 3.6 μm *Spitzer* image from the paper by Bik *et al* (2010) that shows excited gas on the outer-rim of the bubble region and the positions of some field stars and cluster members. The triangles are stars with excess infrared emission; the white stars are regular field stars, the diamonds are the positions of protostars (class 0/I infrared sources), and the squares are the positions of stars with an accretion disk (class II infrared sources). The HII region is the northern part of the excited gas.

RCW 34 (RA=08:56:28.1, DEC=-43:05:58, J2000) is a high-mass star-forming region at a distance of 2.5 kpc (see Bik *et al* 2010) away from the Sun. It is visible in the optical and has an associated methanol maser suggesting that there is very young high-mass star formation in the associated molecular cloud. The maser is located past the ionization front, just north of region III in Figure 1.4. At the centre of the HII region is an O8.5V star, VdBH 25a, which has a neighbouring B0.5-1V and B2-3V star. All 3 are the exciting stars for the HII region, according to Bik *et al* (2010), see region II in Figure 1.4. The ionized gas of the HII region forms part of a bubble region, which includes various low- and intermediate-mass stars with an excess emission characteristic to class II *NIR* PMS stars. The HII region is shown in a 3.6 μm Spitzer image from Bik *et al* (2010) in Figure 1.3. The bubble region spans an angular distance of $10'$ in the eastern-western direction and $7.5'$ in the northern-southern direction. The presence of the maser and the main sequence exciting stars in the HII region show that there are stars that formed at two epochs of star formation in RCW 34. The low-mass pre-main sequence stars that were catalogued by Bik *et al* (2010) may have formed during another star-forming epoch, it is not exactly clear when they formed and requires further investigation.

The exciting star VdBH 25a was classified as an O star by Vittone *et al* (1987). A follow-up in-depth study on VdBH 25a and the ionised gas around this exciting star was performed by Heydari-Malayeri (1988). An extinction of $A_V = 4.2$ was derived for VdBH 25a, and the extinction similar to this mag-

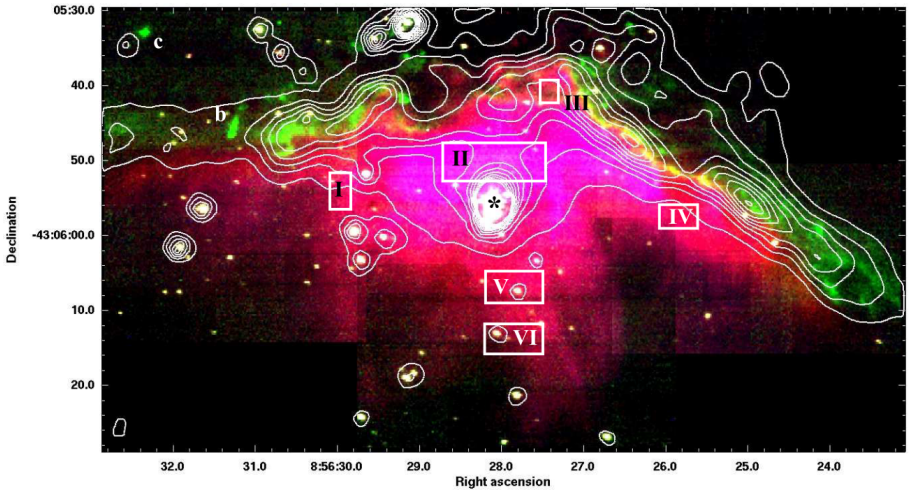

Figure 1.4: The HII region is shown as a colour-composite from the *SINFONI* data that was used by Bik *et al* (2010). The position of VdBH 25a (just below II) is shown with an star symbol and the contours are different fluxes from the 3.6 μm image. The separation of the bubble region (south of V), the HII region (All of the regions I-V) and the molecular cloud (north of III) to the north of the HII region can be clearly seen here.

nitude was measured by Bik *et al* (2010) to the PMS stars in the bubble region. It was discovered that the excited gas that is ejected from the HII region into the bubble clearing is at very high velocities (Heydari-Malayeri (1988) measured it as $\sim$ 100 km.s^{-1}), similar to the cork that pops free from a champagne bottle. The two B stars that were discovered by Bik *et al* (2010) are not as close to the ionization front as VdBH 25a, but they contribute to a fraction of the ionisation of the HII gas.

There is a molecular cloud north of the ionisation front that was studied by Pagani *et al* (1993) using CO mapping of the region. The ionisation front is region III in Figure 1.4 and the CO cloud is shown — with the contours — in Figure 1.5. The molecular cloud at the north of the HII region extends even further north, with a hot, dense core next to the ionisation front bordering on the HII region, which hosts the activating source for the maser. Further away from the dense core the molecular cloud becomes more diffuse. The typical density of the molecular cloud is a few hundred particles per cubic centimetre, and a typical temperature is that of 30-60 K. Only the molecular cloud extending north away from the HII region was mapped — nothing else in the surrounding field.

The molecular cloud was recently observed with the *NANTEN2* and *ASTE* telescope by Hayashi *et al* (2017), where the possible triggering of star formation in the region is attributed to the collision of two molecular clouds. The observations with *NANTEN2* are shown in Figure 1.6. The total mass of the molecular clouds that formed this region is speculated by Hayashi *et al* (2017) to have been $\sim 2.7 \times 10^4$ M$_\odot$ with the remnant molecular cloud to have a total mass of $\sim 10^3$ M$_\odot$. The velocity profiles of the molecular cloud show that there are two clouds moving away from VdBH 25a, these clouds collided supersonically and the collision lasted 0.2 Myr. Hayashi *et al* (2017) speculates that during the intersection period between the two initial clouds, VdBH 25a formed. The collission may also have been the trigger for the formation of the young star that is responsible for the methanol maser, as well as the low-mass population in the bubble region.

The population of PMS stars in the bubble region that were discovered by Bik *et al* (2010) were classified using *NIR* spectroscopic observations with *SINFONI* in the H and K_s bands. The population is a mixture of PMS G- to K stars, while others are already on the main sequence. According to Bik *et al* (2010), the formation of the stars occurred in a southern to northern direction. Moreover, there are three regions in RCW 34, based on stellar ages, according to Bik *et al* (2010). This is the bubble clearing with a mix of PMS and main sequence stars, the HII region, and then the denser molecular

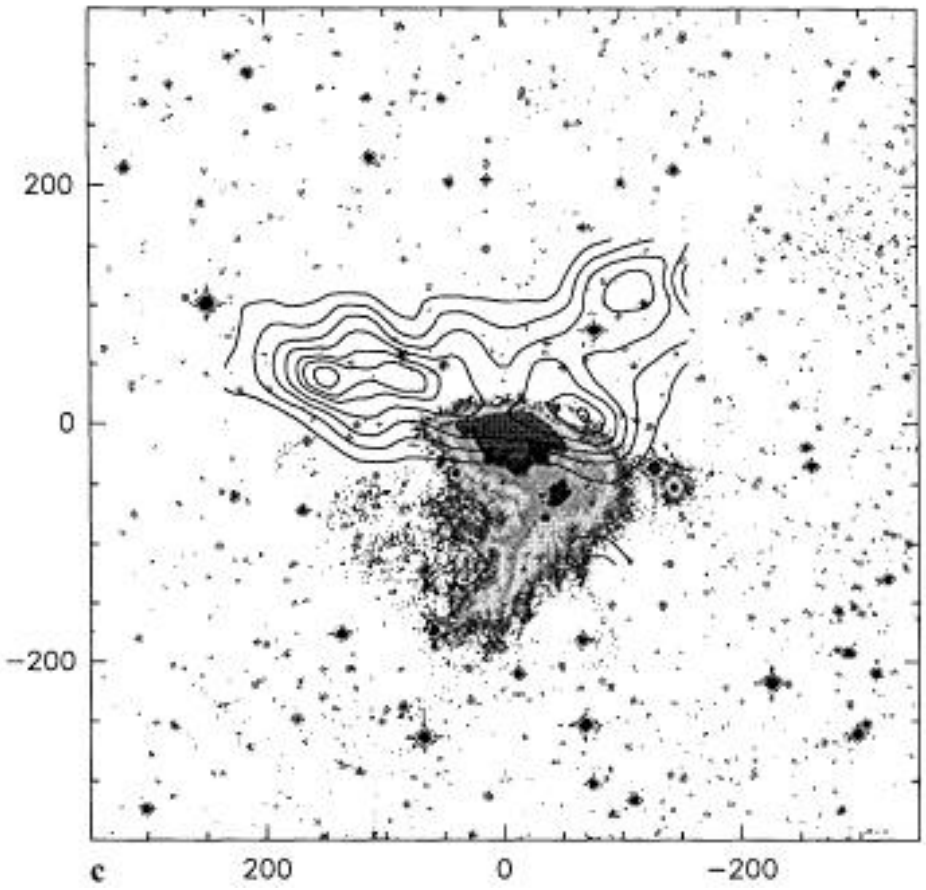

Figure 1.5: This is a CO(J:1-0) radio map of the molecular cloud to the north of the HII region taken from the paper of Pagani *et al* (1993). The rest of the molecular cloud was not imaged, but this image shows how far the molecular ridge — which contains class 0/I infrared sources — stretches to the north.

cloud to the north of the HII region that has some class 0/I *NIR* sources. If the high-mass VdBH 25a star formed over a collision period of 0.2 Myr, as suggested by Hayashi *et al* (2017), it is not known when the main sequence and PMS stars discovered by Bik *et al* (2010) formed. The methanol maser must be associated with a very young high-mass star that formed very recently; and it is located at a position of high extinction, according to the CO map in Figure 1.5.

The large number of *NIR* sources discovered by de Villiers (2009) across the field, and the group of PMS stars in the bubble region by Bik *et al* (2010) leave some questions unanswered: How many low-mass cluster members are associated with RCW 34, and how big is the cluster? Bik *et al* (2010)'s description of the three regions in RCW 34 sketches a clear picture of the star-formation history of the region, but the extent of the molecular clouds are not taken into account. The results from the study by Hayashi *et al* (2017) show how far the dense northern region continues, and the low-resolution extinction maps do not include all the possible low-mass members of the cluster. It is still not known how long star formation kept on occurring, and how far the triggered star formation — due to the interaction between the initial molecular clouds — continued. The question of how large the population of PMS stars are, how far the cluster extends and what may be the triggering mechanisms for the formation of the low-mass population in RCW 34, will be addressed in this thesis.

1.2.2.2 *NGC 2626*

The high-mass star-forming region NGC 2626 (RA=08:35:32, DEC=-40:40:18) is located in Vela and lies at a distance of 950 pc, according to van den Bergh & Herbst (1975) and 1.26 kpc according to

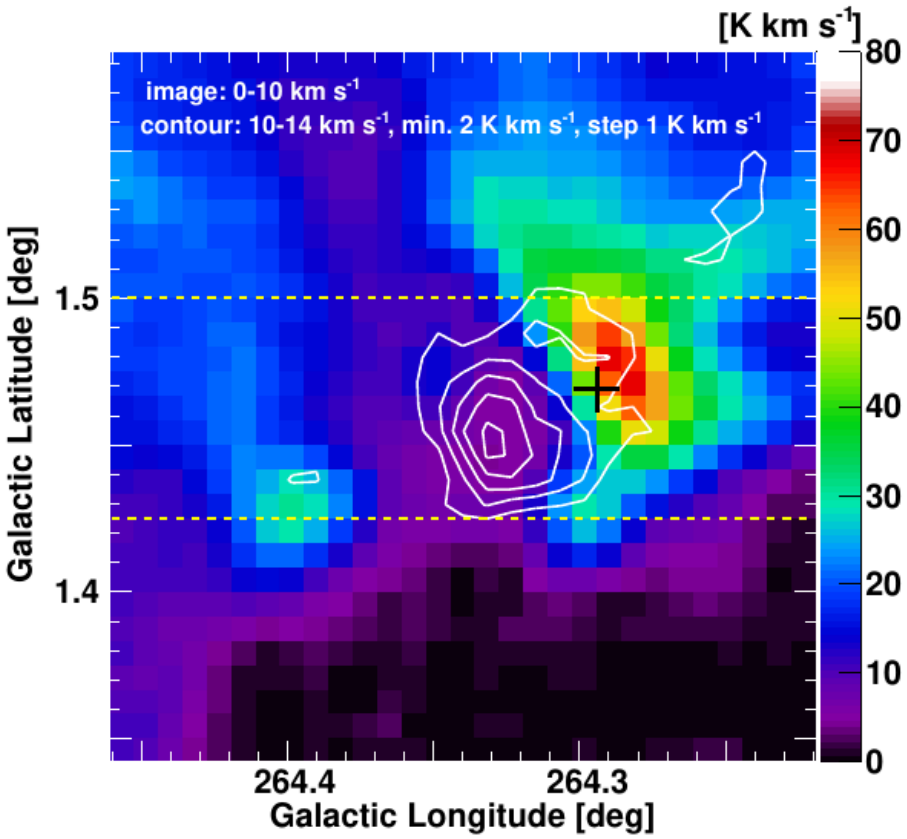

Figure 1.6: The *NANTEN2* observations that were used in the study by Hayashi *et al* (2017) are shown as a colour-composite of the CO(J:2-1) for velocity ranges from 0-14 km/s. The position of VdBH 25a is shown with a black cross, and excited gas that was detected in 8 μm *Spitzer* data is shown as the yellow contour.

Gahm & Malmort (1980). NGC 2626 presents at least two phases of star formation: (1) A 6.7-GHz methanol maser which is indicative of a very young high-mass star; (2) a collection of low-mass stars that have Hα-emission (see Mueller & Graham 2000), class II infrared sources that show excess emission characteristic of CTTs, and a few deeply embedded class 0/I infrared sources (see Sharma *et al* 2016) that are in a closely associated molecular cloud, SFO 54 (from the catalogue by De Vries *et al* 2002). Further salient features of NGC 2626 are that there is a Herbig-Haro object (HH-132) which is very close to the methanol maser. The driving star (IRAS 08337-4028) of the outflow of HH-132 has dispersed much of its embedding molecular cloud SFO 54. There are also two interesting objects that occupy the same field of view, (1) The B1V (VdHB 17a) exciting star with an associated reflection nebula RCW 27 (see Urquhart *et al* 2009) and (2) EM Velorum, F6III (a giant star) which presents strange variability (see Cieslinski *et al* 1997).

Mueller & Graham (2000) discovered 32 stars Hα-line emission in a field that spans $6' \times 6'$ and was centred on EM Velorum. Moreover, a follow-up study by Sharma *et al* (2016) discovered more PMS stars, where many were class II and class 0/I *NIR* sources were found in the molecular cloud to the north of HH-132. Sharma *et al* (2016) used *Spitzer* Mid-infrared (MIR) and *ISPI NIR* data to classify the extent of the cluster associated with NGC 2626, based on the angular distance between nearest neighbours, and profiled the molecular cloud. The position of class II and class 0/I sources are shown in the first image of Figure 1.8 as red and yellow points, respectively. The young class 0/I sources cluster closer together in the area of the molecular cloud, and the class II sources are distributed across the whole $10' \times 10'$ field that was studied. In the second image of Figure 1.8 the surface density of nearest neighbour distances are plotted together with an extinction map of the molecular cloud. Sharma *et al* (2016) classified EM Velorum as a class II infrared source.

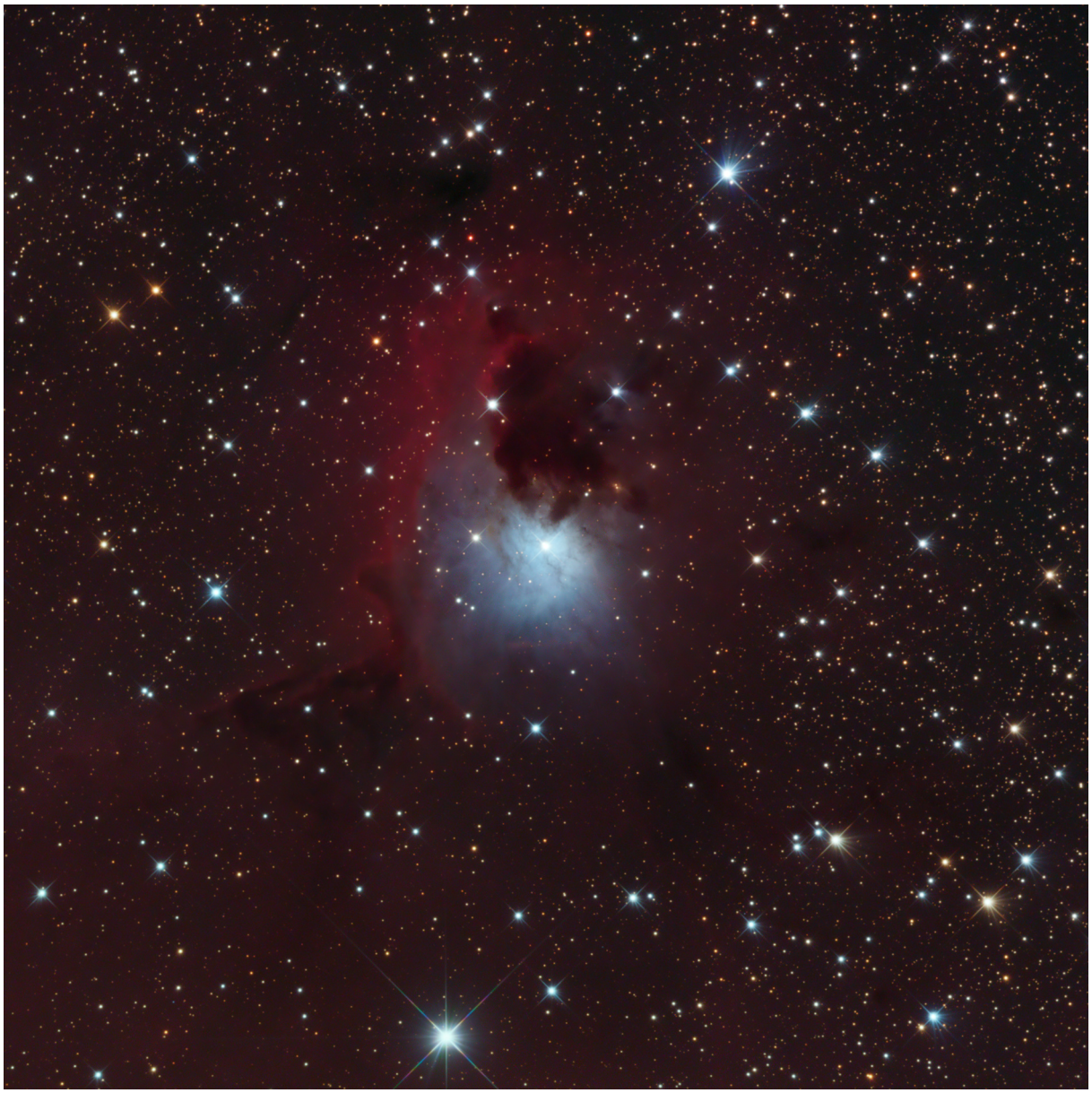

Figure 1.7: A colour image was taken by the *CEDIC* team (Bernhard Hubl, Christoph Kaltseis, Wolfgang Leitner, and Herbert Walter, Image processing by Bernhard Hubl) taken from Hacienda Los Andes on a TEC RC 20″ with a FLI PL16803 with Astrodon filters. The total exposure time is 4.5 hours consisting of L 27 × 6 min / R 6 × 6 min / G 6 × 6 min / B 6 × 6 min.

Pinheiro *et al* (2010) suggests that NGC 2626 and RCW 27 are part of the same system due to the similarities in the measured distances to the sources. However, for this study, they are considered to be two separate regions. The distance to NGC 2626, which was measured by Pinheiro *et al* (2010) of 950 pc, will be used.

1.2.3 Justification for this research project on RCW 34 and NGC 2626

1.2.3.1 *RCW 34*

From the work that was done by Vittone *et al* (1987), Heydari-Malayeri (1988), Bik *et al* (2010), van der Walt *et al* (2012), and Hayashi *et al* (2017) this project seeks to determine: (1) How many low-mass members are associated with RCW 34? (2) What a detailed extinction map of the RCW 34 environment looks like? (3) And how far does the cluster extend? The results from the paper by

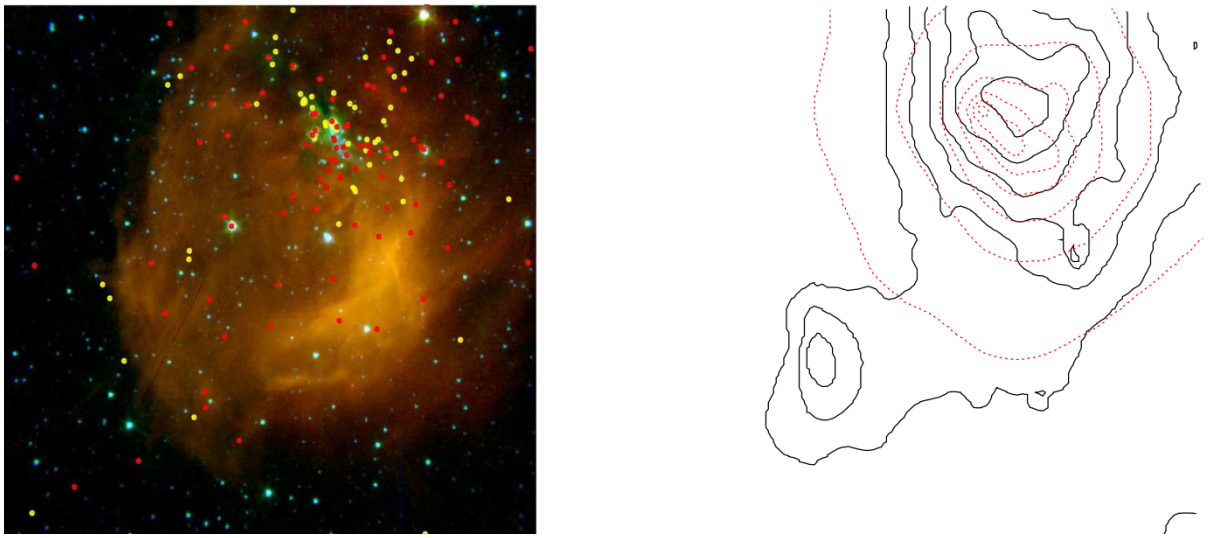

Figure 1.8: A colour-composite image of NGC 2626 and a CO-extinction map that was taken from Sharma *et al* (2016). The colour-composite image shows class 0/I *NIR* sources as yellow dots and class II objects as red dots.

van der Walt *et al* (2012) were supposed to address the question of how many cluster members there are that are associated with RCW 34 and how big the cluster is — using the incorrect transformation equations for the *2MASS* photometric system rendered incorrect results. There is no optical photometry or spectroscopy that has been published of low-mass members in the cluster of RCW 34 — this thesis seeks to fill this gap. Morevover, the contradictory statements by Hayashi *et al* (2017) and Bik *et al* (2010) about the rate and direction in which the formation of the low-mass stars formed in RCW 34 give reason for further investigation. This study will focus on ascertaining the properties of low-mass members that are associated with RCW 34 and determining the physical extent of the cluster. By knowing how many low-mass stars there are in the cluster and how far they are distributed, a basic understanding of its star-formation history can be constructed by knowing their ages. By knowing the star-formation history of RCW 34 it may be possible to derive the relationship between the low-mass and high-mass stars. It may even provide an answer as to what may have been the triggering mechanism for the formation of both the low-mass and high-mass stars.

1.2.3.2 *NGC 2626*

The study by Mueller & Graham (2000) only showed 32 stars with Hα-emission, which suggested that there is a young cluster associated with NGC 2626, but not how old or how big the cluster is. Sharma *et al* (2016) did a thorough investigation of the cluster members that are associated with NGC 2626, but the investigation formed part of a larger study on clusters associated with reflective nebulae. Due to this the individual low-mass members in NGC 2626 may not have received the required attention to accurately determine their spectral class, or at what evolutionary stage they may be. The extinction maps that are presented have low resolutions, when compared to the size of the region. The driving source of HH-132 and the cavity that it seems to carve in the molecular cloud, as well as its proximity to the maser, requires more investigation — specifically the way that the molecular cloud's structure is influenced by this source.

1.3 Thesis outline

With the scientific basis of this study justified, and a thorough background of the two star-forming regions given the outline for the remainder of this thesis is as follows:

Chapter 2: Theoretical and photometric fundamentals gives a thorough theoretical background of star-formation theory. It begins with an overview of the fundamental physics involved in

the collapse of a molecular cloud under its gravitational field to form stars. Following this there is an explanation of how dense cores form from dense filamentary structures, as well as how accretion disks form around protostars. The evolution of protostars to classical T Tauris is then discussed followed by an explanation of the main hydrogen burning sequence. Finally, different types of pre-main sequence stars and the difference between high-mass and low-mass star formation are explained. This theoretical background is followed by a short section on the fundamental photometric tools that are used to study young clusters. An *NIR* colour-colour and colour-magnitude diagram are used to explain how to identify young stars and determine how young stars evolve up to the main sequence.

Chapter 3: Near-infrared imaging and extinction maps is a large chapter that starts with a description of the photometric tools that were used to study all of the cluster members in both stars-forming regions. The effects of extinction on the measured quantities from the embedded members are explained. This is followed by the derivation of a custom extinction law for RCW 34 and NGC 2626. The custom extinction laws are then used with the reddened light of field stars behind each star-forming region to build an extinction map. Finally, the sources that presented excess emission in their *NIR* colours, which are characteristic to pre-main sequence stars, are analysed.

Chapter 4: Optical imaging is a chapter which starts by describing the different optical observations that were performed on the star-forming regions, and why *VPHAS+* survey provided the best suited data to analyse for the goals of this study. Next, the cluster members were tested for Hα-emission and where they lie relative to the cluster's centre. This was then compared to the stars that showed excess emission in their *NIR* colours from the previous chapter.

Chapter 5: Spectroscopy of the Hα-emission candidates was performed on the stars that were most likely pre-main sequence stars by their *NIR* and *SuperCOSMOS* colours. This is a crucial chapter, because spectral classification is performed on all of the candidates, determining if a star shows Hα-emission, and if it has a Li-absorption line — indicating an upper limit to a star's age independent of the photometry.

Chapter 6: Synthesis of the multi-wavelength data brings all the results of the previous three chapters together. The sources that showed excess *NIR*-emission, those that showed photometric Hα-emission, and the spectroscopic results are compared against each other. A common *NIR*, optical colour-colour, and colour-magnitude diagram is used for all of the different stellar groups, to test each group for excess emission against theoretical evolutionary models. From the optical colour-magnitude diagrams for both RCW 34 and NGC 2626 a mass and age distribution is constructed for each cluster.

Chapter 7: Final discussion, summary and conclusion delivers an answer to where the results shown in this study — and the conclusions that were made — fit into the larger picture of answering the questions that still exist in star-formation theory. Comments are given on the stellar populations of these two star-forming regions and recommendations for future work are given. Lastly a summary and conclusion is given for this research project.

CHAPTER 2: THEORETICAL AND PHOTOMETRIC FUNDAMENTALS

2.1 Physical concepts needed for star-formation theory

Star formation starts with the collapse of a molecular cloud or part thereof (more specifically a dense core) under its gravitational field. Inhomogeneous dense clumps then start to attract each other to form larger dense cores (see Chapter 2 of Bodenheimer2011 and Bisnovatyi-Kogan2011). The formation of dense cores occur in filamentary structures that are formed by magnetic fields and turbulent processes in the molecular clouds (see André *et al* 2014). The amount of material in the core that contributes to the gravitational field increases over time because surrounding matter is free falling into the core's gravitational field. Most of the infalling matter already has angular momentum contributed by the internal gas motion of the molecular cloud. When the material gets caught in the core's gravitational field it already has angular momentum due to the slow rotation of the molecular cloud. An accretion disk is formed around the dense core (see Hayashi & Matsuda 2001), due to the amount of material that has gained angular momentum in this manner. When the density of the core has reached a mass of 0.05 $M_\odot$ hydrogen burning can occur and the protostar delivers energy output as radiation (see Hayashi 1961). The accumulation of more matter will cause an increase of radiation that is emitted, so that an energy balance is established between the expansive radiation pressure, and the contractive gravitational force. Once a star has reached the equilibrium point it reaches the main sequence and becomes stable (see Collins 2003). To better understand the physics involved in the formation of stars a theoretical basis needs to be given. The first step in this process is the collapse of a molecular cloud under its own gravitational field, a fundamental description of the physics involved is given below.

2.1.1 Gravitational potential energy

Ellsworth-Bowers *et al* (2015) gives the typical mass, density, and size of a molecular cloud as $m = 10^4$ $M_\odot$, $n = 10^3$ cm^{-3}, and 10 pc, respectively. Any structure that has such a large mass and physical size will collapse under its own gravitational field. For any two particles with masses M and m which are a distance r apart, the gravitational potential energy is:

$$U = -G\frac{M\ m}{r} \tag{2.1}$$

To calculate the gravitational potential energy, U of an ideal spherical core, one needs to calculate the gravitational potential energy of each particle of the cloud. The potential energy of particle i with a mass, m_i at a radial distance, r_i from the centre of mass of a dense core with a mass M_c is:

$$\mathrm{d}U_i = -G\frac{M_c\ m_i}{r_i} \tag{2.2}$$

Suppose that the ideal spherical core in Figure 2.1 has a uniform density, ρ, and is composed of an ensemble of particles, each with a mass m_i. A shell of these particles at a radius, r from the centre has a thickness of dr and a total mass of $m = \sum_i m_i$. The total volume of the shell is $4\pi r^2\mathrm{d}r$ and the total mass is:

$$m = 4\pi r^2 \rho\ \mathrm{d}r = \sum_i m_i \tag{2.3}$$

Replacing this mass into the equation for the differential potential energy gives the total potential energy of the particles in the shell as:

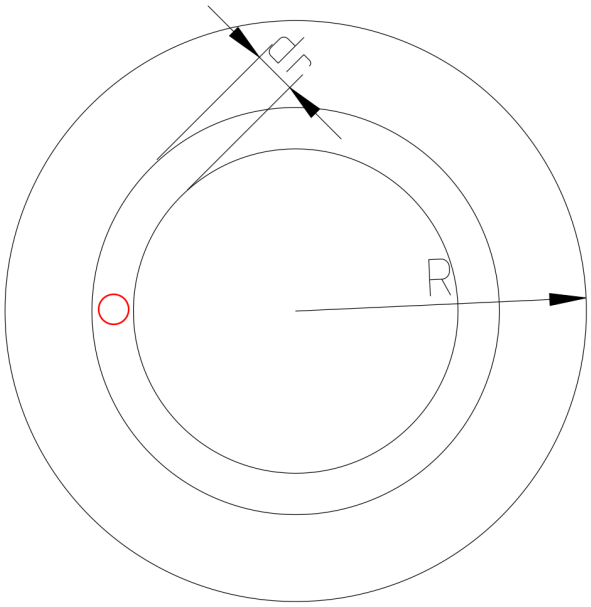

Figure 2.1: A graphical illustration for an ideal spherical molecular cloud with a radius R, composed of differential slices, each with a thickness dr. The red circle is a single particle with a mass m_i.

$$\mathrm{d}U = -G\frac{M_c \pi r^2 \rho}{r}\ \mathrm{d}r \tag{2.4}$$

The total potential energy of the spherical core is then the integral over all of the differential shells in the core, or:

$$U = -4\pi G \int_0^R M_c\ \rho r\ \mathrm{d}r \tag{2.5}$$

To calculate the total value of the potential energy U, the density ρ and molecular cloud mass M_c are required and both are dependent on the radius r. The potential energy can be approximated by assuming that ρ is constant and equal to an average ρ_{avg}, implying:

$$\rho_{\text{avg}} = \frac{M_c}{\frac{4}{3}\pi R^3} \tag{2.6}$$

$$M_c \sim \frac{4}{3}\pi r^3 \rho_{\text{avg}} \tag{2.7}$$

Substituting the core mass into the total potential energy, it can be integrated as:

$$\begin{aligned} U &\sim -4\pi G \int_0^R \left(\frac{4}{3}\pi r^3 \rho_{\text{avg}}\right) \rho r\ \mathrm{d}r \\ &\sim -\frac{16\pi^2}{3} G \rho_{\text{avg}}^2 \int_0^R r^4\ \mathrm{d}r \\ &\sim -\frac{16\pi^2}{15} G \rho_{\text{avg}}^2 R^5 \end{aligned}$$

Substituting the mass of the core M_c back into the total potential energy gives:

$$U \sim -\frac{3}{5}\frac{GM^2}{R} \tag{2.8}$$

Which is the potential energy of a symmetric spherical core, which is the analogue to a prestellar core.

2.1.2 Virial theorem

The gas in a molecular cloud is stable enough that it is considered to be in hydrostatic equilibrium. The virial theorem can be used to describe the energy balance between the gravitational force of all the individual particles, and the thermal kinetic energy of the particles making up the molecular cloud. To use the virial theorem for a molecular cloud, one has to take all of the forces that have an influence on the dynamics of the cloud into account. Stahler & Palla (2005) gives a general expression for hydrostatic equilibrium in a molecular cloud, which also includes the general magnetic field. For a molecular cloud that is moving with a general velocity $\mathbf{u}$, that has an internal pressure P, and gas density of ρ, the gravitational potential energy relative to the rest of the galaxy is measured with Φ_g. An expression for the random internal motions of the gas inside of the molecular cloud is c_{motion}. If the current density of the molecular cloud is $\mathbf{j}$, and it generates a magnetic field per unit volume $\mathbf{B}$ that acts in all directions, then the general hydrostatic equation of the molecular cloud is:

$$\rho \frac{D\mathbf{u}}{Dt} = -\nabla P - \rho \nabla \Phi_g + \frac{1}{c_{\text{motion}}} \mathbf{j} \times \mathbf{B} \tag{2.9}$$

with $\frac{D\mathbf{u}}{Dt}$ the convective time derivation of the fluid velocity. The magnetic field $\mathbf{B}$ and current density $\mathbf{j}$ can be related with Amperé's law, so that the hydrostatic equalibrium can be rewritten as:

$$\rho \frac{D\mathbf{u}}{Dt} = -\nabla P - \rho \nabla \Phi_g + \frac{1}{4\pi} (\nabla \cdot \mathbf{B}) - \frac{1}{8\pi} \nabla |\mathbf{B}|^{\mathbf{2}} \tag{2.10}$$

The third term on the right in the expression represents the tension associated with the curved magnetic field lines. The last term is the gradient of scalar magnitude pressure, $\frac{|B|^2}{8\pi}$; it is analogue to the thermal pressure, but it is not always isotropic. Stahler & Palla (2005) expresses the relation for hydrostatic equilibrium across the entire molecular cloud by taking the scalar product with the vector $\mathbf{r}$, and integrating over the volume. The equation for mass continuity and Poisson's equation are imported in terms of the density ρ. The order of differentiation was interchanged, and consecutive integration was done a few times so that the virial theorem is given by Stahler & Palla (2005) as:

$$\frac{1}{2} \frac{\delta^2 I}{\delta t^2} = 2K + 2E_{\text{th}} + U + E_B \tag{2.11}$$

Here I is the moment of inertia, K the total kinetic energy of the molecular cloud, E_{th} the random thermal motion of the particles inside the cloud, U the gravitational potential energy, and E_B is the potential energy associated with the magnetic field. Stahler & Palla (2005) expresses the energy terms as integrals, and K, E_{th}, and E_B are positive integrals, with the integral for U being negative. If the total kinetic energy, the thermal energy of the particles, or the energy associated with the magnetic field can not match the gravitational energy U, then the molecular cloud would collapse under its gravitational field. Before star formation occurs in the cloud, the forces cancel each other out and the system is in virial equilibrium, or mathematically:

$$2K + 2_{\text{th}} + U + E_B = 0 \tag{2.12}$$

Tayler (1994) gives a much simpler version of the virial theorem, where only the thermal motion of the particles inside the molecular cloud, as well as the gravitational potential energy of the molecular cloud, is taken into account. The virial theorem then states that:

$$2E_{\text{th}} + U = 0 \tag{2.13}$$

which suggests that if the internal thermal energy is larger than the gravitational potential energy, a molecular cloud would expand and loose energy adiabatically. Also, if the gravitational potential energy were dominant the molecular cloud would collapse in on itself.

This expression can be applied to a molecular cloud with a mass M and a radius r, so that the virial velocity v_{vir} and the virial mass M_{vir} can be calculated. The gravitational potential energy can be substituted with $U = -\frac{GM^2}{r}$, and the thermal kinetic energy of the particles with $E_{\text{th}} = \frac{1}{2} M v_{\text{vir}}^2$. The expression for the virial theorem is then:

$$2\left(\frac{1}{2}Mv_{\rm vir}^2\right) - \frac{GM^2}{r_0}$$
$$\rightarrow mv_{\rm vir}^2 = \frac{GM^2}{r}$$
$$\rightarrow v_{\rm vir} = \sqrt{\frac{GM}{r}}$$

The virial velocity is the minimum velocity with which the random thermal motions of the particles inside the cloud should move for the cloud to be in virial equilibrium. The escape velocity for any symmetric spherical object is:

$$v_{\rm esc} = \left(\frac{2GM}{r}\right)^{\frac{1}{2}} \tag{2.14}$$

The velocity of the thermal motion of particles inside a molecular cloud that is in virial equilibrium is smaller than the escape velocity of the cloud. This means that a molecular cloud can be hydrostatically stable so that no matter escapes and it does not collapse in on itself. The virial mass can be calculated from the virial velocity as:

$$M_{\rm vir} = \frac{v^2 r}{G} \tag{2.15}$$

If a molecular cloud has a mass higher than the virial mass it will collapse on itself, and if it has a mass smaller than the virial mass, it dissolves due to the thermal motion of the particles in the cloud.

2.1.3 Jeans criteria and mass

2.1.3.1 *Jeans mass*

The equation for virial mass gives the mass which a molecular cloud needs to have to remain in equilibrium between thermal expansion and gravitational collapse. However, stars form from the collapse of a molecular cloud under its own gravitational field. To test whether a molecular cloud will collapse under its gravitational field Sir James Jeans considered the theoretical construct shown below. The gravitational potential energy can be expressed as:

$$U \sim -\frac{3}{5}\frac{GM_c^2}{R_c} \tag{2.16}$$

where M_c is the mass and R_c the radius of the cloud. The typical temperature for a molecular cloud is so low that the gas can be considered to act as a monatomic gas with three degrees of freedom. The cloud's internal kinetic energy due to the random motion of the gas particles can be estimated as:

$$E_{\rm th} = \frac{3}{2}NkT \tag{2.17}$$

Here N is the total number of particles, which can be rewritten in terms of the mass of the cloud M_c, the mean molecular weight μ, and the mass of one hydrogen atom m_H. By substituting these expressions into the condition for the collapse of the molecular cloud one has:

$$\frac{3M_c kT}{\mu m_H} < \frac{3}{5}\frac{GM_c^2}{r} \tag{2.18}$$

The initial density of the cloud ρ_0, is constant throughout the cloud so the radius can be substituted in terms of the mass and density:

$$R_c = \left(\frac{3M_c}{4\pi\rho_0}\right)^{\frac{1}{3}} \tag{2.19}$$

If the radius is substituted into the condition for spontaneous collapse, then the mass required for the collapse is calculated as:

$$\frac{3M_c kT}{\mu m_H} < \frac{3}{5} G M_c^2 \left(\frac{4\pi\rho_0}{3M_c}\right)^{\frac{1}{3}}$$
$$\rightarrow M_c > \left(\frac{5kT}{G\mu m_H}\right)^{\frac{3}{2}} \left(\frac{3}{4\pi\rho_0}\right)^{\frac{1}{2}}$$

M_c should be larger than the Jeans mass, M_J or symbolically:

$$\left(\frac{5kT}{G\mu m_H}\right)^{\frac{3}{2}} \left(\frac{3}{4\pi\rho_0}\right)^{\frac{1}{2}} \sim M_J$$
$$\rightarrow M_c > M_J$$

This criterion is known as the Jeans criterion which states that if a molecular cloud has a mass greater than the Jeans mass, it will spontaneously collapse in on itself. The only parameter that plays a role in the condition for the Jeans mass is the temperature of the gas T, which is the only determining factor to the internal kinetic energy of the particles in the molecular cloud.

The Jeans criteria can also be rewritten in terms of a critical density, so that if a molecular cloud has a density above a critical density — or the Jeans density — it will also collapse in on itself:

$$\rho_J \simeq \frac{3}{4\pi M_c^2} \left(\frac{5kT}{G\mu m_H}\right)^3 \tag{2.20}$$

Just like the Jeans criterion is expressed in terms of a molecular cloud's mass it can be expressed in terms of the radius of the molecular cloud, or what physical size a molecular cloud should be to spontaneously collapse on itself. The Jeans criteria can be rewritten in terms of the radius, or:

$$\frac{3M_c kT}{\mu m_H} < \frac{3}{5}\frac{G}{R_c}\left(\frac{4\pi\rho_0 R_c^3}{3}\right)$$
$$\rightarrow R_c > \left(\frac{15kT}{4\pi G\mu m_H \rho_0}\right)^{\frac{1}{2}}$$
$$\rightarrow R_c > R_J$$

where

$$R_J \sim \left(\frac{15kT}{4\pi G\mu m_H \rho_0}\right)^{\frac{1}{2}} \tag{2.21}$$

which is called the Jeans length.

The properties of a typical molecular cloud were given at the beginning of this section from Ellsworth-Bowers *et al* (2015) as a mass, density, and size of $m = 10^4$ $M_\odot$, $n = 10^3$ cm^{-3}, and 10 pc. These properties are used in the equations for the Jeans mass, Jeans density and Jeans radius. In each calculation of the Jeans criteria a typical temperature for the gas in a molecular cloud is given as 10 K by Stahler & Palla (2005). The Jeans mass, Jeans radius, and Jeans density respectively are:

$$M_J \sim \left(\frac{5kT}{G\mu m_H}\right)^{\frac{3}{2}} \left(\frac{3}{4\pi\rho_0}\right)^{\frac{1}{2}} = 198.84\ M_\odot$$
$$R_J \sim \left(\frac{15kT}{4\pi G\mu m_H \rho_0}\right)^{\frac{1}{2}} = \left(\frac{15k10\ \mathrm{K}}{4\pi G\mu m_H 10^3.\mathrm{cm}^{-3}}\right)^{\frac{1}{2}} = 0.08\ \mathrm{pc}$$

The Jeans mass is an ideal case where there is no external pressure on a molecular cloud. In reality, there is always the gas of the ISM outside of a molecular cloud that exerts some pressure on the

molecular cloud. If the pressure of the ISM is P_0, then the minimum mass that is required for a molecular cloud to collapse is given by the Bonner-Ebert mass, as:

$$M_{BE} = \frac{c_{BE} v_T^4}{P_0^{1/2} G^{3/2}} \tag{2.22}$$

with the isothermal sound speed as:

$$v_T \sim \sqrt{kT/\mu m_H} \tag{2.23}$$

and the dimensionless constant c_{BE} with a value:

$$c_{BE} \sim 1.18 \tag{2.24}$$

taken from Carroll & Ostlie (2006).

2.1.3.2 *The free-fall time*

A way to estimate the maximum lifespan of a molecular cloud is to estimate the free-fall time for particles from the outer edge of the cloud towards the middle of the cloud. The movement of the particles will only be influenced by the pull of the gravitational field from the middle of the molecular cloud. If the energy of the other terms in the condition of the virial theorem is smaller than the gravitational potential energy, then the free-fall time can give an estimate for the lower limit of a molecular cloud's age.

The derivation of the free-fall time is taken from Carroll & Ostlie (2006). For this derivation, suppose an ideal spherical symmetric cloud which has no outward pressure gradient that opposes the inward acceleration from gravitational collapse is negligible. If the outer edge of the sphere starts from rest to collapse inward at a radial distance of r_0, then its gravitational potential energy is converted to kinetic energy. Due to the conversion of gravitational potential energy to kinetic energy, the change in energy will be the difference between the potential energies:

$$\frac{1}{2} M v^2 = \frac{GM^2}{r} - \frac{GM^2}{r_0} \tag{2.25}$$

This expression can be rewritten so that the velocity changes to a positive value $v = \frac{\mathrm{d}r}{\mathrm{d}t} = \sqrt{\frac{2GM}{r} - \frac{2GM}{r_0}}$. This expression can be integrated to give a value for the free-fall time:

$$t_{ff} = \int_{r_0}^{0} \frac{\mathrm{d}t}{\mathrm{d}r}\, \mathrm{d}r = -\int_{r_0}^{0} \left[\frac{2GM}{r} - \frac{2GM}{r_0}\right]^{-1/2} \mathrm{d}r \tag{2.26}$$

With the substitution of r/r_0 with θ to simplify the integral and factorising all the constants, the integral comes down to a value of $\pi/2$, which leads to a general expression for the free-fall time:

$$t_{ff} = \left[\frac{3\pi}{32 G\rho}\right]^{1/2} \tag{2.27}$$

The free-fall time is the period that an unperturbed homogeneous sphere will take to collapse towards a specific point. This would be the upper limit for the lifetime of a molecular cloud.

The free-fall time for the average molecular cloud, which has a density of $\sim 10^3$ cm^{-3} is then:

$$t_{ff} = \left[\frac{3\pi}{32 G\rho}\right]^{1/2} = \left[\frac{3\pi}{32\ G 10^3.\mathrm{cm}^{-3}}\right]^{1/2} = 2101346 \text{ seconds} \sim 24 \text{ days}$$

2.1.3.3 *Fragmentation of molecular clouds*

These derivations are for the ideal case of a spherically symmetrical molecular cloud. In reality, there are no instances where a molecular cloud undergoes a symmetrical collapse into a star. There are many external influences and internal forces which cause a molecular cloud to fragment. The fragmentation of the molecular cloud leads to a cascading effect from which the cluster eventually forms. The best way to understand a real scenario for the collapse of a molecular cloud is by using a model such as the one developed by Field *et al* (2006), which shows the fragmentation of a molecular cloud — specifically how supersonic turbulent motions are driven by gravitational instabilities.

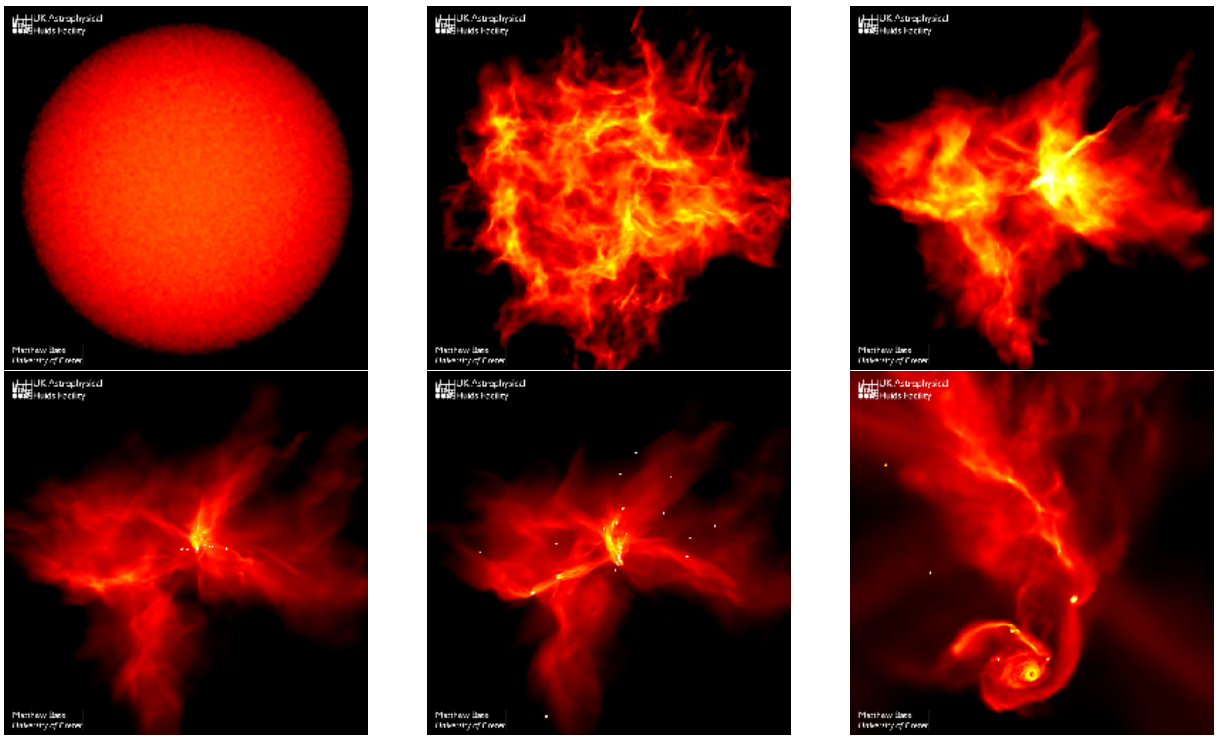

Figure 2.2: Illustration of a numerical model for the collapse of a molecular cloud under the influence of internal turbulent forces taken from numerical models from Mathew Bate. Starting as a spherical symmetric shape in the top left panel, the symmetry becomes distorted in the second panel due to self-gravitation and turbulence. Young star-and-disk systems start to form from the dense filament. In the lower right panel the last instance of the model is shown where a few low-mass systems are ejected from the molecular cloud.

Figure 2.2 show six different stages of a numerical model for the formation of a cluster out of a spherical symmetric molecular cloud. The evolutionary sequence starts from the top left panel and shows different stages up to the last panel at the bottom right. The first two panels shows the collapse of the symmetrical shape of the molecular cloud due to in the influence of internal turbulent forces. From the third to the fifth panel young star-and-disk systems form from the dense core, much of the formation is a product of shock waves from the turbulence. The last panel gives a closer look at the star-and-disk systems. There are various mass objects which range from brown dwarfs to low-mass stars. The particular differences between these objects are not important, however, they serve the purpose of showing the different products which form from a molecular cloud which collapses under the influence of self-gravitation and internal turbulence. Once the cluster has reached an age of more than 10 Myr most of the low-mass members would have evolved to where they start the main sequence hydrogen burning phase. At that evolutionary phase many cluster members would have broken loose from the initial cluster, to still be considered as part of the cluster any star should still be gravitationally bound to the rest. The distance at which a star falls outside of the gravitational potential well of the cluster is called the tidal radius, if a star moves outside of the tidal radius it is not considered as part of the cluster anymore.

2.1.4 Low-mass star formation

2.1.4.1 *The first dense cores*

Ward-Thompson & Whitworth (2011) states that the formation of low-mass stars starts with the formation of the first core which forms from the initial contraction and non-violent collapse of the molecular cloud. The cloud's internal magnetic support is eroded by ambipolar diffusion causing perturbations in the contraction of the molecular cloud. In regions with higher density, the magnetic flux leaks out quicker so that the density increases, causing an accelerated infall of surrounding material. This is a temporary state where a first dense core forms, and later leads up to the formation of a protostar. The theoretical description will not include rotation or magnetic support, because this simplified case will not differ much from what physically happens.

The large-scale equilibrium dynamics that were used previously to describe the collapse of a molecular cloud breaks down when the formation of a star is described. As the density of a central clump increases with time, it becomes opaque for the thermal infrared radiation being emitted by the young dense core. As a clump accretes more matter, the compression at the core continues, causing the internal pressure to rise. The increase of the clump's internal pressure causes a deceleration of infalling matter, and also causes the newly accumulated matter to settle slowly into the hydrostatic structure. For the gas to settle into the hydrostatic structure, some of its energy is lost in the form of infrared radiation. This process of settling gas continues over time until the clump has grown significantly larger. This recursive process of matter falling in on the core and increasing the internal pressure continues until the core stops expanding.

To determine what happens with the internal temperature of the gas falling into the newly forming core, the mean temperature can be calculated by using the virial theorem. Ward-Thompson & Whitworth (2011) gives the virial theorem in the form:

$$2K + 2E_{th} + U + E_B = 0 \tag{2.28}$$

where K is the total kinetic energy of all the gas, and E_{th} is the random thermal motion of particles. The gas of the molecular cloud behaves like a monatomic gas at these low temperatures. A monatomic gas has three degrees of freedom, meaning the total thermal kinetic energy of the molecular cloud can be calculated as $E_{th} = \frac{3}{2}Nk_BT = \frac{3}{2}P = \frac{3}{2}nRT$. The energy associated with the magnetic field and the total kinetic energy can be ignored, because the dense cores form in regions where the rotational and magnetic forces do not remain stable for long. The potential gravitational energy U is roughly equal to $\frac{-GM^2}{R}$, if the mass is M, and the radius is R. If the ideal gas law is applied as before the internal energy becomes:

$$E_{th} = \frac{3}{2}\int P \ \mathrm{d}^3x = \frac{3}{2}\frac{RT}{\mu}M \tag{2.29}$$

where the total number of moles is equal to n, and is substituted by M/μ, and μ is the volume-averaged molecular weight. The bulk kinetic energy of the molecular cloud and the magnetic energy can be ignored, therefore if the thermal and gravitational energy is substituted into the virial theorem. The temperature T is equal to:

$$T = \frac{\mu}{3R}\frac{GM}{R} = 850 \text{ K}\left(\frac{M}{5\times10^{-2}\ \mathrm{M}_\odot}\right)\left(\frac{R}{5\ \mathrm{AU}}\right)^{-1} \tag{2.30}$$

The temperature is much higher than the rest of the molecular cloud, and it has an average mass density of 10^{-10} g.cm^{-3}. This escalating process will cause the internal temperature to keep on rising and then eventually surpass 2000 K. The majority of the gas in the core consists of molecular hydrogen, H_2, which will start to undergo collisional dissociation, and the temperature will start to level off. The average interstellar hydrogen mass fraction is $X = 0.70$, giving an average thermal energy per molecule of $3k_BT/X = 0.74$ eV. This energy is much smaller than the 4.48 eV that is needed to dissociate a single hydrogen molecule. During this transition period, a small fraction of dissociated

hydrogen indicates that most of the compression work of gravity is absorbed in the dissociation process, without a significant increase in the temperature.

The increasing density in the core causes an outward expansion of the region that contains atomic hydrogen. The dissociation of molecular hydrogen takes up a significant amount of the internal energy resulting in a slow temperature rise. Thus, any compression that is caused by perturbations will cause a rise of internal pressure that results in the core becoming gravitationally unstable. This shows that the regions that contain atomic hydrogen can not remain stable for very long before the whole structure collapses and results in an end to the core.

2.1.4.2 *The main accretion phase and its luminosity*

With the repetition of the dissociative process of collapsing gas, the central region reaches a temperature high enough to ionise hydrogen. A protostar will not undergo any other internal transitions and will remain dynamically stable. Such young objects will have a radius a few times larger than $R_\odot$ and a mass of 0.1 $\mathrm{M}_\odot$ which would have an internal temperature of 10^5 K. This means the object can be considered stellar if it has a mass density in the order of 10^{-2} g.cm^{-3}.

The gas that keeps getting added is moving supersonic and has a free-fall velocity of $v_{ff} = (2G\mathrm{M}_*/r)^{1/2}$. The loss of kinetic energy from the free-falling gas due to thermal pressure from the core is relatively small in relation to the gravitational potential energy. The protostellar mass M_* is equal to $\dot{M}t$, if the star has a steady accretion rate of $\dot{M}$ over a time period t. The gravitational force decreases as a function of distance from the core, and with increasing distance towards the core, the expansive thermal force becomes dominant over the gravitational force. The transition of free-fall collapse occurs at a radius R_{ff}, where the velocity $v_{ff} = v_T$, or $G\dot{M}t/R_{ff} = v_T^2$, with v_T the isothermal sound speed. The condition can be rewritten to obtain an expression for the accretion rate as:

$$\dot{M} = \frac{v_T^2 \dot{R}_{ff}}{G} \tag{2.31}$$

The rise in the protostellar mass gradually increases the supersonic infall region, so that the cloud collapse proceeds in an inside-out manner. This is where the main accretion phase starts for the protostar.

The maximum radius from where matter could be accreted to a star which formed over a period t and has a mass of M_* is:

$$R_{\max} = \frac{G\mathrm{M}_*^2}{2\Delta E_{\mathrm{int}}} = 60 R_\odot \left(\frac{\mathrm{M}_*}{\mathrm{M}_\odot}\right) \tag{2.32}$$

This maximum radius $R_{\max}$ is larger than the true radii of solar-type protostars ($R_* << R_{\max}$). The direct result of this accretion is the youngest types of T Tauris, which are smaller by an order of magnitude. This shows that L_{rad} can not be ignored as stated earlier, but it has to be close to the accretion luminosity which is given by:

$$L_{\mathrm{acc}} = \frac{G\mathrm{M}_*\ \dot{M}}{R_*} = 61 L_\odot \left(\frac{\mathrm{M}_*}{1\ \mathrm{M}_\odot}\right)\left(\frac{\dot{M}}{10^{-5}\ \mathrm{M}_\odot yr^{-1}}\right)\left(\frac{R_*}{5R_\odot}\right)^{-1} \tag{2.33}$$

Here L_{acc} is the energy per unit time released by infalling gas which converts all of its infalling kinetic energy to radiation as it lands on the young star's surface. The radiation luminosity L_{rad} is very much equal to the accretion luminosity L_{acc} all the way throughout the accretion phase. This is true even if the gas interacts with an accretion disk before hitting the star's surface — under the assumption that the sum of the thermal and kinetic energy is relatively small when hitting the surface. This assumption requires the star not to rotate close to the speed where it will become structurally unstable. The assumption has been proven true with observations, according to Stahler & Palla (2005).

The radiation from accretion is mostly generated close to the young star's surface and is caused by accreting matter shocking onto the star's surface. Additional radiation is caused by nuclear fusion and quasi-static contractions of the star's interior. The contractions do not contribute significantly to the

accretion luminosity for low and intermediate mass stars ($M_* \leq 8\ M_\odot$). A protostar is a mass-gaining star, where most of the luminosity stems mainly from the external accretion of matter which escapes the parental cloud, and gradually degrades into the infrared as it travels outward. Infrared radiation can propagate through the immense column density of dust which embeds the young forming cloud. The dust absorbs most of the optical radiation, and these objects are only detectable at wavelengths longer than 1 μm. This implies that deeply embedded; young PMS stars have to be observed in the infrared or at longer wavelengths.

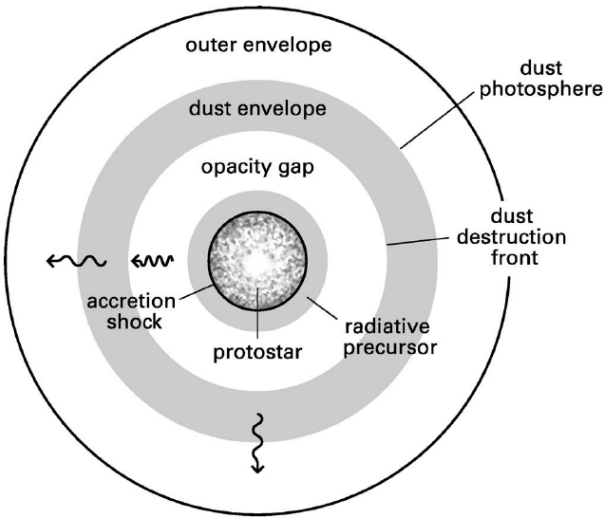

Figure 2.3: An illustration of a protostar which is accreting matter and where most of the radiation comes from the conversion of gravitational potential energy to radiation.

Figure 2.3 gives an illustration of how the radiation from the infalling matter diffuses outward. The accretion shock forms the outer layer of the star, all of the matter on the interior of the star is settling with a low velocity. The matter deep on the inside of the star is turbulent because of the nuclear fusion reactions at the core of the star.

2.1.4.3 *Dust envelope*

In Figure 2.3 the gas that falls on the star originates from the outer envelope. In the outer layer, the gas temperature rises gradually as a function of density, because of the efficient cooling produced by the dust in the gas. Most of the infalling matter is predominantly transparent to the protostellar radiation, but as time passes, the infalling gas continues to be more compressed, and the radiation eventually becomes trapped by the higher opacity from the dust grains. The effective extent of the radiation surface area for radiation from the protostar is detected as $R_{\rm phot}$ at wavelengths longer than 1 μm. The radiation radius is represented by the dust photosphere in Figure 2.3.

The dust envelope is a region which is opaque to the protostar's radiation and bounded by the radiation radius $R_{\rm phot}$. At the point where the temperatures in this region surpass 1500 K, the dust grains start to evaporate. The infalling gas collisionally dissociates at temperatures higher than 2000 K and lets most of the radiation through. This is known as the opacity gap. The radiative precursor which is even more on the inside of the star is where the collisional ionisation of the gas, and consequent rise in opacity takes place. This is located right outside of the accretion shock.

2.1.4.4 *Disk formation*

During the formation of a star, the above envelope falls towards the protostar, but it gets distorted by infalling trajectories. If the material has enough angular momentum, it lands first in an accretion disk and spirals towards the star's surface over due time. Figure 2.4 gives an illustration of a T Tauri star and its accompanying disk.

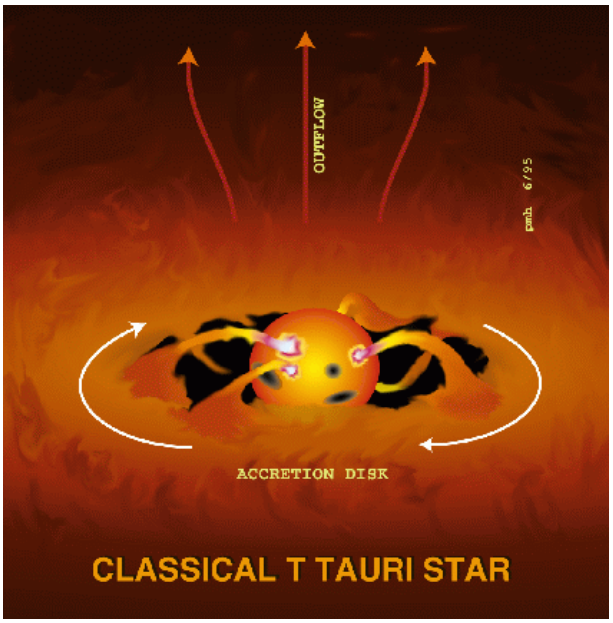

Figure 2.4: A graphic illustration of a young star and its accretion disk. Matter is accreted at a rate of $\sim 10^{-7}$ $M_{\odot}.yr^{-1}$ from the infalling envelope which collects matter at a rate of $\sim 10^{-5}$ $M_{\odot}.yr^{-1}$. Up to 10% of the accreted material is ejected from the system as high-velocity winds. Image taken from the University of Oregon's website.

The dynamics of the disk can be described with a classical model, but it is not really of interest for

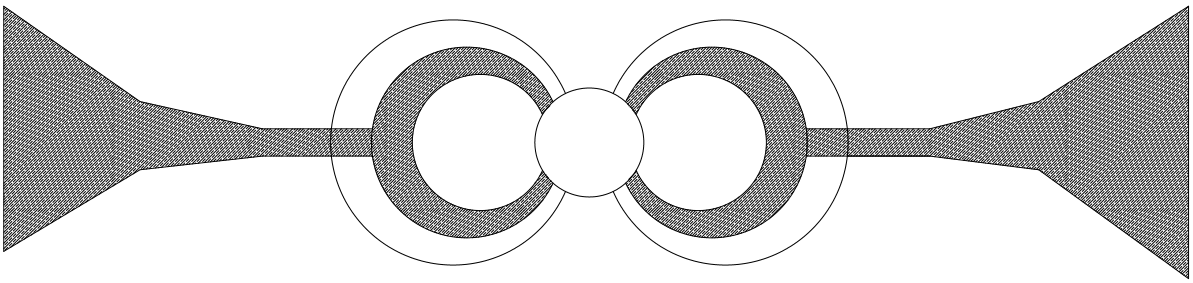

Figure 2.5: The accretion disk is dependent on the radial distance from the star. At distances far away from the star the disk fans out to a broader shape.

this thesis to give a full description of the model. Hartmann (1998) describes the disk as thin, close to the star, and fanning out from the disk shape the further one moves away from the star. This means that the shape of the disk has a dependence on the radial distance away from the star, as is shown in Figure 2.5. Close to the star the force of the magnetic field is stronger than the gravitational force pulling in the material, so material that has the correct angular momentum components are captured by magnetic fields and shocked onto the star's surface. If matter is not captured by the magnetic field, the infalling matter will overshoot the star and escape as an outflow, if it has high enough velocity.

2.1.5 The classification of pre-main sequence objects

The spectral energy distribution (SED) of young stars shows excess emission which originates from circumstellar material and not just from the core/protostar. If the emission is compared to the emission from a photosphere of a main sequence star, then the accretion disk contributes additional emission at wavelengths longer than 1 μm [$\log \lambda \sim 0$]. The amount of emission from heated dust in the accretion disk changes with time. As a pre-stellar core matures to a pre-main sequence star its emission at longer wavelengths decreases. The excess emission from a young star decreases as a function of time and is an indication of how young the star is.

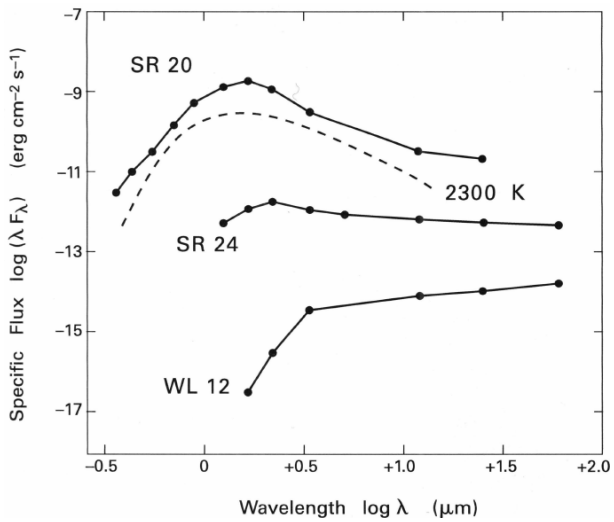

Figure 2.6: The SEDs for three different stars in the ρ Ophiuchi dark cloud complex. From the bottom to the top are class I, II and III infrared source, as well as the dashed line which represents the SED of a blackbody with a temperature of 2300 K.

According to Hartmann (1998) the temperature of heated dust at a distance of R in an accretion disk, around a star with a radius of R_*, and an effective surface temperature of $T_{\rm eff}$ is calculated with:

$$T_d^4(R) \sim \frac{T_{\rm eff}^4}{\pi}\left(\frac{R_*}{R}\right)^3 \tag{2.34}$$

To have strong emission at a wavelength of $\lambda \sim 3$ μm [$\log\lambda \sim 1.098$] the dust needs a temperature of $T_d \sim 1000$ K, which will be at a disk radius of $R_0 \sim 4$ R_* for a central star with a radius of $R = 2$ $R_\odot$, and an effective temperature of $T_{eff} \sim 4000$ K. For the dust in the accretion disk to have strong excess infrared emission at $\lambda = 3$ μm [$\log\lambda \sim 1.098$], the dust has to be optically thick. If a dust-to-gas ratio is taken — similar to the ISM — an optical depth of unity would require a column density of $\sum 0.2$ g.cm^{-2}. The amount of gas that is required to emit excess *NIR*-emission has a mass of $\sim 10^{-10}$ M$_\odot$, which is relatively small for an accretion disk. Figure 2.6 shows the three different classes of *NIR* sources with excess emission; the middle profile on the graph is the typical SED of a classical T Tauri. CTTs are usually K or M stars, for a K star which has a surface temperature of $T_* = 4000$ K the maximum flux for a blackbody at that temperature in $\lambda F_\lambda = 3670$ μm$/T$. At longer wavelengths, the emission profile of the disk — described with the Raleigh-Jeans form ($\lambda F_\lambda \propto \lambda^{-3}$) — decreases, causing the disk to become optically thin in the MIR wavelength range.

In Figure 2.6 the dereddened SEDs are shown from three different sources that were observed in an *NIR* survey of the embedded stars in the L1688 cloud of ρ Ophiuchi, performed by Stahler & Palla (2005). A very strong infrared excess can be seen in the spectrum of WL 12, where the logarithm of the flux is plotted as a product of λF$_\lambda$. The peak of the spectrum from a late-type star would be at 1 μm [$\log\lambda \sim 0$]. However, the flux from the spectrum that includes the accretion disk keeps on increasing up to 60 μm, and starts to fall somewhere past the end of the spectrum. The increasing flux from 1 μm to 60 μm [$\log\lambda$ from 0-4.09] comes from the accretion disk alone, and not from the star's SED. For SR 24 the flux has a shallow negative slope in the mid- and far-infrared regime, and for SR 20 there is strong fall from where the spectrum starts to resemble the profile of a blackbody. The extra infrared emission in the SEDs for WL 12 and WR 24 emanates from heated dust grains. This excess emission does not show the spectral profile typical to that of a blackbody spectrum with a high enough temperature, meaning that the dust must be close to the star. The dust grains are either present in the matter that is falling to the star, or have been left behind after the collapse has ended, as described in Lada (1998).

To distinguish between the different stages of the evolution of PMS stars, a classification system was defined by Andre & Montmerle (1994). In this system the classification starts at the earliest stages

where a pre-stellar core is still heavily embedded in the formation cloud. The following subsection will describe the different classes of infrared sources that show excess emission. Their classification is based on the infrared spectral index:

$$\alpha_{IR} = \frac{\mathrm{d}\log(\lambda F_\lambda)}{\mathrm{d}\log\lambda} \tag{2.35}$$

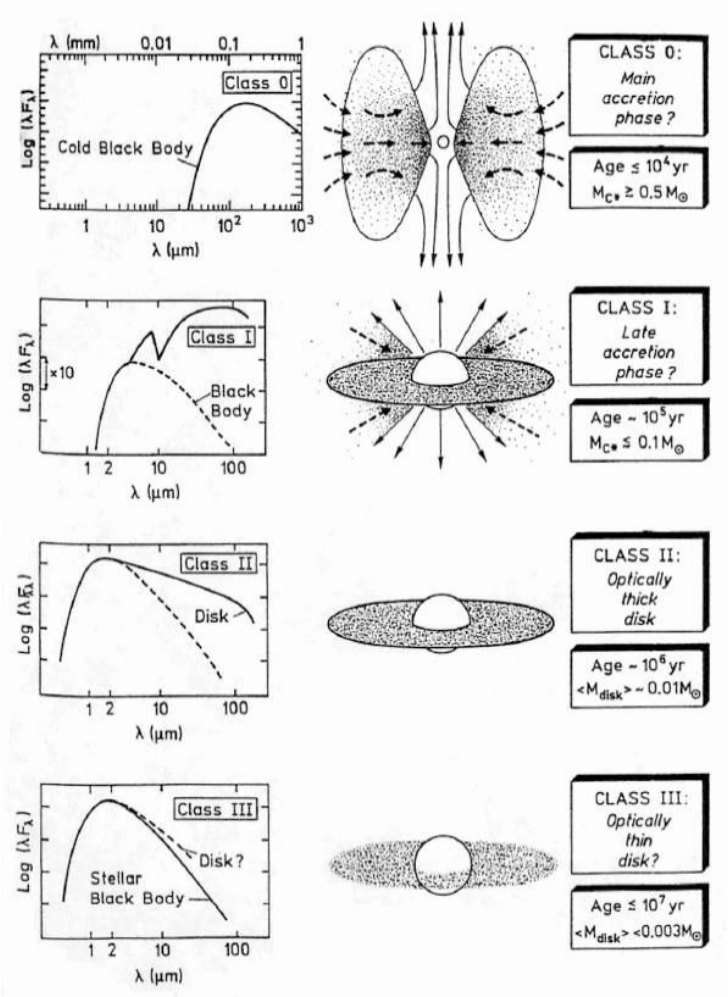

Figure 2.7: This is a reproduction of Figure 8 found in Andre & Montmerle (1994), illustrating the evolutionary phases of PMS low-mass stars.

2.1.5.1 *Class 0 sources*

Class 0 infrared sources are pre-stellar cores and are found in dense filamentary clumps that are so deeply embedded in the parental molecular cloud that their emission can only be seen in the millimetre and far-infrared wavelength regions. No flux is detectable from these sources at wavelengths shorter than 10 μm, even with a central star in a specific dense core. Just like class I sources, the emission for class 0 sources peak in the millimetre and far-infrared wavelength regions. Their emission profile usually peaks at centimetre wavelengths, meaning the class 0 sources are dominantly surrounded by cold dust, even more than class I sources. The SEDs of these objects are similar to a single blackbody, but they have very low temperatures — in the range of 20-30 K — and are associated with highly energetic, bipolar outflows. The energy of the outflows can only come from the release of the gravitational energy of matter falling towards the protostars. Class 0 source outflows are more energetic than those of class I sources. Class 0 sources are called the youngest (and thus the original) protostars by Andre & Montmerle (1994) and Hartmann (1998), yet it is not known if class 0 objects are a precursor

for class I objects. Numerically class 0 sources only make up 10% of embedded sources, and they have lifetimes in the order of $\sim 10^4$ yr (see Andre & Montmerle 1994, André 1994, Lada 1998, Hartmann 1998 and Lada & Lada 2003.

2.1.5.2 *Class I sources*

Sources like WL 12 for which $\alpha_{IR} > 0$, are classified as Class I infrared sources. They have excess emission broader than a blackbody distribution, and their SEDs have a characterised positive slope (α) for $\lambda > 2.2\mu$m. The SEDs of these sources peak in the sub-millimetre and in the far-infrared indicative that the emission is dominated by the emission from cold dust. The flux in the SEDs increase as a function of wavelength at $\lambda > 2.2$ μm, producing much excess emission due to large amounts of circumstellar material. Most of these objects can not be described on an HR diagram as protostellar, and are found deeply embedded in molecular clouds. The means that it is very rare that they show emission in the optical. The sources are often associated with bipolar molecular outflows which are fueled by the release of the gravitational potential energy when falling in towards a protostar. In the Ophiuchus region that was studied by Stahler & Palla (2005), class I sources are many times more luminous than class II sources. The typical luminosity for the class I sources is $3L_{\odot}$, but for class II sources the typical luminosity is $0.6L_{\odot}$. The typical age for class I sources are given in Hartmann (1998) as $1 - 5 \times 10^5$ yr, which means that with an accretion rate of 10^{-5} $M_{\odot}.yr^{-1}$ a solar mass star would accrete matter in 10^5 yr.

2.1.5.3 *Class II sources*

Sources like SR 24 which are not as deeply embedded as class I sources have an infrared spectral index of $-1.5 < \alpha_{IR} < 0$. They are young stellar objects (YSOs) which are surrounded by less circumstellar material than protostellar objects. The SEDs of class II sources are broader than that of a single blackbody and the emission profile peaks at either optical or *NIR* wavelengths. The excess in the *NIR* arises from the circumstellar accretion disk; it is far less than the excess emission that is exhibited by class I sources, according to Stahler & Palla (2005).

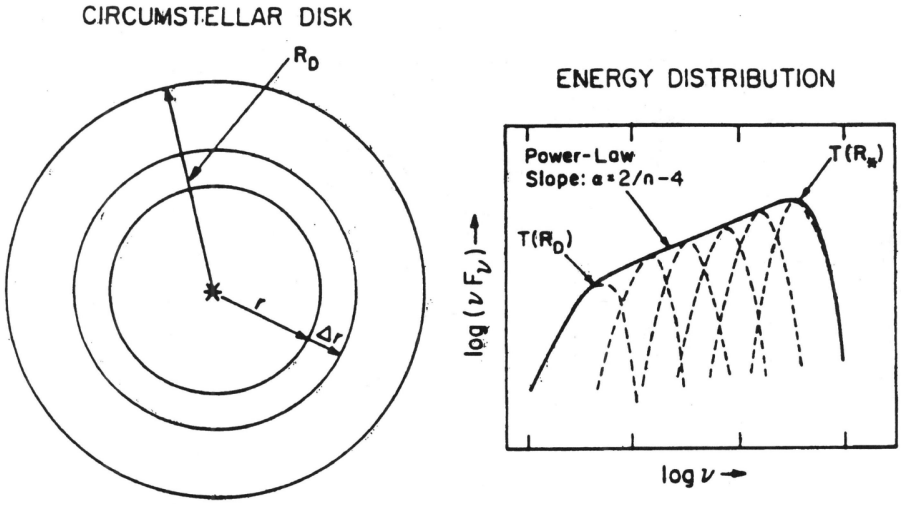

Figure 2.8: A schematic diagram of the spatially thin, optically thick disk and the emergent energy distribution. The illustration on the right is a superposition of blackbodies at different temperatures, the images were taken for Lada (1998).

The first models of Lynden-Bell & Pringle (1974) already described the peak in excess emission in the near-infrared for stars that were surrounded by luminous accretion disks. The best way to describe the system is to envision an optically thick disk which is spatially thin, and surrounds a young star which emits radiation in all directions — similar to a blackbody. The disk would be composed of

concentric annuli (as shown in Figure 2.8) with a radial dimension is ΔR and the area is $2\pi R\Delta R$. Each annulus radiates as a blackbody of temperature $T(R)$. The emergent spectrum of the disk will be the superposition of a series of blackbody curves of varying $T(R)$, shown in the right half of Figure 2.8.

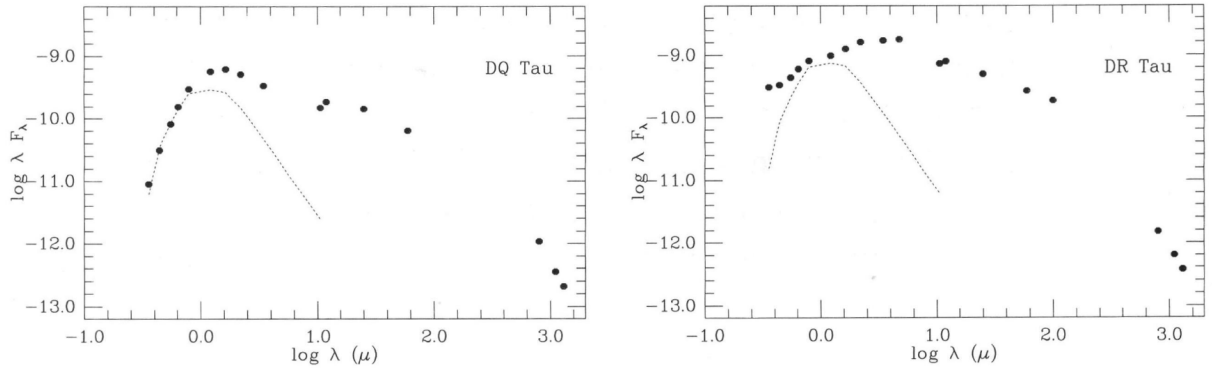

Figure 2.9: Here two SEDs are shown for stars in the Taurus molecular cloud, the vertical axes show the flux in erg.cm^{-1}s^{-1}. The dotted curve is the SED for the weak line T Tauri star LkCa7, which is a K7-M0 PMS star which does not show any signs of accretion. The excess long-wavelength emission is immediately evident, but the short wavelength excess emission is more difficult to detect, except in the strong-emission star DT Tau, the diagrams were taken from Hartmann (1998).

Figure 2.9 shows the SEDs of two T Tauri stars from the Taurus molecular cloud where the broadened blackbody spectrum for the accretion disks are seen, as well as the breaks in the spectral lines at wavelengths near $\sim$ 100 μm. The breaks are an indication of a transition between optically thick and optically thin regions. An optical depth of 1 at 100 μm is equivalent to a visual extinction of $A_v = 1000$ which is in a different class to the extinction of $A_V = 1$, which is typical to what one would measure in an optical study. The breaks in the SEDs shown in Figure 2.9 indicates that there have to be direct lines of sight in the circumstellar material around PMS stars where radiation passes through and is not absorbed by dust.

Adams *et al* (1987) examined the composite SED of seven class II sources; it was discovered that the infrared portion of the spectrum could be modelled by a power-law function in the form of $T(R) \sim R^{-n}$, where n is the index of the disk temperature gradient, which varies from 0.6 to 0.75. Wien's law, or, $\lambda_{\max} = 2.90 \times 10^{-3}/T$, describes that higher temperatures emit photons with shorter wavelengths of higher energies. The fitted power-law for the IR part of the spectrum which is radiated by the disk can be written in terms of Wien's law as:

$$\nu \sim T(R) \sim R^{-n} \tag{2.36}$$

If the temperature gradient in the disk can be described by a power-law similar to Wien's law, then the energy spectrum also has to follow to a power-law slope in frequency or wavelength. The differential form of the luminosity can be used to calculate the relation for the energy spectrum. The radius dR can be written in terms of dν as $\mathrm{d}R \sim \mathrm{d}\nu R^{(n+1)}$. Substituting d$R$ in terms of dν and $T(R)$ in terms of R^{-n} into the differential expression for the luminosity and taking the other variables as constants gives an expression:

$$L_\nu \, \mathrm{d}\nu \sim R^{(2-3n)} \, \mathrm{d}\nu \tag{2.37}$$

Now the luminosity can be written just in terms of the frequency ν using $R \sim \nu^{-1/n}$:

$$L_\nu \, \mathrm{d}\nu \sim \nu^{(-1/n)(2-3n)} \sim \nu^{(3-\frac{2}{n})} \tag{2.38}$$

For an SED, it will mean that $\nu L_\nu \sim \nu^{(4-2/n)}$ or $\alpha = \frac{2}{n} - 4$ where α is the slope of the SED when it is plotted as a function of $\log \lambda$ (see Lada 1998).

The power-law shape that is seen in the infrared portion of Class II SEDs strongly suggests that the IR excess occurs in an optically thick circumstellar disk, where the temperature gradient is directly reflected in the slope of the SED. The temperature gradient and spectral slope is the same that is predicted for a flat passive disk, where the luminosity comes from the reprocessing and re-radiation of light that it has absorbed from the central star as explained by Lada (1998). Class II IR sources can be seen in wavelengths from the infrared up to the ultraviolet. In the optical strong emission lines and continuum emission are seen, however, most observational information is found in the infrared. Class II sources typically show properties that are characteristic to CTTs, meaning that they are low-mass, PMS stars that exhibit emission lines, variable emission, and excess emission in the infrared and the ultraviolet.

Properties characteristic to T Tauri stars are given in Lynden-Bell & Pringle (1974) as: **(1)** The angular momentum of the collapsing protostellar clouds cause substantial rotation of the accretion disk around the young stars, **(2)** The accretion powers the excess optical and ultraviolet emission, **(3)** Infrared excess emission arises from the circumstellar accretion disks. The disk emission of a typical T Tauri star is mainly powered by: **(1)** The absorption of radiation from the host star and **(2)** the local accretion energy that is released.

The accretion onto the T Tauri star is modified by a stellar magnetic field similar to highly-enhanced solar-type activity (coronal X-ray emission, flares and starspots). The magnetic field is strong enough to keep the accretion disk from falling to the star's surface. Strong magnetic fields disrupt the inner disk, and the matter is channelled to follow magnetic fields that lead the material to fall on the star's surface. The energy of the accreting material is dissipated when the rapidly-moving magnetospheric gas shocks onto the star's surface causing a hot continuum emission. For more detail see Uchida & Shibata (1984) and Hartmann (1998).

T Tauri stars produce broad emission lines that are most likely produced from the magnetospheric accretion columns where the gas moving towards the star is moving with free-fall velocities. The emission lines from these columns are asymmetric around their specific wavelengths — identical to asymmetric radio emission lines of radio sources (see Calvet & Hartmann 1992 and Hartmann 1994 for more details). The asymmetrical shape around the central wavelength value for each emission line suggests that the highest velocity material is non-uniformly distributed (see Reipurth *et al* 1996). The extent of how much the emission lines are red/blue shifted is subject to how fast the material is orbiting the star, and at what angle the source is observed (see Reipurth *et al* 1996 and Lago *et al* 1998). Classical T Tauri stars emit strong hydrogen emission lines, specifically the Hα-emission line which is an indicator of how large the accretion disk is that is orbiting the host star. CTTs also emit many forbidden spectral lines in the optical. The forbidden lines are emitted from stellar winds that orbit close to the surface of the young star and are blue shifted. The absence of red-shifted emission is interpreted as strong support fir there being an occulting disk close to the star's surface, according to Edwards *et al* (1987) and Appenzeller & Wagner (1989). The Balmer emission lines most likely originate from mass loss and mass accretion in CTTs according to Bertout *et al* (1993). The mass accretion and ultraviolet excess are most likely caused by disk accretion onto the star's surface at rates of $\sim 10^{-8}$ $M_{\odot}.yr^{-1}$, which is much lower relative to the infall rates of protostars.

CTTs are visible in both the optical and the *NIR* so they can be examined on an HR diagram. They can be compared to theoretical evolutionary models, like those by Siess *et al* (2000), and have typical ages younger than 1-3 Myr. These theoretical models are usually only for diskless PMS stars, or just the photospheric emission of PMS stars, making the comparison of CTTs to isochrones and evolutionary lines very difficult.

2.1.5.4 *Class III sources*

Class III infrared sources are stars that have evolved to a stage past the accretion disk, so they do not exhibit excess infrared emission. Their SEDs are characterised by reddened blackbody functions,

which means that the emission from the short-wavelength region is absorbed by surrounding dust and remitted at longer wavelengths. The emission from these sources peak in the optical and *NIR* parts of the spectrum, and the emission decreases at wavelengths longer than 2 μm more steeply than class II infrared sources. The agreement between the SEDs of class III infrared sources and the SEDs of black-bodies at specific temperatures had lead to the conclusion that the emission comes from photospheres of young stars. The young stars do not show excess infrared emission, but their light could substantially be influenced by foreground dust (see Lada 1998).

Class III sources are also visible in the optical, like class II sources, but they do not show strong optical excess emission. Class III sources include young main sequence stars, and more mature PMS and Zero age main-sequence stars (ZAMS) that are no longer associated with an accretion disk and can be analysed on an HR diagram, together with evolutionary models. These stars are still more luminous than the similar spectral class star on the main sequence, and are either considered to be classical PMS stars, or that the emission from these stars only come from their photospheres — meaning that they can be compared to PMS evolutionary models. Most of these sources have matured in the range of 5-10 Myr and are no longer regarded as T Tauri stars. Because these stars are still relatively young and they do not have the characteristic excess emission — like the class II sources — it is difficult to distinguish these stars from field stars. For more on the properties of class III infrared sources (see Feigelson *et al* 1987).

One characteristic of class III sources is that they are strong variable X-ray emission sources. With the use of an X-ray survey, the number of class III sources in the Taurus region was catalogued and the number was roughly the same as for class II sources. A class III source is called a weak-line T Tauri star, because it does not show any or very little Hα-emission — like the star SR 20 with a spectral index of $\alpha_{\mathrm{IR}} < -1.5$. Most of these details were described by Stahler & Palla (2005) and Lada (1998).

2.1.6 High-mass star formation

One of the main questions that star-formation theory still needs to answer is how exactly does high-mass star formation occur. A high-mass star is an O or B star with a mass larger than 8 $\mathrm{M}_{\odot}$, which means that the main sequence lifetime of the star is less than about 50 Myr. This is how long it would take to burn through its hydrogen fuel supply, according to the evolutionary models of Siess *et al* (2000). Battersby *et al* (2017) states that it is not yet known what exactly the relationship is between the formation of low-mass cluster members and high-mass star forming regions. The clusters can either form from slow, hydrostatic, global contractions of the molecular cloud, or quickly and dynamically. Dib (2014) also states that the hierarchy of star formation in high-mass star-forming regions is not yet known; Does a high-mass star form, and do lower-mass stars form from the matter which is accumulated in the environment surrounding the high-mass star? Alternatively, do low-mass stars form across a whole molecular cloud, and some of the low-mass protostellar cores attract each other and merge to form a high-mass prestellar core?

It is widely accepted that the formation of low-mass stars occurs according to the model by Shu *et al* (1987). The star forms through the gravitational collapse of a prestellar core, which is followed by an accretion disk which contributes matter for about 10 Myr. High-mass stars reach the zero-age main sequence before the end of their accretion phase. When the protostellar core reached a mass of 10 $\mathrm{M}_{\odot}$ the conditions are right for hydrogen fusion to ignite the core. The radiation pressure and stellar winds from these objects are strong enough to halt any further mass accretion. The open question according to Faustini *et al* (2009) is how is it possible that objects heavier than 10 $\mathrm{M}_{\odot}$ still form. Some hypotheses have been formulated:

- Accretion rates of up to three orders of magnitude higher than in the case of low-mass stars (see Cesaroni 2005).

- Non-spherical accretion geometries dominated by magnetic fields (see Nakano 1989, Yorke 2002 and Keto 2003).

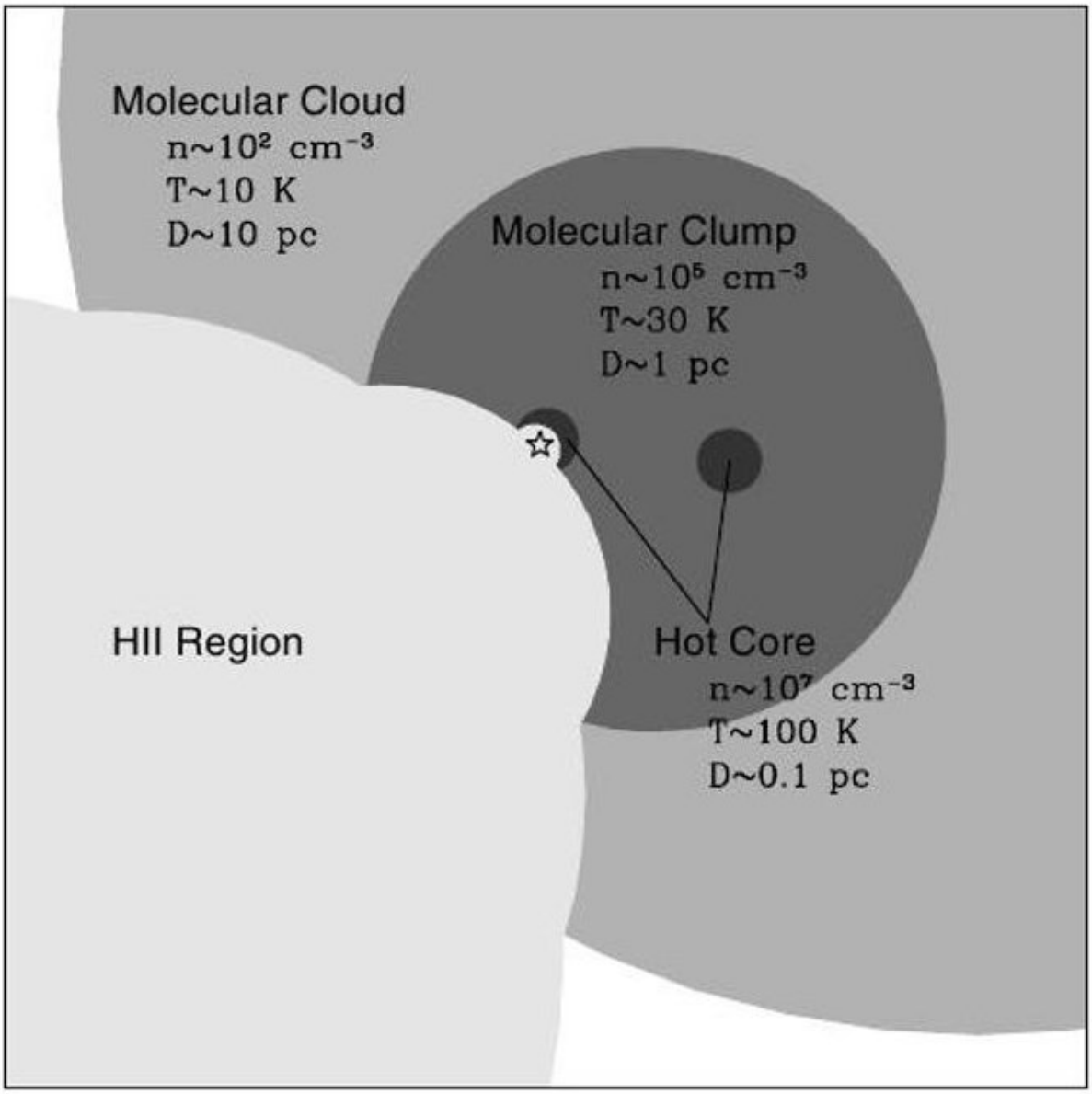

Figure 2.10: This illustration shows the hierarchical structure in high-mass star-forming regions. The clouds form dense clumps which have cores, a high-mass star forms in a molecular cloud and starts to form a hot molecular core which initially forms an ultracompact HII region. The illustration was taken from Kim & Koo (2001).

- The formation of massive stars by the merger of multiple low-mass pre-stellar objects in dense protostellar clusters (see Bonnell *et al* 1998 and Bally & Zinnecker 2005).

There may be different versions of star formation that can occur. Deharveng *et al* (2005) gives different examples of different versions of high-mass star-forming regions. One interesting model is where an HII-region sweeps up the embedding material until it becomes gravitationally unstable, collapses, and forms a new massive star near the border of an HII region. The different hypotheses for the formation of massive stars have observationally distinct consequences, not only for the existence of accretion disks and the morphologies of outflows, but also for the stellar population associated with the young high-mass star:

- In the case where direct accretion occurs, there should be some massive stars that form in isolation. These should have very little or no low-mass stars associated with them.

- On the other hand, a coalescence model predicts that there should be a halo of low-mass stars that form around a young high-mass star. The stellar density of the low-mass stars in this model would be very high, in the range of 10^4 stars.pc^{-3} (see Bally 2002).

To test these different models, the populations associated with high-mass star-forming regions have to be studied in detail. The generally accepted assumption is that massive star formation always occurs in clusters and the embedding environment gets affected by the star's winds and emitted radiation, as explained by Lada (2005). *NIR* photometry has proven to be very useful in studying deeply embedded young clusters and ultra-compact HII regions. By studying the evolutionary progress of these deeply embedded populations, some insight may be gained on the mechanisms and processes involved in high-mass star formation (see Anandarao *et al* 2008). The appearance of such ultra-compact HII regions that are deeply embedded in a molecular cloud the formation of a massive star earlier than a B3 star (see Shepherd & Churchwell 1996).

In many star-forming regions, there are multiple or single OB stars present. The dominant ultraviolet emission and the strong stellar winds from these stars strongly affect the molecular clouds. These conditions blow away and clear the environments embedding these OB stars. The movement of the gas by these OB stars can hinder the formation of low-mass stars near the massive stars, but it can trigger the formation of low-mass stars further in the molecular clouds (see Elmegreen & Lada 1977 and Schmeja 2010). Embedded clusters and the bullet-shape of the magnetosphere from young stars are sometimes found to be aligned with expanding HII shells. This suggests that the formation of the low-mass stars were triggered by external compression from OB stars (see Phelps 1997 and Schmeja 2010).

Battersby *et al* (2017) performed a study on various high-mass star-forming regions, where ultra-compact HII regions and regions with class II methanol masers were used to determine the lifetimes of high-mass star-forming regions. They discovered that the dense molecular environments spend 70% of their ages starless — meaning that the high-mass stars have not yet formed and the last 30% of their ages are in the star-forming phase. The star-forming phase occurs when the gas temperature rises due to the formation of a high-mass star which heats up the gas. Different phases in the lifetime of embedded high-mass star-forming regions were determined by the identification of the duration of methanol masers, and the continuum emission from the dust in the hot regions of the star-forming regions. The time-periods involved in the study of the regions showed that masers form in a short period before a high-mass star turns on and starts to form an ultra-compact HII region. The mechanisms involved in the formation evolution of the high-mass stars during the ultra-compact HII regions expand, and the gas around the high-mass star starts to heat up.

The evolution of dense filamentary structures in molecular clouds that start to form prestellar cores have been well studied with Herschel, for example, the studies by Marsh *et al* (2017), Mowat *et al* (2017) and Pattle *et al* (2017). Dense filaments collapse mainly under gravitational force at free fall speeds to form the prestellar cores that lead to low-mass star formation. The link between the filamentary structures and the precursors for high-mass stars is still not fully understood yet.

2.1.7 The initial mass function

The distribution for the masses of stars that form as a cluster out of a molecular cloud is known as the initial mass function (IMF). Ward-Thompson & Whitworth (2011) describes the IMF $\Phi(M)$, as the fraction, S, of the total mass from a molecular cloud that is formed into stars. The total number of stars in a mass interval $(M, M + \mathrm{d}M)$ is given by:

$$N_M \, \mathrm{d}M = S\Phi(M)M \, \mathrm{d}M = 1 \tag{2.39}$$

The IMF was first conceptualised by Salpeter (1955) where observational data was fitted as a power-law for stars with masses between 0.4 $\mathrm{M}_\odot$ and 10 $\mathrm{M}_\odot$, the power-law had the form:

$$\Phi(M) \, \mathrm{d}M \simeq KM^{-2.35} \, \mathrm{d}M \tag{2.40}$$

where K is a constant. The IMF can only be measured from young populations in clusters, where all of the stars have the same age. In some populations it has been discovered that the IMF is a piece-wise power-law between different mass ranges. The most common form of the broken power-law IMF that is accepted today is from the paper by Kroupa (2001):

$$\Phi(M)\ \mathrm{d}M \simeq KM^{-2.3}\ \mathrm{d}M : M > 0.5\ \mathrm{M}_{\odot}$$
$$\Phi(M)\ \mathrm{d}M \simeq KM^{-1.3}\ \mathrm{d}M : 0.5\ \mathrm{M}_{\odot} \geq M > 0.08\ \mathrm{M}_{\odot}$$
$$\Phi(M)\ \mathrm{d}M \simeq KM^{-0.3}\ \mathrm{d}M : 0.08\ \mathrm{M}_{\odot} \geq M \geq 0.01\ \mathrm{M}_{\odot}$$

The IMF can also be represented on a log-normal distribution which is given in Maschberger (2013)

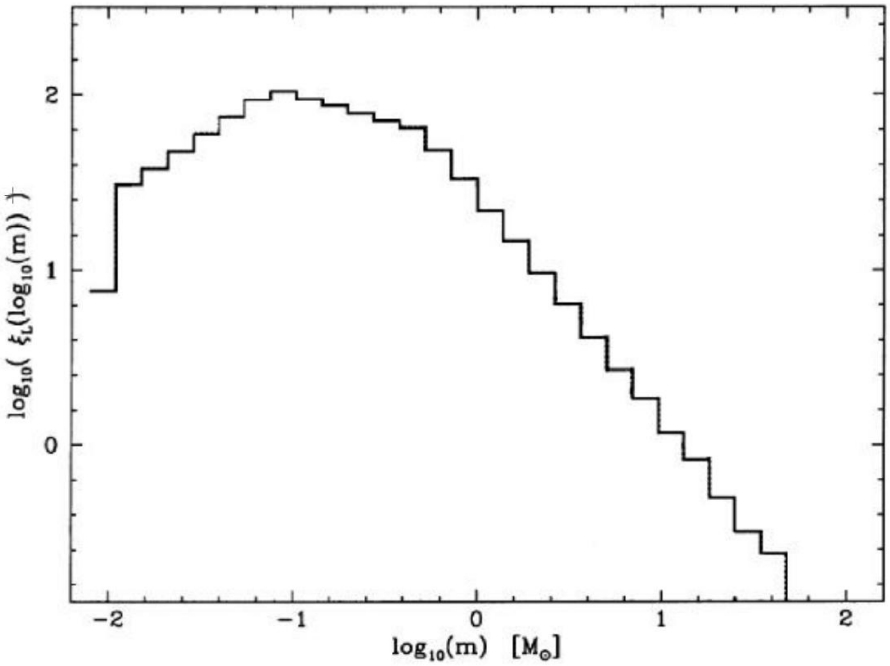

Figure 2.11: This IMF was taken from Figure 1.12 in Ward-Thompson & Whitworth (2011). The function is plotted as $\log(\xi)$ where $\xi = M\Phi(M)$ against $\log(m)$ where $m = M/\mathrm{M}_{\odot}$.

in the form:

$$\Phi(M)\ \mathrm{d}M \simeq 0.584\ \mathrm{M}_{\odot}^{-1} \exp\left(-1.54 \log^2\left[\frac{M}{0.22\ \mathrm{M}_{\odot}}\right]\right) \tag{2.41}$$

One of the main objectives of star-formation theory is to understand why the IMF varies very little between different star-forming regions, and if the little variance that is experienced is due to the difference in environments, or if there are other factors. The IMF of a star-forming region can be determined by fitting a power-law to the mass distribution of a cluster on a log-normal scale.

2.2 Fundamentals of photometry

The only information that is available to study young stellar cluster members is the light emitted by them. To measure the light, condense the measurements into results, and then understand as well as correctly interpreting the results, is very difficult. To aid in the understanding of the results in the rest of this thesis the most basic principles will be discussed in this section.

The light that is emitted by stars is electromagnetic radiation quantified in energy packets, or photons. Photons have a propagation direction and energy that is measured with $E = h\nu$ in eV. Carroll & Ostlie (2006) states that one can measure the energy flux of photons with a specific wavelength, and which are travelling in a certain direction over a unit-surface area. For a differential energy range the energy flux of the photons moving across the unit-surface area can be measured. The total energy flux for

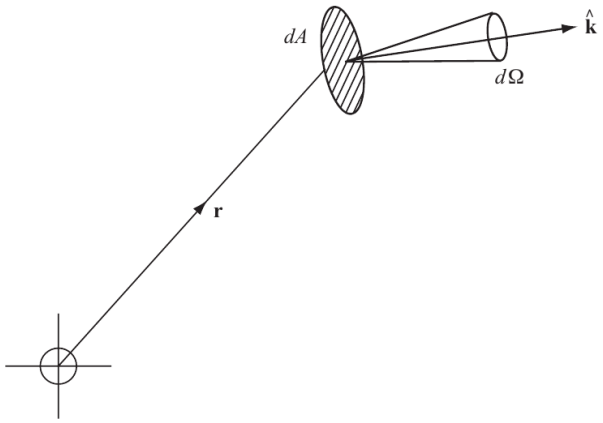

Figure 2.12: The path followed by light in the direction of vector r that propagates through a surface element $\mathrm{d}A$ with a normal vector $\hat{\mathbf{k}}$ at a solid angle $\mathrm{d}\Omega$.

photons of a specific frequency that moves over unit-surface area can be calculated with intensity I_ν. The intensity I_ν is the amount of radiant energy per unit frequency interval over ν, over a solid angle, across a unit-area per unit time. Mathematically it can be expressed as:

$$I_\nu(\mathbf{r},\hat{\mathbf{k}})\mathrm{d}\nu\mathrm{d}A(\mathbf{r},\hat{\mathbf{k}})\mathrm{d}t\mathrm{d}\Omega(\hat{\mathbf{k}}) \tag{2.42}$$

This expression gives the amount of radiant energy in the infinitesimal frequency interval, $(\nu,\nu+\mathrm{d}\nu)$, which passes through an infinitesimal element of area $\mathrm{d}A(\mathbf{r},\hat{\mathbf{k}})$, which has a position r, and a unit normal $\hat{\mathbf{k}}$ around a differential solid angle $\mathrm{d}\Omega(\hat{\mathbf{k}})$ over a time interval $(t,t+\mathrm{d}t)$. This is the intensity at a specific frequency interval. To get the total intensity of light the integral is:

$$I(\mathbf{r},\hat{\mathbf{k}}) = \int_0^\infty I_\nu(\mathbf{r},\hat{\mathbf{k}})\mathrm{d}\nu, \tag{2.43}$$

which measures the total amount of radiant energy summed over all frequencies, passing through the unit area at position $\mathbf{r}$, into unit solid angle about the unit normal $\hat{k}$ to that area. The radiation field of any stellar object can be described by the Planck equation which is used to describe the electromagnetic emission at a frequency ν from a blackbody with a surface temperature of T:

$$I_\nu(\mathbf{r},\hat{\mathbf{k}}) = B_\nu(T) = \frac{2h\nu^3}{c^2}\left(e^{\frac{h\nu}{kT}}-1\right)^{-1} \tag{2.44}$$

where k is the Boltzmann constant, and h is the Planck constant. The monochromatic flux of light, F_ν can be defined as:

$$F_\nu(\mathbf{r},\hat{\mathbf{k}})\mathrm{d}\nu\mathrm{d}A(\mathbf{r},\hat{\mathbf{k}})\mathrm{d}t \tag{2.45}$$

which gives the net amount of radiant energy in a frequency interval $(\nu,\nu+\mathrm{d}\nu)$. The light crosses the infinitesimal frequency interval $(\nu,\nu+\mathrm{d}\nu)$, over the infinitesimal element of area $\mathrm{d}A(\mathbf{r},\hat{\mathbf{k}})$ at position r in the time interval $(t,t+\mathrm{d}t)$, irrespective of the propagation direction of the light relative to the normal vector $\hat{\mathbf{k}}$.

The standard way of measuring a star's brightness is the magnitude scale, the definition of which have archaic origins. Hipparchus first catalogued stars that could be seen with the naked eye and classified them on a magnitude scale. The brightest stars had a magnitude of 0, and the faintest objects had a magnitude of 6. With the advent of photometers in the nineteenth century William Pogson discovered that the magnitude classification is a rough geometric progression in flux F. A regularizing system was introduced where a magnitude difference of 5 corresponds to a brightness ratio of 100:1. The magnitude scale is still in use today, and a magnitude that is directly measured from an object is called an apparent magnitude — this is where the distance and extinction to the object are not taken

into account. The relationship between the measured magnitude (m) and the flux emitted by the object is:

$$m = -2.5 \log_{10}(F) + K \tag{2.46}$$

Here K is a constant which is often chosen so that the measurements between different systems agree. In the standardisation of the modern system, Vega has a magnitude of $m = 0$. If the total apparent bolometric flux is used in equation 2.46, m is then called the apparent bolometric magnitude. The difference between two sources of different magnitudes is calculated as:

$$\Delta m = m_1 - m_2 = -2.5 \log_{10} \left(\frac{F_1}{F_2} \right) \tag{2.47}$$

The luminosity of a source can also be expressed on the magnitude scale. A source's absolute magnitude is the apparent magnitude of the source at a distance of 10 parsecs in clear space. The relation between the apparent and absolute magnitude is:

$$m - M = 5 \log_{10}(r) - 5 \tag{2.48}$$

where M is the absolute magnitude, r the actual distance to the object in parsecs and the difference between the apparent and absolute magnitudes $m - M$ is called the distance modulus. The distance modulus also takes the inverse square law for the decrease in a source's flux into account. The following section of this chapter starts with a discussion on extinction, or in other words, the type of material that the observed light encounters on the way to an observing telescope.

2.2.1 Extinction

The light that is captured by a telescope originates from sources in the Milky Way or beyond and is subjected to interaction with the ISM. This interaction implies that the intensity of the light, I_λ that is observed with a telescope does not have the same intensity, I_0 that was emitted from the specific source. The decrease in the intensity is caused by the interaction between the incident light and dust particles in the ISM, and particles in the atmosphere. The phenomenon of extinction and its effects on observed light was first documented by Trumpler (1934).

The initial intensity of light with a wavelenght λ at the star is $I_\lambda(l = 0)$. It can also be represented with a magnitude of $m_0(\lambda) = -2.5 \log_{10} I_0(\lambda)$. The light's intensity changes as a function of the distance from the source, l so that the intensity measured above the Earth's atmosphere is $I_\lambda(l)$. As before, the intensity above the Earth's atmosphere has an equivalent magnitude, $m_\lambda(l) = 2.5 \log_{10} I_\lambda(l)$. When the light interacts with particles in the atmosphere, its intensity decreases due to scattering and absorption of photons by particles in the Earth's atmosphere, $I_\lambda(l) = I_\lambda(0) e^{-\kappa_\lambda l}$ so that the total intensity that is measured:

$$\begin{aligned} -2.5 \log_{10}(I_\lambda(l)) &= -2.5 \log_{10}(I_\lambda(0)) + 2.5 \kappa_\lambda \log_{10}(e) \\ m_\lambda(l) &= m_\lambda(0) + 1.086 \tau_\lambda \end{aligned}$$

Thus,

$$m_\lambda(l) - m_\lambda(0) = 1.086 \tau_\lambda = -2.5 \log_{10} \left(\frac{I_\lambda(l)}{I_\lambda(0)} \right) \tag{2.49}$$

The difference in the measured magnitudes is caused by the interaction of the emitted light from the star with dust in the Milky Way's Galactic plane. This decrease in light is called the extinction and has to be taken into account when the absolute magnitude of the star is calculated. A measure of the amount of light that is lost when propagating through a specific medium can be measured by the optical depth, τ_λ. The optical depth, τ_λ is a measure of how much material the light propagates through, if l is the thickness of the material, σ the attenuation cross section, and n is the number density. The optical depth is $\tau_\lambda = \int_0^l \sigma n(z) \, \mathrm{d}z$. The optical depth, τ_λ is equal to the natural logarithm for the ratio of the initial intensity of the light entering the medium and the intensity of light leaving the medium:

$$\tau = \ln \left(\frac{I_\nu(0)}{I_\nu(\tau_\nu)} \right) \tag{2.50}$$

The relation between the extinction measured in magnitudes, which was defined in equation (2.49), and the optical depth is:

$$A_\lambda = 1.086\tau_\lambda \tag{2.51}$$

Extinction has a wavelength dependence which is governed by the power-law, $A_\lambda = \lambda^{-\beta}$, which is given by Cardelli *et al* (1988). The extinction suffered by incident light is directly proportional to the amount of dust which it propagates through. The wavelength dependence implies that light at shorter wavelengths (around 3000Å) suffer more extinction than at longer wavelengths (around 7000Å). Physically the incident light is either scattered, or absorbed and remitted at longer wavelengths by dust particles. An object will appear to have more emission at longer wavelength bands; this effect is called reddening.

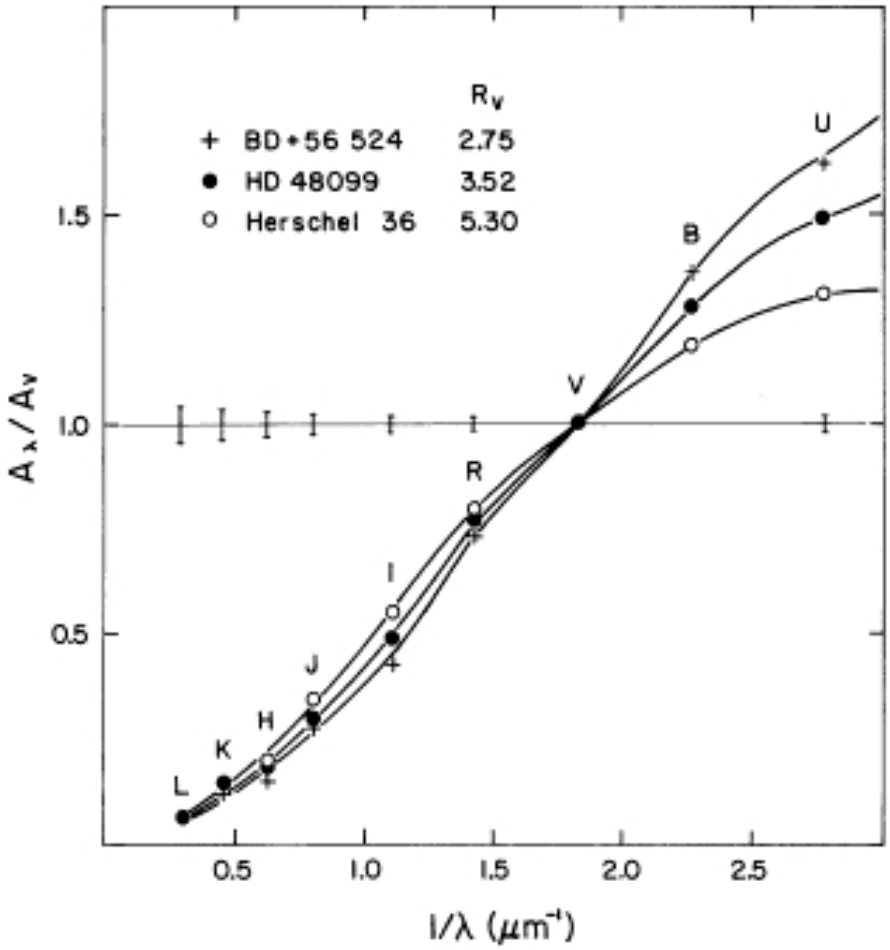

Figure 2.13: An illustration of extinction as a function of wavelength in the different directions of the Milky Way's Galactic plane. It shows the ratio of the measured extinction relative to the extinction in the visual magnitude band. The illustration was taken from the paper by Cardelli *et al* (1989).

To better understand the wavelength dependence of extinction, suppose the intensity of light emitted from a star is measured at two different wavelengths, $I_{\lambda_1}(0)$ and $I_{\lambda_2}(0)$. The ratio of these two measured intensities, or $\frac{I_{\lambda_1}(0)}{I_{\lambda_2}(0)}$ is called the colour of the object, and is measured in magnitudes as:

$$-2.5\log_{10}\left(\frac{I_{\lambda_1}(0)}{I_{\lambda_2}(0)}\right) = m_{\lambda_1}(0) - m_{\lambda_2}(0) \tag{2.52}$$

Above the atmosphere, the intensity of light at each wavelength range would have suffered extinction

by propagating through the Galactic plane. The intensities above the atmosphere are:

$$I_{\lambda_1}(l) = I_{\lambda_1}(0)e^{-\kappa_{\lambda_1} l}$$
$$I_{\lambda_2}(l) = I_{\lambda_2}(0)e^{-\kappa_{\lambda_2} l}$$

or in terms of the optical depth:

$$\Delta m_{\lambda_1}(l) = 1.086\tau_{\lambda_1} = A(\lambda_1)\Delta m_{\lambda_2}(l) = 1.086\tau_{\lambda_2} = A(\lambda_2) \tag{2.53}$$

The ratios of the specific intensities are:

$$\frac{I_{\lambda_1}(l)}{I_{\lambda_2}(l)} = \frac{I_{\lambda_1}(0)}{I_{\lambda_2}(0)} e^{-(\kappa_{\lambda_1} - \kappa_{\lambda_2})l} \tag{2.54}$$

In terms of magnitudes the ratio is:

$$-2.5\log_{10}\left(\frac{I_{\lambda_1}}{I_{\lambda_2}}\right) = -2.5\log_{10}\left(\frac{I_{\lambda_1}(0)}{I_{\lambda_2}(0)}\right) + 2.5(\kappa_{\lambda_1} l)\log_{10} e - 2.5(\kappa_{\lambda_2} l)\log_{10} e$$
$$-2.5\log_{10}(I_{\lambda_1}) - (-2.5\log_{10}(I_{\lambda_2})) = -2.5\log_{10}(I_{\lambda_1}(0)) - (-2.5\log_{10}(I_{\lambda_2}(0))) + 1.086(\kappa_{\lambda_1} l) - 1.086(\kappa_{\lambda_2} l)$$
$$(m_{\lambda_1} - m_{\lambda_2}) = (m_{\lambda_1}(0) - m_{\lambda_2}(0)) + 1.086(\kappa_{\lambda_1} - \kappa_{\lambda_2})l$$
$$\implies (m_{\lambda_1} - m_{\lambda_2}) - (m_{\lambda_1}(0) - m_{\lambda_2}(0)) = 1.086(\tau_{\lambda_1} - \tau_{\lambda_2})$$

If the difference in intensity is calculated in terms of two different bands in the Johnson-Cousins filter system, for instance, the blue B and visual V bands, the colours are:

$$(B-V) - (B-V)_0 = 1.086(\tau_B - \tau_V) \sim E(B-V) \tag{2.55}$$

if $A_V = 1.086\tau_\nu \implies E(B-V) = A_B - A_V$.

The reddened colour can be used to calculate the extinction for one of the bands that was used in the calculation of the colour. This is under the assumption that there is a constant relation between the reddening and the extinction:

$$A_V = R_V E_{B-V} \tag{2.56}$$

The relation R_V is the ratio of the total extinction suffered by that all of the light that is emitted by the observed star to the selective visual extinction, or the extinction suffered in just one specific band, $E^{\nu=\lambda_2}_{\nu=\lambda_1}/E^{\nu=\inf}_{\nu=0}$. The value of R_V was empirically determined as, $R_V = 3.05 \pm 0.15$ for the average density of the ISM (1 particle.cm^{-3}) in the Galactic plane by various astronomers like Whitford (1958) and Johnson (1968). If the visual extinction A_V is known, then R_V can be used to calculate the extinction in any other band using the extinction law that were determined by Nandy *et al* (1976), Schultz & Wiemer (1975), Rieke & Lebofsky (1985), Lombardi *et al* (2006) and Stead & Hoare (2009). The most general extinction law that is used for sources in the Milky Way's Galactic plane is given in Table 2.1 and was determined by Rieke & Lebofsky (1985).

The environments in which young stellar clusters form and evolve to the stage of the main hydrogen burning sequence have typical densities in the range of $(10^2 - 10^3)$ cm^{-3} (see Bodenheimer 2011). The high extinction causes optical observations to become almost impractical when using anything smaller than a 10-m telescope. At wavelengths longer than 1 μm it becomes possible to study sources with high extinction. The light emitted by young embedded stars at wavelengths in the JHK_s *NIR* photometric system that was developed by Bessell & Brett (1989) has been shown by Lada *et al* (1993) and Lada *et al* (2007) to suffer the least extinction. This *NIR* photometric system is the most direct way of observing and studying a young cluster. The reason is that the bands have a respective mean throughput at 1.25 μm, 1.65 μm, and 2.6 μm. By using a typical 1.5-m *NIR* telescope it is quite easy to detect and study most of the deeply embedded sources from a star-forming region situated at a distance of a few kpc. The following two subsections will describe how the results from *NIR* imaging are used to study young embedded clusters.

Table 2.1: The broadband filter names, mean transmission wavelength, the band minus the visual band's excess as a ratio to $(B-V)$ excess, and then the ratio of the specific band's extinction to the visual extinction.

Filter	Peak throughput [Å]	$\frac{E(\lambda-V)}{E(B-V)}$	$\frac{A_\lambda}{A_V}$
U	3663	1.64	1.531
B	4361	1.00	1.324
V	5448	0.00	1.000
R	6407	-0.78	0.748
I	7980	-1.60	0.482
J	12350	-2.22 ± 0.02	0.282
H	16620	-2.55 ± 0.03	0.175
K_s	21590	-2.744 ± 0.024	0.112

2.2.2 Different photometric systems and their transformation relationships

2.2.2.1 Calibration to a standard photometric system

There is not one specific photometric system that is used over the various wavelength regimes, for example — Table 2.1 gives the bands of the Johnson-Cousins photometric system. The peak throughput in Table 2.1 is the wavelength at which the maximum luminous flux propagates through the specific band. The Johnson-Cousins photometric system was developed at the start of digital photometric imaging where the B and V bands were inherited from the era of photographic plates. The Johnson U band was introduced with digital imagers and the R_C and I_C Cousins bands were later added to include light with longer wavelength. When referring to the Johnson-Cousins system the set of abriviations for the bands, $UBVR_CI_C$ are used, where the band names refer to the specific wavelength region of each band, namely, ultraviolet, blue, visual, red, and infrared respectively.

Another optical photometric system which is used in general was initially developed for the Sloan Digitised Sky Survey (SDSS). The system's abreviated band names are $u'g'r'i'z'$ and are called ultraviolet, green, red, infrared, and near-infrared respectively. The Sloan photometric system was developed with the aim of performing photometry on high red shifted galaxies. However, the transmission of the bands as a function of wavelength is much better defined than the Johnson-Cousins system. Both systems are shown in the left panel of Figure 2.14.

For reference the transmission curves of the JHK_s *2MASS* photometric system are included in the right panel of Figure 2.14. The bands in the *2MASS* photometric system were developed around the atmospheric windows in the *NIR*. The Johnson-Cousins, SDSS, and *2MASS* systems are shown here because they are all relevant to this specific study.

When performing photometry on a source that is of scientific interest with a telescope, a CCD and filter band is used to take an image. The magnitudes derived from the flux (T) that is measured from the observed image is called the instrumental colours and magnitudes:

$$m_{\text{inst}} = -2.5 \log_{10} \left(\frac{F}{t_{\text{exp}}} \right) \tag{2.57}$$

The instrumental colours and magnitudes are subject to many factors, such as atmospheric extinction and the optical setup that was used. The instrumental colours and magnitudes are different for each instrumental setup, to be comparable to the measurements taken with other instruments, they have to be transformed to a standard system which is independent of the instrumental setup or atmospheric conditions. By eliminating the effects of atmospheric extinction, the magnitude that would be measure above the atmosphere — called the apparent magnitude — can be calculated.

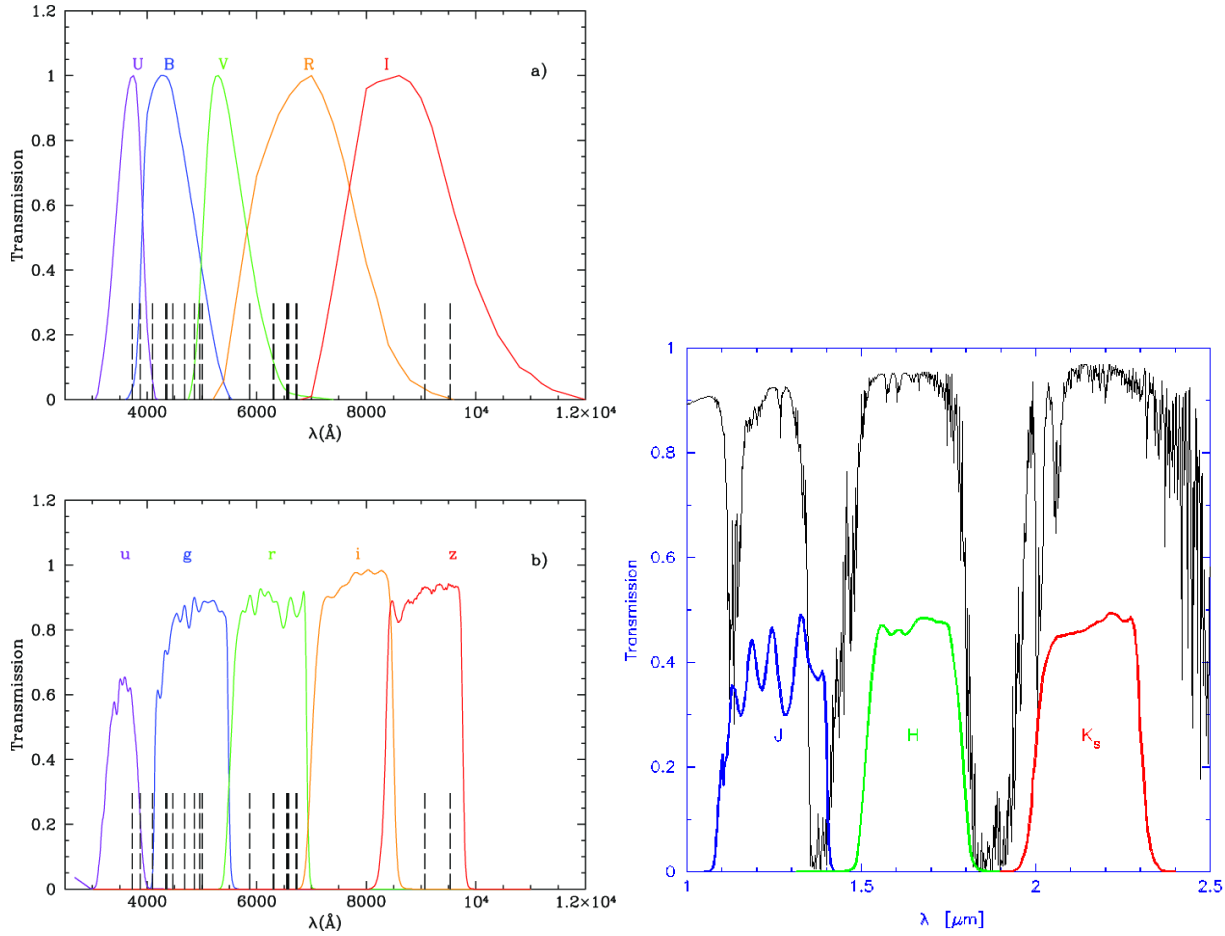

Figure 2.14: The left panel shows transmission as a function of wavelength for the different bands in the Johnson-Cousins and Sloan Digitised Sky Survey (SDSS) photometric systems, respectively. The Figure in the left panel was taken from García-Vargas *et al* (2013). The right panel shows the transmission as a function of wavelength for the *2MASS* photometric system.

There are two ways of transforming from the measured instrumental colours and magnitudes to a standard system:

1. By using standard stars of which the colours and magnitudes are known the effects of atmospheric extinction can be eliminated.
   If the chromatic flux from a star incident on the layer is F_λ, then the decrease in the flux, dF_λ, on passing through the layer will be proportional to F_λ and the length of path followed by the light. The change in the flux will thus be

$$\mathrm{d}F = -\kappa_\lambda F_\lambda \sec(z)\mathrm{x} \tag{2.58}$$

   and the proportionality constant, κ_λ is the absorption coefficient. The absorption coefficient is dependent on the composition of the material through which the light propagates, meaning the length of the path, x, followed by the light. The expression can be solved both from the top of the atmosphere to the bottom of the atmosphere

$$\int_t^b \mathrm{d}F/F = -\sec(z)\int_t^b \kappa \mathrm{d}x, \tag{2.59}$$

   or the ratio of the flux of light at the top of the atmosphere to the that at the bottom of the atmosphere:

$$F_b/F_t = F/F_0 = e^{-\sec(z)\int_t^b \kappa \mathrm{d}x} \tag{2.60}$$

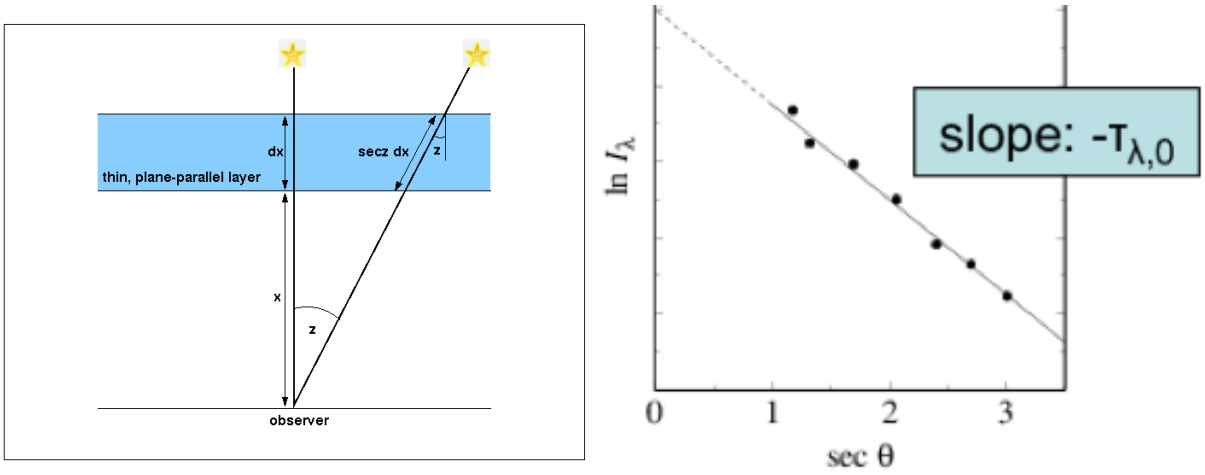

Figure 2.15: The path light follows through the atmosphere that is emitted by a star that is at an angle z relative to the zenith.

The flux at the top (F_t) and at the bottom (F_b) of the atmosphere have respectively been renamed, $F_t = F_0$, and $F_b = F$. The flux at the bottom of the atmosphere, F_b, is measured with the telescope. Using the relation between flux and magnitudes, this expression can be rewritten in terms of magntiudes:

$$m - m_0 = -2.5 \log_{10} (F/F_0) = -2.5 \log_{10} \left[e^{-\sec(z) \int_t^b \kappa \mathrm{d}x} \right] = 2.5 \sec(z) \log_{10} e \int_t^b \kappa \mathrm{d}x \tag{2.61}$$

A constant $k = 2.5 \log_{10} \int_t^b \kappa \mathrm{d}x$ is introduced, so that the apparent magnitude (m_0) can be calculated from the instrumental magnitude m:

$$m = m_0 + k \sec(z) \tag{2.62}$$

By observing a standard star, or preferably multiple standard stars, during a single night the constant k can be calculated. For higher precision calibrations a second extinction term which is colour dependant is introduced:

$$m = m_0 + k \sec(z) + k_2 C \sec(z) \tag{2.63}$$

The factor C is the colour index across two different bands, for example $C = (B - V)$ is the colour term for the B and V bands. When solving the constants k and k_2 and converting the magnitudes from instrumental to apparent, a zero-point is required for converting from the instrumental magnitude to the apparent magnitude of the standard star:

$$m_{\mathrm{zp}} = m_{\mathrm{std}} - m_{\mathrm{inst}_{0\ \mathrm{std}}} \tag{2.64}$$

The calibrated magnitude of the star that is of scientific interest is calculated by adding the apparent magnitude's zero-point to the instrumental magnitude:

$$m = m_{\mathrm{zp}} + m_{\mathrm{inst}_0} \tag{2.65}$$

If the instrument setup, telescope, and filter system perfectly matches the system which was used, the calibration to the standard system can be done with:

$$m_{\mathrm{std}} - m_{\mathrm{inst}_{0\ \mathrm{std}}} - m_{\mathrm{zp}} = 0 \tag{2.66}$$

In practice the setups never match perfectly to each other, thus a colour term is needed to correctly calibrate to a standard system:

$$m_{\mathrm{std}} - m_{\mathrm{inst}_{0\ \mathrm{std}}} - m_{\mathrm{zp}} = kC \tag{2.67}$$

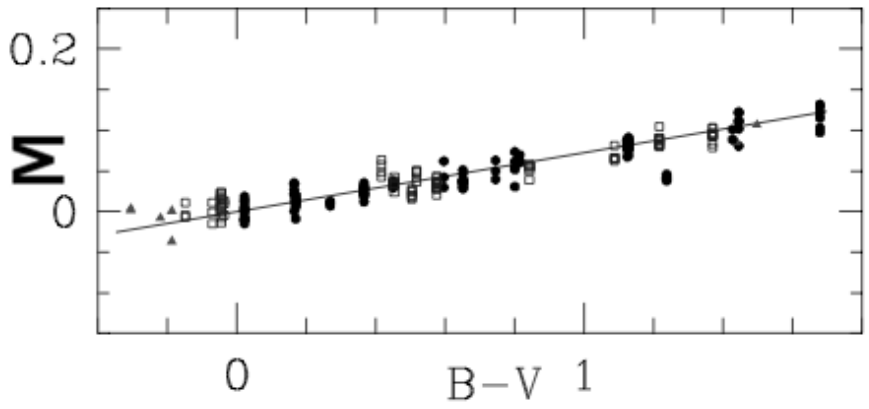

Figure 2.16: The difference between the catalogued magnitude for standard stars and the calibrated colour ($M = m_{\rm std} - m_{\rm inst_0\ std} - m_{\rm zp}$) as a function of the colour $(B - V)$.

where k is the colour term and C is the colour index, for example $C = (B - V)$. The colour term is equal to the gradient of the plot of the difference for the plot of $m_{\rm std} - m_{\rm inst_0\ std} - m_{\rm zp}$ against C which shows the difference between catalogued magnitudes of standard stars and their calibrated magnitudes as a function of the colour. The $y-$intercept is set to 0, using a zero-point calculated from a star with $(B - V) = 0$. This plot is shown in Figure 2.16.

2. When more than one image is stacked together the airmass for all of the component images differ. Implying that the calibration from instrumental colours and magnitudes to a standard photometric system is not possible using standard star observational data. On the other hand it is possible to calibrate the measured instrumental colours and magnitudes to a standard system if the colours and magnitudes of stars in the observed field are already known. Suppose the colours and magnitudes of 30 stars in the observed field are taken from a survey or other observational data, then the following calibration equations can be used:

$$M_{\rm std} \quad = m_{\rm inst} + k_1 C_{\rm inst} + k_0 C_{\rm std} \quad = k_2 C_{\rm inst} + k_3 \tag{2.68}$$

The standard colours and magnitudes are $C_{\rm std}$ and $M_{\rm std}$ respectively. For the calculation of the magnitude M_{std} the specific band's magnitude has to form part of the colour index $C_{\rm inst}$. An example of this is if B is calculated then the $(U - B)$ or $(B - V)$ colour index has to be used and not the $(R - I)$ colour term. This calibration is similar to the transformation equations that were used by van der Walt *et al* (2012) and were shown in Chapter 1.

2.2.2.2 Transformation between different photometric systems

When the observed colours and magnitudes have been calibrated to a standard photometric system it can be compared to theoretical models or other observations. One problem that is encountered when using theoretical models — or other observational data — is that not all data is available in the same photometric system, for example, a theoretical model only gives output in Johnson-Cousins colours and magnitudes but the observations were done in the SDSS photometric system. It is possible to transform from the Johnson-Cousins to the SDSS and the other way around. Figure 2.14 shows that bands in each of these two systems capture light over a significant amount of the same wavelength range. There are transformation equations between these two systems given in the literature, which were all derived empirically. Jordi *et al* (2006) give the following set of transformation equations:

$$
\begin{aligned}
g - V &= a_1 (B - V) + b_1 & \delta (g - V) &= a_1 \delta (B - V) + b_1 \\
r - i &= a_2 (R - I) + b_2 & \delta (r - i) &= a_2 \delta (R - I) + b_2 \\
r - z &= a_3 (R - I) + b_3 & \delta (r - z) &= a_3 \delta (R - I) + b_3 \\
r - R &= a_4 (V - R) + b_4 & \delta (r - R) &= a_4 \delta (V - R) + b_4 \\
u - g &= a_5 (U - B) + b_5 (B - V) + c_5 & \delta (u - g) &= a_5 \delta (U - B) + b_5 \delta (B - V) + c_5 \\
g - B &= a_6 (B - V) + b_6 & \delta (g - B) &= a_6 \delta (B - V) + b_6 \\
g - r &= a_7 (V - R) + b_7 & \delta (g - r) &= a_7 \delta (V - R) + b_7 \\
i - I &= a_8 (R - I) + b_8 & \delta (i - I) &= a_8 \delta (R - I) + b_8
\end{aligned}
$$

Table 2.2: Coefficients for the 'global' transformations between *UBVRI* and *ugriz*. This table is a reproduction of Table 3 in the paper from Jordi *et al* (2006).

Colour	Colour Term	Zeropoint	Range
$g - V$	$(0.630 \pm 0.002)(B - V)$	$-(0.124 \pm 0.002)$	
$r - i$	$(1.007 \pm 0.005)(R - I)$	$-(0.236 \pm 0.003)$	
$r - z$	$(1.584 \pm 0.008)(R - I)$	$-(0.386 \pm 0.005)$	
$r - R$	$(0.267 \pm 0.005)(V - R)$	$+(0.088 \pm 0.003)$	$(V - R) \leq 0.93$
$r - R$	$(0.77 \pm 0.04)(V - R)$	$-(0.37 \pm 0.04)$	$(-0.37 \pm 0.04) > 0.93$
$u - g$	$(0.750 \pm 0.050)(U - B) + (0.770 \pm 0.070)(B - V)$	$+(0.720 \pm 0.040)$	
$g - B$	$-(0.370 \pm 0.002)(B - V)$	$-(0.124 \pm 0.002)$	
$g - r$	$(1.646 \pm 0.008)(V - R)$	$-(0.139 \pm 0.004)$	
$i - I$	$(0.247 \pm 0.003)(R - I)$	$+(0.329 \pm 0.002)$	

The set of equations for the errors directly follows from the original set of transformation equations. The equations work in general for standard stars. Other transformation equations from the SDSS to Johnsons-Cousins system were derived by Jester *et al* (2005) for stars and redshift ≤ 2.1 quasars, Karaali *et al* (2005) for stars, Bilir *et al* (2005) for dwarf stars, West *et al* (2005) for M and L dwarf stars, and Rodgers *et al* (2006) for main sequence stars. Each set of equations differ from the others, and may work the best for the calibration of a specific type of observation. The point that is made with the different sets of calibration equations is that there is no rule set in stone when transforming from one photometric system to another, irrespective of the wavelength regime that is being used. It is a complex and difficult problem when deciding which photometric system should be used when performing photometric studies, and whether it will be necessary to convert the measurements to a different photometric system. Even when well calibrated photometric equations are used on observations with small errors, there are systematic errors which arise when converting from one photometric system to another. This Implies that magnitudes and colours which were transformed from one photometric system to another may have uncertainties/errors larger than the magnitudes measured in a native photometric system.

2.2.2.3 Completeness of photometric studies

A measurement to the quality of the photometry that is performed on an image, specifically when studying open clusters is, the completeness of source detection on the image. The completeness of source detection is described by Chiu *et al* (2016) as an indication of the fraction of the objects which are detected above a specific detection threshold above the noise level on an image. The completeness is inversely proportional to the detection threshold, meaning that the completeness decreases with an increasing detection threshold because the required signal-to-noise ratio of a source is higher. With an increased threshold the quality of source detection also increases, meaning that the number of sources which are not spuriously detected by the detection becomes higher.

The completeness can be quantified relative to a the number of sources detected in terms of a limiting magnitude. The number of sources which are detected by the analysis software can be compared too the number of sources which are detected in an image with a longer exposure time, or which was stacked from more than one image. This becomes important for stacked images, or a study where

faint sources are of scientific interest. By comparing the number of sources that were detected over a normalised area between two different images will aide in determining a limiting magnitude. Another way of determining the completeness, is to use the uncertainties in measured magnitudes of the detected sources as a function of the observations' depth.

Rykoff *et al* (2015) gives a relation between the uncertainty in a magnitude and the completeness measured relative to the limiting magnitude of the survey. In Figure 2.17 the completeness is shown for extra-Galactic sources from the SDSS survey. It was shown that the completeness can be approximated with a simple linear function, in the form of:

$$c = (e/2)\left[1 - \mathrm{erf}\left(\frac{m - m_0}{\sqrt{2w}}\right)\right] \tag{2.69}$$

Rykoff *et al* (2015) showed that when using the uncertainty plotted against the magnitude measured, a cut-off magnitude can be chosen. Accordingly the fraction of observations which are brighter than the chosen magnitude, or have an error smaller than the co-responding cut-off uncertainty can be used to calculate the completeness of the chosen set.

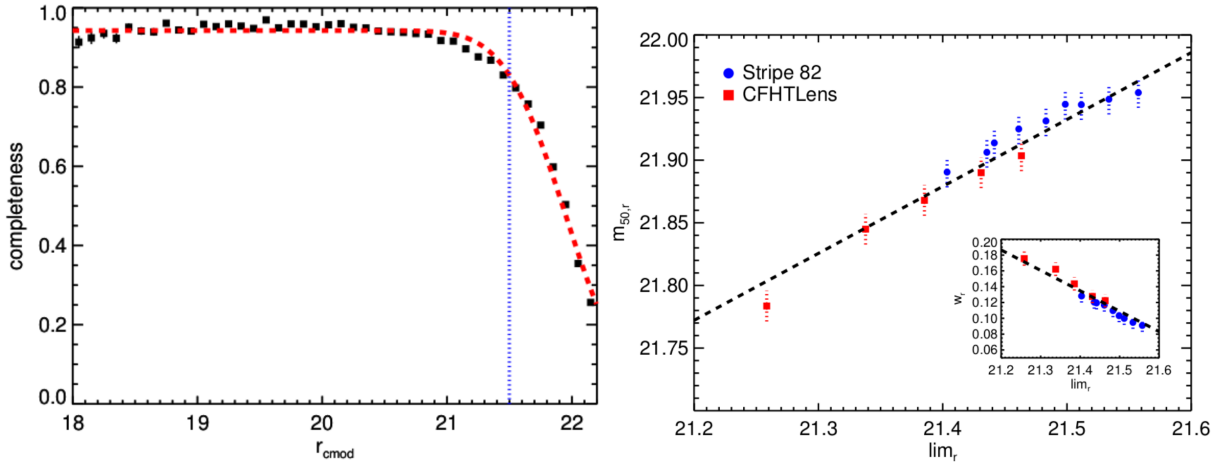

Figure 2.17: Both panels were taken from Rykoff *et al* (2015). The left panel shows the completeness as a function of the r_{cmod} magnitude for the 8'th data release of the SDSS. The red dashed line shows the fit of a functional form equation for the completeness measure for galaxies (equation 2.69) observed with the SDSS. The blue dotted line shows the 10σ limiting magnitude. The errors are smaller than the data points, except for the brightest magnitudes. The right panel shows the completeness parameter m_{50} at which 50% of the galaxies were detected as a function of the local depth measured from r_{cmod} in the left panel.

2.2.3 Colour-colour diagrams

The most useful tool for analysing the stars in a young stellar population is a $(J - H)/(H - K_s)$ colour-colour diagram. To determine which spectral class a specific star is and if it is a main sequence star, its colours have to be compared to the intrinsic colours of each spectral class. In the literature it is shown that each spectral type has a set of intrinsic photometric colours on the main sequence. Different main sequences are shown in Figure 2.18.

Figure 2.18 shows three different versions of the main sequence that were taken from the literature. Each main sequence by Koornneef (1983), Straižys & Lazauskaitė (2009), and the website of Mamajek (`http://www.pas.rochester.edu/emamajek/EEM_dwarf_UBVIJHK_colors_Teff.txt`) show the intrinsic colours that were measured and corrected for extinction of every stellar spectral type. The three main sequences do not show the exact same colours for different spectral types, but it does show that there is a high level of agreement between the colours of specific spectral classes. If the error of each spectral type's intrinsic colours and the different distributions of the main sequence are all considered to be correct, then it can not be seen as an infinitesimally thin line. The main

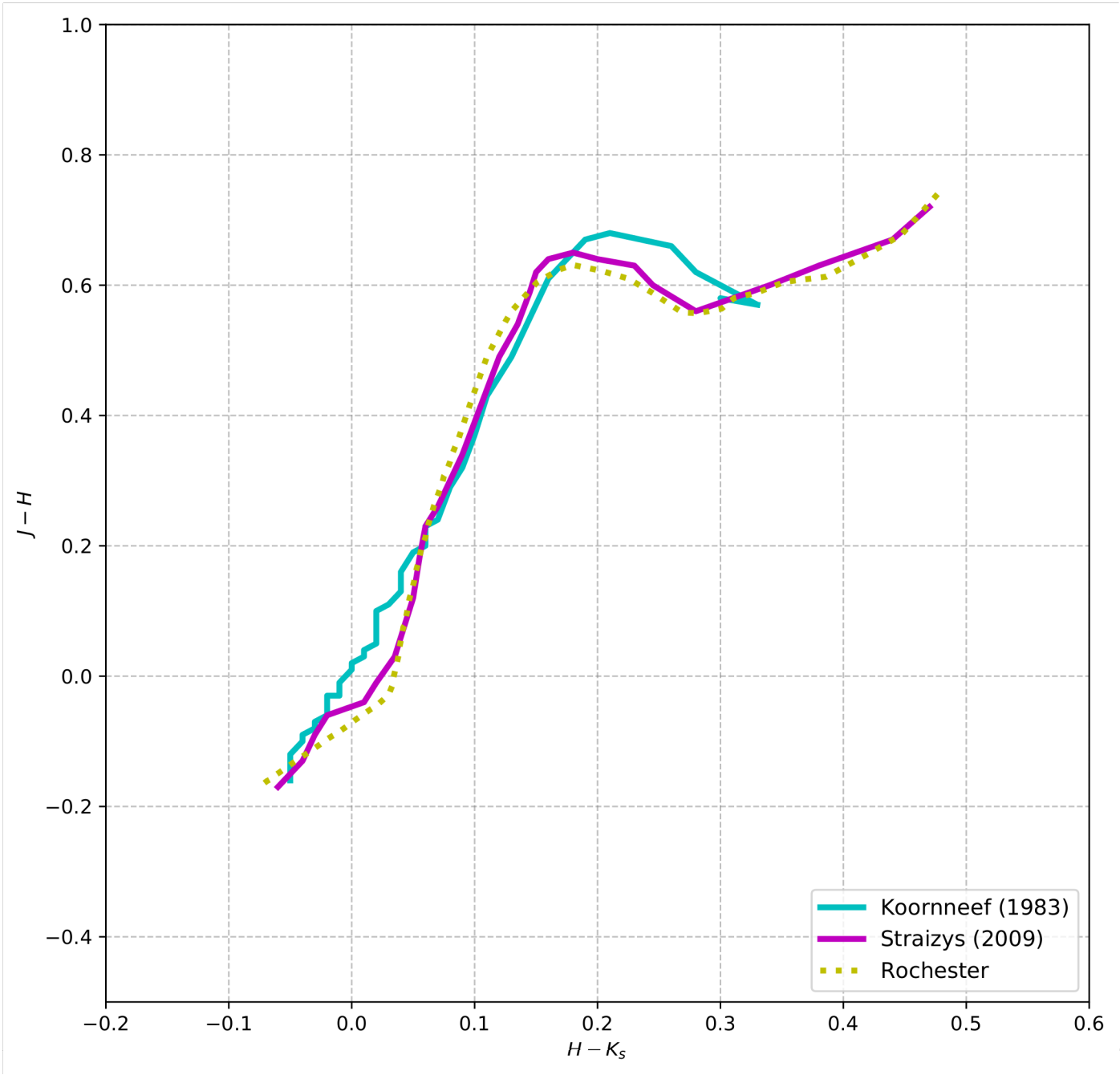

Figure 2.18: The intrinsic colours for different sprectral class main sequence stars are plotted as they are given by Koornneef (1983) and Straižys & Lazauskaitė (2009). A combination of data from Pecaut & Mamajek (2013) and Pecaut *et al* (2012) was taken for dwarf stars which was compiled by Eric Mamajek and is publicly available from his website (`http://www.pas.rochester.edu/emamajek/EEM_dwarf_UBVIJHK_colors_Teff.txt`).

sequence should rather be described as a distribution that has the profile of a thick band. This is the general case for any representation of the main sequence of stars on a color-colour, colour-magnitude or Hertzsprung-Russel diagram. For a detailed description see Carroll & Ostlie (2006), Collins (2003), Hansen *et al* (2004), Kippenhahn *et al* (2012), and Russell (1913).

Figure 2.19 shows the distribution of dwarfs in the Galactic polar region on a colour-colour and colour-magnitude diagram. The $(J-H)/(J-K_s)$ colour-colour diagram shows the thickness of the main

sequence of dwarf stars that are observed in the Galactic polar region. This region was specifically chosen because there is very low extinction. The main sequence on a $(J-H)/(H-K_s)$ colour-colour diagram will have a similar distribution, which is not just illustrated by a thin line, but a broad colour-distribution. For classification purposes the main sequence from the study by Koornneef (1983) will be used for this study, because it is the best representation of the intrinsic colours of each spectral type.

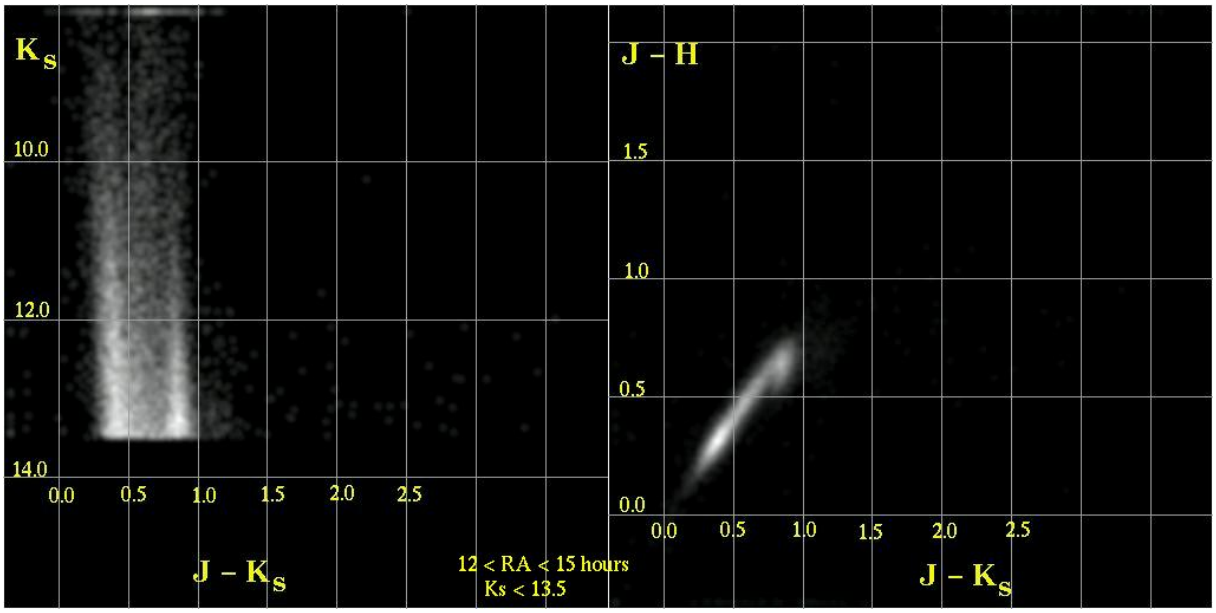

Figure 2.19: The dwarf field stars in the *2MASS* catalogue that were observed over the Galactic polar region $12 < RA < 15$, and were brighter than $K_s < 13.5$. This set of images were taken from the *2MASS* website.

Figure 2.20 shows the main sequence from Koornneef (1983) together with the two outer most reddening lines at O3 and M4 stars. The light from any star that is observed will be subject to interstellar extinction and will appear in the region marked with the red ellipse. The area that is represented by the blue ellipse is the most probable area where reddened field stars may appear, but in reality, a reddened star can lie anywhere around this area, or around the main sequence. The area represented by the blue ellipse only shows the stars that can be dereddened to a specific spectral type on the main sequence. If a star's light only interacts with the material in the Galactic plane, then the extinction is proportional to the distance to the star, and is given by Whittet (1992) as $\langle A_V \rangle = 1.8$ kpc^{-1}. The observed colours of the stars in the Galactic plane will show reddening, similar to the colours of the stars in Figure 2.21.

A young PMS star will show intrinsic excess emission in its *NIR* colours due to heated dust in an accompanying accretion disk. Meyer *et al* (1997) showed that there exists an empirical indicator for the excess emission shown by CTTs, called the CTT locus. The CTT locus and its upper and lower 1σ limits are the green dashed lines in Figure 2.20. It is very rare to see an unembedded CTTs free from its parental molecular cloud. Such a case would place its colours somewhere between the upper and lower limits of the CTT locus. However, in most cases, a CTTs would be reddened and fall somewhere in the region of the blue ellipse, above the CTT locus' upper limit in the area of the yellow ellipse.

Lada & Adams (1992) explains that class 0/I infrared sources, or protostars, may also appear in the regions above the yellow ellipse, but they are usually much further away from the CTT locus. They are usually found in the area shown by the pink ellipse and may have more extinction. They may lie at higher extinction than the pink ellipse. The extinction for these sources is usually between 10-40 A_V ($\simeq 1 - 4A_{K_s}$). It is unusual to find CTTs that are so reddened, so a rough distinction is made between a class I and class II IR source based on the extinction that they show in their *NIR* colours. The distinctive regions are shown with the yellow and pink ellipses. The Herbig Ae/Be separation line

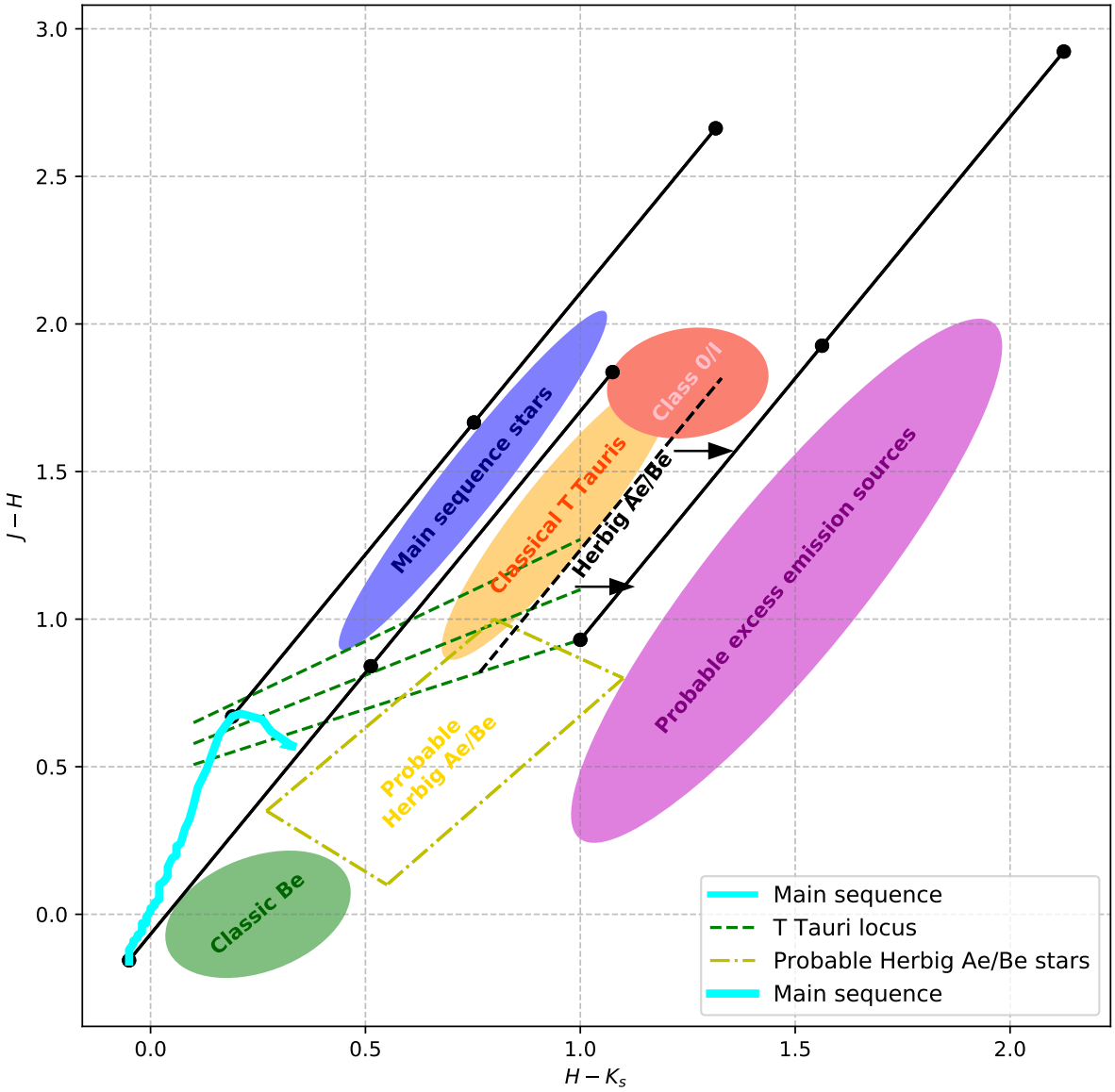

Figure 2.20: An *NIR* colour-colour showing the intrinsic colours of main sequence stars, reddening vectors with $A_{K_s} = 1$, intervals and the regions where PMS stars will appear.

is plotted as the black dashed line, and if a star shows so much excess emission that it lies past this specific line, then it is most likely a Herbig Ae/Be star (see Lee *et al* 2005). If a source has significantly more excess emission than the Herbig Ae/Be separation line, in the region of the purple ellipse, then it can either be a flat-spectrum excess emission source, or a Class I IR object. With so much excess emission it is not possible to determine which type of source it is. If a source lies below the lower limit of the CTT locus, in the areas outlined by the yellow rectangle, then it is most likely a Herbig Ae/Be star (see Hernández *et al* 2005). For this region, it is not possible to say with certainty whether a source is a Herbig Ae/Be star. If a star lies between the yellow rectangle and the main sequence, then it most likely a classic Be star (see Lee & Chen 2009).

WTTs are not so obvious to identify on a colour-colour diagram, CTTs stars are, because the photosphere is already visible with very little contributing emission from an accretion disk. There may still be enough heated dust around the star that it has excess emission and it lies somewhere between the CTT locus and a particular spectral class on the main sequence.

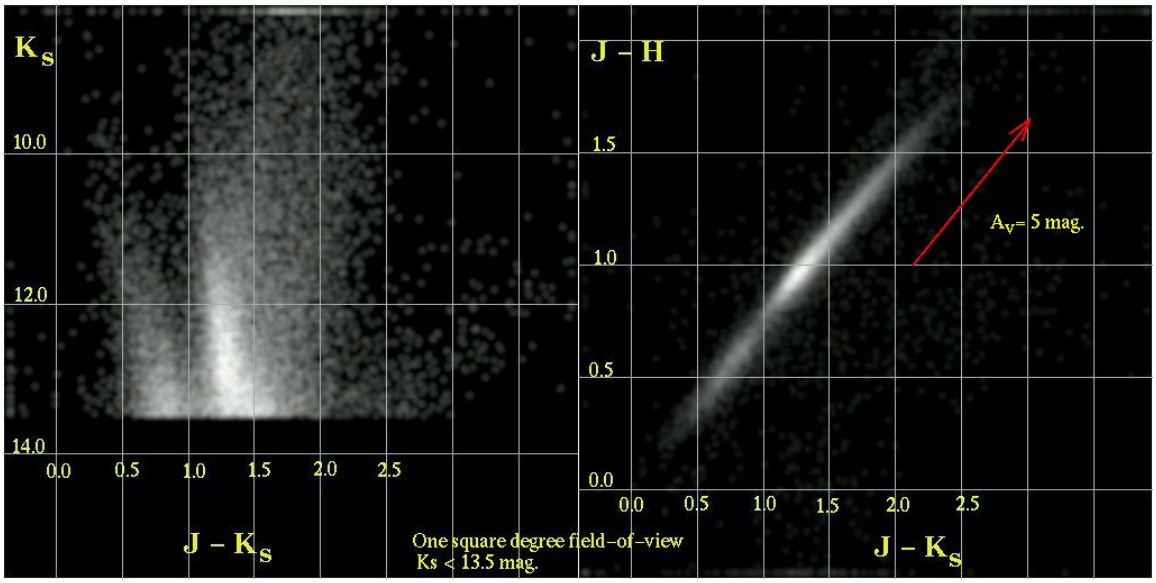

Figure 2.21: All of the dwarf field stars in the *2MASS* catalogue that were observed with magnitudes brighter than $K_s < 13.5$.

2.2.4 Colour-magnitude diagrams

Colour-colour diagrams are very useful for identifying sources that show excess emission due to circumstellar material, but there is no known way in identifying at what evolutionary stage a PMS star is. A colour-magnitude diagram (CMD) can be used to gauge at what evolutionary stage a PMS star is. However, CMD is a representation of a Hertzsprung-Russel diagram where the magnitude is a representation of a star's luminosity, and the colour is a representation of its temperature (see Devorkin 1977).

In Figure 2.22 different isochrones were calculated for various ages using the theoretical models by Siess *et al* (2000) together with evolutionary lines for discrete stellar masses. An evolutionary line suggests that a PMS star will start with a luminosity higher, and temperature lower than it would have on the main sequence. As a PMS star matures over the first 3 Myr, it accumulates more matter from its accompanying accretion disk. This increases its mass which contracts the radial size due to a stronger gravitational field. The radial contraction causes the effective surface area emitting radiation to shrink, and the radiation flux from the photosphere to reduce (see Sandage 1956 and Stahler 1983). A smaller area for the photosphere implies a lower luminosity and an increase in the temperature, due to a much higher internal pressure (see Hansen *et al* 2004, Henyey *et al* 1955, and Hayashi 1961). The lower luminosity will result in a smaller intensity of the emitted light, and the increased temperature implies that the measured colours become brighter. The magnitude of the colour additionally decreases, because the accretion disk dissipates at higher temperature, so there is no more excess emission.

It is possible to characterise the properties of a young cluster using just the apparent magnitudes on a colour-magnitude diagram. The distance modulus first has to be deduced from the apparent magnitudes that were observed for the cluster members. If the cluster members have been corrected for distance, and it is possible to correct them for extinction, then a colour-magnitude diagram will give an estimate to the spectral class and the age for each star.

Chapter 3 will describe how the observational data was obtained and reduced. A section in Chapter 3 describes how the data was used to derive a custom extinction law and build an extinction map from the field stars behind RCW 34 and NGC 2626. By using the extinction maps the populations of stars showing excess emission in RCW 34 and NGC 2626 can be dereddened and properly studied; extra attention is given to the excess emission sources in the last section of Chapter 3.

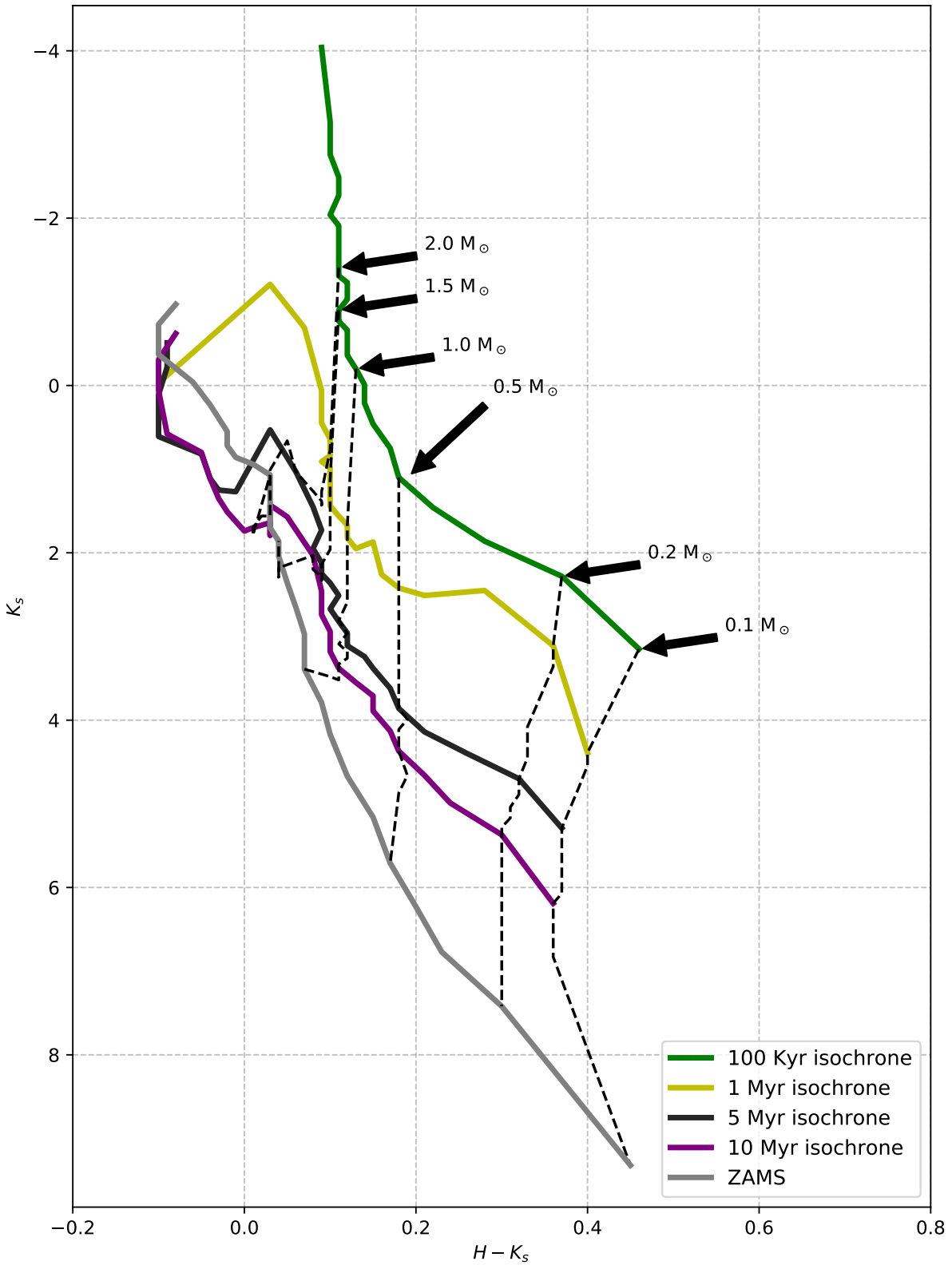

Figure 2.22: A colour-magnitude diagram that shows isochrones from 10^5 yr up to the main sequence, as well as the evolutionary lines that different stellar spectral types will follow in between the different isochrones up to the main sequence.

CHAPTER 3: NEAR-INFRARED IMAGING AND EXTINCTION MAPS

3.1 Introduction

This chapter gives a description of the data acquisition, reduction, and the results of the near-infrared imaging used to determine properties of the two high-mass star-forming regions RCW 34 and NGC 2626. The chapter starts with a section on the data acquisition and then details how an automated reduction pipeline was written to speedily reduce the large datasets into usable results. The results were used to derive a custom extinction law, construct an extinction map of each star-forming region, and also identify which stars present excess *NIR* emission, characteristic to PMS stars. The chapter ends with a two part analysis. First there is an analysis of the spatial distribution of the stars with excess emission, and secondly where they lie relative to the high-mass star, molecular cloud, and other stars in the field surrounding each star-forming region.

3.2 Data acquisition and reduction

3.2.1 Observations

The telescope that was used for the *NIR* imaging in this project is the 1.4-m Infrared Survey Facility *IRSF* telescope at SAAO, Sutherland. The imaging instrument used was the SIRIUS camera, which has a $7.7' \times 7.7'$ field of view, and a pixel resolution of 1024×1024 pixels on HAWAII detectors. The camera splits the beam of incident light into three seperate beams so that the J, H, and K_s imaging is done simultaneously. Each imager is identical and has a gain of $5.0e^-$/ADU and read-out noise of $30e^-$. The pixel scale for the SIRIUS camera is $0.457''$ per pixel. Images that are taken with a *NIR* imager need to be dithered, because the detectors usually have large bad areas that consist of hot or dead pixels/columns.

The observations used in this project were conducted on different dates. The first set of observations of NGC 2626 and RCW 34 were made by GG Nyambuya in 2005. This set of observations was performed for a different reason than for this study, but the data fulfills the requirements for this project. A second, third, and fourth set of observations on RCW 34 were performed by the author during January 2012, October 2013, and January 2014. Some of the data obtained during 2012 was unusable due to a malfunction on the cold shutter, causing it not to open all the way, resulting in thermal contamination on some of the images. The observations that were done in October 2013 were done in the wrong season, resulting in the source only being visible after 02:30 in the morning. The time that the source was visible at an airmass low enough to detect the faint cluster members that are the main focus of this project, was an hour before dawn. To gain deep imaging, many dedicated hours of observations at low airmass were required.

In 2014 a larger field around RCW 34 was observed with the goal to construct a mosaicked image spanning $\sim 16' \times 16'$. The mosaic was built from observations in the N, S, E, W, NE, NW, SE, and SW direction, each with a $250''$ offset from the central star VdBH 25a. The observations on each of the off-set fields were done to the same total exposure time. They also had enough of an overlap so that a complete image, without gaps, could be built.

During the observations of 2014, a set of standard stars selected from Persson *et al* (1998) were also observed in the first and second observation run. They were selected because they are the stars in the catalogue closest in proximity to RCW 34 and NGC 2626. These stars were supposed to be observed

for calibrating each of the dithered observations, and an analysis of members that presented variability was also supposed to be done. This variability analysis turned out to be beyond the scope of this project, due to time constraints.

A *NIR* imager is sensitive to temperature fluctuations, which means that dark images were taken at the beginning and the end of each night. Flat field images were only observed on 13 January 2014; not many were taken because they only served as a back-up plan, if the master flat fields in the reduction software packages did not deliver good reduced images.

The reduction process was used to build a single image from a set of dithered images. A set would be a standard collection of 10 images dithered with a $20''$ radius around a central point, each having an exposure time of 30 seconds. The resulting image was a median combination of the ten images, totalling 5 minutes of exposure time and pointing to the central point of the dithering radius.

3.2.2 Reduction

The total storage size of the unreduced data was $\sim$ 185 GB, and reducing the data by hand with a package like `IRAF` resulted in a monumental task. The owners of the telescope at the University of Nagoya were contacted to ask about a reduction pipeline. They were in the process of switching from an old *perl* based pipeline to a new *PyRAF* version (*PyRAF* is a Python shell that can call `IRAF` tasks). This Python-based pipeline, *pyIRSF* is terminal based and runs various commands in the following order:

1. Put the raw frames taken on a specific date in a directory `rawdata`.

2. Create a working directory where the observational logs and parameter files are stored. Then run `mkobslog.py` in the working directory so that all of the headers for the files in the `../rawdata/` directory are read and an observational log `obslog` is created. Inspect the `obslog` file and remove all entries for flat field images.

3. After a set of custom flat field images are created they must be put into the working directory.

4. Run the command `sirius.py param` to create the parameter file `sirius.param` that will be used by the pipeline. This file needs to be edited so that the correct operations are done when the pipeline is run. In order to edit the file the following decisions must be made:
   - Whether to reduce only a single band's images or all of the images.
   - Whether the pre-made flat field images or the master flat field images should be used.
   - At what reduction step should the pipeline be stopped: after dark and flat correction, sky subtraction, or after all of these reduction steps?
   - Whether cosmic rays should be removed.
   - The images be corrected for linearity.
   - Whether the pipeline should use the `cfitsio` library for compressed FITS files.
   - Whether all of the images that were taken of the same object, should be combined.

   For all of the *NIR* data, the images were corrected for cosmic rays and linearity; and the master flat field images were used.

5. Next the command `sirius.py set` is executed to build the file lists for the dithered images that should be combined. The file lists containing the sky images are also compiled.

6. The pipeline is executed by running `sirius.py run` so that the bias correction and dark current frame is subtracted from each science image, and is divided by the flat field image. Thereafter the sky is subtracted, and the dithered images are median combined into a usable science image.

7. Once the pipeline is done producing the science images, World Coordinate system (WCS) needs to be projected into the headers. In the *pyIRSF* pipeline a script by the name `sirwcs2.py`

is supplied that queries an online catalogue and calculates the WCS transformations. This is done by taking the Right ascension (RA) and Declination (DEC) coordinates from the science image's header, and downloading the catalogue entries for the stars close to those coordinates from the *2MASS* survey. The script then detects the brightest unsaturated stars in the science image and runs a pattern recognition algorithm between the survey sources and those detected in the science image. Once the WCS transformations have been calculated, they are written to the science image's header.

When all of the science images had been reduced, and the WCS transformations had been applied, it was possible to combine these images into a stacked image. From this deep image, it was possible to detect and analyse the faintest sources that were deeply embedded in the parental molecular cloud.

For the deep image stacking the *MONTAGE* software package was used. This is an automated mosaicing package that was developed by NASA using an adapted version of the MOPEX, an algorithm which was conceptualised and developed by the Spitzer Science Center[1]. *MONTAGE* uses the WCS transformations for an image and a simple star detection algorithm to determine where different images overlap. The package can also be used to match the backgrounds for a mean or median pixel value where the images overlap; the matching can be smoothed using an iterative process.

During the stacking of the deep images, a vignetting effect on each component image had a degrading effect on the outer parts of the built image. This was corrected by trimming off the vignetted area on each of the component images and then building the deep image. Each deep J, H, and K_s image of the mosaicked $16' \times 16'$ image underwent 10 000 background smoothing iterations. This ensured that there were no differential background differences. This made the precision of the photometry that was performed very accurate.

A deep image was built for NGC 2626 from all of the images that were observed in 2005; this deep image was composed of 36 images, each having an exposure time of 300 seconds. This gives a total exposure time of 10 800 seconds (3 hours) in each of the J, H, and K_s bands. To investigate the extent of the cluster associated with RCW 34 the area surrounding the HII region was observed, with 40 component images in the central and seven surrounding fields (∼3h20min exposure time). This extended field span $15.9' \times 15.9'$ is a big enough area to ensure that all of the embedded members, extending up to the outer edges of the cluster would be detected.

3.2.3 Photometric pipeline

To perform precise photometry on the various images, an automated pipeline was written as a `Python` script. The script calls up various `IRAF` and `python` commands in such a manner that it determines the parameters for each image before running the tasks needed for the photometry.

The first step of the pipeline was to determine what would be the most efficient FWHM value for star detection, and then performing PSF photometry. To get this optimal FWHM value for each image an instance of `source extractor (sextractor)` was run to determine where most of the stars on the image were. They are shown in the second slide of Figure 3.2. These stars were detected using a blind value for the detection area parameter in `sextractor`. Next, the stars were sorted according to their instrumental magnitudes, choosing the brightest ones to determine the optimal FWHM. The number of stars that were used to determine the FWHM parameter given to the pipeline was 100. By having the pixel coordinates for each of the brightest stars, the radial extent for each star's profile was determined. This was done by iterative stepping from pixel-to-pixel starting in the central coordinates up to a distance where the number of counts was equal to the background value. The FWHM was calculated as the pixel value where the number of counts was half of the difference between the maximum and the sky-value.

[1]It is funded by the National Science Foundation under Grant Number ACI-1440620, and was previously funded by the National Aeronautics and Space Administration's Earth Science Technology Office, Computation Technologies Project, under Cooperative Agreement Number NCC5-626 between NASA and the California Institute of Technology.

(a) NGC 2626.

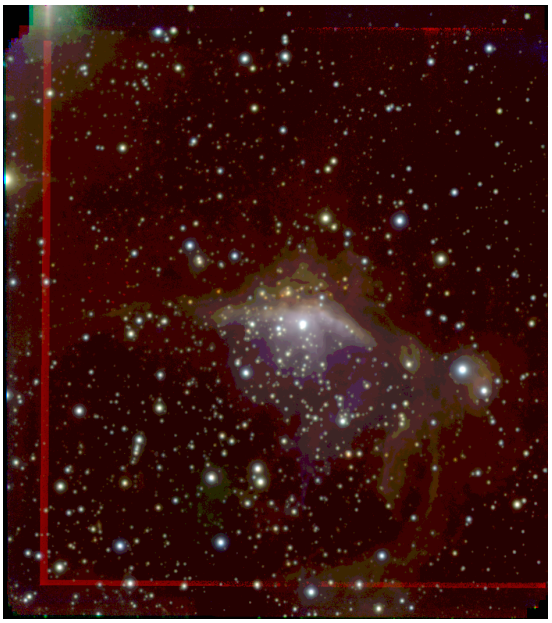

(b) Central part of RCW 34.

(c) Mosaicked region around RCW 34.

Figure 3.1: Pseudo-colour image of the deep stacked image of NGC 2626, the deep central part of RCW 34, and the mosaicked area around RCW 34. The field of view of each panel is $\sim 7.9' \times 7.9'$, $\sim 7' \times 7'$ and $\sim 15.9' \times 15.9'$ respectively. In each image north is towards the top and east is towards the left of each image. The J band is blue, the H band is green, and, the K_s band is red.

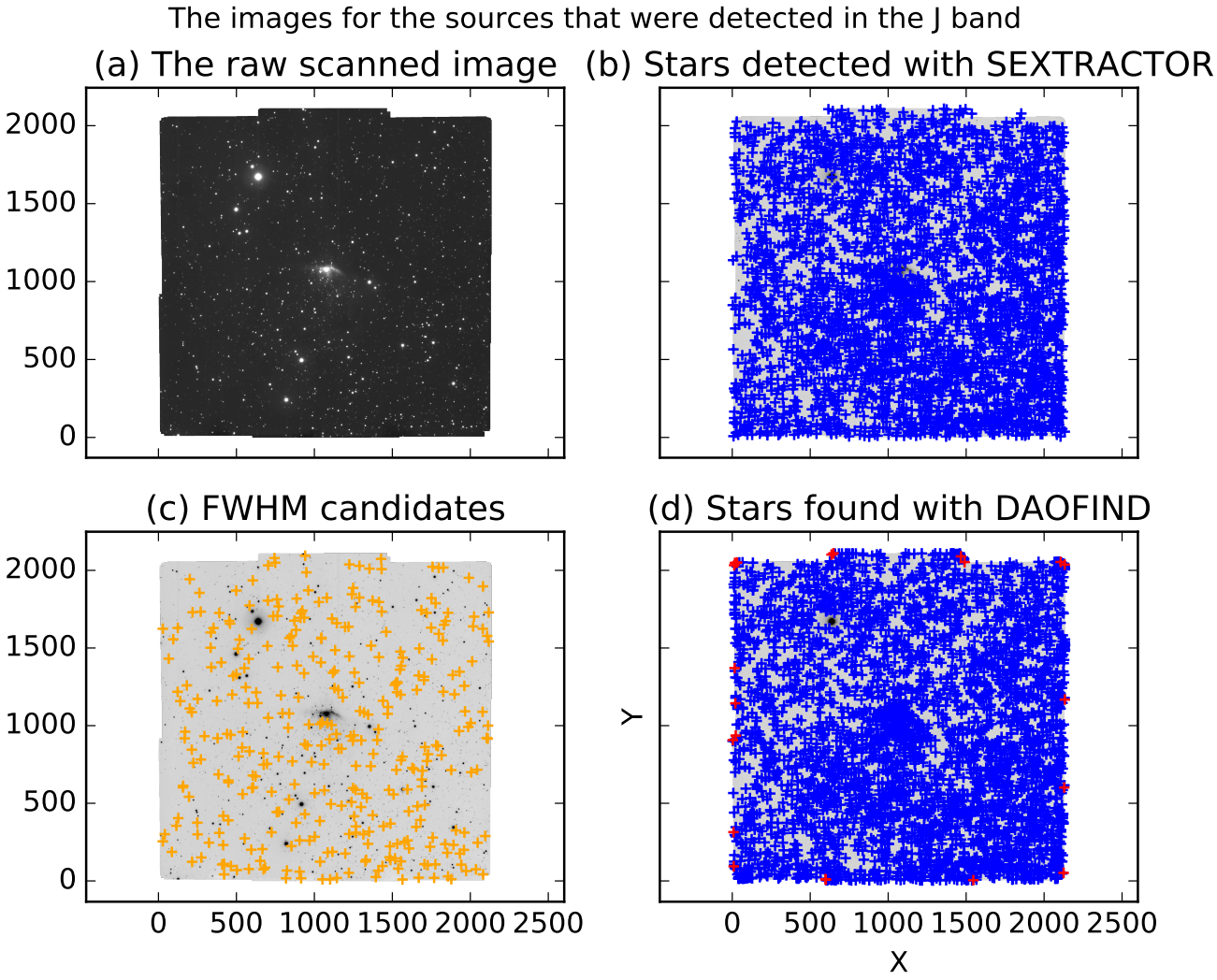

Figure 3.2: Plots for the stars that were detected using `sextractor`, those used to calculate the ideal FWHM for the photometry on the science image, and the stars that were detected using `daofind`. These plots are for the $J-$band mosaicked area surrounding RCW 34 (see Figure 3.1c). On the $x-$ and $y-$axis of each subfigure the pixel coordinates are shown.

Next the `daophot.daofind` routine was run with all of the required parameters to detect most of the stars on the image; they are shown in slide (d) of Figure 3.2. It may seem strange to first run `sextractor` and then `daofind`. However, the reason for this is that `sextractor` runs much faster than `daofind` and the latter writes the coordinate files in the correct format that will be used by packages to perform the photometry. The most important parameters that were required by `daofind` were the sky, detection-threshold, and saturation values. For the SIRIUS camera, the saturation value was 30000 ADUs, and the sky value was measured as the median value across the whole image. A detection threshold of 3σ was used to detect most of the stars on the image.

For the second step, a point-spread function (PSF) needed to be fitted on the brightest unsaturated stars on the image. Those that were used to calculate the FWHM value were also used to construct the PSF. They were used because their emission profiles extend over the largest number of pixels on the image. If a PSF was correctly fitted for these stars it was simply scaled down for the fainter sources. To properly fit a PSF, the stars that were used to fit the PSF fitting should not be too close to other fainter stars. A PSF was fitted using a radius of $2\times$ FWHM. A Poisson noise-distribution

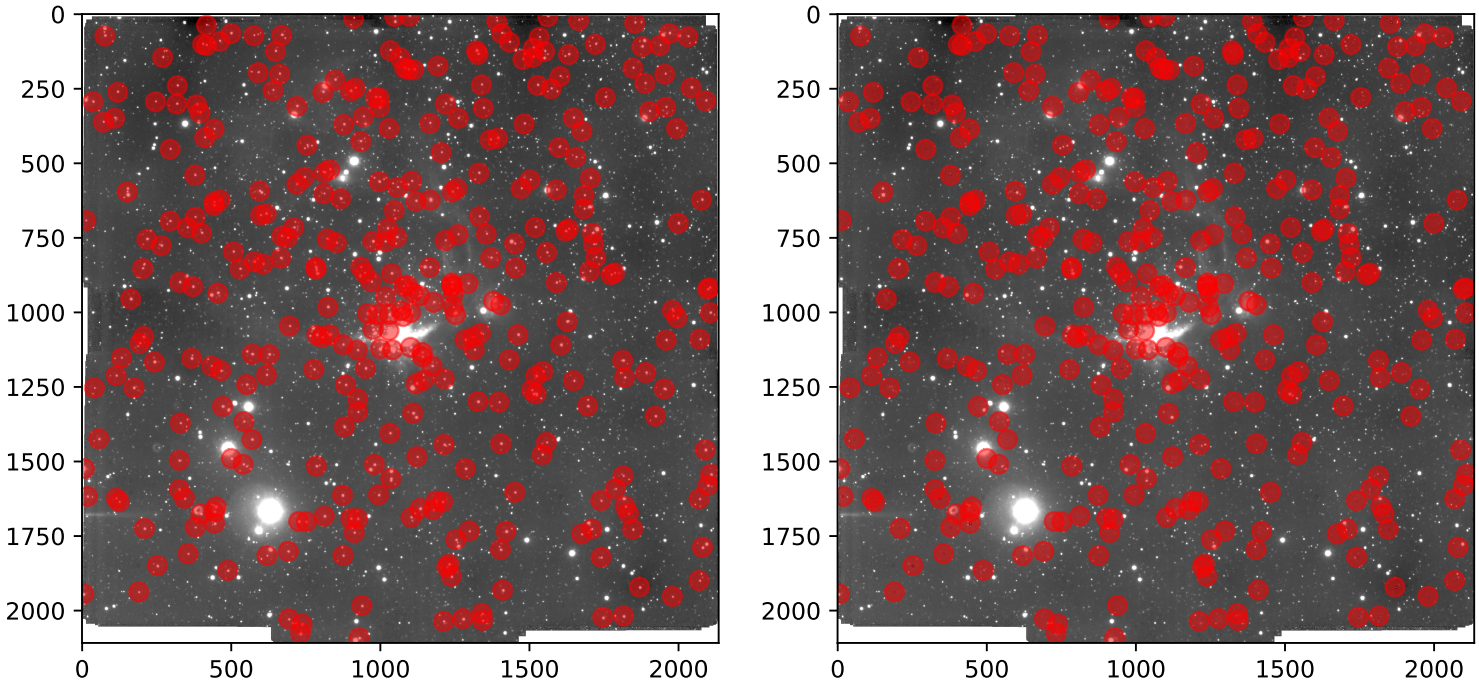

Figure 3.3: The left panel shows the original K_s-band image. The right panel shows where the most prominent stars, that were used to fit the PSF, are subtracted. The positions of these stars, before and after subtraction, were shown with the red dots. The image is plotted on a $\log_{10}$ scale between an upper and lower gray-scale limit of $\log_{10} 10\ 300$ ADU and $\log_{10} 10\ 500$ ADU, which show most of the faint sources and nebulous gas relative to the background.

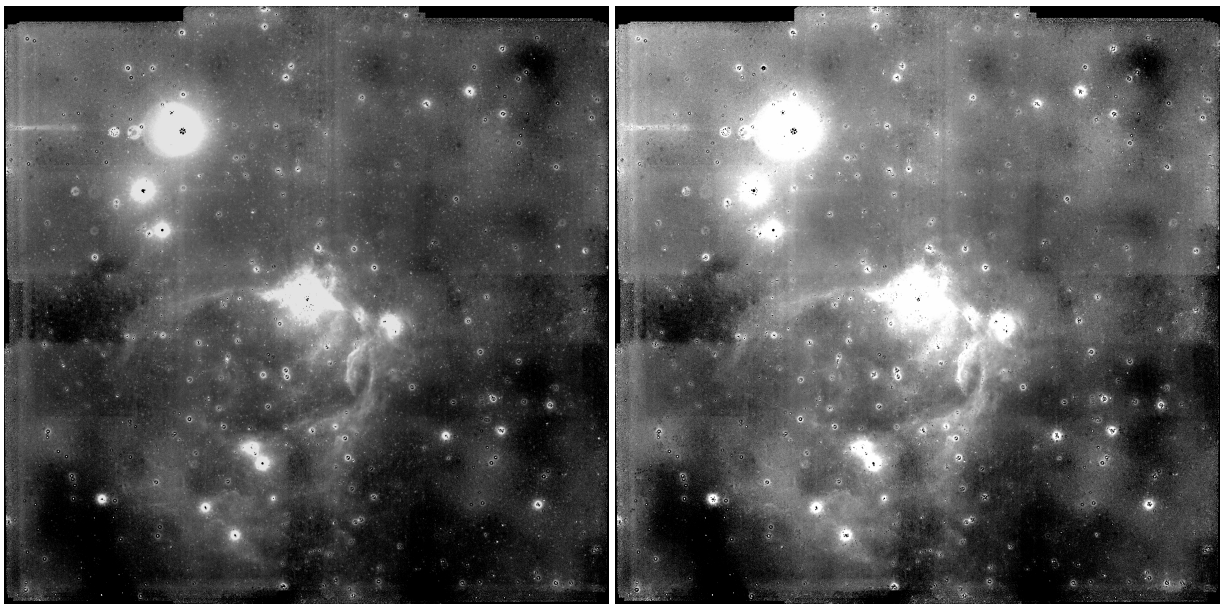

Figure 3.4: The image in the left panel shows all of the bright sources that were subtracted using the PSF. Take note that there are many faint sources that were not detected using the first round of `daofind`. The image in the right panel shows how all of the bright and faint sources were subtracted using the PSF from the original image. The same grayscale limits from Figure 3.3 are used to show how the faint sources were subtracted.

was used to fit the sky. A maximum number of 15 fitting iterations and an upper limit of 50 rejections were chosen to get a smoothed PSF. The quality of the PSF was evaluated on how well the profiles of the stars that were used to construct the PSF were subtracted from the original image.

The newly constructed PSF was then used on all of the stars that were detected by `daofind`. It was scaled to the magnitude that was measured by the aperture photometry earlier on. By using the PSF, the typical stellar profile of the stars in the cluster was modelled for the best fit. Precision photometry like this is very important for crowded fields like the cluster associated with RCW 34 and NGC 2626. This is because aperture photometry can not be used due to the proximity of the stars to each other. The PSF was then evaluated for all of the stars that were subtracted by visually inspecting the image after the PSF was subtracted for each star. If a very good fit was accomplished only the background of the image, devoid of stars, would be seen.

In the stacked images that were used in this project, there were usually very faint cluster members that would not be detected by the first run of `daofind`. With a proper PSF subtraction on all of the stars that were detected by `daofind` in the first round, their emission profiles should have had no leftover light, and the light measured at their positions should have been indistinguishable from the background. The second round of stellar detection were then run on the image from which the fainter stars that were not detected in the previous subtraction round were removed with the fitted PSF. These were easily detected with a lower σ threshold, because the fainter stars would be more distinguishable from the background than in the initial image, since all of the brighter sources were now subtracted. These fainter stars would now be concatenated into the initial file with pixel coordinates of detected sources. The PSF fitting was then run on the stars that were detected in the first and second round of detection. The fainter sources required that all of the stars on the image be correctly grouped when the PSF is fitted for each star. Once the PSF had been fitted on each of the stars on the image, and they have been subtracted, the resulting image should have been void of any stars. Only the black background and some nebulous gas would be left.

The pipeline was run on each image. The final photometric files of the mosaicked image that contained the instrumental magnitudes that, were measured by the pipeline were all read into a data file. The data files for the J, H, and K_s instrumental magnitudes were individually transformed from pixel to WCS coordinates, using the coordinate transformations from each of the fit images. After the photometric measurements were finished, the pipeline wrote the correctly measured instrumental magnitudes, pixel coordinates, and RA/DEC to an `ascii` data file.

3.2.4 Calibration to the *2MASS* system

With the realisation of the calibration mistake that was made in the study by de Villiers (2009) (see section 1.4 for the discussion), various calibration experiments were performed with different sets of the data to be sure that calibration was performed correctly for this project. It was decided to transform the instrumental *IRSF* magnitudes and colours to the *2MASS* system. The effect of transforming the magnitudes and colours for images that were observed at different airmasses to the *2MASS* was investigated. This was to ensure that the transformation of the same stars in the same field would come down to the same values in the *2MASS* system. The calibration of the same sources that were observed at different airmasses is a very valid test for the calibration that will be performed on all of the observed images. The reason for this is that it ensures that the calibration is not incorrect as in the previous deep *NIR* study on RCW 34. It also tests how well the calibration of a highly reddened magnitude and colour of the same sources compares to a much less reddened measurement. If the calibrated colours and magnitudes at high and low airmass agree, then the calibration method that will be used for the mosaicked images will be correct.

In Figure 3.5 the colours and magnitudes calibrated to the *2MASS* system of two images that were observed at different airmasses are shown. The observations of RCW 34 were obtained on the night of 11 February 2014 at 21:30 and the following morning at 02:00, respectively, at an airmass of 1.708 and 1.018. To test the effects that the calibration would have on a stacked image, the two images were combined in the same manner as the stacked images, using the `MONTAGE` package. This was done by building a median combined image from the low and high airmass images.

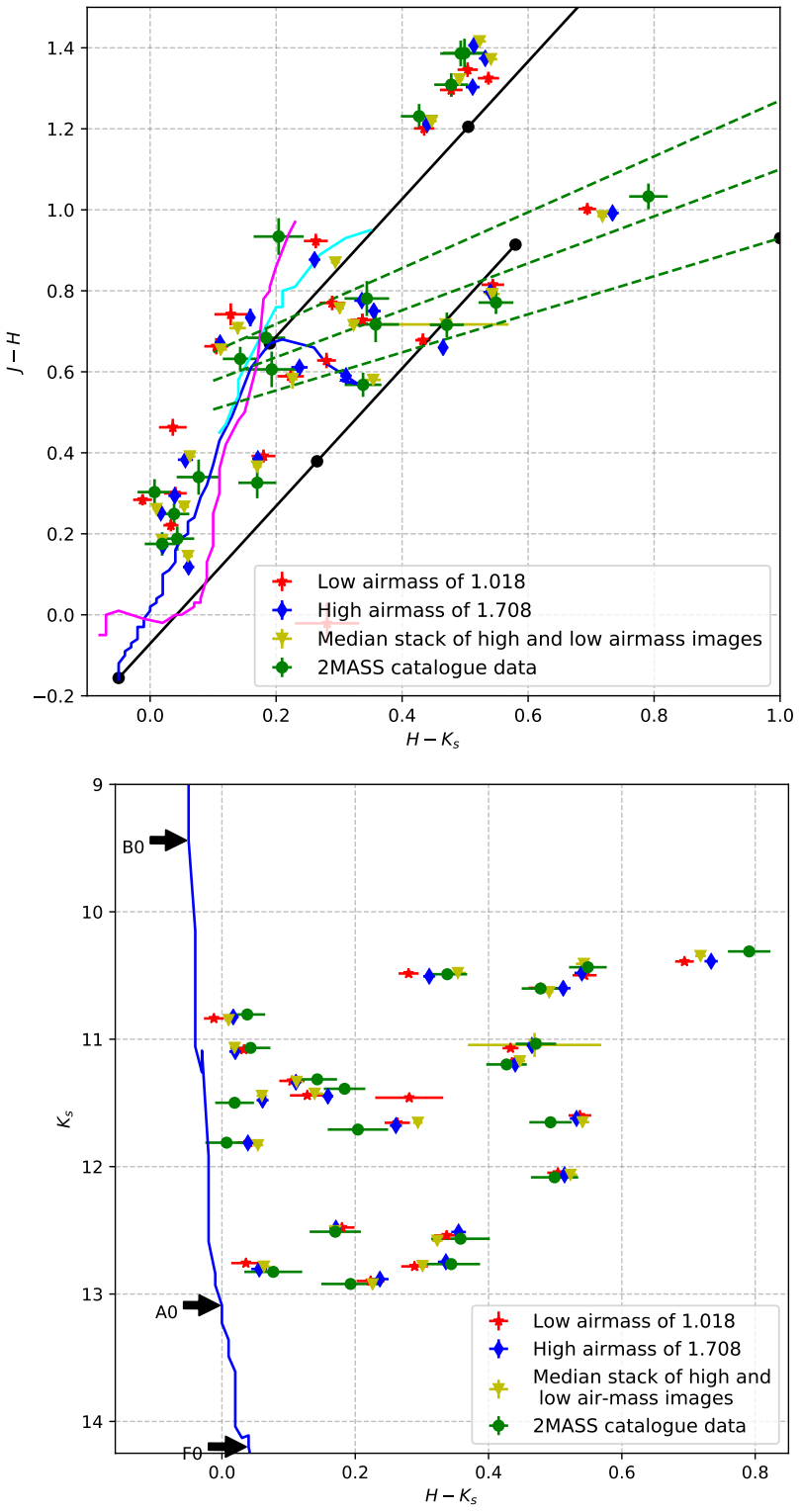

Figure 3.5: Demonstration of calibrating directly to the *2MASS* colour system from the *IRSF* colour system. The brightest 20 unsaturated stars in each image were chosen, calibrated to the *2MASS* system and plotted alongside its colours from the *2MASS* catalogue. The first diagram shows the calibrated $(J-H)$ and $(H-K_s)$ colours that were transformed in equations 3.4, 3.8, and 3.12. The second diagram shows the calibrated K_s and $(H-K_s)$ colours and magnitudes that were transformed with equations 3.4, 3.8, and 3.12.

The first image of Figure 3.5 shows a set of colours that were transformed from the instrumental colours to the *2MASS* colours. The second image shows magnitudes that were transformed from the instrumental magnitudes to the *2MASS* system, which included a $(H - K_s)$ colour correction. The transformation equations that were used for the calibration of the high airmass and low airmass instrumental observations to the *2MASS* system are:

$$(J-H)_{2MASS}^{\text{Stacked}} = 1.1175 \times (J-H)_{IRSF}^{\text{Stacked}} - 0.1937 \tag{3.1}$$
$$(H-K)_{2MASS}^{\text{Stacked}} = 1.0485 \times (H-K)_{IRSF}^{\text{Stacked}} + 0.8064 \tag{3.2}$$
$$K_{2MASS}^{\text{Stacked}} = K_{IRSF}^{\text{Stacked}} - 0.0578 \times (H-K)_{IRSF}^{\text{Stacked}} - 1.4085 \tag{3.3}$$
$$\tag{3.4}$$

$$(J-H)_{2MASS}^{\text{Low airmass}} = 1.0907 \times (J-H)_{IRSF}^{\text{Low airmass}} - 0.2238 \tag{3.5}$$
$$(H-K)_{2MASS}^{\text{Low airmass}} = 1.0703 \times (H-K)_{IRSF}^{\text{Low airmass}} + 0.8558 \tag{3.6}$$
$$K_{2MASS}^{\text{Low airmass}} = K_{IRSF}^{\text{Low airmass}} + 0.0587 \times (H-K)_{IRSF}^{\text{Low airmass}} - 5.3970 \tag{3.7}$$
$$\tag{3.8}$$

$$(J-H)_{2MASS}^{\text{High airmass}} = 1.0294 \times (J-H)_{IRSF}^{\text{High airmass}} - 0.2307 \tag{3.9}$$
$$(H-K)_{2MASS}^{\text{High airmass}} = 1.0428 \times (H-K)_{IRSF}^{\text{High airmass}} + 0.8299 \tag{3.10}$$
$$K_{2MASS}^{\text{High airmass}} = K_{IRSF}^{\textit{High airmass}} + 0.0877 \times (H-K)_{IRSF}^{\text{High airmass}} - 5.1959 \tag{3.11}$$
$$\tag{3.12}$$

These equations are used to calibrate the measurements of the high and low airmass, and the median stacked image's measured magnitude and colours, to the *2MASS* photometric system. The three sets of transformed magnitudes and colours should be equal to each other, or at least within each other's measured errors. In Figure 3.5 all 20 stars that were used for the calibration to the *2MASS* system are plotted, as well as their original *2MASS* magnitudes and colours. The colour-colour diagram shows that the transformed colours of the high and low airmass, as well as the stacked images, are close to the original *2MASS* data. On the colour-colour diagram the calibrated data group is so close together for each star, that even for a crowded group of measurements close to the main sequence the individual groupings are apparent. On the colour-magnitude diagram the measurements for individual stars are more apparent and show, for example, all of the calibrated measurements of the stars that have $13 \leq K_s \leq 12$. This is very little differences between the 4 data sets. If the errors on the colours of each star are taken into account, the transformed colours and magnitudes are very close to each other, so any transformation of this nature can be accepted as correct. In both the diagrams of Figure 3.5 the calibrated colours and magnitdes of each star group together, indicating that the calibration of stars with different magnitudes are all accurate.

The light profiles from the stars of the image that was taken at higher airmass suffer much more extinction and scattering than those from the low airmass image. This creates larger errors and a worse fit to the PSF than the sources on the low airmass image, yet the calibrated *2MASS* colours and magnitudes are within acceptable thresholds from the other colours and magnitudes. The scattering of the calibrated colours and magnitudes are not within each other's error margins, but close enough that the calibrated colours and magnitudes give an accuracy acceptable for precise photometry. The effects of higher extinction and more scattered light on images that were taken at high airmasses will have a depreciating effect when compared to the images that were observed at very low airmasses. This negatively influences the image that results from the stacking of images at high and at low airmasses. This was taken into account when the deep images were stacked from a large number of images, so that the images which were taken at an airmass higher than 1.5 were not used in the stacking of the

deep images. The varying effects of the quality in measured colours and magnitudes caused by the airmass has to be taken into account when stacking a large number of images together. However, the uncertainties on the 20 stars that were measured on the image that were observed at an airmass of 1.708 are in the same order as the measurements from the images that were taken at an airmass of 1.018. The uncertainties on sources with an apparent magnitude of ~ 20 or fainter, will be significant enough that it will not be as precise as the colours and magnitudes shown in the demonstration of the calibration at different airmasses. When the deep images were stacked it was not necessary to assign a weight to each elementary image based on its airmass because the majority of the images were taken at airmasses lower than 1.2, and those with an airmass higher than 1.5 were removed. If a weight was assigned to the each elementary image based on its airmass, it would make a significant improvement on the uncertainties measured on the sources with an apparent magnitde of 20, or fainter.

It must be kept in mind that when more images are combined into a stacked image, the precision will be higher when the measurements are made from a median combined image. The reason for a higher precision from a stacked image is that the signal (point sources) to noise (the background) ratio of the stacked image is much higher. Photons that do not come from the specific source, but which are incidental on the CCD, compromise the desired signal. These incident photons also carry a statistical variation of fluctuations in the photon arrival rate, which is called the photon noise. There is also inherent CCD noise which creates electrons that are indistinguishable from the photoelectrons. The noise can be reduced by stacking more than one image of the source together. The noise measured from an image that is stacked out of a number N images is reduced by a factor of $\sqrt{N}$.

In Figure 3.5 it is shown that the calibration equations to a standard photometric system for a selected few stars on images that were taken at a high airmass, low airmass, or for a stacked image, the transformed colours and magnitudes were accurate enough in the standard photometric system to be considered equivalent to each other. In other words, the transformed colour and magnitudes of the 20 stars resulted in equivalent *2MASS* colours and magnitudes from the three different images. The direct transformation from the instrumental photometric system to the *2MASS* system is due to the similarities in the JHK_s band in both the *IRSF* and the *2MASS* photometric system. In Table 1.A of the dissertation by Kato (2007) a set of conversion equations between the *IRSF* and *2MASS* photometric systems is given. These equations can be used to transform *IRSF* photometric data which have been calibrated with standard star data to the *2MASS* photometric system. The calibrations for the stacked images in this study will not use the transformation equations from Kato (2007). The calibration is done directly to the *2MASS* system, and not calibrated to the *IRSF* photometric system with standard star data and then to the *2MASS* system.

In both the images of RCW 34 and NGC 2626 the 60 brightest, unsaturared stars which matched in the JHK_s images, and are also present in the *2MASS* catalogue, were selected to calculate the transformation equations between the instrumental colours and magnitudes to the *2MASS* system. The J-magnitudes of the 60 stars used for the calibration ranged between $\sim$9 and $\sim$15 in both the images of RCW 34 and NGC 2626. They were chosen far enough from any other sources so that they did not have any apparent contamination from any other stars.

The transformation equations that were used to calibrate the instrumental colours and magnitudes to the *2MASS* system for RCW 34 are,

$$\begin{aligned}
J_{2MASS} - J_{\rm inst} &= 0.0919 \times (J-H)_{\rm inst} - 4.8814 \\
J_{2MASS} - J_{\rm inst} &= 0.0632 \times (J-K_s)_{\rm inst} - 4.8310 \\
H_{2MASS} - H_{\rm inst} &= 0.0286 \times (J-H)_{\rm inst} - 4.6952 \\
H_{2MASS} - H_{\rm inst} &= 0.1289 \times (H-K_s)_{\rm inst} - 4.6143 \\
K_{2MASS} - K_{\rm inst} &= 0.0644 \times (J-K_s)_{\rm inst} - 5.5137 \\
K_{2MASS} - K_{\rm inst} &= 0.3271 \times (H-K_s)_{\rm inst} - 5.3224
\end{aligned}$$

$$
\begin{aligned}
(J-H)_{2MASS} &= 1.0713 \times (J-H)_{\rm inst} - 0.2104 \\
(J-K_s)_{2MASS} &= 1.0351 \times (J-K_s)_{\rm inst} - 0.6184 \\
(H-K_s)_{2MASS} &= 0.8683 \times (H-K_s)_{\rm inst} - 0.7164.
\end{aligned}
$$

The transformation equations for NGC 2626 are,

$$
\begin{aligned}
J_{2MASS} - J_{\rm inst} &= 0.0187 \times (J-H)_{\rm inst} - 0.7066 \\
J_{2MASS} - J_{\rm inst} &= 0.0055 \times (J-K_s)_{\rm inst} - 0.6865 \\
H_{2MASS} - H_{\rm inst} &= -0.0481 \times (J-H)_{\rm inst} - 0.5004 \\
H_{2MASS} - H_{\rm inst} &= -0.1305 \times (H-K_s)_{\rm inst} - 0.5908 \\
K_{2MASS} - K_{\rm inst} &= -0.0267 \times (J-K_s)_{\rm inst} - 1.3094 \\
K_{2MASS} - K_{\rm inst} &= -0.1001 \times (H-K_s)_{\rm inst} - 1.3587 \\
(J-H)_{2MASS} &= 1.0592 \times (J-H)_{\rm inst} - 0.2039 \\
(J-K_s)_{2MASS} &= 0.9986 \times (J-K_s)_{\rm inst} - 0.6429 \\
(H-K_s)_{2MASS} &= 0.8683 \times (H-K_s)_{\rm inst} - 0.7332.
\end{aligned}
$$

In RCW 34 there were 7460 sources which matched between the JHK_s bands. A criterion was chosen that the error of all magnitudes and colours should be less than 0.05 ($\delta J \leq 0.05$; $\delta H \leq 0.05$; $\delta K_s \leq 0.05$; $\delta(J-H) \leq 0.05; \delta(H-K_s) \leq 0.05$). In NGC 2626 there were 1278 sources that matched between the JHK_s, bands of which 953 sources conformed to the criterion of the error in each colour and magnitude is smaller than 0.05. The completeness of the data set is 82%, 87%, and 83% with a limiting magnitude of 19.36, 18.15, and 17.66 in the J, H, and K_s bands respectively.

3.3 Analysis and results

3.3.1 Derivation of a customised extinction law using linear regression

The extinction law by Rieke & Lebofsky (1985) is usable for most sources in the Milky Way plane which are not deeply embedded in molecular clouds. Light propagating through regions with a density and temperature drastically different from the Galactic average will not obey the same extinction law as the rest of the Galactic plane. In cold and dense molecular clouds, the dust particels have different physical properties than in other environments, see in-depth explanations by Whittet (2001), Weingartner & Draine (2001), and Román-Zúñiga *et al* (2010). To set up a custom extinction law for these environments, high precision, deep photometry is required of stars embedded in the material and field stars behind the molecular clouds. In the following sections the distribution of the calibrated colours of stars in RCW 34 and NGC 2626 will be compared to the extinction laws of Rieke & Lebofsky (1985) and Cardelli *et al* (1989), and it will be shown that a custom extinction law is required.

It is possible to observe field stars behind these dense clouds in the near- and mid-infrared with very sensitive telescopes, such as the *IRSF* or *Spitzer*. Examples of customary extinction laws that were constructed with MIR *Spitzer* photometry are the studies by Indebetouw *et al* (2005) on RCW 49; Flaherty *et al* (2007) on Orion A, NGC 2068, NGC 2024, Serpens, and Ophiuchus; Chapman *et al* (2009); and Román-Zúñiga *et al* (2010) on Barnard 59. If the extinction laws of Rieke & Lebofsky (1985) or Cardelli *et al* (1989), which are accepted anywhere in the Galaxy, are used for RCW 34 and NGC 2626 the embedded sources may be dereddened incorrectly, leading to misinterpretation of the photometric data. A distribution showing the number density for the fields surrounding RCW 34 are shown in Figure 3.6 together with the extinction laws of Rieke & Lebofsky (1985) and Cardelli *et al* (1989). The majority of the sources do not lie parallel to the reddening vectors of either reddening law, suggesting that a custom extinction law should be derived for this specific field. A custom extinction law has to be constructed from only the photometric data of the stars in each field and a separate control field. Ascenso *et al* (2012) explains that deriving an extinction law from only photometric data is a linear regression problem that determines the best fitting reddening-vector on a colour-colour diagram. The reddening vector (β_λ) is an indicator of how much reddening a star suffers and it can also be measured by the excess on each colour-axis $\beta_\lambda = (E_{\lambda-K_s}/E_{H-K_s})$ on a $(\lambda - K_s)/(H-K_s)$

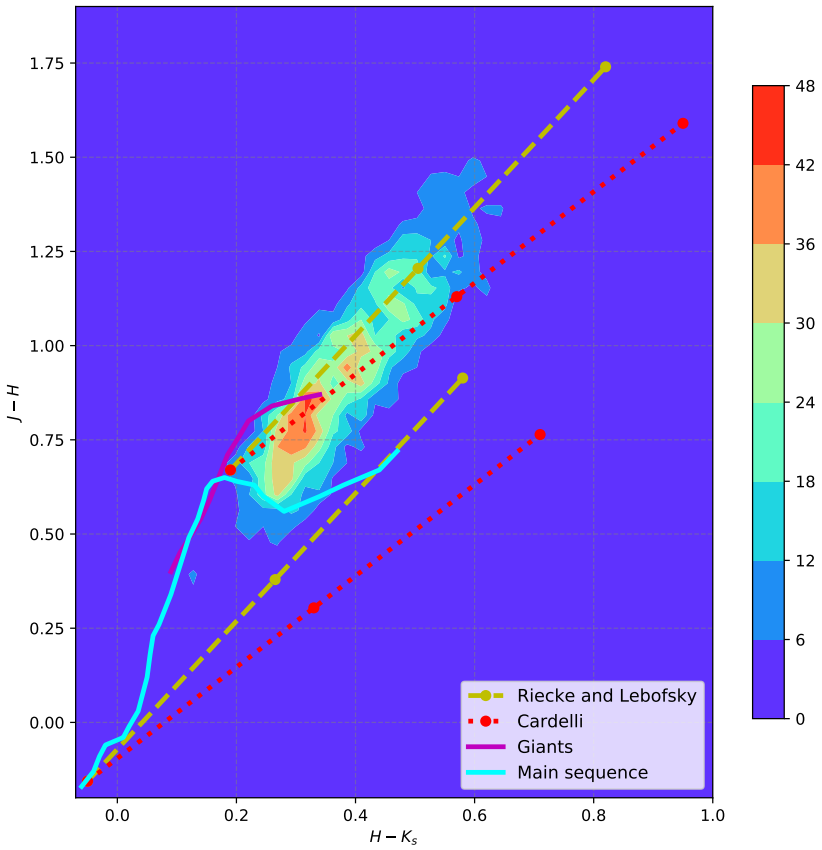

Figure 3.6: A number density distribution for all of the stars in the field surrounding RCW 34, together with the extinction laws from Rieke & Lebofsky (1985) and Cardelli *et al* (1989).

diagram. An extinction law for A_λ/A_{K_s} is calculated as:

$$\frac{A_\lambda}{A_{K\,s}} = \left(\frac{A_H}{A_{K\,s}} - 1\right)\frac{E_{\lambda-K_s}}{E_{H-K_s}} + 1 \tag{3.13}$$

To fully understand the linear regression method that is used to calculate the reddening vector, a mathematical basis will be given for the statistics which were first conceptualised by Akritas & Bershady (1996). The reasons why this is explained in thorough detail are: (1) Both the variables on the X- and $Y-$axes have intrinsic errors and scattering that are dependent on the differences of two magnitudes. The error on any magnitude increases as the magnitude becomes fainter, and very faint sources can not be measured with the same precision as bright sources; (2) When determining an extinction law for $\lambda = J$ from a $(J-H)/(H-K_s)$ diagram, both colours are interdependent on the H magnitude giving the $X-$ and $Y-$magnitudes a correlation; (3) The stars behind the molecular cloud are a random collection of different spectral types, affecting the scatter for the colours that are used to determine how much extinction is caused by the dust in the molecular cloud.

This method is more complex than the optimised linear regression method, but was developed to calculate the best extinction law for a specific field that is observed in the infrared. The mathematical proof of the statistical model that was derived by Akritas & Bershady (1996) is given in Annexure A. The following adjustment from the **o**rdinary **l**east **s**quares (OLS) method to the **bi**variate **c**orrelation **e**rrors

and intrinsic scatter (BCES) method, and implementation in the derivation of the *LinES* method was taken from Ascenso *et al* (2012).

In the derivation given in Annexure A the variables X_{1i} and X_{2i} are represented by two measured quantites, which each have a respective measurement error, $\epsilon_{1i}, \epsilon_{2i}$. If you take $X_{1i} = x$ and $X_{2i} = y$ in a colour space with a single β parameter, which represents the reddening slope, that has to be determined, the equation A.5 can be reduce to:

$$\beta_{\rm OLS} = \frac{{\rm Cov}(x, y)}{{\rm Var}(x)} \tag{3.14}$$

The variance and covariance in these cases are defined for variable sets x and y with averages $\bar{x}$ and $\bar{y}$:

$${\rm Var}(x) = \frac{1}{N}\sum_{i=0}^{n}(x_i - \bar{x})^2 \tag{3.15}$$

$${\rm Cov}(x, y) = \frac{1}{N}\sum_{i=0}^{n}(x_i - \bar{x})(y_i - \bar{y}) \tag{3.16}$$

In equation 3.14 the effect of the errors on the ${\rm Cov}(x, y)$ and ${\rm Var}(x)$ can be compensated for. Thus, so each datapoint (x_i, y_i) is affected by an error so that the measured value is actually $(x'_i, y'_i) = (x_i, y_i) \pm (\epsilon^x_i, \epsilon^y_i)$. By substituting (x_i, y_i) with (x'_i, y'_i) in equation 3.15 and 3.16 the variance and co-variance's definitions change to:

$${\rm Cov}(x', y') \mapsto {\rm Cov}(x, y) + {\rm Cov}(\epsilon^x, \epsilon^y) \tag{3.17}$$

$${\rm Var}(x') \mapsto {\rm Var}(x) + {\rm Var}(\epsilon^x) \tag{3.18}$$

Now that the variances and covariances for the errors and the original quantities are incorporated into the definition for β, equation 3.14 can be rewritten in terms of (x', y'):

$$\beta_{\rm BCES} = \frac{{\rm Cov}(x, y) - {\rm Cov}(x', y')}{{\rm Var}\, x - {\rm Var}(\epsilon^x)} \tag{3.19}$$

In equation 3.19 the variance and the covariance for the errors have to be known. For example, if $x = (H - K_s)$ and $y = (J - H)$ then the variance and co-variance on the errors would be (see Ascenso *et al* 2012 for a detailed derivation):

$${\rm Cov}(x', y') = -\sigma^2_H \tag{3.20}$$

$${\rm Var}(\epsilon^x) = \sigma^2_H + \sigma^2_{K_s} \tag{3.21}$$

where σ_H and σ_{K_s} are the mean photometric errors in the H and K_s bands.

Equation 3.19 can easily be implemented in a measured data set, but it does not work when an extinction law for a specific field is built. This is because it requires x to be measured without error - which is unrealistic for actual data. Akritas & Bershady (1996) and Ascenso *et al* (2012) state that the $\beta_{\rm BCES}$ can only be used if the intrinsic scatter is not known. When an extinction law is constructed the internal scatter of the measured data can be determined by using high precision photometry of a control field. The variance and covariance for the colours of the control field are just the summations of the variance and co-variance caused by intrinsic scatter of the stars and the photometric errors for the control field. The reddening vector on a colour-colour diagram can then be calculated with the following equation:

$$\boxed{\beta_{LinES} = \frac{{\rm Cov}(x, y) - {\rm Cov}(\epsilon^x, \epsilon^y) - {\rm Cov}(x^{cf}, y^{cf}) + {\rm Cov}(\epsilon^{cf\ x}, \epsilon^{cf\ y})}{{\rm Var}(x) - {\rm Var}(\epsilon^x) - {\rm Var}(x^{cf}) + {\rm Var}(\epsilon^{cf\ x})}} \tag{3.22}$$

This linear regression method is called *LinES* (**Lin**ear regression with **E**rrors and **S**catter). It has been thoroughly tested by Ascenso *et al* (2012) for robustness when there exists a correlation between the errors. It is therefore assumed that this method can be trusted and applied without question to the data for RCW 34 and NGC 2626.

3.3.1.1 *Implementation of the LinES method on the stellar fields around RCW 34 and NGC 2626*
To construct extinction laws for RCW 34 and NGC 2626 the variables in equation 3.22 will have to be $x = (J - H)$ and $y = (H - K_s)$, so that the reddening vector's slope can be calculated as:

$$\boxed{\beta_J = \frac{\begin{array}{c}[\mathrm{Cov}\left((J-H),(H-K_s)\right) - \mathrm{Cov}\left(\delta(J-H),\delta(H-K_s)\right)] - \\ [\mathrm{Cov}\left((J-H)_{cf},(H-K_s)_{cf}\right) - \mathrm{Cov}\left(\delta(J-H)_{cf},\delta(H-K_s)_{cf}\right)]\end{array}}{\mathrm{Var}(J-H) - \mathrm{Var}(\delta(J-H)) - (\mathrm{Var}(J-H)_{cf} - \mathrm{Var}(\delta(J-H)_{cf}))}} \tag{3.23}$$

The extinction law that is defined in equation 3.13 can be rewritten for this case as:

$$\beta_{LinES}\frac{A_\lambda}{A_{K_s}} = 1 - \left(\frac{A_H}{A_{K_s}} - 1\right).\beta_\lambda \Rightarrow \frac{A_J}{A_{K_s}} = 1 - \left(\frac{A_H}{A_{K_s}} - 1\right).\beta_{J\,LinES} \tag{3.24}$$

To correctly apply the *LinES* method, the two science fields for RCW 34 ($l = 264.29,\ b = +1.46$) and NGC 2626 ($l = 259.97,\ b = -0.06$) were used together with a control field at the same Galactic latitude as RCW 34, but 10 degrees in the positive direction of the Galactic longitude ($l = 274.31,\ b = +1.46$). The control field does not have to be observed to the same depth as the science fields, because it should only give an indication of the typical colour distribution for a random sample of stars in the same direction of the Milky Way and should not have any obvious structures that cause extinction. To calculate a statistically sound extinction law for each science field, all of the stars in each science field that are brighter than the sensitivity limit of the control field were selected for the calculation of the extinction law. All of the stars in the science fields are shown in Figures 3.7 and 3.8 where a cut-off magnitude of $K_s = 16.407$ was used.

When an extinction law was calculated for each science field, the assumption made by Ascenso *et al* (2012), that the ratio $A_H/A_{K_s} = 1.57$ is valid for each science field, was used, as was initially determined by Rieke & Lebofsky (1985). The reason for this assumption is that the ratio of H and K_s relative to the A_V extinction is the same in the different directions of the Milky Way plane, as was shown by Cardelli *et al* (1989). For other bands at shorter wavelengths, the ratio of the extinction in the specific band relative to the visual extinction is dependent on which direction in the Milky Way the extinction is measured. In equation 3.24 the ratio for A_H/A_{K_s} is required to calculate A_J/A_{K_s} and determine the slope for the reddening vector.

Substituting the data for each science field into equation 3.22 gives respective results for $(\beta_{LinES})_{\mathrm{RCW\ 34}} = -3.068$ and$(\beta_{LinES})_{\mathrm{NGC\ \ 2626}} = -2.772$. Using these values in 3.24 gives the extinction law as:

$$\left(\frac{A_J}{A_{K_s}}\right)_{RCW\ 34} = 2.726 \tag{3.25}$$

and

$$\left(\frac{A_J}{A_{K_s}}\right)_{NGC\ 2626} = 2.559 \tag{3.26}$$

It must be stated that the calculated value of A_J/A_{K_s} is an average across each field. If a smaller part of the science field was used in the same calculation, a different answer should be expected. This is the result of using a different set of field stars in equation 3.23, which will have different covariance and variance values for each term in the calculation of β_J. For example, the calculated value for β_J of the deep central field of RCW 34, which is shown in Figure 3.1b, was $\beta_J = -2.453$ ($A_J/A_{K_s} = 2.379$). This is between the values for the extinction laws by Rieke & Lebofsky (1985) and Cardelli *et al* (1989). The results of the deep central field, including its extinction laws, are not discussed, because: (1) The goal of this project is to look at the cluster as a whole, and (2) the quality of the mosaicked images of RCW 34 is high and deep enough that all of the information of the central region can be

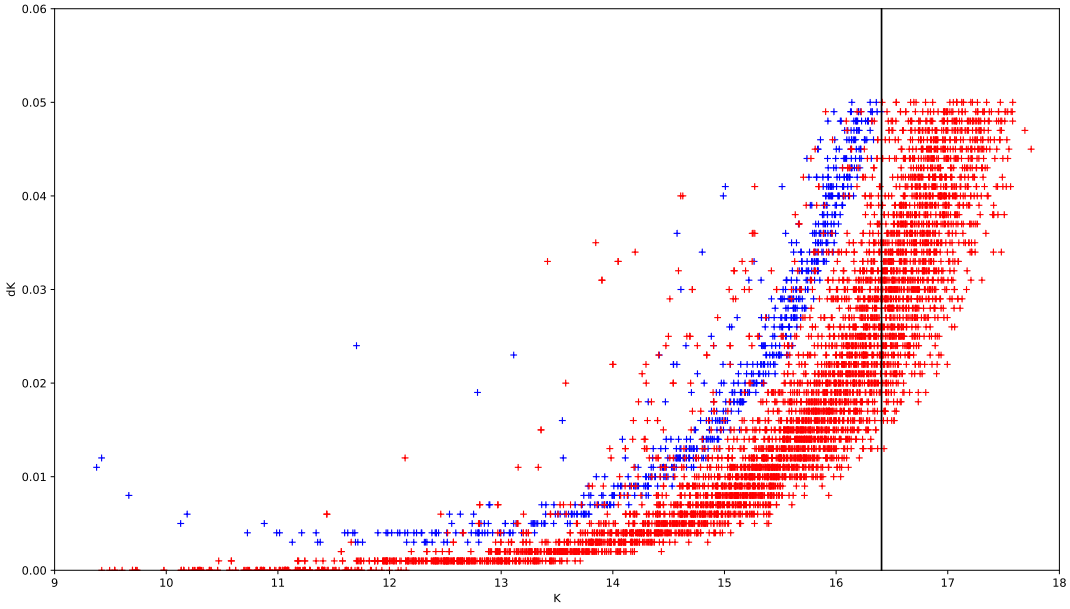

Figure 3.7: Out of the 5270 stars that were observed in the vicinity of RCW 34 there were 3756 brighter than $K_s = 16.407$ and were used to contruct an extinction law for the field with the *LinES* algorithm. The blue data points are stars from the control field, and the red points are the stars from the science field. The sensitivity limit of the control field was used as a cut-off magnitude for the stars that were used to calculate the extinction law in the science field.

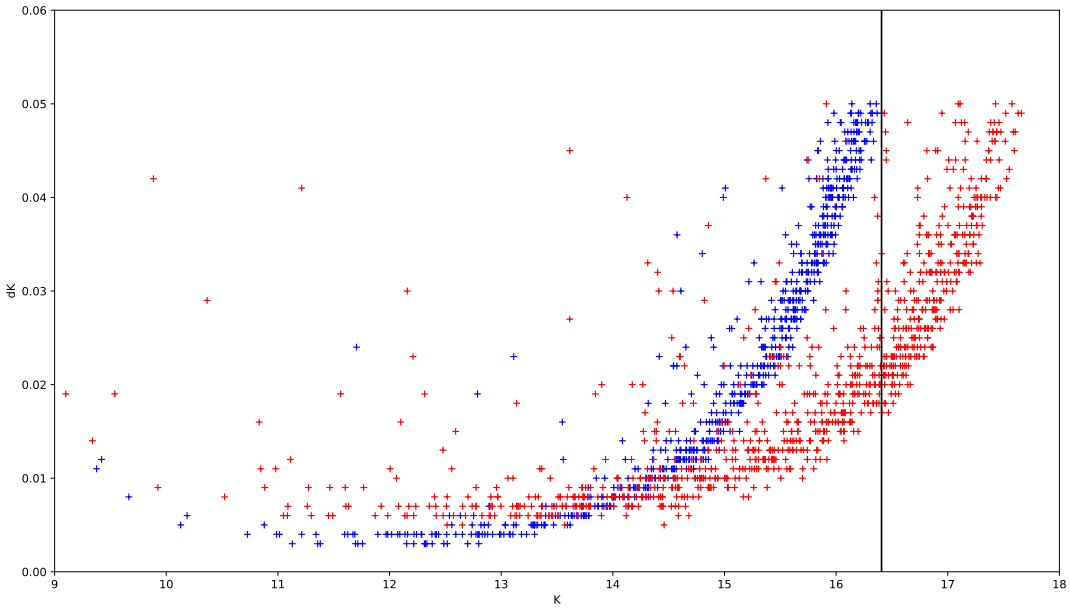

Figure 3.8: Out of the 953 stars that were observed in the vicinity of NGC 2626 there were 607 that were brighter than $K_s = 16.407$ and were used to contruct an extinction law for the field with the *LinES* algorithm.

deduced from the mosaicked images.

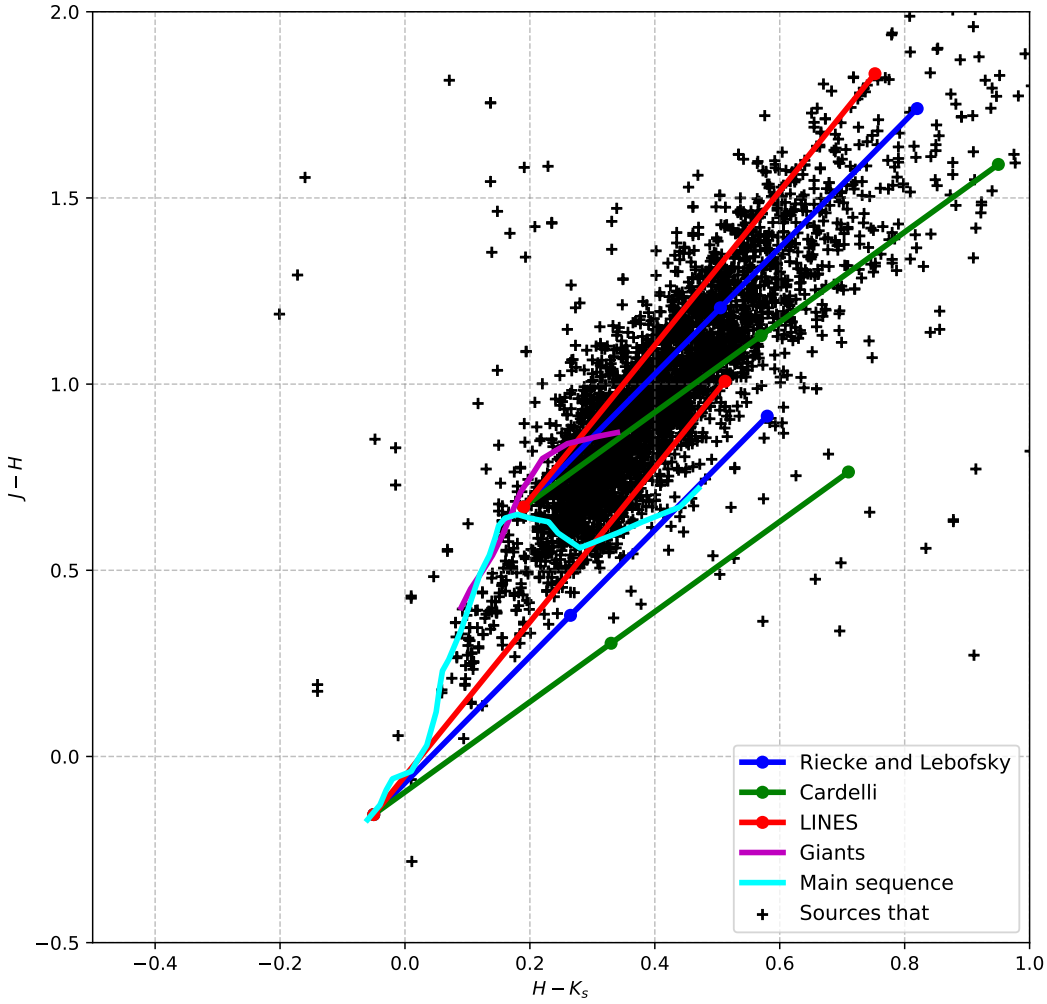

Figure 3.9: All the stars in RCW 34 that were brighter than the sensitivity limit of the control field together with the extinction laws by Rieke & Lebofsky (1985), and Cardelli *et al* (1989) and the custom *LinES* extinction law.

Figure 3.9 shows all of the stars in the field surrounding RCW 34 that are brighter than the sensitivity limit of the control field and were used to calculate a custom extinction law for RCW 34. The newly calculated *LinES* extinction law lies parallel to the population of reddened stars. The other extinction laws of Rieke & Lebofsky (1985) and Cardelli *et al* (1989) would clearly give incorrect dereddened results if applied to this specific field.

In Figure 3.10 the number density distribution of all the stars in the field surrounding RCW 34 is given, together with the three extinction laws. It is clear that the *LinES* extinction law lies parallel to the full population of stars in the science field. This extinction law will be used to identify PMS stars with excess *NIR* emission and to build extinction maps of the region around RCW 34.

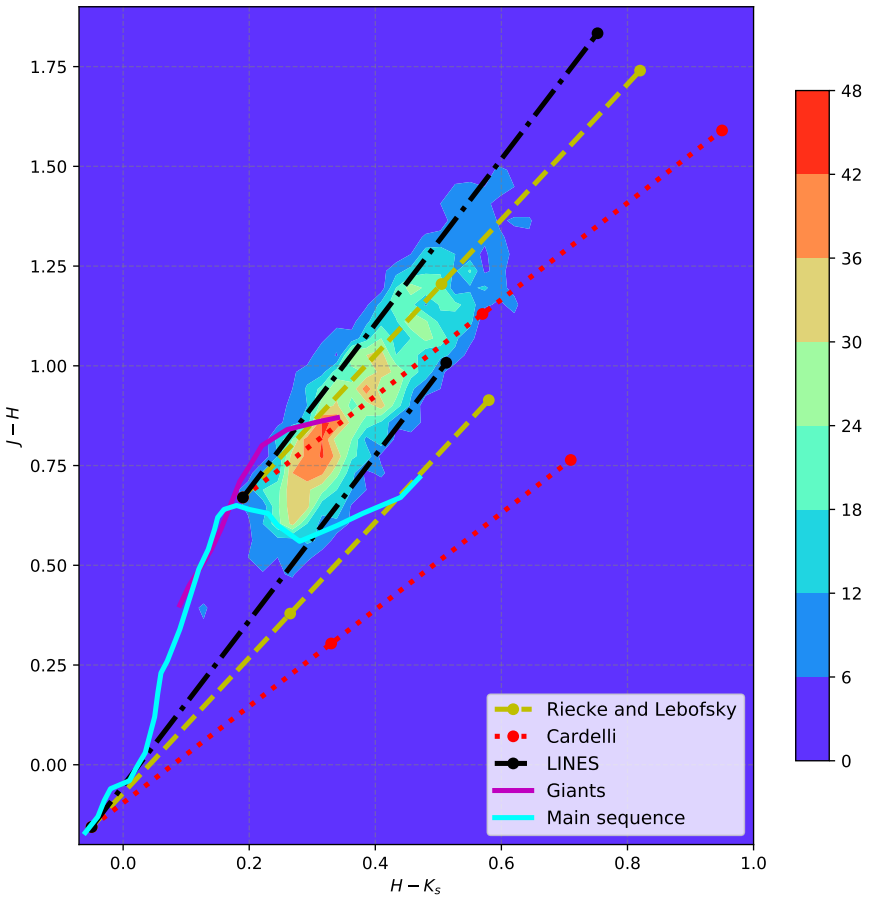

Figure 3.10: The number density of stars in the science field around RCW 34. The two extinction laws derived by Rieke & Lebofsky (1985) and Cardelli *et al* (1989) are shown together with the custom derived *LinES* extinction law for the stars in the science field surrounding RCW 34.

3.3.1.2 *Extinction laws for RCW 34 and NGC 2626*

The extinction laws that were calculated for the fields of RCW 34 and NGC 2626 from the *LinES* algorithm are given in Table 3.1. The calculated ratio of $\frac{A_J}{A_{K_s}}$ was used together with the assumption that the ratio of $\frac{A_J}{A_V} = 0.282$ is correct for all of the science fields. First the ratio of $\frac{A_{K_s}}{A_V}$ is calculated as $\frac{A_{K_S}}{A_V} = \frac{A_J}{A_V}\frac{A_{K_s}}{A_J} = 0.282 \times \frac{1}{2.726} = 0.103$. For the ratio of $\frac{A_H}{A_V}$ the newly calculated ratio $\frac{A_{K_s}}{A_V}$ is used, $\frac{A_H}{A_V} = \frac{A_H}{A_{K_s}}\frac{A_{K_s}}{A_V} = 1.56 \times 0.103 = 0.161$.

Table 3.1: The ratios of the extinction in the respective J, H, and K_s bands are given to a magnitude of extinction in visual extinction.

λ	Rieke & Lebofsky (1985) $[\frac{A_\lambda}{A_V}]$	Cardelli *et al* (1989) $[\frac{A_\lambda}{A_V}]$	*LinES*: RCW 34 $[\frac{A_\lambda}{A_V}]$	*LinES*: NGC 2626 $[\frac{A_\lambda}{A_V}]$
J	0.282	0.282	0.282	0.282
H	0.175	0.190	0.161	0.172
K_s	0.112	0.114	0.103	0.110

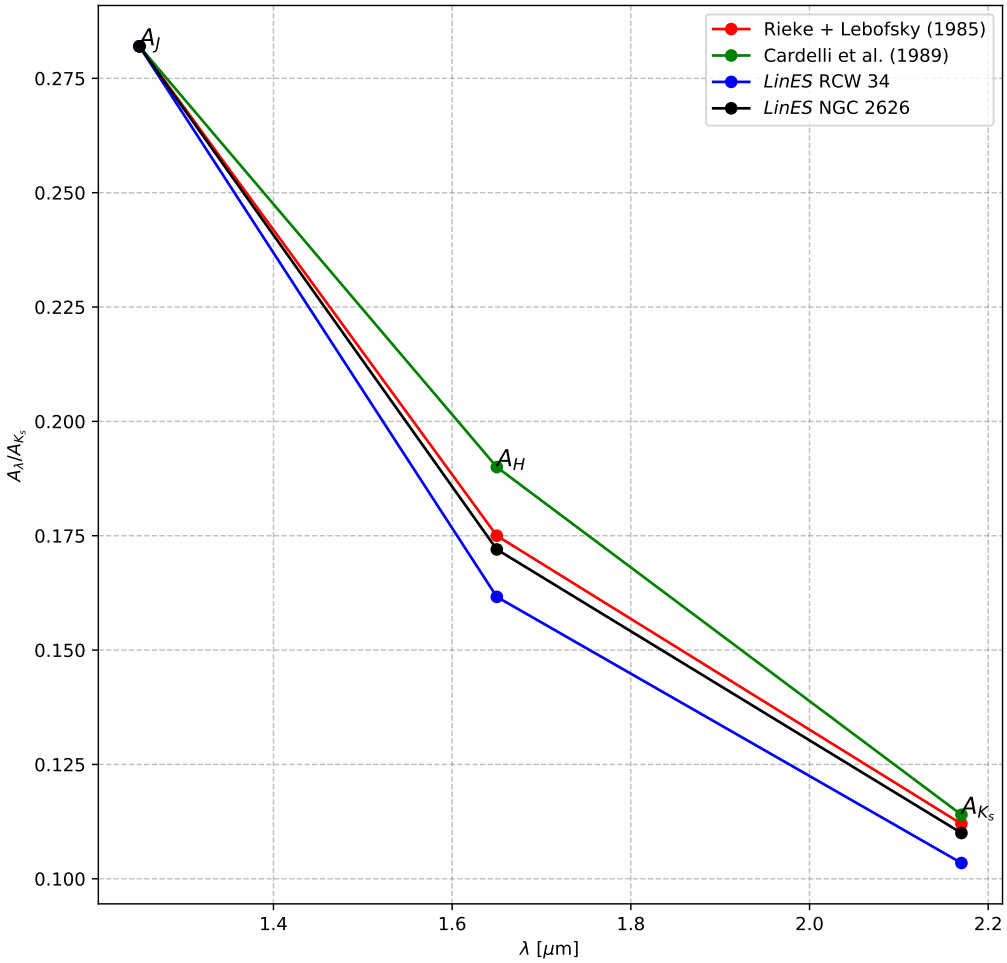

Figure 3.11: A graphic depiction of extinction in the J, H, and K_S bands relative to visual extinction for different extinction laws.

The difference between the extinction laws of Rieke & Lebofsky (1985), Cardelli *et al* (1989), and the custom *LinES* cases for RCW 34 and NGC 2626 are shown in Figure 3.11 and Table 3.1. The ratio of $\frac{A_J}{A_V}$ was constant for all of the extinction laws according to the assumption that was used to calculate the other ratios. The *LinES* extinction law for NGC 2626 lies parallel to the extinction law of Rieke & Lebofsky (1985). The values of $\frac{A_H}{A_V}$ and $\frac{A_{K_S}}{A_V}$ for RCW 34 are smaller than the other extinction laws, implying that extinction that is measured as A_{K_s} from *NIR* data will give a visual extinction that is smaller than the other extinction laws. Applications of the calculated extinction laws as reddening vectors for *LinES* on the mosaicked field of RCW 34 are best shown on a colour-colour and colour-magnitude diagram along-side the extinction laws by Rieke & Lebofsky (1985) and Cardelli *et al* (1989) in Figures 3.12 and 3.13, as well as for NGC 2626 in Figures 3.14 and 3.15.

In Figure 3.12 the colour-colour diagram is shown for stars in the field around RCW 34 together with reddening vectors for the extinction laws by Rieke & Lebofsky (1985), Cardelli *et al* (1989), and the custom calculated *LinES* case. Each reddening vector is drawn for $A_V = 10$, starting at three different positions: (1) The high-mass end of the main sequence, (2) the position of the M4 stars, on the knee of the main sequence and (3) the end of the CTT locus' lower limit.

The distinction between main sequence stars, and stars with excess emission, is the reddening vector, starting at the high-mass end of the main sequence. The stars that can be dereddened onto the main sequence, according to the distinguishing reddening line, are assumed to be main sequence field stars. Those that lie to the right of the reddening line are assumed to be excess emission sources. If a

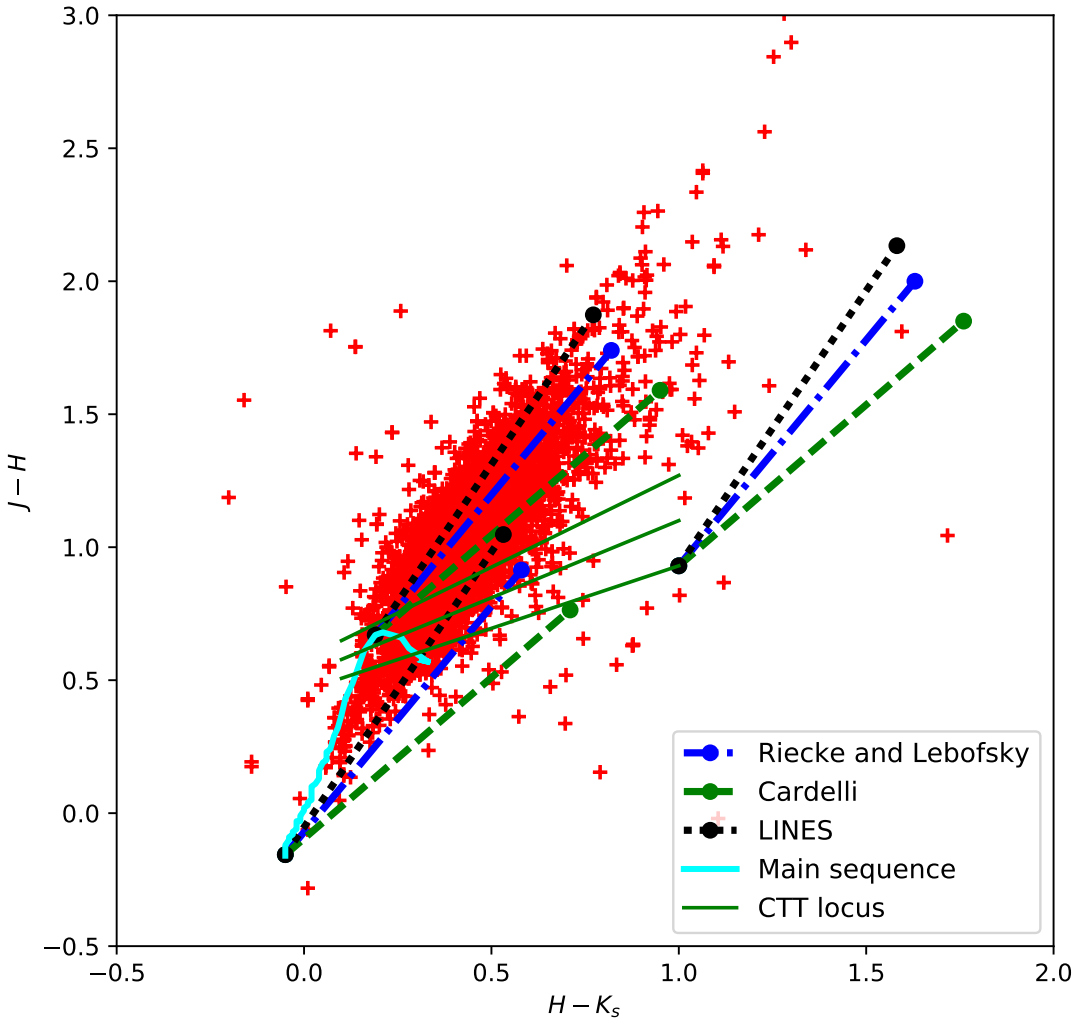

Figure 3.12: The colour-colour diagram shows the 5270 sources in the field surrounding RCW 34, and illustrates a comparisson between the extinction laws by Rieke & Lebofsky (1985), Cardelli *et al* (1989), and the custom extinction law that was derived using the *LinES* algorithm.

reddening vector with a steep slope is used, such as the *LinES* extinction law, instead of the Rieke & Lebofsky (1985), then the number of excess stars is much higher than the alternative. The majority of the population lies parallel to the reddening vector of the Rieke & Lebofsky (1985) extinction law. If this reddening vector was used for the whole field, then the reddening vector that extends from the knee of the main sequence would imply that there is a very large number of stars that would be dereddened onto the giant and supergiant sequences. Figure 3.10 shows a comparison between the distribution of reddened stars and the custom reddening vectors. It also shows that the reddening vector given by the *LinES* extinction law lies parallel to the majority of the reddened sources in RCW 34. This shows that the optimization of the *LinES* method is the best fit for the data, and it is the correct choice for the reddening law that should be used for the science field, RCW 34. If the reddening vector of *LinES* was used, then the number of excess sources would be much higher and the calculated visual extinction of each source would be significantly smaller.

The implications of using an incorrect extinction law would be disastrous, because an incorrect reddening vector would be used to deredden all field stars to the correct spectral class on the main sequence. A possible result would be mistaking a PMS star as a main sequence star that is used to measure the extinction at a certain position, and is used in the construction of an extinction map. This would generate artificial structures in any extinction map, that is built from the *NIR* data, and cascade throughout the rest of the data that measures extinction from the specific maps.

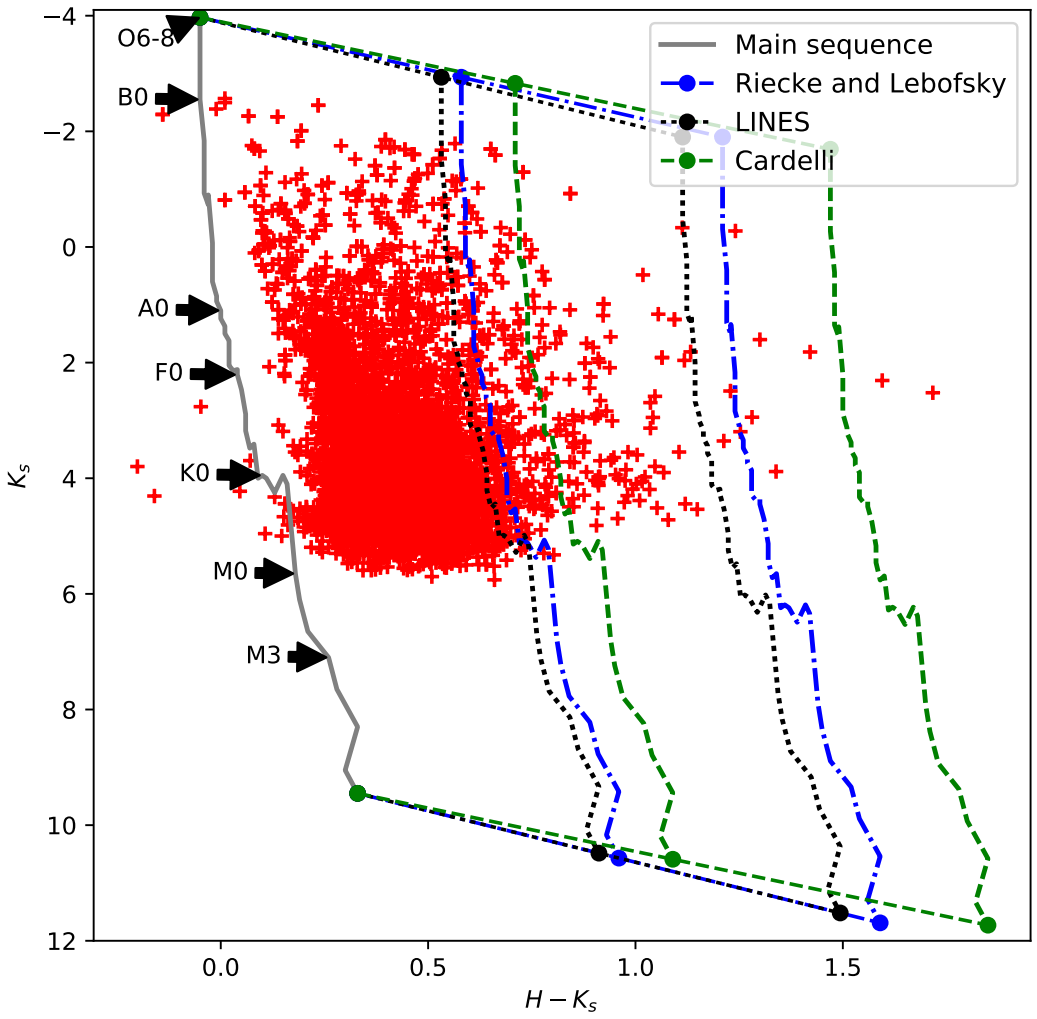

Figure 3.13: The colour-magnitude diagram comparing the extinction laws as in Figure 3.12 for RCW 34.

The colour-magnitude diagram shown in Figure 3.13 shows the $K_s/H-K_s$ plot for the stars in RCW 34. The main sequence and the reddening vector for each of the three extinction laws are shown for $A_V = 10$ and $A_V = 20$ magnitudes. The ratio of $\frac{A_H}{A_{K_s}}$ shows the difference between the extinction laws for Rieke & Lebofsky (1985) and Cardelli *et al* (1989), as well as why the reddening vectors of *LinES* and Rieke & Lebofsky (1985) lie parallel to each other. The ratio of $\frac{A_V}{A_{K_s}}$ is the reason why the extinction step length differs between the reddening vectors of *LinES* and Rieke & Lebofsky (1985).

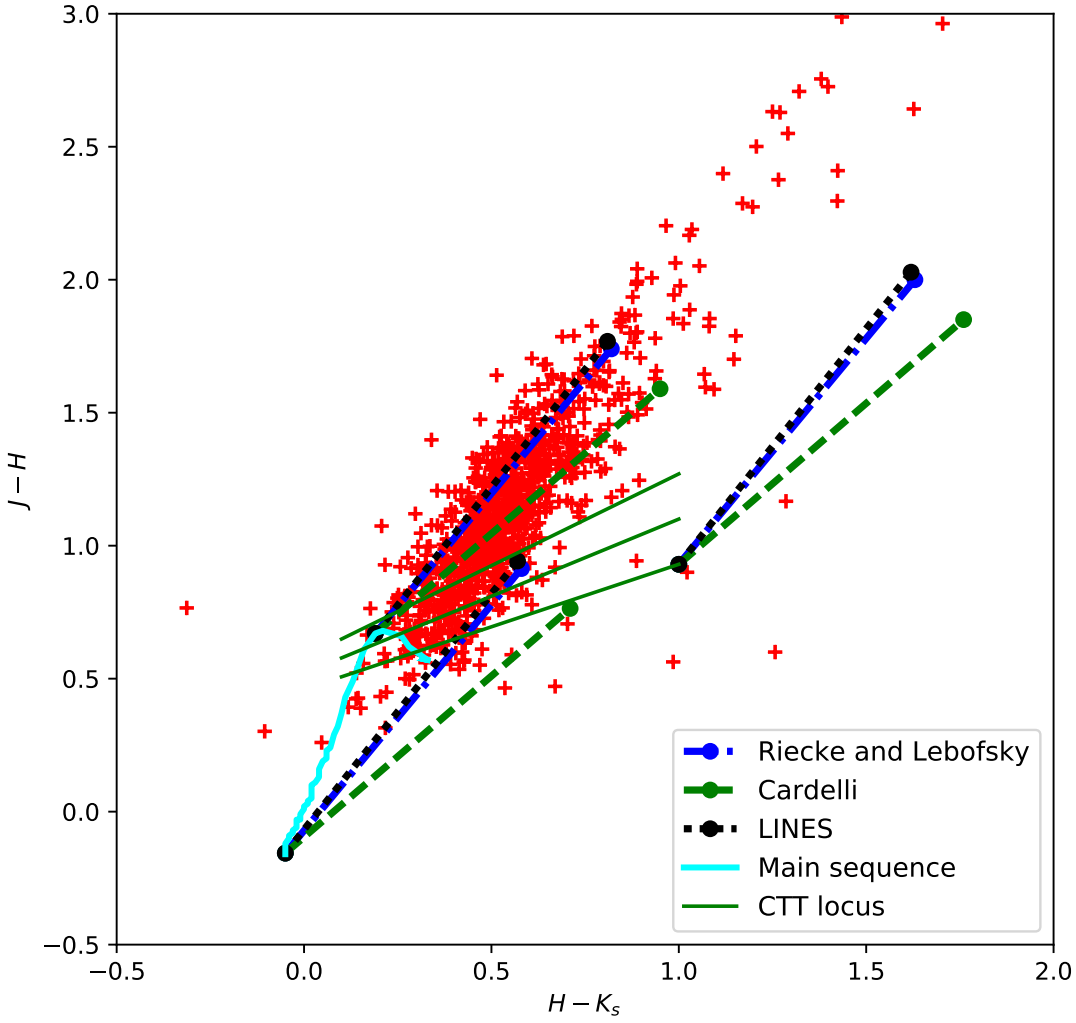

Figure 3.14: The colour-color diagram shows the 953 sources in the field surrounding NGC 2626 and illustrates a comparisson between the extinction laws by Rieke & Lebofsky (1985), Cardelli *et al* (1989) and the customised extinction law that was derived using the *LinES* algorithm.

Figure 3.14 shows that the derived *LinES* extinction law for NGC 2626 has a slope much closer to that of Rieke & Lebofsky (1985). This similarity implies that Rieke & Lebofsky (1985)'s extinction law can be used for the other photometric results.

The colour-magnitude diagram shows that the reddening vectors for the *LinES* and Rieke & Lebofsky (1985) extinction laws are similar. From the identical reddening vectors it is apparent that the *LinES* optimization method results in the extinction law of Rieke & Lebofsky (1985). It also implies that the main sequence that is reddened with the two different extinction laws lie on top of each other.

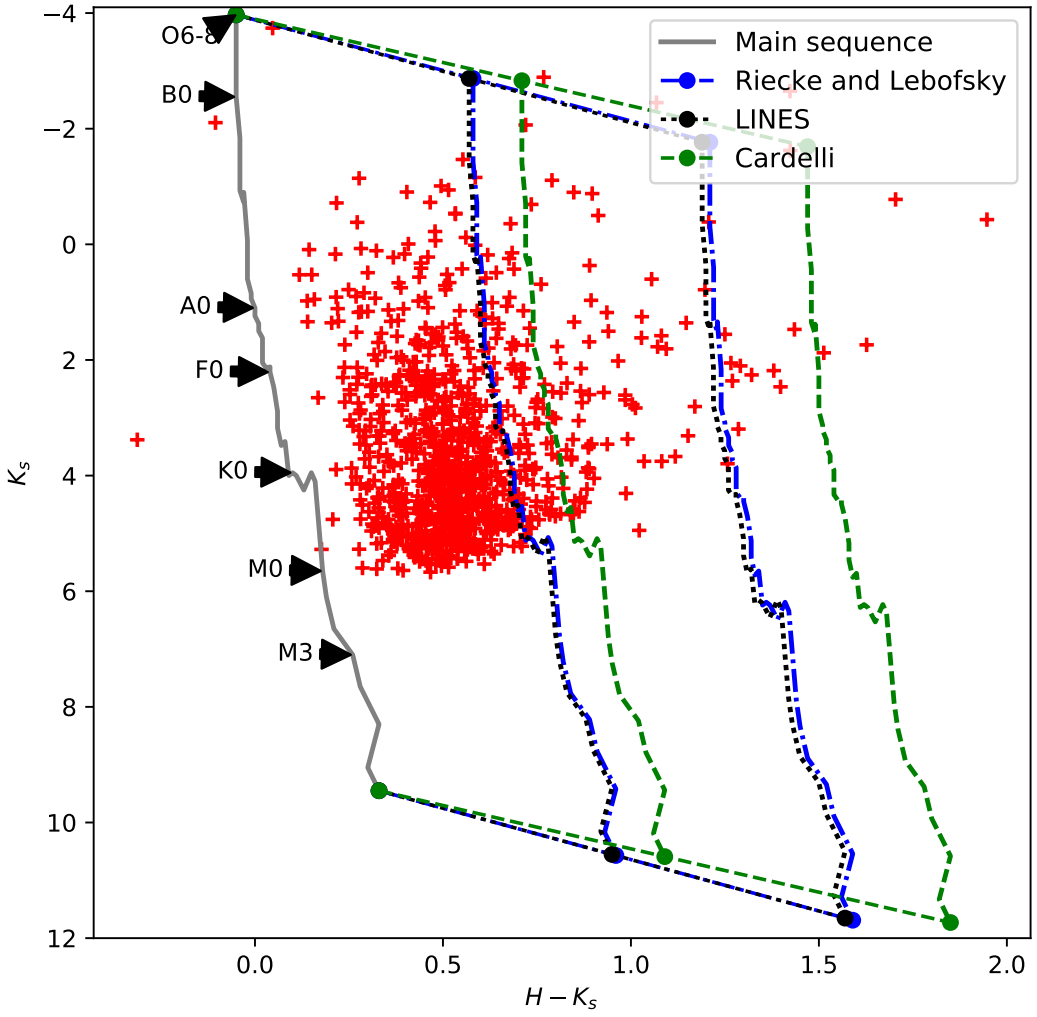

Figure 3.15: The colour-magnitude diagram comparing the extinction laws as in Figure 3.14 for NGC 2626.

3.3.2 Construction of extinction maps: *NICEST LinES*

By only using the calibrated colours and magnitudes it is not possible to determine how much colour excess and reddening there is in the measured magnitudes of a star. This is due to interstellar extinction or possible circumstellar material. A way to determine how much reddening is caused by extinction for a specific field star, is to deredden it to the main sequence. If the extinction is known for enough field stars across a science field, an extinction map can be built by interpolating for the extinction in the regions between dereddened field stars. An interpolation method *NICE* (**N**ear-**I**nfrared **C**olour **E**xcess) was first proposed by Lada *et al* (1993), where the average extinction at a specific point can be calculated based on the excess colour distribution of the surrounding background stars. A practical application of the the *NICE* method introduced by Lada *et al* (1993) was not well developed in the initial publication. The method was documented much more comprehensively and explained in detail by Lada *et al* (2007), it was a revised version of *NICE*, titled *NICER* (**N**ear-**I**nfrared **C**olour **E**xcess **R**evised). The general idea for the *NICER* method is to calculate a weighted average for the extinction at a specific point in a science field, based on the extinction measured for field stars around

that specific point. The extinction for the field stars is measured as the difference between the observed colours and the intrinsic colours for each spectral type on the main sequence as is given by Koornneef (1983). The *NICER* method does have some shortcomings, as it introduces a bias anywhere on an extinction map where structures smaller than a pixel are present and suffers contamination from foreground stars. These shortcomings of *NICER* were corrected by Lombardi (2008) with the introduction of *NICEST*. The *NICEST* method corrects for inhomogeneities in molecular cloud extinction maps, making it tailored to small scale structures. The resulting extinction map built with *NICEST* thus has a higher resolution than *NICER* extinction maps.

The first step in the construction of the extinction map requires an estimate of the extinction for each field star. Any background star in the science field may be subject to extinction, because the structure of the molecular cloud is not known yet. The assumption can be made that the intrinsic colour distribution for the science field's background stars, is equivalent to that of the control field. This assumption does not mean that there is no extinction for the stars in the control field, but it implies that if there were no molecular clouds in the science field, the colour distribution of the field stars should look like the colour distribution of the control field:

$$(H - K_s)_{\text{Intrinsic}} \equiv \langle H - K_s \rangle_{\text{Control field}} \tag{3.27}$$

Using the assumed intrinsic colour value, the excess emission for each star's colour can be calculated by:

$$E(H - K_s) = (H - K_s)_{\text{Measured}} - (H - K_s)_{\text{Intrinsic}} \tag{3.28}$$

When applying this technique to regions where active star formation is occurring, there has to be a distinction between stars that may be PMS stars and field stars. The candidate PMS stars, will not only have colour excess due to extinction suffered because they are enveloped in the embedding material. They will also have excess emission from a circumstellar disk, which reprocesses photospheric radiation (see Koerner *et al* 1993 and Strom 1993), and the heating of gas and dust by accretion (see Lynden-Bell & Pringle 1974, Kenyon & Hartmann 1987, Bertout *et al* 1988, and Adams *et al* 1987). Therefore, the measured colours are:

$$(H - K_s)_{\text{Measured}} = (H - K_s)_{\text{Intrinsic}} + E(H - K_s)_{\text{Extinction}} + E(H - K_s)_{\text{Circumstellar material}} \tag{3.29}$$

A distinction can be made between candidate PMS stars and field stars on a colour-colour diagram with the reddening line that extends from the high-mass end of the main sequence. In Chapter 2, Figure 2.20 shows the regions where reddened main sequence stars lie, and where PMS stars with excess *NIR* emission lie past the high-mass reddening line.
In Figure 3.16 the distinction between reddened field stars and candidate PMS stars is made for both the populations of RCW 34 and NGC 2626. The red data points are the field stars that can be dereddened onto the main sequence. They will be used to construct the extinction map. The blue data points are candidate PMS stars and can not be used in the construction of the map. A reddening vector was constructed for each reddened field star to the main sequence. There exists a degeneracy for some of these stars, because the reddening vector overlaps with two different spectral types on the main sequence.

Figure 3.17 shows a star that can be dereddened onto the main sequence giving a measurement for the extinction, A_{K_s}. It also shows the degeneracy for this star between two spectral types on the main sequence. It can either be a G1 or an M7 star. On a colour-colour diagam the main sequence peaks at the colours of an M4 star — referred to as the knee on the main sequence — and then comes down in both the positive and negative $(H - K_s)$ directions. To overcome the degeneracy, an assumption was made that the field stars have a mass distribution similar to that of the stars in the Milky Way plane. The mass distribution of the Milky Way's field stars are given in Parravano *et al* (2011) as a separate power-law for the lower stellar masses ($\Psi \propto m^{\gamma}; \gamma = 0.57$), and higher stellar masses ($\Psi \propto m^{\Gamma}; \Gamma = 0.57$). Along with this is a characteristic mass $M_{ch} = 0.42$, which distinguishes between lower and higher masses and gives a smoothly joined two-piece power-law (see De Marchi *et al* 2010 for the original form) as:

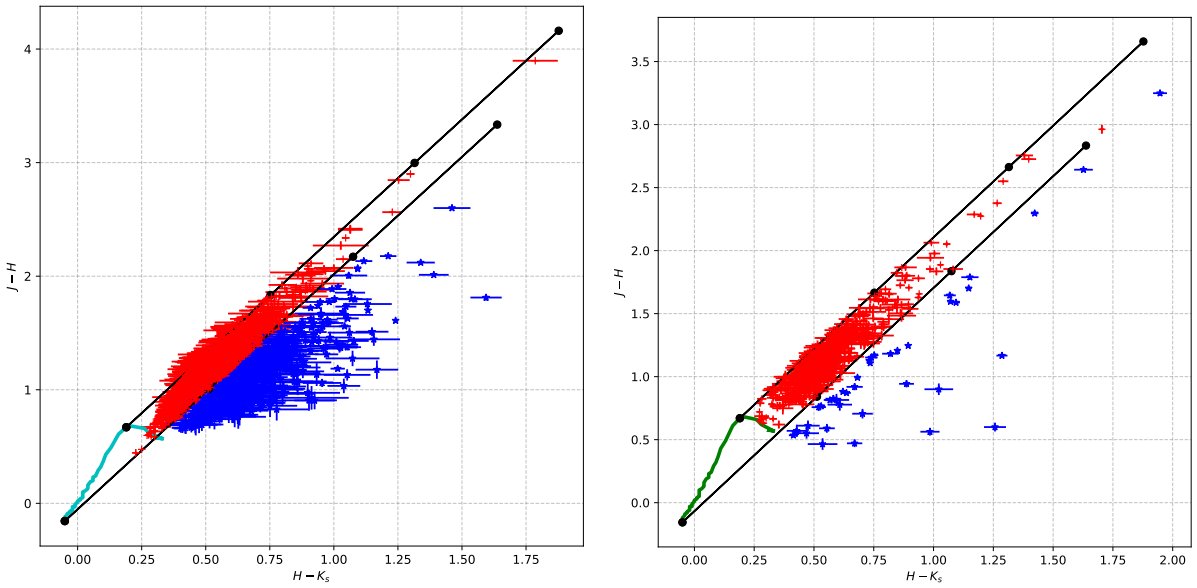

Figure 3.16: There were respectivley 593 and 39 stars shown as blue data points in the field surrounding RCW 34 (left panel) and NGC 2626 (right panel) that showed excess *NIR* emission and can be considered as probable PMS stars. The other stars shown in red are considered as reddened main sequence stars.

$$\Psi_{\text{Parravano}}(m) = km^{-\Gamma}\left[1 - \exp\left(\frac{m}{M_{ch}}\right)^{\gamma+\Gamma}\right] \tag{3.30}$$

If the reddening vector for any of the identified main sequence stars in the population of RCW 34 and NGC 2626 had a degenerate solution, both of the masses were calculated. A simple Monte-Carlo model was used to determine to which one of the two masses on the main sequence the specific field star should be dereddened. The IMF value for each of the two possible masses were calculated with equation 3.30 and normalised so that they added up to 1. The distinguishing stellar type between the different legs of the main sequence is the M4 star, which has a mass of 0.22 $M_{\odot}$:

$$P_{\text{Parravano}}(m < 0.22\ M_{\odot}) + P_{\text{Parravano}}(m > 0.22\ M_{\odot}) = 1 \tag{3.31}$$

An uniformly distributed, random value x between 0 and 1 was calculated, and if $x \leq P_{\text{Parravano}}(m <$ M4 star) it would be dereddened onto the lower mass, otherwise the higher mass would be used. The randomisation process was repeated 500 times so that each field star with a degenerate main sequence solution had 500 different solutions of either ending up on the higher or lower mass end. A most likely average A_{K_s} value was then calculated for each field star from the 500 repetitions. This solution was applied to each of the science fields.

The outcome for each averaged calculation is a position on the reddening vector between the different legs of the main sequence for each star that has a degenerate solution, as shown in Figure 3.17. The majority of the averaged points lie towards the stars with a mass lower than an M4 star. The distribution of the averaged points is determined only by the mass distribution, $\Psi_{\text{Parravano}}(m)$.

For each field star that was dereddened there is spatial data as a set of RA and DEC coordinates, and an A_{K_s} measurement. When the science field is viewed as an extinction map at this stage, it looks like a collection of pencil-beam extinction measurement points spread over an empty background. The execution of the *NICER/NICEST* method fills in the rest of the extinction background. The extinction map is constructed by calculating a weighted average $\hat{A}_{K_s}$ value on a pixel-to-pixel basis for each point, $\mathbf{x}_i$. This is the same smoothed interpolation method that was described in Lombardi

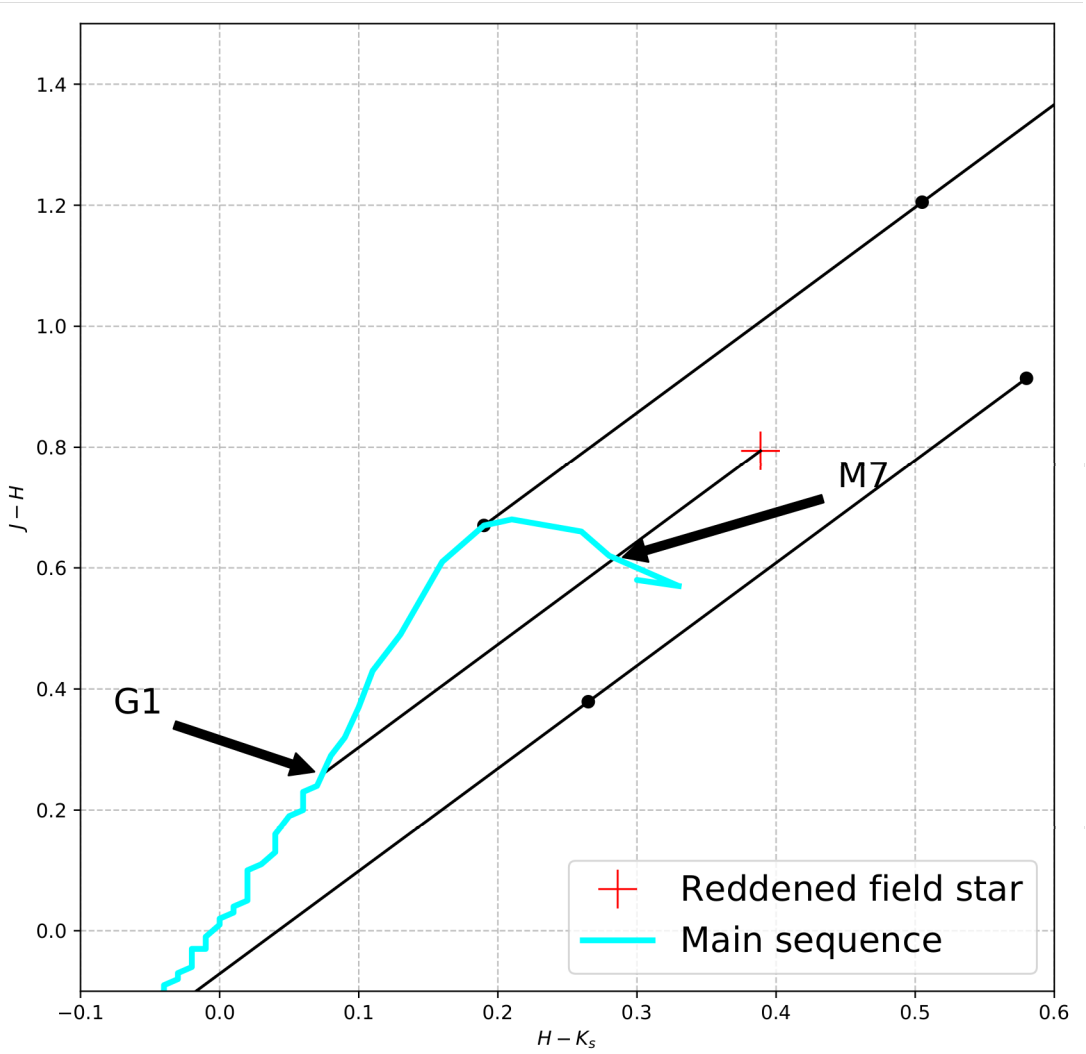

Figure 3.17: The reddened field star has two possible spectral types to which it can be dereddened. A Monte-Carlo simulation was used to select the most probable solution.

(2008), where the weighted average is defined as:

$$\hat{A} = \frac{\sum_n w_n(\mathbf{x}_i, \mathbf{x}_n) A_n}{\sum_n w_n(\mathbf{x}_i, \mathbf{x}_n)} \tag{3.32}$$

For each instance where $\hat{A}_{K_s}$ is calculated at a pixel position $\mathbf{x}_i$ there are a number, n stars that contribute to the calculation of the extinction. The n stars are all from the population of dereddened main sequence stars, each with its own A_{K_s}, and within a radial distance r_{trunc} from the pixel at $\mathbf{x}_i$. Each contributing star is assigned a weight w_n, using the radial distance between the star and the pixel $w_n \propto (\mathbf{x}_n - \mathbf{x}_i)$. Enough surrounding field stars are included for each calculation of $\hat{A}_{K_s}$ and an objective size is therefore chosen for the detection/truncation radius. The choice for the size of the detection/truncation radius is based on the angular distance between field stars. The radius is be large enough that the typical field star density is included in the radius size. The size of the detection/truncation radius is the parameter that affects the resolution of the resulting extinction map. The resolution of the map determines the structural correlation length of the final map, meaning that if the resolution is chosen too small a very low S/N is given. If the resolution is chosen too big any small-scale structures of the molecular cloud are averaged out by an overwhelming number of contributing field stars.

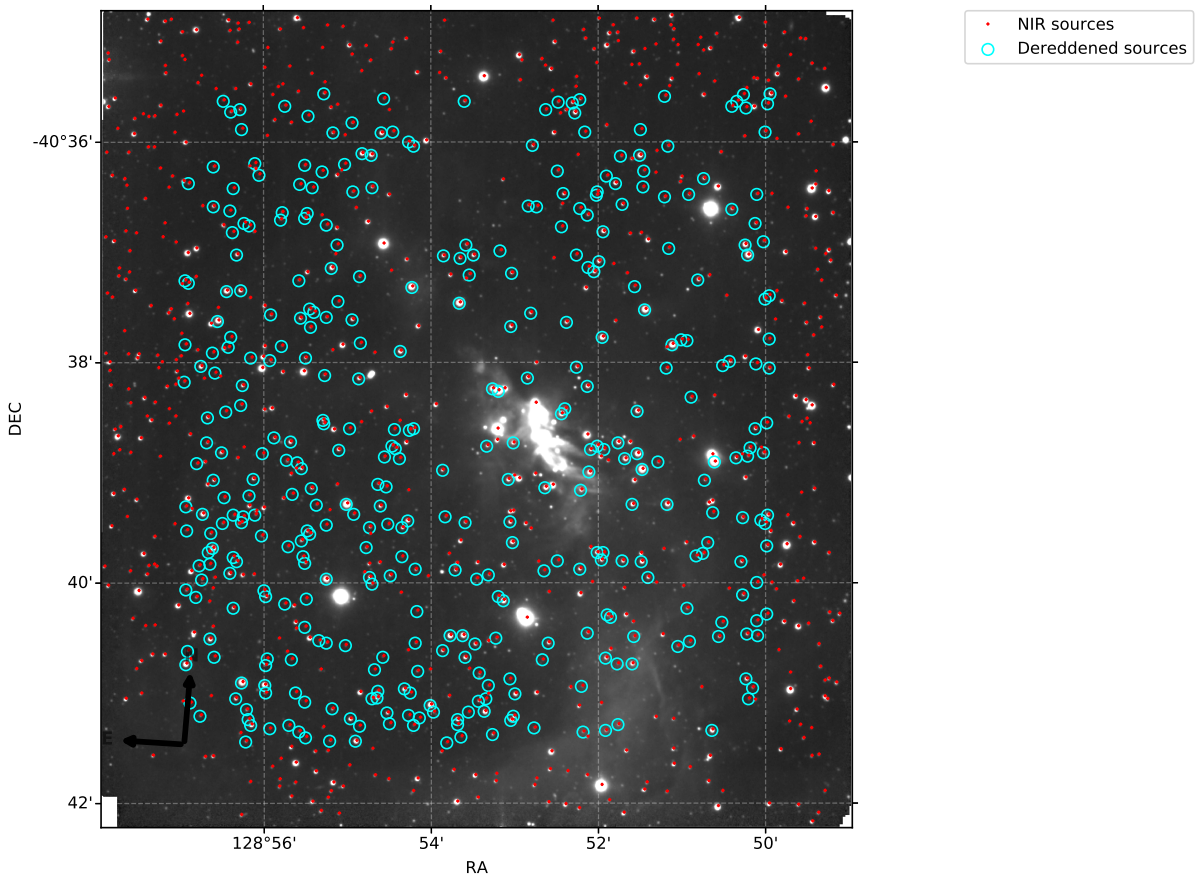

Figure 3.18: The position of the field stars that were used to construct the extinction map for the whole science field. The extinction for each star is only known at its point. The stars marked as the red dots are all of those that were detected in the *NIR* bands and those with the blue circles are the stars that were dereddened onto the main sequence and whose A_{K_s} extinctions are used to build the *NICEST* map. The rest of the extinction map is interpolated and smoothed from this pencil-beam type of map.

The error for $\hat{A}_{K_s}$ is calculated as:

$$\left(\delta\hat{A}_{K_s}\right)^2 = \frac{\sum_{n=1}^{N}\left(w_n^2\,\mathrm{Var}\left(A_{K_s}^{(n)}\right)\right)}{\sum_{n=1}^{N}(w_n)^2} \tag{3.33}$$

Here N is the total number of stars within the detection radius and $\mathrm{Var}\left(A_{K_s}^{(n)}\right)$ is the variance over all of the A_{K_s} values for the field stars that are used to calculate $\hat{A}_{K_s}$.

Lombardi (2008) states very clearly that equation 3.32 introduces a bias in the calculated column density when building an extinction map of a molecular cloud. Some of the more complex structures of the molecular cloud can be lost due to this bias in the method. This bias can be seen when performing star counting in a field where the surface density of stars changes from the Galactic average, ρ_0 to a lower surface density of field stars due to a molecular cloud, or other structure, causing extinction:

$$\rho(\mathbf{x}) = \rho_0.10^{-\alpha k_\lambda A_\lambda(\mathbf{x})} \text{ or } \rho(\mathbf{x}) = \rho_0.10^{-\alpha k_J A_J(\mathbf{x})} \tag{3.34}$$

In equation 3.34, α is the slope of the number of counts in Rieke & Lebofsky (1985) α is given as 0.34 mag^{-1} and $k_\lambda = A_\lambda/A$ is the extinction law in the λ band. The change in the density of field stars

is shown for $\lambda = J$, because the shorter wavelength bands are most affected by high extinction. To correct for the bias that exists in equation 3.32, the weight function w_n firstly has to take into account the decrease in density of field stars shown in equation 3.34 and secondly it has to be normalised $\left(\sum_n w_n = 1\right)$,

$$\begin{aligned} w_n(\mathbf{x}_i, \mathbf{x}_n) &= w'_n(\mathbf{x}_i, \mathbf{x}_n).\rho(\mathbf{x}_i, \mathbf{x}_n) \\ w_n(\mathbf{x}_i, \mathbf{x}_n) &= w'_n(\mathbf{x}_i, \mathbf{x}_n).10^{-\alpha k_\lambda \hat{A}_n} \end{aligned} \tag{3.35}$$

The weight function $w'(\mathbf{x}_i, \mathbf{x}_n)$ is a normalised Gaussian function that is multiplied with the column density correction factor $\rho(\mathbf{x}_i, \mathbf{x}_n)$.

Lombardi (2008) points out that the introduction of the correction factor to the weight function w_n creates a non-linearity in the calculation of $\hat{A}_n$ in equation 3.32. The non-linearity creates a new bias towards large extinctions, since the original $\hat{A}$ calculated from 3.32 is symmetrically distributed around A, but with the correction factor $\left(10^{\alpha k_\lambda \hat{A}_n}\right)\left(\hat{A}_n\right)$ will be skewed against values that are larger than $\left(10^{\alpha k_\lambda A_n}\right)(A_n)$. This means that the correction of the bias for cloud sub-structures introduces a bias related to the scattering of the individual extinction values. Details of the statistical nature of the newly created bias is discussed in Lombardi (2008). The magnitude of this newly created bias is $B_{\text{error}} = \beta \frac{\sum_n w_n \sigma_n^2}{\sum_n w_n}$, where $\{\sigma^2\}$ are the set of variances on the set of corresponding extinctions $\{A_n\}$ that are used to calculate $\hat{A}_n$. A term correcting for the new bias has to be introduced in the calculation of $\hat{A}_n$ in equation 3.32:

$$\hat{A} = \frac{\sum_n w_n(\mathbf{x}_i, \mathbf{x}_n) A_n}{\sum_n w_n(\mathbf{x}_i, \mathbf{x}_n)} - \beta \frac{\sum_n w_n \sigma_n^2}{\sum_n w_n} \tag{3.36}$$

Equation 3.36 can now be applied to each of the science fields, using the β_{LinES} and the dereddened A_{K_s} values for the field stars.

To ensure that a smoothed extinction map, showing realistic structure, is built the extinction for all field stars, $\{A_{K_s}^{(n)}\}$ should be evaluated. All foreground stars have to be eliminated from the population of field stars that are used to construct the extinction map of RCW 34 and NGC 2626. The elimination of a field star is based on the extinction of each star. If the extinction to a star is less than the average extinction that is caused by dust in the Milky Way plane at the distance of RCW 34, $\langle A_V \rangle_{\text{cutoff}} = \frac{2500 \text{ pc}}{1.8 \ A_V.\text{kpc}} = 4.5$, it has to be a foreground star. For each instance where $\hat{A}_{K_s}$ is calculated at a specific position it is done from a weighted average of a number of n surrounding field stars that are behind the star-forming region. It is very important that no foreground stars are included in the population of stars that are used for any instance where $\hat{A}_{K_s}$ is calculated.

Before a discussion is given about the extinction maps, it has to be emphasised how important the choice of the detection/truncation radius of each field is. It has already been stated that the choice of the size of the detection radius determines both the amount of information that one gets about small-scale structures in the molecular cloud, as well as the S/N for the extinction map. An objective value should be assigned to the detection/truncation radius. The radius should be big enough that the average field star density is included in each calculation of $\hat{A}_{K_s}$. If the radius is too small, numerical errors will arise in areas where there are large statistical fluctuations in the field density. The radius should also not be too big, because any small-scale structures in the molecular cloud may be averaged out causing a loss of structural information. An objective way of choosing the detection/truncation radius would be to consider the distribution of angular distances between all pairs of stars over the whole science field. The spatial stellar density should keep on increasing as a function of radius until the density reaches the Galactic plane average, where the density will start to flatten off. Such a distribution is shown in Figure 3.19 for RCW 34; the distribution stops increasing at around 200 pixels,

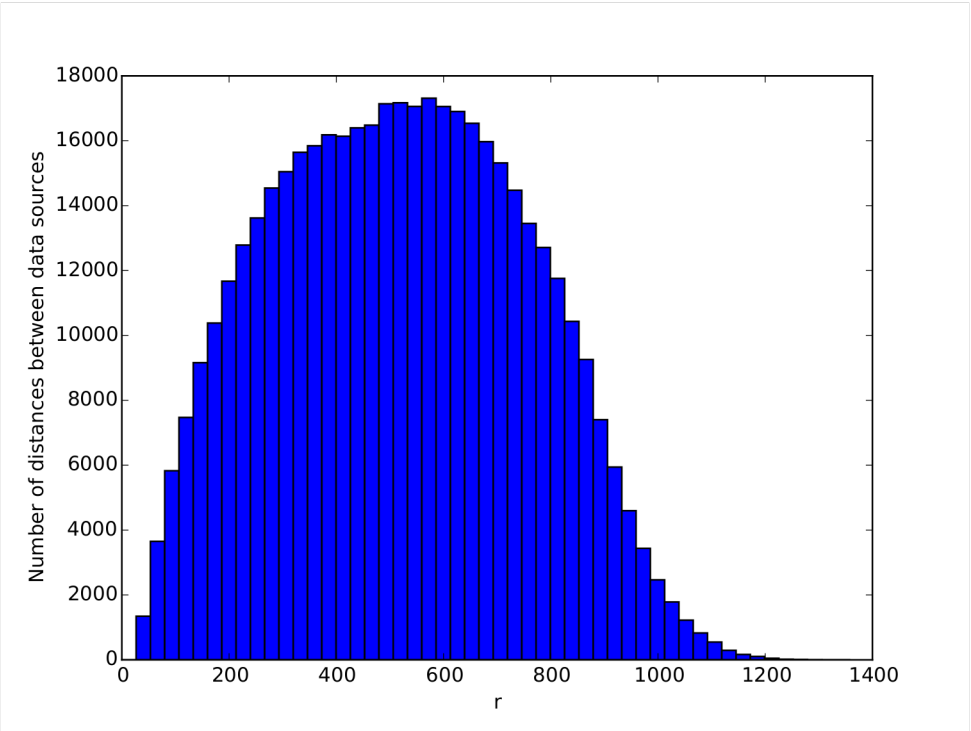

Figure 3.19: In this figure, the number of combinations for angular distance between different stars is shown as a function of the number of pixels between pairs for RCW 34. The initial increase in many combinations for small distances shows a density lower than the average and would probably be too small for a detection radius. Moreover, the decrease in many combinations at the larger distances shows the cut off effect that the image's border has on the field star density.

or 91 arc-seconds. This was the size of the radius chosen for the construction of the extinction map of RCW 34. The weight that is assigned to each contributing field star is calculated with a Gaussian function which has a radius equivalent to the detection/truncation radius. This size is an indicator of how big the Gaussian should be around each pixel where $\hat{A}_{K_s}$ is calculated. The reason is that a Gaussian of this size would span enough of an area to include the typical field star density. The same radius can not be used for both RCW 34 and NGC 2626, because the density of field stars differ in the individual directions. Angular expanse of each field of view also determines how large a radius can be chosen. A detection/truncation radius of $45''$ is used for the Gaussian in each instance that is calculated for $\hat{A}_{K_s}$ in the field surrounding NGC 2626. To illustrate the influence that a differing size of the detection/truncation radius has on the resulting extinction map, various radius sizes are used in the construction of an extinction map for NGC 2626. The resulting extinction maps of NGC 2626 for three different truncation/detection radii are shown in Figure 3.20 and discussed thereafter.

To illustrate the choice of the truncation/detection radius on the resulting extinction map, three different sizes of the detection radii were chosen, respectively as $r_{\text{detect}} = 10''$, $r_{\text{detect}} = 30''$, and $r_{\text{detect}} = 70''$ and are shown in Figure 3.20. Choosing r_{detect} too small does not include enough field stars that contribute to areas with high extinction to add enough information to interpolate in the construction of the extinction map, resulting in a patchy structure. If r_{detect} is chosen in the range of the spatial extent of the molecular cloud the smoothing of *NICEST* washes out some of the smaller scale structures of the molecular cloud, defeating the purpose of the correction for the small scale structures of *NICEST* above *NICER*.

The S/N ratio will be different for $\hat{A}_{K_s}$ in each pixel, because the stars and the contributing weight for each of those stars change for each instance in the calculation of $\hat{A}_{K_s}$. To demonstrate this phenomenon S/N maps are shown in Figure 3.20 the extinction maps for the same detection/trun-

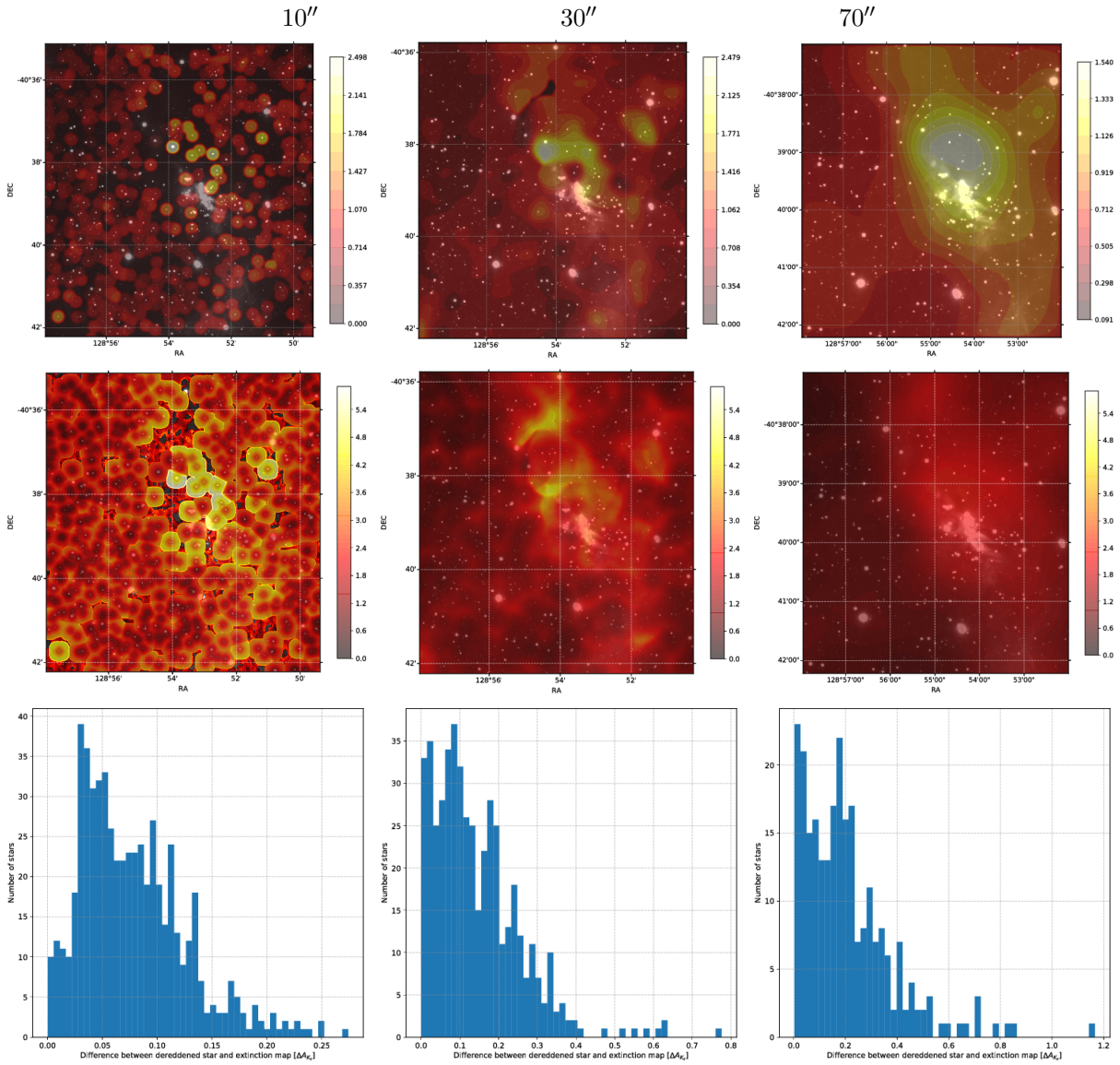

Figure 3.20: The effects of choosing a different truncation/detection radius for the construction of an extincion map is shown for NGC 2626. The upper three panels show extinction maps that were built using *NICEST LinES* with a respective detection/truncation radius of 10″, 30″ and 70″. The middle set of panels is the $\log(S/N) = \log\left(\frac{\hat{A}_{K_s}}{\delta\hat{A}_{K_s}}\right)$ for the same set of radii. The bottom set of diagrams is the absolute value of differences between the extinction that was measured for each field star from the colour-colour diagram and the extinction at its position on the extinction map.

cation radius. The S/N in each pixel is calculated as the ratio $\frac{\hat{A}_{K_s}}{\delta\hat{A}_{K_s}}$. The three graphs showing the natural logarithm of the calculated S/N are all plotted on the same scale to make comparison possible.

The high S/N in the case of the 10″ is due to too few stars that contribute to the calculation of the $\hat{A}_{K_s}$, and the results are not realistic. As for the 30″ truncation radius a higher number of stars contribute to the calculation of $\hat{A}_{K_s}$, so that a single star is not the only contributor to the calculation of $\hat{A}_{K_s}$, and a more realistic structure is shown in the extinction map. For the 70″ radius the S/N decreases, because of the larger number of stars that contribute to the calculation of $\hat{A}_{K_s}$. This means that a proper mix of stars that have low and high extinctions is used and can not be distinguished from each other. The maximum S/N for the 10″, 30″, and 70″ extinction maps are 5500, 4600, and 2400,

respectively. The maximum S/N values for the $10''$ and $30''$ radii are mainly an artificial construct due to the unrealistic structures in the extinction map. The $70''$ radius' lower S/N ratio is a result of the overly averaged extinction error map, which gives the resulting S/N map. The three different sizes that were chosen show a progression in the numerical method which builds the extinction map from small discrete structures to an overly smoothed map. This progression is directly proportional to the density of field stars behind the star-forming region, meaning the density will change from RCW 34 to NGC 2626. If this interpolation method is applied anywhere else in the Milky Way, it is still dependent on the exposure time of the image that is used to measure the number of field stars behind the structures. The right choice of the truncation/detection radius will have enough field stars that contribute to the calculation for each instance of A_{K_s}, without loosing the smaller scale structures of the molecular cloud due to oversmoothing.

The last three graphs in Figure 3.20 show the distribution of the difference between the value of A_{K_s} for each field star that was dereddened on the colour-colour diagram, and the extinction at the same position on the extinction map. The difference is the absolute value between the extinction measured from the dereddened colours and the extinction measured from the map at the same position. The distribution of $r_{\text{detect}} = 10''$ is concentrated between the $0 \leq \hat{A}_{K_s} \leq 0.2$, indicating that for most of the field stars the difference between the dereddened extinctions and the extinction map are very small. It can not give an objective measure between the dereddened colours from the colour-colour diagram and extinction map, due to the unrealistic, patchy extinction map that was built — the radius was just too small. For the $30''$ and $70''$ the radius is big enough that a continuous structure in the extinction map has been constructed. The distributions for the difference between the dereddened extinction and the extinction map fo $r_{\text{detect}} = 30''$ and $70''$ are not as large as for $10''$ because of a continuous structure in the extinction map. The distribution for the difference $\Delta A_{r'}$ of $30''$ is not as flattened as the $70''$ at larger differences, but has a higher number peak at smaller differences. This suggests a radius of an optimal size, smaller than $70''$ will give the most structural information of the molecular cloud in NGC 2626, the least difference between the dereddened A_{K_s} value, and the weight average $\hat{A}_{K_s}$ at the same position. In other words, the most accurate extinction map that can be derived with *NICEST LinES*.

By using (1) the distribution of the distance between field stars, (2) the S/N maps (3) how realistic the structures in the extinction map are and (4) the distribution of ΔA_{K_s}, a truncation/detection radius was chosen. A very important criteria for point (3) is that the detection/truncation radius is big enough that it gives a realistic extinction map with continuous structures. However, this is not true the doughnut shaped, discontinuous structures in the of map of the $10''$ radius, because no molecular cloud has been seen with that type of structure. The truncation/detection radii were respectively chosen as $45''$ and $65''$ for NGC 2626 and RCW 34. The chosen radius of the Gaussian that is used to build the extinction maps can be used to calculate the resolution of the maps. Juvela & Montillaud (2015) explains that the resolution will be the FWHM of the chosen Gaussian, meaning that NGC 2626 and RCW 34 will have respective resolutions of $\sim 35''$ and $\sim 51''$, because the relationship between the detection radius and the resolution is $\left(\frac{\text{Truncation radius}}{3} \times 2.35\right)$. Any structures that are smaller than the specific resolution of the extinction map will not be visible/discernable, because it will be averaged and smoothed out by the *NICEST* algorithm.

If a foreground star is included by accident in the stellar population which was used to construct the extinction map — because it has an extinction higher that the cutoff extinction — it will not have a drastic impact on the structures in the extinction map. The reason for the small contribution of a foreground star is that each pixel on the extinction map is built from a weighted average of field stars that are included in the truncation/detection radius. This will cause the effects of a single few foreground stars to be outweighed by the contribution of the extinction measured to field stars behind the star forming region. Any and all background stars make a positive contribution to the construction of the extinction map, even the faintest sources have a positive contribution because the sources with an error larger than 0.05 have been removed from the data set before the extinction maps were built.

3.3.3 Extinction maps from different extinction laws *NICEST*

In the previous subsection, the different extinction laws are shown on colour-colour and colour-magnitude diagrams. In this subsection the usage of these extinction laws with the *NICEST* algorithm are shown in the construction of extinction maps. Together with the maps, the position of sources that showed excess emission, according to the applied extinction law, are plotted. No explanation will be given about the molecular cloud and the environment surrounding the star-forming regions, but only about the resulting extinction maps. The extinction law by Rieke & Lebofsky (1985) and the custom derived *LinES* extinction law for NGC 2626 are identical in Figure 3.14, so they will deliver the same resulting extinction map. Only the extinction laws by Cardelli *et al* (1989) and the *LinES* extinction law that was derived for RCW 34 will be applied in an extinction map of the area surrounding NGC 2626.

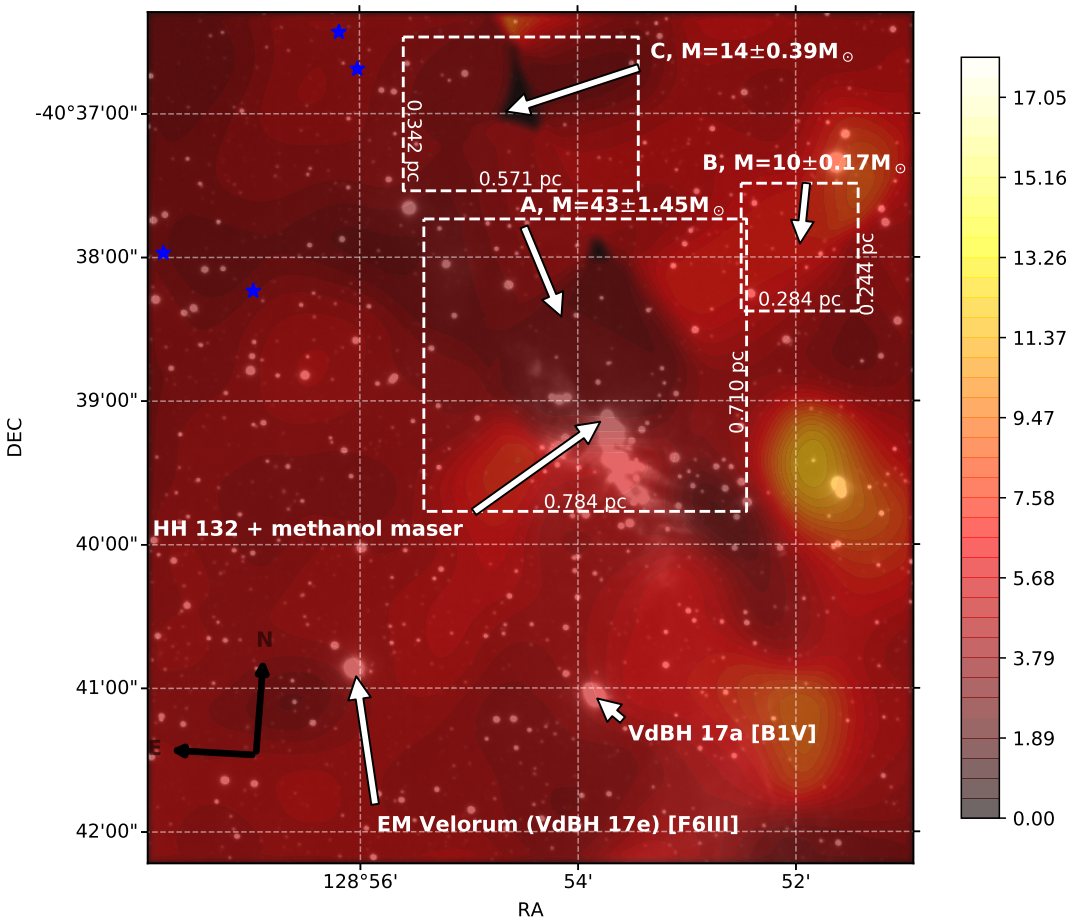

Figure 3.21: The extinction map that was built of the field surounding NGC 2626 using the extinction law by Cardelli *et al* (1989), as well as all of the excess emission sources that were identified using the extinction law.

In Figure 3.21 the extinction map was built using the extinction law by Cardelli *et al* (1989). The dense regions in the extinction map are not in the same positions as the extinction maps that were presented by Sharma *et al* (2016) (see Figure 1.8). The low-density regions, especially the one at the centre of block C and the one at the top of block A, do not agree with any of the structures seen in Figure 1.8. This inconsistancy between the CO map and the extinction map built using the extinction law from Cardelli *et al* (1989), suggests that something is wrong with the construction of the extinction map.

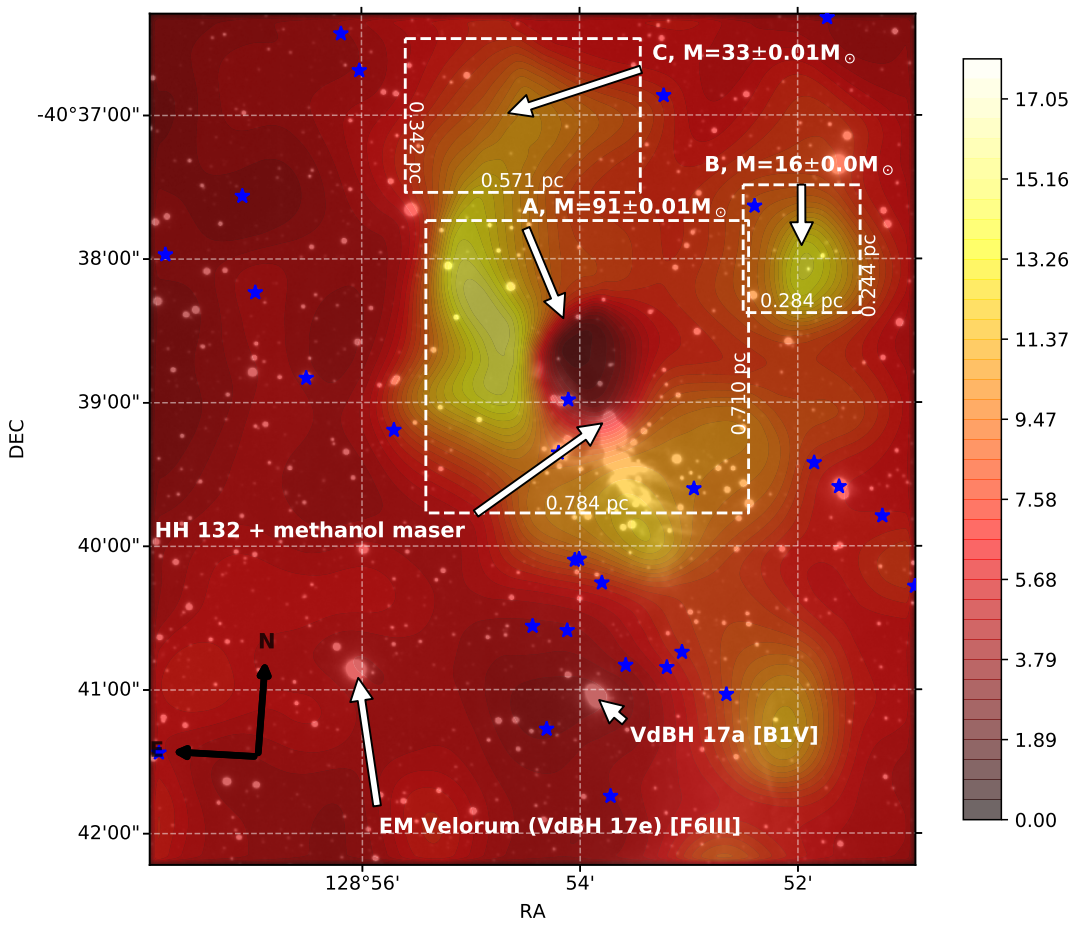

Figure 3.22: The extinction map that was built of the field surrounding NGC 2626 using the custom extinction law that was calculated with the *LinES* algorithm, as well as all of the excess emission sources that were identified using the extinction law.

The extinction map for NGC 2626 was built with the custom *LinES* exinction law that was derived for RCW 34 is shown in Figure 3.22 and illustrates what happens if an incorrect extinction law is used. The map shows regions with very low extinction, where the CO map from Sharma *et al* (2016) shows some of the highest extinction, and in some regions where Figure 3.22 show low extinction there are dense structures in the CO map. This is caused by the reddening vector for *LinES* on the colour-colour diagram, which eliminates the majority of the field stars that can be reddened onto the main sequence. This implies that stars that would be classified as main sequence stars, using the extinction law from Rieke & Lebofsky (1985), they are incorrectly classified as excess emission stars using the *LinES* extinction law. This extinction map is a result of using a custom extinction law that was derived for a specific region and can not be used for data in a different region.

The *LinES* and Rieke & Lebofsky (1985) extinction laws used to build the two extinction maps also show the location of the stars that showed excess emission according to each specific extinction law. For both maps built with the *LinES* and Cardelli *et al* (1989) extinction laws the sources with excess emission are in different locations than in Figure 1.8. The dense structures in each of the extinction maps do not show resemblance to the CO map. Testing the use of different extinction laws in the construction of the extinction map emphasize how important it is choosing the correct extinction law, and checking the results with existing extinction results. From the colour-colour diagrams with the distribution of all the stars detected in NGC 2626, and these extinction maps it is apparent that the extinction law from Rieke & Lebofsky (1985) is the correct choice for NGC 2626. In the following section, the custom *LinES* extinction law for RCW 34, and the extinction law by Rieke & Lebofsky

(1985) for NGC 2626 are used together with the calibrated field stars to build extinction maps with the *NICEST* algorithm.

3.4 Results and discussion

3.4.1 Extinction maps and spacial distribution of PMS stars in RCW 34

3.4.1.1 *NICEST LinES* extinction map

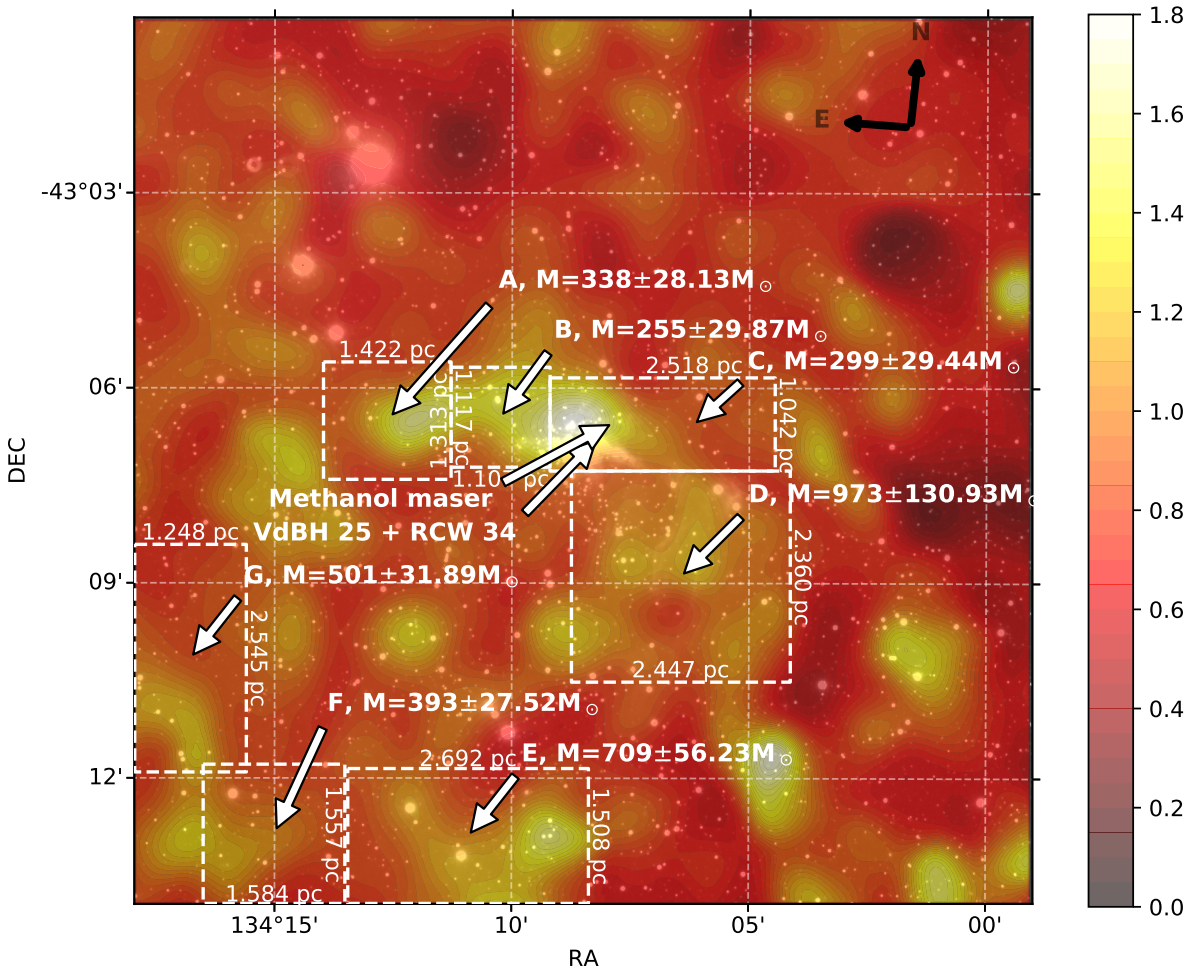

Figure 3.23: The *LinES* extinction law was used to build an extinction map of the $15.9' \times 15.9'$ mosaicked image from the excess emission in field stars surrounding RCW 34. The *NICEST* algorithm used a $65''$ detection radius to build the extinction map in magnitude units of A_{K_s}.

The extinction map of the $15.9' \times 15.9'$ field around RCW 34 is shown in Figure 3.23. It contains some interesting objects and structures in the embedding molecular cloud. In the centre of the field is the arch-shaped HII region which embeds the exciting stars, i.e. an O8.5V and two young B stars. The HII region is the separation between the molecular cloud towards the north which was first documented by Pagani *et al* (1993) and a bubble-shaped clearing where young PMS stars are located (see Bik *et al* 2010). Most of the material in the centre of the bubble region have been cleared out by the OB stars and the low-mass young cluster members. It is not known how much of the initial molecular cloud is still present in the molecular cloud from which the cluster formed, but some of the embedding matter surrounds the bubble region.

The bright source in the upper-left corner of the image causes the *NICEST* routine to break down, because its angular size is too big for photometric measurements with the chosen aperture range in the reduction pipeline. In Figure 3.4 the brightest sources have been removed with the PSF photometry,

however this specific source could not be removed. This bright source has such a large emission profile that only some of the light at the center of its emission profile was removed by the PSF photometry. The rest of the profile could not be removed by the parameters used in the PSF photometry that worked in the subtraction of other sources' light emission profiles from the image. All of the sources that were detected in the light-profile of this bright source were removed from the measured datasets. The lack of field star data at this position becomes very clear from the extinction map that was built with the numerical routine; it seems that there is physically nothing at this position while the images show sources at this position.

3.4.1.2 *Comparisson between NICEST LinES maps and CO extinction maps of RCW 34*
Of the remnant matter that still surrounds the bubble region, there are seven big clumps, which each have high extinctions ($A_{K_s} > 0.75$) where star formation may still occur. The regions are named A-G as indicated in Figure 3.23. Before the properties of these dense regions are reported or discussed, they can be used to test the accuracy of extinction maps that were built with *NICEST LinES*. This is done by comparing CO maps of clumps A, B, and C that were observed by Pagani *et al* (1993).
In Figures 3.23 and 3.24 the structure of the molecular cloud can be compared on the extinction maps. In a private communication with Pagani the original data of the CO map was requested, but it does not exist anymore, which only left the imaging data published in the paper. Meaning in Figure 3.24 the image was taken from the paper by Pagani *et al* (1993). Without the available CO data it is not possible to plot the CO map and mark the dense regions A-G, which were identified in the *NICEST LinES* extinction map for comparison. Thus comparisson between the CO maps and the *NICEST LinES* extinction maps can only be performed visually. In Figure 3.24b clumps A, C, and a part of D can be seen, as well as clump B in Figure 3.24d. The identical structures of clumps A-D between the CO and *NIR* data is a confirmation that the method that was implemented in the field around RCW 34 and then consequently NGC 2626 is correct. This is similar to the testing that was done by Lada *et al* (2007) who compared CO extinction maps with *NICER/NICEST* extinction maps of the Pipe nebula.

Clumps A-G form the outer parts of the bubble clearing that was studied by Bik *et al* (2010). In Figure 3.25 nebulous gas can be seen all along the inside of the bubble region. This is the only observational indicator different from the *NIR* observations in this study, namely, that there are dense structures on the side opposite to VdBH 25a of the bubble clearing. It is only from the *NICEST LinES* extinction maps that the extent of these clumps become apparent and the question about future star formation arises.

3.4.1.3 *Physical properties for remnants of the molecular cloud*
It is possible to deduct physical properties of the molecular cloud from the extinction map that was built with *NICEST LinES*. Using the distance, the physical area that is represented by a pixel on the extinction map, and the visual extinction read from the extinction map at the pixel's position, the total matter contained in a pixel on the extinction map can be determined. The total matter in each pixel can be calculated from the visual extinction measured at each pixel's position using a column density-to-visual-extinction relation given by Whittet (1992) as $2.21{\times}10^{21}\ \frac{\text{particles}}{A_V.\text{cm}^2}$. To calculate the total matter that is contained in each pixel from the column density, the physical area that is represented by a single pixel on the image has to be calculated. This was done by using the pixel scale of the imager to calculate the radial angular size of each pixel in the RA and DEC directions. The distance to RCW 34 was used as 2.5 kpc (see Bik *et al* 2010) so that the area represented by a pixel is:

$$\begin{aligned}&\text{Physical surface area represented by a single pixel} =\\&\left(\text{Pixel scale on RA} \times \frac{\pi}{180^\circ} \times \text{distance}\right) \times \left(\text{Pixel scale on DEC} \times \frac{\pi}{180^\circ} \times \text{distance}\right)\\&= \left(0.457\ \text{arcsec} \times \frac{\pi}{180^\circ} \times 2500\ \text{pc} \times 3.086 \times 10^{18} \frac{\text{cm}}{\text{pc}}\right)^2 = 2.805 \times 10^{32}\ \text{cm}^2\end{aligned}$$

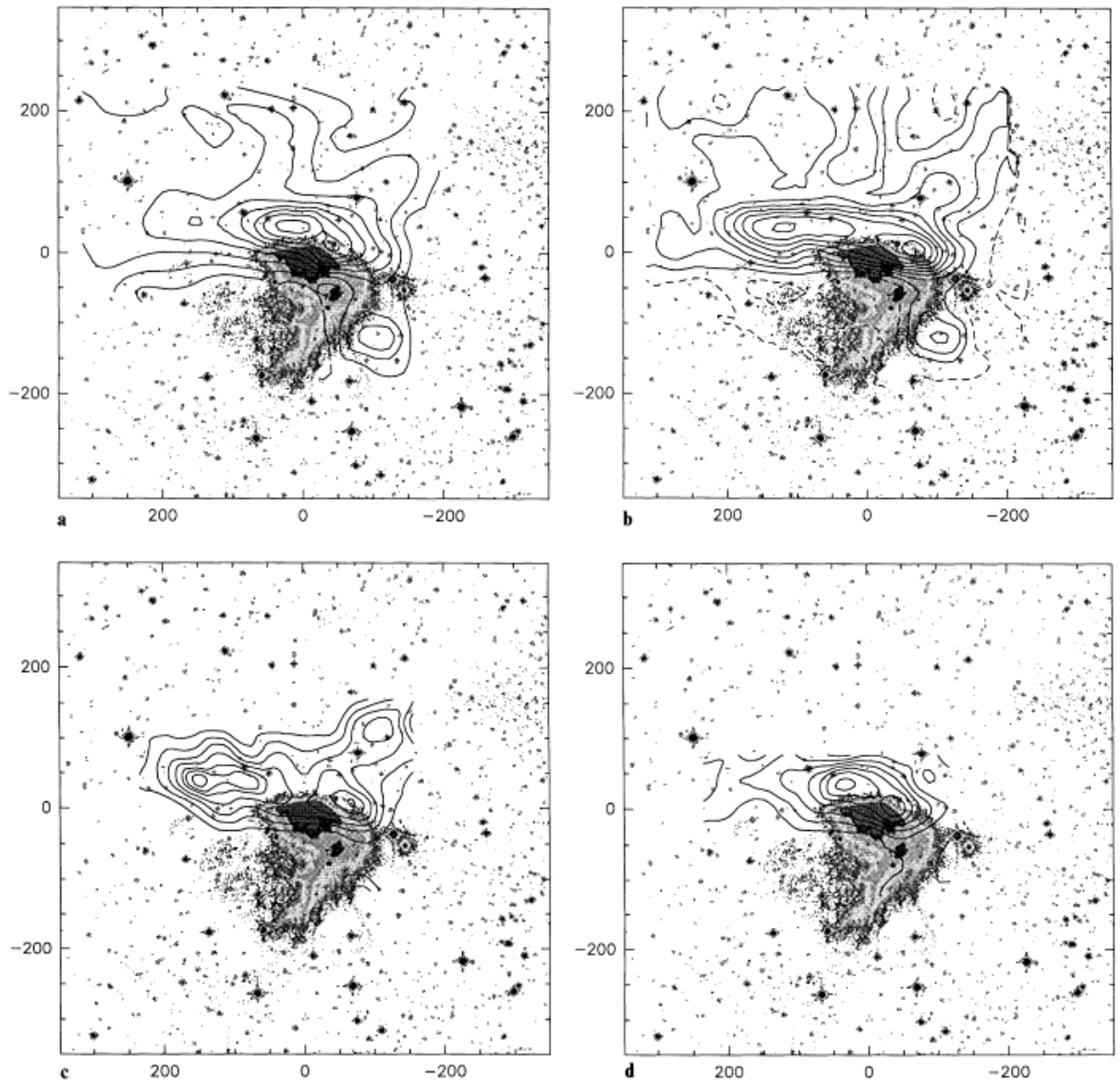

Figure 3.24: The CO maps from Pagani *et al* (1993) were used to compare with the extinction maps that were built with *NICEST LinES*. (**a**) ^{12}CO($J:1\rightarrow0$) integrated area between 0 and 15 km.s^{-1}, levels (5-85) K km.s^{-1} by steps of 10. (**b**) ^{13}CO($J:1\rightarrow0$) integrated area between 2 and 11 km.s^{-1}, levels 1-13 K km.s^{-1} by steps of 1.5. (**c**) C^{18}O($J:1\rightarrow0$) integrated area between 4 and 10 km.s^{-1}, levels 0.1 to 0.9 K km.s^{-1} by steps of 0.2 plus 1.0 and 1.1 K km.s^{-1}. (**d**) C^{32}S($J:2\rightarrow1$) integrated area between 0 and 12 km.s^{-1}, levels 0.5 to 6.5 K km.s^{-1} by steps of 1.

The product of the column density, the surface area represented by a pixel and the extinction in that specific pixel, was then multiplied by hydrogen's atomic mass to get the total mass of embedding material observed in that pixel. Using the mass of the matter in each pixel the total mass of the dense clumps A-G could be calculated. The total mass for a clump was taken as the sum over all of the pixels which had an extinction higher than $A_V = 5$ ($A_{K_s} = 0.517$). An extinction of $A_V = 5$ was chosen because the average extinction in the Milky Way's plane is $A_V \sim 4.5$. A more conservative threshold for dense material in RCW 34 was chosen to be certain that the mass of only dense material in RCW 34 was calculated. The masses for clumps A-G were thus calculated as given in Table 3.2:

In Table 3.2 a rough estimate for the density is given for each clump. This was calculated by assum-

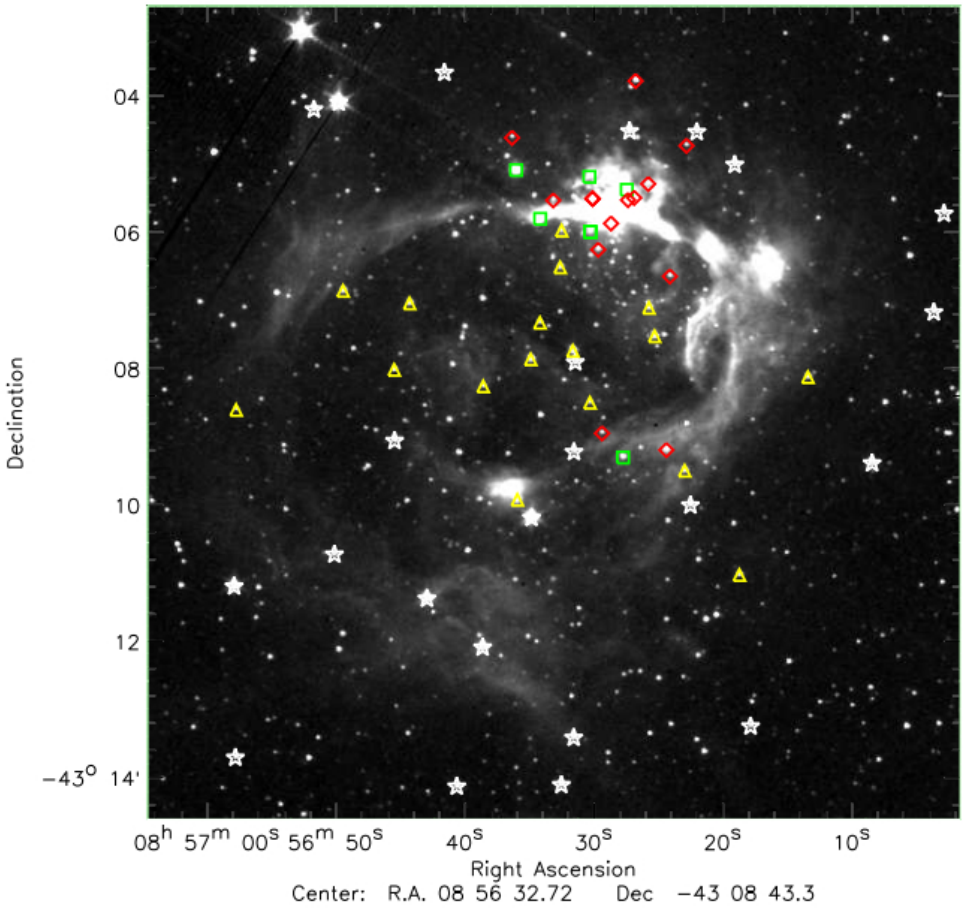

Figure 3.25: A Spitzer/IRAC 3.6 μm image that was taken from Bik *et al* (2010). The red diamonds and yellow traingles are class 0/I and class II objects, respectively.

Table 3.2: Properties of dense regions in RCW 34 measured from the *NICEST LinES* extinction map.

Clump	Length [pc]	Width [pc]	Mass [$M_\odot$]	Error of mass [$\delta M_\odot$]	Average density [cm^{-3}]
A	1.422	1.313	266.50	10.65	970
B	1.107	1.118	184.92	7.22	1305
C	2.518	1.042	247.84	11.62	362
D	2.447	2.360	709.93	44.54	485
E	2.692	1.508	560.73	27.29	496
F	1.584	1.557	324.19	15.54	790
G	1.248	2.545	434.35	22.87	7237

ing that each clump is a symmetric ellipsoid that has a length and width, also given in the table. The density was then calculated for the number of hydrogen atoms in that specific volume. The calculated density of A is in the same order as the density that was measured by Pagani *et al* (1993) from the CO data. The consistency between Pagani *et al* (1993)'s CO data and the rough density calculation means that the temperature that was measured by Pagani *et al* (1993) can also be used to calculate a Jeans mass. By calculating the Jeans mass the possiblity for future star formation is tested.

A Jeans mass of 72 $M_\odot$ and a Jeans length of 0.0513 pc was calculated for a temperature of 17 K and a density of 10^3 cm^{-3} which was measured by Pagani *et al* (1993) from $^{12}CO(J:1\rightarrow 0)$. The masses for A-G exceed the Jeans mass implying that there is a possibility for future star formation in these clumps. Clumps A and D-G have the highest promise of future star formation, because of the mass measured for each cloud is higher than the Jeans mass for the specific density and temperature

measured by Pagani. Of the clumps that hold the highest promise of future star formation, E and G extend further than the field of view that is shown in Figure 3.23. Clumps E and G are also physically larger than the extent of the field studied, and also have masses higher than shown in Table 3.2.

In clump B it is possible that VdBH 25a may have triggered star formation by perturbing gas from the outside of each clump into its interior. However, clump C may be dissolved by photo-evaporation by VdBH 25a and the two B stars, because Bik *et al* (2010) measured a velocity of 16 ± 8 km.s^{-1} on the ridge of ionized gas, which separates the HII region and the molecular gas. If the ionized gas keeps moving with the same velocity it will take somewhere between (42-128)$\times 10^5$ yr to cross the 1.042 pc distance across clump C. This period is much shorter than the 2×10^5 yr period that was stated by Hayashi *et al* (2017) as the formation period of the high-mass star and other cluster members formed during cloud-cloud collision. The amount of material in clump C was shown by Pagani *et al* (1993) to be more than the amount calculated from the mass measured from the *NIR* extinction map. Thus it is very likely that the speed at which the ionization will commence will not remain at 16 ± 8 km.s^{-1}, or if it does, it will take much longer to clear out — anywhere in the range of (42-128)$\times 10^5$ yr. It is possible that more star formation may occur in the environment surrounding RCW 34.

3.4.1.4 *Uncertanties in the extinction map of RCW 34*

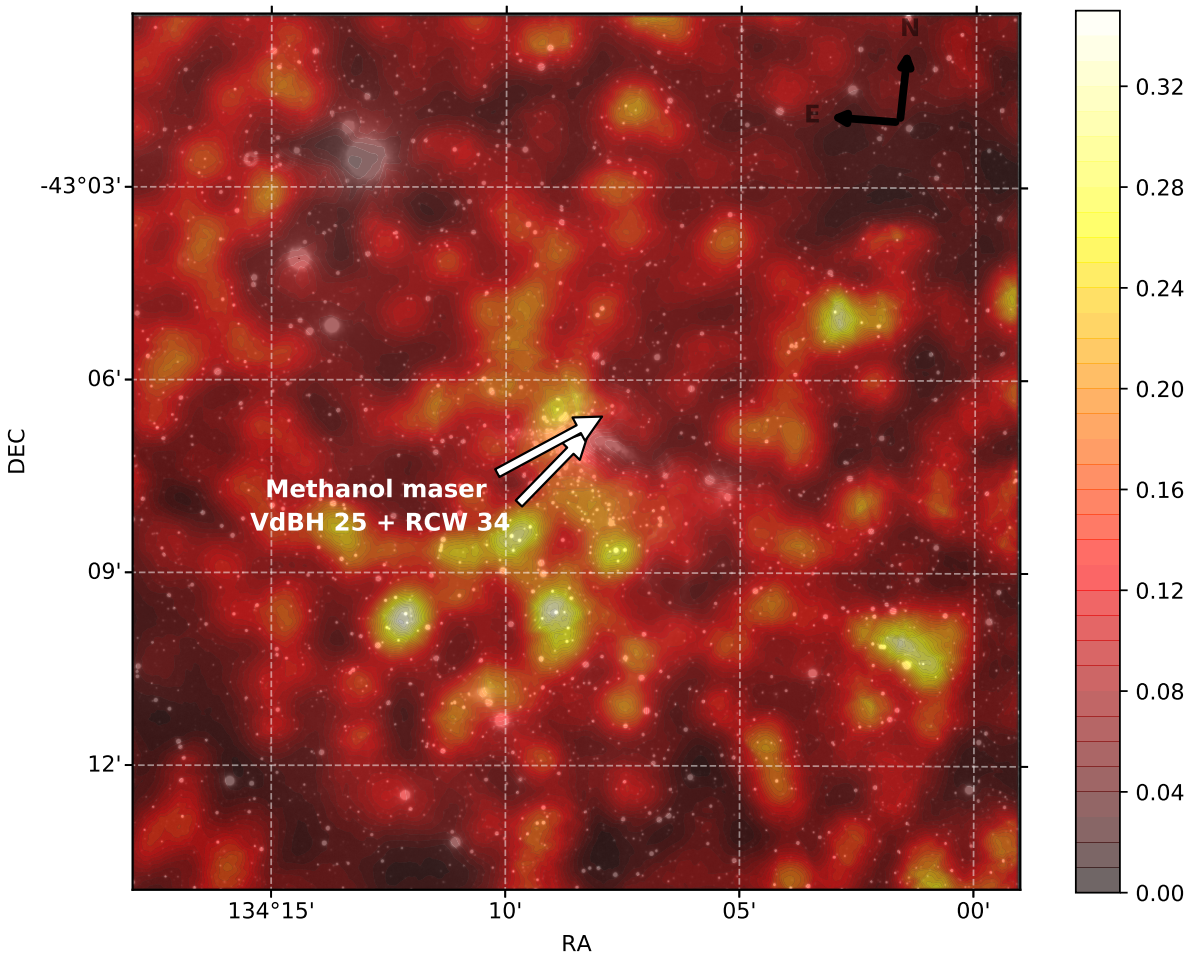

Figure 3.26: The error, δA_{K_s} for the extinction map of RCW 34.

Figure 3.26 shows the error at each pixel coordinate. This error was calculated using a weighted average from the measured extinction in each contributing field star's error, $\frac{\delta(J-H)}{\delta(H-K_s)}$. At some positions with high extinction, there is a corresponding high error. This is because of a lower field star density at high extinction. In the regions with higher extinction the field stars behind the molecular clouds

have a fainter magnitude implying that a higher error is also measured. The relation between errors and magnitudes are shown in Figure 3.7 and 3.8.

3.4.1.5 *Quality tests of the extinction maps: S/N map and the distribution for the difference between the dereddened and extinction map A_{K_s} values of RCW 34*

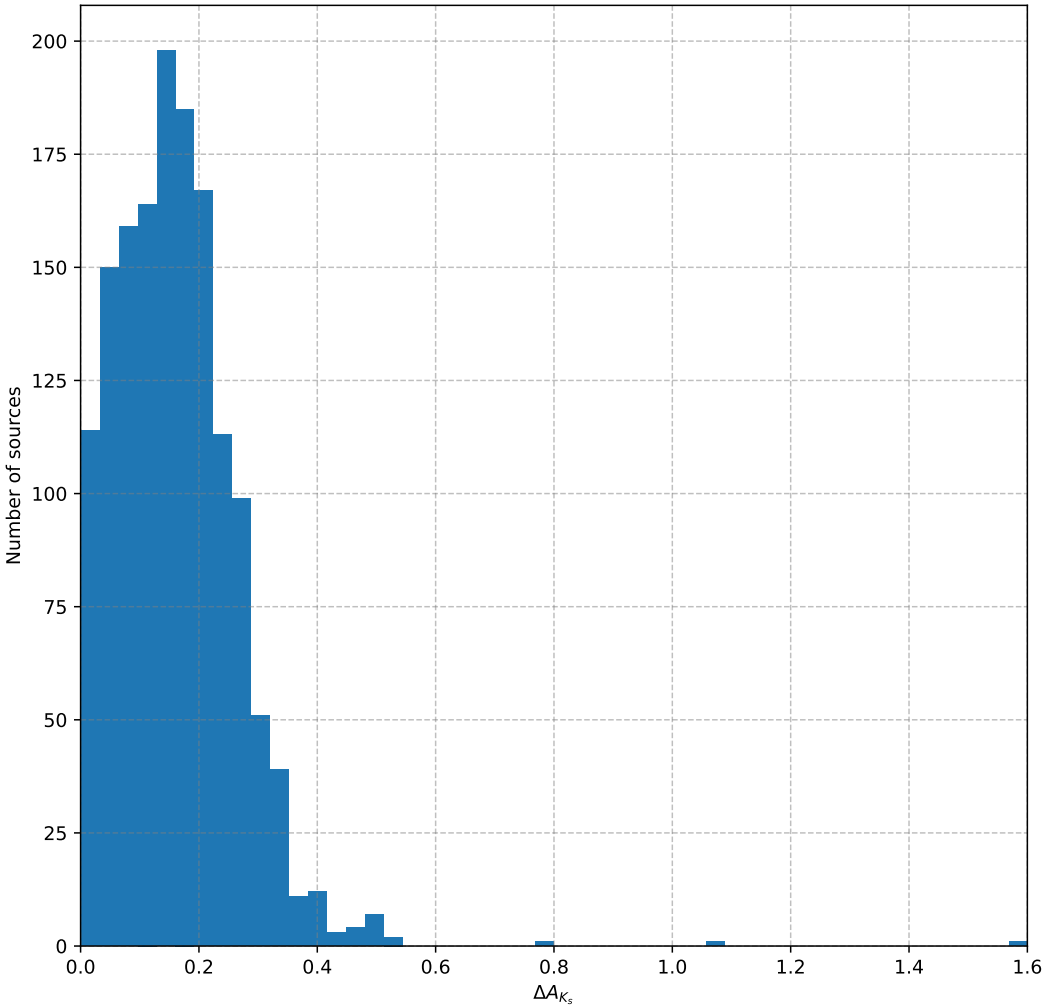

Figure 3.27: The difference between the dereddened colours on the CCD and the $\hat{A}_{K_s}$ value for the field stars in the extinction map around RCW 34

Figure 3.27 shows a histogram of the difference between the dereddened A_{K_s} magnitudes from the colour-colour diagram, and the weighted average $\hat{A}_{K_s}$ from the extinction map. The distribution of the differences between the dereddened extinctions and the measured extinctions from the map are similar to the distributions for NGC 2626 shown in Figure 3.20. The difference is that RCW 34 has a significantly larger density of field stars that were used to build the extinction map. This is reflected in the distribution of the difference between the dereddened extinction and the extinction measured at the same position on the extinction map, with the majority of the differnces as $\Delta A_{K_s} \leq 0.4$. The mean difference is $\hat{\Delta} A_{K_s} = 0.161$, and the standard deviation is $\sigma_{\Delta A_{K_s}} = 0.105$, which reflects the small range of differences for the stars that were used to construct the extinction map. This implies that the extinction map has little deviation between the weighted average that was calculated from the surrounding field stars and the extinction measured from dereddening the field star to the main sequence. In other words, the correct size truncation/detection radius was chosen allowing for a very accurate extinction map to be constructed.

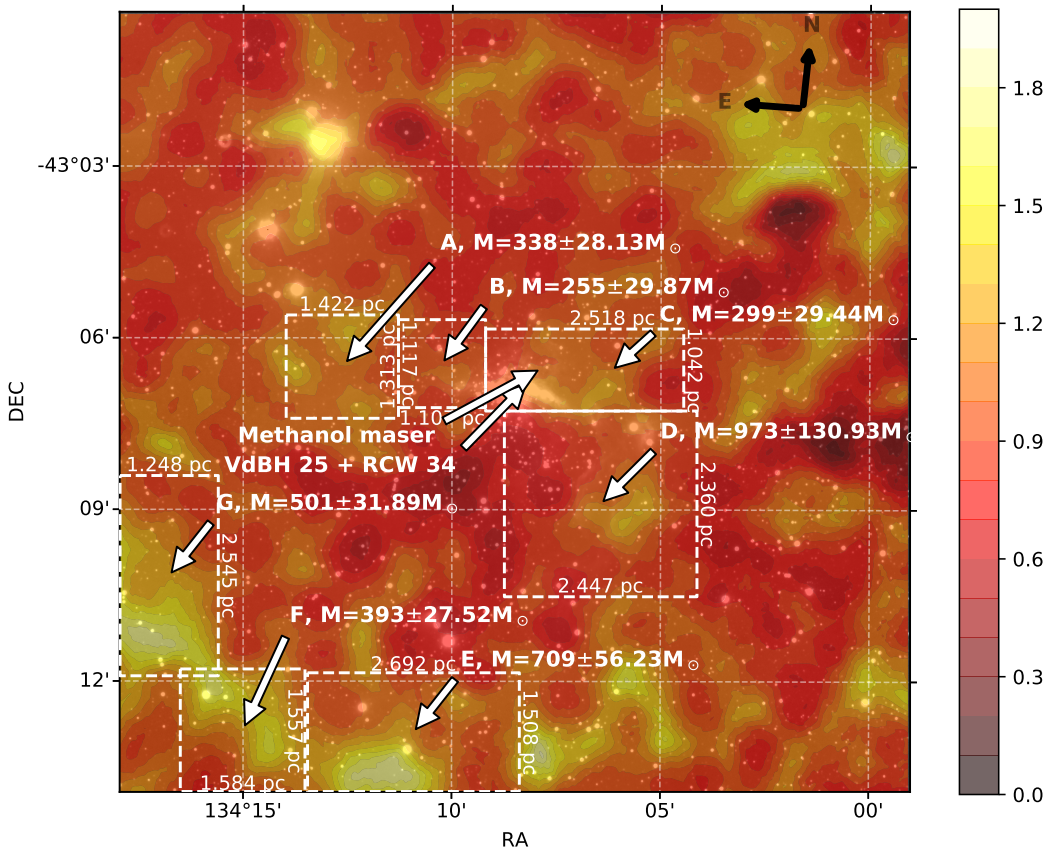

Figure 3.28: The logarithm of the signal-to-noise ratio, $\log_{10}(S/N) = \log_{10}(\frac{\hat{A}_{K_s}}{\delta\hat{A}_{K_s}})$ for the extinction map of RCW 34.

Figure 3.28 shows the logarithm (base 10) of the S/N map for the *NICEST LinES* map of RCW 34. The map is very complex, but from some regions with high extinction there is a high S/N, especially for clumps E-G. While clumps A-D have S/Ns that are comparable to the rest of the map. With a S/N for regions with high extinction that is comparable to the rest of the map, it is expected that for higher extinctions (A_{K_s}) the error also increases (δA_{K_s}), or that there is some proportionality between the extinction and its error, $\delta A_{K_s} \propto A_{K_s}$. This implies that the precision of the extinction map is high in regions with high extinction and a corresponding S/N like clumps E-G.

3.4.1.6 *Concluding remarks on the NICEST LinES extinction map of RCW 34*

The error map, S/N map, and the distribution of dereddened extinction magnitudes are all tests that indicate that the extinction map that was constructed with *NICEST LinES* gives a very accurate representation of the molecular cloud remnants in RCW 34. The extinction map also shows much more structure than the CO map by Pagani *et al* (1993), especially at areas with low extinction ($A_V \sim 2-5$). This improvement of the *NIR*-based extinction maps above CO extinction maps was also seen by Kong *et al* (2015) in the California molecular cloud, and Juvela & Montillaud (2015) in an all-sky *NICER/NICEST* extinction map based on *2MASS* data.

Photometry of the $15.9' \times 15.9'$ field made it possible to truly see how much remnants of the initial molecular cloud are left. These remnants stretch further than any previous study could show. The only other proof of clumps E-G was a *Spitzer/IRAC* 3.6 μm image from Bik *et al* (2010), which simply show excited gas on the inside of the bubble region. It is not possible to state how much further

clumps E and G extend away from the bubble clearing without the necessary observational data. The physical sizes and the masses of the remnant dense regions hold strong promise for future star formation, especially those far away from the HII region on the south-western part of the bubble region.

3.4.2 Extinction maps and spacial distribution of PMS stars in NGC 2626

3.4.2.1 *The environment around NGC 2626 and the NICEST extinction map*

There are more stars that can be associated with the cluster in NGC 2626 than in RCW 34, making the environment around the star-forming region more complex. There are three bright emission stars situated in the observed field. There is, an irregular variable high-mass star EM Velorum (see Gahm & Malmort 1980), the high-mass star CD-40 that is the exciting star for the HII region RCW 27 (see Reed 2003), and the Herbig-Haro object HH-132 which has an associated reflective nebula that is very prominent in the K_s-band image. It has been shown by Mueller & Graham (2000) and Sharma *et al* (2016) that there are young PMS stars in the region around NGC 2626, specifically in the dense cloud north of HH-132.

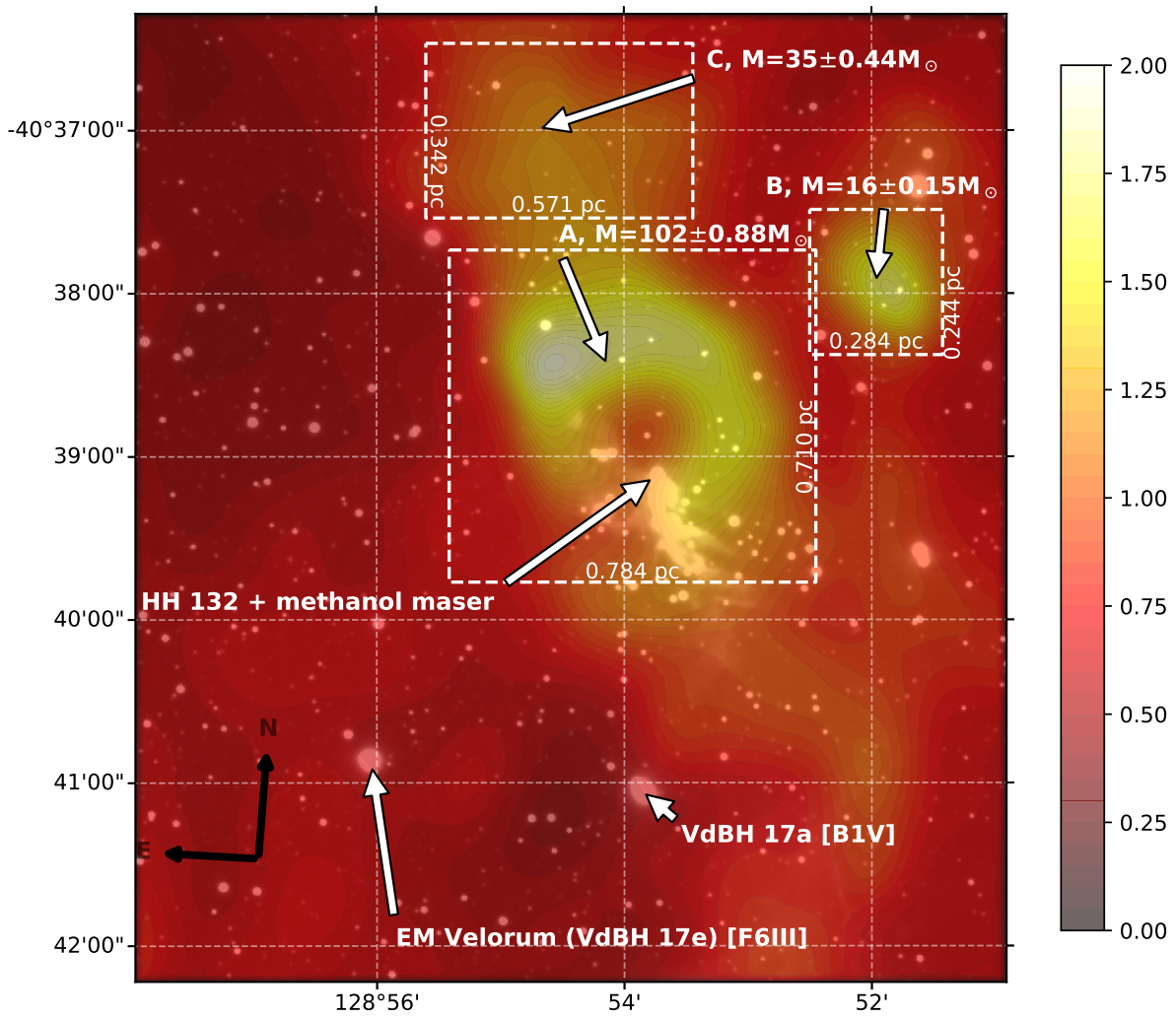

Figure 3.29: The *NICEST* algorithm was used to construct an extinction map of NGC 2626 using a 45″ detection radius. All of the high-mass and stars prominently mentioned in the literature in the field is also shown.

The extinction map of NGC 2626 in Figure 3.29 shows the molecular cloud at the northern part of NGC 2626 (cloud A), and a cavity around the star associated with HH-132. The cavity in the molecular cloud could only be cleared out by the bipolar outflows from the driving star of HH-132. The reason for this is that the nebulous gas that was ejected by HH-132 lies aligned with the clearing, and it flows parallel to the outer edges of the dense remnants to the west of HH-132. The other side of the bipolar outflow is not visible most likely due to a projection effect.

There are two dense regions north and north-west of cloud A. These two are most likely remnants of the same molecular cloud from which the young cluster formed. These dense clouds are significantly smaller than A, but the presence of class 0/I on the inside, and class II IR objects on the outskirts of cloud A raises the question of whether star formation may also occur in them. It is most likely that formation may occur in C, because it is much bigger than B. The only way to answer this question is to compare the masses of clouds B and C with a possible Jeans mass.

3.4.2.2 *Physical properties of the molecular cloud remnants near NGC 2626*

The same procedure was followed for measuring the masses of dense clumps in NGC 2626 as for RCW 34. NGC 2626 is 1.2 kpc away, which determines the physical size that is represented by a pixel, and affects the mass that was calculated for each molecular cloud. The same column density to extinction relation of $2.21\times10^{21}\,\frac{\text{particles}}{\text{A}_\text{v}.\text{cm}^2}$ was also used. It is assumed that the gas in clouds A-C are roughly at the same temperature as those in RCW 34, which is ~20 K. The same simplistic density calculation was done using the assumption that each dense region is a symmetrical ellipsoid. Much higher densities were measured for clouds A-C than for RCW 34, all of which are given in Table 3.3. A Jeans mass for a molecular cloud with a temperature of 20 K and a density of 3×10^3 cm^{-3} is 51 M$_\odot$.

Table 3.3: Properties of dense regions in NGC 2626 measured from the *NICEST LinES* extinction map.

Clump	Length [pc]	Width [pc]	Mass [M$_\odot$]	Error of mass [δM$_\odot$]	Average density [cm^{-3}]
A	0.784	0.710	98.91	1.11	2188
B	1.107	1.118	14.55	0.23	5609
C	2.518	1.042	33.96	0.51	2694

3.4.2.3 *Uncertainties in the extinction map and the signal-to-noise diagram for NGC 2626*

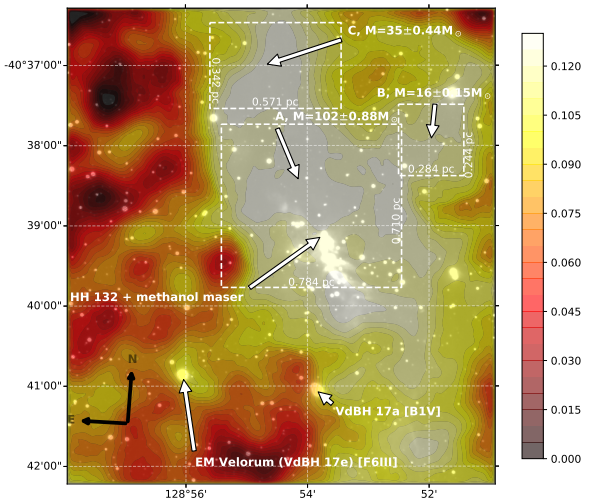

Figure 3.30: The error, δA_{K_s} for the extinction map of NGC 2626.

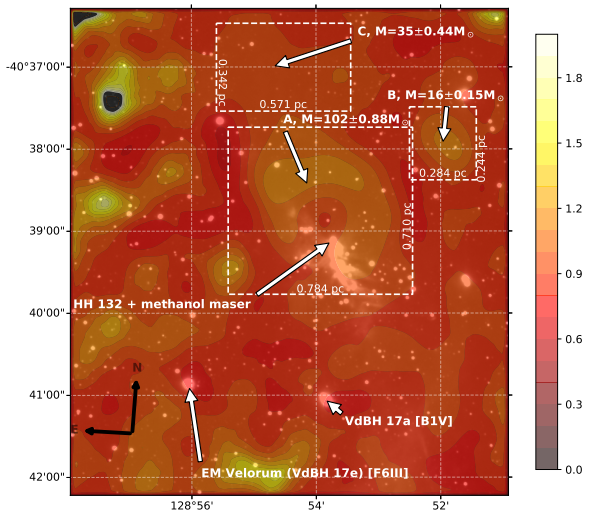

Figure 3.31: The signal-to-noise diagram for the extinction map of NGC 2626 drawn on a logarithmic scale.

Figure 3.30 shows the error map that was built with *NICEST LinES* of NGC 2626. The uncertainties in this extinction map are significantly higher than in the case of RCW 34. This is a direct result of the much higher extinction in clouds A-C. With such a high extinction the number of field stars that are visible through the cloud is much lower than in the case of RCW 34. Therefore the photometric errors are significantly bigger, because the light from the field stars behind clouds A-C undergo much more reddening. The S/N diagram in Figure 3.31 shows that for areas of high extinction, the S/N is a bit better than for areas with low extinction. This is similar to some of the dense regions in RCW 34 which also have a high S/N.

3.4.2.4 *Concluding remarks for the extinction maps of NGC 2626*

The extinction maps that were built using *NICEST LinES* in NGC 2626 show some of the dense structures that are also shown in CO maps by Sharma *et al* (2016), specifically, cloud A. Cloud A was also the only region that showed promise for future star formation. However, with the driving star of HH-132 pumping gas into cloud A and the population of young stars that was discovered by Sharma *et al* (2016), there is a chance that all of the dense gas will be dissolved in the near future.

3.4.3 Colour-Colour diagrams

3.4.3.1 *RCW 34*

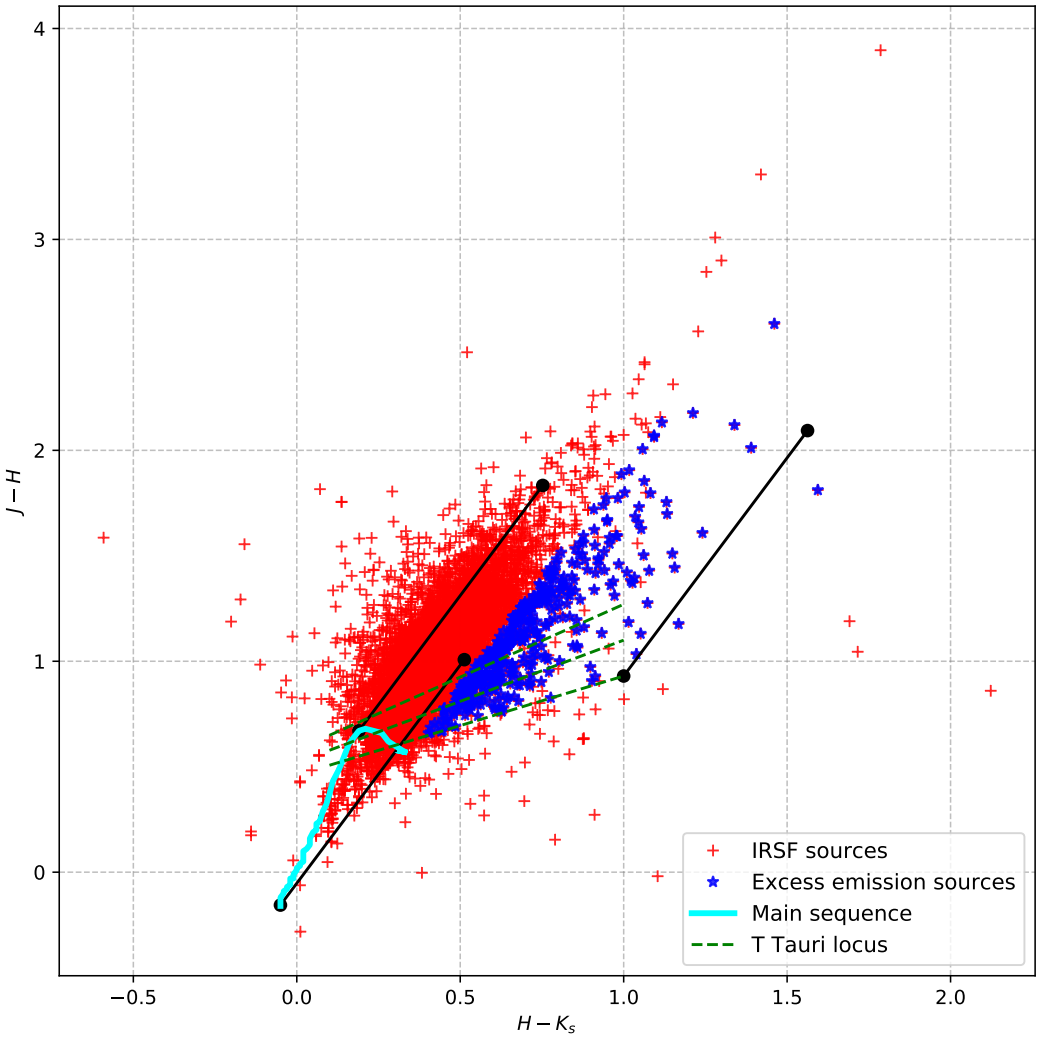

Figure 3.32: All of the 5273 sources including the 399 probable PMS stars that were observed in the field of RCW 34 and calibrated to the *2MASS* system.

There were 7460 sources that matched in the J, H, K_s bands across the field of RCW 34 of which 5273 had errors in their measured colours smaller than 0.05; $\delta(J-H) \leq 0.05$ and $\delta(H-K_s) \leq 0.05$, and their magnitudes $\delta J \leq 0.05$, $\delta H \leq 0.05$, and $\delta K \leq 0.05$. Of the 5273 stars, there were 586 that showed excess emission characteristic to PMS stars. These are respectively shown in Figure 3.32 as red crosses and blue stars. Of the 586 excess emission sources, there are 187 that can not be dereddened to somewhere between the upper and lower limits of the CTT locus. Their colours are either under the lower limit of the CTT locus, or they have more excess emission past the reddening vector of the lower limit. The sources that do not show excess emission are shown as red crosses and are considered to be field stars that can be dereddened onto the main sequence.

The red-crossed sources that fall between the reddening vectors that extend upward from the high-mass end and the degeneracy split of the main sequence at the colours of an M4 star were dereddened onto the main sequence. The sources that lie above the reddening vector that extends upward from an M4 star on the main sequence are either main sequence, giant, or supergiant stars. The uncertainty as to where these stars should be dereddened, eliminated them from the remainder of this study.

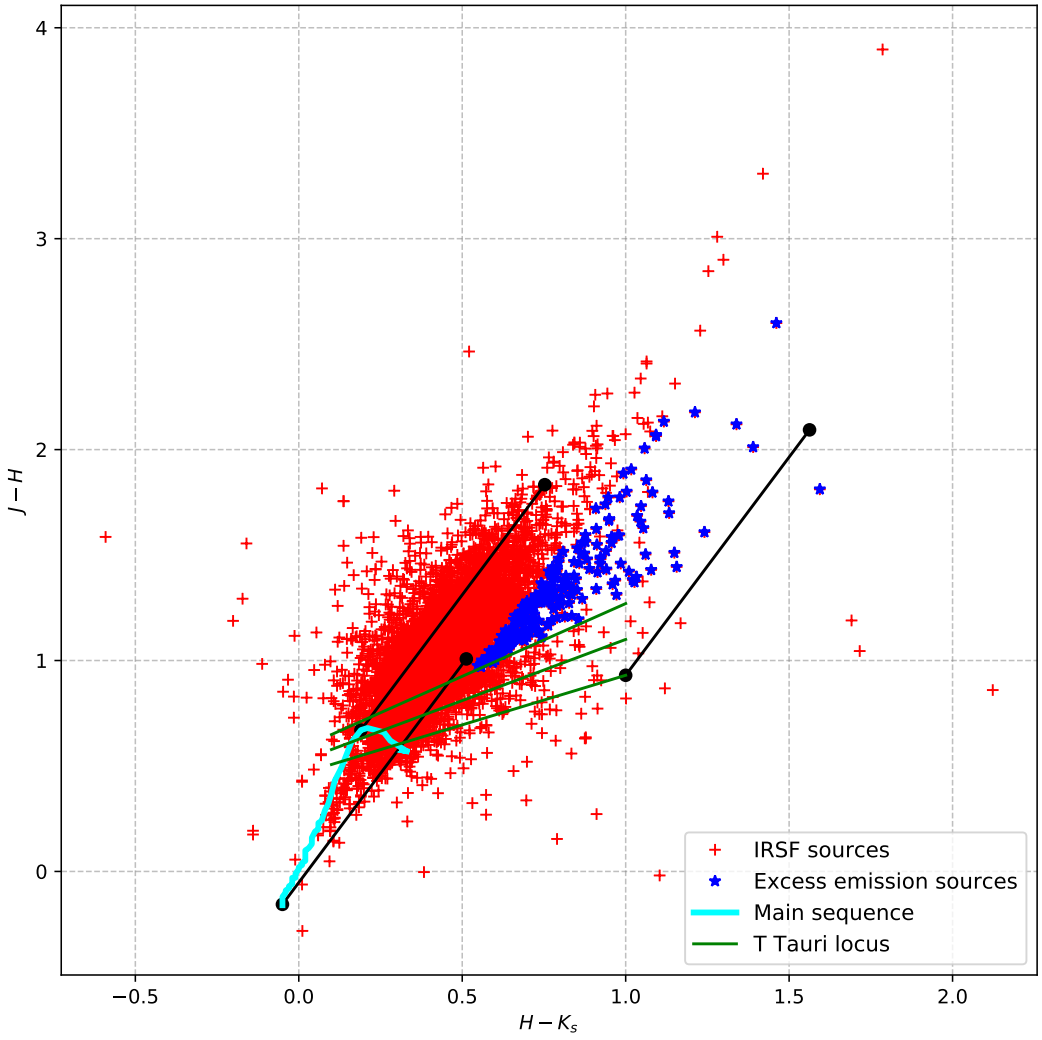

Figure 3.33: All of the detected sources that were plotted in Figure 3.32 are shown here as red crosses. The blue sources are the excess emission sources out of the 399 sources shown in Figure 3.32. These are assumed to be CTTs, and can be dereddened to somewhere between the upper and lower limits of the CTT locus. The extinction for these dereddened CTTs are also used in the construction of the extinction map.

The majority of the excess emission sources lie above the lower limit of the CTT locus. In other words, it is possible to deredden them to some position between the upper or lower limits of the CTT locus. It is not possible to truly say if a star is a CTTs without knowing the exact extinction to the source. If the total extinction has been compensated for, the remaining colour excess can only originate from hot circumstellar material, and it can be tested against the CTT locus. To test whether all of the sources that lie above the higher limit of the CTT locus (the blue sources in Figure 3.33) are CTTs that can be dereddened to a position somewhere between the upper and lower limits of the CTT locus. The sources that lie between the upper and lower limits of the CTT locus will remain at that specific position, because it is assumed that the extinction to those sources is zero. The dereddened position on the colour-colour diagram will be a randomised position, with the highest probability being on the CTT locus and the other random positions — that are generated according to a normal distribution — between the upper and lower limits of the locus.

In Figure 3.32 the majority of the reddened excess emission sources can be dereddened to some position between the upper and lower limits of the CTT locus, under the assumption that they are reddened CTTs stars. A good test is to look at what their dereddened colours are, if the extinction is read at each star's position from the extinction map that was built from the field stars alone. Thereafter the measured extinction at the same point on an extinction map — that was built with the excess emission sources dereddened — is compared to a position between the upper and lower limits of the CTT locus. The difference between the extinction measured from the different maps at that specific point would not show a large difference if the assumption that the excess emission stars that are dereddened to between the limits of the CTT locus is true.

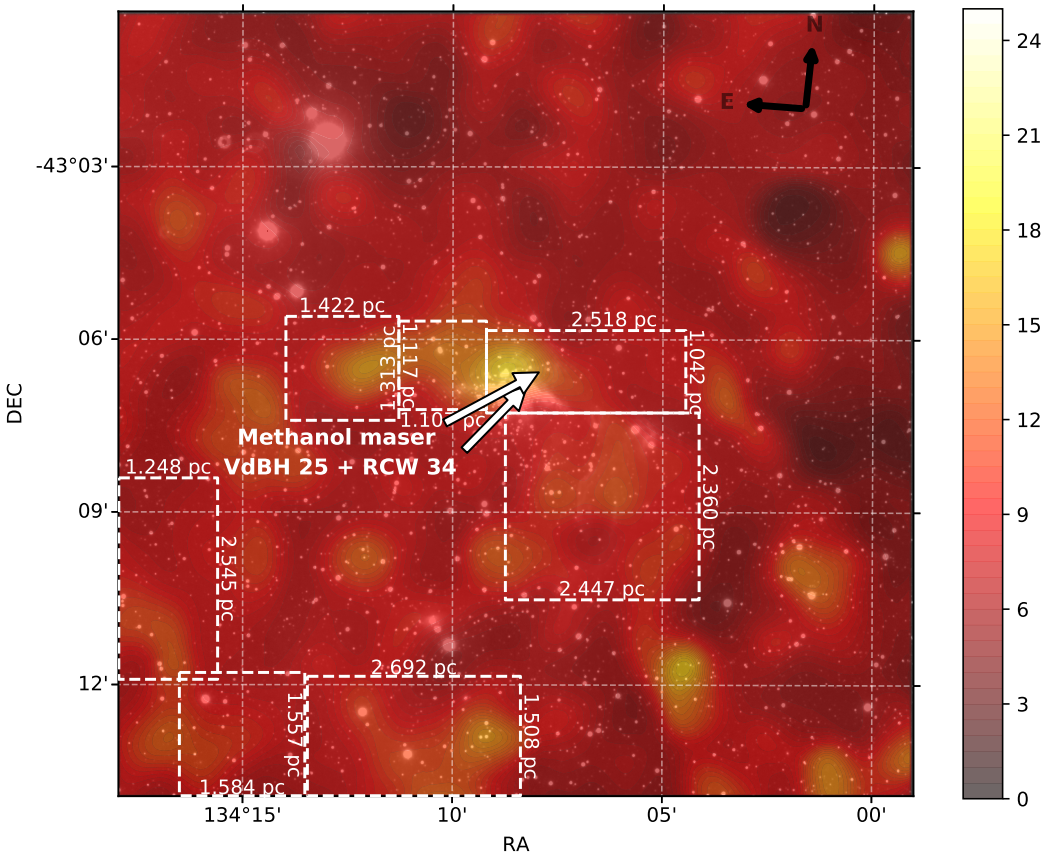

Figure 3.34: The extinction map that was built using the population of field stars that fall between the upper and lower dereddening vectors that extend from the MS in Figure 3.32, and the excess emission sources that lie above the lower limit of the CTT locus.

Figure 3.34 shows the extinction map that was built using the field stars that were used in the building

of the extinction map in Figure 3.23, as well as the excess emission sources that were dereddened to a position between the upper and lower limits of the CTT locus. The location of dense regions in Figure 3.23 differ from those in Figure 3.34. This is caused by the influence of the dereddened CTTs and those that were already between the upper and lower limits of the CTT locus, which were assigned an extinction of $A_V = 0$. There were 152 extra stars that contributed to the construction of the extinction map in Figure 3.34. This is 10% more than what was previously used in the construction of the map in Figure 3.23. No new dense clumps can be seen in Figure 3.23, if compared to Figure 3.34, the only significant difference is in the structure of the dense clumps. The dense structures are in slightly different positions with the addition of more stellar sources, for example, B's densest part is closer to VdBH 25a in Figure 3.23, than in Figure 3.34. The slight differences between the extinction maps do not show enough information regarding the excess sources that were dereddened to a position between the limits of the CTT locus.

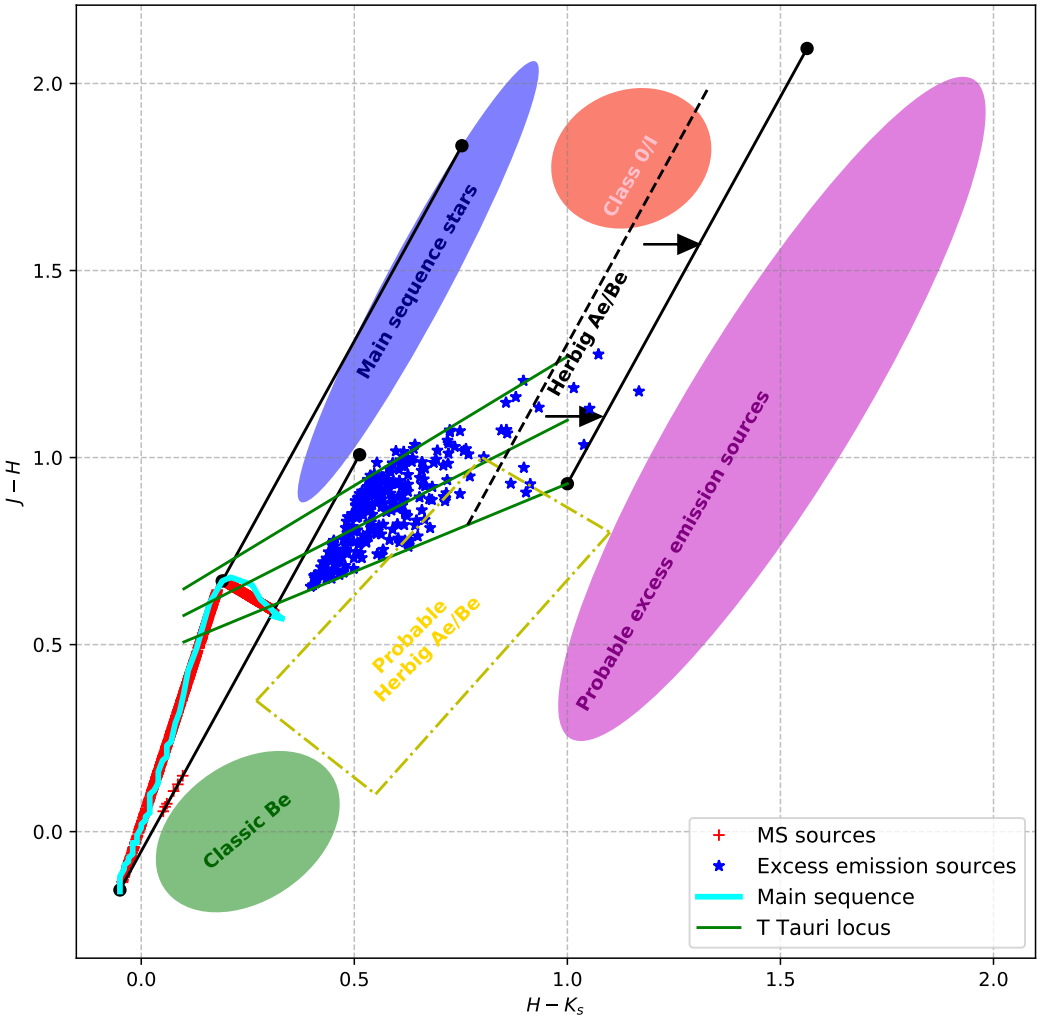

Figure 3.35: The dereddened colour-colour diagram of the sources that were used in the construction of the extinction map in Figure 3.34.

All of the dereddened sources are shown in Figure 3.35, the field stars are dereddened to the most probable position on the main sequence. The sources that were above the upper limit of CTT locus in Figure 3.32 are dereddened to a position between the limits of the CTT locus. All of the sources that initially had colours between the limits of the CTT locus had no extinction, or $A_V = 0$ was assigned to each one, and this zero extinction value was also used in the construction of the extinction map in Figure 3.34.

The results of dereddening the excess emission stars to some position between the CTT locus' limits, and dereddening them using the extinction map that was built using only the field stars must be compared. This comparison can only be seen on a colour-colour and colour-magnitude diagram. On a colour-colour and colour-magnitude diagram, it is possible to compare the validity of the assumption that the stars that lie above the upper limit of the CTT locus are either reddened CTTs or other excess emission sources. In Figure 3.32 the excess emission sources may either be reddened CTTs that can be dereddened to somewhere between the CTT locus, or other types of excess emission sources that can not be dereddened to a specific location. The excess emission sources that could not be dereddened to the CTT locus were dereddened using the extinction from the map in Figure 3.34 and are shown on a colour-colour diagram in Figure 3.36.

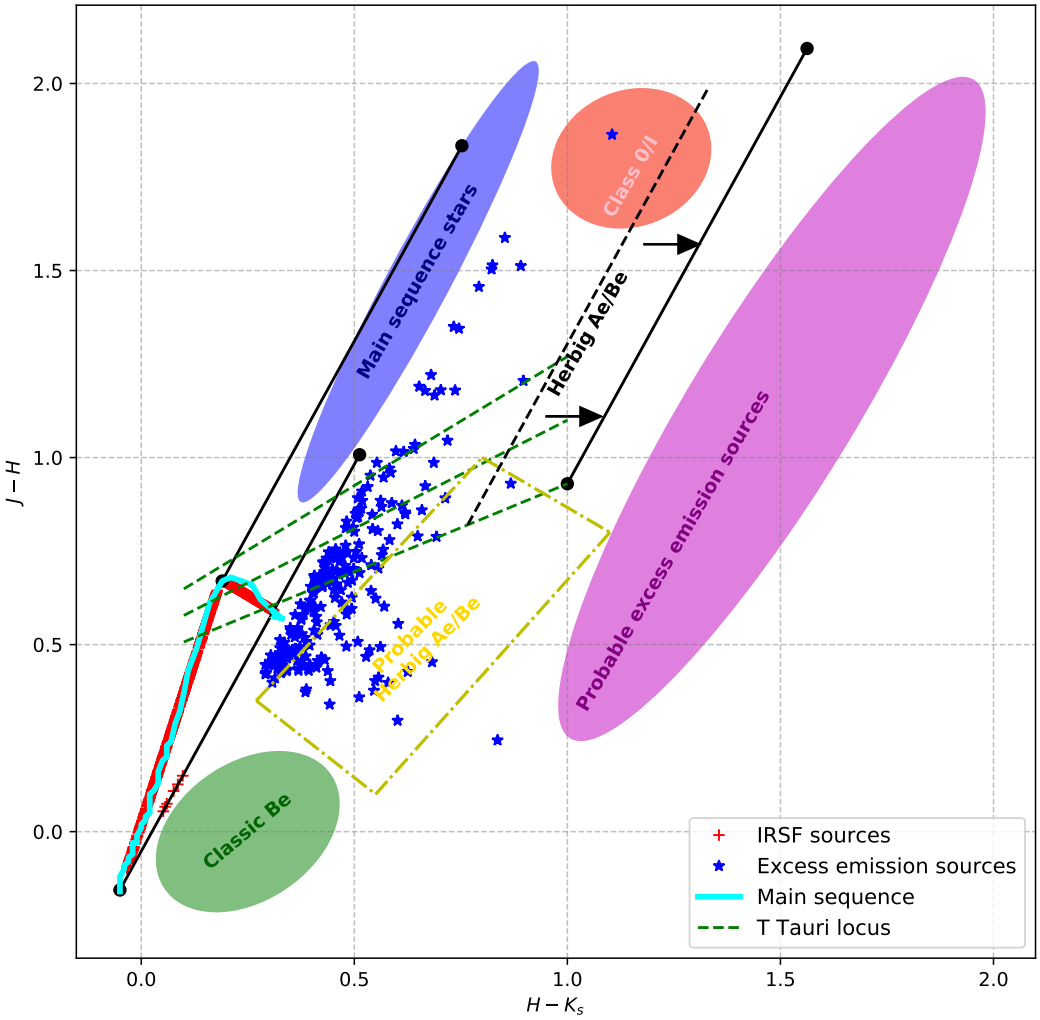

Figure 3.36: Out of the 5273 sources in Figure 3.32 there were 3179 stars dereddened with *NICEST LinES* methods, as well as the 399 PMS stars.

The dereddened field stars are shown as the red crosses on the main sequence, and the excess emission sources are shown at their dereddened positions. The excess emission sources in Figure 3.36 were dereddened using only the extinction map that was built from the field stars behind RCW 34, and not the additional set of excess emission sources that were dereddened to a position between the upper and lower limits of the CTT locus. Using the extinction map built only from the field stars behind RCW 34 implies that the majority of the excess emission sources lie below the lower limit of the CTT locus. This suggests that they are more evolved than the colour-colour diagram in Figure 3.36 would

suggest. There are only 28 sources that lie between the limits of the CTT locus. This is 6% of the population of excess emission sources. The distribution of these dereddened sources is very unlikely. It would imply that the majority of excess emission sources in RCW 34 are Herbig Ae/Be stars, with just 28 CTTs stars. If an IMF was constructed from these numbers it would be top-heavy, not just in that 49 sources — 12% — would have a mass less than 2.5 $M_{\odot}$, but the power-law would be the opposite than anywhere else in the literature! This is very improbable, because that IMF of RCW 34 would show many more A/B stars than K/M stars. Any IMF in the literature shows that the larger number of stars in an open cluster are lower-mass K/M stars. The most likely conclusion from this result is that the extinction map that was built from just the field stars behind RCW 34 is incorrect, and the assumption that the reddened colours of excess emission sources above the upper limit of the CTT locus, can be dereddened to somewhere between the limits of the CTT locus is correct. This implies that the extinction map that should be used to deredden any source in RCW 34 should include the extinctions of the excess emission sources that were assumed to be reddened CTTs.

3.4.3.2 *NGC 2626*

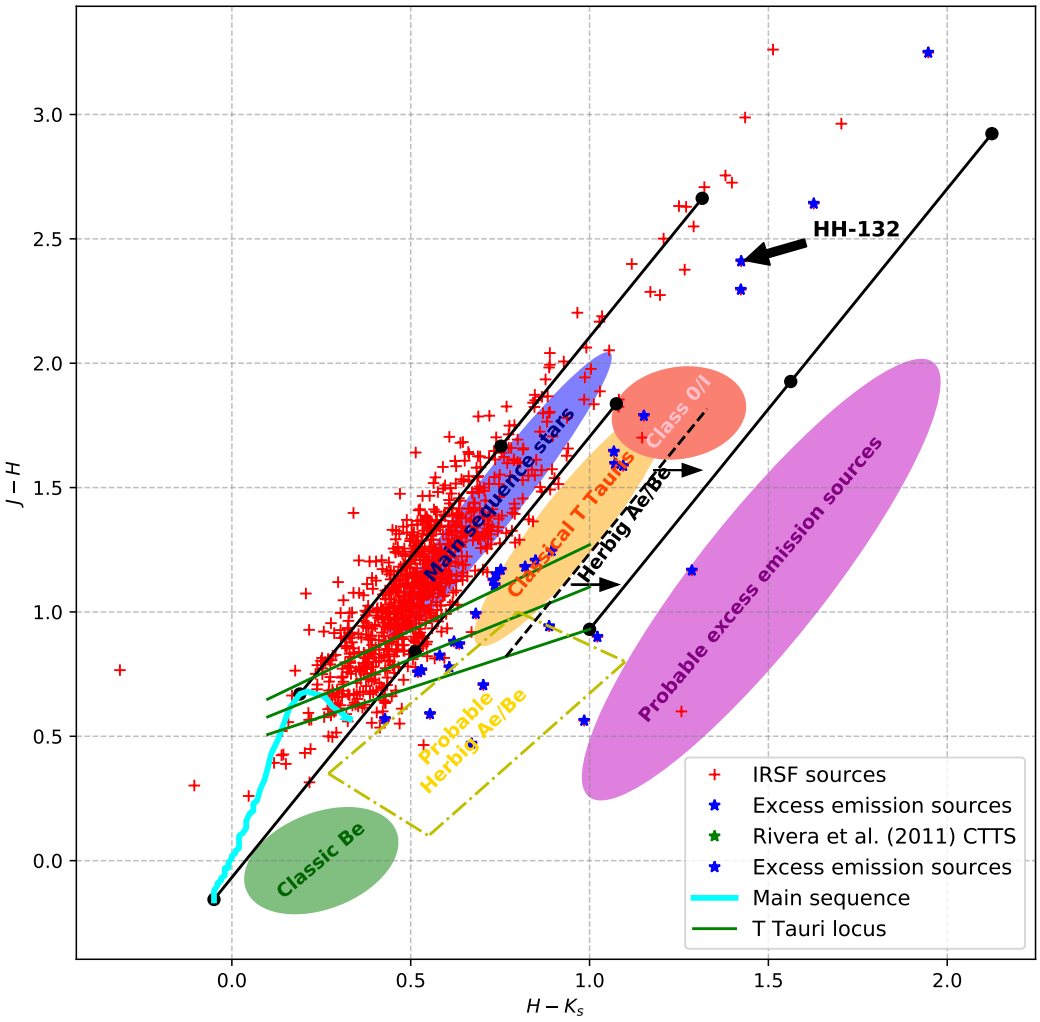

Figure 3.37: All of the 953 sources that were observed in NGC 2626 and were calibrated to the *2MASS* system.

In Figure 3.37 all of the sources in NGC 2626 that were calibrated to the *2MASS* photometric system are shown. The same criteria in the errors of the colours and magnitudes for selecting sources in RCW 34 was used in NGC 2626, so that a source should have $\delta(H - K_s) \leq 0.05$, $\delta(J - H) \leq 0.05$, $\delta J \leq 0.05$, $\delta H \leq 0.05$ and $\delta K \leq 0.05$. Of these 953 sources, there were 29 sources that showed

excess emission, of these sources, eight lie between the upper and lower limits of the CTT locus. The majority of the stars in Figure 3.37 can be dereddened to either the main sequence or to some position on the CTT locus. There are also nine sources that present colours with very strong colour excess; they may be class I type *NIR* sources. Moreover, there are four sources that cannot be dereddened onto the CTT locus, because they are outside of the reddening vector limits, or below the lower limit of the CTT locus. There are also five sources that lie low in the yellow rectangle, meaning that they are most likely Herbig Ae/Be stars.

The few sources that lie above the CTT locus in Figure 3.37 are so few, that they will not make any difference in the construction of the extinction map if they are dereddened to the CTT locus and used in the *NICEST* algorithm. The number of excess emission sources that are in RCW 34 can make a difference in the construction of the extinction map of that region. For the few in NGC 2626 the extinction for these excess emission sources is taken from the extinction map.

The star driving HH-132 shows excess emission and is at a position of high extinction according to Figure 3.37. According to the extinction map, this driving star has low extinction. The strong excess emission on the colour-colour diagram suggests that the star is very young, possibly a class 0/I NIR source. The strong excess emission in the colours for the driving star may be emission from the jets that were included when photometry was performed on the image.

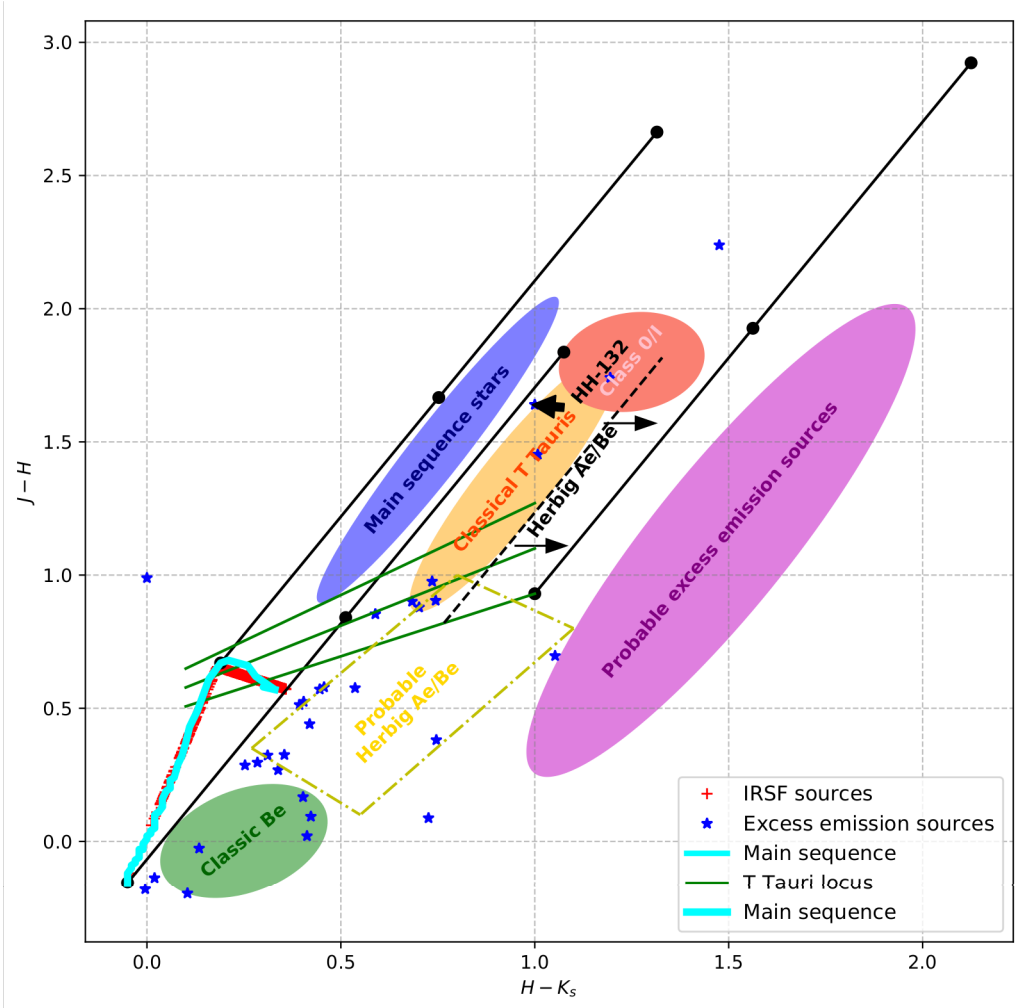

Figure 3.38: Out of the 953 sources in Figure 3.37, 437 were dereddened with the *NICEST LinES* method and are shown with 25 probable PMS stars.

All of the field stars were dereddened onto the main sequence and the stars that showed excess emission were dereddened according to the extinction map. There are five sources that are between the CTT locus' limits and four that are still above the upper limit. Any sources that lie between the limits of the CTT locus are considered to be CTTs. The excess emission sources that remain above the upper limit of the CTT locus, and have high extinction, are probably the class 0/I *NIR* sources. The majority of excess emission sources lie below the lower limit of the CTT locus fourteen of which are potentially Herbig Ae/Be stars, and seven may be classic Be stars. The exact distinction between these two groups is not very precise, it may be that some of these stars may be included in the incorrect classification scheme.

The colours for the star driving HH-132 were dereddened with an extinction of $A_{K_s} = 0.77$ or ($A_V = 7.01$) which places it at a position still above the upper limit of the CTTs locus. There are two possibilties for the dereddened colours of the driving star for HH-132. Either it is a very young star, or the excess emission includes emission from the jets that were included when the PSF photometry was performed. If the excess emission is only from the driving star they indicate that it is a very young source. This together with the presence of the maser at the almost same position suggests that it is the same young star that is driving both the maser and the Herbig-Haro outflow. There are many *NIR* sources which are counterparts to the driving sources of masers, as shown by Walsh *et al* (1999).

3.4.4 Colour-Magnitude diagrams

In this subsection, the magnitudes for every star on the colour-magnitude diagrams have all been respectively corrected for the distance to RCW 34 and NGC 2626. The colour-magnitude diagrams are plotted for the $K_s/(H - K_S)$ bands, specifically for the use of the A_{K_s} magnitude from the extinction maps. If a star is dereddened, then the measured A_{K_s} magnitude can be used directly from the extinction map and would not have to be converted with an extinction law. The magnitudes for every star on the colour-magnitude diagrams have all been respectively corrected for the distance to RCW 34 and NGC 2626. For each region there are two colour-magnitude diagrams. The first diagram shows the measured colours and magnitudes, while the second colour-magnitude diagram is corrected for extinction. The dereddening was for the field stars from the colour-colour diagrams, and the sources with excess emission from the position on the extinction maps. On each colour-magnitude diagram isochrones, as well as evolutionary tracks, are shown for models that were developed by Siess *et al* (2000). There are isochrones plotted at ages of 10^5, 10^6, 5×10^6, 10^7 yr and a ZAMS with mass intervals at $M_* = 0.1$ $M_\odot$, 0.2 $M_\odot$, 0.5 $M_\odot$, 1.0 $M_\odot$, and 2.0 $M_\odot$. The mass intervals were chosen specifically for the mass ranges where CTTs are the most prominent ($M_* < 2$ $M_\odot$). The evolutionary tracks show the evolution of a specific spectral type from the earliest stages when it becomes detectable, up to the main sequence.

3.4.4.1 *RCW 34*

The magnitudes for the stars in Figure 3.39 were all corrected for a distance modulus of $2.5 \times \log_{10} \frac{2500 \text{ pc}}{10 \text{ pc}}$ after the calibration of the apparent magnitude and colour to the *2MASS* with the following equations:

$$K_{2MASS} = K_{IRSF} + 0.3271 \times (H - K)_{IRSF} + -5.3224$$
$$(H - K)_{2MASS} = 0.8683 \times (H - K_s)_{IRSF} + 0.7164$$

The stars that were identified as field stars in the colour-colour diagram are plotted here as red crosses and the stars with excess emission as blue stars. In Figure 3.39 the field stars, excess emission stars, and any other cluster members associated with RCW 34 are distributed in such a way that no distinction can be made between cluster members and non-cluster members. Similarly, the studies on the ONC by Hillenbrand & Carpenter (2000), and NGC 7538 by Ojha *et al* (2004) were not able to distinguish between cluster members and the field stars on a colour-magnitude diagram. There are few bright or massive stars and the number increases for fainter sources, which are best described by

the power-law in the mass function of Parravano *et al* (2011).

The sources that show excess emission in Figure 3.32 are mixed amongst field stars sources that also have $(H - K_s)$ colour excess, which are most likely caused by reddening. The number of sources also increase as a function of the magnitude, so that the number of low-mass sources that show excess emission is synonymous with the mass distribution for the field stars. In a study by Ingraham (2012) a criterion of $(H - K_s) > 0.7$ was used to classify stars with a mass smaller than 3 $M_\odot$ as CTTs. Using the same criterion would not work for RCW 34 because are too many sources that have colours $(H - K_s) > 0.7$. Different criterion for CTTs were given by Rivera-Ingraham *et al* (2011) who chose excess emission sources that lie above the lower limit of the CTT locus — similar to the proposed assumption that was used in the case of RCW 34.

In Figure 3.39 no evolutionary classification can be done without the correct dereddening, but in Figure 3.40, the field stars have been dereddened according to the extinction calculated from the colour-colour diagram. The excess sources have been dereddened according to the extinction measured from the extinction map. All of the field stars shown in Figure 3.40 were used in the construction of the extinction map of RCW 34, so they are field stars located behind the star-forming region, and they have colours between the reddening vectors that extend up from the main sequence on the colour-colour diagram in Figure 3.32. There are no dereddened field stars that lie between the evolutionary lines of $M_* = 0.5$ $M_\odot$ and $M_* = 1.0$ $M_\odot$. This is because of the degeneracy in the dereddening onto the main sequence from stars at a higher or lower mass than an M4 star on the colour-colour diagram.

The position to which the field stars are dereddened can not be compared to the isochrones and the evolutionary models, because the distance to each field star is not known. It is assumed that each field star is a main sequence star to deredden them to the main sequence on the colour-colour diagram. The sources that show excess emission are all assumed to be members of the cluster associated with RCW 34 so they can be compared with the isochrones/evolutionary lines.

3.4.4.2 *Excess sources dereddened to the CTT locus*

In Figure 3.41 the distinction between the field stars and the excess sources are more apparent than in Figure 3.40. The excess emission sources have a distribution of dereddened colours/magnitudes that show a number of sources that can be considered to be Herbig Ae/Be stars, due to their K magnitudes. The other excess sources can be interpreted as CTTs, specifically under the assumption that these stars were dereddened to somewhere between the limits of the CTT locus. The excess emission of the assumed CTTs does not make it possible to compare them with the evolutionary models of Siess *et al* (2000), which are just a representation of the photospheric emission of PMS stars.

There are 37 stars that lie above the dashed line that distinguishes between an A9 spectral star and lower-mass stars in Figure 3.41, which are considered to be Herbig Ae/Be. This is far less than the stars that were dereddened using the extinction map that was built just using the field stars. This implies that the assumption that most of the excess emission sources above the upper limit of the CTT locus in Figure 3.32 is reasonable for the majority of the assumed CTTs, and to where they were dereddened on the colour-magnitude diagram. There are 373 excess emission sources that are fainter than the Herbig Ae/Be line which are considered to be CTTs. The shortcoming of the evolutionary models and isochrones by Siess *et al* (2000) is that the models only use the photospheric emission for PMS stars and not their accompanying discs. This shortcoming hinders the possiblilty of determining the age for these stars and estimating when the last epoch of star formation occurred in RCW 34. The models only make it possible to put an age estimate on naked T Tauri stars, not anything younger than a WTTs or roughly 10 Myr.

By comparing the distribution of the excess emission sources in Figure 3.40 with those in Figure 3.41 the distribution relative to the field stars is remarkable. If the distribution of the dereddened excess sources — which were dereddened only uses the extinction from the map — in the colour-colour dia-

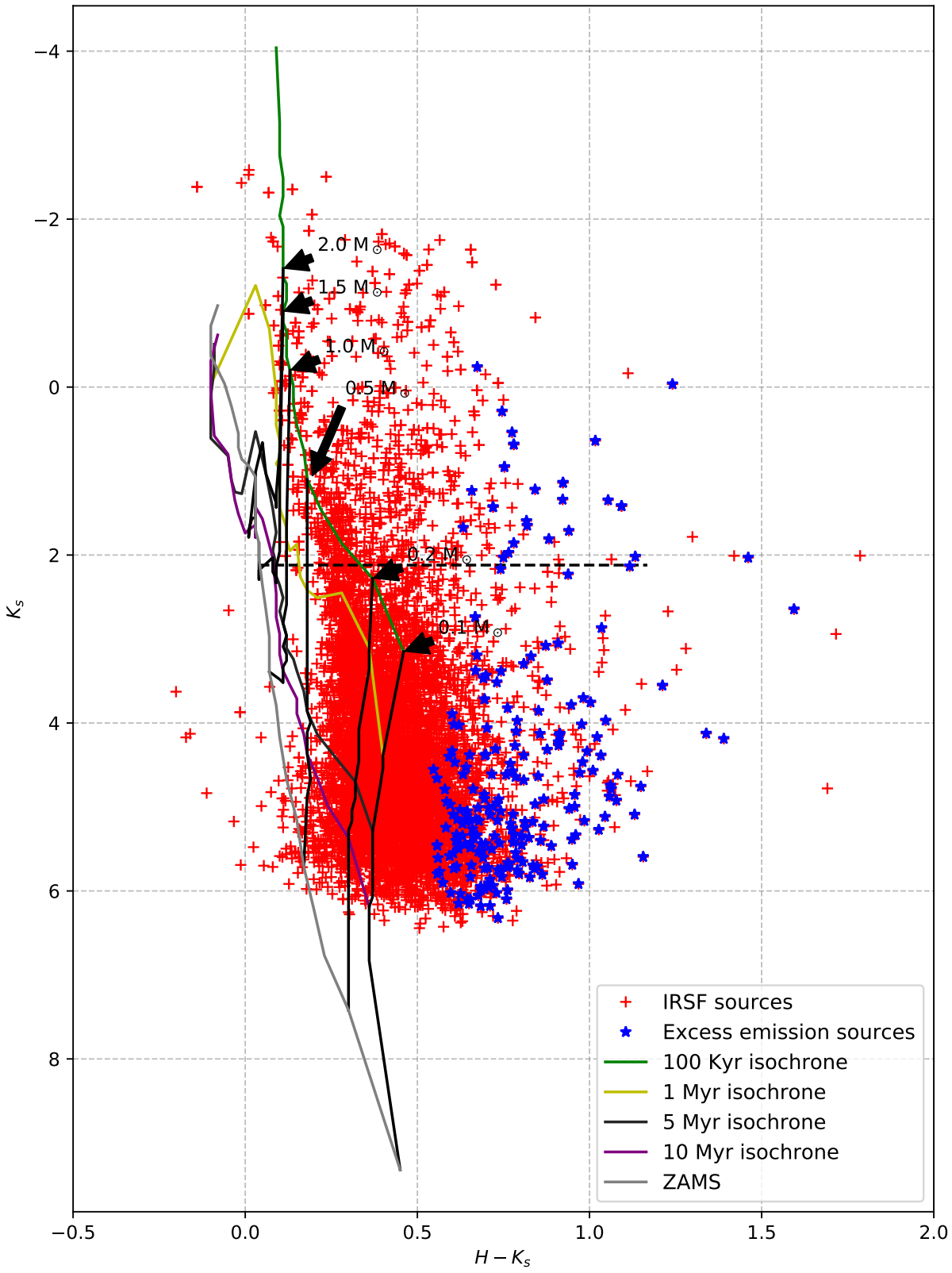

Figure 3.39: All of the 5273 sources that were observed in RCW 34 and were calibrated to the *2MASS* system. These are the absolute magnitudes which have not been dereddened from the extinction map.

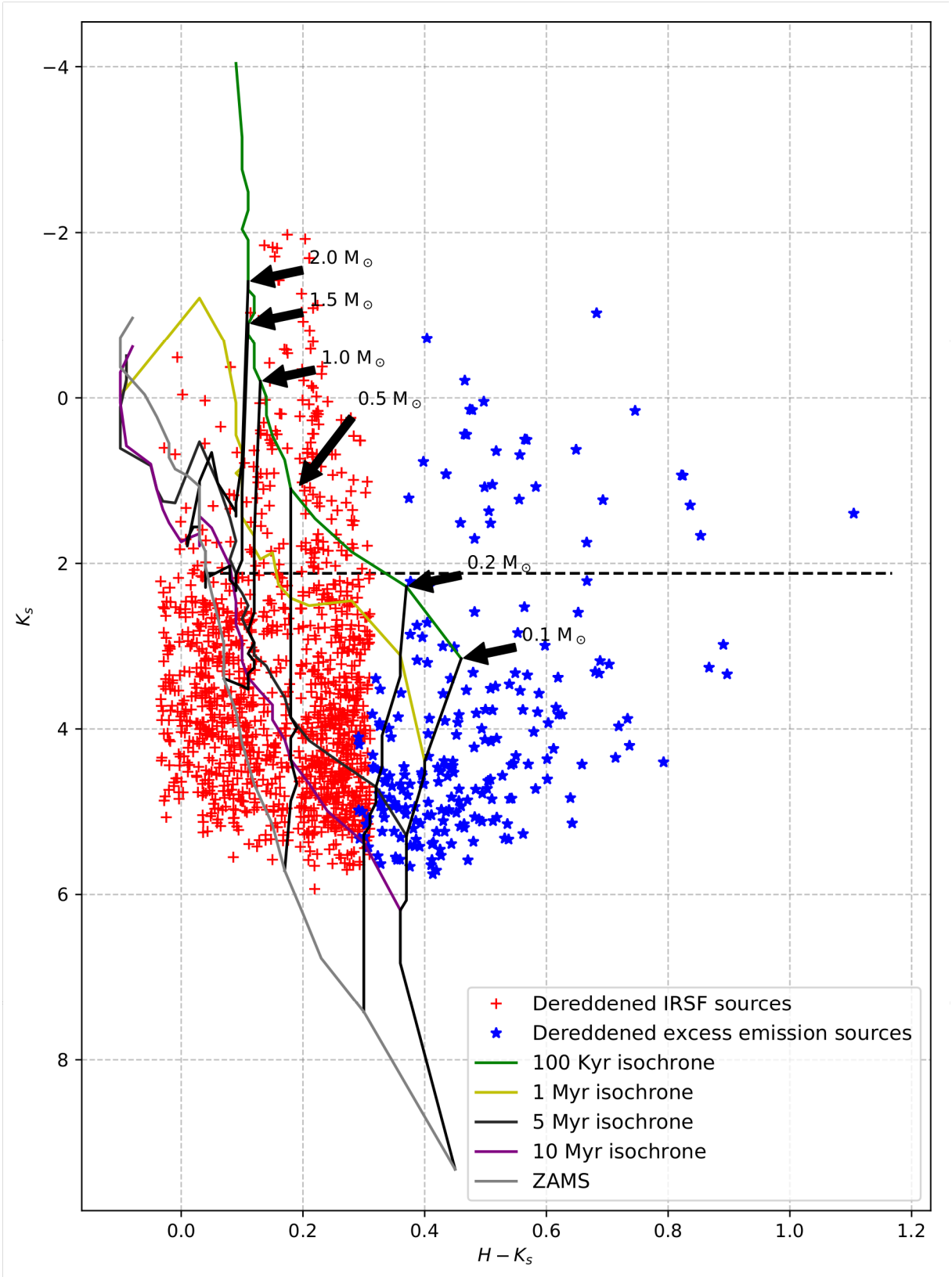

Figure 3.40: Out of the 5273 sources in Figure 3.39 there were 3179 stars dereddened with *NICEST LinES* methods, as well as the 399 PMS stars.

gram is valid in Figure 3.35, then the dereddened excess emission presents unrealistic colours. From the colour-magnitude diagram in Figure 3.41 a clear distinction can be seen between the CTTs and

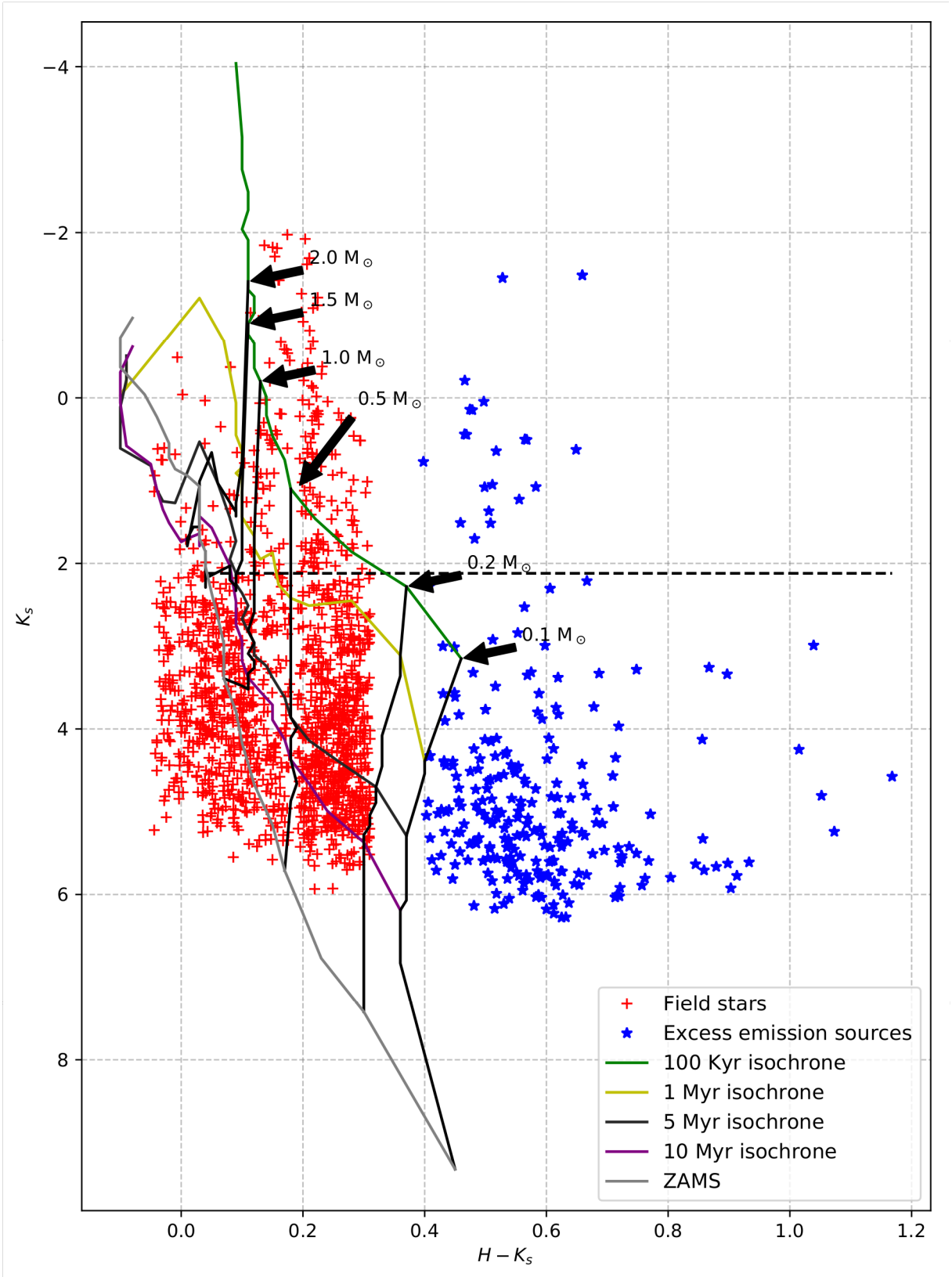

Figure 3.41: The colour-magnitude diagram for the field stars that were dereddened onto the main sequence, and the excess emission sources that were dereddened onto the CTT locus.

the field stars.

3.4.4.3 *NGC 2626*

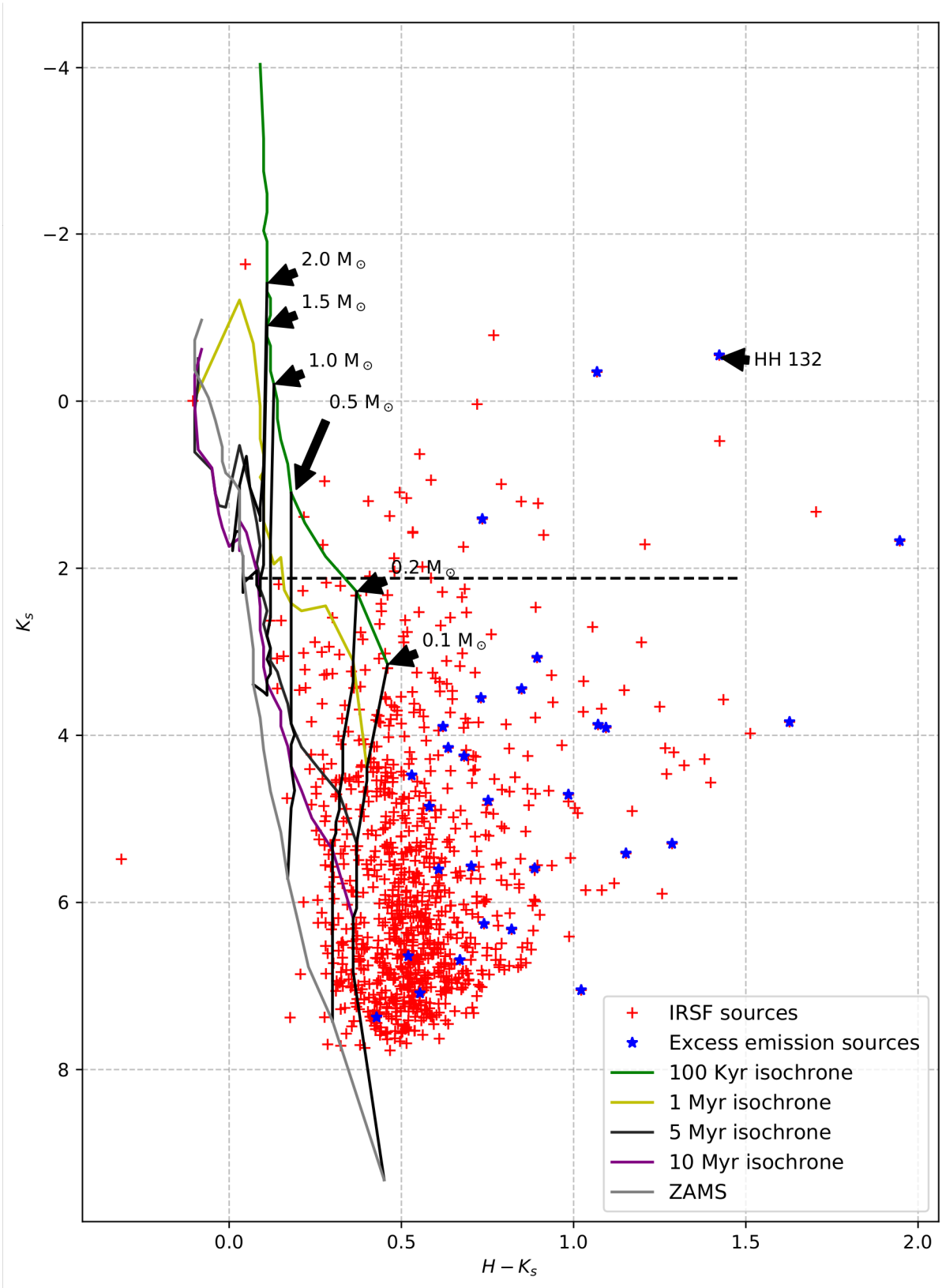

Figure 3.42: All of the 953 sources that were observed in NGC 2626 and were calibrated to the *2MASS* system.

In Figure 3.42 all the sources that were detected in NGC 2626, and calibrated to the *2MASS* system are shown. The sources that showed excess emission are the blue stars, and the other red crosses are the field stars. The K_s magnitude and the $(H - K_s)$ colours were calibrated with the equation:

$$K_{2MASS} = K_{IRSF} - 1.3587 - 0.1001 \times (H - K_S)_{IRSF}$$
$$(H - K_s)_{2MASS} = 0.8678 \times (H - K_s)_{IRSF} + 0.7332$$

The calibrated magnitudes were corrected for a distance modulus of $5 \times \log_{10}\left(\frac{950 \text{ pc}}{10 \text{ pc}}\right) = 9.88$ so that the isochrones and evolutionary tracks can be compared to the data for NGC 2626. The colour and magnitudes of sources that showed excess emission are distributed between the other sources that were detected in the field. There is no apparent grouping on the colour-magnitude diagram of the cluster members associated with NGC 2626 that separates them from the field stars. The only way to compare the sources that showed excess emission with the PMS evolutionary models of Siess *et al* (2000), is by dereddening these sources with the help of the extinction map.

In Figure 3.43 all of the field stars that have an extinction larger than the average extinction in the Galactic plane $(A_V^{\text{cut off}}) = \frac{1.8 A_V}{\text{kpc}} = 1.8 \times 0.95 = 1.71$, are shown with dereddened colours and magnitudes. The extinction for the dereddened main sequence stars were taken from the dereddening on the colour-colour diagram. The sources that show excess emission were dereddened according to the extinction that was measured from their position on the extinction map. The colours and magnitudes of the field stars in Figure 3.43 can not be compared to the evolutionary tracks/isochrones, because the distance to each one is unknown, and it is assumed that each one is a main sequence star. It is only the stars that show excess emission that can be associated with NGC 2626 and be compared to the evolutionary lines.

The majority of the dereddened field stars appear to have masses between the range of $0.2 \text{ M}_\odot \leq \text{M}_* \leq 0.5 \text{ M}_\odot$. This classification can be made regardless of the distance to the specific sources, because the colours do not change significantly over the PMS evolutionary process for these low-mass stars. There may be some cluster members that were incorrectly classified as field stars. As mentioned before, it is almost impossible to distinguish between field stars and cluster members with absolute certainty. Radial velocity measurements would have aided in distinguishing between field stars and cluster members.

There are 30 stars that presented excess emission and were dereddened according to the extinction map at their specific positions. Of these 30 stars, there were 20 that had so much excess emission that they could not be compared to the evolutionary models of Siess *et al* (2000). These 20 sources may be are either Class 0/I infrared sources, have flat infrared spectrums, or they may be binary systems. Without individual spectra of these sources, there is no way to discern which types of objects these sources may be.

The star activating the Herbig-Haro outflow, or HH-132 is shown at its reddened position in Figure 3.43. In order to compare the dereddened colours and magnitude to the evolutionary models by Siess *et al* (2000), the star has to be very young, due to the excess emission in the colours. Its magnitude is significantly brighter than the evolutionary tracks that are used to classify the excess emission sources, which means that the star's mass is higher than 2 $\text{M}_\odot$. The location of the methanol maser right next to the activating star of HH-132 strongly suggests that it is the same source that activates the Herbig-Haro object and the maser, similar to the studies by Palla & Prusti (1993), Palla *et al* (1995), and Walsh *et al* (1999).

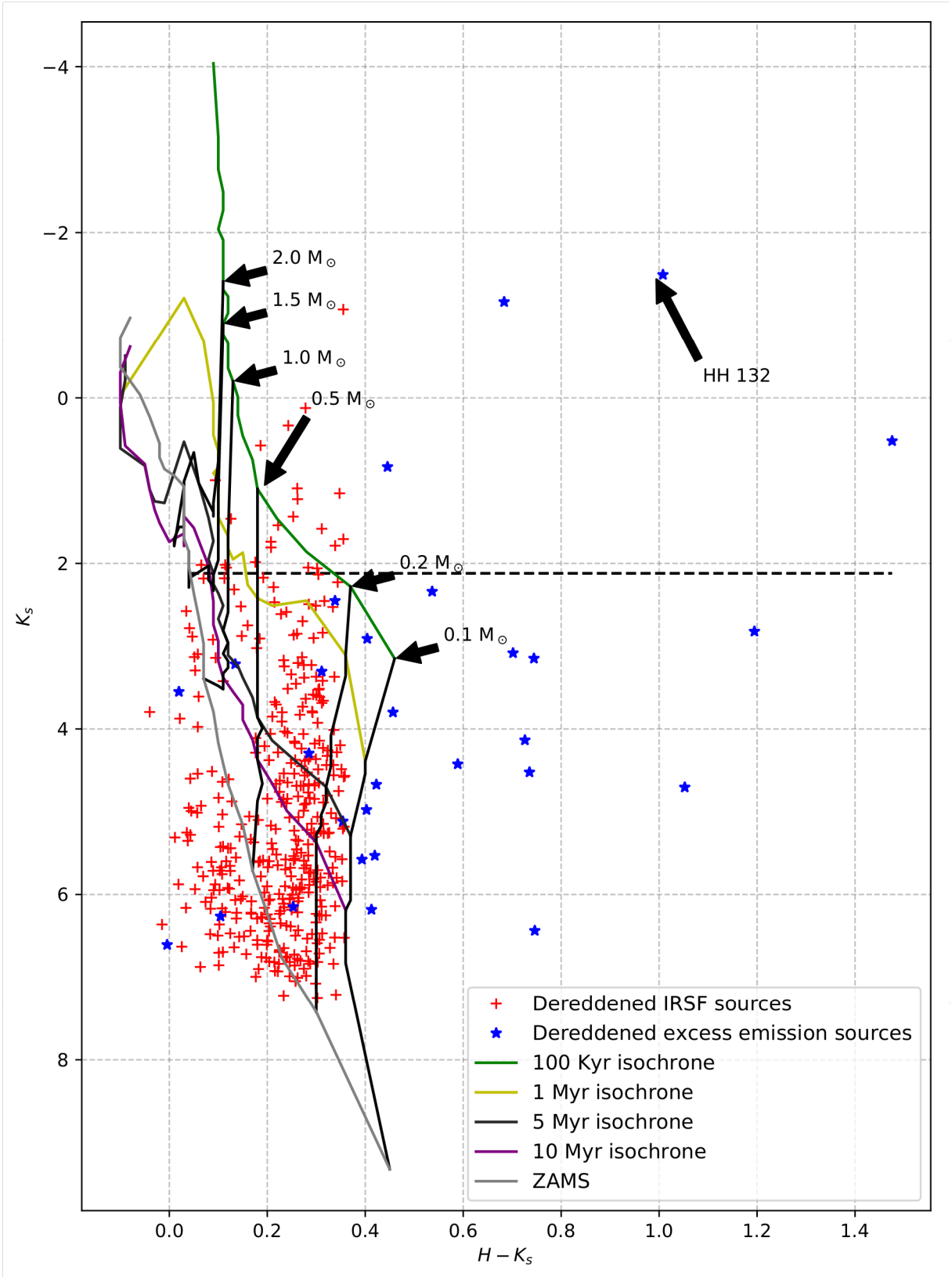

Figure 3.43: Out of the 953 sources in Figure 3.42, 437 were dereddened with the *NICEST LinES* method and are shown with 25 probable PMS stars.

3.4.5 Spatial distribution of *IRSF* sources

In the previous subsection, the colour-colour and colour-magnitude diagrams were used to discuss the properties of the field stars and then for the stars that showed excess emission in the fields of RCW 34 and NGC 2626. Their spatial distribution will be discussed in this subsection. It is important to understand where the sources that show excess emission are relative to the high-mass stars, the HII region, the maser, and the dense remnants of the molecular cloud. The extent of the excess emission sources shows how big the star-forming regions are, which may help answer the question as to what may have triggered the formation of the low-mass members associated with each star-forming region.

3.4.5.1 *RCW 34*

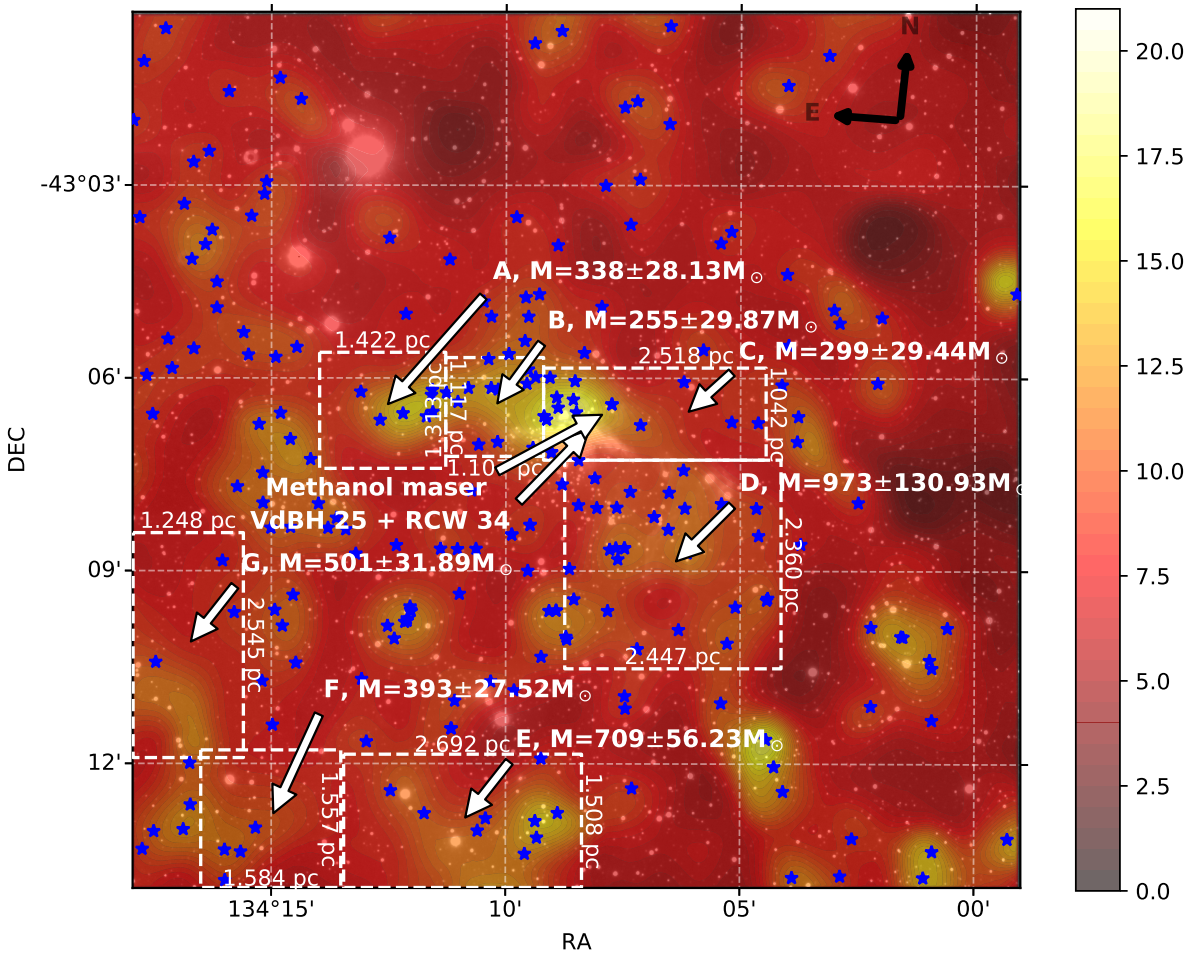

Figure 3.44: The location of the *IRSF* sources that showed excess emission (blue stars) relative to the structures shown by the extinction map in RCW 34.

The spatial distribution of the sources that show excess emission is shown in Figure 3.44 as the blue stars, and the position of the maser and VdBH 25a are pointed out with big arrows and the contours of the *NICEST LinES* extinction map. The excess emission sources are distributed across the whole $15.9' \times 15.9'$ field of RCW 34. They cluster closer together in the area directly surrounding the HII region and are more sparsely distributed further away from the HII region.

The position of the excess sources relative to the seven dense regions A-G is interesting, in the centre of each of these clumps there are a few excess emission sources. The excess emission sources are uniformly distributed in areas of the extinction map where the extinction is higher than $A_V \sim 7$. There are not a large number of sources that cluster in regions A-G. The highest number that group together is in

the dense region north of VdBH 25a where clump B and C join. This is the same position where the highest density of the molecular cloud is shown in the *NANTEN2* observations of Hayashi *et al* (2017).

There are more sources that show excess emission in the bubble region, as was discovered by Bik *et al* (2010), than the larger field. However those excess emission sources outside of the bubble region have not previously been documented. The most likely scenario for star formation here is as mentioned by Hayashi *et al* (2017) that two molecular clouds collided, which triggered the formation of the excess sources in the bubble region. The formation of VdBH 25a, the driving source of the maser, and the high density of excess emission stars next to these high-mass stars may have occurred at the densest part of the molecular cloud. It is hard to understand the exact occurrence of events due to the complex dynamics involved in the merger of the two molecular clouds. The most likely scenario is that the bubble shape is the aftermath of how the two molecular clouds interacted with each other, analogous to the collision of two spherical waves on the surface of a pond. The unanswered question is why there are excess emission sources that extend further than the ($10' \times 7.5'$ or $\sim 7.2 \times 5.45$ pc^2) bubble region, or whether the star-forming region is larger than $\sim 11.6 \times 11.6$ pc^2 covered by the whole field of view.

The excess emission sources lie on the ridges of different densities of the extinction map, for example, the groupings at the top north-western corner of the extinction map. It is possible that RCW 34 forms part of a larger star-forming region than the HII and bubble regions suggest. It may only be shown by the far-reaching distribution of the excess emission stars. Alternatively, the far reaching excess emission stars that lie outside of the bubble region may form part of a different star-forming region that is projected over the same field as RCW 34. The distribution of the dereddened excess emission stars on the colour-magnitude diagram in Figure 3.41 shows no distinctive sub-group of stars that would fit a specific isochrone. This implies that they are not part of a group of stars that formed at the same instance in a different star-forming region. None of the excess emission stars show signs that another star-forming region is in the same field of view as RCW 34, but they all are most likely associated with RCW 34.

It is difficult to determine how large the cluster associated with RCW 34 is, based only on the position of the excess emission sources. The high number of stars in the field also make it difficult to determine which stars are cluster members and have evolved to the main sequence. The results of Bik *et al* (2010) showed that there are definite main sequence cluster members in the bubble region. A way to test how far the cluster extends, is to look at the projected stellar surface density, the density is higher for a cluster than the typical density of field stars.

In Figure 3.45 the stellar surface density of the field around RCW 34 is shown, using the average number of stars at a specific radial distance from VdBH 25a. The density initially picks up from 0 to 0.013° ($0.78'$ or 0.56 pc), peaks at 0.015° ($0.9'$ or 0.65 pc), has a stable density up to 0.03° ($1.8'$ or 1.3 pc), and then decreases to 0.053° ($3.18'$ or 2.31 pc) and has an average up to the last few bins. At 0.12° ($7.2'$ or 5.23 pc) the density starts to stabilise and is considered to be the average field density, which only starts to decrease at the last few bins. The furthest decrease in density is due to the decrease in surface area that is measured when the circular shapes run over the square edge of the images. The decrease in the stellar surface density at a radius of 2.31 pc means the cluster spans ~ 5 pc. The effects of choosing the centre for the surface density measurement at VdBH 25a in such a complex environment might be the explanation for the gradual decrease in the surface density of the stars. If the stellar surface density had been measured from a position different than VdBH 25a, then the density profile might have looked different.

The surface density of the stars in Figure 3.45 shows the extent of the young stars in the bubble region. This star-forming region is very complex with the distribution of the high-mass stars, the young stars in the bubble region, and the excess emission stars extending past the bubble region and across the whole field. Hayashi *et al* (2017) explained that the star formation in RCW 34 was triggered by the collision of two molecular clouds. This explains the number of young stars in the bubble region which

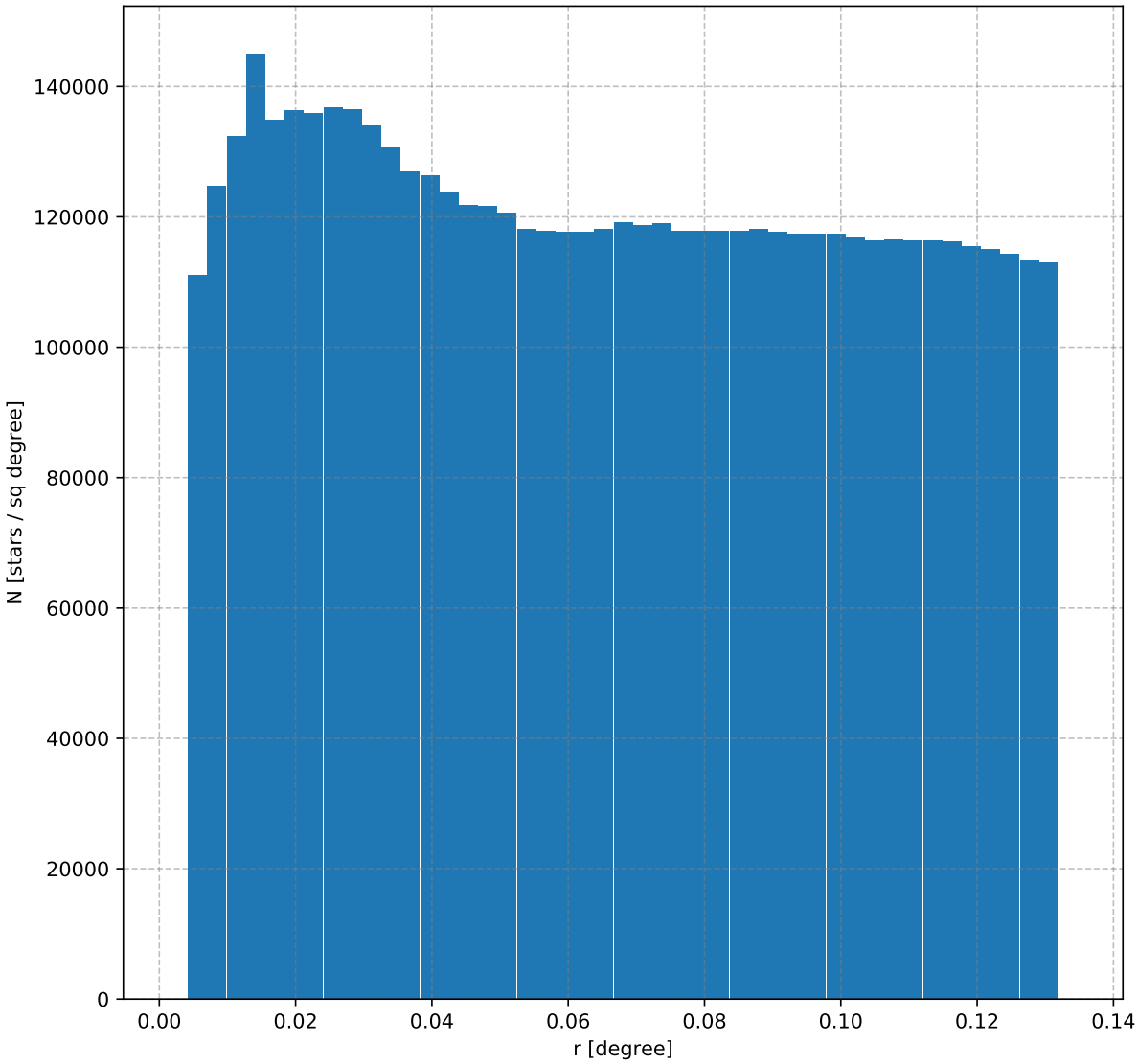

Figure 3.45: The stellar surface density as a function of radial distance from the star VdBH 25a.

must have formed just after the collision. However, their results cannot explain the distribution of the excess emission sources across the rest of the field. It is possible that star formation was occurring in both molecular clouds before the collision, and the higher number of sources that formed in the bubble region occurred after they crossed paths. Without proper motion observations that show in which direction each star in the field is moving it is impossible to sketch the full history of the star-forming region, or to identify the cluster members moving in a general direction relative to the other stars in the field of view.

3.4.5.2 *NGC 2626*

In Figure 3.46 the position of the excess emission stars are shown as blue stars together with the position of EM Velorum, HH-132, VdBH 17a, and the *NICEST LinES* extinction maps. The excess emission sources discovered in this study physically have the same size span as was shown in the study by Sharma *et al* (2016) ($5' \times 5'$). Sharma *et al* (2016) stated that the FIII6 star is a star with excess colour emission and is considered in that study as a PMS star. It is good to see that there is a very young star, which has not yet contracted to the same size as a main sequence star at such a distance away from the main sequence, is not embedded at high extinction. The physical extent of the cluster

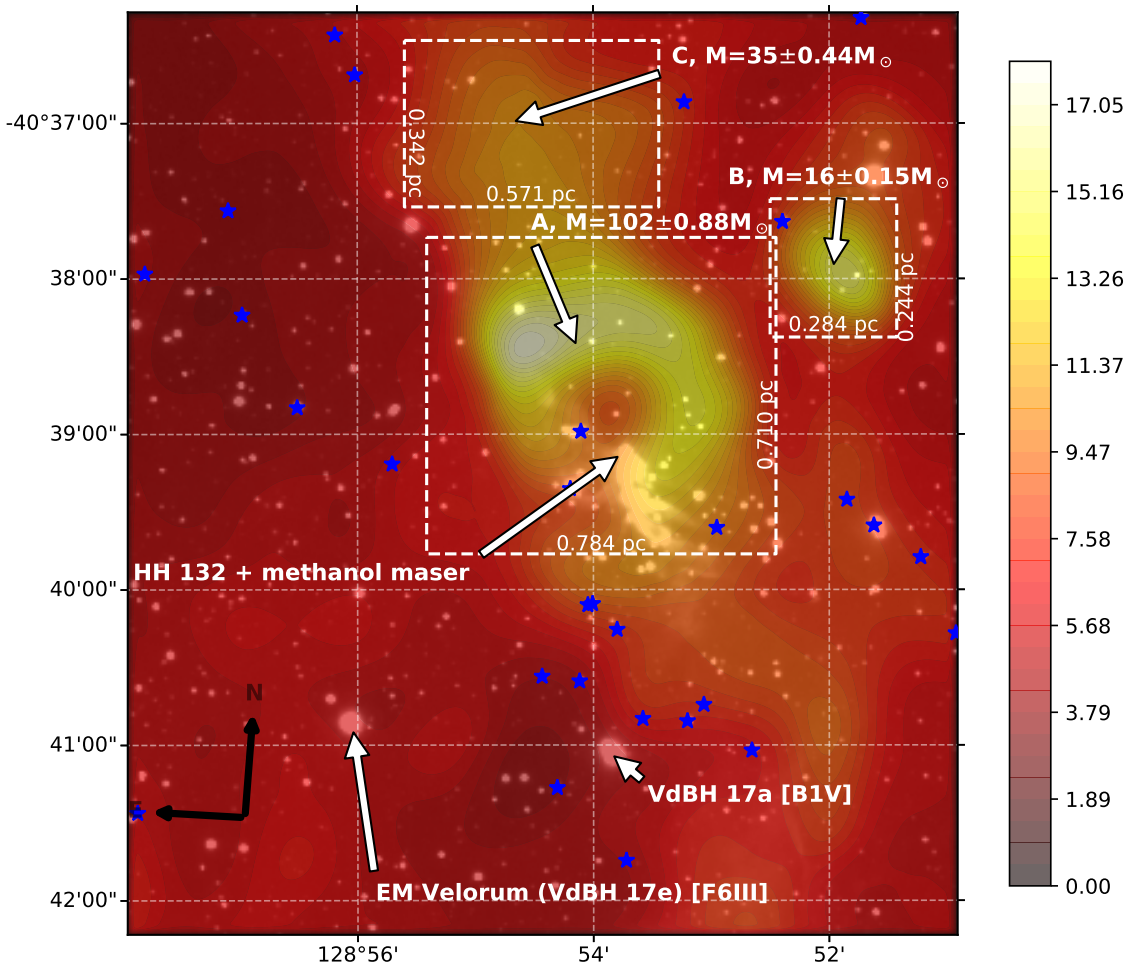

Figure 3.46: The location of all the *IRSF* sources and those that showed excess emission surrounding NGC 2626.

associated with NGC 2626 is thus considered to be larger than the field of view that was studied in this chapter.

3.5 Summary and conclusion

This chapter has covered a very large portion of the work for this thesis. In particular it has looked at near-infrared results of RCW 34 and NGC 2626, from the observations with the *IRSF* up to the extinction maps and spatial distribution of the low-mass stars in each field. This chapter also contains the most information relating to the young low-mass stars associated with each star-forming region, specifically regarding how much excess emission they provide, as well as an indication of how large each star-forming region is. The results on RCW 34 showed that there are indeed CTTs that are located further from the HII region than previous studies in the literature have shown. The results that were found by de Villiers (2009) were in principle incorrect, yet the spatial distribution of the PMS stars is true. The results for NGC 2626 confirm the same conclusions that were made in other studies from the literature by Mueller & Graham (2000) and Sharma *et al* (2016) regarding the expansion of the cluster associated with NGC 2626, the remnants of the molecular cloud, and the number of PMS stars that showed excess emission. The extinction maps from this study of NGC 2626 showed that the driving star of HH-132 forms a cavity in the molecular cloud, which other studies did not mention. This cavity and the presence of the maser right next to the driving star suggests that there is more to the star than the literature can explain.

3.5.1 The custom *LinES* extinction laws

The custom extinction law that was derived for RCW 34 was based on a linear optimization method that uses a dataset which has intrinsic errors and scatter. The colour distribution of the reddened sources lie along the derived reddening vector. The custom extinction law gave many sources with excess emission and was used to build extinction maps of the region surrounding RCW 34. The extinction law must be correct, because the extinction map that was built with the extinction law also agreed with extinction maps that were derived from CO observations. The extinction law for NGC 2626 was identical to the most generally accepted case for the Milky Way's Galactic plane. All of these results show that the method that was used to derive the extinction laws with *LinES* is correct, and that a method that works mainly in the mid-infrared is in general also applicable to near-infrared data.

3.5.2 Extinction maps

The extinction map that was built of RCW 34 was done with field stars dereddened to the main sequence and excess emission stars that were dereddened to a position between the upper and lower limits of the CTT locus. The resulting extinction map was used to dereddened all of the stars in the field and will be used in the following chapters to deredden the other imaging results. The structures in the resulting extinction map agree with CO observations from Pagani *et al* (1993) and Hayashi *et al* (2017), yet the *NICEST LinES* extinction has a much higher resolution. The extinction map for NGC 2626 shows structures with high extinction that propagate around the driving star for HH-132. The same star has blown away a significant amount of the gas in the molecular cloud, and it can be seen in the extinction map.

3.5.3 Colour-colour diagrams

The colour-colour diagrams for RCW 34 show that there are many stars in the field that have excess emission, which is characteristic to CTTs stars. The assumption that most of the stars with excess emission that lie above the CTT locus, can be dereddened to somewhere between the upper and lower limits of the CTT locus can be considered plausible. The reason for this is that the excess emission sources that were dereddened using just the extinction map built from the field stars in Figure 3.38 are incorrect in classifying the larger number of excess emission sources as classic Be stars. The most logical alternative to the sources not being classic Be stars is that they are reddened CTTs that can be dereddened to a position between the upper and lower limits of the CTT locus. The colour-colour diagram for the region around NGC 2626 showed that the driving star for HH-132 may be a very young source, and it may have strong excess emission. There were not as many sources with excess emission detected as is shown in the literature. The reason for this is that the field that was studied was much smaller than the studies by Sharma *et al* (2016), and the 1.4-m *IRSF* telescope is not as sensitive as the 4.0-m Blanco telescope that was used in the previous study.

3.5.4 Colour-Magnitude diagrams

The colour-magnitude diagram for RCW 34 showed that the sources with excess emission on the colour-colour diagram stand out from the other stars with the amount of excess emission in the dereddened colours. These sources showed various ages when compared to the evolutionary models of Siess *et al* (2000), and many had so much excess emission that they could not be compared to the evolutionary models. The evolutionary models are for naked photospheric emission and do not include excess emission from circumstellar material. The few low-mass sources that are comparable with the evolutionary lines show colours characteristic to late M-class stars. The colour-magnitude diagram for NGC 2626 shows that the dereddened colours and magnitude for the driving star of HH-132 is characteristic to a high-mass star. At least it has a mass higher than an A star, which would possibly make it a Herbig Ae/Be star.

3.5.5 Spatial distribution of excess emission source

The spatial distribution of the stars with excess emission in RCW 34 are found in regions with some high extinction and the structure of the remnants of the molecular clouds from which these stars formed. The majority of the excess emission stars formed in regions with high extinction, especially in the regions that border the HII region. The spatial relation between the excess emission line star

and the regions with high extinction show that there is low-mass star formation occurring in a region with spatial extent larger and deeper than the studies by Bik *et al* (2010) and Hayashi *et al* (2017) discovered. The spatial distribution of the stars with excess emission around NGC 2626 shows that star formation occured in such a large region as was shown in the study by Mueller & Graham (2000) and Sharma *et al* (2016). The number of sources is less than Sharma *et al* (2016) discovered in the region, because of the expanse of the field that was observed with the *IRSF*.

CHAPTER 4: OPTICAL IMAGING

4.1 Introduction

In this chapter a discussion will be given of the optical observations of the low-mass cluster members that are associated with RCW 34 and NGC 2626. It starts with an explanation of how the data was gathered, reduced, and analysed. It details how applicable extinction laws give a a relation between the *NIR* and optical photometry, for each respective region, which is used to deredden magnitudes and colours from the *NIR* extinction maps. Discussion is also had around how and why it was difficult to obtain precise optical photometry for the faint, young cluster members in RCW 34 and NGC 2626. The chapter then moves onto detailing how colour-colour diagrams are used to identify young stars with excess ultraviolet and Hα-emission. This includes an explanation on how narrowband Hα imaging can be used to identify young PMS stars emitting light from the heated matter in their accompanying accretion disks, without obtaining spectroscopy of individual cluster members. Thereafter a discussion on how masses and ages are determined for young stars that are identified as sources with excess ultraviolet and Hα-emission. The chapter closes with a discussion on the spatial distribution of these young stars relative to the structures seen in the extinction maps and the rest of the cluster.

4.2 Data acquisition

In a previous optical study by Czanik (2013), the observations of RCW 34 were done with the 1.0-m telescope and were initially not obtained to study the faint cluster members. The lack of the needed sensitivity resulted in inconclusive findings. For this project, longer exposure times with higher sensitivity were necessary to obtain the required high-precision measurements from the suspected faint sources. To obtain the precision optical photometry necessary for this project, a proposal was submitted for photometry on the **S**outh **A**frican **L**arge **T**elescope (*SALT*). The time allocation committee rejected the proposal and advised that the observations could apparently be performed on a smaller telescope. There are no optical telescopes available in South Africa that are smaller than *SALT*, but still large enough to detect the faint sources associated with RCW 34 and NGC 2626, and which can be observed and be absolutely flux calibrated. An attempt was made to obtain observing time for time on the 3.58-m New technology telescope (NTT)-telescope at ESO, La-Silla by submitting a proposal with the help of an European Southern Observatory (ESO) collaborator, Stefan Kimeswenger. Due to over-subscription the time was not allocated. After the applications for *SALT* and the NTT were submitted, survey data became publicly available for *SuperCOSMOS*, and later *VPHAS+*, which had the precise and sensitive photometry needed for this study. The following section will give an outline of the different data sources considered for this project. The parts of the data gathering that were not used, for example, the observations on the 1.0-m telescope and the *KMTNet* telescope are included, because the data analysis helped with the improvement of the photometric reduction pipeline.

4.2.1 *SuperCOSMOS* photometric survey

Frew *et al* (2014) explains that *SuperCOSMOS* is a digitisation of photographic plates observed as part of a survey in the southern Galactic plane. The survey was conducted as 3-hour long Hα exposures and 15-minute short-red band filters on the *AAO/UKST*. What makes the *SuperCOSMOS* survey relevant for this project is that its Hα observations started at the position of the Vela supernova remnant, and expanded to a large part of the constellation. The regions that were observed include both RCW 34 and NGC 2626. The scanned images have a resolution of 10 μm over an angular distance of 0.67″, which is higher than the DSS-I (25 microns) and the DSS-II (15 microns). Even though the survey is a digitised version of old photographic plates, the high sensitivity and accuracy of its measurements still makes it very relevant.

Figure 4.1: A digitised Hα filter image of RCW 34 (left panel) and NGC 2626 (right panel) extending a $15' \times 15'$ field of view. The images have not been continuum subtracted.

In Figure 4.1 Hα images are shown of the regions around RCW 34 and NGC 2626. These images show the detailed structure of the ionised gas surrounding each star-forming region that was visible in the survey images. The resolution and sensitivity of the digitised scans are high enough to show some of the faint low-mass PMS sources that are in the field of RCW 34 and NGC 2626.

Hambly *et al* (2001c) compares other surveys to the *SuperCOSMOS* data saying it has a higher sensitivity and smaller errors than the DSS-II, and is the only Hα survey of the southern hemisphere that has this precision. Hambly *et al* (2001b) explains the scanning process of the *SuperCOSMOS* machine and how an automated pipeline does digitised photometry on the images. The photometry is done by converting a measured intensity to a magnitude, and calibrating to a standard photometric system. The plates that were scanned had an angular size of 3×3 square degrees making precision photometry quite difficult. Hambly *et al* (2001a) further explains how the algorithms for astrometric calibration to the Tycho-2 system was calculated so that sources with $R \sim 18$ was aligned up to $0.2''$, and for $R \sim 22$ the alignment was up to $0.3''$. Hambly *et al* (2001b) shows that the photometric calibration is accurate up to 0.3 magnitudes for $R_S < 15$, have 5% errors for sources that have magnitudes of $19 < R_s < 15$, and for any sources fainter than $R_s \sim 19$, the error is in the range of 10%. The small number of sources that were detected in the previous optical study by Czanik (2013) suggests that if there are young PMS members in the cluster of RCW 34, they will be very faint. This means that the calibrated magnitudes will have at least 10% errors.

A young PMS star will show Hα-emission from its accretion disk. The amount of Hα-emission will depend on how young the star is. A star which is younger than 3 Myr will show very strong Hα-emission from the accretion disk. The Hα-emission will start to decrease after 3 Myr, as the accretion disk starts to dissipate with age. Once the star reaches an age of 10 Myr, there will be practically no more emission from the accretion disk. To separate the Hα-emission from the continuum emission in the short-red filter, the $(R_S - H\alpha)$ colour is used. This colour is independent of the magnitude of the star in each filter. On a $R_S/(R_S - H\alpha)$ colour-magnitude diagram the relevant age and mass of a young cluster member can be measured against theoretical evolutionary models.

Even though the quality and precision of the *SuperCOSMOS* survey is remarkable for a digitised version of photometric plates, it was not deep enough to match the sensitivity and accuracy of the *IRSF* observations. A detailed analysis of the images showed many dust marks, scratches, and other

artefacts that were present on the photographic plate. The 10% photometric errors for the faintest sources also did not give the precision that was required for the optical part of the observations. It was decided that alternative optical photometry was needed to test whether the sources that were presented as faint in the optical photometry was consistent with the excess *NIR*-emission.

4.2.2 Observations with the 1.0-m telescope at Sutherland

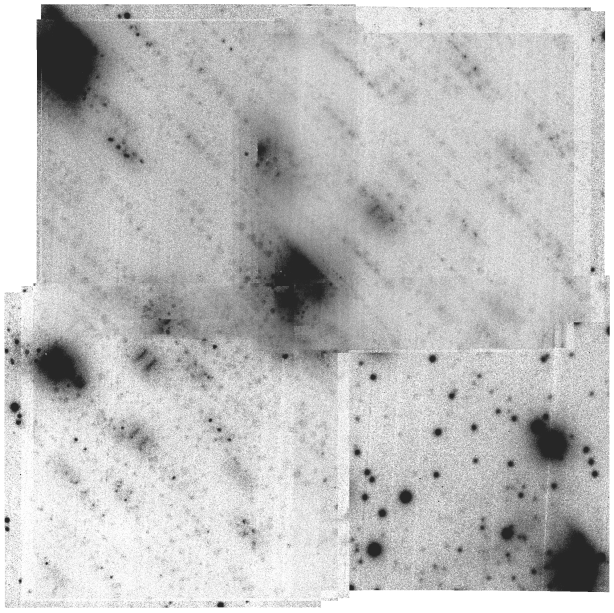

Figure 4.2: A stacked image of individual images that were observed with the 1.0-m telescope at SAAO, Sutherland. A median z' filter image was built from 15 individual images with the *MONTAGE* software package. The best astrometric solution for each was manually calculated for each individual image. The stacking was done from misaligned images, rendering the final product unusable.

The *NIR* results showed how faint the young cluster members around RCW 34 and NGC 2626 were. With these results known, another attempt of observations on the 1.0-m telescope was requested during December 2015, so that planning could be done accordingly. This time around, precision photometry of the faint members was the sole purpose of the observations. Two weeks were allocated from 2-15 December. The observations were performed using u', g', r', i', and z' SDSS filters, as well as the Hα filters on the STE 4 imager which has a $5' \times 5'$ field of view on the 1.0-m telescope. Sloan filters were chosen, because they have better-defined cut-off profiles over very specific wavelength ranges, and the results could be compared to more recent studies performed with *IPHAS/VPHAS+* survey data. The limited field of view on the imager resulted in various observations having to be taken of the fields surrounding RCW 34 and NGC 2626.

The high extinction at the sources and the narrow bandwidth of the Sloan filters resulted in a few detectable sources on individual images. Approximately ten sources were detected in the u'-band, and at most thirty in z'-band. The sources detected on the optical images were used to calculate astrometric solutions manually for each image. There were not enough bright sources located across each image to perform precision astrometry. An automated astrometric solution package on the *astrometry.net - NOVA* website was used to calculate astrometric solutions for the optical images. The *NOVA* package required the pixel scale of the imager and the coordinates of the central pixel in each field. The astrometric solutions from both a manual and automated system were so inaccurate that a mosaic could not be built with the *MONTAGE* package, resulting in an image as shown in Figure 4.2. The misalignment in the astrometric solution of the individual images rendered the stacked images unusable due to the position of individual stars differing between the different elementary images. These results, similar to the preliminary study by Czanik (2013), proved that the 1.0-m telescope is not sensitive enough to perform optical studies on faint, low-mass PMS stars in regions

with high extinction. A more sensitive instrument was needed for the optical photometry of this study.

4.2.3 *KMTNet* (Korean Microlensing Telescope Network)

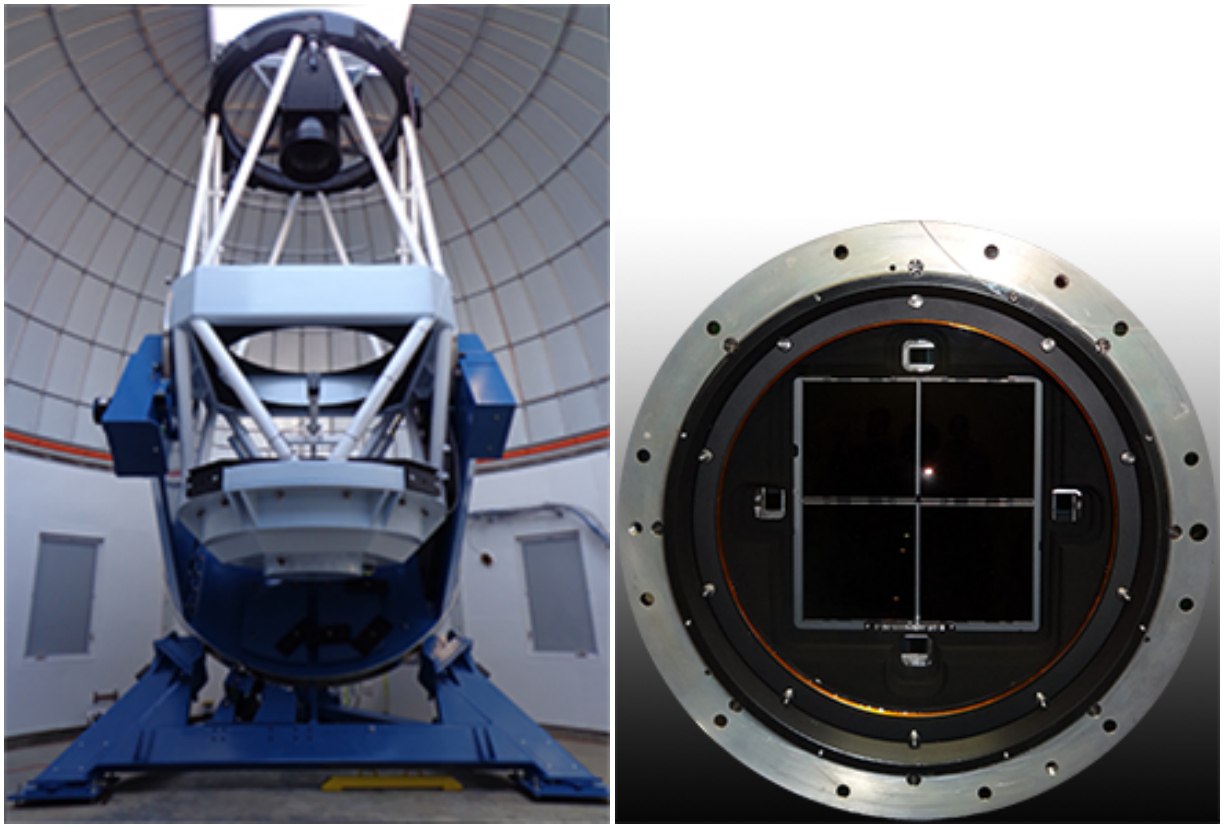

Figure 4.3: The first image is a photograph of the 1.6-m *KMTNet* telescope located at SAAO, Sutherland. The second image is of the 340 mega pixel science CCD that is used on the *KMTNet* telescope.

After the observations on the 1.0-m telescope did not deliver any usable results an application was submitted for observations on the new 1.6-m *KMTNet* (**K**orean **M**icrolensing **T**elescope **Net**work) telescope. The *KMTNet* telescope is part of a Korean operated three-leg telescope network located in Sutherland (SAAO), Cerra Tololo (CTIO) and Siding Spring (SSO). The main scientific purpose of the network is hunting microlensing events/transients (see Henderson *et al* 2014). Each *KMTNet* telescope has a large 340-megapixel camera covering 4.2 square degrees. The CCD is an array of 4 imagers with a 373″ gap along the y-axis and a 184″ gap along the x-axis between the CCDs (see Kim *et al* 2016). A single image is a 4-part Multi-extention fits (MEF) file, that takes up 682.6 MB storage space.

Three nights of observation time were allocated from 12/02/2016-14/02/2016 for RCW 34 and NGC 2626, resulting in $\sim$ 220 GB of raw data. Observations were performed in B, V, R, and I Johnson-Cousins filters, with respective exposure times of 120, 90, 60, and 60 seconds. These observations were centred on RCW 34 and NGC 2626, as well as standard star observations. There were 30 images taken in each band of both RCW 34 and NGC 2626, which means that there was a total exposure time of 3600 seconds, 2700 seconds, 1800 seconds, and 1800 seconds in the B, V, R, and I bands respectively of RCW 34 and NGC 2626. To practically deal with the reading and writing of the reduction of the large images on a desktop computer, a reduction script was written to streamline the processing.

The *MSCRED* (**M**osai**c** **red**uction) package in *IRAF* was used, because it was developed to reduce multiple entry Flexible image transport system (FITS) files. The reduction script performed the following steps:

- A master BIAS image was built as a median stacked image from all of the bias images taken.

- Each *KMTNet* image had four FITS entries respectively, named **M**, **K**, **T**, and **N** that corresponds to a specific imager. Each FITS entry for an imager has 32 sub-entries, each sub-entry a smaller FITS image that has a specific row and column entry on a specific imager. These 32 entries all come from 8 different amplifiers on each imager. Each of the **M**, **K**, **T**, and **N** imager entries was written to a separate FITS file, starting the image name with the specific filter of each individual. A new header entry was generated for each FITS file.

- Each newly created FITS image was corrected for BIAS, overscan, and trimmed according to the pre-set parameters in the header entry.

- Each image did not have a value associated with the dark time in its headers, so it was corrected to the same value of the exposure time. A few dark images with exposure times of 120 seconds were supplied with each night's observations; a master dark image was built for each night's dataset. To correct the science images for dark current, the master dark image was scaled according to the specific dark time parameter in the header.

- A median combined sky-flat image was used together with a master dome flat image to apply flat-field correction to each science image.

- After each science image was reduced, it was cleaned of bleed trails. A bleed trail is where light spills over from the point-like profile of a star to adjacent columns of pixels. The cleaning parameter of the bleed trails had a width of 3 pixels, and an average value that a bleed trail would have above the background value was 5000 ADUs.

- A second order polynomial was fitted over a reduced image so that the difference in the background levels could be calculated between the 32 different readout images. There were 100 points selected across the x- and y-axis. The fitted polynomial was used to correct the background levels between the readouts. After the background correction, all 32 readouts were combined into a single FITS image.

- The large field of view on the *KMTNet* images causes a very complex astrometric calculation for each reduced image. Across the whole 4.2 square degrees image, a 4% WCS distortion was the result of projecting light from spherical optics onto a square-shaped imager. When a single **M**, **K**, **T**, and **N** reduced science image was submitted to the astrometry.net software package, incorrect WCS solutions were calculated when the centre of each science image — and its corresponding RA and DEC were given to the software package. The WCS calculations were done by trimming each **M**, **K**, **T**, and **N** science image to a quarter of its original size. The star-forming region, in each instance was located in the middle of the four science CCDs; each observation had a small offset in the RA and DEC so that a mosaic would result in a deep composite of each star-forming region. The estimated point for the WCS calculations was given to the astrometry.net software as the corner of each science exposure closest to the star-forming region and its estimated RA and DEC coordinates. For the smaller science images spanning 1×1 degree, where the distortion of the larger field is trimmed away, precise WCS transformations were calculated. Stacked images resembling Figure 4.4 were built from high precision astrometry on the component images.

The mosaicked image was stacked with the *MONTAGE* software package. The alignment between the component images was very precise in the corners where the WCS calculation estimates were started. On the outer corners of the image, there are offsets to the astrometry which did not make it possible to perform good photometry between the different images. The areas where the astrometry has strong offsets are not of interest to this study, since it is more than a degree away from the star-forming regions. When the images were supposed to be calibrated to a standard photometric system,

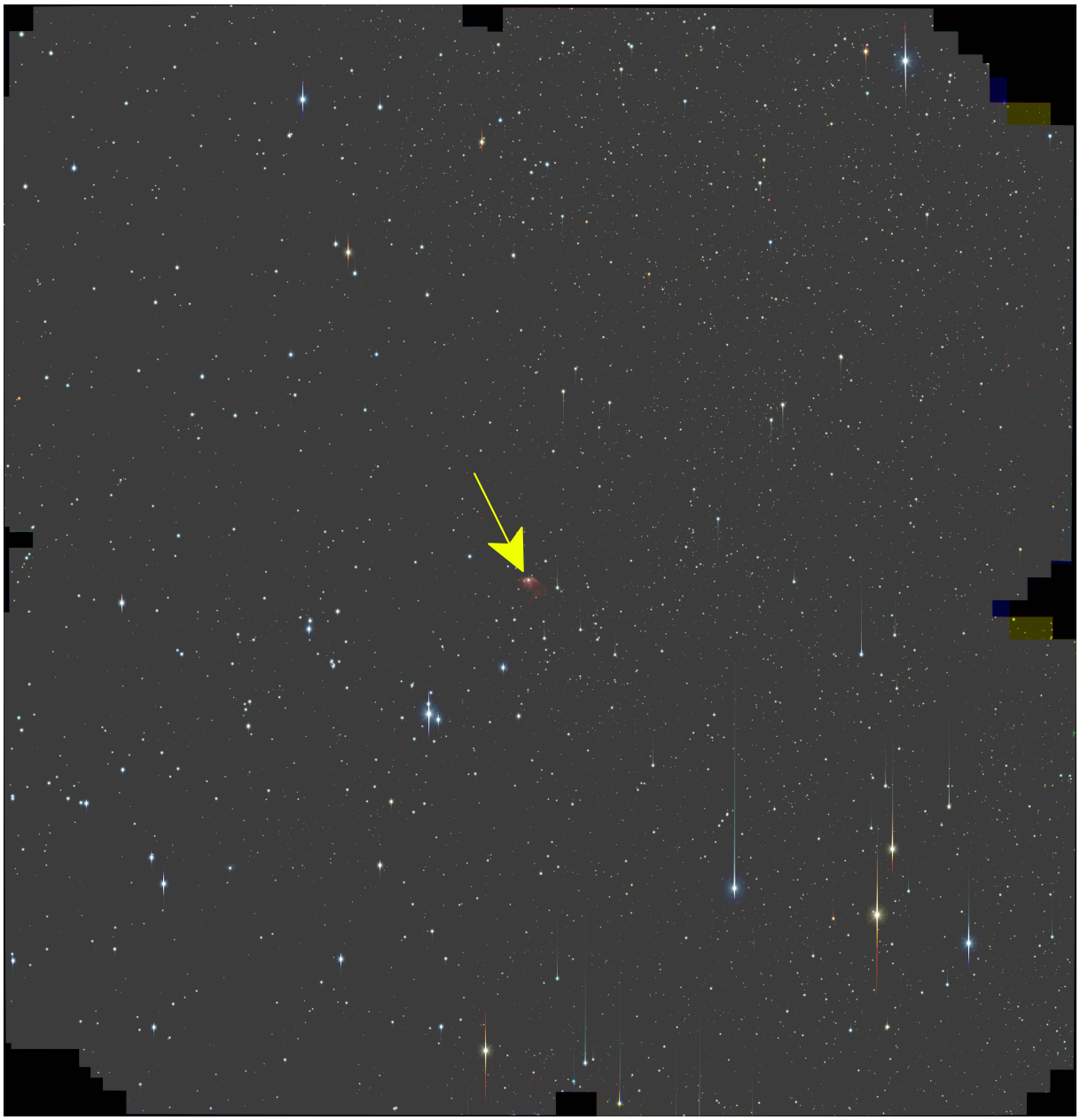

Figure 4.4: A pseudo-colour image centered on RCW 34 that was constructed from the B, V, and R broadband images that were observed with the *KMTNet* telescope.

it was discovered that with the service observations, the standard star was left in the gap between the science CCDs. The standard star was not observed in dither-mode, as in the case of the science images. With a lack of standard star data the photometric calibration would be done using either survey data, or using other known magnitudes/colours of stars that were included in the images of RCW 34 and NGC 2626. If survey data was used for the calibration of the *KMTNet* data similar to the *IRSF* data, it was decided a search for survey data that was already reduced and calibrated would be performed. The reason for this is that the *KMTNet* data was not obtained in the SDSS photometric system, and did not include Hα imaging, which was the initial goal of using the 1.0-m telescope.

4.2.4 *VPHAS+* (The VST photometric Hα survey)

From the literature on various star-forming regions it was clear that the northern hemisphere based *IPHAS* survey, and its southern hemisphere counterpart *VPHAS+*, was ideal for studying star-forming regions. The *VPHAS+* (**V**LT **P**hotometric **H**α **S**urvey) is a survey conducted in the optical u', g',

r', i', and Hα bands. It covers the Galactic plane and bulge at a 1″ seeing, with a sensitivity that can detect objects fainter than 20'th magnitude in all filters (see Drew *et al* 2014). It is the southern counterpart of the *IPHAS* survey conducted on the Isaac Newton telescope of the Galactic plane with a coverage of 5 degrees above and below the Galactic plane from the northern hemisphere (see Drew *et al* 2005).

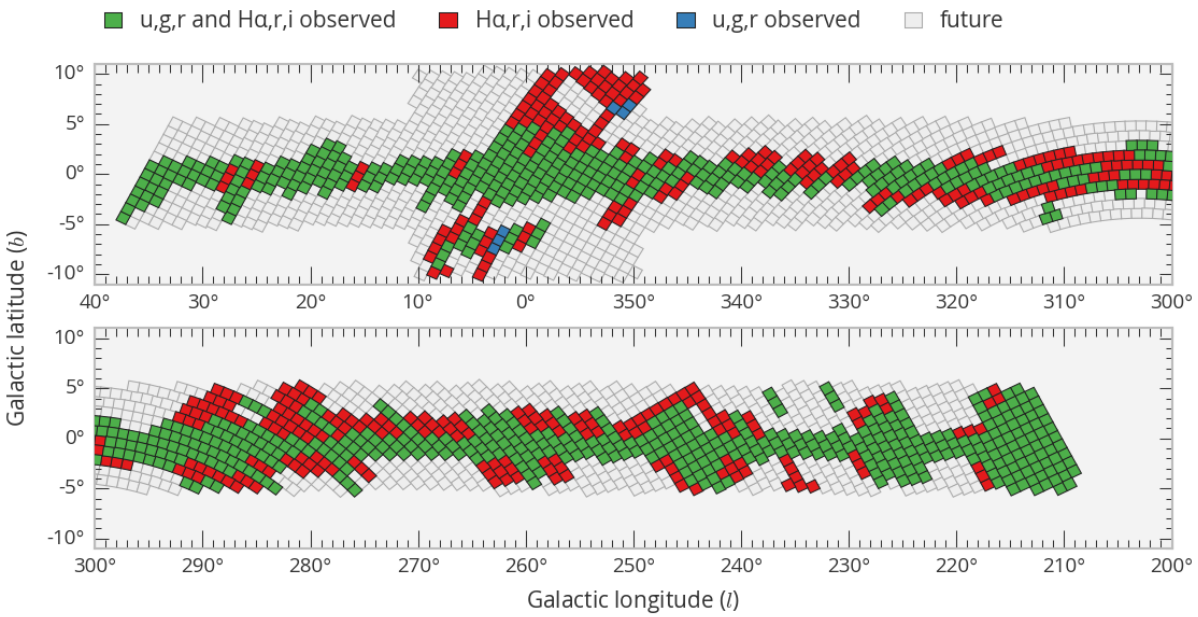

Figure 4.5: The progress of the *VPHAS+* survey up to the end of August 2015 as shown on the survey's website (http://www.vphasplus.org/survey.shtml). The different colours correspond to which filters have been observed.

The survey is supposed to cover ∼2000 square degrees along the Galactic bulge and plane. The area is 5 degrees in Galactic latitude from the central part of the Galactic plane and 10 degrees in latitude and longitude along the bulge. Observations are performed on an intermittent basis during dark and grey periods, so that the u', g', r' (blue) and r', i', $H\alpha$ (red) reduced data are released at different periods. The survey is an ongoing project with the final goal of observing objects of up to 20'th magnitude with 5σ precision.

The *VPHAS+* survey is the best source for the optical photometric data for this project because:

- The VST (**V**LT **S**urvey **T**elescope) is a 2.61-m telescope located in Cerro Paranal at 2635 m above sea level, and it is mainly dedicated to the *VPAHS+* survey. The 268-megapixel OmegaCAM covers an area of 1 square degree and has a sensitivity that can not be matched by any equipment at the SAAO site.

- The chosen filters of the survey makes it very efficient in finding stars with Hα-emission from a $(r' - H\alpha)/(r' - i')$ colour-colour diagram. The spectral class of a star can be estimated, as well as how much Hα-emission is given off by the accretion disk.

- The *SuperCOSMOS* survey does not have data for all of the filters that the *VPHAS+* survey has, nor is the photometric system as easily comparable with existing data. Furthermore, the *VPHAS+* bands follows into the optical wavelengths from the *IRSF* bands.

The third data release (DR3) gave photometric results in all filters for the regions around NGC 2626, but none for RCW 34. Private e-mail communication with the PI of the *VPHAS+* survey, Janet Drew, provided reduced photometric data for RCW 34 and its surrounding region.

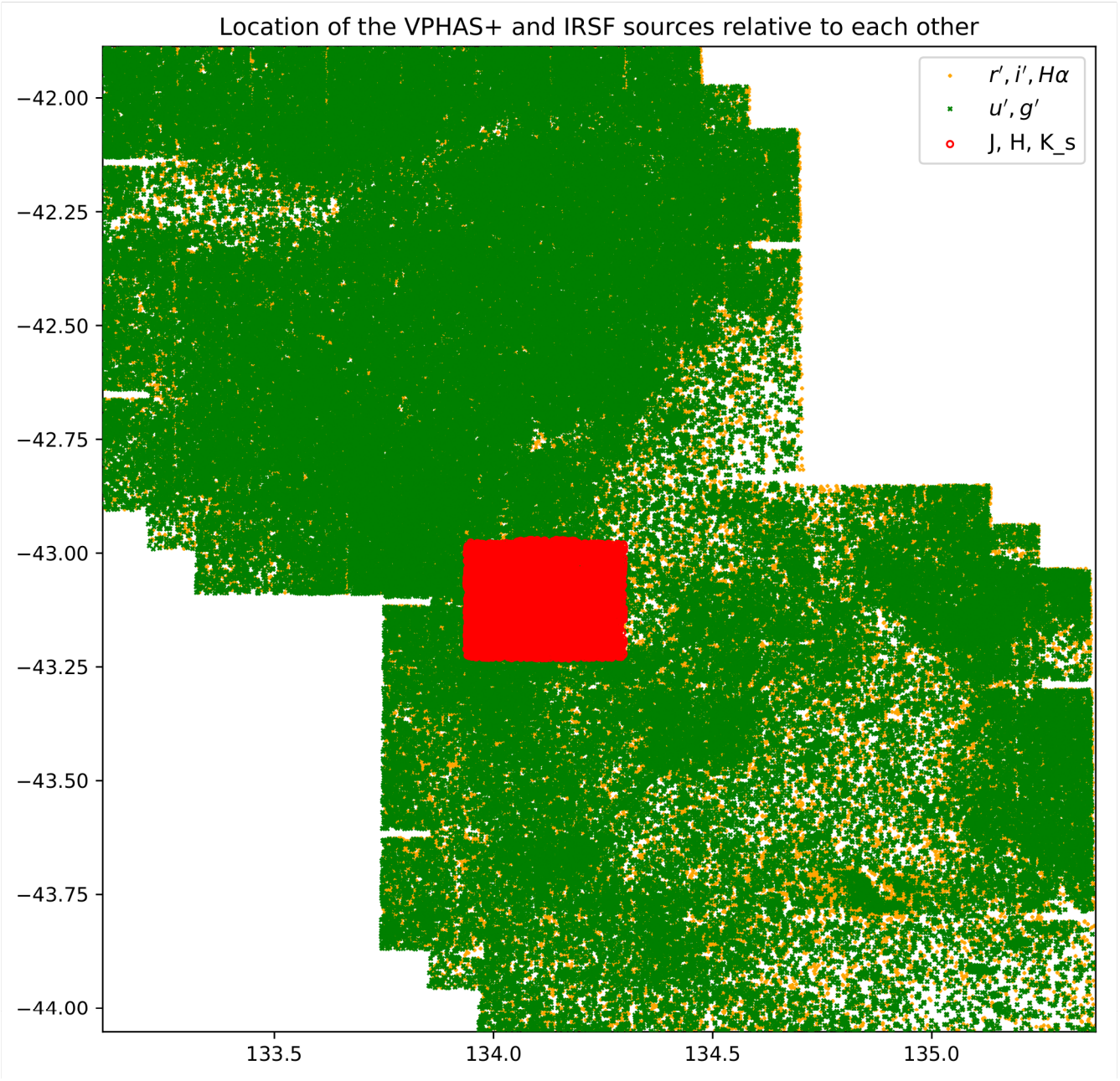

Figure 4.6: The overlap between the *IRSF* and *VPHAS+* red (r', i',Hα) and blue (u', g', r') datasets for the region around RCW 34.

4.2.4.1 *Optical extinction measured from NICEST LinES maps*

The extinction maps constructed with the *NICEST* interpolation method are used to calculate the optical extinction to detected sources with excess ultraviolet and Hα-emission. Davenport *et al* (2014) gives the ratios for a R_V=3.1 extinction law between the SDSS and the *2MASS* photometric systems. A custom *NIR* extinction law was derived for RCW 34, which gives a relation between A_J/A_{K_s} that is different from the general extinction law that is used in the Galactic plane or the case of NGC 2626. The ratio of A_J/A_{K_s} is used to derive a J-band extinction map, and then the ratio of A_J/A_V given in Davenport *et al* (2014) is used to derive a visual extinction map. From the A_J extinction map for RCW 34 the custom *NIR* extinction law has already been applied, and it is assumed that the extinction law relating the extinction in the optical bands to the extinction in the J-band, is valid for RCW 34 if the custom *NIR* extinction law has already been applied from the K_s to J band. From the

A_V map a conversion to an $A_{r'}$ extinction map is done and is used to deredden the optical colours and magnitudes. The *LinES* method can not be applied to the optical bands, so an assumption is made that the general case used in the Milky Way's Galactic plane are valid in all directions. The same ratio of extinction between the optical bands to the J-band are valid for RCW 34 and NGC 2626. Thus, if the extinction in the J-band can be calculated from the custom *NIR* extinction law, the relation between the visual extinction and the SDSS system can be used to deredden stars in the *VPHAS+* data.

$$A_J/A_V = 0.282 \text{ and } A_J/A_{r'} = 0.15 \tag{4.1}$$

$$A_{r'}/A_V = \left(\frac{1}{A_J/A_{r'}}\right) \times A_J/A_V \tag{4.2}$$

$$A_{r'}/A_V = \frac{1}{0.282} \times 0.15 \tag{4.3}$$

$$A_{r'}/A_V = 0.53 \tag{4.4}$$

Equation 4.4 is used to derive a relation between the r' and V-band from the *LinES* extinction law. The relations between all of the SDSS bands are given in Table 4.1.

Table 4.1: The median wavelength and extinctions relative to the r' band for the bands used in *VPHAS+* survey.

Filter	λ [Å]	$A_\lambda/A_{r'}$	$\sigma(A_\lambda/A_{r'})$
u'	3542	1.83	0.02
g'	4770	1.39	0.01
r'	6231	1.00	-
i'	7625	0.76	0.01

The extinctions ratios in Table 4.1 are used to deredden sources on the $(u'-g')/(g'-r')$ colour-colour diagrams, and the $r'/(r'-i')$ colour-magnitude diagrams. The visual extinction is required to deredden stars on a $(r'-H\alpha)/(r'-i')$ colour-colour diagram with the use of a reddening vector scheme given in Drew *et al* (2005).

To calculate the extinction for the colours involving the Hα filter, a reddening scheme was developed by Drew *et al* (2014). The scheme has a basis of using SEDs for stars of different spectral types and assigning an Hα-emission line at various equivalent widths to the different spectral types. The reddening vector is shown in Figure 4.7 for an A0V star. The extinction vector is curved due to the wavelength dependence of the extinction law which has to be used with the precision photometry of the *VPHAS+* data. The reddening vector can be simplified with a straight line, because the errors of the transformed extinction between the different bands will be bigger than the small difference between the curved reddening vector from Drew *et al* (2005) and a straight line. A least squares fit was applied to the three points showing the extinction law in Figure 4.7.

In the following section, the colour-colour and colour-magnitude diagrams will be presented and discussed. In the first part of the colour-colour diagrams, stars with Hα-emission are identified from the $(r'-i')/(r'-H\alpha)$ diagram. A classical T Tauri star has excess emission in its $(r'-H\alpha)$ colour. Next, sources with excess blue emission are identified on $(u'-g')/(g'-r')$ diagrams. The excess blue emission is characteristic to young classical T Tauri stars and is caused by matter moving at supersonic speeds along magnetic tubules from the accretion disks, and shocking onto the surface of the young stars. In the colour-magnitude subsection, the dereddened stars are compared to evolutionary lines of different spectral classes and isochrones. Attention is given to the stars with properties characteristic to young PMS stars on the colour-magnitude diagrams. Lastly, the spatial distribution of the stars with Hα-emission and *NIR* excess that was detected in the optical is analysed regarding the rest of the cluster.

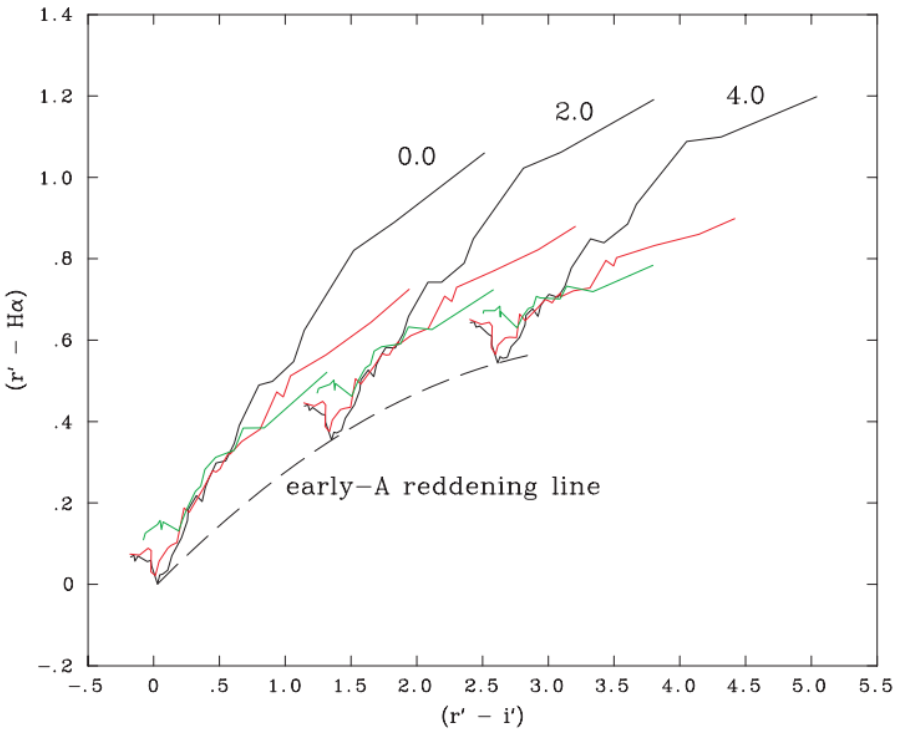

Figure 4.7: The extinction curve that is displayed in Figure 5 of Drew *et al* (2005) for the interstellar extinction law for R=3.1. The main sequence is drawn as the black line while the giant and supergiant sequences are drawn as red and green. The reddening positions agree to excess $E(B-V) = 0.0,\ 2.0$ and 4.0. The dashed line shows the reddening locus for an A0V star.

4.3 Results

4.3.1 Colour-colour diagrams

In this subsection, the stars that have excess u'-emission will first be determined from a $(u'-g')/(g'-r')$ colour-colour diagram. The stars that present excess Hα-emission are identified from a $(r'-H\alpha)/(r'-i')$ colour-colour diagram. On the $(u'-g')/(g'-r')$ diagram the zero-age main sequence (ZAMS) from the models by Siess *et al* (2000) is used to represent the intrinsic colours for main sequence stars. Young PMS stars will show excess ultraviolet emission in their $(u'-g')$ colours. The matter shocking onto the young star's surface causes a strong increase in the emission at wavelengths shorter than 4500Å. In the spectra of most classical T Tauris, there is veiling caused by radiation from heated circumstellar material. For young stars, there is more veiling observed in their spectra, due to more heated dust in the circumstellar disk. The heated dust will present an emission profile at around 5300Å which has a width of ∼500Å. These features in a star's spectra will show in $(u'-g')$ as a colour excess and $(g'-r')$ as a colour decrease. If a star has strong excess ultraviolet emission the $(u'-g')$ colour will show excess emission, more than the main sequence. An empirical measure for the excess u'-emission emitted by a classical T Tauri is documented by Venuti *et al* (2014) and is plotted as the black dashed line on Figures 4.8 and 4.9. Any classical T Tauri star with excess emission from matter shocking onto the star's surface, will have a $(u'-g')$ colour smaller than the segregation line with the equation $(u'-g')_{\rm ref} = 1.312 \times (g'-r')_{\rm obs} + 1.03$. This line is represented as the red dashed line in Figures 4.8 and 4.9. A main sequence star will lie above the line and a young PMS star will lie below it. In the data from Venuti *et al* (2014), the excess u' line has a difference of 0.5 magnitude on the $(u'-g')$ axis to make a clear distinction between a distribution of WTTs and stars that are CTTs. That same difference is applied to this study and the segregation line between WTTs and CTTs is plotted as the red dashed line. If the star has strong veiling then $(g'-r')$ colour will have a colour excess more than the main sequence stars. In Figures 4.8 and 4.9 the stars with excess ultraviolet emission will appear more to the bottom of the figure and those with veiling will appear more to the left.

4.3.1.1 *RCW 34*

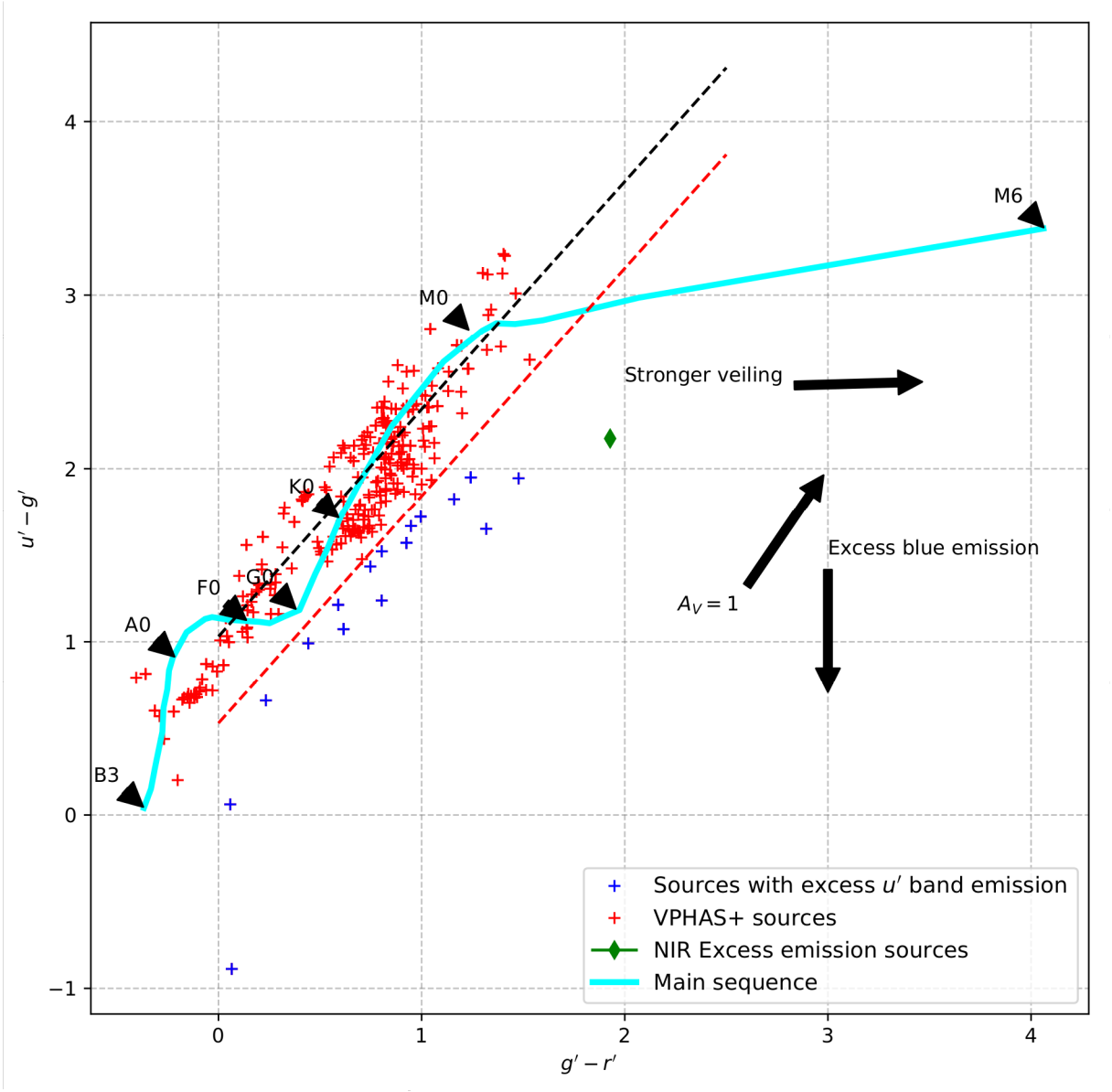

Figure 4.8: $(u' - g')/(g' - r')$ colour-colour diagram for *VPHAS+* sources in RCW 34. PMS stars with excess ultraviolet emission will lie below the red excess emission line, whereas main sequence stars will lie inline with the black dashed line. The stars with strong veiling will lie more towards the right side of the excess emission line, relative to the black main sequence line.

In Figure 4.8, 338 sources are shown, all of which had magnitudes detectable in the u', g', and r' bands and could be dereddened using the *NICEST LinES* extinction maps. The limiting magnitudes for that data set shown in Figure 4.8 are 18.18, 19.73, and 21.68 in the u', g', and r' bands respectively. It is not surprising that the u'-band's limiting magnitude is in the range of ~ 18, due to the extinction in the region, and the short exposure time with which the images were taken on the *VLT* survey telescope. The limiting u'-magnitude has a negative effect on the number of sources that are studied in this colour-colour diagram. The effects of extinction on the u'-band effectively eliminates the sources with excess *NIR*-emission, which are only found in areas with extinction higher that $A_V \sim 7$ on the *NIR* extinction map. From the 399 sources with excess *NIR*-emission, and the 338 sources that were detected in the u'-band, it is surprising that only a single source matched. This indicates that the u' imaging was not deep enough to detect any of the excess *NIR*-emission sources. The dereddened

colours for the source with excess *NIR*-emission that is shown in Figure 4.8 has excess u'-emission. There were only 21 sources with excess u'-emission, which is a very small number of CTTs if compared to the number of *NIR* excess emission sources. The other 317 sources all have colours that place them close to, or on the main sequence. These sources can not be foreground stars, because all of the foreground stars, which had an extinction smaller than the cutoff extinction, were eliminated. This is similar to the elimination of foreground stars in Chapter 3. Extinction due to the dust in the embedding gas makes detection of the embedded sources very difficult at short optical wavelengths, especially with the large distance towards RCW 34. It would require a substantially longer exposure time on a large telescope to get accurate u'-band photometric measurements of all the sources that have excess *NIR*-emission.

4.3.1.2 *NGC 2626*

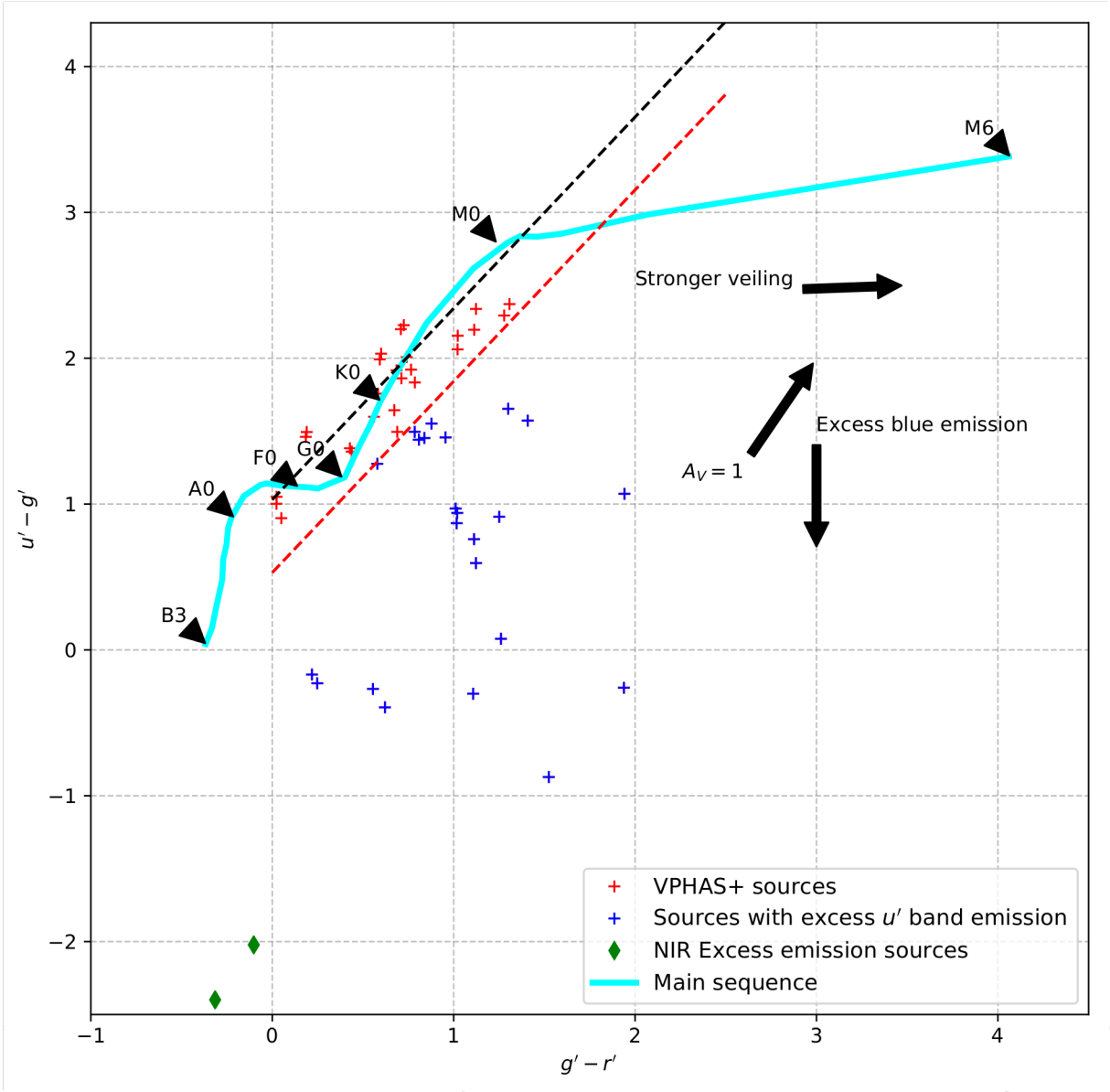

Figure 4.9: $(u' - g')/(g' - r')$ colour-colour diagram for *VPHAS+* sources in NGC 2626. PMS stars with excess blue emission will lie below the red excess emission line, where main sequence stars will lie inline with the black dashed line. The stars with strong veiling will lie more towards the right side of the excess emission line, relative to the black main sequence line.

Figure 4.9 shows the dereddened colours for 51 sources that matched between the u', g', and r' bands,

of which 14 also had excess *NIR*-emission. The limiting magnitudes are 19.27, 21.81, and 21.13 in the u', g', and r' respectively. The limiting magnitude of the u'-band does determine which sources are studied on the colour-colour diagram. The u'-band of NGC 2626 is one magnitude more sensitive than for RCW 34, due to the closer proximity and fewer structures with high extinction. The limiting magnitude of $u' \sim 19$ implies that the completeness of possible CTTs stars in NGC 2626 is expected to be higher than in RCW 34, because these sources have strong excess blue emission in the optical, and there is less extinction in this region. There are 23 stars that show excess u'-emission according to the dereddened colours. If a star shows excess emission, then the colour-colour diagrams can not be used to determine what the spectral type star is, because the younger stars will most likely have strong veiling in their spectra. The stars with excess u'-emission that also has veiling will not just appear far below the excess emission line, but also towards the right from the excess emission line. For example the three stars with $(g' - r') = 2$ may have both strong veiling, and excess u'-emission. It is not possible to test how much excess u'-emission and veiling is given off by these stars without knowing from which spectral type the emission in each colour should be measured. This shows that fully understanding the results from these colour-colour diagrams is not possible without extra information.

4.3.2 Hα-emission sources

In Figures 4.11 and 4.13 the stars that were detected in r', i', and Hα are dereddened according to the *NICEST LinES* extinction map. From the A_K *NIR* extinction map a A_J extinction map was derived with the custom *NIR* extinction law. The assumption made earlier — that the extinction law relating the J-bands's extinction, A_J to the visual extinction, A_V is still valid when the custom *NIR*-extinction law was used to derive the A_J extinction map from the A_{K_s} extinction map — is made again here. This implies that the relation between the visual extinction A_V, and the extinction in the SDSS bands given by Davenport *et al* (2014), together with the relation between the visual extinction and Hα-band given by Howarth (1983) as $A_V = 0.796 \times A_V$ is also still valid. This same technique was used to deredden *VPHAS+* Hα sources on a $(r' - H\alpha)/(r' - i')$ colour-colour diagram by Barentsen *et al* (2011).

The colour-colour diagrams will indicate which stars have excess Hα-emission. This excess Hα-emission is a consequence of a strong Hα-emission line, which is characteristic of a classical T Tauri star. The main sequence used on the colour-colour diagrams was taken from a paper by Drew *et al* (2014) where the typical $(r' - H\alpha)$ flux was calculated from spectral models. The $(r' - i')$ colour on the colour-colour diagram is used as an indicator of the star's spectral type.

4.3.2.1 *RCW 34*

Figure 4.10 shows the dereddened $(r' - H\alpha)/(r' - i')$ colours and errors of the sources that are in the field of RCW 34. There are dereddened colours for 1593 stars shown in Figure 4.10 certainty of the measured accuracy of the magnitudes is 95%, and the errors are smaller than 0.1 magnitudes in each of the Hα, r', and i' bands. The red crosses are the sources that have flux in the $(r' - H\alpha)$ colour, higher than the typical continuum flux of a main sequence star in this colour. The excess emission in the $(r' - H\alpha)$ colour is characteristic of a star with an Hα-emission line. The main sequence shown here serves as the separation between different spectral types using the $(r' - i')$ colours, similar to studies by Drew *et al* (2014), Barentsen *et al* (2013), and Kalari *et al* (2015). Adding the excess emission to the same main sequence serves as the separation between main sequence and Hα-emission line stars. A star is classified as an Hα-emission line star according to the $(r' - H\alpha)$ colours — regardless of the error on the measurement. This is shown in Figure 4.11.

216 out of the 1593 stars show Hα-emission sources in Figure 4.11, and are plotted as red crosses. The spectral classification is based on the $(r' - i')$ colours of the stars, which are distributed between A and M stellar types. The majority of these stars fall between the K5 and M4 stars, which show the peak of the mass function for the stars in the field. This same peak of stars between K5 and M4 stars is present in the stars with excess Hα-emission, showing that the mass function for the cluster is similar to that for the rest of the field.

The strength of the Hα-emission line is proportional to the $(r' - H\alpha)$ colour, which implies that the

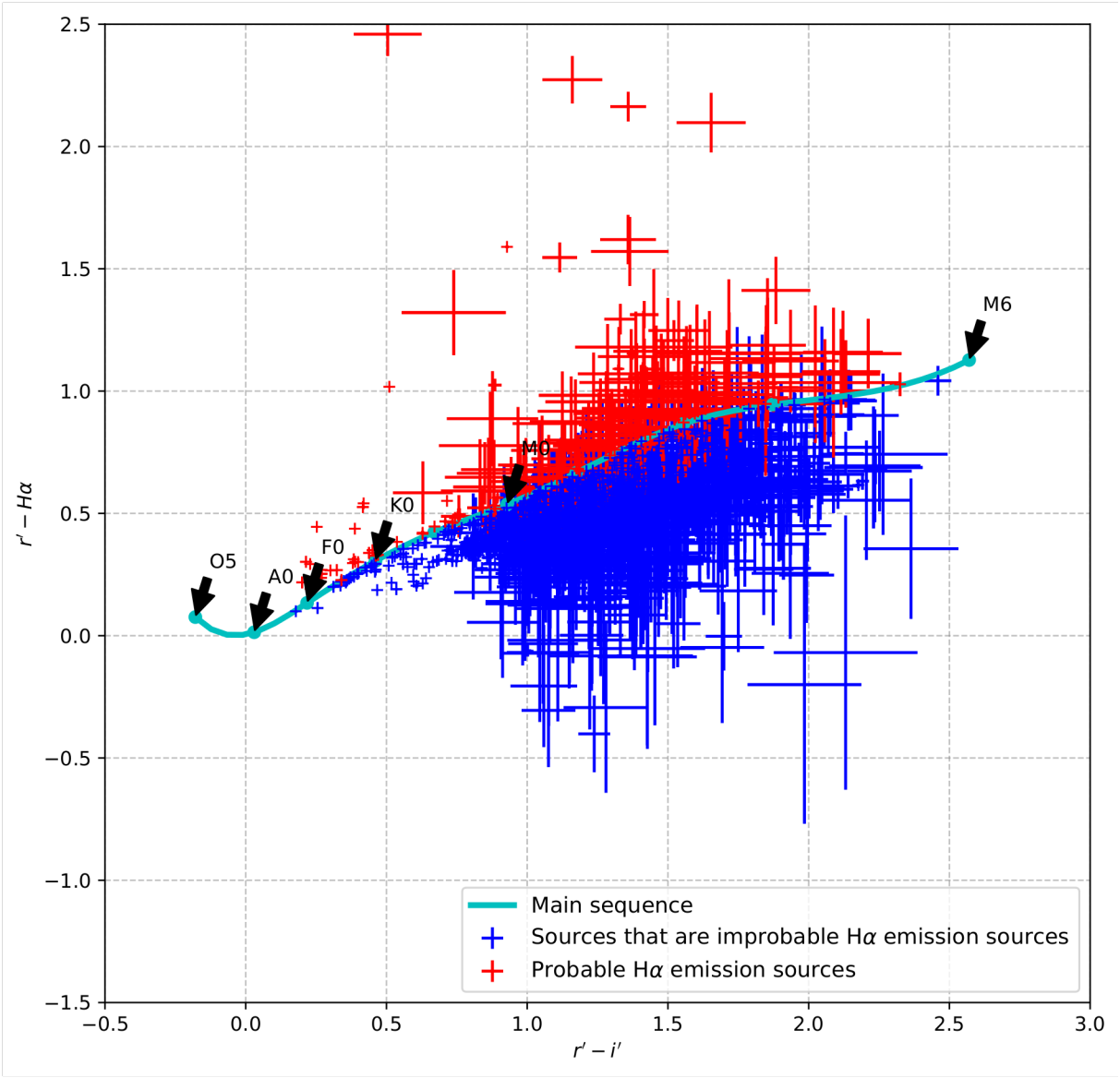

Figure 4.10: $(r' - H\alpha)/(r' - i')$ colour-colour diagram for all of the *VPHAS+* stars in RCW 34.

excess $(r' - H\alpha)$ is a indicator of more Hα-emission from the source. Most of the stars with excess Hα-emission are close to the main sequence, and can either be main sequence or WTTs. There were only four sources with excess u'-emission that matched to sources with Hα-emission. These are shown as the magenta circles. The low number of sources with excess u'-emission which also shows excess $(r' - H\alpha)$ emission, can only be attributed to extinction, which makes the other sources with excess u'-emission undetectable.

The simulated main sequence of Drew *et al* (2005) gives a relation between the difference in the $(r' - H\alpha)$ colour, and the equivalent line width that is present in the $H\alpha$-emission line strength. The more excess that is measured in the $(r' - H\alpha)$ colour, the larger the equivalent width of the Hα-emission line star would be. For an equivalent width of 10Å, the excess from the main sequence will be $\Delta(r' - H\alpha) = 0.1$, meaning any star with an excess of more than 0.1 is a CTTs. Out of the 216 stars with excess $(r' - H\alpha)$ emission, there were 88 that showed Hα-emission characteristic to CTTs, and are plotted as green crosses in Figure 4.11. The number of sources with properties characteristic to CTTs that were detected in the optical, is a small fraction of the number of sources that showed similar properties in the *NIR*. The other 128 sources that had excess $(r' - H\alpha)$, but less than the CTTs

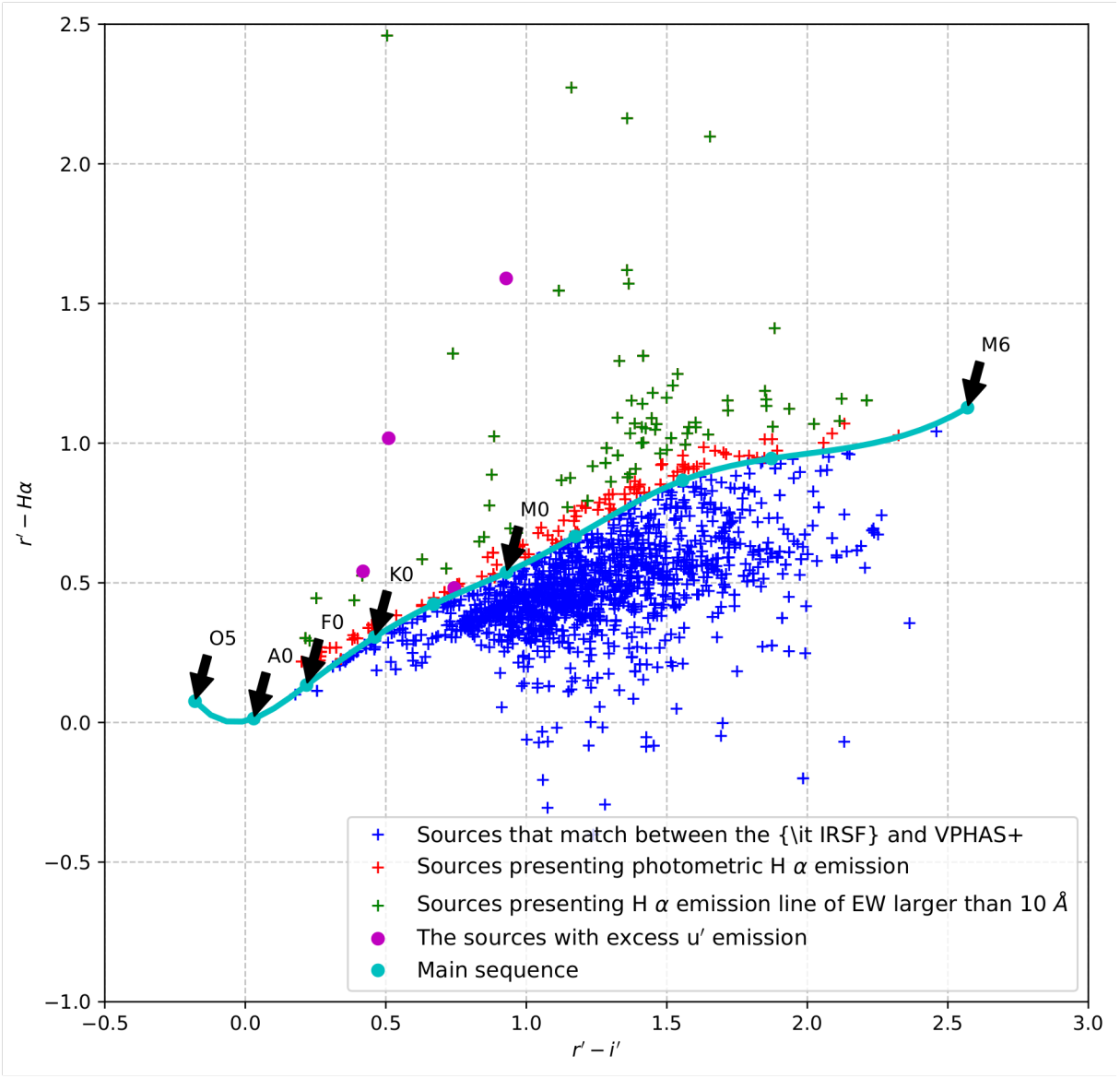

Figure 4.11: $(r' - H\alpha)/(r' - i')$ colour-colour diagram without errorbars for all of the *VPHAS+* stars in RCW 34.

segregation line, have excess emission that can classify them as WTTs. The 128 stars (62%) that are viewed as WTTs might be main sequence stars which may suffer contamination from Hα-emission from nebulous gas. This possibility has to be kept in mind because of the close proximity of the large number of these stars to the main sequence, and the fact that the threshold for excess Hα-emission is so small when relative to the errors on the measured colours.

It should be possible to estimate the number of T Tauri stars that are expected to form in RCW 34, however it is a very difficult number to estimate. For this estimate, the mass of the molecular cloud from which the CTTs and WTTs are forming, the star-formation efficiency, the period for how long star formation has been occurring, and the IMF of RCW 34 are known. The regions where any further star formation is likely to occur, are the dense clumps that were identified in the *NIR*-extinction map that was constructed in Chapter 3. The masses measured from that same extinction map are taken in the estimate for the number of T Tauris stars that are expected to have formed. Murray (2011) conducted a large survey on giant molecular clouds, where the star formation efficiency ranged anywhere from 0.02 to 0.2, with an overall average of 0.16. If it is assumed, just for this estimate, that

RCW 34 has a star formation efficiency of 0.16, then the mass of the dense clumps that will result in stars is given in the following table.

Table 4.2: The estimate for the mass of the stars forming out of the dense clumps A-G in RCW 34.

Clump	Mass [$M_\odot$]	Total mass of stars formed [$M_\odot$]
A	266.50± 10.65	42.62± 1.70
B	184.92± 7.22	29.59± 1.15
C	247.84± 11.62	39.65± 1.85
D	709.93± 44.54	113.59± 7.13
E	560.73± 27.29	89.72± 4.37
F	324.19± 15.54	51.87± 2.49
G	434.35± 22.87	69.50± 3.66

The question remains — what the IMF is that the cluster in RCW 34 will obey? The two most general IMFs that are found in open clusters is either a Kroupa (2001) or Salpeter (1955) power-law. If a Salpeter (1955) power-law is used, the number of sources will have to be calculated in the mass range from 0.5 $M_\odot$ to 3 $M_\odot$, or:

$$\begin{aligned} \xi(m)\mathrm{d}m &= \xi_0 \left(\frac{m}{\mathrm{M}_\odot}\right)^{-2.35} \left(\frac{\mathrm{d}m}{\mathrm{M}_\odot}\right) \\ \rightarrow\ \xi(m) = \int_{m_1}^{m_2} \mathrm{d}m &= \xi_0 \int_{m_1}^{m_2} \left(\frac{m}{\mathrm{M}_\odot}\right) \left(\frac{1}{\mathrm{M}_\odot}\right) \mathrm{d}m. \end{aligned}$$

To get the constant ξ_0 the IMF that will deliver the O8.5 star is used,

$$\begin{aligned} 1 &= \xi_0 20^{-2.35} \\ \xi_0 &= \tfrac{1}{20^{-2.35}} = 1141.35. \end{aligned}$$

The number of sources that would form in the mass range of T Tauris are

$$\xi = 1141.35 \int_{0.5}^{3} m^{-2.35}\mathrm{d}m = 1141.35 \left(-\frac{1}{2.35}\right) \left[3.0^{-1.35} - 0.5^{-1.35}\right] \sim 1128.$$

This is the total number of stars in the mass range of T Tauris that will form from the molecular cloud out of which VdBH 25a has formed. The typical lifespan of a giant molecular cloud is given by Murray (2011) as $\sim$ 27 Myr. If star formation has occurred in RCW 34 over only a period of 0.2 Myr then it is expected that only a fraction of the expected 1128 sources have already formed. To estimate what fraction of the expected T Tauri stars have already formed is a very complex problem. This is because there are many factors that affect the number of stars which form at specific stages in the lifetime of a molecular cloud. For example, the presence of VdBH 25a can perturb the molecular cloud's structure, and either disrupt or trigger more star formation. This leaves the number of T Tauri stars which have formed after 0.2 Myr in RCW 34 still as an open question. This example does give a rough estimate to how many stars would form from the molecular cloud out of which VdBH 25a has formed. Comparing the 1128 sources that are expected to still form with the 216 sources identified with Hα-emission means that only 20% of the expected number of stars have formed. Yet, the masses given in Table 4.2 add up to 436.54 ± 9.86 $M_\odot$. If all of this material formed into an ensemble of stars at the lower limit of T Tauris, only $\sim$ 837 stars would form. This is far under the number of stars that would form from the molecular cloud from which VdBH 25a formed; if the total mass of the material formed stars with masses varying over the whole range of the IMF, the number of stars would be smaller than 1128. This may imply that the star-formation efficiency may be less than the average for star-forming regions in Milky Way. This adds to the complexity of the question of how many stars will form from the molecular cloud in RCW 34, and how much is expected to still form from the remaining material.

4.3.2.2 *NGC 2626*

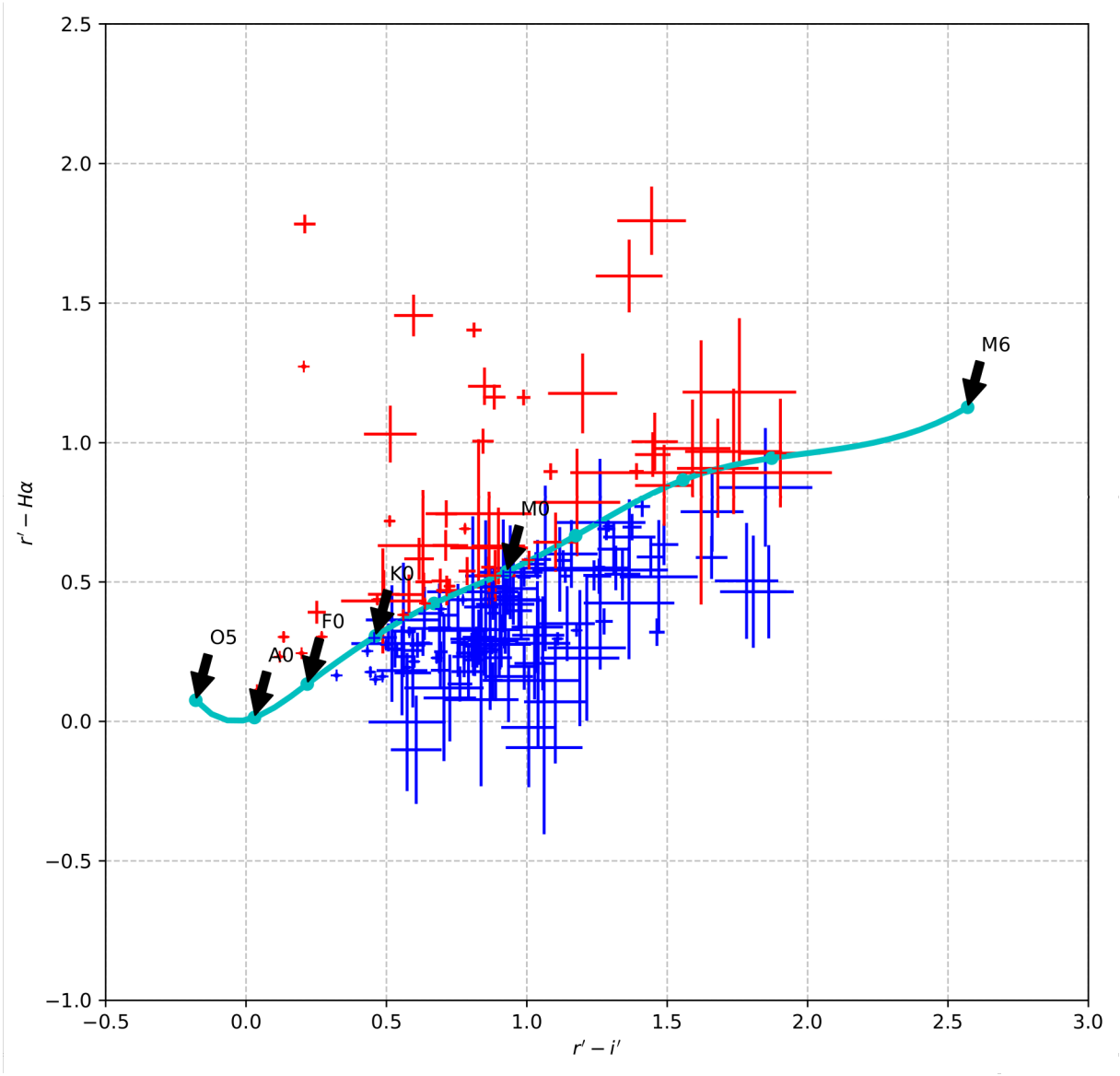

Figure 4.12: $(r'-H\alpha)/(r'-i')$ colour-colour diagram for all of the *VPHAS+* stars in NGC 2626.

Figure 4.12 shows the $(r'-H\alpha)/(r'-i')$ colours for 181 stars of which 30 have excess emission in the $(r'-H\alpha)$ colour indicating an Hα-emission line. A smaller number of stars associated with NGC 2626 are expected when compared with RCW 34, as it is a smaller star-forming region. The smaller number of stars that show Hα-emission makes it significantly more difficult to determine how the mass function for NGC 2626 would look — there are single stars that have excess emission for each spectral class. The number of sources in the *NIR* data and from the study by Sharma *et al* (2016) suggests that there should be more sources with Hα-emission in the field, however, they may not be detectable due to high extinction. Figure 4.13 shows the colours of the Hα colour-colour diagram without the errors.

Twenty stars had an excess emission in the $(r'-H\alpha)$ colours similar to an Hα-emission line width more than 10Å. Barentsen *et al* (2013) showed that any source that has an excess emission of $(r'-H\alpha) > 0.1$ is most probably a CTT. A similar analysis of excess emission sources was done by Barentsen *et al* (2011) in IC 1396 , which is located at a distance of ∼735 pc — which is very similar to NGC 2626, suggesting that the same measure for excess emission can be used in this analysis. In NGC 2626,

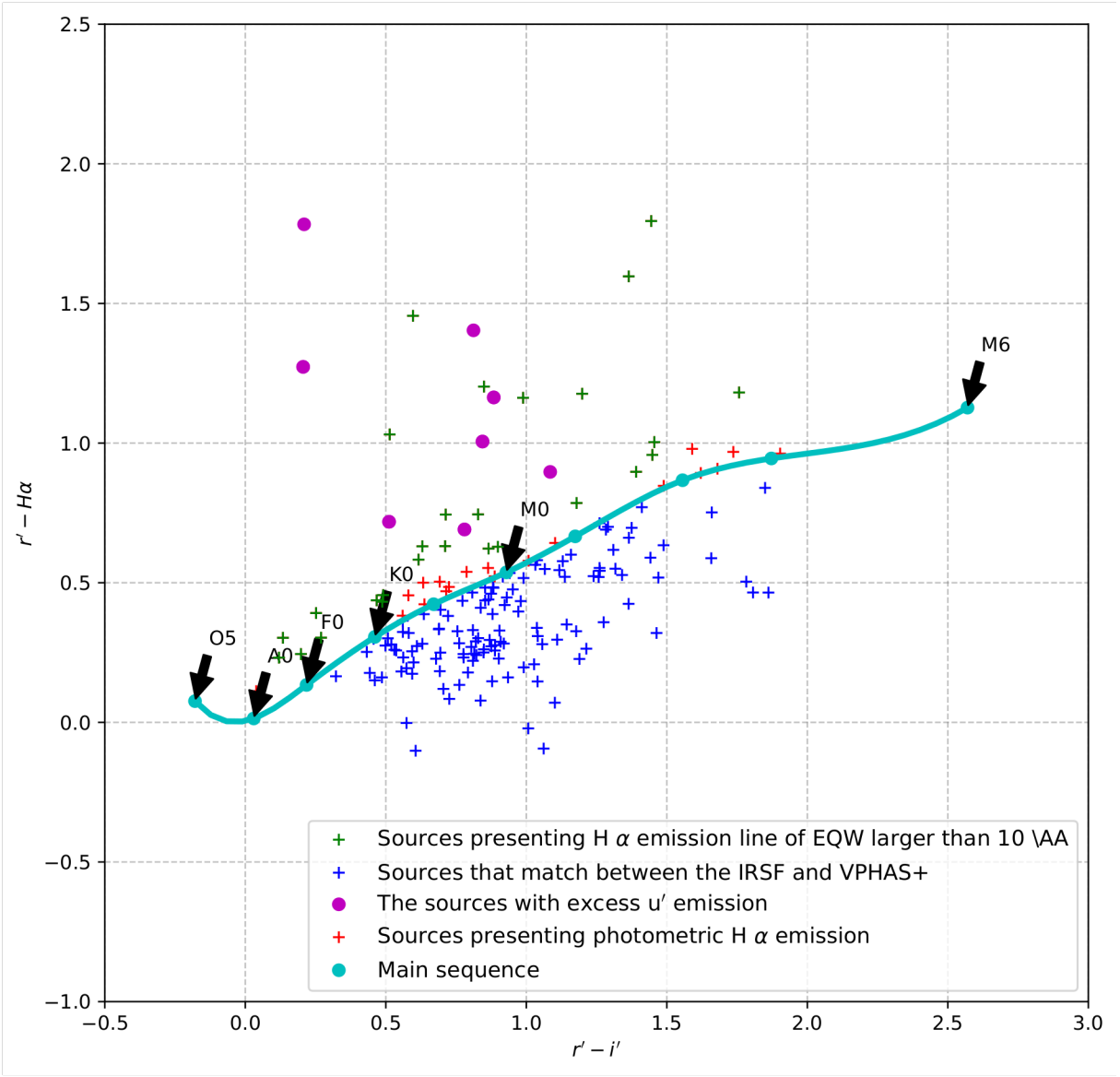

Figure 4.13: $(r' - H\alpha)/(r' - i')$ colour-colour diagram without errorbars for all of the *VPHAS+* stars in NGC 2626.

118 sources showed $(r' - H\alpha)$ excess emission in the part of the colour-colour diagram characteristic to CTTs. Of these 118 there were 109 that were verified with *2MASS* counterparts that had excess *NIR*-emission. Comparing the higher number of Hα excess emission sources of Barentsen *et al* (2011) with those in NGC 2626 can be explained by: (1) The low extinction to the sources in IC 1396, most of the young sources were discovered in parts of the star-forming region where the dense matter have been cleared out. The position for most of the young sources in the study by Sharma *et al* (2016) was in the dense cloud north of HH-132. This suggests that the extinction of these sources was too high to detect in the optical. (2) The sources with excess Hα-emission in IC 1396 have a radial distance of up to 35 pc from each other. If NGC 2626 is the physical size of the $10' \times 10'$ field that was studied by Sharma *et al* (2016), then it is 10% the size of IC 1396. Without very deep *NIR* observations that span a region larger than the full extent of NGC 2626, it is not possible to test how large the cluster truly is with a 2-point correlation function or stellar surface density measurement. In a region (IC 1396) that may be ten times larger than NGC 2626, there are only five times more Hα-emission sources.

The number of sources with Hα-emission that were detected in the *VPHAS+* data is less than the

number of sources that were detected by Sharma *et al* (2016), thus estimating the number of sources that is expected to be detected in NGC 2626 is unnecessary. Without a substantially larger number of sources, an IMF can not be constructed for NGC 2626, meaning an the IMF from a similar star-forming region is assumed. A Kroupa (2001) IMF is assumed for NGC 2626, due to the similarities to IC 1396 which has a Kroupa (2001) IMF according to Barentsen *et al* (2011). There are only a few sources with colours that can be identified as M4-M6 stars, but this is the most abundant number of sources according to a Kroupa (2001) IMF. A possible reason for the lack of stars at these masses is that they can not be detected in the optical, most likely due to the effects of extinction. There were 8 sources with excess u'-emission that also showed excess $(r' - H\alpha)$ emission and all of them except for 1 have masses higher than early M stars. All of these 8 stars also have an excess $(r' - H\alpha) > 0.1$ which definitely shows that they are CTTs and are younger than 3 Myr.

These results show that it is difficult to measure the Hα-excess emission from a $(r' - H\alpha)/(r' - i')$ diagram both for RCW 34 and NGC 2626. For both a custom derived extinction law for RCW 34, and the general extinction law of the Galactic plane for NGC 2626, the dereddening is not very accurate. The comparison between the dereddened $(r' - i')$ colours for the stars in both RCW 34 and NGC 2626 to the main sequence is not very accurate, due to the large uncertainties introduced by dereddening from an extinction map that was derived in a different wavelength regime. The equivalent width (EW) of the Hα-emission line affects the total flux of the continuum in the r'-band. If a star has an Hα-emission line with a significantly large EW, 10Å in the case of a CTT, its magnitude measured in the Hα narrow band will be significantly brighter than a star of the same spectral type which has just continuum emission measured in the same band. A star with an Hα-emission line with a significantly large EW, will also affect the continuum emission measured in the r'-band. A larger Hα EW implies more emission measured in the r'-magnitude. The uncertainties in the dereddened colours imply that the only way to distinguish between stars that show Hα-emission and the main sequence, is if $(r' - H\alpha) > 0.1$ more than the main sequence. This distinction which is used for the seperation of CTTs, WTTs and the main sequence have been tested thoroughly by Barentsen *et al* (2011), Barentsen *et al* (2013) and Kalari & Vink (2015).

For the stars that have an excess of $(r' - H\alpha) > 0.1$ and are classified as CTTs, there exists a relation between the colour excess and the EW of the Hα-emission line. The relation was derived from a Bayesian statistical analysis on specific stars by Barentsen *et al* (2013), using the $(r' - H\alpha)$ excess emission and the Hα EWs from a study by Dahm & Simon (2005). The relation between the colour excess and the EWs is linear when the inferred photometric EW and measured spectroscopic EW are plotted on a log-log scale. The relation will differ between star-forming regions, because the measured flux is not compensated for distance. The errors involved with the relation between the measured spectroscopic EW and the derived photometric EW is significantly high and it is not used for this study.

4.3.3 Colour-magnitude diagrams

4.3.3.1 *RCW 34*

The *VPHAS+* data provided by Janet Drew differ in format from the data products that are in the public data releases. In the provided datasets two overlapping observations were combined, and those with errors smaller than 0.1 magnitudes were used for the optical photometry. In Figure 4.14 there are 1597 *VPHAS+* sources that were of high enough photometric quality in the red bands (r', i', and Hα) that they could be used in conjunction with the *NIR* photometry. For the analysis only $r'/(r' - i')$ diagrams were used, because the extinction in the u' and g' bands was too high to detect any of the sources that showed excess *NIR* or Hα-emission.

In Figure 4.14 the main sequence is represented by a ZAMS model that was taken from the paper by Siess *et al* (2000). The reddening vector shows how much a star's colours and magnitudes will shift when reddened for a value of $A_V = 1$. The magnitudes were corrected for the distance modulus of RCW 34: $r'_{\text{distance modulus}} = 5 \times \log_{10}\left(\frac{2500 \text{ pc}}{10 \text{ pc}}\right) \sim 12$, but not yet dereddened. In Figure 4.14 there

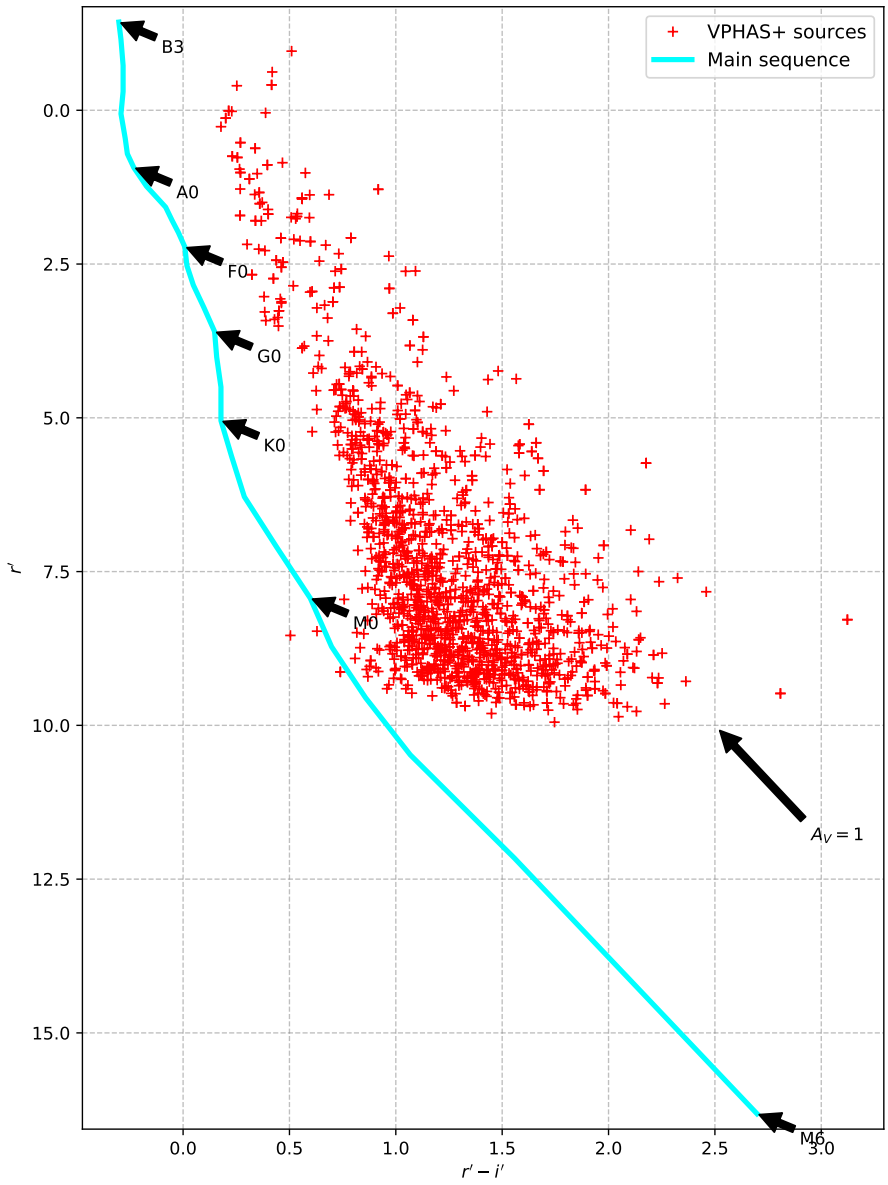

Figure 4.14: The measured $r' - i'$ colours and distance corrected r' magnitudes for the red sources in RCW 34.

is no apparent distinction between stars that may be cluster members and field stars. There is no obvious way of distinguishing between cluster members and field stars on the densely populated colour-magnitude diagram, similar to the study by Kalari & Vink (2015). The only way that young cluster members/possible CTTs can be identified is either by using excess emission in their *NIR* colours, or by identifying which ones have Hα-emission.

Figure 4.15 shows the sources that matched between red *VPHAS+* and unreddened *NIR* sources. Out of the dereddened stars that showed both *NIR* and Hα excess emission, only 59 stars matched, and they are the only stars that can be associated with the young cluster of RCW 34. The 216 sources that showed Hα-emission are separated into two distinctive groups. This first group comprises 128 sources that had an excess of $(r' - H\alpha) < 0.1$, and are represented by red crosses, while the second group consists of the remaining 88 sources, that had an excess of $(r' - H\alpha) > 0.1$, and are represented by green crosses. The other *NIR* excess emission sources were most likely too faint — because of extinction — meaning they could not be detected in the optical.

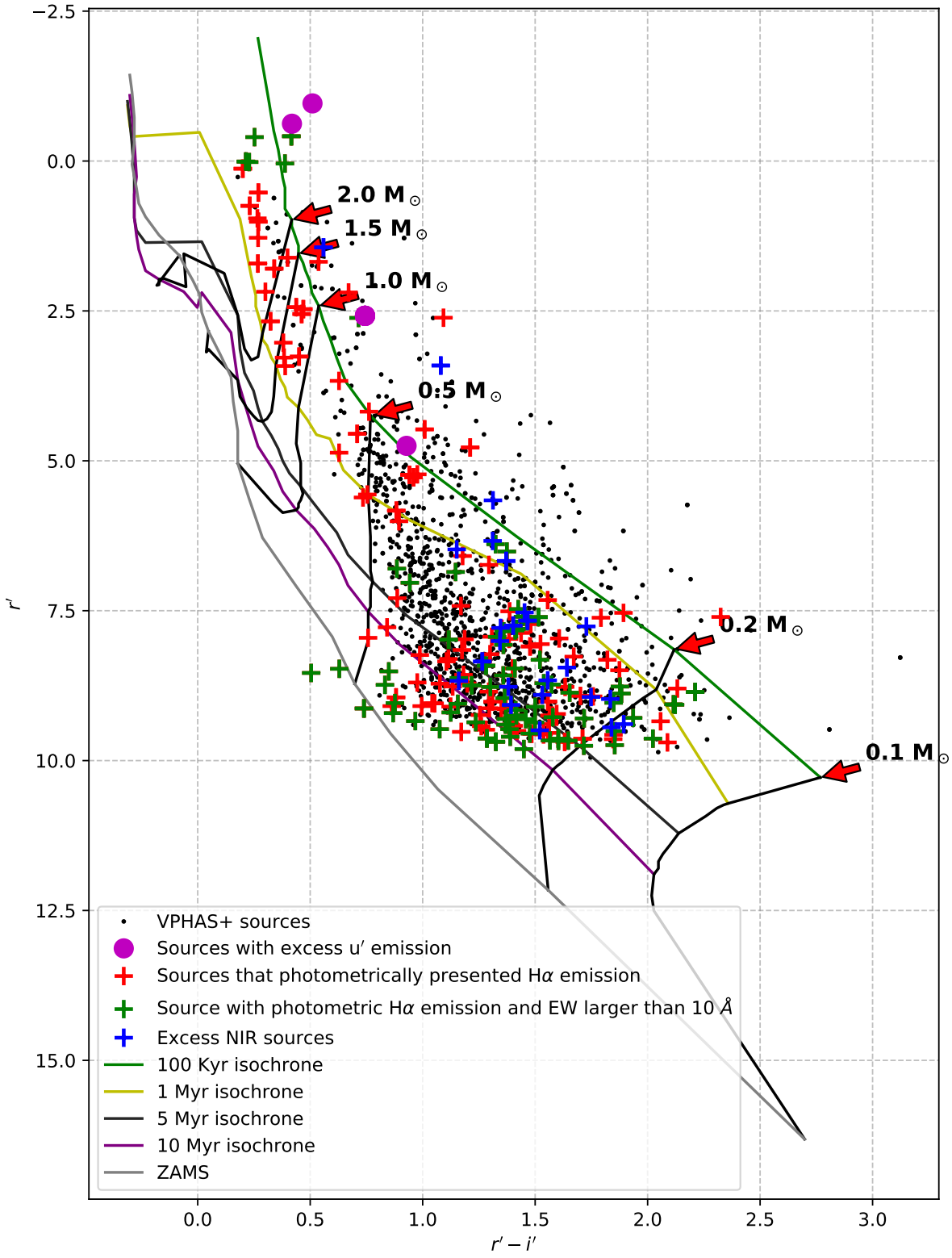

Figure 4.15: The colours and magnitudes for 1597 *VPHAS+* sources that were dereddened according to the *NICEST LinES* extinction map.

All of the stars in the field surrounding RCW 34 that are not associated with an excess *NIR*-emission or Hα-emission source are plotted as black dots. Foreground stars were eliminated from this population

by matching all sources with the foreground stars that were identified during the construction of the *NIR* extinction map. For all of these black dots that are shown in Figure 4.15, a distinction can not be made between field stars and cluster members. In general, it is very difficult to distinguish between field stars and cluster members without a very technical process, such as the one that was followed by Drass *et al* (2016) which required CO data, spectroscopy, radial velocities, and more precise *NIR* photometry, where brown-dwarfs and sub-dwarf stars could be detected.

The 59 sources that could be matched to those with excess *NIR*-emission are shown as blue crosses in Figure 4.15. There are three sources that lie above the youngest isochrone, so they are eliminated. The other 56 excess *NIR*-emission sources have masses between (0.2-0.5) $M_{\odot}$ (all later than M0 stars), and are younger than 10 Myr. Of the 128 sources that are considered to be Hα-emission sources, but do not have enough $(r' - H\alpha)$ colour excess to be CTTs, 8 lie above the youngest isochrone. The other 120 show very young ages between 100 kyr and 1 Myr for sources heavier than 0.5 $M_{\odot}$. For sources with masses lower than 0.5 $M_{\odot}$, the majority of the sources have ages between 1 Myr and 10 Myr. The derived ages suggest that an epoch of star formation for intermediate mass stars occurred less than 1 Myr ago. This is consistent with the results from the study by Hayashi *et al* (2017), who stated that the high-mass star formation in RCW 34 was triggered by the collision of two molecular clouds ∼0.2 Myr ago. The separation between the stars with masses higher and lower than 0.5 $M_{\odot}$ is curious, and suggests the same as the *NIR* photometry — that there was a formation of stars with masses lower than 0.5 $M_{\odot}$. This occurred before the collision of the two molecular clouds over an expanse larger than the collission area of the two molecular clouds. For the 88 stars that showed excess Hα-emission characteristic to CTTs, 9 lie outside the limits of the isochrones/evolutionary tracks. Of the remaining 79 stars, there are 3 that are younger than 1 Myr that have masses higher than 2 $M_{\odot}$, meaning they are too heavy to be classified as CTTs stars. From the remaining 76 stars, there are 13 that are older than 10 Myr, so that 63 fall within the age and mass limits of CTTs stars. All of these 63 stars are at different evolutionary stages, suggesting that there was an ongoing star-formation process before the collision of the two molecular clouds. The sources with excess u'-emission are all high-mass stars, or they are the only sources that are luminous enough that they can also be detected in the u'-band. All of these sources show colours and magnitudes — if compared to the evolutionary lines — that indicates they are part of the young population that formed in the short period after the collision of the two molecular clouds.

The evolutionary lines and isochrones tell a more detailed story on an optical colour-magnitude diagram. This is because the excess emission from the accretion disk seen in the *NIR* does not feature in the optical. The only optical feature of the accretion disk that is detectable in the r' band, is the Hα-emission line, which does not contribute a significant fraction of the total flux, except for cases with strong Hα-emission. The isochrones are just like the main sequence, not an infinitesimally thin line, but serve as approximate indicators of the age of a pre-main sequence star. Each photometric point has an error, and the extinction map that was used for each star also has an uncertainty. All of these photometric measurements and their associated errors contribute to an indication of the age of these young sources, but do not give a precise answer. There are two facts that can be concluded from the evolutionary process shown in Figure 4.15: (1) The stars heavier than 0.5 $M_{\odot}$ did not start to form before the collision of the two molecular clouds discovered by Hayashi *et al* (2017). (2) There was an ongoing process of star formation for stars with masses lower than 0.5 $M_{\odot}$ before the molecular clouds collided.

4.3.3.2 *NGC 2626*

Figure 4.16 shows the 939 stars in the field of NGC 2626 that matched in the r', i', and Hα bands. All of this optical data was obtained from the ESO point source data archive. The extinction map that was built with the *NICEST* interpolation method of the region surrounding NGC 2626 was used to calculate the extinction to each of these stars.

Of the 939 stars, there are 14 stars that showed excess *NIR*-emission, 55 that showed Hα-emission more than the main sequence, and 35 with Hα-emission strong enough that they can be characterised

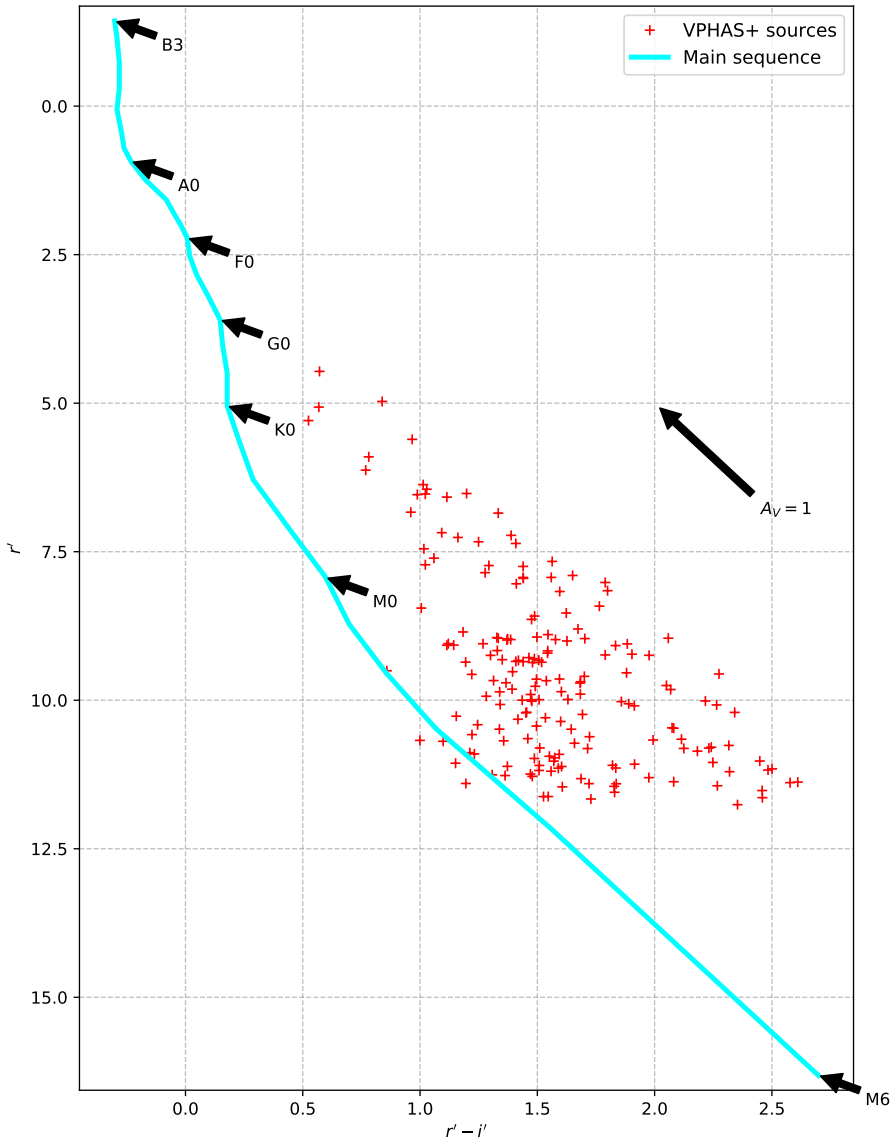

Figure 4.16: The measured $(r' - i')$ colours, and distance corrected r' magnitudes for the red sources in NGC 2626.

as classical T Tauri stars. All these sources have the same symbols as in Figure 4.15 so that the black dots are field stars; the blue crosses present excess *NIR*-emission, the red dots WTTs and the green crosses CTTs. The reddening vector shows how much a star's magnitude and colours will be dereddened for $A_V = 1$. The 15 sources with excess u'-emission are all at various phases of the formation when compared to the evolutionary models. All of these sources are also the brighter ones in the region; the lower-mass sources might have been detectable with a more sensitive telescope.

Of the stars that presented excess *NIR*-emission, there are 3 that do not fall in the region of the graph where they can be measured against an isochrone or evolutionary line. All the other *NIR* excess emission stars have masses between 0.2 $M_\odot$ and 0.5 $M_\odot$, and are older than 1 Myr. All of the stars that present Hα-emission more than the main sequence, but less than the CTTs, are younger than 10 Myr. Two of these have masses more than 2 $M_\odot$ and can not be CTTs stars. Those that have masses lower than 2 $M_\odot$ are considered to be WTTs. The rest of the Hα-emission stars all have masses between (0.2-1) $M_\odot$ and are between 100 kyr and 10 Myr old. Of the 35 stars with Hα-emission characteristic to CTTs stars, there are 3 that can not be aged, while the rest show different evolutionary phases

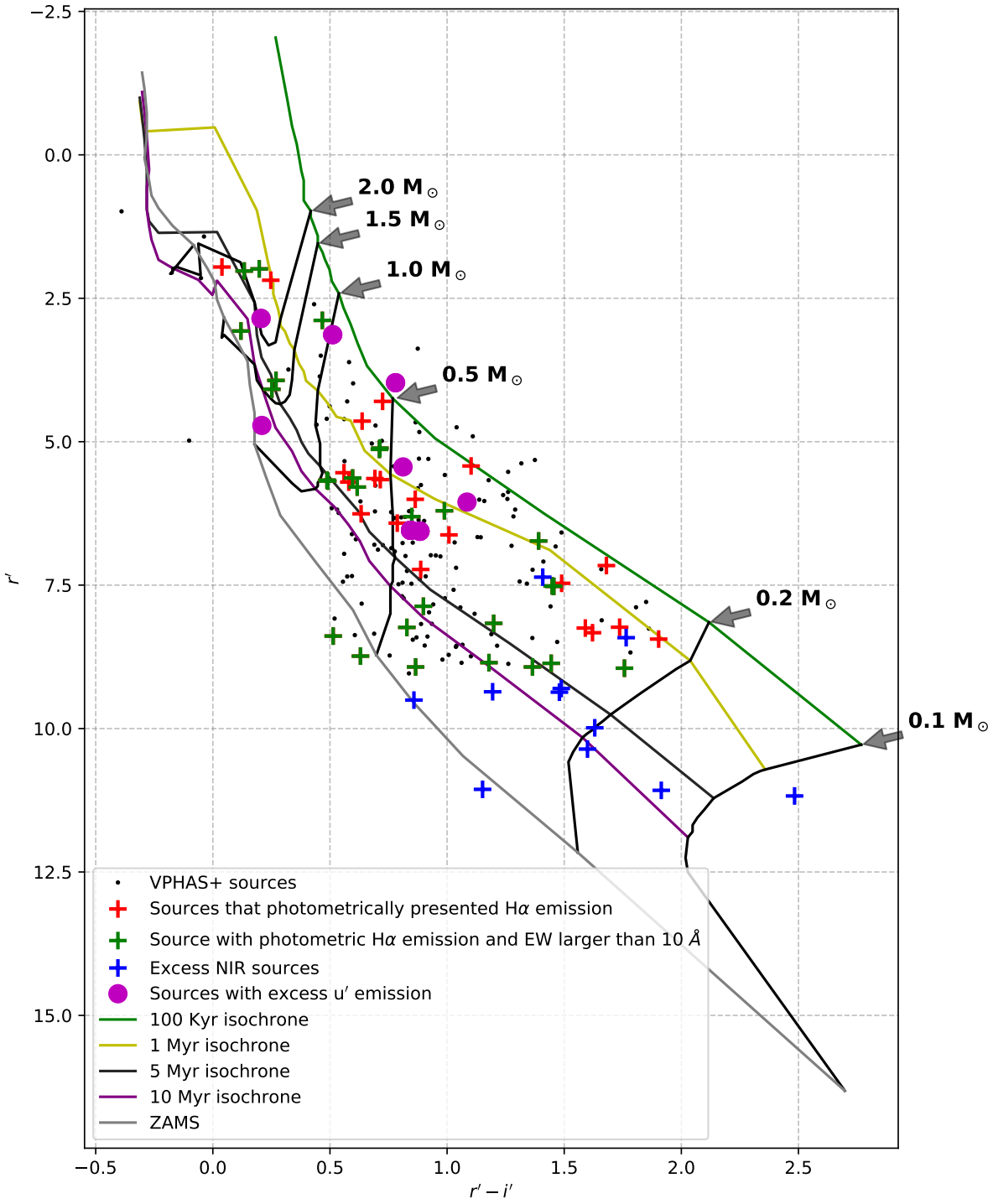

Figure 4.17: The colours and magnitudes for the 939 *VPHAS+* sources in NGC 2626 that were dereddened according to the *NICEST LinES* extinction map.

at different masses. This suggests the same continuous star-formation process that was discovered by Sharma *et al* (2016) by means of the numerous class 0/I and II *NIR* sources. The results for NGC 2626 suggests that there was a continuous star-formation process occurring in the region, rather than the different epochs of star formation seen in RCW 34.

4.3.4 Spatial distribution of Hα-emission sources

The *VPHAS+* data provided a photometric measure for the strength of the Hα-emission line exhibited from the excess emission in the $(r' - H\alpha)$ colour. The stars that have an Hα EW > 10Å have an excess of $(r' - H\alpha) > 0.1$ relative to the main sequence and can be considered to be CTTs stars. Those that have $(r' - H\alpha)$ colour excess more than the main sequence, but not enough to be considered CTTs stars, can be considered to be WTTs. In this subsection, the spatial distribution of these optically classified CTTs and WTTs is discussed in the same context as the optical colour-colour and colour-magnitude diagrams.

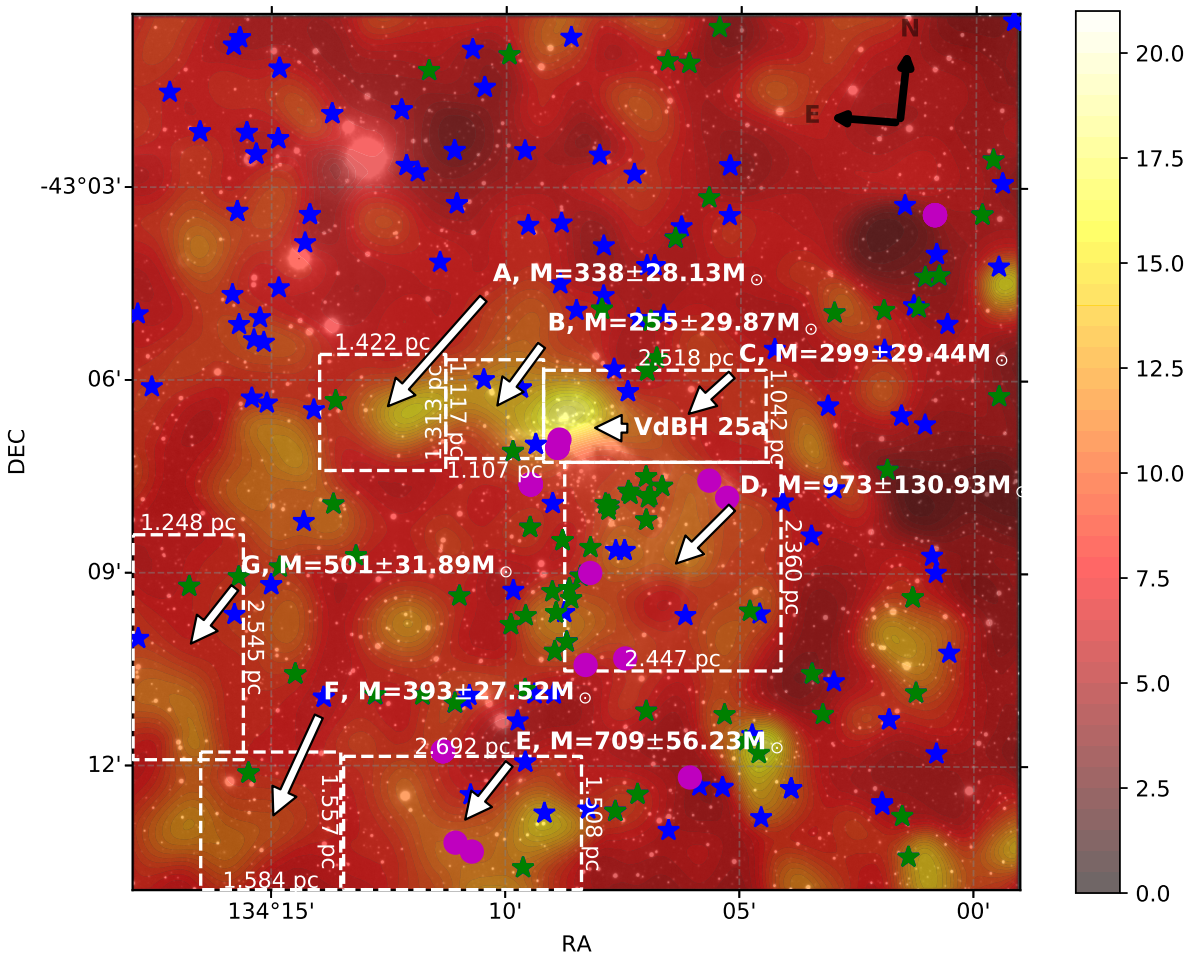

Figure 4.18: The spatial distribution of the stars that showed Hα-emission from the dereddened *VPHAS+* $(r' - H\alpha)$ colours in RCW 34. The sources with an EW < 10Å are plotted as blue stars, and the sources with a photometric EW > 10Å are plotted as green stars. North is towards the top of the image and east is towards the left.

Figure 4.18 shows the spatial distribution of the different classified Hα-emission stars relative to the HII region and the remnant molecular cloud. Similar to the spatial distribution of the *NIR* excess emission stars, those that photometrically showed Hα-emission are distributed across the whole field. Most of the CTTs stars appear in the bubble region and on the outer edges of regions containing dense molecular remnants. From the HII region, there are two collections of stars expanding outward. One set that expands towards the north and another that expands towards the east. The star trail towards the north of the HII region is right along the densest region of the two colliding molecular clouds. These were most likely formed during the collision — which also formed VdBH 25a and the young star associated with the maser. The densest number of CTTs are on the outer ridge, just south of the HII region in the bubble region (region D) and aligns with the star trail towards the north of the HII region. Hayashi *et al* (2017) and the *NICEST LinES* maps show a cavity at the position of

this dense number of CTTs in region D, where all of the stars surround a dense molecular clump. The ridge of CTTs that come from the north of the HII region and align with the stars in this cavity all lie on the outer edge of a denser part that is shown by Hayashi *et al* (2017) as the ridge of two colliding molecular clouds. The position of the stars with excess u'-emission are in the bubble clearing, at the dense intersection of the molecular clouds and along the intersection of the two colliding clouds north of the HII region. These indicate that some of the youngest stars are located at the intersection of the two molecular clouds. The position of these stars together with the position of the stars with an Hα EW > 10Å suggests that the collision between the two molecular clouds was the triggering mechanism for the youngest stars.

The stars with $(r' - H\alpha)$ excess that is equivalent to Hα EW < 10Å can be considered to be WTTs. They are distributed more uniformly across the field surrounding RCW 34, and are located in the north eastern and south western quarters of the image. They are not as densely distributed in the bubble region as the CTTs, but are in the same dense locations. Over the rest of the field, these stars are not concentrated at specific structures as is the case of the CTTs. The spatial distribution of these stars and their ages suggests that there was an epoch of low-mass star formation across the whole region. This means that there was possible low-mass star formation occurring in each of the two molecular clouds before the collision. The high-mass star formation and next generation of low-mass star formation were triggered by the collision. It has to be emphasised that these WTTs may be main sequence stars whose errors can place their $(r' - H\alpha)$ flux below that of the main sequence.

Figure 4.19 shows the location of the stars that exhibited excess Hα-emission according to the $(r' - i')/(r' - H\alpha)$ colour-colour diagram in NGC 2626. The stars with Hα EW > 10Å are considered to be CTTs, and those with EW < 10Å to be WTTs. The CTTs and WTTs are distributed across the whole field, similar to the spatial distribution of Hα-emission stars shown by Mueller & Graham (2000). Mueller & Graham (2000) studied a $10' \times 10'$ field where 32 Hα-emission sources are located around HH-132. They were identified based on their $(R_s - H\alpha)$ colour. For all of the stars observed by Mueller & Graham (2000), the $(R_s - H\alpha)$ colour was normalised to zero for a main sequence star, and those with a colour excess more than 0.5 were considered to be Hα emitters. There are only 16 stars from the study by Mueller & Graham (2000) that are in the field shown in Figure 4.19. The 47 sources shown in Figure 4.19 show many more sources at different phases of star formation than Mueller & Graham (2000), and there are no sources that match between the two different datasets. Even though the Hα-emission sources were identified in two different photometric systems, the lack of any matching between the datasets can be attributed to two possibilities: (1) Bad astrometric conversions between the different datasets; (2) The Hα-emission sources may be variable, which implies that different sources were detected with the *VPHAS+* data than by Mueller & Graham (2000). If this is the case, then the Hα-emission sources from Mueller & Graham (2000) show the star-forming region is larger than the field for this study.

The spatial distribution of the sources with excess u'-emission are in regions with extinction in the range of $A_V \sim 7$. All of these sources are on the outer edges of the star-forming region, as the same distance from HH-132 than the Hα-emission sources. Their positions and the positions of the stars with Hα-emission emphasise that there are many young stars around the molecular cloud. They show that there are stars younger than 10 Myr at a significant distance from the dense molecular cloud. The WTTs were only detected in the regions with low extinction, showing that the gas has been blown away with due time. The CTTs detected in the *NIR* results and discovered in the study by Sharma *et al* (2016) in the dense molecular remnants of region A, were not detected in the optical due to the high extinction. The high number of Hα-emission sources across the field show that there is more star formation occurring in the remnant molecular clouds associated with NGC 2626 than Sharma *et al* (2016) and Mueller & Graham (2000) discovered.

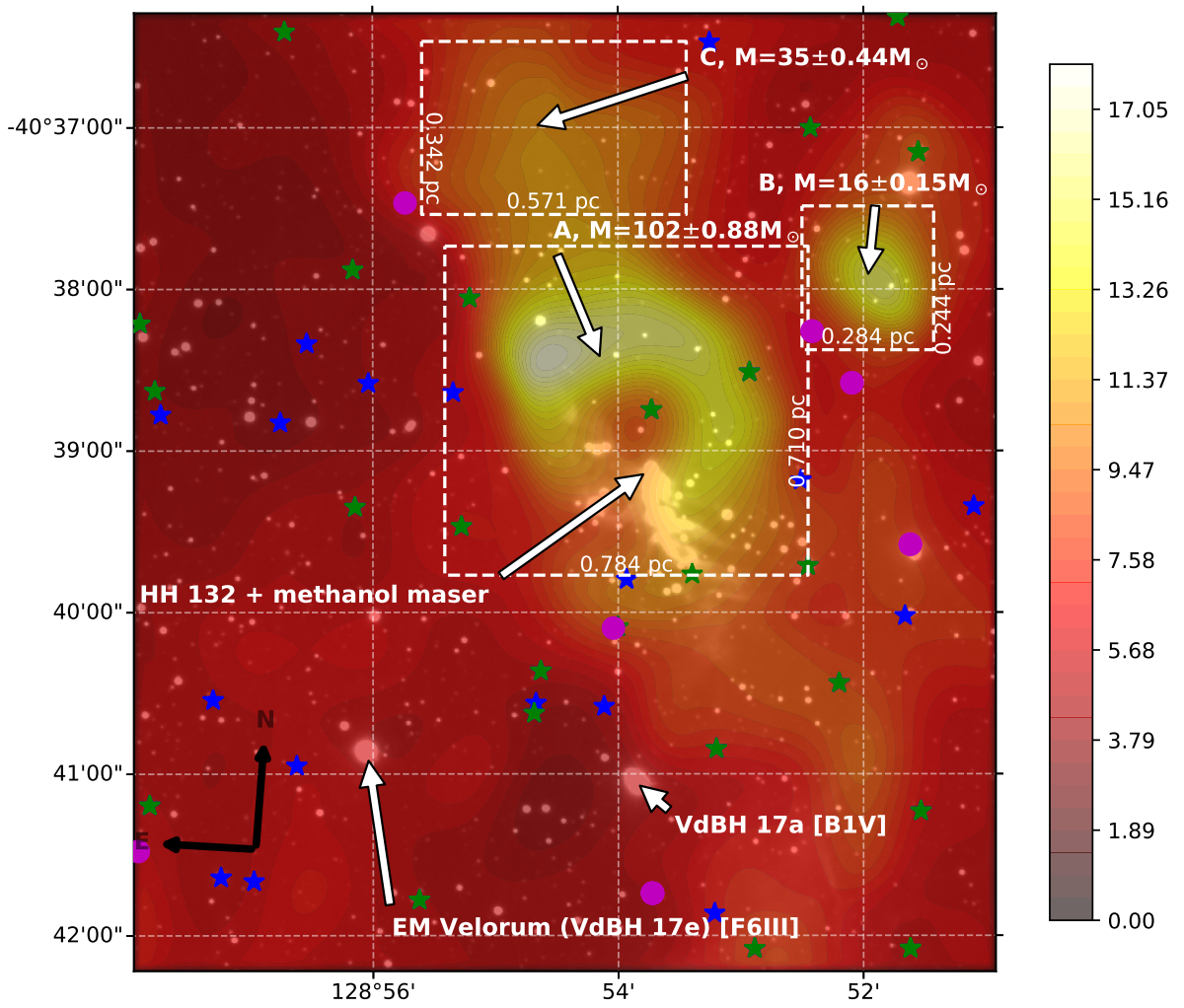

Figure 4.19: The spatial distribution of the stars that showed Hα-emission from the dereddened *VPHAS+* $(r' - H\alpha)$ colours in NGC 2626. The sources with an EW < 10Å are plotted as the blue stars and the sources with a photometric EW > 10Å are plotted as green stars. North is towards the top of the image and East is towards the left.

4.4 Summary and conclusion

In this chapter young stellar sources with an accompanying accretion disk which gives off Hα-emission, were identified on $(r' - i')/(r' - H\alpha)$ diagrams. For RCW 34 there were 216 sources of which the majority are K and M stars. The spatial distribution of the Hα-emission sources suggests that there is low-mass star formation on a scale larger than Bik *et al* (2010) and Hayashi *et al* (2017) discovered. The ages of these stars on the colour-magnitude diagram also shows that there was a more recent epoch of star formation than the uniformly distributed low-mass Hα-emission stars show. This recent star formation was most likely caused by the collision of the molecular clouds, as stated by Hayashi *et al* (2017). The Hα-emission stars discovered in NGC 2626 show star formation across the whole region that was investigated in this study. The Hα-emission source identification showed sources at different locations than the *NIR* excess emission sources.

Sources were also tested for excess u' emission on $(u' - g')/(g' - r')$ diagrams, but only a few were detected in RCW 34 and NGC 2626, due to sensitivity limitations. The collection of stars in RCW 34 that were dereddened according to the *NICEST LinES* extinction map lie at the higher-mass end of the main sequence, where only three stars with excess u'-emission were identified. The dereddened stars at the high-mass end of the main sequence were most likely foreground stars that were incor-

rectly dereddened, and no other stars associated with RCW 34 were detected. The young stars in NGC 2626 that showed excess u'-emission are all younger than 10 Myr, and are at various stages of PMS evolution. They were detected because of the low extinction around NGC 2626, and are an indicator of recent star formation in NGC 2626 much futher than just the dense molecular remnants in region A.

The young Hα and excess *NIR*-emission sources that were detected in the optical were associated with a spectral class and age measured relative to the evolutionary and isochrones models on $r'/(r'-i')$ diagrams. The colour-magnitude diagram for RCW 34 shows a distinct separation of very young and more evolved stars around 0.5 $M_\odot$ (M0-M1 stars). The more evolved WTTs have masses higher than 0.5 $M_\odot$ while the majority of the CTTs have masses lower than 0.5 $M_\odot$. The higher number of stars with $M_* \leq 0.5$ $M_\odot$ can be described with the mass function of the star-forming region. The more evolved low-mass CTTs are explained by Beltran & de Wit (2015) in that the stability of an accretion disk around a star is dependant on the star's mass. The separation between the two groups around 0.5 $M_\odot$ shows that there was an event between 100 kyr and 1 Myr that triggered the formation of stars heavier than 0.5 $M_\odot$. A logical explanation for the event was the collision between the molecular clouds that was discovered by Hayashi *et al* (2017). An event such as this collision between two molecular clouds, of which both already had star formation occurring, is not common in other star-forming regions. The event will have an impact on the mass function and the evolution of the cluster.

The distribution of *NIR* excess, and Hα-emission stars on the colour-magnitude diagram of NGC 2626 shows a smaller star-forming region, with an even spatial distribution of stars that show Hα and *NIR* excess emission. The majority of these young stars have ages spanning from about 1 Myr to 10 Myr suggesting that there is a continuous star-formation process occurring in NGC 2626.

CHAPTER 5: SPECTROSCOPY OF Hα- EMISSION CANDIDATES WITH *SALT*

5.1 Introduction

In this chapter the analysis of spectroscopic observations that were performed with *SALT* on low-mass cluster members associated with RCW 34 and NGC 2626 will be discussed. In a previous optical study, Czanik (2013) discovered five stars with Hα-emission. The observations for that was done using long-slit spectroscopic observations from the 1.9-m telescope in Sutherland. The study by Czanik (2013) served as a preliminary investigation for this chapter and showed that there are CTTs in RCW 34 with Hα-emission, and that they were optically detectable.

5.1.1 Preliminary spectroscopic study of Hα-emission stars around RCW 34

The study by Czanik (2013) used observational data from 2002 and 2011, where single and then four other stars with strong Hα-emission were discovered, respectively. All five Hα-emission stars had spectral features, shown in Figures 5.2-5.6 which resemble K/M stars (see Morgan *et al* 1943). The study by Bik *et al* (2010) showed that there are many more young cluster members associated with RCW 34, while the results by van der Walt *et al* (2012) suggested an even larger cluster than already known. All of the Hα-emission stars discovered by Czanik (2013) are located in the bubble region of RCW 34, where Bik *et al* (2010) discovered the youngest cluster members. The results from van der Walt *et al* (2012) raised the question if there are cluster members of RCW 34 outside of the bubble region. The results from the deep *NIR* photometry in Chapter 3 and the *VPHAS+* photometry in Chapter 4 show that there are young stars in RCW 34 extending further out than the bubble region. There is no optical spectroscopic study on NGC 2626 reported in the literature. The observations from the 1.9-m telescope all lasted longer than an hour's exposure time, implying that it is not sensitive enough to do a time-efficient optical spectroscopic investigation on low-mass cluster members in RCW 34, and similarly in NGC 2626. To get a strong signal-to-noise ratio (S/N) for any low-mass cluster member which suffers significant extinction and to do it in a time-effective manner, a larger instrument was required.

Figure 5.1 shows the position and Figures 5.2-5.6 show the spectra of the 5 stars with Hα-emission that were discovered in the preliminary study. The *NIR* photometry from Chapter 3 and optical photometry from Chapter 4 suggest that there are many more young cluster members with potential Hα-emission. *SALT* is sensitive enough to perform a time-efficient investigation on the stars in each region which have the highest probability of showing Hα-emission. In this chapter Hα-candidates that were observed with *SALT* around RCW 34 and NGC 2626 are analysed and spectroscopically classified. The stars which presents the strongest Hα-emission lines are analysed in more detail. The equivalent width of the Hα-emission line for these stars is measured and used to distinguish between WTTs and CTTs. The Hα-line profile is also analysed to determine what the emission source from the heated gas surrounding the young star is — either outflows, and/or accreting matter.

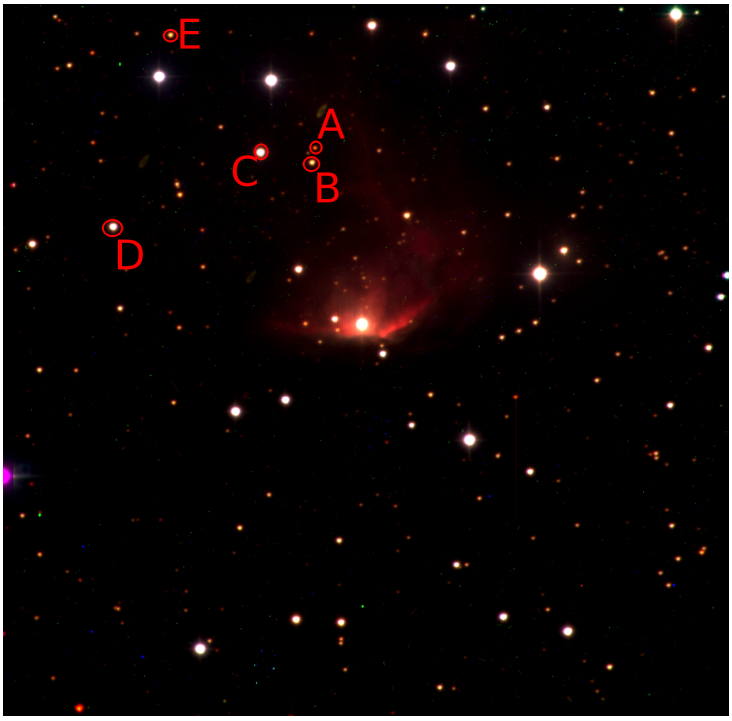

Figure 5.1: The location of the 5 stars that were discovered to have Hα-emission in the project by Czanik (2013).

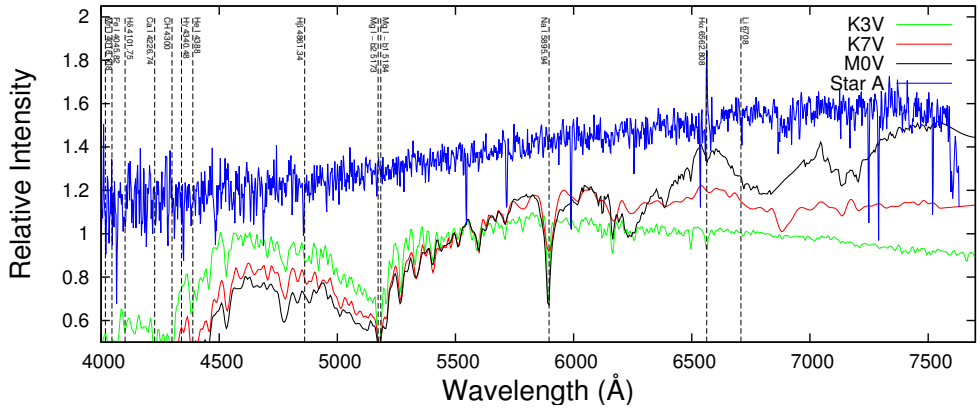

Figure 5.2: The spectrum for star A in Figure 5.1 from the study by Czanik (2013).

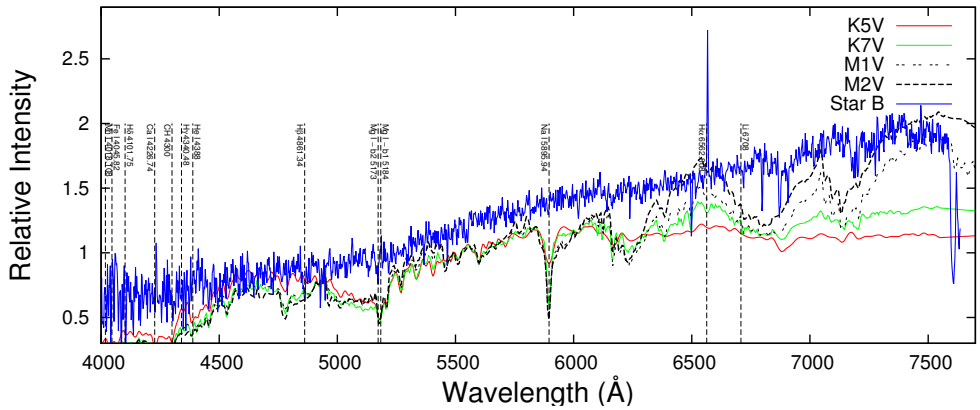

Figure 5.3: The spectrum for star B in Figure 5.1 from the study by Czanik (2013).

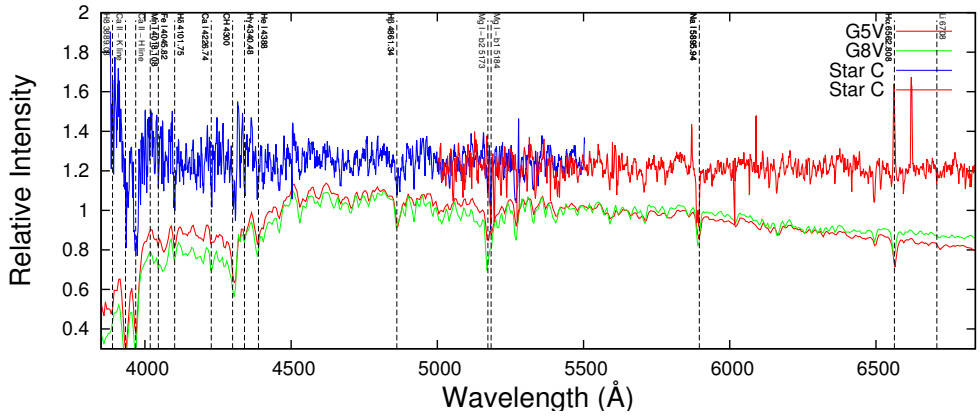

Figure 5.4: The spectrum for star C in Figure 5.1 from the study by Czanik (2013).

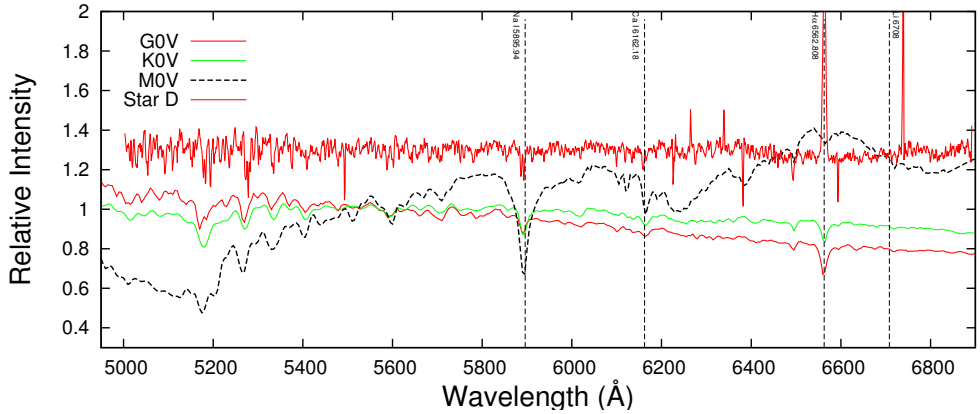

Figure 5.5: The spectrum for star D in Figure 5.1 from the study by Czanik (2013).

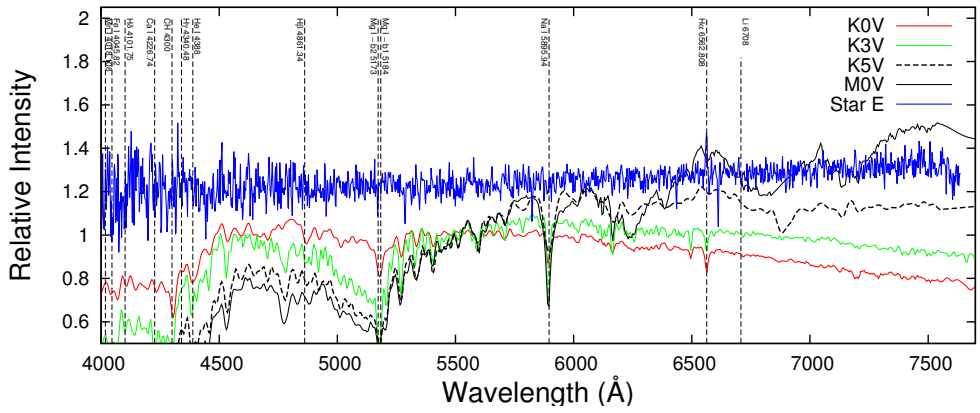

Figure 5.6: The spectrum for star E in Figure 5.1 from the study by Czanik (2013).

5.2 Data acquisition and reduction

5.2.1 The South African Large Telescope

From the outcomes of the photometry on small telescopes it is clear that none of them are sensitive enough to obtain a significantly high S/N on the faint objects in a realistic exposure time. Similarly, each individual spectrum in the preliminary study was done with more than an hour's exposure time on the 1.9-m, making a larger study of the low-mass stars in either RCW 34 and NGC 2626 unpractical. The only telescope that is sensitive enough to perform optical spectroscopy on numerous faint objects is *SALT*. The following subsection serves as an introduction and thorough description of *SALT* and the instruments used to observe Hα-candidates. It has to be emphasized that most of the material in this introduction on the design and observation modes of *SALT* was taken from the *SAAO/SALT* website. It has been edited to fit into this context, but remains mainly the same, there is no published literature other than the website which have a more comprehensive overview of these technical details.

5.2.1.1 Telescope design

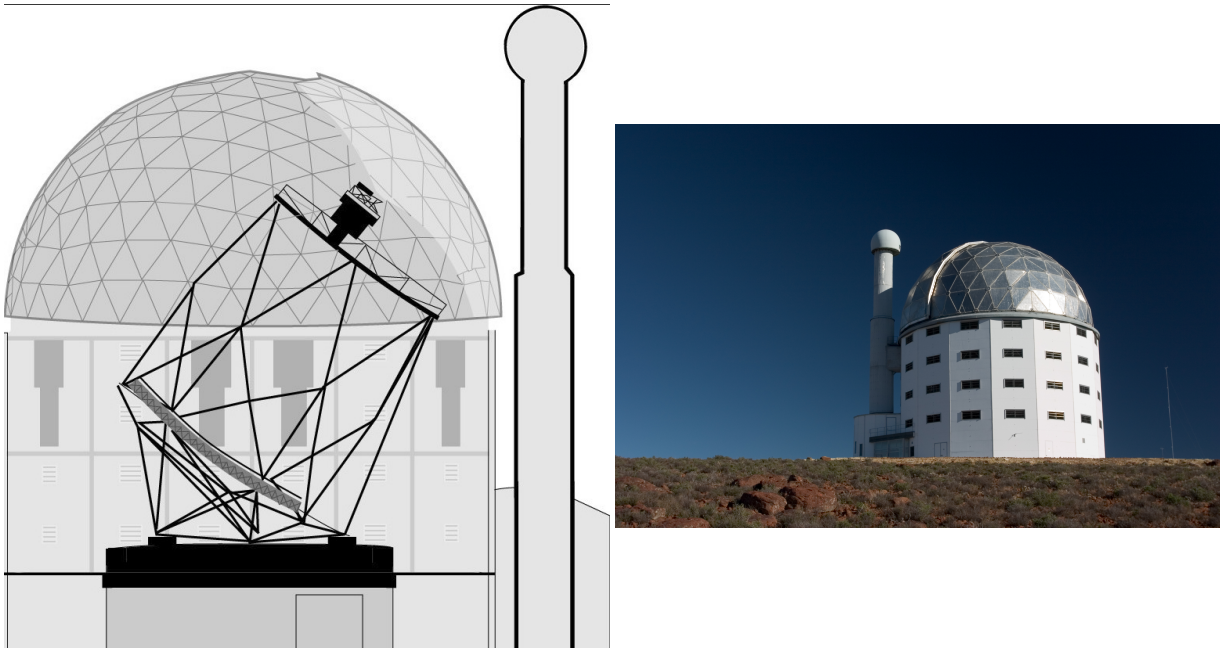

Figure 5.7: The left panel displays a schematic of *SALT*'s structure which includes the tracker, primary mirror, dome and building. The right panel shows a photo taken from outside *SALT*.

The **S**outh **A**frican **L**arge **T**elescope (*SALT*) is the largest single optical telescope in the southern hemisphere, and amongst the largest in the world. It has a hexagonal primary mirror array spanning 11-m, comprising 91 individual 1-m hexagonal mirrors. The telescope structure is a solid 45-ton steel structure which rests on four feet. *SALT*'s novel design is a fixed-elevation (53° above the horizon) telescope which constrains the field of view to an annulus covering 12.5% of the sky at any time, or 70% of the observable sky. The conceptual design was taken from the Hobby Eberly Telescope (HET) in Texas, which resulted in a significant cost saving in exchange for added complexity of the optical and control system.

5.2.1.2 Tracker and payload

The function of the tracker is to carry and position the optical payload in the required position and orientation so that the light collected from the primary mirror can enter the Spherical Aberration Corrector and is ultimately directed to one of the science instruments. The tracker is supported by the telescope structure at the nominal position for half the radius of curvature of the primary mirror. The telescope structure supports all the interfaces of the tracker to the rest of the telescope system.

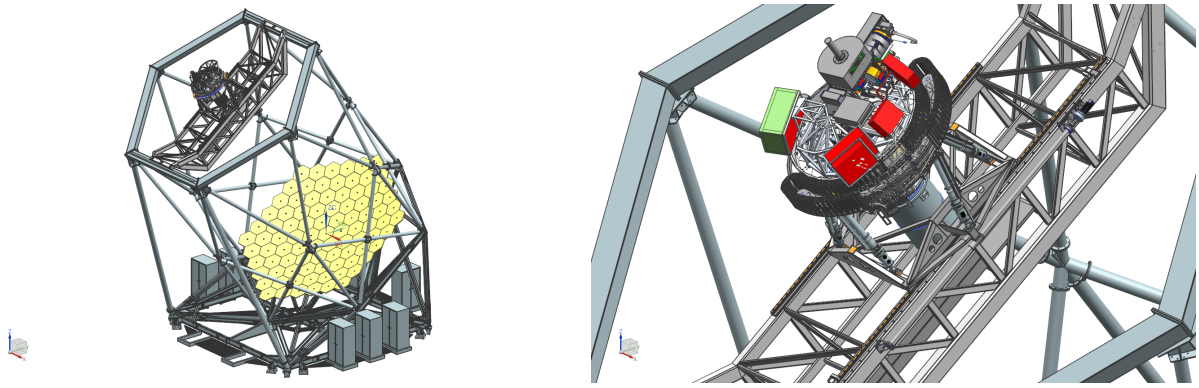

Figure 5.8: The left panel is a schematic of the primary mirror of *SALT*, and the right panel shows the tracker and payload which carries all of the optical equipment.

The total mass that can be supported by the tracker, inclusive of its own weight is nominally at 4.5 ton. The mass of the optical payload alone is ∼750 kg.

5.2.1.3 Primary mirror

The primary mirror is a collection of 91 hexagonal mirror segments, each with a diameter of 1.0-m and a spherical shape. Together these segments make up a spherical mirror — 11-m in diameter — the largest in the southern hemisphere. Each segment is manufactured in Russia from Astrositall, a glass-ceramic with a very low thermal expansion coefficient. The mirrors were sent from Russia to Kodak in the USA to be figured. Aluminium is used as the reflective material on the mirror surface which is replaced at least once a year. Each mirror rests on a specially designed mount that allows it to move in tip and tilt using three pistons. This makes it possible for all the segments to be aligned so that they approximate a single monolithic spherical mirror. The mirror segments are supported by a very stiff steel truss that ensures the mirrors stay in place. In the near future, edge sensors will be installed on all the mirror segment which will monitor their positions relative to each other. Any change in position for a segment would be detected and corrected, keeping the mirror in shape and ensuring good image quality.

5.2.1.4 MOS mode on the RSS

Due to the clever design of the payload-system, *SALT* can easily accommodate different instruments for either photometric observations, such as *SALTICAM* which serves as the acquisition camera as well as a science imager and photometer, or the Robert Stobie Spectrograph (RSS). The RSS was designed and built for *SALT* by the University of Wisconsin-Madison and Rutgers University. The RSS is designed to to take advantage of the improved blue/UV throughput of *SALT* as well as its access to a science field of $8'$ diameter. The RSS is capable of normal long-slit and multi-object spectroscopy (MOS) to resolutions of $R \sim 12000$. Additionally, it can perform Fabry-Perot imaging spectroscopy and narrow-band imaging. The MOS capabilities of the RSS made it the ideal instrument to obtain optical spectra of numerous spectral candidates in both RCW 34 and NGC 2626, in a realistic time frame.

Kobulnicky *et al* (2003) gives a detailed summary of the different operation modes of the RSS. The RSS was first commissioned in 2004. It covers the optical wavelength range from 3200-9000Å and has a $\sim 8'$ field of view. The RSS can take spectra in either the MOS, long-slit, Fabry-Pérot, or imaging modes. One thing that should be kept in mind is that *SALT* has a moving pupil due to the fixed angle of the primary mirror. During long exposures the tracker with the payload moves, which changes the effective aperture of the telescope, resulting in an ever changing flux of light falling on the imager. In other words the observed data can not be absolutely flux calibrated, but it can be partially flux calibrated if the spectrum of a spectro-photometric standard is available. Using the spectro-photometric standard star's spectrum and flat-field observations, scientific observations can

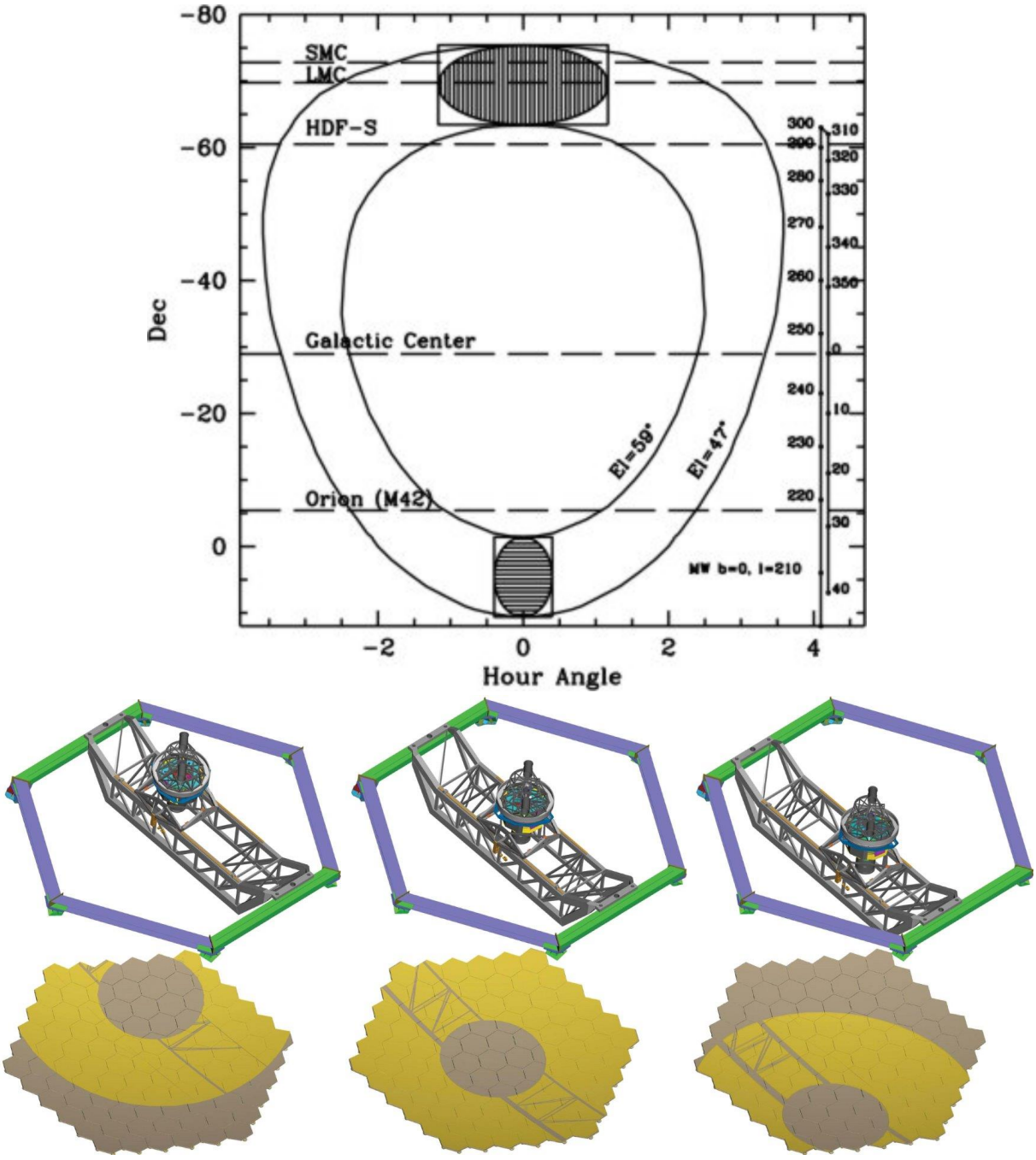

Figure 5.9: The top panel shows the visibility annulus of objects observable with *SALT*, as an angle of declination and hour angle. The hashed regions show the range of motion for the tracker at two different declinations. The bottom three panels show the pupil (yellow region) for three different tracker positions. The grey areas are non-illuminated parts of the mirror.

be relatively flux calibrated - or in other words the shape of the continuum can be determined. The optical design of the RSS is described by Burgh *et al* (2003). An important fact to take note of is that when MOS observations are performed with the RSS, the propagation path for each slit is different, which implies that the dispersion angle for each these paths are different to each other when interacting with the grating. This results in a wavelength dependence on the position at which light falls on the imaging CCD. This effect is shown on the right panel of Figure 5.10.

The sequence of steps for MOS observations is given by Kobulnicky *et al* (2003) as: (1) Slew the

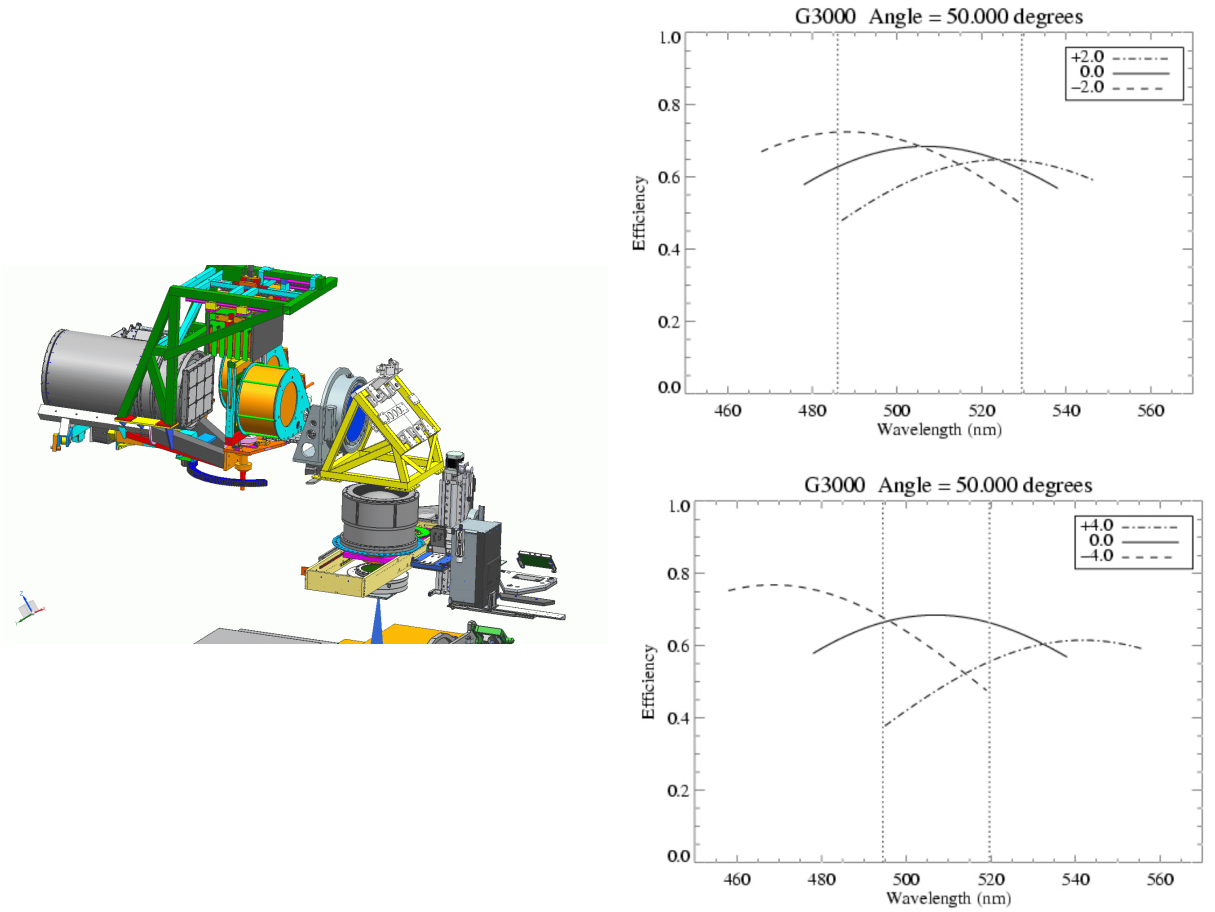

Figure 5.10: The left panel shows the optical design of the RSS. The right panel shows the wavelength dependence of light falling onto different positions of the CCD.

telescope and tracker to the desired field. (2) Take an image of the science field with *SALTICAM* or the RSS. (3) Insert a mask with slits at the positions of the spectral candidates into the RSS. (4) Take an image with the RSS of the field and mask, to assure that the alignment of the slit is correct. (5) Fine-tune the pointing relative to the guide stars are done. (6) Insert the desired grating and rotate it to the desired angle. (7) Take the exposure of the science images.

5.2.2 Selection of candidates

The MOS mode on the RSS (**R**obert **S**tobie **S**pectrograph) on *SALT* was used for the stars in the field surrounding RCW 34 and NGC 2626. The sources which had the highest probability of being CTTs, and were bright enough to be observed in the optical, were chosen. The *VPHAS+* photometry was not available when the application was submitted for the second semester of 2015, therefore *SuperCOSMOS* and *IRSF* photometry was used to select the most probable CTTs. A priorty scoring

Table 5.1: The grating complement that is available for the RSS.

Grating Name	Wavelength Coverage [Å]	Usable Angles [°]	Bandwidth per tilt [Å]	Resolving Power [1.25″ slit]
PG0300	3700-9000		3900/4400	250-600
PG0900	3200-9000	12-20	$\sim$ 3000	600-2000
PG1300	3900-9000	19-32	$\sim$ 2000	1000-3200
PG1800	4500-9000	28.5-50	1500-1000	2000-5500
PG2300	3800-7000	30.5-50	1000-800	2200-5500
PG3000	3200-5400	32-50	800-600	2200-5500

system was developed for the sources that matched between the *IRSF* and *SuperCOSMOS* datasets using the J-band magnitude, the $(H - K_s)$, colour and the $(R_s - H\alpha)$ colour. The J-magnitude was used as a measure for a source's brightness in the optical, because the median wavelength for J is the closest to optical wavelengths. The limiting magnitude for the 1639 sources that matched between the *IRSF* and *SuperCOSMOS* in RCW 34 was $J = 17.99$. For NGC 2626 there were 143 sources that matched between the *IRSF* and *SuperCOSMOS* datesets. The limiting magnitude was $J = 19.29$. In RCW 34 and NGC 2626 there were 439 and 47 sources respectively that showed excess *NIR*-emission, and fulfilled the criteria for selection as candidates for observation with *SALT*.

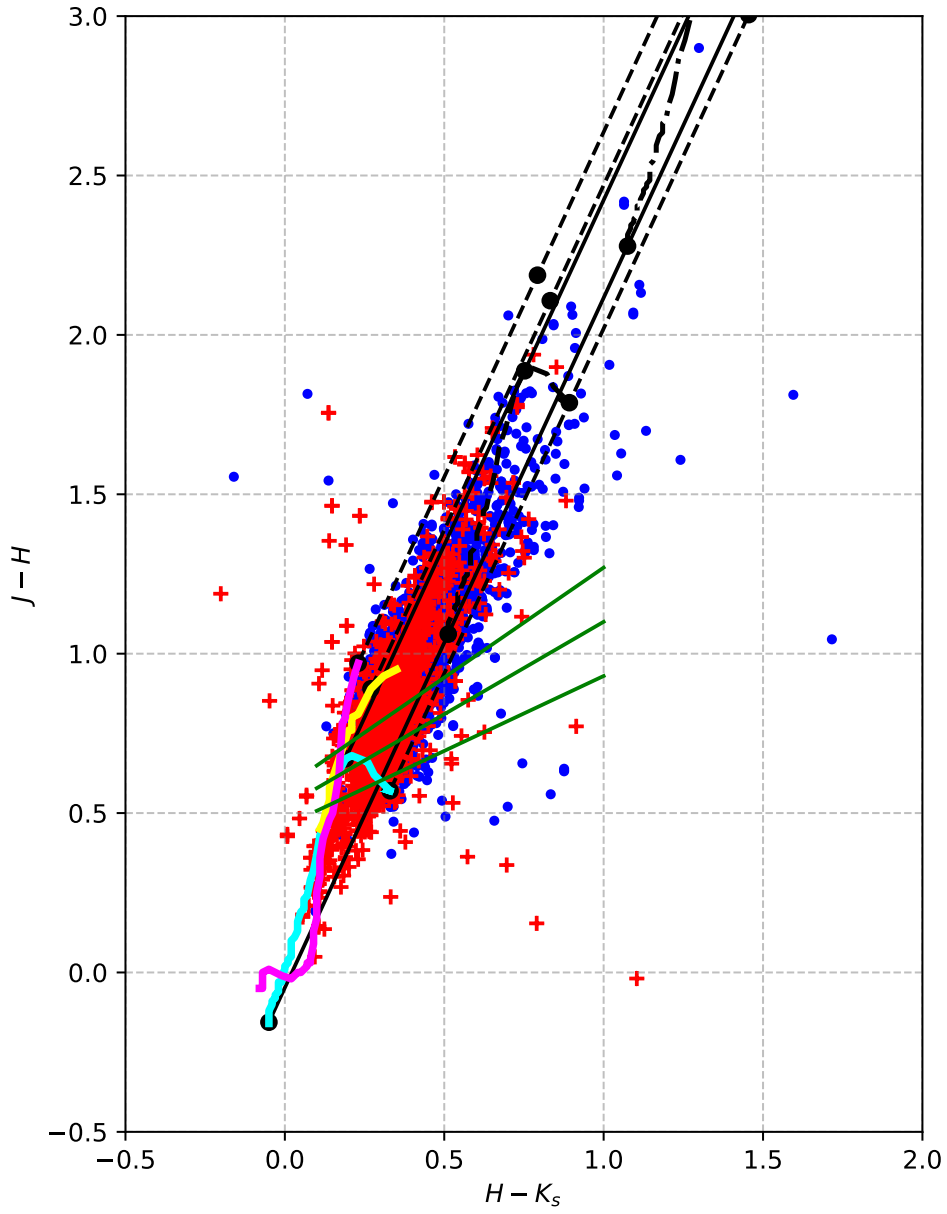

Figure 5.11: The 1639 sources in RCW 34 that matched between the *IRSF* and *SuperCOSMOS* datasets. The red crosses are the sources with $(R_S - H\alpha)$ characteristic to excess Hα-emission, and the blue dots do not have excess Hα-emission. The main sequence, giant, and super giant locus is plotted with a cyan, yellow, and magenta line respectively.

Figures 5.11 and 5.12 show the sources that matched between the *IRSF* and *SuperCOSMOS* datasets. In each graph the sources with excess $(R_s - H\alpha)$ colour excess — which is an indicator for excess Hα-

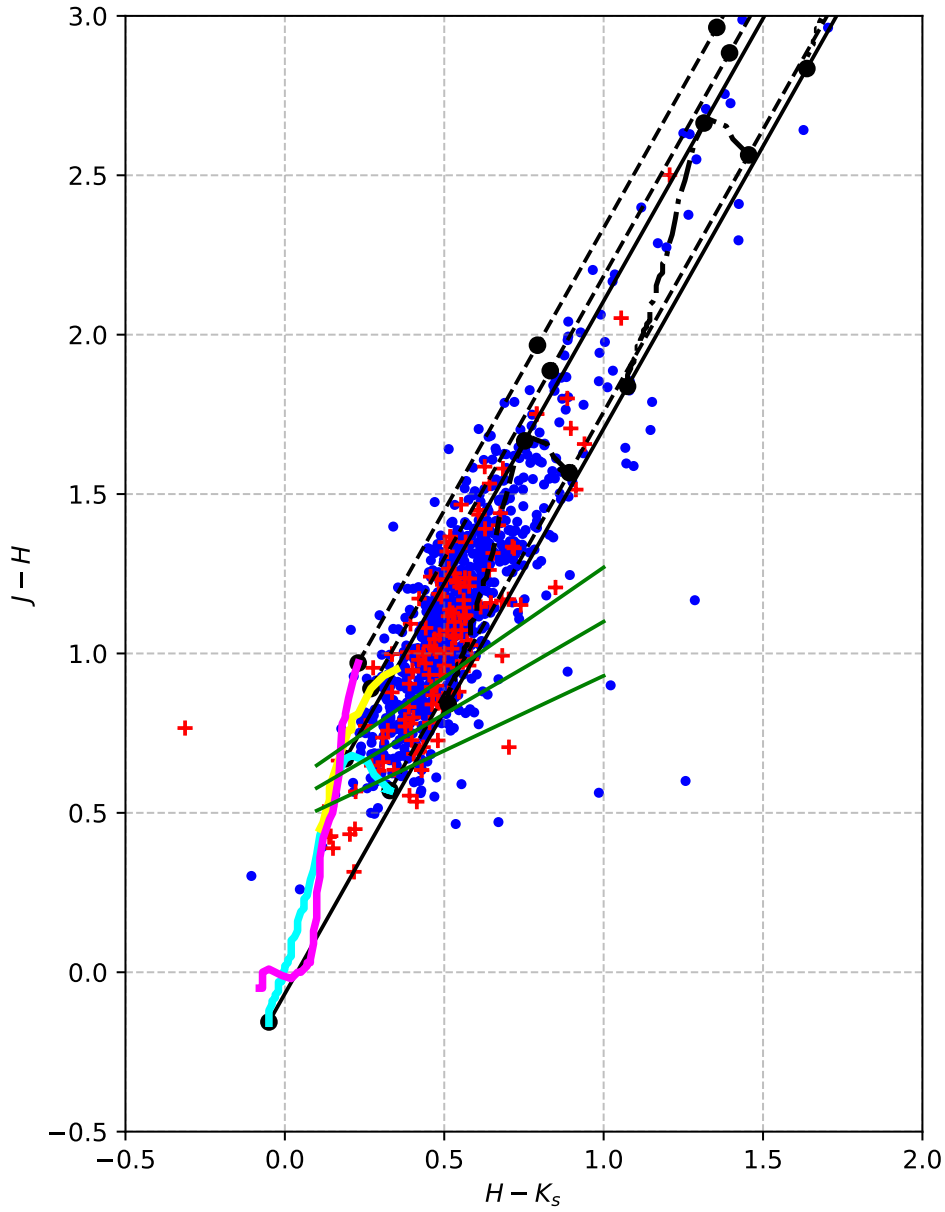

Figure 5.12: The 953 sources in NGC 2626 that matched between the *IRSF* and *SuperCOSMOS* datasets, the red crosses are the sources with $(R_S - H\alpha)$ characteristic to excess Hα-emission and the blue dots do not have excess Hα-emission. The main sequence, giant and super giant locus is plotted with a cyan, yellow and magenta line respectively.

emission — are plotted as red crosses. The sources which did not show $(R_S - H\alpha)$ excess are plotted as blue dots. The majority of the distribution lies between the upper and lower reddening vectors, which would suggest that most of these sources could be dereddened to the main sequence and is the typical distribution for a long exposed image taken of field stars. The majority of the blue sources lie between the upper and lower reddening vectors, they are very likely reddened main sequence stars and will not be considered as candidates. The red sources between the upper and lower reddening lines were added to the pool of candidate stars. There are sources without excess Hα-emission which show excess *NIR*-emission, this was shown by Gras-Velázquez & Ray (2005) to be the case of some WTTs where there was not a significant amount of Hα-emission but they did show excess *NIR*-emission. Each colour-colour diagram illustrates how high the priority of a source is considered to be. Those with Hα-emission and strong colour excess $(H - K_s)$ have the highest priority for being selected as

a candidate for spectroscopic observations. A priority index was calculated for the sources shown in Figures 5.11 and 5.12, using the colours and magnitudes as described in the previous paragraph:

$$p_{(H-K_s)} = 1 - \frac{(H-K_s)_{MAX} - (H-K_s)}{(H-K_s)_{MAX} - (H-K_s)_{MIN}} \tag{5.1}$$

$$p_{(R_s-H\alpha)} = 1 - \frac{(R_s-H\alpha)_{MAX} - (R_s-H\alpha)}{(R_s-H\alpha)_{MAX} - (R_s-H\alpha)_{MIN}} \tag{5.2}$$

$$p_J = \frac{J_{MAX} - J}{J_{MAX} - J_{MIN}}. \tag{5.3}$$

These three factors were multiplied to calculate a general priority for each stellar candidate, $p = p_{(H-K_s)} \times p_{(R_s-H\alpha)} \times p_J$. The maximum value for the respective parameters are not all associated with a single source, thus no source has a general priority score equal to 1. The general priority will from now on just be called the observation priority for a source, or the priority.

When observing in MOS mode on the *RSS*, spectra can at most be taken for 20-30 sources in a single instance. The colour priorities $p_{(H-K_s)}$ and $p_{(R_s-H\alpha)}$ were calculated so that the sources with the largest excess emission have the highest priority. A source with the largest excess emission in either colour would have a colour of $(H-K_s)_{MAX}$, so the priority would be $p_{(H-K_s)} = 1 - \frac{(H-K_s)_{MAX} - (H-K_s)_{MAX}}{(H-K_s)_{MAX} - (H-K_s)_{MIN}} = 1 - 0 = 1$. The priority for J is proportionally based on a value between 0 and 1 for the brightest and faintest J-magnitude in the population of candidates. If J_{MAX} is the faintest of the population, then the highest priority will be for the brightest source in the population, $\frac{J_{MAX} - J_{MIN}}{J_{MAX} - J_{MIN}} = 1$. The distribution for the resulting priorities is shown in Figure 5.13, and these priorities were used in the *RSS* slitmask software package. The slitmask tool selects the most likely, brightest sources that have the correct spatial distribution so that they can be observed in MOS mode. The priority for each star is used by the spatial optimization routine of the slitmask tool to select the maximum number of sources with the highest priority of being observed. A priority of 1 was manually assigned to the stars causing the HII regions in RCW 34 (VdBH 25a) and NGC 2626 (the driving star of HH-132). The other sources with a priority smaller than 1 were subject to the selection of the spatial optimization of the slitmask tool. The sources given to the mask creation routine all had a priority score high enough that each had a very high likelihood of being bright CTTs.

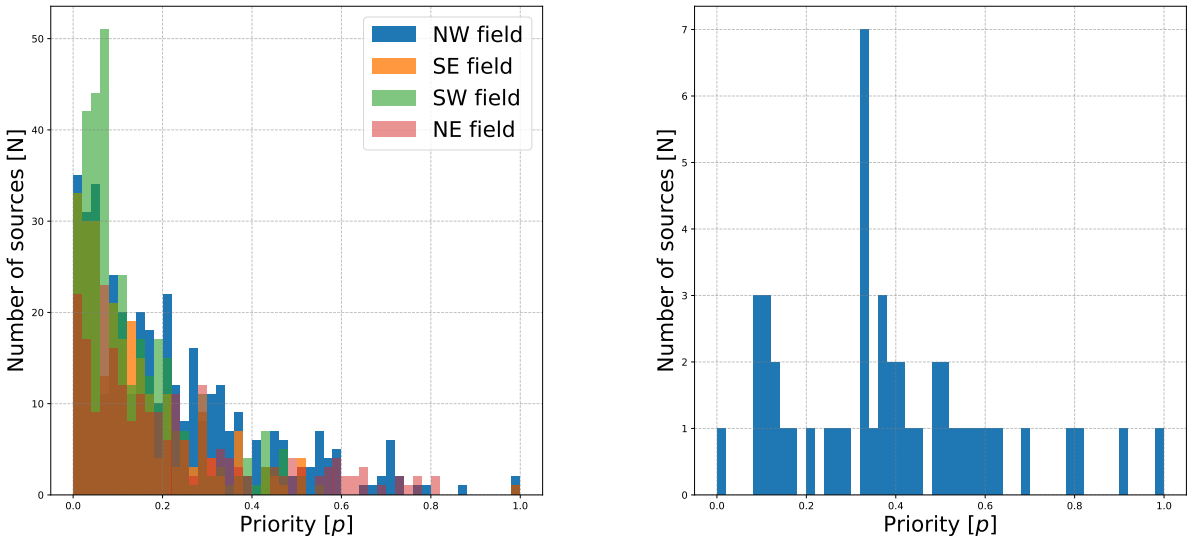

Figure 5.13: The distributions of observation priorities that were calculated using equation 5.3 for the 4 fields around RCW 34 (in the left panel) and for NGC 2626 (in the right panel).

The distribution for the priorities that were used for the selection of *SALT* candidates are given in Figure 5.13. For RCW 34 there are not many sources that fulfill the criteria of having excess emission in their $(R_s - H\alpha)$ and $(H - K_s)$ colours, and a bright J-magnitude. This resulted in the selection of a large number of sources with a relative low priority, as shown in the first diagram of Figure 5.13. Only 20-30 sources can be observed with a single instance in MOS-mode, meaning that there are just a few sources that were initially selected in the construction of the slitmask. *SALT* has a field of view which spans $\sim 7' \times 7'$, which is smaller than the region that is of interest to this study around RCW 34. Therefore, 4 separate fields were observed for RCW 34 in the directions NE, NW, SE, and SW from the HII region, resulting in 75, 185, 142, and 104 candidate sources, respectively. For NGC 2626 there are 189 sources, all shown in the distributions of Figure 5.13. The source with a manually assigned priority of $p = 1$ (the star causing the HII region) is also shown in each of the distributions of RCW 34 and NGC 2626. Both distributions show very few stars with a high priority; the number of stars increase for lower priorities. The distribution for the priority, p, reflects that there are a few sources that satisfy all 3 criteria, namely: strong excess emission in both colours and a bright J-magnitude. Some sources may present a strong $(H - K_s)$ excess emission, but their J-magnitude may be too faint to be optically detectable, or some other combination, resulting in a low general priority. This implies that the spatial distribution optimization algorithm has to choose between a few high priority sources and a larger number of low priority sources. This low number of high priority sources may be restrictive to spatial selection, and if they are too close to one another then the spatial optimization algorithm may throw them out.

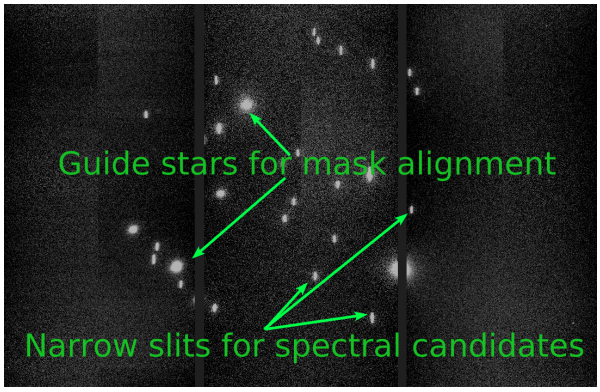

Figure 5.14: The stars that are projected through the slits on the slitmask.

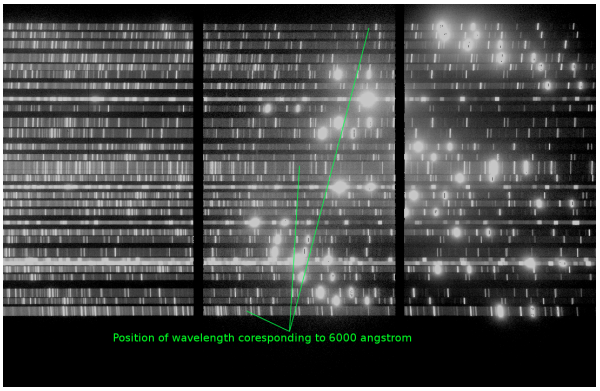

Figure 5.15: An arc image showing the centre of the image and the location of the different slits on the imager.

The MOS observations were done with a mask in which small slits are laser cut for each candidate. To correctly disperse the light from the candidate sources the slits are only 1.25 arc-seconds wide. These slits are too small to accurately align the slitmask and the telescope during instrumentation setup, thus large slits need to be separately cut for bright stars in the field which serve as alignment targets. At least three bright guide stars are selected in a science field as the alignment targets. The guide stars were chosen on the outer edges of the slitmask so that alignment of the mask would be accurate enough for long exposure times. The positions of the spectroscopic candidates are the narrow, long slits, and the slits for guide stars are the bright, square slits. Both types are shown in Figure 5.14. For the observation of spectral candidates in RCW 34 and NGC 2626, a maximum number of sources were fit onto a slitmask, because a single long-time exposure was going to be performed. For the layout design of the mask, a beta-version of the slitmask tool in the `proptools` routine of the *PySALT* package was used. A candidate list was compiled for the stars in the field with the strongest general priority p. The slitmask tool used the priority parameter (p) and the location of all the candidates when choosing spectroscopic candidates. An optimised layout of the slits on the mask had to be chosen to maximize the number of spectroscopic sources. All of the candidates that were given to the slitmask tool had a priority less than 1, due to the way that it was calculated. The software uses the priority so that a p-value of 1 is assigned to a source that has to be observed. For sources with a priority p less than

1 the mask tool's optimization algorithm chooses the sources with the highest priority and the best spatial distribution to maximize the number of slits on the mask. For each slitmask, the brightest three stars — which were not too close together — were selected as guide stars for the alignment of the slitmask. For a candidate, a rectangular slit is cut with an angular size of $1.25'' \times 8''$ whereas for the reference stars, a slit is $5'' \times 5''$. The guide stars are assigned a priority $p = -1$, which tells the masktool that the specific star is a guide star and should be on the mask. The position of the stars with p=1 and p=-1 are placed on the mask and the position of the sources with $p < 1$ optimized around these. During the optimisation routine of the slitmask tool, the p-value for each candidate is used as a weighted criteria to position the maximum number of sources around the $p = 1$ source and guide stars. The positions chosen needs to avoid the overlap of two spectral profiles on the dispersion grating or the imager. If the positions of the slits were not correct and they were located very close to each other, then the spectral profiles shown in Figure 5.15 would be projected over each other and their light would cross-contaminate each other's spectra.

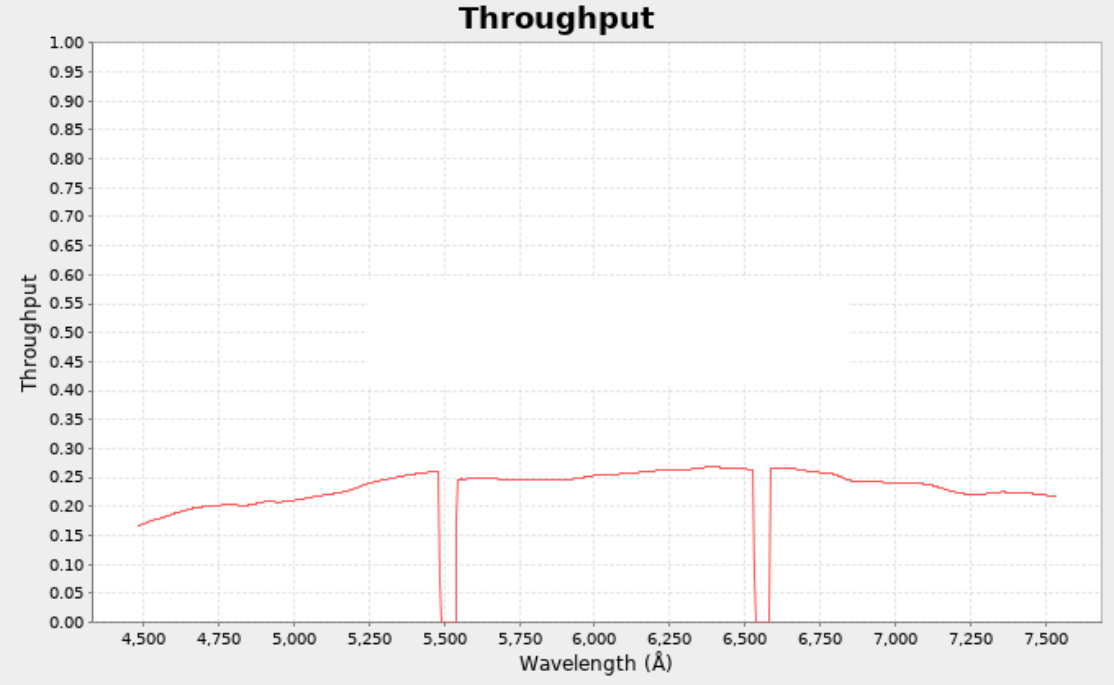

Figure 5.16: The throughput of light onto the RSS chip showing the gaps between the different CCDs across the wavelength range.

When the light of a star propagates through the slit in the mask to the dispersion grating and then onto the imager, the position of the slit affects the wavelength range that is captured on the imager. The position of the central wavelength shifts with a few Å as the slit moves away from the centre of the imager. This means that slits that lie on the outer limits of the mask will have a wavelength offset of 200Å blue-wards or red-wards in the spectrum, away from the central wavelength of the slit at the centre of the mask. The imager of the RSS has two gaps from the blue end to the red end of the wavelength range. The shift of the pixel position of the central wavelength range are shown on the position of the spectral profiles projected onto the imager, as shown by the green indicator lines in the right panel of Figure 5.15. Any planning that is done for specific spectroscopic features has to compensate for both the wavelength shift, due to the position of the slit, and the gaps in the imager. The projection of a simulated source from the exposure time calculator is shown in Figure 5.16. For any higher or lower y-axis position the wavelength range will shift according to the distance. A throughput similar to that of the source in Figure 5.16 for a source at the upper edge of the image, will span from $\sim 4700 - 7700$Å and have a central wavelength of ~ 6200Å.

The candidate sources were chosen from the $15.9' \times 15.9'$ field centered on VdBH 25a in the HII region of RCW 34 and a $7.8' \times 7.8'$ field surrounding HH-132 in NGC 2626. As previously mentioned, the *IRSF* and *SuperCOSMOS* photometric results were used to construct the list of candidates. The effective field of view that can be observed with the RSS is $\sim 7' \times 7'$ which would require four separate instances of observations to include all of the candidates surrounding RCW 34 that were identified from the *NIR* photometry. The candidates around NGC 2626 could be observed in a single instance.

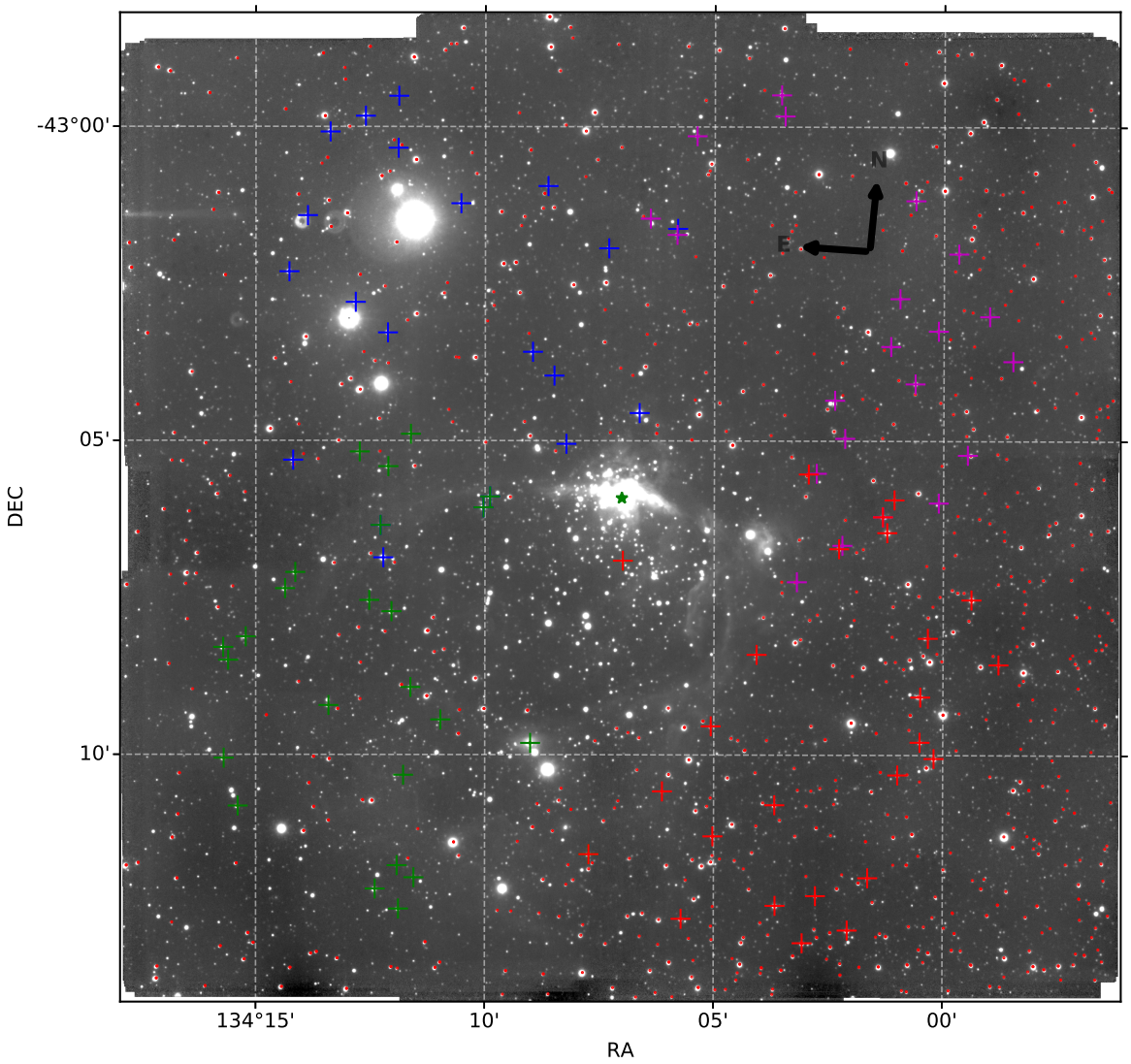

Figure 5.17: The sources that were selected in four distinctive fields surrounding RCW 34 for observation with *SALT*. The individual candidates in the NE, NW, SE, and SW fields are the blue, magenta, green, and red crosses, respectively.

The spectroscopic candidates that were selected by their priority parameter p, together with their positions according to the slitmask tool, are shown in Figure 5.17. There were four fields selected from the area directly surrounding RCW 34: NE, NW, SE, and SW. The positions of the selected stars in the respective fields are indicated with blue, purple, green, and red crosses respectively. All of the selected sources are not too close to any nebulosity and they are diversly positioned across each field, giving a good sample of sources across the field. The selected positions are separated enough from the nebulous gas that any contamination from the nebulous gas is a minimum.

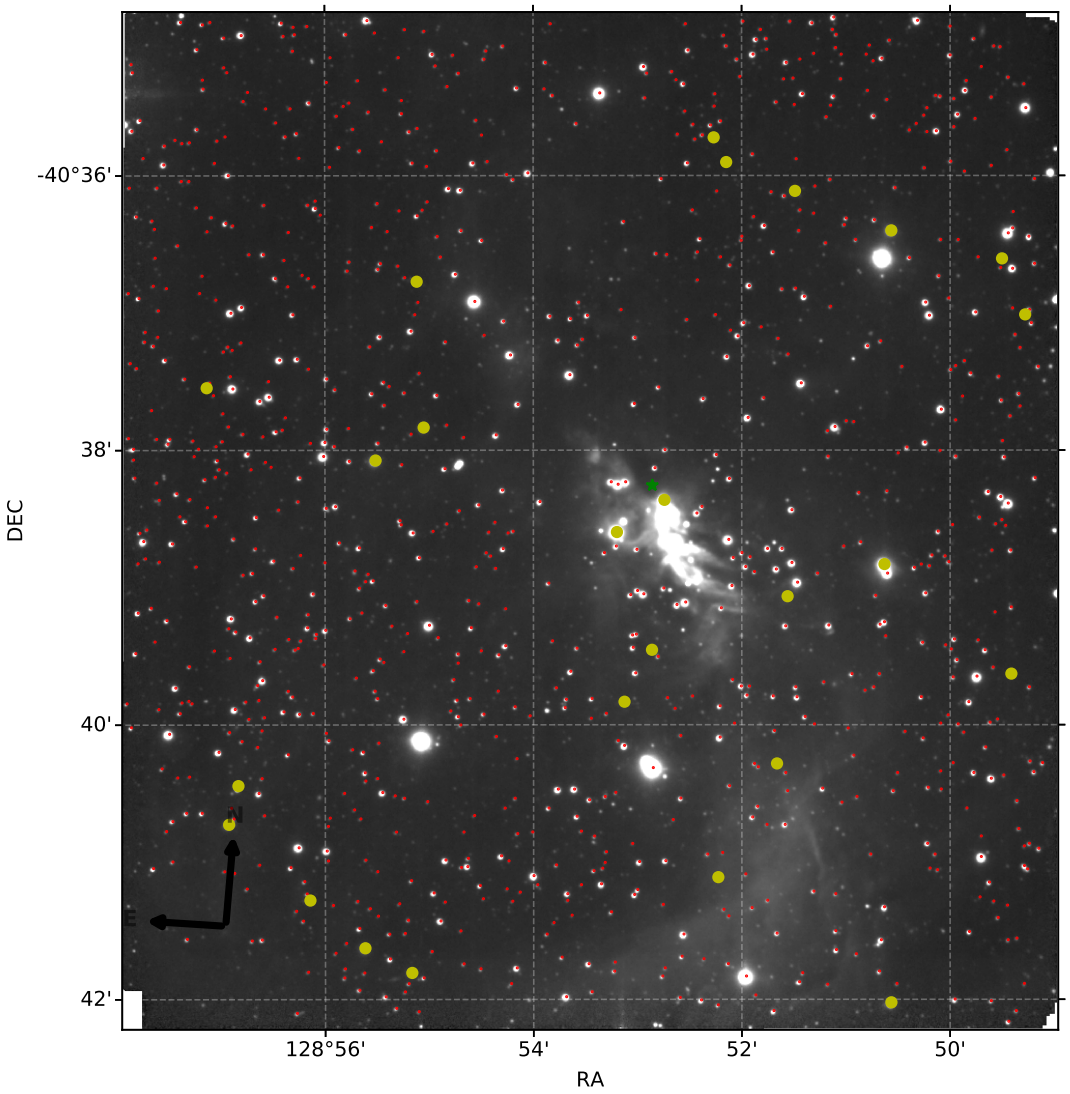

Figure 5.18: The sources surrounding NGC 2626 selected for observation with *SALT*.

5.2.3 Exposure time calculation

During phase I of the time application process the total exposure time required for observations is requested. To calculate the correct exposure time the RSS exposure time calculator was used. The spectrum of a bright star ($V = 15$) that was observed in 2011 from the study by Czanik (2013) was used for the simulations. This spectrum is shown in Figure 5.19. The calibrated flux and the corresponding magnitude were used to calculate the expected flux from a fainter source. The calculated flux for the faint source was then used to calculate an effective exposure time for a desired S/N of 20. A V-band magnitude of 20 was assigned to the source, and the instrument setup was changed that high-resolution spectra could be obtained from the candidates.

Grating number PG1300 was chosen, because it has an effective wavelength range from 3900-9000Å, and an observable wavelength range spanning 2000Å with a resolving power of 1000-3200. Due to the faint emission from the selected sources no filter was used in the instrumentation setup. The two spectroscopic features that were the primary focus of this investigation were the Hα-emission line at 6562.18Å, and the Li-absorption line at 6707Å. Any other spectroscopic features were a bonus and would be necessary to determine the spectral type of the star. This also ensured that the blue spectrum was assigned a priority 3, which would only be observed with *SALT* when the atmospheric conditions were not optimal, for example if it was non-photometric overcast. The consequences of

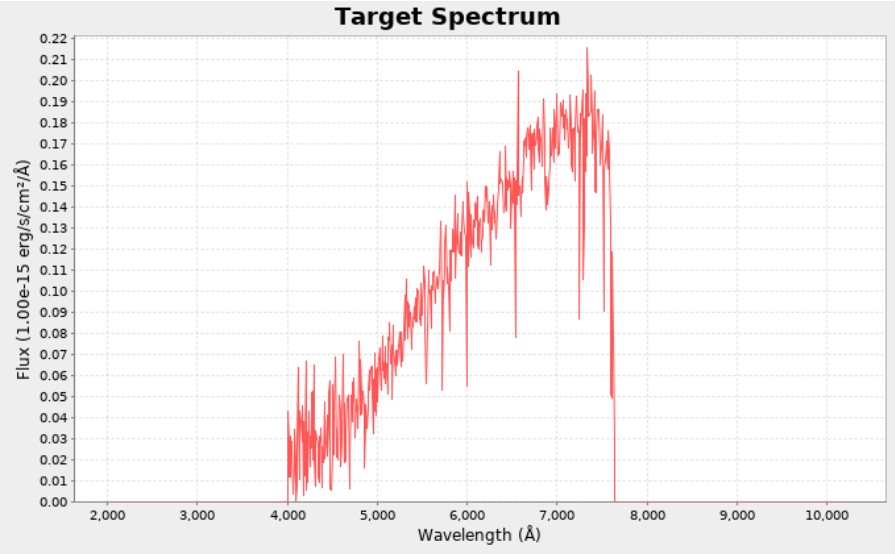

Figure 5.19: The spectrum that was observed in 2011 on the 1.9-m telescope as part of the study by Czanik (2013) which was used for exposure time simulations on the RSS.

the blue spectrum having a priority 3 is that there were no blue spectral observations obtained for RCW 34. To obtain enough light from the faint sources a binning of 2×2 was chosen. The shift in central wavelength across the imaging chip and the limitation of the 2000Å spectral range has a consequence that a separate blue and red spectrum had to be observed. The red spectrum would concentrate on the Hα-emission line as the central feature of its observations, and the blue spectrum would continue from the end of the wavelength range from the red dataset. For the blue part of the spectrum, the camera angle was 39.25°, and the grating angle was 44°. The red setup had a camera angle of 50.4° and a grating angle of 25.25°.

5.2.4 Data acquisition and reduction

The phase II part of the time allocation was approved, and observations performed at different periods resulted in a combined exposure time of 46170.2 seconds dedicated to the spectroscopic observations. The time assigned and observed on each field is given in the Table 5.2.

Table 5.2: The number of slits, exposure time dedicated, and the time when the obervations were done with *SALT* of the 4 fields around RCW 34, and the single field of NGC 2626.

Block	Obs Time	Priority	Target	Obs Date	Number of slits
RCW 34 NE RED	2159	2	RCW 34 NE	2015-12-07	26
NGC 2626 RED	2159	2	NGC 2626	2016-01-09	30
NGC 2626 BLUE RUN #1	3635	3	NGC 2626	2016-02-29	30
RCW 34 NW RED	2159	2	RCW 34 NW	2016-02-12	26
RCW 34 SE RED	2159	2	RCW 34 SE	2016-02-13	32
RCW 34 SW RED	2159	2	RCW 34 SW	2016-02-15	29
NGC 2626 BLUE RUN #2	3435	3	NGC 2626	2016-04-14	30

A dataset which had basic image reduction in the form of crosstalk and trim correction was downloaded from the *SALT* website. The downloaded product directory contained the alignment, arc, flat field, and science field images, all of which are shown in Figures 5.20-5.23. The science field that was observed through the RSS, without the slitmask or the grating, is shown in Figure 5.20 for NGC 2626. Once the alignment of the RSS was close to the correct position for the spectral observations, the slitmask was placed over the RSS and the alignment stars were used to get the mask in the correct position. The resulting light from all the stars through the slitmask, without being projected onto the spectral grating is shown in Figure 5.21. If the grating was placed between the slitmask and the imager, the resulting spectrum for each star is shown in Figure 5.23. The light from the arc lamp shone through the slitmask, for wavelength calibration is shown in Figure 5.22.

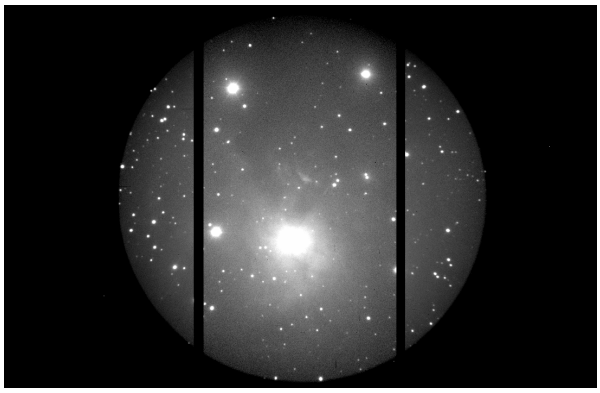

Figure 5.20: The view of NGC 2626 taken with the RSS imager before the slitmask is placed in the instrument.

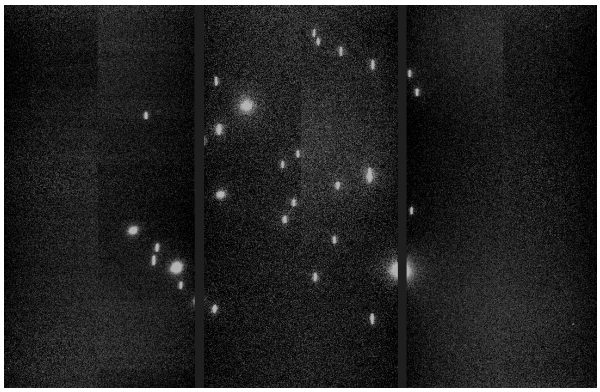

Figure 5.21: The view with the RSS when the slitmask is placed into the instrument.

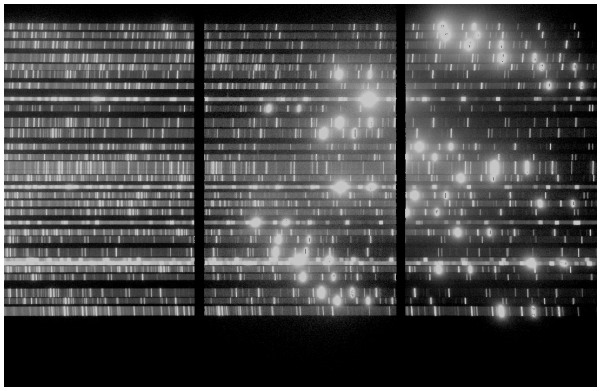

Figure 5.22: An arc image that is used for wavelength calibration for every star's profile that is observed through a different slit.

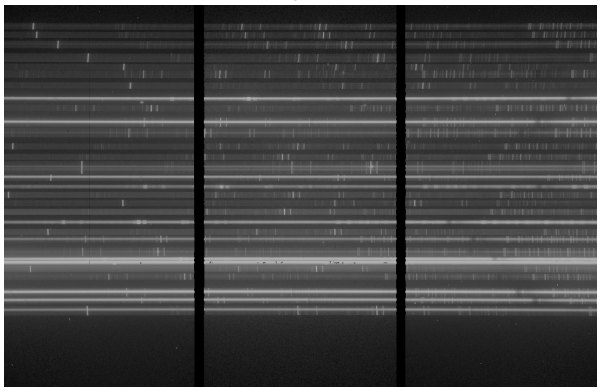

Figure 5.23: The downloaded image from the RSS that includes the spectral profile of each star observed from a different slit.

Cosmic rays were removed from the science image using a python adaption of the La Cosmic routine that was developed by Dokkum (2001). To get the spectroscopic observations from the single science frame image, as shown in Figure 5.23, to a status where it can be analysed, an automated pipeline developed by Matt Hilton was used. No citation to a publication for the pipeline is available for referral, only the online address on github: `https://github.com/mattyowl/RSSMOSPipeline`. Private e-mail communication with the author of the software insured that the arc lamp standards for Ar on grating PG1300 at 2×2 binning were included into the package. The package initially only had the Ar arc lamp standard for grating PG0900 as part of the package. The pipeline initially reduces the science field and performs BIAS, DARK, and flat fielding correction.

As part of the scientific dataset standard star observations were requested, so that flux calibration could be performed on the science images. It is not possible to perform absolute flux calibration with *SALT*, due to the ever changing pupil, but standard star spectra can be used to correct the continuum profile for the observed spectra. Standard star data was requested but it were not available for the nights on which the observations were performed.

The pipeline is fully automated with the identification of the position of each spectral profile from the science field and the arc images. The position of each slit identified by the pipeline is shown on the science field image in Figure 5.24. The individual spectral profiles are trimmed according to the pixel coordinates from the slitmask. The unique position of each slit has a y-coordinate that is positioned on a star's a profile with the same size that is outlined in the science field image. Once the individual spectral profiles have been trimmed out of the science field image the same slit outline is trimmed

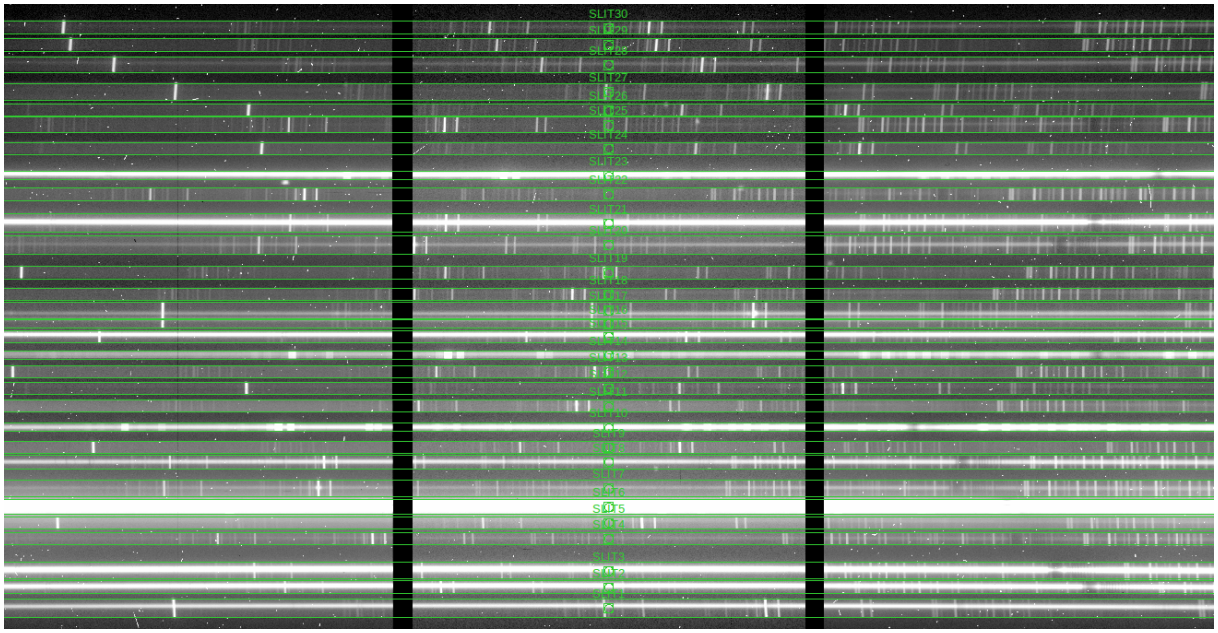

Figure 5.24: The individual slit regions of each star that is trimmed out by the pipeline from the science image.

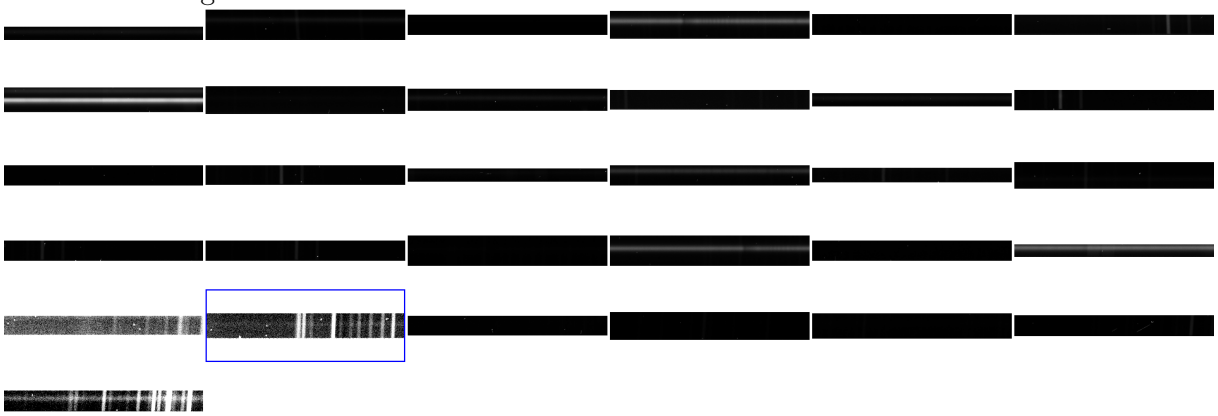

Figure 5.25: The individually trimmed stellar profiles. The spread of the skylines across the stellar profiles show that the profiles were precisely trimmed by the pipeline.

out from the arc images, as shown in Figure 5.25. With the same pixel regions for the individual stellar candidates and trimmed arc regions, the pipeline identifies the best wavelength solutions for each spectral profile.

To perform the wavelength calibration on the individual spectral profiles the Ar arc library for the PG1300 grating that was observed with a 2×2 binning was given to the pipeline. The wavelength solutions were done iteratively for the slits in RCW 34's NE, NW, SE, SW, and NGC 2626's red, and blue datasets resulting in a median wavelength offset in each dataset of 2.778Å, 2.856Å, 2.277Å, 2.6554Å, 2.857Å, and 7.854Å, respectively. The wavelength offsets were calculated using the wavelength difference for all of the skylines that were identified in each scientific spectral slit. The skylines and their corresponding wavelengths are shown in Figure 5.29.

After the wavelength calibration was done the spectral profile of each star had to be corrected for skylines. A straight line was fitted through the spectrum of the star and the width of the spectrum's light distributed on the images was measured so that the maximum amount of light from the star was extracted. The skylines from the atmosphere covered a much wider area than the star's spectral profile. The spectrum of the star on the imager is the horizontal bright band across Figure 5.30,

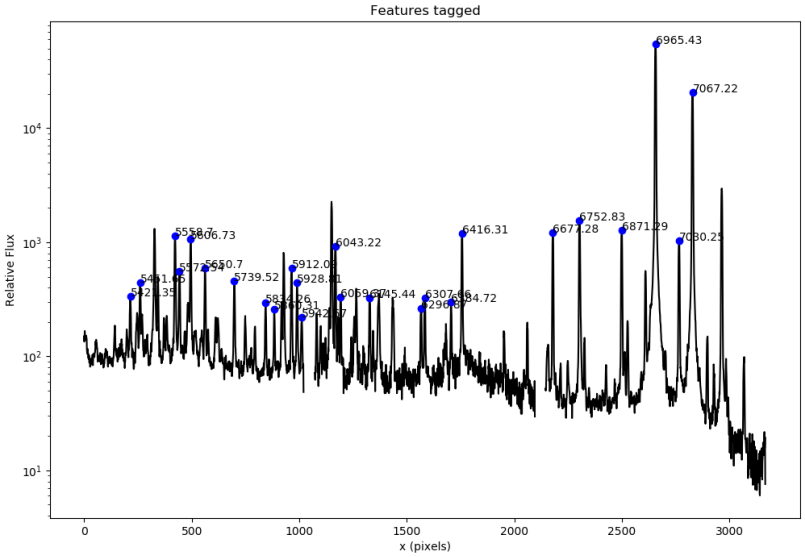

Figure 5.26: The arc lamp features that were used for the wavelength calibration.

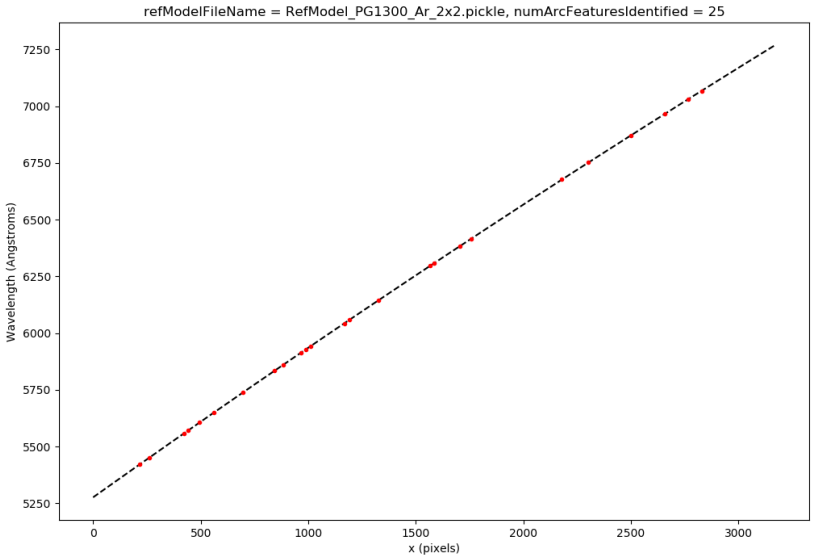

Figure 5.27: The linear transformation that was caculated between the pixel values and wavelength values.

and a skyline is the perpendicular bright line, both are clearly indicated. The observations were all taken during grey time and in non-photometric conditions, meaning that the skylines were the most prominent spectral features and dominated the spectrum of a faint star ($r' > 20$). The regions of the slit that do not have emission from the star's spectral profile would have emission lines from the atmosphere extending further away from the centre of the star's spectral profile to the outer edges of the slit. A standard atmospheric model for the skylines that were observed in Sutherland, were used by the pipeline to identify and eliminate the skylines from the stellar spectral profile. The skylines that cover the wavelength range that was calculated from the wavelength transformation equations were used to identify the skylines that were present in the spectral profile of the star. The identified skylines

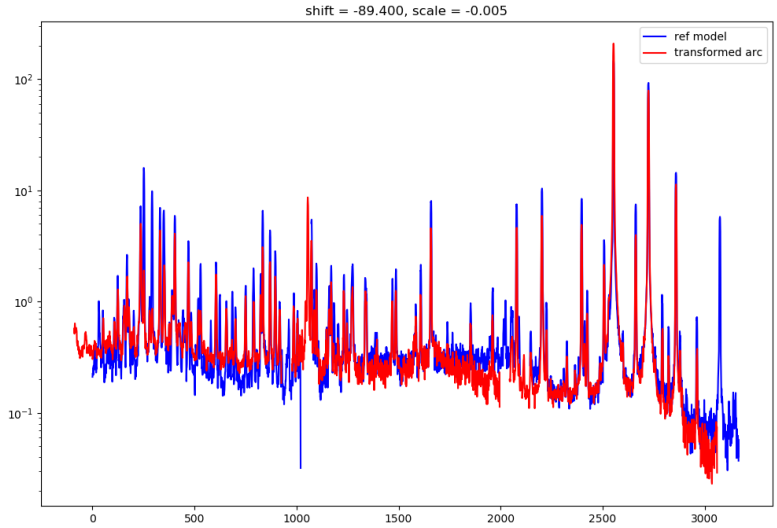

Figure 5.28: A comparisson between the library arc lamp and the arc lamp projection through slit 1.

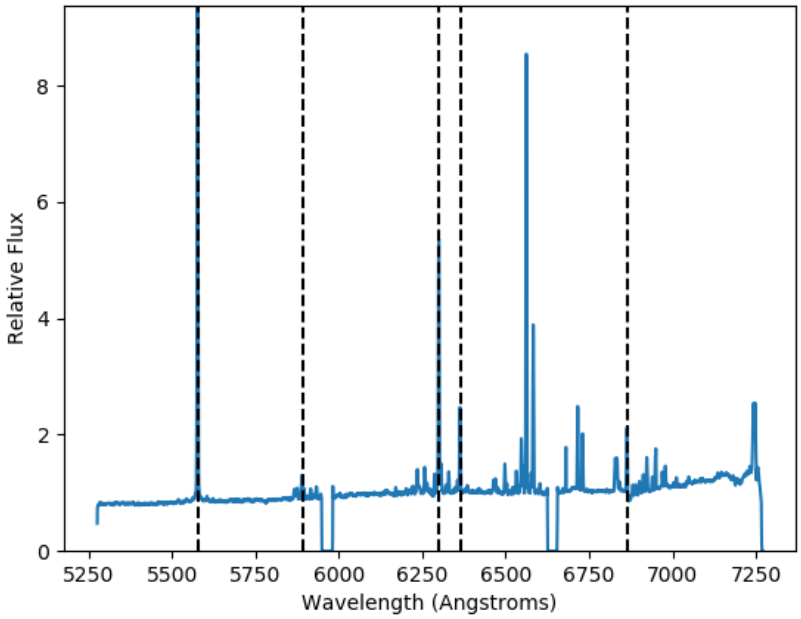

Figure 5.29: The skylines that were identified and subtracted from the spectra.

were used to calculate the precision of the wavelength calibration by taking the difference between the wavelength measured from the science image and the characteristic wavelength of each skyline. The identified skylines were subtracted from the star's spectral profile. The skylines that were identified in slit 1 of NGC 2626 are shown in Figure 5.29. Background subtraction was also performed as part of the skyline subtraction routine. The background profile was constructed by taking the combined average of the three rows above and below each star's spectrum. After the skylines and background were subtracted from the spectra, all of the light of the spectral profile were added together to form a 1D spectrum that was used for emission/absorption-line identification and measurements.

Figure 5.30: The trimmed stellar profile from the science image, the bright line across the center of the image is the star's spectrum and the bright perpendicular line is a skyline.

Under ideal circumstances a set of observations would be taken for each mask positioned next to the star, but not directly positioned in the slit. This would make it possible to subtract any nebulous emission that may be included in the emission from each star. The averaged background subtraction did remove some nebulous emission, but may have been subject to circumstellar emission — under ideal circumstances the subtraction of the spectrum from the nebulous emission would not have this contamination. The time constraints for *SALT* led to the decision that such a request, would take more observational time and have a negative effect on the application for observation time. Thus, it was assumed that any nebulous emission from gas that may be included in stellar spectra was subtracted together with the sky lines and the average background subtraction.

5.3 Analysis and results

After the spectroscopic data were reduced and collapsed into 1D spectra, the spectra were analysed for prominent absorption and emission lines. The *SpecViz* software package was used to measure the **e**quivalent **w**idth (EW) of each detected Hα-line in the red regime, irrespective if it was an emission/absorption line. The same package was used to measure the signal-to-noise ratio (S/N) for the Hα emission/absorption line and Li-absorption line in the red regime and the Hβ and Hγ lines in the blue regime. The Hα-profile was inspected by eye and the number of stars that have an Hα-emission, Hα-absorption, or an undetermined Hα-profile in RCW 34 and NGC 2626, are given along in Table 5.3.

Table 5.3: The number of stars according to their Hα-line profiles.

Starforming region	Hα emission	Hα absorption	Undetermined Hα profile
RCW 34	18	52	22
NGC 2626	11	8	4

Even though the spectra were partially flux calibrated, absolute flux calibration could not be performed because the spectra of a spectro-photometric standard was not available. One consequence of this was that the shape of the continuum could not be determined for any of the observed spectra. Each continuum was normalised relative to the maximum feature in the spectrum, and then flattened by fitting a 3'rd-degree polynomial through each spectrum. For the signal-to-noise ratio, the noise measurement was taken as the standard deviation of the continuum, excluding any features that may be either absorption or emission lines. For the signal strength it would be the maximum value of an emission line, or the minimum value of an absorption line. The ratio of the maximum/minimum value divided by the noise level is the respective S/N for the emission/absorption line. For a positive identification of a spectral line the S/N has to be greater than 3. Figure 5.31 gives a depiction of the region around the Hα-emission line which was used to measure the S/N. The green highlighted regions were used to measure the standard deviation, or the noise level of the spectra. The wavelength ranged from 6480-6505Å was not included in the calculation of the noise because it may potentially be an absorption line. A conservative approach was taken when choosing which parts of the spectrum were used to calculate the noise, the reason being that if any spectral features were included the noise measurement would be inaccurately high.

In *SpecViz* the EW is measured for the Hα-emission/absorption line and any other prominent emission/absorption line by distinguishing the line from the continuum. Two regions in the pre-flattened continuum were selected so that an average value of the continuum flux could be measured. A baseline was plotted between the middle of the two regions. The total flux over the wavelength range that was

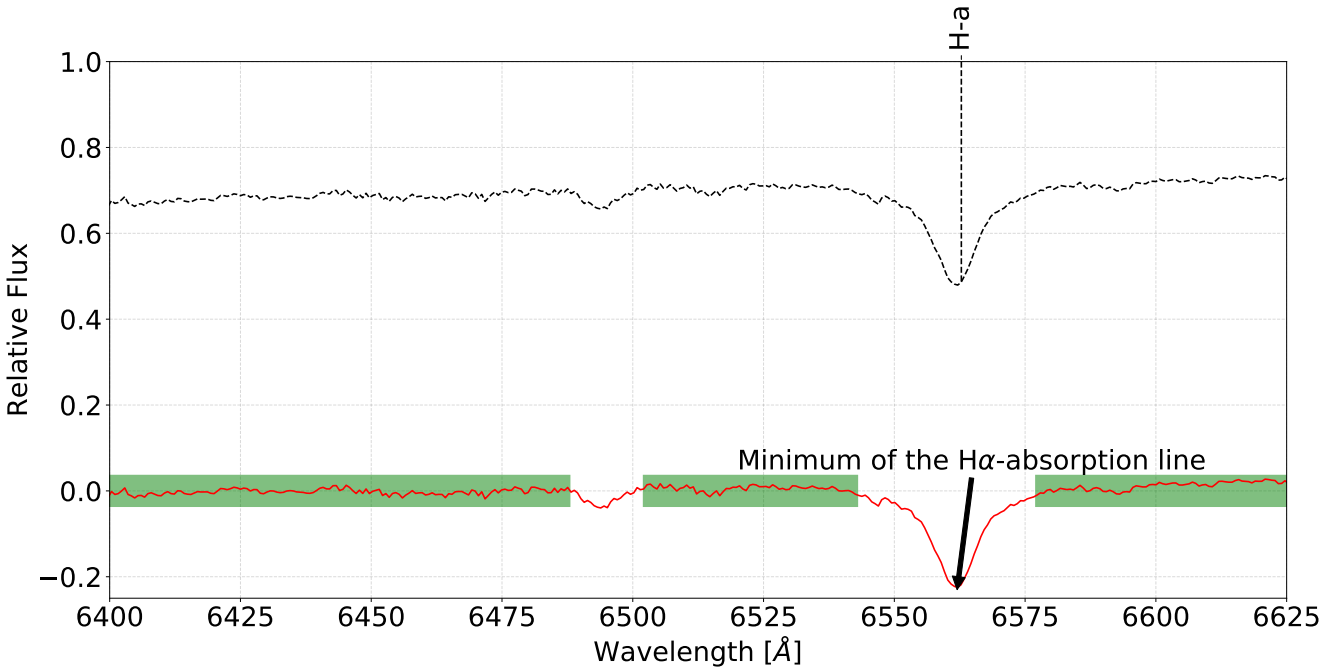

Figure 5.31: The region around the Hα absorption line of slit 9 in the south-eastern field of RCW 34. The dashed black line shows the normalised original spectrum, and the red spectrum is flattened with a third degree polynomial. The spectrum highlighted by the green regions were used to determine the standard deviation of the featureless spectrum — or in other words the noise. The ratio of the Hα-line's minimum to the noise is the S/N for Hα.

covered by the spectroscopic feature is subtracted form the average continuum flux. The measured flux is the equivalent line width that is taken up by the emission/absorption line from the continuum emission — irrespective of the spectral feature's shape. Even though the observed spectra were not absolutely flux calibrated, the equivalent width of the absorption/emission line could be measured relative to the partially flux calibrated spectrum. Many CTTs show signs of variable emission due to the dynamics of the circumstellar material, this results in a variable Hα-emission line profile. It was shown by Herczeg & Hillenbrand (2014) that measurements from many local T Tauri stars differ when observed over long periods. A time-variable Hα-emission line profile is influenced by the interaction of the star, the accretion disk, strong magnetic fields, and the volatile nature of the circumstellar material. For some of the stars that showed Hα-emission in this study, both the Hα-absorption line from the photosphere and the emission line from the circumstellar material were observed. For a case like this, it was not easy to determine the age of the star, based on the EW of the Hα-emission line; the observed flux is a superposition of the flux from the emission and the absorption lines. The interesting cases which had a high S/N for the Hα-emission line ($S/N \geq 5$), or the where Hα-emission line has an interesting profile, such as a combination for an absorption and emission line —not just an emission of absorption line— were analysed in more detail.

The spectroscopic classification was done with the PyHammer package, which is a Python implementation of an automated IDL optical spectroscopic classification package, developed by Covey *et al* (2007). The PyHammer package can be applied to any stellar spectrum across the wavelength range of 3650-10200Å. The algorithm distinguishes the most prominent absorption and emission lines in the spectrum from the continuum and iteratively matches the best fit between the identified lines and a spectral standard library. The classification is based on the ratios relative to each other, of the equivalent widths of spectral features detected and measured by the package. Identification is based on which lines were detected and the ratios of equivalent widths of those lines, and not on the shape of the continuum — meaning that spectra do not have to be flux calibrated to be classified. The spectra in the library has an average resolution ∼2000 according to Kesseli *et al* (2017). The RSS simulator

showed that the instrumental setup gave a resolution of ∼2000 for the red spectra, and ∼1900 for the blue spectra. The similar resolutions between the spectral library and the *SALT* spectra makes the classification with PyHammer ideal. The classification is done according to the Morgan & Keenan (MK given in Morgan *et al* 1943) spectroscopic classification system. The PyHammer package is unique by being the first package that has an empirical database of metallicity indicators that includes a large collection of M stars. The package does the classification by intelligently using iterative index matching between the input spectrum and its spectral standard library. Initial identification of the spectral type was done by measuring the EW of 34 spectral lines from the individual spectral library entries, listed in Table 5.4. There are various templates for each spectral type in the standard library, thus a weighted mean and the variance of each index value were measured and give an indication of the uncertainties. The identified spectral lines from the input spectrum are compared to the weighted means from the corresponding spectral lines of the entire spectral library. The comparison is done on a χ^2-test between the lines that are measured from the spectrum, and the mean and variance values of the indices from the spectral library. The smallest χ^2-value between the spectral library and the input spectrum is given as output.

Table 5.4: The spectroscopic indices that are used to perform spectroscopic classification and determine metallicity with PyHammer. Taken from Table 4 in Kesseli *et al* (2017).

Spectral Index	Numerator (Å)	Denominator (Å)
Ca II K	3923.7-3943.7	3943.7-3953.7
Hγ	4086.7-4116.7	4136.7-4176.7
Ca I 4227	4216.7-4236.7	4236.7-4256.7
G band	4285.0-4315.0	4260.0-4285.0
Hγ	4332.5-4347.5	4355.0-4370.0
Fe I 4383	4378.6-4388.6	4355.0-4370.0
Fe I 4404	4399.8-4409.8	4414.8-4424.8
Hβ	4847.0-4877.0	4817.0-4847.0
Mg I	5152.7-5192.7	5100.0-5150.0
Na D	5880.0-5905.0	5910.0-5935.0
Ca I 6162	6150.0-6175.0	1620.0-6145.0
Hα	6548.0-6578.0	6583.0-6613.0
CaH2	6814.0-6845.0	7042.0-7046.0
CaH3	6960.0-6990.0	7042.0, 7046.0
TiO5	7126.0-7135.0	7042.0-7046.0
VO 7434	7430.0-7470.0	7550.0-7570.0
VO 7445	7350.0-7400.0, 0.5625;[a] 7510.0-7560.0, 0.4375	7420.0-7470.0
VO-B	7860.0-7880.0, 0.5; 8080.0-8100.0, 0.5	7960.0-8000.0
VO 7912	7900.0-7980.0	8100.0-8150.0
Rb-B	7922.6-7932.6, 0.5; 7962.6-7972.6, 0.5	7942.6-7952.6
Na I	8177.0-8201.0	8151.0-8175.0
TiO8	8400.0-8415.0	8455.0-8470.0
TiO 8440	8440.0-8470.0	8400.0-8420.0
Cs-A	8496.1-8506.1, 0.5; 8536.1-8546.1, 0.5	8516.1-8526.1
Ca II 8498	8483.0-8513.0	8513.0-8543.0
CrH-A	8580.0-8600.0	8621.0-8641.0
Ca II 8662	8650.0-8675.0	8625.0-8650.0
Fe I 8689	8684.0-8694.0	8664.0-8674.0
FeH	9880.0-10000.0	9820.0-9860.0
Color region 1	4550-4650	4160-4210
Color region 2	5700-5800	4160-4210
Color region 3	7480-7580	4160-4210
Color region 4	9100-9200	4160-4210
Color region 5	10100-10200	4160-4210

Note: [a]Indices with more than one numerator entry contain two numerator regions and a weight for each region, e.g., lower limit of region 1 — upper limit region 1, weight of region 1; lower limit of region 2 — upper limit of region 2, weight of region 2.

Table 5.5: The spectrocopic standards from the atlas by Pickles (1998) and Jacoby *et al* (1984) that were used to test the classification of PyHammer

Given spectral type	Guessed spectral type	Guessed [Fe/H]	User specified spectral type	User specified [Fe/H]
Pickles A0	A2	-1.5	A0	0
Pickles B0	O9	0	B0	0
Pickles F0	F1	-0.5	F0	0
Pickles F4	F4	-0.5	F4	-0.5
Pickles F6	F6	-1	F6	-1
Pickles G0	G0	-1	G0	-1
Pickles G4	G4	-0.5	G4	-0.5
Pickles G8	G6	-0.5	G8	-0.5
JHC A0	A2	-1	A0	-1
JHC A9	F4	0	A9	0
JHC B0	O9	0	B0	0
JHC G1	G6	0	G1	0
JHC K0	G8	-0.5	K0	-0.5
JHC M0	M1	0	M0	0
JHC M5	M5	0.5	M5	0.5
JHC O9	O9	0	O9	0
JHC K0	G9	-1.5	K0	-1
JHC K4	K5	-1	K4	-1
Pickles M0	M0	0	M0	0
Pickles M3	M3	0.5	M3	0.5
JHC M6	M7	-0.5	M6	-0.5
JHC O5	O9	0	O5	0

In tests performed by Kesseli *et al* (2017) on the package, 50% of spectral classifications were correct and 80% were one metallicity bin, or one spectral sub-class from the correct classification. To test whether the classification of PyHammer was correct, specifically when the input spectra have different wavelength resolutions than the standard spectral library, the package was tested with the data from different spectral atlases. The atlases used were the Pickles (1998) (Pic) and Jacoby *et al* (1984) (JHC) optical spectroscopic databases and the resolution for each is 2.0Å and 1.5Å respectivly. The package needed to rebin each input spectrum so that the measured indices for the 34 spectral features, shown in Table 5.4, could be correctly compared to the standard library that was used for classification. A spectral standard was chosen for an O5, B0, A0, F0, K0, M0, and M6 star, each with a metallicity of -0.5, from each atlas and given as input to PyHammer. The difference between the input spectral class and the output given in Table 5.5 shows that, at most, the spectral classes differ with two sub-classes. For example, in the first entry, when an A0 star was given as input, the output was delivered as an A2 star. The spectra of most of the sources are quite noisy, due to high extinction, meaning that the determination of the exact spectral class is challenging. The results from PyHammer were acceptable, within reason, to get an indication of the spectral class of each star.

5.3.1 Properties of all the stars observed with *SALT*

The *IRSF* and *VPHAS+* magnitude for each star that was observed with *SALT* are given in this sub-section. The pipeline that was used for reduction only gave a name and a spectrum for a specific slit. To find the matching RA/DEC coordinates of a specific slit name, the pixel coordinates from each slit was taken from the science image, as shown in Figure 5.24. The numbering of the slits started from 1 at the first y-pixel position where light from a slit was registered on the imager. Each slit number followed recursively where each was positioned at a higher y-pixel value. Using the known y-pixel coordinates and RA/DEC positions taken from the slitmask, and the matching RA/DEC coordinates from each photometric set, the corresponding RA/DEC were matched up. By knowing which RA/DEC coordinates matched between the slit numbers and the photometric data, the different datasets were bridged, which implied that the star associated with the individual slit was known.

In the following tables the Hα-line profile for each star is represented as emission, absorption, or undetermined by an E, A, and U, respectively. If a star did have an emission or absorption Hα line profile which could be visually identified, but the Hα S/N is less than 3 the feature is indicated as either a respective E or A together with a question mark next to the profile indicator. If the equivalent

width could be measured then it is shown in the column following the Hα-line profile's column. The convention is that an emission line has a negative EW and an absorption line has a positive EW. If a star has a hybrid Hα-profile, then the net EW measured is given.

5.3.1.1 *RCW 34*

Table 5.6: Properties for the spectroscopic candidates in the north-eastern field of RCW 34.

Slit name	Spec Type	u'	g'	r'	i'	Hα	J	H	K_s	Li S/N	Hα S/N	Hα line profile	Hα EW [Å]	$\frac{[Fe]}{[H]}$
NE 1	K5			18.82	16.71	18.22	12.41	10.81	10.24		20	E	-3.17	-2
NE 2	M1			18.84	17.04	18.21	13.38	12.04	11.49	3.1	79	E	-38.07	0.5
NE 3	A7			16.87	15.78	16.52	13.52	12.90	12.54		0.4	U		-0.5
NE 4	M6			17.20	15.96	16.76	13.68	12.94	12.59	3.5	19	E	-3.81	-0.5
NE 5	M5			16.87	15.78	16.52	13.52	12.90	12.54		9.5	E	-0.72	0
NE 6	M1	13.25	13.11	12.76	12.50	12.64	12.04	11.85	11.70		32	A		0
NE 7	K5			13.52	13.11	12.04	11.85	11.70	17.38		23	A	4.14	-2
NE 8	K1	13.92	13.62	13.00	12.73	12.75	12.17	11.87	11.72		17	A	5.18	-1.5
NE 9	K7						12.17	11.87	11.72		24	A	0.63	0
NE 10	K0	21.11	18.93	16.87	15.86	16.48	13.93	13.24	12.92		3.0	A	0.11	-1
NE 11	G6	20.38	18.65	17.09	16.18	16.67	14.41	13.74	13.45		13	A	2.22	0.5
NE 12	K3	16.76	15.93	15.02	14.64	14.72	13.90	13.41	13.19		26	A	4.03	0
NE 13	M3	20.38	18.65	17.09	16.18	16.67	14.41	13.74	13.45		16	A	3.80	0.5
NE 14	M5	14.59	14.31	13.79	13.45	13.56	12.85	12.53	12.39		1.2	A?	0.94	-0.5
NE 15	M2						12.85	12.53	12.39		11	A	2.43	0
NE 16	M0	20.48	18.43	16.62	15.57	16.23	13.72	13.06	12.73		1.1	A?		0
NE 17	K1	19.42	17.90	16.26	15.46	15.88	13.78	13.19	12.91	3.2	42	A	16.41	0
NE 18	F3	16.12	15.49	14.66	14.34	14.39	13.58	13.19	12.97		11	A	2.33	0
NE 19	M8						13.58	13.19	12.97		0.1	U		-0.5
NE 20	K5			17.65	15.98	17.10	12.53	11.32	10.84		0.2	U		0
NE 21	G8						12.53	11.33	10.84		3.0	E	-6.56	0.5

Table 5.7: Properties for the spectroscopic candidates in the north-western field of RCW 34.

Slit name	Spec Type	u'	g'	r'	i'	Hα	J	H	K_s	Li S/N	Hα S/N	Hα line profile	Hα EW [Å]	$\frac{[Fe]}{[H]}$
NW 1	M7	19.93	18.70	17.35	16.55	17.01	14.99	14.40	14.12		8.2	E	-6.39	-0.5
NW 2	G8			18.03	17.14	17.61	15.40	14.60	14.31		18	E	-0.16	0.5
NW 3	G0			19.33	18.05	18.69	16.27	15.51	15.18		26	A	9.56	-0.5
NW 4	O9						11.75	11.00	10.61		15	A	4.16	0
NW 5	A7						12.21	11.84	11.63		2.4	E?		-0.5
NW 6	M2						16.36	15.32	15.31		3.2	E	-0.44	0
NW 7	F0			18.16	16.83	17.61	14.06	12.99	12.55		9.8	A	2.35	0
NW 8	K5			18.95	17.49	18.52	14.62	13.77	13.31		7.6	A	0.79	0
NW 9	K2			18.54	17.59	18.21	15.51	14.88	14.56	3.3	35	A	1.66	0
NW 10	G7						14.60	13.90	13.64		19	A	0.04	0
NW 11	G9			19.80	18.16	19.26	14.86	13.63	13.14		5.2	U		-2
NW 12	K5						14.86	13.63	13.14		10	A		0.5
NW 13	A6			17.57	16.73	17.21	15.14	14.50	14.19		0.5	U		0.5
NW 14							12.20	11.84	11.63		0.2	U		0
NW 15							13.19	12.71	12.51		3.4	A	0.90	0
NW 16	F4			18.05	17.08	17.63	15.01	14.32	13.99		9.5	A	1.62	0
NW 17	M1						15.01	14.32	13.99		2.2	A?	0.25	-0.5
NW 18	M1			18.89	17.24	18.12	15.25	14.46	14.08		3.9	A		0
NW 19	M0	17.18	16.22	15.39	14.96	15.12	14.15	13.65	13.45		4.7	A	0.06	0.5
NW 20	A1	15.19	14.87	14.27	13.89	14.03	13.20	12.77	12.60		0.1	U		0

Table 5.8: Properties for the spectroscopic candidates in the south-eastern field of RCW 34.

Slit name	Spec Type	u'	g'	r'	i'	Hα	J	H	K_s	Li S/N	Hα S/N	Hα line profile	Hα EW [Å]	$\frac{[Fe]}{[H]}$
SE 1	M2	18.13	16.39	15.11	14.40	14.69	13.26	12.57	12.37		8.4	E	-0.04	0.5
SE 2	F1	18.31	16.94	15.55	14.73	15.19	13.22	12.62	12.34		26	A	4.98	-0.5
SE 3		15.19	14.73	14.07	13.61	13.81	12.80	12.43	12.27		9.7	E	-0.77	
SE 4		15.25	14.32	13.41	12.86	13.12	11.83	11.41	11.22		11	E	-1.56	
SE 5	F0						11.78	11.00	10.61		9.9	A	4.38	0
SE 6	M1	15.25	14.32	13.41	12.86	13.12	11.84	11.41	11.22		0.1	U		0
SE 7	G9	18.13	16.39	15.10	14.40	14.69	13.26	12.57	12.37		4.1	E	-0.05	0.5
SE 8	K7			17.42	15.97	16.97	13.44	12.61	12.20		4.2	A	0.27	1
SE 9	F2			18.84	17.04	18.21	13.38	12.04	11.49		19	A	3.91	0
SE 10	K2	19.72	17.77	16.27	15.34	15.96	13.57	12.98	12.66		0.1	U		0.5
SE 11	G3			17.20	15.97	16.76	13.68	12.94	12.59		26	A	5.26	
SE 12	G9	19.20	17.54	16.08	15.21	15.89	13.68	13.17	12.88		14	E	-0.02	-1.5
SE 13		21.20	18.89	17.06	15.96	16.69	13.94	13.33	12.95		0.6	U		
SE 14	F9			18.65	17.07	18.06	13.99	12.89	12.45		14	A	3.52	-1
SE 15	F6	21.23	19.07	17.53	16.23	16.85	14.50	13.89	13.57		14	A	6.35	0
SE 16	F4			18.89	17.24	18.12	15.25	14.46	14.08		2.4	A?		0
SE 17				18.25	17.17	17.83	15.15	14.37	14.03		0.7	U		
SE 18	M0	14.55	13.58	12.84	12.38	12.67	11.37	11.03	10.82		12	A	2.03	0
SE 19	K4	21.20	18.89	17.06	15.96	16.69	13.94	13.33	12.96		14	A	5.09	-0.5
SE 20		20.08	17.92	16.32	15.34	16.00	13.49	12.93	12.60		0.2	U	1.29	
SE 21		20.59	18.42	16.69	15.64	16.35	13.75	13.17	12.81		0.1	U		
SE 22	M3			18.51	17.28	18.12	15.08	14.37	14.01		10	E	-2.04	-1
SE 23	F1			16.63	15.53	16.21	13.57	12.88	12.54		11	A	6.45	0
SE 24	A6	20.37	18.46	16.93	15.88	16.39	14.31	13.53	13.26		20	A	4.31	-1
SE 25	M6	20.46	18.50	14.07	13.61	13.81	12.80	12.43	12.27		0.2	U	3.39	-0.5

Table 5.9: Properties for the spectroscopic candidates in the south-western field of RCW 34.

Slit name	Spec Type	u'	g'	r'	i'	Hα	J	H	K_s	Li S/N	Hα S/N	Hα line profile	Hα EW [Å]	$\frac{[Fe]}{[H]}$
SW 1	G8			18.72	17.23	17.89	14.94	14.13	13.80		11	A	0.98	0.5
SW 2	F5										18	A		0
SW 3				17.62	16.20	17.11	13.35	12.21	11.77		3.0	E	-0.35	
SW 4		14.13	13.84	13.33	12.97	13.10	12.46	12.06	11.92		0.2	U		
SW 5		18.85	17.19	15.92	15.08	15.64	13.35	12.81	12.50		6.3	A	0.56	
SW 6		18.85	17.32	15.92	15.11	15.54	13.41	12.77	12.53		4.9	E	-0.58	
SW 7	K4	18.84	17.68	16.44	15.71	16.14	14.39	13.75	13.50		16	A	2.62	-1.5
SW 8	K3	14.13	13.84	13.33	12.97	13.10	12.46	12.06	11.92		9.1	A	1.10	-0.5
SW 9	F7	16.55	15.22	14.30	13.83	13.99	13.04	12.54	12.35		12	A	20.59	-1
SW 10	F2			15.92	15.11	15.54	13.41	12.77	12.53		12	A	3.56	0
SW 11	M0	15.19	14.87	14.27	13.89	14.03	13.20	12.77	12.60		0.1	U		0
SW 12		20.57	17.85	15.88	14.76	15.41	12.48	11.55	11.20		0.4	U		
SW 13	F2	16.66	15.88	15.10	14.64	14.81	13.90	13.38	13.20	4.2	31	A	13.82	0
SW 14	G8	17.82	16.80	15.82	15.25	15.50	14.19	13.67	13.44		9.1	A	1.75	0.5
SW 15	M0	18.84	17.68	16.44	15.71	16.13	14.39	13.79	13.50		7.6	A	0.46	0
SW 16	M1						14.57	14.01	13.68		0.1	U		0
SW 17	O9	18.31	16.94	15.55	14.73	15.19	13.22	12.62	12.34		14	A	3.46	0
SW 18	K0			18.73	17.69	18.35	15.56	14.81	14.46		16	A	3.99	0
SW 19	M2	15.19	14.73	14.07	13.61	13.81	12.80	12.43	12.27		0.5	U		
SW 20	K1	21.22	19.20	17.54	16.62	17.13	14.79	14.09	13.81		6	A	0.68	0
SW 21	G8	19.72	17.91	16.53	15.79	16.10	14.53	13.76	13.55		3.3	A	0.33	0.5
SW 22	M2						14.53	13.76	13.55		14	E	-1.62	0
SW 23	G3			17.77	16.89	17.36	14.91	14.09	13.79		10	A	0.81	0
SW 24							13.26	12.57	12.37		0.4	U		
SW 25							13.56	12.87	12.54		0.2	U		

In Tables 5.6-5.9 the properties measured from each Hα-emission candidate are listed. The spectra ranging from 6500-6600Å of the stars with the most prominent Hα-emission lines are shown in the next

subsection, these sources are also highlighted in Tables 5.6-5.9. The full spectra of these stars, and the others given in these tables are shown in Annexure B, characterised according to their Hα-line profile. Out of the 92 stars observed, there were 18 stars that showed Hα-emission, 52 with Hα-absorption, and 22 with an undetermined Hα-profile. Observations with *SALT* can be flux calibrated using standard star data that is obtained close to the time of observation. There was no standard star data available, meaning that the shape of the continuum could not be determined. Each spectrum was flattened by subtracting the fitted polynomial from the spectrum. The flattened spectra of each star, as well as the flattened spectra of the closest matching spectral type from a standard library is shown in Annexure B. It has to be noted that the spectra of M stars have very strong absorption lines, which may appear that the polynomial was not correctly subtracted from the spectrum — this effect is only a result of very strong absorption lines. For the blue spectra the polynomial fit was not as precise as the red spectra, the reason being that the extracted spectra had a lower sensitivity at the maximum and minimum wavelength for each spectra. This meant that there was a stronger decrease of counts in the spectrum at the maximum and minimum wavelength ends of each spectrum. Higher and lower order polynomials were fit to the blue spectra, but this resulted in over and under fitting respectively at the maximum and minimum wavelength ends of each spectrum. A third order polynomial remained the best fit, despite having a residual effect at both the maximum and minimum ends of each blue spectra.

The stars that were used for alignment of the slitmasks were not analysed and are not shown in the tables. For a positive detection of a spectral line its S/N must have been greater than 3. There were 19 stars with a Hα $S/N < 3$, of these 19 there were 4 with an apparent absorption line and 1 with an apparent emission line. The visually identified shape of the Hα profile of these 5 stars are noted, but it is not considered as a definite detection of an Hα-line of NE 14, NE 16, NW 5, NW 17, and SE 16. There are 5 stars that have a Li-absorption line with a $S/N > 3$, of which 2 have an Hα emission line and the other 3 have an absorption line.

Most of the young cluster members are still deeply embedded in the molecular cloud, which implies that there is a significant amount of dust which absorbs a fraction of the light emitted by the young stars, resulting in flatter spectroscopic features. Very young stellar objects have veiling caused by continuum emission from heated circumstellar material. Additionally, the veiling weakens the signal on spectroscopic features and makes the classification of these objects very difficult (see Stuewe & Schultz 1994). To eliminate the veiling from some spectra of very young stars, as was demonstrated by Gahm *et al* (2008), extra spectroscopic observations is needed from circumstellar material around each star. It was not possible to obtain these type of observations for any of the stars in RCW 34 or NGC 2626. There also does not seem to be a correlation between the Hα S/N for a star's spectra and its optical magnitudes. The cause for this apparent lack of correlation between the Hα S/N and the optical magnitudes is not known.

In most of the spectra around RCW 34 the O_2 (6884Å and 6388Å) skylines dominated over the star's spectral emission and could not be fully removed with sky subtraction. The majority of T Tauri stars studied in the literature are K and M stars which, according to Herczeg & Hillenbrand (2014), feature TiO at wavelengths of 6250Å, 6800Å, 7140Å, 7700Å, and 8465Å. Herczeg & Hillenbrand (2014) gives a very detailed description of how the veiling in spectra can be calculated using the flux ratios at specific wavelengths. The absolute flux of the TiO absorption lines were primarily used to determine the veiling for their sample in their study, which included 283 T Tauri stars. In order to use the same method the spectra needs to be absolutely flux calibrated. With no standard star data available the spectra could be absolutely flux calibrated, and the veiling was calculated mainly from the blue wavelength region of the spectrum, which was not available for the stars around RCW 34. This made it difficult, because only the red spectrum was observed for the stars in RCW 34, and the blue spectrum for the sources in NGC 2626 was so noisy that little information could be derived. For most cases where a star has very strong veiling, there are strong emission lines in the spectrum, emitted by circumstellar material or nebulous gas. For most of the stars around RCW 34 the red spectral data mainly showed absorption lines, suggesting that there was no strong veiling in any of the spectra. Even if a young

star had little veiling, many weak absorption lines would be undetectable. If the strength of the lines was affected by veiling it would influence the spectral classification of the star. For the PyHammer method, where a star's spectrum was compared to a standard library, the effects of veiling could not be objectively assessed without testing the correct classification of a star with veiling, of which the spectral type was known. However, the strength of veiling differed at various wavelengths, and some spectral features were not as sensitive to it as others. It was reasonable to assume that PyHammer gives an indication of a star's specific spectral class and metallicity, even though in many cases the low S/N and veiling casted a strong uncertainty over the precision of the indication. Important comments on the spectra of the exciting star, number of Hα-emission stars in each of the four fields, and the number of stars with an Hα-absorption or undetermined line profile are given in the following paragraphs. The comments of the SE region is discussed in a paragraph separate from the NE, NW and SW region, because it had the most stars with Hα-emission and Bik *et al* (2010) showed that there are indeed young CTTs in the bubble region.

(a) VdBH 25a was included as a candidate star in both the NW (slit 4; Figure B.36 in the annexure) and SW (slit 17; Figure B.68 in the annexure) and was classified as an O9V star with PyHammer. Heydari-Malayeri (1988) classified the star as an O8.5V by removing the circumstellar material's emission from the star's spectrum. The close match of the classification for the spectrum of VdBH 25a which included circumstellar emission with PyHammer to that of the cleaned spectrum by Heydari-Malayeri (1988) showed that PyHammer's results for VdBH 25a is accurate.

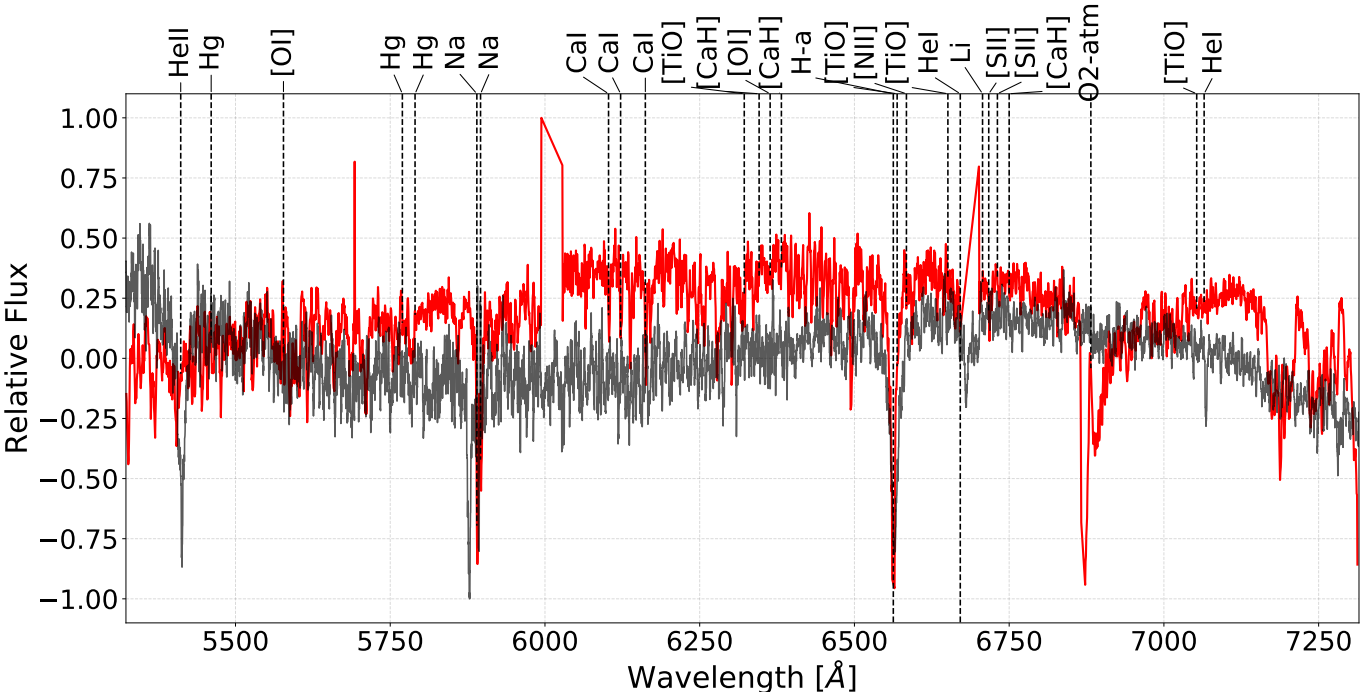

Figure 5.32: The flattened red spectrum of VdBH 25a that was observed through slit 4 in the north-western field of RCW 34. The grey spectrum is the spectral standard of an O9 star, which was the best match to the spectrum of VdBH 25a.

(b) The NE, NW and SW fields are the regions where most of the molecular cloud with high extinction is located. The NE field covers a region where most of the sources with excess *NIR*-emission are located around the outer arch of the HII region. The *SALT* candidates in the NE field were selected across the whole field based on the calculated priority p, and the location optimization algorithm by the `proptools` package. The 5 stars in the NE field that show Hα-emission are on slit numbers 1, 2, 4, 5, and 21 (Figures B.1, B.2, B.3, B.4, and B.5 in the annexure) and are K5, M1, M6, M5, and G8 stars, respectively. The stars in slits 2 and 4 have the Li-(6708Å) absorption line, for slit 1, 5, and

21 the absorption line was not detected. Star 17 in the NE field also had a Li-(6708Å) absorption line, and had an Hα-absorption line — This may be a young PMS star without an accretion disk. The 4 stars presenting Hα-emission in the NW field are in slit numbers 1, 2, 5, and 6 (Figures B.6, B.7, B.8, and B.9 in the annexure) and are M7, G8, A7 and an M2 stars, respectively. The only star with a Li-absorption line in the NW field is the one in slit 9, which also has a Hα-absorption line. The 3 stars in the SW field that show Hα-emission are slits 3, 6, and 22 (Figures B.19, B.20, and B.21 in the annexure), where only the last one could be classified and resembles a G3 star. The 11 stars that showed Hα-emission are a relativly small fraction of the stars that were initially selected as candidates for observation with *SALT*. Of these 11 stars there were only 2 with a Li-absorption line, which is a definite indicator that they are CTTs which are younger than 3 Myr. The other 2 with Li-absorption lines show that there are young PMS stars in the region, which may be older than 3 Myr. The exact location of the stars that showed Hα-emission will be discussed later in this chapter.

(c) The SE field (Bubble region) spans most of the region that is surrounded by the dense molecular cloud and the HII region. There were six stars that showed Hα-emission in the bubble region; the higher number of young stars was supported by the *NIR* and optical photometry, and the studies of Bik *et al* (2010) and Hayashi *et al* (2017). The stars with Hα-emission in the bubble region were summarised in Table 5.8, and their spectra were shown in Figures B.10-B.18 in the annexure. Their spectral classes range from A6 to M3 stars — significantly higher masses than the other Hα-emission line stars in the surrounding regions. The collision of the two molecular clouds that were discovered by Hayashi *et al* (2017) may have triggered the formation of higher mass stars. The presence of these higher mass stars contributed to the clearing of the region faster than the surrounding areas. For seven of the stars in the bubble region no spectral type could be determined, this higher number of unclassified stars may have been due to a lack of absorption lines. The extinction in the bubble region was quite low, so the lack of absorption lines was most likely caused by spectral veiling from circumstellar material.

(d) The stars with Hα-emission were mostly classified with spectral types ranging from A6-M7 with corresponding masses of 1.83-0.09 $M_{\odot}$. All of the masses for these stars fell within the mass range of T Tauri stars. Many of these stars with Hα-emission have noisy spectra and are located in regions with low extinction. If they did not have faint broadband magnitudes (~ 20) then it was a strong sign of veiling from circumstellar material which hid absorption lines that would be detectable in naked photospheric emission. Only the star from slit 2 in the NE field had an Hα EW of $\sim$ 38Å, yet this could not be the only CTTs in the field around RCW 34. The other stars that showed Hα-emission had an EW smaller than 10Å and were most likely WTTs, with ages older than 3 Myr. The number of sources with excess *NIR*-emission suggested that there would be many more CTTs in RCW 34, but the many factors which contributed to p and the spatial distribution of the sources in the selection of *SALT* candidates eliminated these stars. Leading to only 1 star with an equivalent larger than 10Å that was spectroscopically confirmed to be a CTTs.

(e) The stars with Hα-absorption lines and unresolved profiles surprisingly made up most of the sources that were observed with *SALT*. This outcome realised because the sources which did not have the highest priority p were selected as candidates that should be observed with *SALT*. The slitmask tool was used to select as many spectroscopic sources as possible in a single field. The parameter p was used, but the location of each candidate also influenced which were selected. With the priority p, the location of each possible candidate and maximization of the number of sources on the slitmask as selection criteria, the specific group of candidates ended up being chosen. The spectra of each star that showed an Hα-absorption and undetermined spectral profile was shown in Annexure B and C.

5.3.1.2 *NGC 2626*

The spectroscopic and photometric properties of the stars in the field of NGC 2626 are given in Table 5.10. The stars in this field were observed both in the blue and red wavelength ranges. The spectra

for both the blue and red wavelength regimes are shown in Annexure C. The blue spectrum covers a wavelength range from 3500-5500Å and the red spectrum from 5500-7500Å. The blue observations were performed on two occasions under a lower priority than the red set. Both instances had some light overcast. The observation conditions and the extinction of the embedded sources resulted in very noisy blue spectra for most of the observed sources. The noisy blue spectra led to the decision that classification be done in PyHammer using only the red spectra. Similar to the results of RCW 34 the S/N was measured for the Hα, Li in the red and the Hβ and Hγ was measured in the blue, for a positive detection for a spectral line would the $S/N>3$. Similar to the case or RCW 34, if a star had an Hα-emission/absorption line, and the $S/N<3$ then the feature is indicated with a question mark next to the emission or absorption indicator. There were 12 stars with Hα-emission, 8 with Hα-absorption, and 5 with an undetermined spectral profile. There were 3 stars with a Li-absorption line, 9 with a Hβ-absorption line, and 6 stars with a Hγ-absorption line. For the 2 stars with a noted Hα-absorption line without a confirmed S/N the shape of the absorption line was noted together with a question mark. The stars which have an Hα-emission or absorption line, but do not have a measured EW in Table 5.10, either cross the gap between the chips, or the continuum had some zero values, resulting in an EW that can not be measured. The driving star for the Herbig Haro object, HH-132, is one of the stars with an Hα-absorption line. It was allocated a priority of 1 and showed surprisingly good spectral results, a whole subsection is dedicated to an analysis of this object.

Table 5.10: All of the properties for the spectroscopic candidates in the fields surrounding NGC 2626. The classification was done with the PyHammer package and were inspectred by eye.

Slit name	Spec Type	u'	g'	r'	i'	Hα	J	H	K_s	Hβ S/N	Hγ S/N	Li S/N	Hα S/N	Hα line profile	Hα EW [Å]	$\frac{[Fe]}{[H]}$
1	B5			21.57	19.54	19.89	14.41	11.91	10.37	23	21		27	A	11.06	0
2	G6	19.09	17.90	16.06	15.25	15.62	14.07	13.52	13.32	14	7.3		26	A	3.59	0.5
3	A6						16.53	15.92	15.50	8.8	3.8		0.1	U		-0.5
4	M0			18.31	16.54	17.48	13.22	12.07	11.30				3.9	A	0.31	0
5				21.09	18.77	20.45	15.69	15.08	14.68				11	E	-1.17	0
6	G7						14.41	11.91	10.37	9.9	10.3		1.6	A?		-2
7	M7			20.34	17.94	19.61	15.10	14.45	14.02				60	E	-26.33	0.5
8	M0			19.25	17.73	18.81	15.00	14.09	13.59				1.2	A?	0.96	0.5
9	M7			19.60	17.91	18.72	14.02	12.46	11.49				0.4	U		0
10	K3	16.71	16.20	15.18	14.66	14.66	13.94	13.35	15.18	4.5			6.1	A	0.62	0
11	F2			18.53	17.05	18.10	14.30	13.36	12.91				0.2	U		-1
12	M8	15.81	15.36	14.36	13.78	14.10	13.00	12.63	12.52				10	E	-7.78	0.5
13	M7			21.06	18.58	19.95	15.37	14.21	13.44				0.0	U		0
14	K5	14.95	14.52	13.64	13.18	13.37	12.59	12.19	12.08				26	E	-0.09	-2
15	M0	21.07	20.97	18.85	17.15	17.79	14.37	13.21	12.57	7.7	5.2		15	A	2.52	0.5
16	K5	19.64	19.27	17.25	15.84	16.30	12.39	10.68	9.54				26	E	-3.69	-2
17	F7	15.93	15.59	14.65	14.13	14.38	13.47	13.07	12.97	9.5			24	E	-60.24	-0.5
18	K5						13.27	10.88	9.34			3.2	18	E	-2.04	-2
19	M7						18.67	17.48	16.81				23	E	-8.05	-0.5
20	G6			20.43	19.33	20.03	16.82	15.88	15.49				25	E	-24.80	-0.5
21	G6						16.68	15.27	14.39	35	15	3.1	38	A	4.99	0.5
22	M0			19.19	17.70	18.52	16.09	15.51	15.09				0.1	U		0.5
23	K6	18.48	17.37	15.80	14.82	15.48	13.16	12.41	12.10	7.8		3.7	30	E	-5.29	-0.5
24	M7						16.63	14.97	13.80				62	E	-4.99	0.5

The stars with an Hα-emission line in NGC 2626 are in a smaller field, and at a closer distance than those in RCW 34. This made it possible to observe the candidates with the highest probability all in a single instance. Out of the 24 stars observed, there were 11 stars that showed an Hα-emission line. Out of the 11 there are 3 stars that had an Hα EW's > 10Å, implying that they are CTTs. The spectral classification of these 3 CTTs is an M7, F7, and G6 star respectively. Only 2 out of the 11 Hα-emission line stars had a Li-absorption line, indicating that these CTTs were younger than 3 Myr. The spectral type of these 2 stars were given by PyHammer as K5 and K6.

5.3.2 The spectra and line profiles for the stars with the most prominent Hα-emission lines

In this subsection the stars which showed the highest S/N or highest EW Hα-emission lines from the previous results are shown and analysed. The sources which had a Hα-emission line which stretched

across only a single, two or three bins, or the Hα-profile varied between the noise level and higher levels between neighbouring bins were not included because it was not clear where the Hα profile started or ended. From the Hα-emission line profiles radial velocity measurements were performed with the equation:

$$v = c\frac{\lambda_0 - \lambda}{\lambda_o}. \tag{5.4}$$

In this equation, $c = 299792.458$ km/s which is the speed of light in a vacuum, λ_0 is the wavelength of the specific spectral profile when observed at rest, and λ is the wavelength at which the specific spectral line was observed from the source. To use this formula the wavelength calibration of the observed spectrum had to be very precise. To explain how important an accurate wavelength calibration is, suppose there is an uncertainty of 1Å in equation 5.4 for the position of the Hα-line. The corresponding uncertainty in velocity would be $\Delta v = \frac{c}{6562.801} = 45.68$ km/s. The projected spectra on the RSS has a binning resolution of 0.32Å per pixel, meaning on a 2×2 binned image a resolution of 0.64Å, or velocity bin resolution of ~ 30 km/s. The uncertainty in the wavelength calibration in the red wavelength regime had an average offset value of ~ 2.8Å. The uncertainty in the wavelength offset, together with the wavelength intervals of the pixels, gave an uncertainty in the wavelength offset of 3.5Å, or 160 km/s. With these large uncertainties it did not make sense giving a detailed analysis for the radial velocities. The corresponding velocity profiles may reveal some information about the dynamics of the gas emitting the light. Most of these stars also featured other emission lines which are prominent in other T Tauris systems. The two most prominent lines that featured in most of the emission line stars observed with *SALT* were the Fe[I]-(5576.097Å) and O[I]-(6300Å) lines. A radial velocity profile was also derived for each using equation 5.4, with their respective wavelengths at rest. The radial velocities calculated for Fe[I] and O[I] were plotted together with the Hα-line, to get an idea of the radial velocity of the star.

The Hα-line profile could reveal much about the heated gas contributing to its extra emission. Even though there was a significant uncertainty in the measured radial velocity, the velocity profile that was derived with equation 5.4 could give information about the gas dynamics around the star-disk system. The velocity profiles were compared with a radiative transfer model of a CTT star-and-disk system by Kurosawa *et al* (2005). The model includes gas that contributes to Hα-emission from both the accretion inflow and wind outflows. The model is complex, because it has to reproduce the full line profile that was observed from the system. It is a radiative transfer model for emission from a magnetospheric-accretion-disk system, where the blue-ward shifted asymmetric component is caused by a partial occultation of the flow of inward falling matter by the stellar photosphere. The model resembles an inverse P Cygni profile for emission from the magnetospheric accretion model. The emission is a result from inflowing material at near free-fall velocities that is projected against hotspots on the stellar surface (see Muzerolle *et al* 2001). The stellar wind outflow is based on a model by Alencar *et al* (2005), where the Hα, Hβ, and Na-doublet lines are best described by a model which include a collimated disk-wind arising from near the inner edge of the accretion disk. The model also takes physical circumstances of the star-disk system into account for the light emitted from the system.

The radial velocity profiles were compared to the different model parameters that influenced the Hα-emission line profile. No physical velocities were measured from the line profile because of the large uncertainties in the wavelength binning and calibration. A qualitative description is given for the line profiles which is the dominating factor in the emission of the Hα-line.

In the following subsection the spectra around the Hα-line of the stars with the most prominent Hα-emission line profiles were shown; for the full spectra of each star in RCW 34 please see Annexure B and for NGC 2626 see Annexure C. The spectra were followed by the velocity profiles for the Hα, Fe[I], and O[I] lines which were plotted together in the same velocity-diagram.

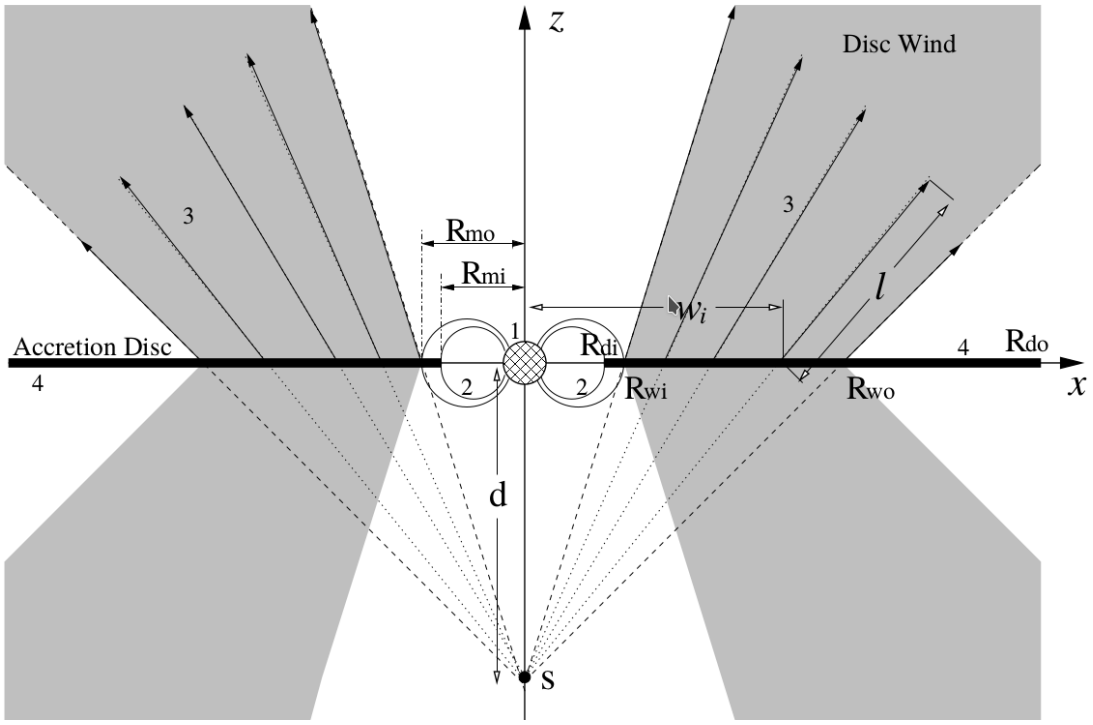

Figure 5.33: An illustration of the radiative transfer model by Kurosawa *et al* (2005) and the physical parameters that are used in the model. It show the different physical contributors in the model by Kurosawa *et al* (2005) that affect the Hα-emission line profile that is observed from a CTTs. The star-disk system model the following properties: $R_* = 2\ R_\odot$, $M_* = 0.5\ M_\odot$, $T_{\rm photosphere} = 4000$ K, $R_{mi} = 2.2\ R_*$, $R_{mo} = 3.0\ R_*$, $\dot{M}_{acc} = 10^{-7}\ M_\odot.yr^{-1}$, $\dot{M}_{wind} = 10^{-8}\ M_\odot.yr^{-1}$, $R_{di} = 2.2\ R_*$ and $R_{do} = 100$ AU. This figure and the three below are taken from Figures 1, 4, 5, and 6, respectively in the paper by Kurosawa *et al* (2005).

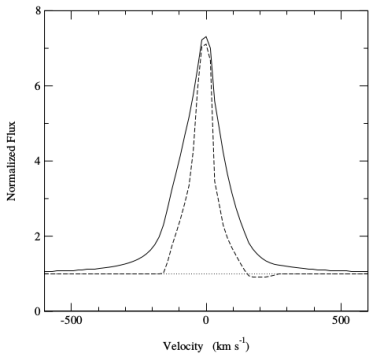

Figure 5.34: The effects of dampening on the Hα-emission line is illustrated. Dampening is affected by the physical conditions of the gas, which includes the hydrogen particle density, the number of free electrons, and other microscopic properties. With an increase in dampening the line broadens and the equivalent width increases.

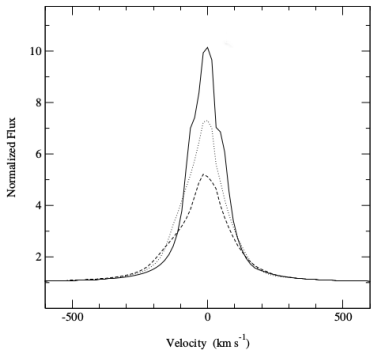

Figure 5.35: The effects of the inclination angle on the emission line. With an increase in the inclination angle the strength of the emission line decreases. The profile also broadens a bit due to the doppler shift that is seen in the infalling gas.

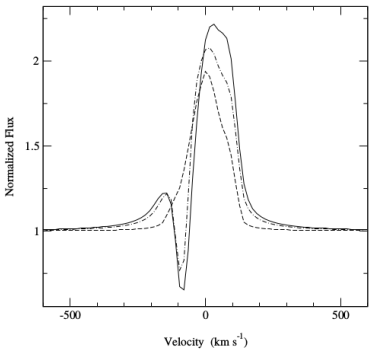

Figure 5.36: The dependency of the Hα-emission line on the source displacement value (d) is shown. If the wind becomes more collimated, the wind emission becomes stronger. The P-Cygni absorption disappears for the model with a small collimation, since the opening angle of the disk wind is larger than the inclination angle.

5.3.2.1 *RCW 34*

For full-page representations of the spectra shown here please refer to Annexure B. The spectra shown in Figure 5.37 only give a high level view of the spectra around each star's Hα-line. The spectra for NE slit 1, 2, 4, SE slit 22, and SW slit 22 have strong Hα-emission lines or interesting profiles which required a more detailed analysis. These spectra have the least noise in the continuum emission. NE slit 2 has two strong emission features next to each other in the region of the Hα-line. There are stars listed in Tables 5.6-5.9, such as NW slit 5, which show an emission feature around the Hα-line, yet the Hα S/N is too small to confirm the presence of the emission line. In these spectra and the others shown in the Annexure, the O_2 skylines at 7621Å and 6884Å are present, because the skylines were dominatingly brighter than the stellar spectra. NE slit 2 and NW slit 5 had a hybrid Hα-line profile; it is an emission line conjoined with an absorption line. Kurosawa *et al* (2005) showed that this is caused by a partial amount of wind-absorption. Moreover the angle between the wind and the inclination angle of the disk is less than 60° which causes the wind not to properly launch from the star. SE slit 12 has an Hα-line profile which shows a broad absorption line, as well as an emission line at the centre of the profile. This Hα-profile is similar to a model by Petrenz & Puls (1996) where the absorption line from the star is seen, and the emission line emanates from a heated stellar wind originating from the star. Other profiles similar to SE slit 12 were observed by Israelian & de Groot (1999) of a very narrow Hα-emission line at the centre of a broad absorption line in P-Cygnus. A P-Cygnus line profile is caused by hot stellar winds leading to strong mass loss. For this case the emission line was much weaker, which may indicate much less mass loss from a stellar wind.

Table 5.11: The width of the Gaussian fitted to each Hα-emission line profile in RCW 34.

Slit	FWHM [km.s^{-1}]	Error [%]
NE slit 1	400±60	15
NE slit 2	235±50	21
	235±50	21
NE slit 4	165±40	24
NE slit 5	140±40	29
	70±30	43
NW slit 2	70±30	43
	220±50	23
SE slit 12	330±55	17
SE slit 22	400±60	15
SW slit 22	1100±135	12

The velocity profiles in Figures 5.38a-5.38h show the Hα, Fe[I], and O[I] emission lines as red, green, and blue plots, respectively. Equation 5.4 was used together with the characteristic wavelength (λ_0) of each line to calculate the radial velocity. The three line profiles were all plotted together in the same velocity diagram. A Gaussian profile was fitted to the Hα-emission line profile in Figure 5.38a, 5.38b, 5.38c, 5.38e, 5.38f, 5.38g, and 5.38h. A Gaussian was fitted to an identified emission/absorption feature, of the fitted parameters the standard deviation was used to get an indication of the FWHM for the emission line. The uncertainty in the wavelength calibration was stated as 3.5Å, which gives an uncertainty of 160 km/s for a velocity measured from the central line velocity. A consequence of the large uncertainties in the velocity measurements is that of the fitted parameters for the velocity profiles only the width of the velocity profile is measured. Thus in Table 5.11 only the FWHM of the fitted Gaussian is given and not the central velocity, because the value fitted for the central velocity is much smaller than the 160 km.s^{-1} uncertainty, due to the wavelength calibration. The uncertainty on each FWHM was calculated by using the uncertainty on each pixel in velocity space ($\sim$ 30 km.s^{-1}, or $\sim$ 15 km.s^{-1} per side), together with the fitting of the Gaussian where the error on the y-axis was taken as the noise level. The error on the Gaussian was calculated as part of the profile fitting. The relative error decreases for the broader Gaussian profiles, because more bins contribute to a better fit for the Gaussian profile, and the uncertainty on each bin decreases relative to the width of the Gaussian. The large uncertainties in the wavelength calibration does imply that the central line velocity cannot

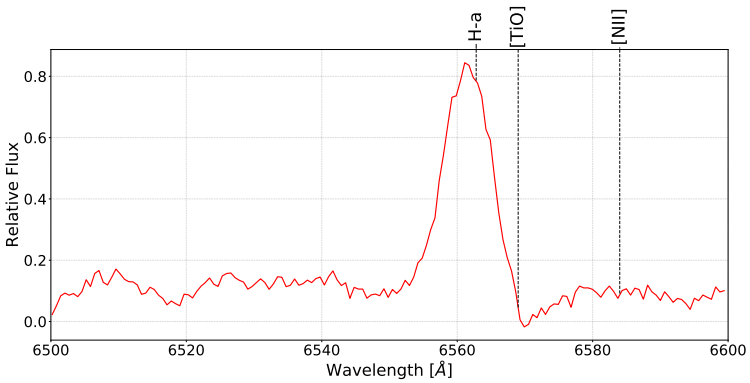

(a) Slit 1 in the NE field of RCW 34

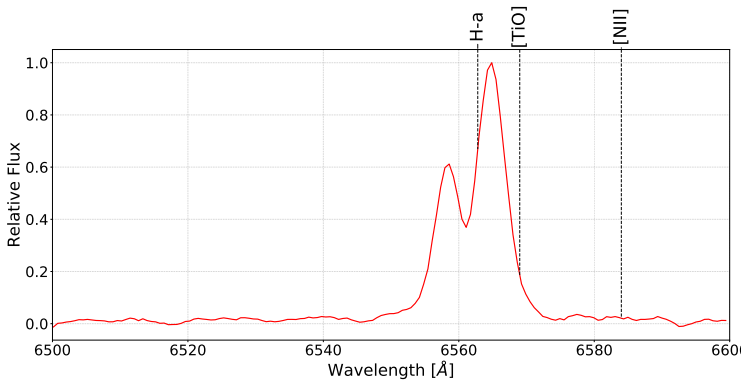

(b) Slit 2 in the NE field of RCW 34

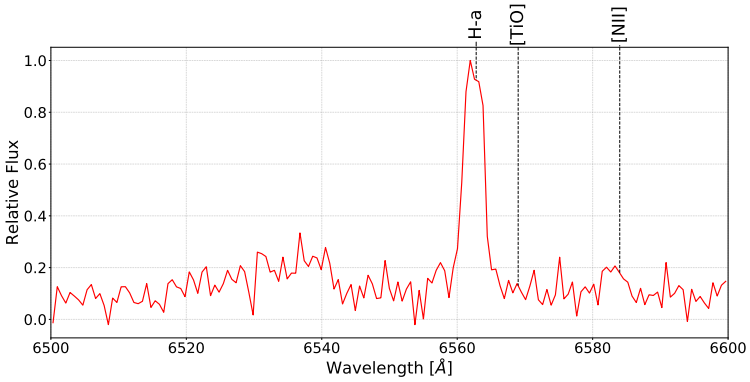

(c) Slit 4 in the NE field of RCW 34

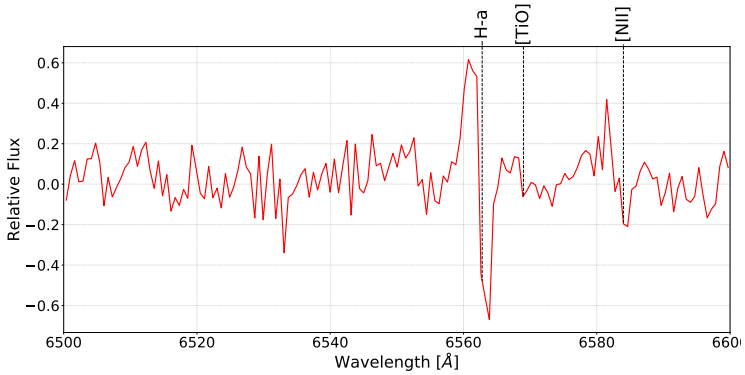

(d) Slit 5 in the NE field of RCW 34

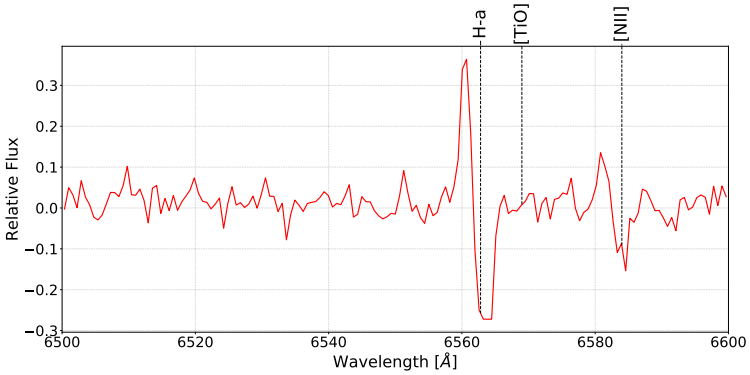

(e) Slit 2 in the NW field of RCW 34

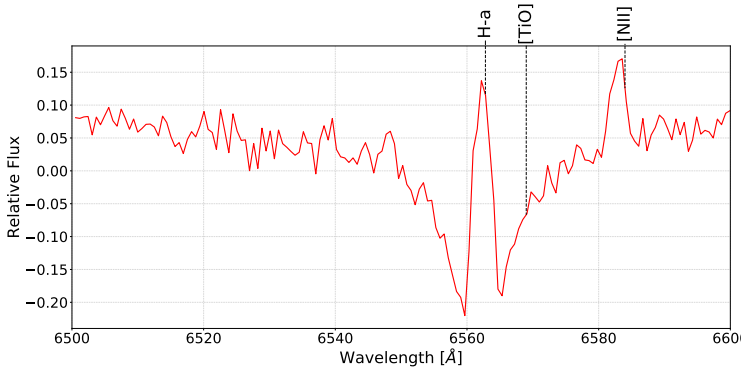

(f) Slit 12 in the SE field of RCW 34

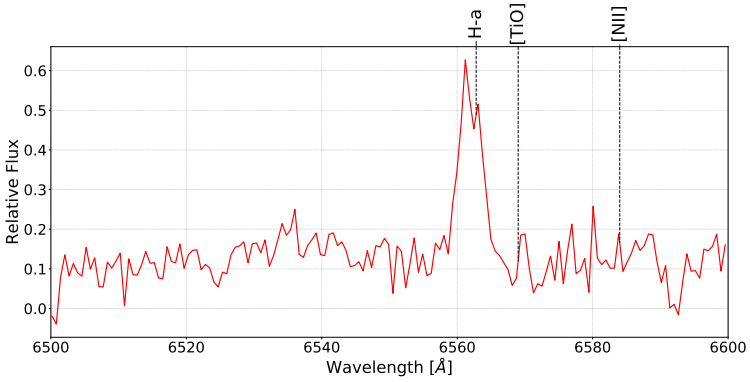

(g) Slit 22 in the SE field of RCW 34

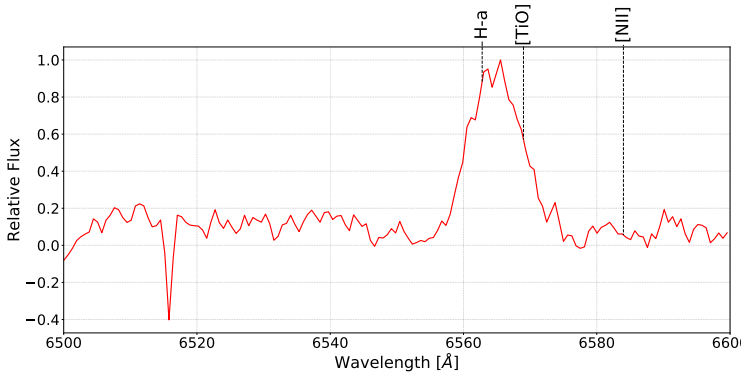

(h) Slit 22 in the SW field of RCW 34

Figure 5.37: The spectral candidates in RCW 34 with the most prominent Hα-emission line profiles.

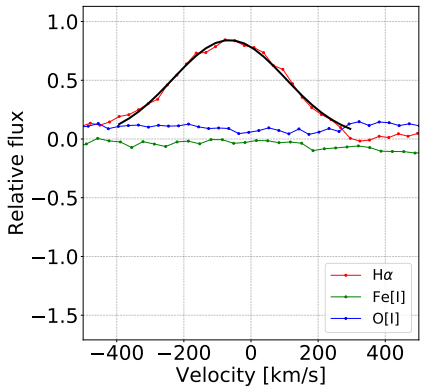

(a) Slit 1 for the NE slit of RCW 34

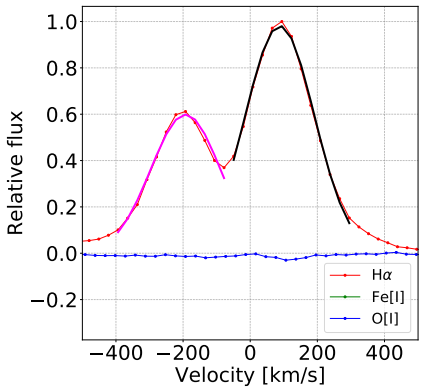

(b) Slit 2 for the NE slit of RCW 34

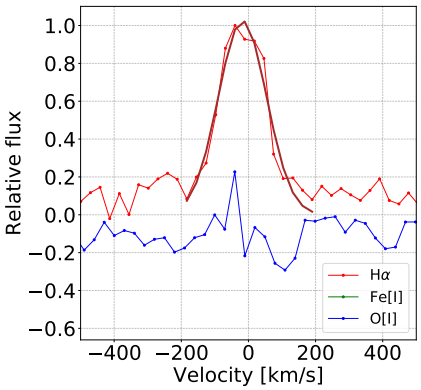

(c) Slit 4 for the NE slit of RCW 34

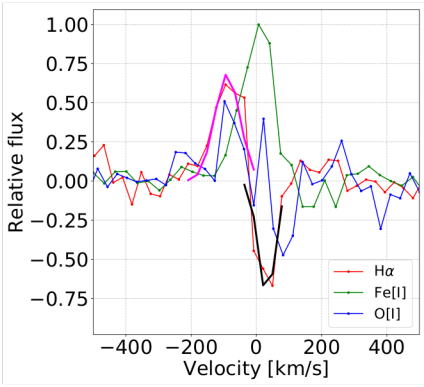

(d) Slit 5 for the NE slit of RCW 34

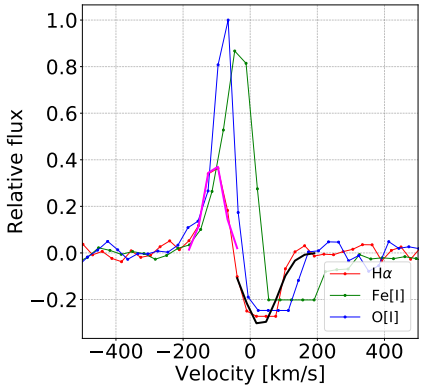

(e) Slit 2 for the NW slit of RCW 34

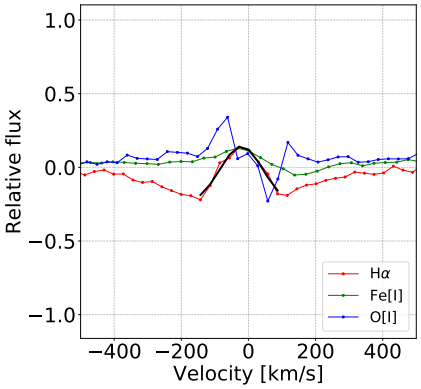

(f) Slit 12 for the SE slit of RCW 34

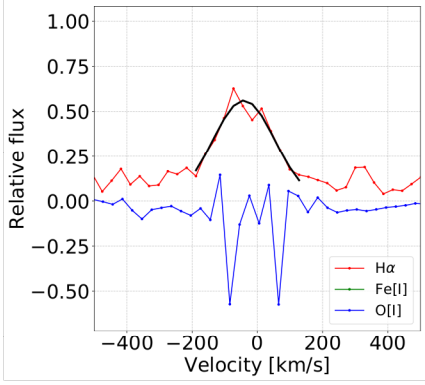

(g) Slit 22 for the SE slit of RCW 34

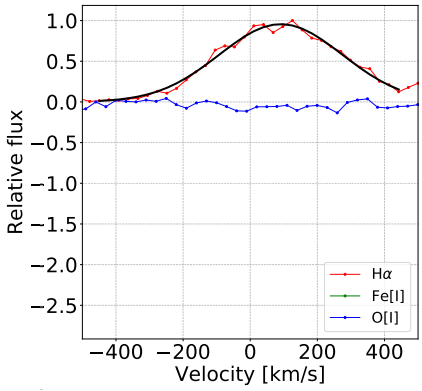

(h) Slit 22 for the SW slit of RCW 34

Figure 5.38: For each star that has an Hα-emission line a Gaussian profile is fit so that the corresponding spread of the emission line can be measured.

be accurately measured, but the width of the velocity profile does give some insight into the physical conditions of the gas contributing to the Hα-emission line profile.

- NE slit 1-(K5 star with $M_* \sim 0.72\ M_\odot$) had a broad Hα-emission line velocity profile and a Gaussian function was fitted to the profile. The standard deviation of the fit Gaussian had an equivalent FWHM of 400 km.s^{-1}. The broadened profile can either be caused by dampening in the disk, or it may be an inclination effect. It may also hold some velocity components from the accretion disk that contribute to the Hα-line emission.

- NE Slit 2-(M1 star with $M_* \sim 0.53\ M_\odot$) has two strong emission features around the Hα-line. Both the Gaussians have an equivalent FWHM of 235 km.s^{-1}. This profile can either be caused by a

binary system where both stars contribute to the Hα-emission, similar to the KH 15D system studied by Hamilton *et al* (2012), or the emission line profile can be caused by bi-polar outflows that dominate the Hα-emission.

- NE slit 4-(M6 star with $M_* \sim 0.1\ M_\odot$) had a strong Hα-emission line, which has a FWHM equivalent to ~ 165 km.s^{-1}. This star had a high Hα S/N of 19, and a Li-absorption line which is an indicator that it is young PMS star, the EW of the Hα line is -3.81 which would not fall under the CTTs but rather WTTs. Magazzu *et al* (1992) showed that WTTs similar to NE slit 4 did have Li-absorption lines with an age older than 3 Myr, but younger than 10 Myr.

- NE slit 5-(M5 star with $M_* \sim 0.15\ M_\odot$) showed a Hα-profile similar to a reverse P Cygni profile, which is a combination of a Hα-emission line conjoined to an absorption line, as shown in Figure 5.36. A separate Gaussian was fitted to the emission component and to the absorption component, each had a respective FWHM of 140 km.s^{-1} and 70 km.s^{-1}. The Hα-line had this profile because Israelian & de Groot (1999) explains that the emission from a P Cygni profile arose from heated gas around the star, and the blue-shifted absorption lobe which emanating from radiation passing through circumstellar material rapidly expanding in the direction of the observer. For this case the Hα-line has a reverse P Cygni profile, which means that the material causing the absorption line was red-shifted — or in other words the material was moving away from the observer.

- NW slit 2-(G8 star with $M_* \sim 0.94\ M_\odot$) showed an Hα-profile similar to that of NE slit 5, a reverse P Cygni profile. Two Gaussian profiles were fit to the emission and absorption line, the respective peaks of the profiles were at -110 km.s^{-1} and 30 km.s^{-1}, and the respective FWHM for each profile was 70 km.s^{-1} and 220 km.s^{-1}.

- SE slit 12-(G9 star with $M_* \sim 0.90\ M_\odot$) had a broad Hα-absorption line with a weak emission line at the centre of the profile. A Gaussian was fitted to the emission component, and it had FWHM of 330 km.s^{-1}. The Fe[I] and O[I] profile seem to have a partial absorption and emission line profile in opposite velocity directions. The model by Petrenz & Puls (1996), for more massive stars, explains that a hot stellar wind leads to extensive mass loss. This star was classified as a G9 star with PyHammer, which may explain why the Hα-emission line is weak relative to an O star which presented a strong narrow Hα-emission line for a very hot stellar wind.

- SE slit 22-(M3 star with $M_* \sim 0.39\ M_\odot$) had a Hα-emission line of which the Gaussian function had a FWHM of 400 km.s^{-1}.

- SW slit 22-(M2 star with $M_* \sim 0.48\ M_\odot$) has an extended Hα-emission line for which the fitted Gaussian had a FWHM of 1100 km.s^{-1}. This flat profile was most likely caused by an inclination effect, and it was difficult to distinguish from continuum emission.

Of the 8 figures shown, the Hα-line was widely distributed over a few velocity bins. All of the velocity profiles showed a prominent emission profile relative to the baseline, and the spectra were flattened in such a manner that the continuum varied around 0. The Gaussian fitted to each Hα-emission line gave an indication of how broad the emission line profile was. With the large uncertainties of the calculated velocities the width of the Gaussian should not be taken as an accurate measurement, but as stated before a rough estimate. The radial velocity that was measured for VdBH 25a by Heydari-Malayeri (1988) was +25.9 km.s^{-1} and is considered as the most accurate radial velocity for the whole cluster.

5.3.2.2 *NGC 2626*

The 5 stars in NGC 2626 that have the most prominent Hα-emission line profiles are shown in Figures 5.39a-5.39e.

- Slit 12-(M8 star with $M_* \sim 0.077\ M_\odot$) and slit 24-(M1 star with $M_* \sim 0.53\ M_\odot$) both had narrow, strong Hα-emission lines with respective S/N of 10 and 62. In both cases the Fe[I] and O[I] emission lines were detected, which suggested that there was nebulous emission present in both cases.

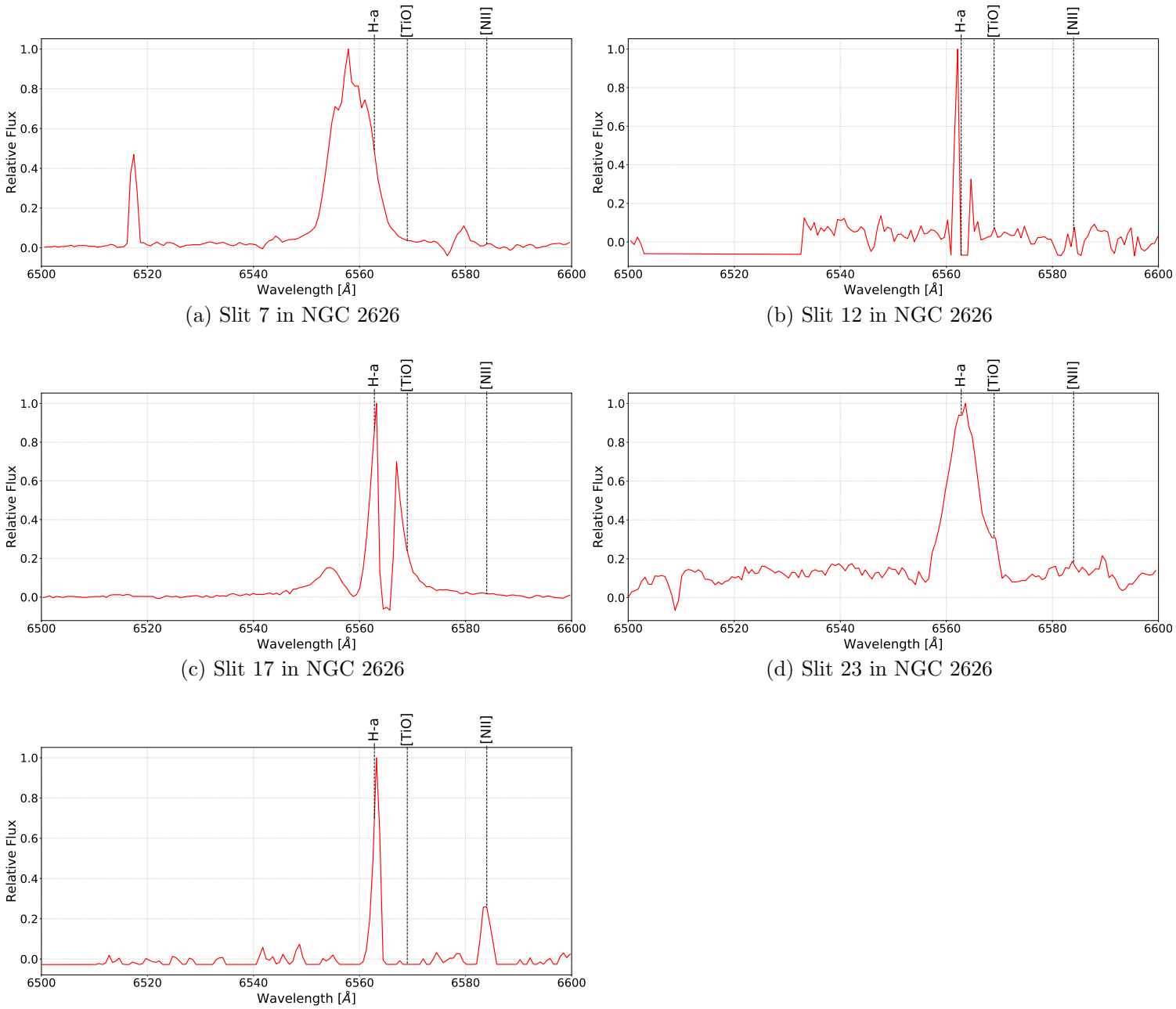

(a) Slit 7 in NGC 2626

(b) Slit 12 in NGC 2626

(c) Slit 17 in NGC 2626

(d) Slit 23 in NGC 2626

(e) Slit 24 in NGC 2626

Figure 5.39: The spectral candidates in NGC 2626 with the most prominent Hα-emission line profiles.

- Slit 7-(M7 star with $M_* \sim 0.09\ M_\odot$) presented a very strong and broad Hα-emission line, which had a S/N of 60 and EW of -26.33. This spectral profile did suggest that Slit 7 was a CTTs. Many other emission lines were also present in the spectrum, these may have originated from circumstellar nebulous emission.

- The Hα-line of slit 18-(K5 star with $M_* \sim 0.72\ M_\odot$) was not analysed here, because the EW was not higher than 10, or the profile was nothing out of the ordinary. It had to be noted that a Li absorption line was detected in its spectrum, thus was most likely a WTTs. Similarly slit 20 had a confirmed Li-absorption line, and a Hα-absorption, this suggested that it may be a naked T Tauri, or as defined in Walter (1986) a young PMS star without a accretion disk.

- Slits 4-(M0 star with M_* ~0.6 $M_\odot$), 14-(K5 star with M_* ~0.72 $M_\odot$), 16-(K5 star with M_* ~0.72 $M_\odot$), and 19-(M7 star with M_* ~0.09 $M_\odot$) had Hα-emission lines, but these did not show any unique characteristics, thus they were not analysed here in detail. Slit 20-(G6 star with M_* ~0.97 $M_\odot$) had a particularly strong Hα-emission line, but it ran over the gap between the imagers, and was thus also ignored.

- Slit 17-(F7 star with M_* ~1.21 $M_\odot$) has a very strong and complex Hα-emission line profile, and other emission lines that include the Fe[I] and O[I] lines. The Hα-emission line has a very broad profile that includes a narrow deep absorption component.

- Slit 23-(K6 star with M_* ~0.70 $M_\odot$) has a broad Hα velocity profile of which the fitted Gaussian had a FWHM of 700 km.s^{-1}. The physical cause for the broad profile may be the result of a projection effect. There was also Li-absorption line confirmed, the Hα emission line's EW was smaller than 10Å, which indicated a WTTs.

Velocity profiles of Hα-emission lines profiles: The properties of the Gaussian functions that were fitted to Hα-emission line profiles are as follow:

Table 5.12: The width of the Gaussian fitted to each Hα-emission line profile in NGC 2626.

Slit	FWHM [km.s^{-1}]	Error [%]
Slit 7	450±60	13
Slit 12	50±25	50
Slit 17	110±40	36
	200±50	25
	270±50	19
Slit 23	670±70	10
Slit 24	70±30	43

- The Hα-line for slit 7 showed a wide profile with fluctuations at the peak of the profile, the Gaussian had a FWHM of 450 km.s^{-1}. According to the models of Hamilton *et al* (2012) a similar line profile was obtained for a binary system. An alternative description for the line profile was given by Kurosawa *et al* (2005) as an inclination effect. If the broad velocity profile was Gaussian then the deviations from a typical Gaussian profile at the peak was caused by a binning effect and not physical circumstances at the source.

- The Hα-line for slit 12 had a narrow Hα-emission line, the best fit Gaussian had a FWHM of 50 km.s^{-1}. The model by Kurosawa *et al* (2005) showed that the width of the Hα-emission line may be dependent on the effects of damping.

- Slit 17 showed two emission lines close together around the Hα-emission line profile, similar to the NE slit 2 for RCW 34. A Gaussian was fit to the red and blue emission features. If the red and blue components were emitted from the same source then their emission profile may be represented by a larger Gaussian emission profile. A large Gaussian was fitted over the emission profiles which were not influenced by the apparent absorption line, thus the tails from -200 to 0 km.s^{-1} and from 200 to 300 km.s^{-1}. The region between these tails was considered to be part of an absorption line, which may be a result of the star's photosphere that was observed. The line profile was also similar to the Hα-profile for the Herbig Ae star BF Ori. Reipurth *et al* (1996) explained that BF Ori is a variable Herbig Ae star which was classified as an A5III by Grinin *et al* (2001). Yet the star in slit 17 was classified as a F7 with PyHammer, eliminating it as a Herbig Ae/Be star. The similarities between BF Ori, the mass loss model by Kurosawa *et al* (2005), and this Hα-line profile were best described by bi-polar outflows.

- Slit 23 has a broad Hα velocity profile of which the fitted Gaussian which had a broad FWHM of

670 km.s^{-1}. The physical cause for the broad profile may have been the result of a projection effect.

- The Hα-line for slit 24 had a strong and narrow profile, of which the Gaussian had a FWHM of 70 km.s^{-1}. Similar to the Hα-profile of the star in slit 12, the model by Kurosawa *et al* (2005) describes the narrow profile to a damping effect.

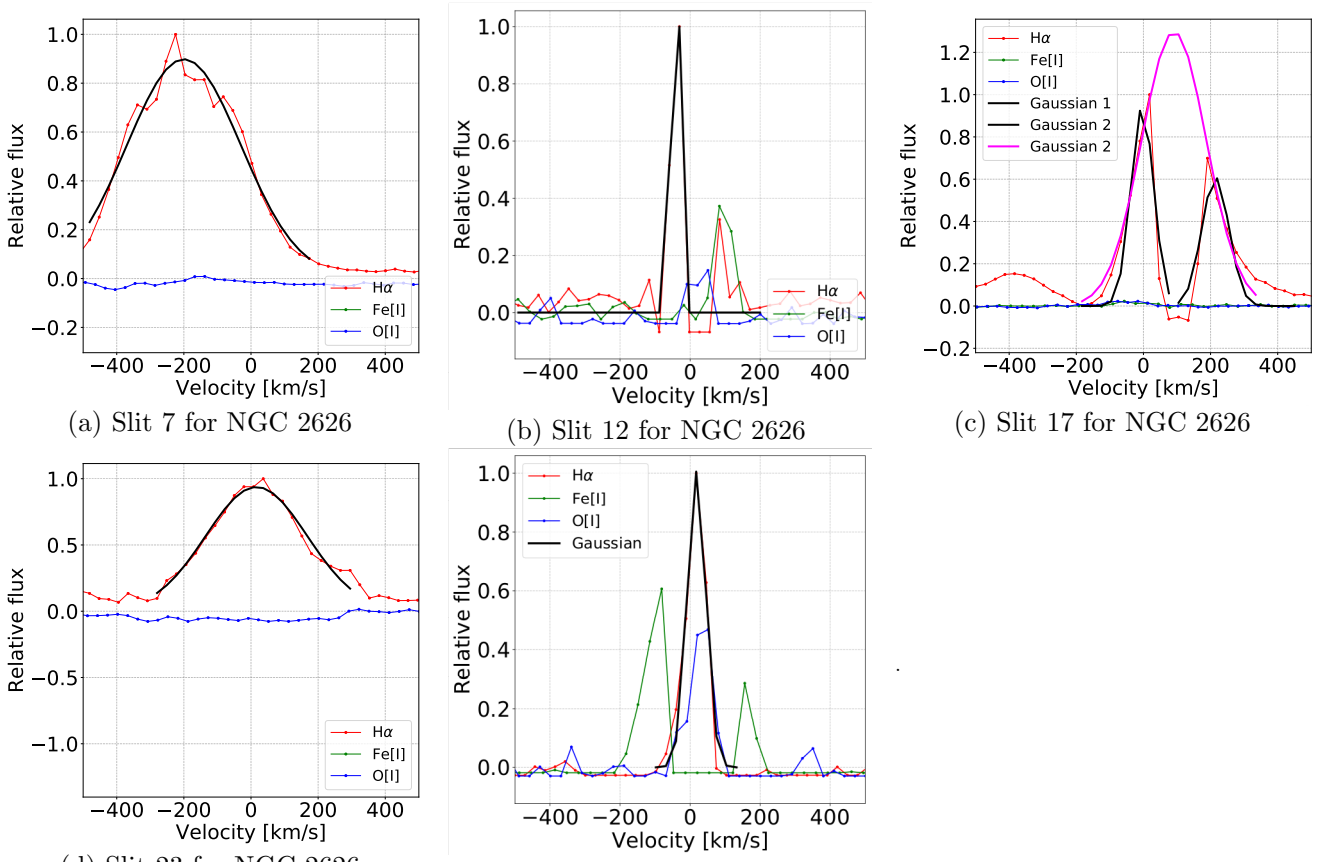

(a) Slit 7 for NGC 2626

(b) Slit 12 for NGC 2626

(c) Slit 17 for NGC 2626

(d) Slit 23 for NGC 2626

(e) Slit 24 for NGC 2626

Figure 5.40: For each star that has an Hα-emission line a Gaussian profile is fit so that the spread of the emission line can be measured.

In each case where the velocity profile was described for RCW 34 and NGC 2626 the FWHM was given. The radial velocity was not derived for any star, due to the large uncertainties involved in the velocity measurements. The FWHM of each line as well as the most likely physical cause for the velocity profile could be described using the models from Kurosawa2005, Hamilton *et al* (2012) and Israelian & de Groot (1999). It is challenging to give a physical description of a Hα-emission line profile without the help of a numerical model; The reason is the Hα-line observed is a collective observation of the star-disk system, as well as any in-flowing/out-flowing gas.

5.3.3 The metallicities for cluster members

The metallicity of a star is a term that is used to describe how much of a star's content is made up of elements heavier than hydrogen or helium (see Carroll & Ostlie 2006). The metallicity of the Sun $\left(Z_{\odot} = \frac{\text{Fe}}{\text{H}}\right)$ has been thoroughly studied (see Asplund *et al* 2009) and it is used as the standard measurment for the metallicity of other stars. This means that the metallicity of any other star is measured relative to that of the Sun: $Z_* = \log_{10}\left(\frac{[\text{Fe/H}]_*}{[\text{Fe/H}]_{\odot}}\right)$.

In the introduction of the results and analysis section it is explained that PyHammer uses the EW of a standard set of 34 spectral lines to iteratively classify input spectra. The metallicity measurement was done in the same method as the spectral classification; the measured line strengths of the

detected absorption lines were compared to a standard spectral library. The library had entries for the different metallicity of each spectral type, and the matching was done using a χ^2-fit between the spectral lines identified in the input spectra and the library. The best fitting match was used, not just for the spectral type classification, but also the metallicity of the star. The precision of the metallicity measurement was not as accurate as the spectral type measurement, but the initial testing of the software gave an indication that the classification was accurate. The spectra of the stars observed with *SALT* in RCW 34 and NGC 2626 suffer more extinction than those in the spectral libraries. The increased extinction may have affect the equivalent widths of the standard spectral lines measured by PyHammer. With the effects of extinction and the inaccuracies in the measurement of the metallicities given by PyHammer, a star's output metallicity was regarded as a rough indication of either solar like or differing, in intervals of $\Delta Z_* = 0.5$. For each group of stars in RCW 34 and NGC 2626 the measured metallicities would serve as an indicator to which metallicity should be used in evolutionary models that were compared to the photometric data in the next chapter.

5.3.3.1 *RCW 34*

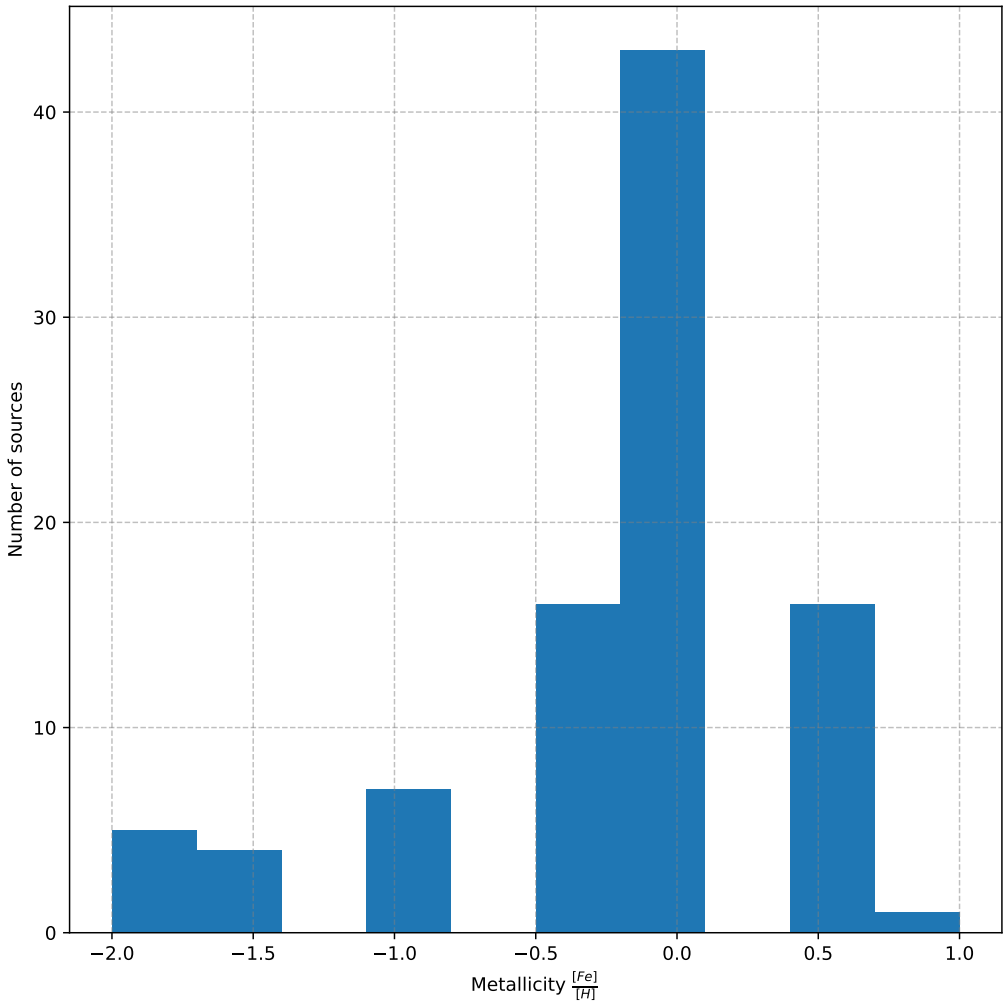

Figure 5.41: The distribution of metallicities measured of the stars observed with *SALT* in RCW 34.

All of the stars in an open cluster form from the same initial molecular cloud, so they should all have the same initial abundances. In an embedded cluster the brightest star, or in the case of RCW 34, the young high-mass star VdBH 25a, would give the best indication for the metallicity of the stars in the cluster. The metallicity for VdBH 25a was not measured by Vittone *et al* (1987) due to very weak iron lines, or by Heydari-Malayeri (1988) who spectroscopically classified it as an O8.5V star. The

stars with Hα-emission were considered to be associated with the star-forming region. There was no definite way of determining whether the stars with an absorption or unresolved Hα-line were either cluster members or field stars. They could not be discarded on this uncertainty, because (1) their metallicities may be more precise than those with an Hα-emission line, and (2) the larger number of stars with an unresolved/absorption Hα-line gave a better contribution to an average metallicity for the cluster.

In Figure 5.41 the distribution of the metallicities of the spectral candidates is shown. All of the stars that were observed with *SALT* were included in the distribution. The majority of the stars (51 out of the 92) had a metallicity of 0 or -0.5, suggesting that the average for the cluster may be in this region. Even though not all of the stars that were included in this population were cluster members, there had to be some that did form part of the cluster. This measurement of the metallicities was a very rough attempt of measuring the average metallicity of the cluster. In the distribution there were stars with a metallicity larger than 0.5, and smaller than -0.5. This difference would mean that the stars had a metallicity with a factor 10 times less, or 10 times more than the metallicity of the Sun. A solar metallicity is typical for most of the stars in the Milky Way plane (see Chen *et al* 2003). A factor difference of 10, or more, would imply a radical difference in the typical conditions from which most clusters in the Milky Way have formed, and is very unlikely. Suggesting that a factor difference of 10 times more, or 10 times less than a solar metallicity may have been a systematic error. The large difference in metallicity classifications may be the reason why some stars are classified into classes with a factor 10 difference with solar metallicity. Upon inspection of NE slit 8, which was classified to have a metallicity of -1.5 the spectrum had a large collection of absorption lines. If the metallicity was determined relative to the Hα absorption line, either the Hα line may have been subject to additional emission from nebulous gas, or the other absorption lines (elements heavier than Hydrogen — meaning metals) may have been subject to veiling. If these absorption lines were subject to anything other than photospheric emission the metallicity may have been incorrectly calculated by PyHammer.

5.3.3.2 *NGC 2626*

In Figure 5.42 the distribution of the metallicity that was derived from the red wavelength regime for all of the spectral candidates in NGC 2626 was given. The star associated with HH-132 had an acceptable Hα (S/N=27), Hβ (S/N=23), and Hγ (S/N=21), suggesting that the spectra observed in the red and blue wavelength regimes were usable for a possible measurement for metallicity, which was 0 in both cases. This star was definitely a member of the cluster in NGC 2626 and served as an indication of the metallicity of the other cluster members. Similar to the distribution of RCW 34, all of the stars observed with *SALT* in NGC 2626 were included in the distribution. Both distributions showed that the majority of sources have a solar metallicity, and it is generally accepted that most open clusters in the Milky Way have a solar metallicity. For reference, Chen *et al* (2003) showed that a large number of clusters have a metallicity between $-0.5 \leq Z_{\odot} \leq 0.5$, which served as a criteria by which the stars in RCW 34 and NGC 2626 with metallicities outside of this range, were considered to be incorrect. If a star had a metallicity that did not fall between $-0.5 \leq Z_{\odot} \leq 0.5$, its spectral classification was also considered with some scepticism.

The method with which PyHammer determines the metallicity for each star is not perfect. It involves finding the best fit between the measured spectral lines and entries in the spectral library. If the spectra is subject to veiling, due to emission from circumstellar material, or strong extinction from the embedding material, then the measurements of the absorption lines used for classification may be biased. In both the populations of RCW 34 and NGC 2626 there were many noisy spectra, of which the spectral classification and metallicity may be incorrect. The metallicity measured for sources with Hα-emission are considered biased, because the photospheric emission is subject to additional emission from circumstellar material. This extra emission affects the EW's measured by PyHammer for the standard indices which were used to classify the star's spectral type and metallicity.

In both the distributions of RCW 34 and NGC 2626 the majority of stars had a metallicity similar to the Sun. But the metallicity of a source can not be used to distinguish a star as a cluster member

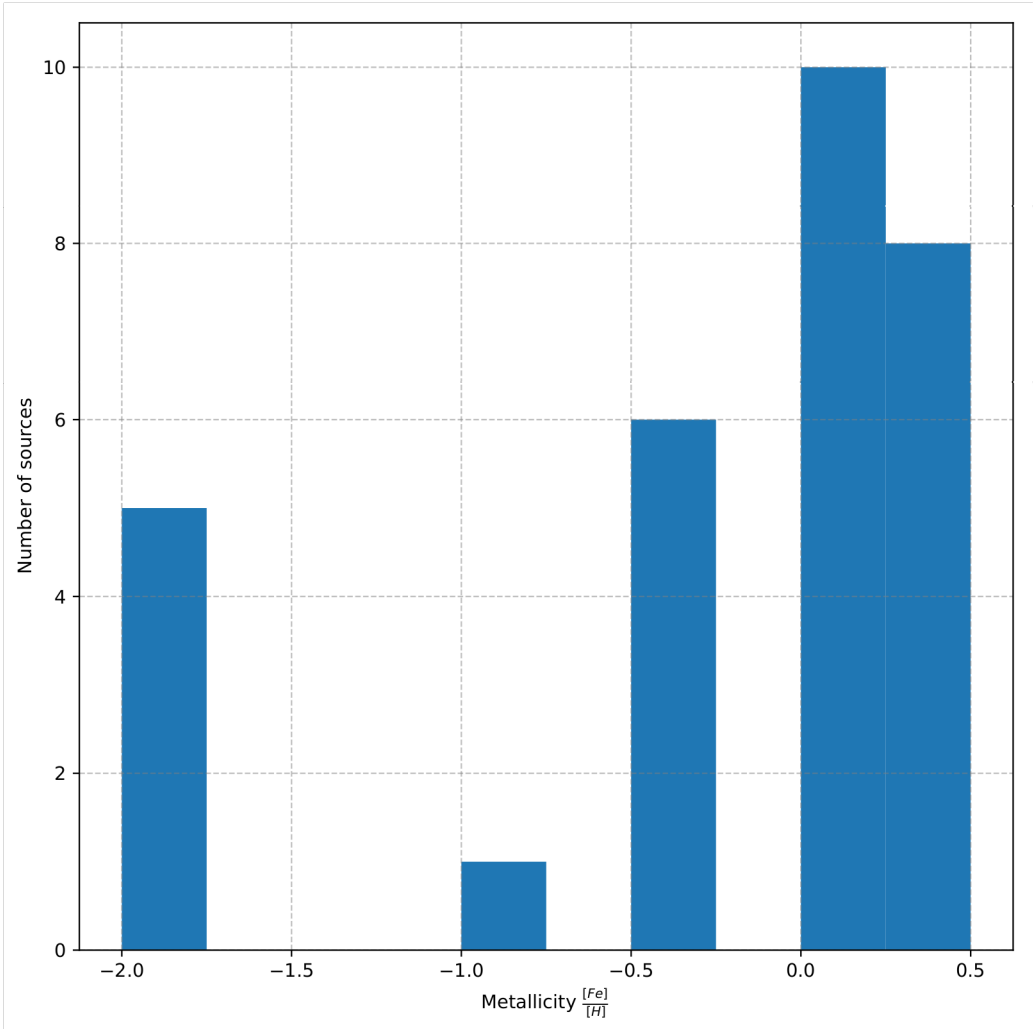

Figure 5.42: The distribution of metallicities measured from the red spectroscopic observations with *SALT* of stars associated with NGC 2626.

or a field star, it only served the purpose of indicating what the average metallicity of stars in the direction of the star-forming region is. It was shown by Paunzen *et al* (2010), Heiter *et al* (2014), and Netopil *et al* (2016) that the overwhelming number of open clusters in the Milky Way have a solar metallicity. This general case is consistent with the results measured from the spectral candidates in both RCW 34 and NGC 2626.

It is expected that the stars in an open cluster should have the same metallicity, because they formed from the same molecular cloud. In reality the members of an open cluster have small variations in their metallicities, due to individual evolution and the different periods at which hydrogen burning switched on. For example, Heiter *et al* (2014) showed the variations between the measured metallicities for cluster members of M 67. All of the cluster members in M 67 do not have a metallicity difference of more than 0.5.

The method with which PyHammer uses the 34 absorption lines shown in Table 5.4 to classify the spectral type of each star is precise enough, to within one spectral sub-class. However, using the method to determine the metallicity for each star in RCW 34 and NGC 2626 is not effective for the red wavelength ranges from 5750-7250Å. The blue spectra for NGC 2626 is not considered for this discussion on the metallicity measurement. The reason is due to the high extinction suffered at short optical wavelengths and the low S/N that was measured for most of the stars in this dataset. PyHam-

mer also give as very rough value for a star's metallicity; the most intervals in which the metallicity classification is done are 0.5, i.e. a metal content difference of a factor 5.

The majority of the sources that were observed with *SALT* in both RCW 34 and NGC 2626 had a solar metallicity according to the distributions shown in Figures 5.41 and 5.42. The metallicity of a star could not be used to classify it as a cluster member, or not, because most of the stars in the Milky Way's plane have solar metallicity, according to Chen *et al* (2003). The metallicity distributions gave an indication of the value that should be used for the input parameter of the metallicity in the evolutionary models by Siess *et al* (2000) which is compared to the photometric data in Chapter 6.

5.3.4 The spatial distribution of the different types of Hα-line sources

5.3.4.1 *RCW 34*

With the information of the metallicities and the spectral types analysed, the spatial distribution of the stars observed with *SALT* were analysed based on their Hα-line profiles. Figure 5.43 showed the

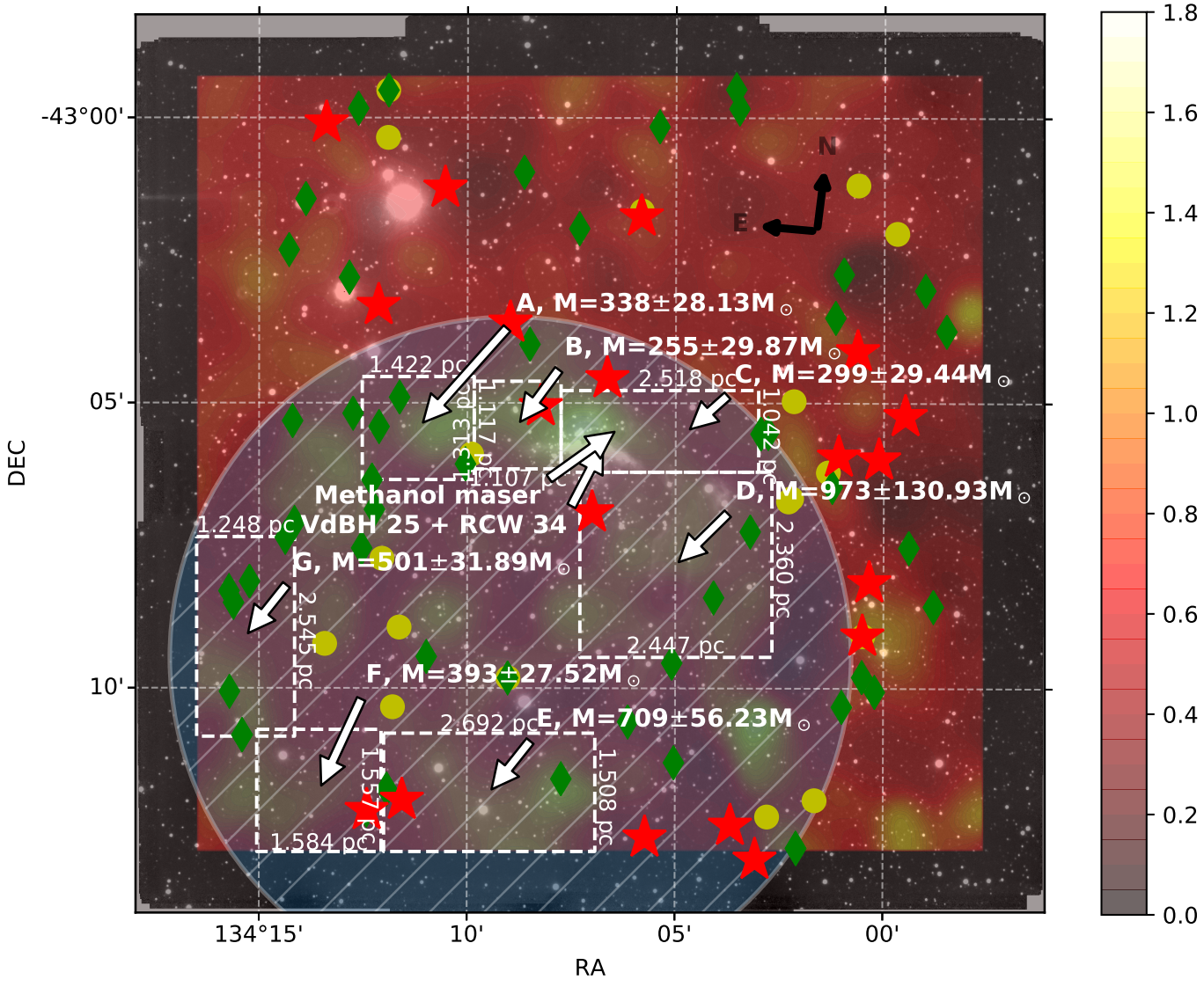

Figure 5.43: The position of each star that was observed with *SALT* in RCW 34 marked on the basis of each star's Hα-profile. The red stars indicate the position of the stars with an Hα-emission line, the green diamonds show the position of the stars with an Hα-absorption line and the yellow dots are the stars with an unresolved Hα-profile.

positions of the stars with an Hα-emission, absorption, and undetermined line profiles as red stars, green diamonds, and yellow dots, respectively. It was very important that the position of the Hα-emission line stars were shown, because these sources indicated where the most recent star formation in RCW 34 occurred. Even though the other stars observed with *SALT* could not be considered as cluster members of RCW 34, it was necessary to show them all.

The bubble region that was described in detail by Bik *et al* (2010) was marked by a grey circle region. Most of the Hα-emission stars were distributed on the outer edges of the bubble region. The majority — except for the four far north and the six far west of the HII region — were in pockets with low extinction ($A_v \leq 10$) in the molecular cloud on the outer edges of the clearing of the bubble region. The four stars far north of the HII region were most likely too far away from the bubble shape that their formation was influenced by the young stars in the bubble shape. They showed that recent star formation in RCW 34 extend past the borders of just the bubble clearing. The four stars directly west of the HII region that grouped around a dense clump, may not have been associated with the bubble region. While the last two sources west of the HII region were close enough to the border of the bubble region that they may also have been associated with its structure. Bik *et al* (2010) noted that the sources in the bubble region were related to each other's formation, either with triggered star formation, or a cascaded sequential formation. It was apparent that the formation of the sources outside of the bubble region were related to those on the inside of the clearing. It was unfortunate that there were no spectroscopic observations done of the stars in the dense intersection of the two colliding molecular clouds. It was expected because the *NIR* and *VPHAS+* data sets showed that there were many young excess sources along the intersection's ridge.

The location of the stars with Hα-absorption lines across the whole field suggested that a fraction of the Hα-candidates that were selected for spectroscopic investigation were field stars. With the overwhelming number of the *SALT* sources being stars with Hα-absorption, and all of them distributed across the whole field, it was clear that the selection of candidates was not done effectively. All of the candidates were selected before the *VPHAS+* data and the correct extinction map of the region was available. If this information was available before the *SALT* observations were done, a different set of candidates would most likely been selected.

5.3.4.2 *NGC 2626*

The positions of the stars that were observed in the field of NGC 2626 and characterised according to their Hα-line profiles were shown in Figure 5.44. The position of the Hα-emission line stars were shown with red stars and they were distributed in the area surrounding HH-132 and the molecular clouds. Of the 17 sources that were shown in Figure 5.44 there were 10 with an Hα-emission line. This means that the selection of the *SALT* sources around NGC 2626 gave a higher number of Hα-emission line stars than for RCW 34. This may have been because NGC 2626 is much closer than RCW 34, meaning that the sources that showed excess emission during the selection process had a bright enough J-magnitude that they were assigned a high priority. These sources and this field of view was not as big as the study by Sharma *et al* (2016), but they suggested that there were as many PMS stars as the *VPHAS+* and *NIR* data showed. They did not give significantly more information about the low-mass star formation in NGC 2626 than the studies by Mueller & Graham (2000) and Sharma *et al* (2016).

The sources with an Hα-absorption line were located at no specific structure in NGC 2626 and may either have been field stars or cluster members. They were most likely selected by the slitmask tool's spatial optimisation algorithm due to their positions, rather than on the basis of their priority score. It is interesting that the driving star of the Herbig Haro object, HH-132, has an Hα-absorption line. It is discussed in detail in the following subsection.

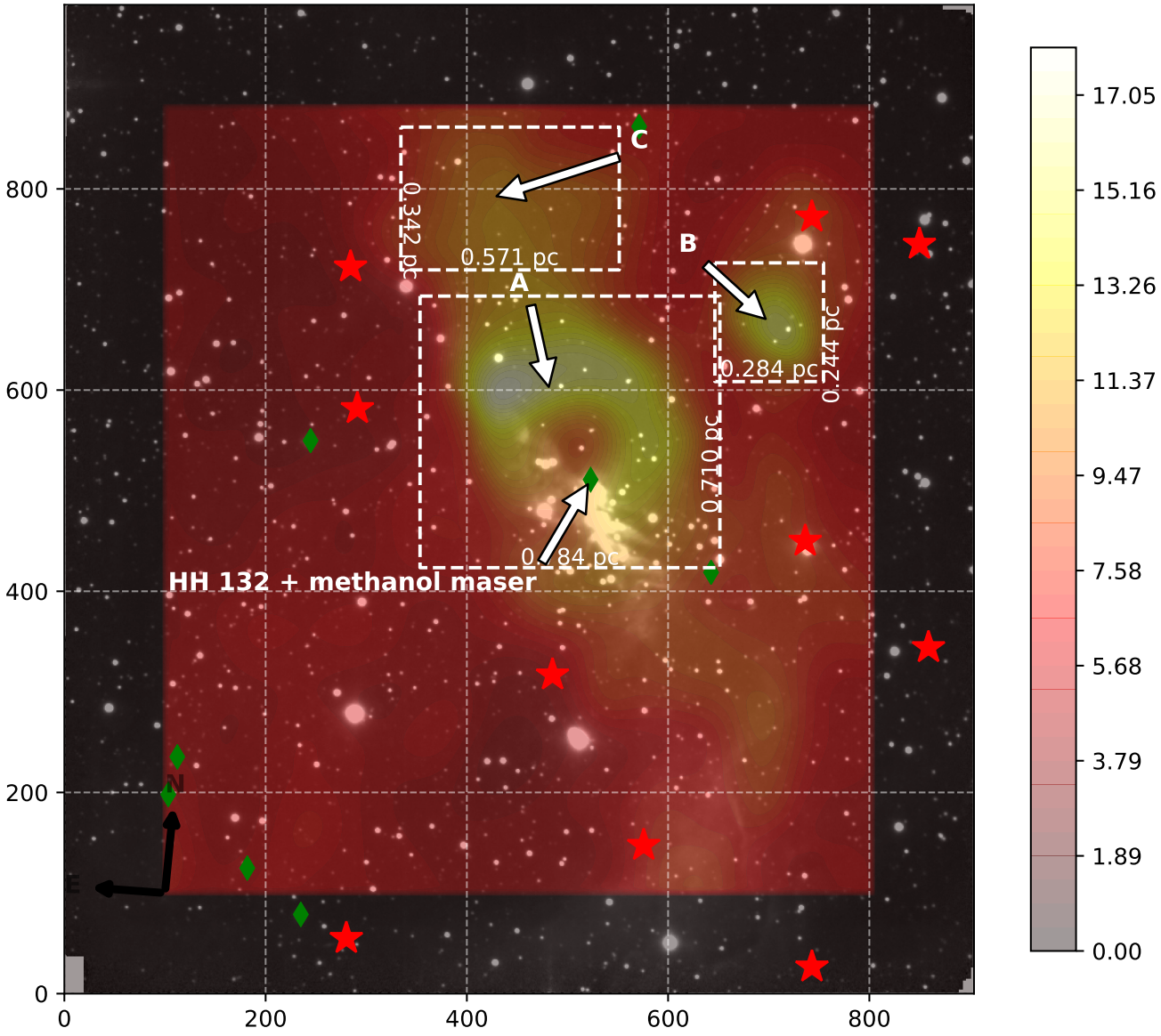

Figure 5.44: The spatial distribution of the *SALT* candidates around NGC 2626 categorised according to their Hα-line profiles. The red stars show the position of sources with an Hα-emission line and the green diamonds show sources with an Hα-absorption line.

5.3.5 The driving star for HH-132

The driving star for the Herbig Haro object, HH-132, was interesting because it was not expected that a star with such strong jets would have such apparent absorption lines. Very young stars have jets with violent outbursts and are characterised by their strong Hα-emission. This case was interesting because a young high-mass star ejected heated gas from its jets which contributed to not just Hα, but other hydrogen emission lines. A Herbig Haro object is nebulous gas that is ejected from a young star's jets and usually moves at high velocities away from the host star. A young star is usually surrounded by circumstellar material with emission that veils the star's photospheric emission in the spectra. Obtaining a high enough S/N for various spectral lines to classify the source — particularly one that is as embedded as this one — in the optical is unique. There is also a maser very closely associated with the driving star for HH-132, and it is suspected that the same star is driving both HH-132 and the maser. The reason for suspecting that the star is also driving the maser is that there is no other high-mass star in the embedded material, and the maser's position is the same as the star

driving HH-132.

Full page spectral representations are given for the star driving HH-132 in Annexure D. The blue and red parts of the spectrum that were observed with *SALT* were shown in Figures 5.45-5.50, together with O5, O9, B0, B2, B5, and B9 stars from the library of standards from PyHammer. The most prominent absorption lines found in young stars were also plotted against the spectra of the star which indicated the hydrogen and other spectral lines in each figure. The best match of a spectral type according to PyHammer was a B5 star with a metallicity of 0, which was plotted in Figure 5.49. The O[I]-(5577.5Å) line features in the spectra of a B2, B5, and B9 shown in Figures 5.48, 5.49, and 5.50 respectively. The line between the library and the B2 and B9 was roughly the same. The spectra for HH-132 did not have He-lines, which would be an indicator of an early B or O star, and the Ca[II]-H and -K lines suggested that the star was closer to a B9 (left panel of 5.50) star than a B2 (left panel 5.48) star. With these spectral indicators it would lead to the conclusion that the star may have been a late B star. The presence of the methanol maser on the other hand did suggest that it was a high-mass star, or a star with a mass higher than 8 $M_{\odot}$ — or in other words an early B star. Without more spectral observations it was not possible to correctly classify the star driving HH-132, but the presence of the methanol maser did show that there was a high-mass star.

It is very rare that a high-mass star-forming region which is associated with a maser is visible in the optical. The environment in which these objects are found has very high extinction resulting in them rarely being seen in the optical. To date there were only ~ 70 of these optically detectable HII regions which were associated with a 6.7-GHz maser in the Milky Way that have been catalogued in the literature. What was even more unique was the optical spectroscopy of a source that was possibly the driving source of a methanol maser — this may have been an observational first. Menten (1991) stated that class-II molecular transitions (of which 6.7-GHz is the most famous) — or better known as class-II masers — are closely associated with infrared sources. The extinction towards these sources is usually so high that it is only possible to obtain spectra in the K-band (2.2 μm) when performing spectroscopic classification. The optical spectra for HH-132 in Figures 5.45-5.50 may have been subject to high extinction, it was $A_V \sim 8$ according to the extinction map in Figure 5.44. These *NICEST LinES* extinction maps gave an indication of the extinction towards an object, but there may have been an opening in the molecular cloud towards this source which was lower than the indicated extinction. The spectra was most likely subject to extinction which affected the strength of the absorption lines which were used in the identification of the spectral type. This implied that the observed spectra from the driving star of HH-132 was different from naked photospheric emission from a similar main sequence star.

In the blue wavelength regime the Hβ and other Balmer hydrogen lines were the most prominent features. Of which the S/N of both the Hβ and Hγ lines were above 20. The other prominent spectral features were the Mg[I]-(5167Å and 5172Å), S[II]-(4068.6Å), Ne[III]-(3967Å), and Ca[II]-(3933.68Å , K-line) lines. In the red wavelength regime the most prominent features were the Hα, O[I]-(5577.5Å), Hg-(5769Å and 5895Å), Na[I]-(D1-5895.94Å and D2-5889.973Å), O[I]-(6303Å and 6302.50Å), He[I]-(6678Å), and He[I]-(7067Å) lines. In O stars there are prominent He-lines, but the H-lines are weak, and in B stars the Mg[II], and Si[II] lines become more prominent. The strength of the most prominent spectroscopic features suggested that this star was an early B star, and the presence of the maser close to the source suggested that it was a star with a mass higher than 8 $M_{\odot}$. The lack of strong He-lines suggested that it was not an O star, however, the H-lines were not strong enough to show that the star was indeed a late B star.

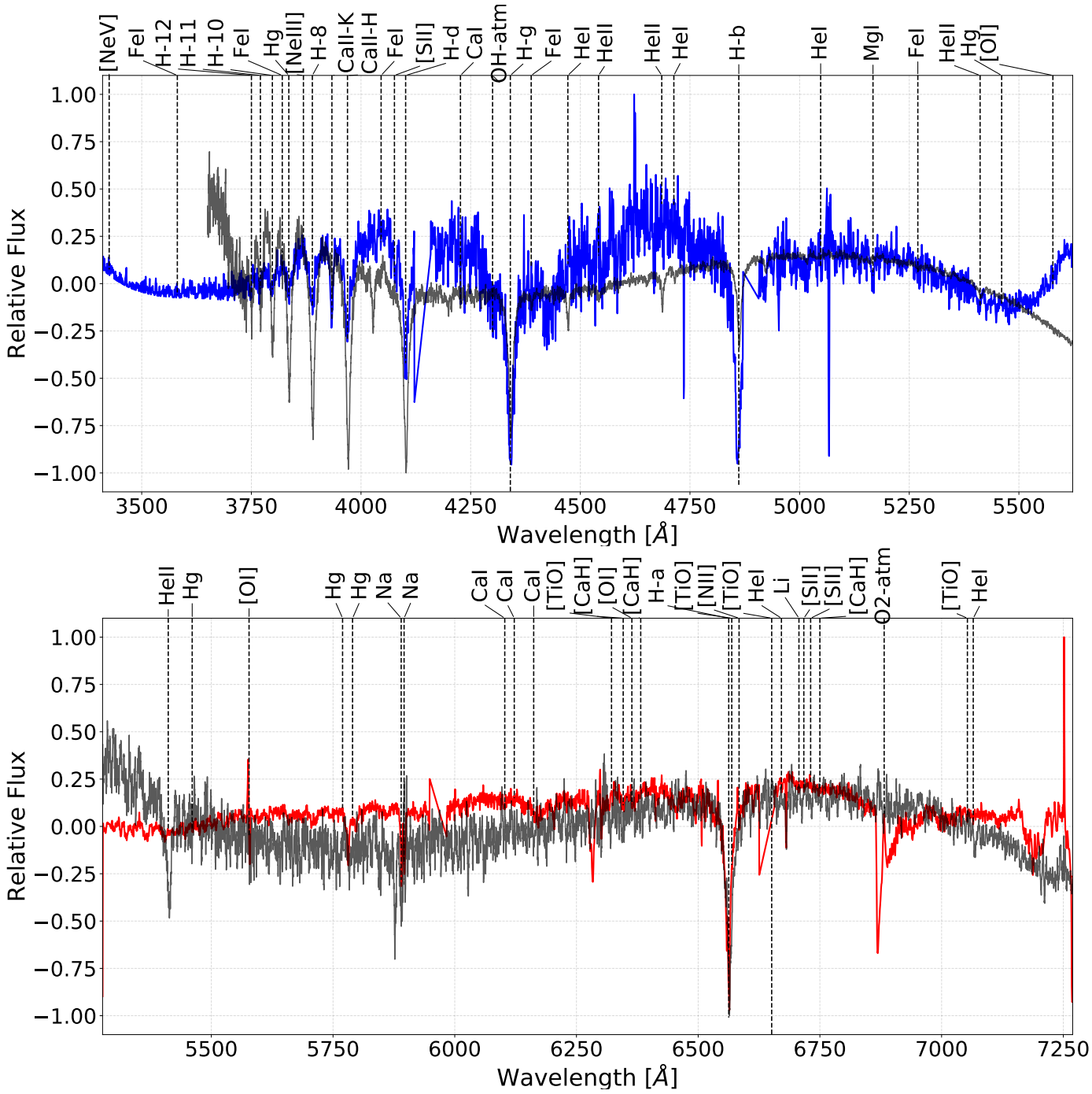

Figure 5.45: The blue and red spectra for the star associated with HH-132 is shown in the top and bottom panel respectively. The flattened spectra of HH-132 is plotted against the spectra of an O5 star.

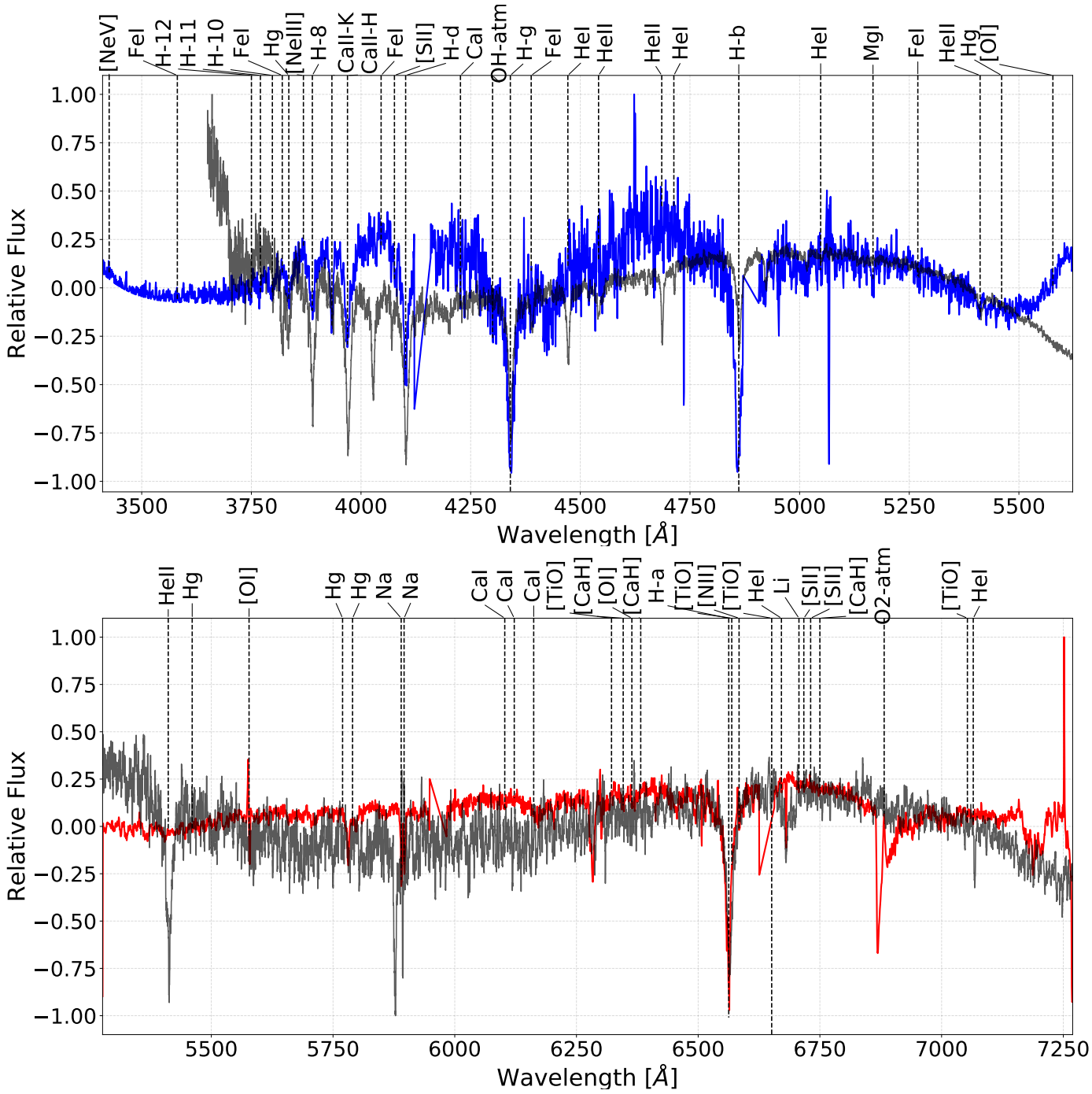

Figure 5.46: The blue and red spectra for the star associated with HH-132 is shown in the top and bottom panel respectively. The flattened spectra of HH-132 is plotted against the spectra of an O9 star.

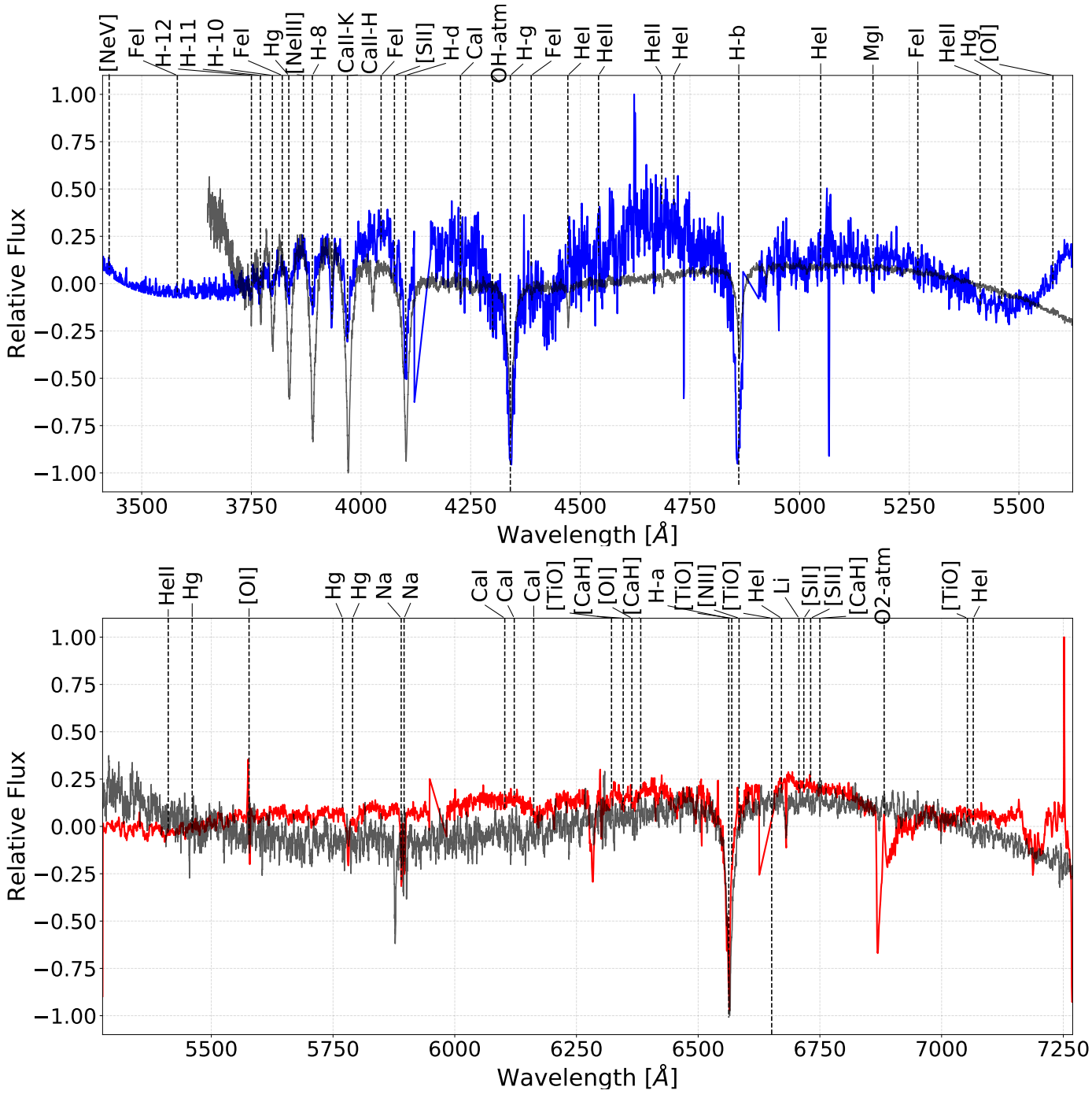

Figure 5.47: The blue and red spectra for the star associated with HH-132 is shown in the top and bottom panel respectively. The flattened spectra of HH-132 is plotted against the spectra of a B0 star.

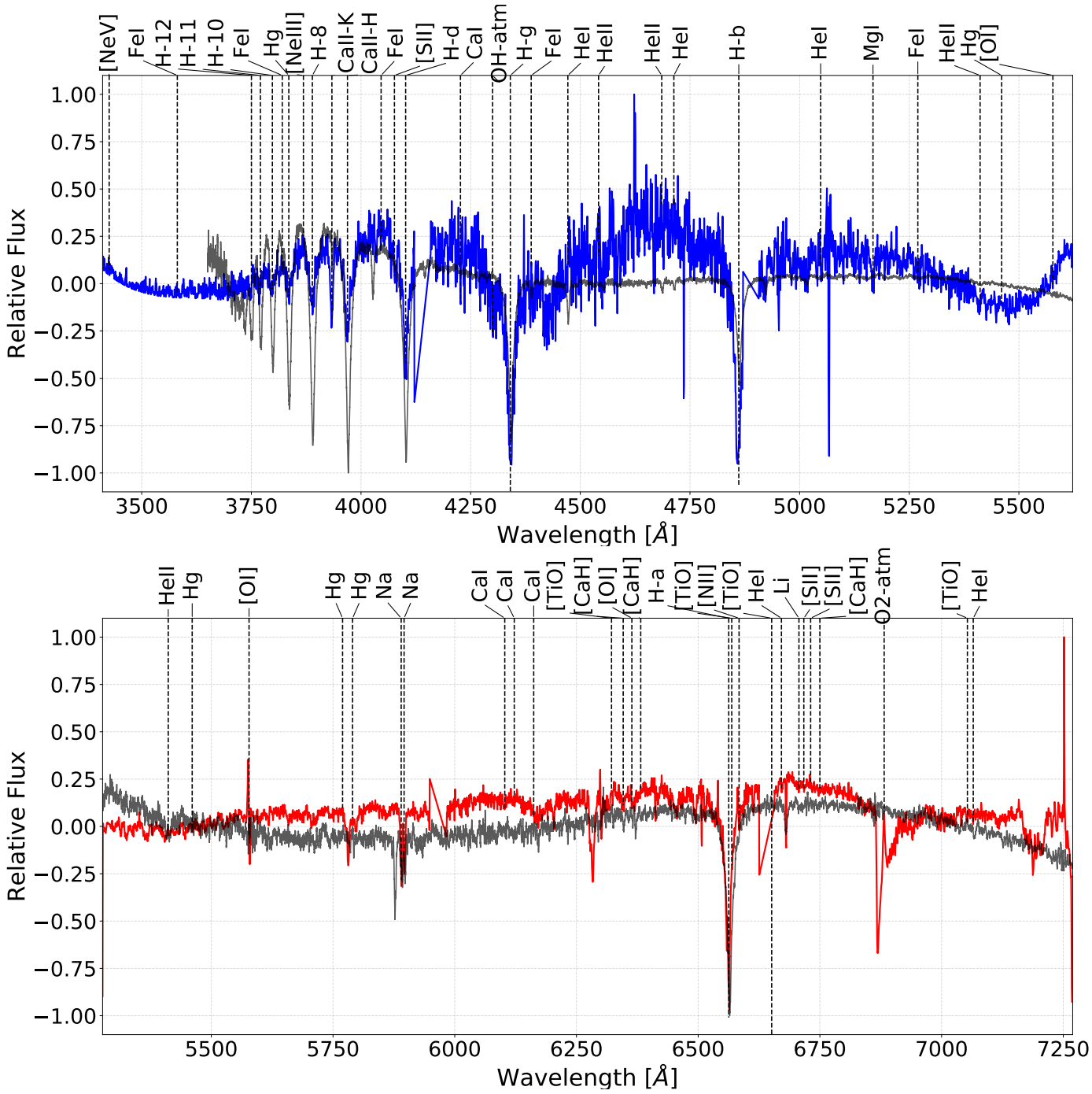

Figure 5.48: The blue and red spectra for the star associated with HH-132 is shown in the top and bottom panel respectively. The flattened spectra of HH-132 is plotted against the spectra of a B2 star.

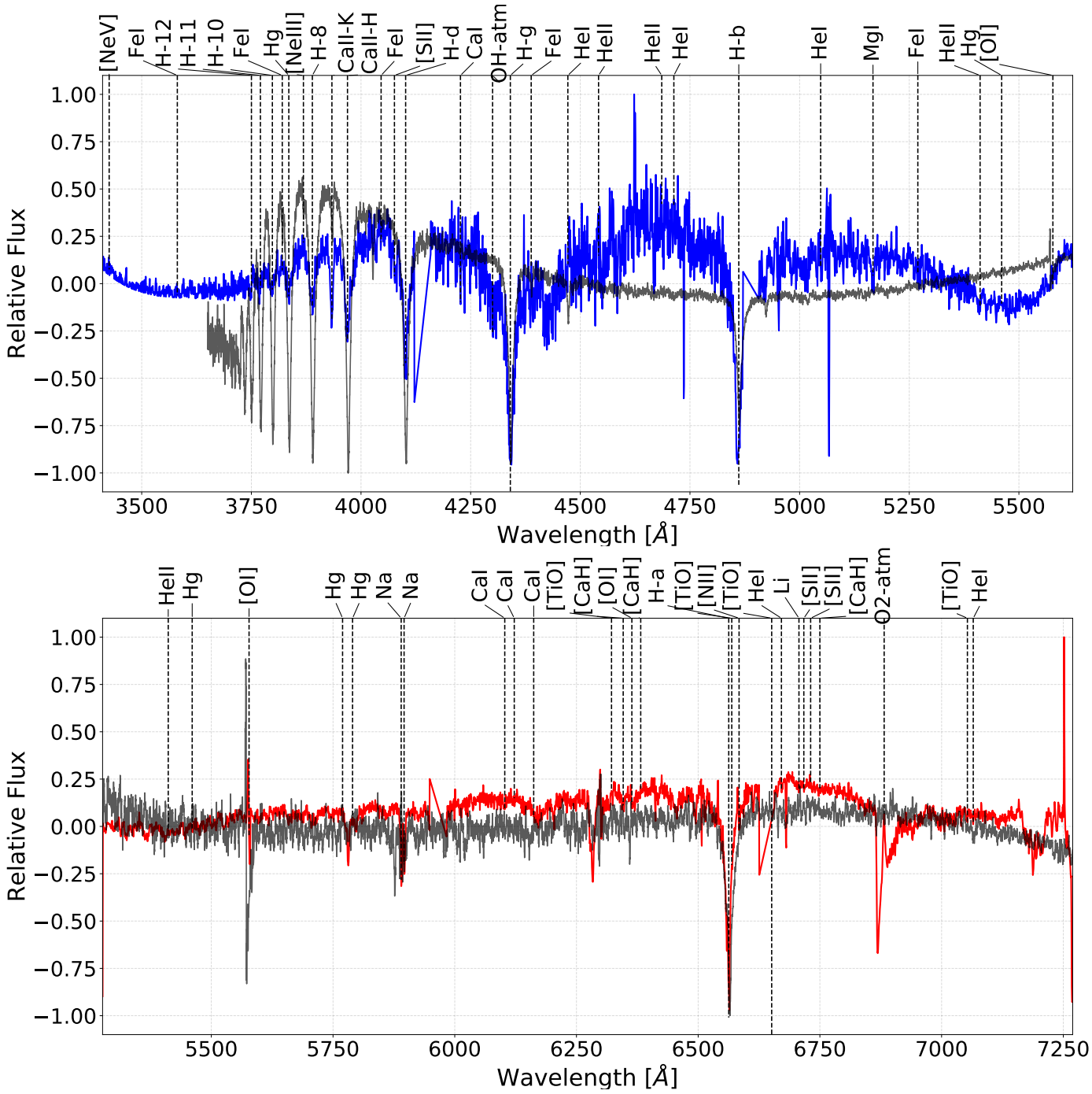

Figure 5.49: The blue and red spectra for the star associated with HH-132 is shown in the top and bottom panel respectively. The flattened spectra of HH-132 is plotted against the spectra of a B5 star.

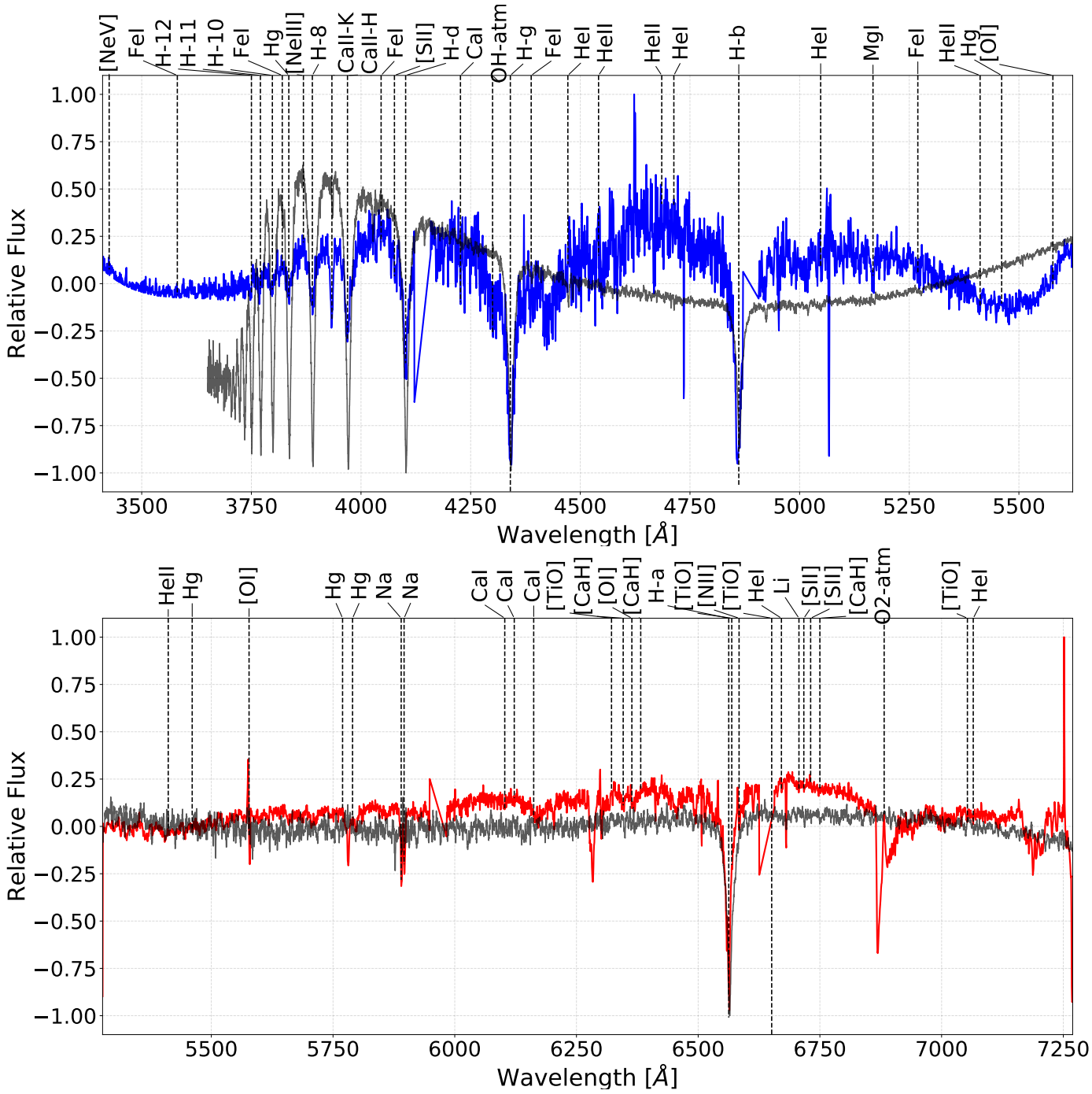

Figure 5.50: The blue and red spectra for the star associated with HH-132 is shown in the top and bottom panel respectively. The flattened spectra of HH-132 is plotted against the spectra of a B9 star.

5.4 Summary and conclusion

In this chapter an analysis was done on spectroscopic observations conducted with the *SALT* telescope, on Hα-emission candidates. The sources were selected on the basis of excess emission in their *SuperCOSMOS*, $(R_S - H\alpha)$ and the *IRSF*, $(H - K_s)$ colours. The results showed that candidates which initially were anticipated to have Hα-emission did not spectroscopically show an Hα-emission line. Also, the position of the stars that had Hα-emission were located in regions where the *IRSF*, *VPHAS+*, and results from the literature showed some of the youngest cluster members.

5.4.1 Spectra and stellar types of the *SALT* candidates

5.4.1.1 *RCW 34*

The spectral classification that was done with PyHammer of the candidates around RCW 34, range between an A6 and a M6 star, or masses ranging from 1.83 $M_\odot$ to 0.1 $M_\odot$. Even though many of the stars could be spectroscopically classified, it could not be determined from the spectra if they are cluster members of RCW 34. The larger number of candidates had an Hα-absorption line, meaning that these stars could either be cluster members or field stars. The only candidates that could be considered as cluster members were the stars with an Hα-emission line. The spectral classification for the emission line stars also ranged from A6 to M7 stars. Bik *et al* (2010) showed spectra for stars ranging from G to K stars, meaning this study discovered a larger variety of spectral types which also span further than just the bubble region. The other spectral results assigned a metallicity to some stars, and a radial velocity was calculated for the stars with the most prominent Hα-line profiles. The average metallicity of the cluster is a solar metallicity. The cluster members that did not have a solar metallicity, either had a systematic measurement error — which occured during classification — or the measurement may have been correct and they could not be considered as cluster members. In either case, the individual metallicities of stars were not considered as very precise, and were only used to calculate the average for the whole cluster. The uncertainties associated with the radial velocities in the emission line spectral profiles did not make it possible to make any indicative measurements. However, the velocity profiles revealed information about the way that the light was emitted from the source and the gas that may also be contributing to the star's emission.

5.4.1.2 *NGC 2626*

Most of the stars that were observed around NGC 2626 showed Hα-emission lines and were considered to be young cluster members associated with NGC 2626. The spectral types of the stars ranged from an early B star driving HH-132, down to a M7 star. The metallicities measured from the spectra of stars in NGC 2626 were only used for the calculation of the average metallicity of the cluster. Most of the spectra in the red wavelength regime had a strong and clear spectral profile, thus the spectral classification could be performed. In the blue wavelength regime, the majority of the spectra for the stars around NGC 2626 were so noisy that no signal could be identified from noise.

5.4.2 The number of stars with Hα-emission out of the candidates

5.4.2.1 *RCW 34*

Out of the 92 stars that were observed in the field surrounding RCW 34, there were only 18 that showed Hα-emission, and there were 22 with an unresolved Hα-profile. The distance to RCW 34 and the instrumentation setup made the selection of Hα-emission candidates challenging. The *IRSF* and *VPHAS+* results suggested that there were many young cluster members with excess emission which were not observed as part of the *SALT* candidates. The areas where most of the young cluster members were prominent around RCW 34 were subject to extinction, or they were too faint ($r' \sim 20$) to practically observe them with *SALT*. The location of most of the Hα-emission line stars was at the outer edges of the bubble region, and north and west beyond the bubble region. If the location and the movement of the molecular clouds that were profiled by Hayashi *et al* (2017) were taken into account, then the Hα-emission line stars were in the location of the denser parts of the two molecular clouds.

5.4.2.2 *NGC 2626*

From the 19 stars shown in Figure 5.44 there were 10 with Hα-emission lines. The larger fraction of sources with Hα-emission showed that the prioritization score worked better in the selection of candidates for NGC 2626 than for RCW 34. This may have been because NGC 2626 is closer than RCW 34, meaning that the sources with excess emission were bright enough ($r' \sim 15$) to be observed with *SALT* for a reasonable exposure time. The extinction for 4 of the 6 stars Hα-emission stars on the extinction map was quite low ($A_V \sim 5$), implying that the spectra were not contaminated too much by the embedding material.

5.4.3 Spatial distribution of Hα-emission line stars

5.4.3.1 *RCW 34*

The instrumentation setup and the majority of possible candidates that were faint in the optical ($r' \sim 20$) made selection of possible candidates around RCW 34 very challenging. The instrumentation setup required that the candidates that were selected around RCW 34 all have roughly the same magnitude. The reason for this was that a good S/N for weak spectral lines used for spectral identification would be obtained from all of the sources for a reasonable exposure time. This eliminated the larger portion of possible candidates, because most of the sources with excess *NIR*- and optical-emission were so faint in the optical that the exposure times on *SALT* was impractical. The location of the stars with Hα-emission was all on the outer edges of the bubble region and some extend north- and westward past the edges of the bubble region. The *NIR* and *VPHAS+* data suggested that there were many more stars with Hα-emission in the remnant molecular cloud around RCW 34. To observe these, more exposure time would be required, and a different selection scheme for candidates should be applied.

5.4.3.2 *NGC 2626*

The stars that show Hα-emission were all located in the region surrounding the star driving HH-132 and the molecular cloud. They were not concentrated at specific locations, like the stars in the bubble region of RCW 34, but were on the outer edges of what seemed to be a larger and older star-forming region. Their location agreed with the positions that were shown from the *IRSF* and *VPHAS+* results and were consistent with the positions from Mueller & Graham (2000) and Sharma *et al* (2016). The region was larger than the extent of the molecular cloud suggested, and may have extended as far as the gas of the bright rim nebulosity. The spectroscopic observations of the Hα-emission line star far away from HH-132 gave some insight into how star formation occurred in the region. The young stars showed that up to the present, there was ongoing star formation in the region and that most of the matter from the forming molecular cloud had been cleared out. The remaining cloud still hosted some of the youngest cluster members in NGC 2626 according to Sharma *et al* (2016), and it was just a matter of time before it was also destroyed by its young members.

5.4.4 The driving star of HH-132

It is interesting that the star that was driving HH-132 had dispersed the molecular cloud so much that there was a clearing big enough that optical spectroscopy showed photometric emission. It was unique that the star driving the methanol maser had cleared enough matter in the line of sight that the extinction was low enough for optical spectroscopy. Measuring the strength of any spectral line, including hydrogen lines and the metallicities, had to be viewed with scepticism. The light emitted from the star was subject to extinction from the surrounding molecular cloud, and possible emission from circumstellar material. In both the red and blue spectra there were not enough metal lines for the star to be classified as an A type or later spectral class. Moreover, there were not enough He-lines suggesting that the star was either a late O or early B star. The presence of the maser suggested that the star must have a mass higher than 8 $M_\odot$, meaning that the star had to be of a spectral type heavier than a B2 and may be a late O star.

5.4.5 Final thoughts and conclusion

In this chapter the candidates were selected based on the excess emission in their *IRSF* and *SuperCOSMOS* colours and J-magnitde. The number of Hα-emission stars in RCW 34 was lower than expected. The cause was the distance to RCW 34, and the instrumental setup which influenced the selection of candidates. The stars in NGC 2626 with Hα-emission were located in positions similar to the results of the imaging in Chapters 3 and 4, as well as the literature. If the *VPHAS+* data and the extinction maps were correct at the time of *SALT* candidate selection, different sets of sources would have been chosen. The PyHammer results were used to calculate the average metallicities for each cluster and were not precise enough to make conclusions about individual measurements. The spatial distribution of Hα-emission cluster members around RCW 34 confirmed the imaging results that the young cluster members extended past the bubble region. More specifically, the Hα-emission cluster members of RCW 34 extending to the north, past the bubble region, were aligned with one ridge of the two colliding molecular clouds. The few stars with Hα-emission in RCW 34 that could be confirmed with spectroscopic observations gave a more defined structure to the cluster. The samples of Hα-emission stars in RCW 34 and NGC 2626 were too small to conclusivly contribute to a detailed star-formation history of either.

CHAPTER 6: SYNTHESIS OF MULTI- WAVELENGTH DATA

6.1 Introduction

In this chapter all of the sources that showed properties characteristic of PMS stars in the *IRSF* and *VPHAS+* data sets are combined into a single data set. Each of these data sets is discussed and they are compared to each other. This is done to determine if the stars which showed properties characteristic to PMS stars in one set of observations also showed in another. This would strongly suggest that such a star is a young cluster member, and not just a field star. This comparission is done by combining the photometric data from Chapters 3 and 4 of the sources that showed excess *NIR*-, u'-, or $H\alpha$-emission. All of the *SALT* sources are added to the data set; not all of them are cluster members but there are so few that their combined spectral and photometric data are analysed together. The synthesised results for RCW 34 and NGC 2626 are presented in two separate sections, and in each section, the results are presented in the same format — by plotting the data for all of the sources on the same diagram. A brief description of the tools used to compare the different groups of stars to each other is given below.

6.1.1 Coordinate matching

By bridging the results from different imaging datasets with each other, the multi-wavelength properties of individual stars can be determined. Bridging the different datasets from the *NIR* and optical imaging for the same stellar sources was easy, because both sets used astrometric calibration from the *2MASS* catalogue. The *SALT* candidates were selected from the coordinates of the *IRSF* data. With the same WCS calibration used for all three datasets, it was just a matter of selecting the corresponding sources from each dataset. The results from the different optical and *NIR* photometry datasets compliment each other and aid in the interpretation of the stellar properties deduced from each individual set.

6.1.2 Imaging results

By using the properties from the measured magnitudes and spectra for each cluster member in RCW 34 and NGC 2626 a bigger set of properties can be derived for the star-forming regions. The individual properties for each star was determined from a $(J-H)/(H-K_s)$ and $(r'-H\alpha)/(r'-i')$ colour-colour diagram, as well as a $r'/(r'-i')$ and $K_s/(H-K_s)$ colour-magnitude diagram. The first part of each section on RCW 34 and NGC 2626 starts with the *NIR* colour-colour diagram, showing all of the sources that are considered to be cluster members. All of the photometric data have been dereddened using the extinction that was measured from the *NICEST LinES* maps in Chapter 3. The *NIR* colour-colour diagram shows the amount of excess emission presented by the stars that were observed with *SALT*, and those with optical excess $(r'-H\alpha)$ and u' emission. The optical $(r'-i')/(r'-H\alpha)$ colour-colour diagrams show the amount of Hα-excess emission of the cluster members.

6.1.3 Optical colour-colour diagrams

The optical colour-colour diagram for $(r'-H\alpha)/(r'-i')$ show the same sources as the *NIR* colour-colour diagram. In Chapter 4 these colour-colour diagrams were used to identify stars which had excess Hα-emission, relative to the main sequence, using the $(r'-H\alpha)$ colour. The same distinction between CTTs and WTTs that was used in Chapter 4 is used in this chapter. Those with $(r'-H\alpha) > 0.1$ above the main sequence were classified as CTTs and those with $(r'-H\alpha) \leq 0.1$ more than the main sequence as WTTs. The $(r'-H\alpha)$ colours of the *SALT*, *NIR*-excess emission, and u'-excess emission sources were compared to the main sequence, to test for excess Hα-emission.

In Chapter 3, a $K_s/(H-K_s)$ colour-magnitude diagram was used because the extinction maps were built from K_s-band extinction so that observed colours and magnitudes could be directly rededdened from the extinction map. In this chapter, only the stars with excess Hα-, u'-, and *NIR*-emission as well as all of the *SALT* sources are shown on the colour-magnitude diagrams. From the colour-magnitude diagrams, the dereddened sources are compared to the main sequence and the evolutionary models by Siess *et al* (2000). The comparison with the evolutionary models are a rough indication of the ages and masses of the sources.

6.1.4 Optical colour-magnitude diagrams

All of the sources that showed excess *NIR*-, Hα-, and u'-emission, and the sources that were observed with *SALT*, are shown on the same $r'/(r'-i')$ colour-magnitude diagram. The optical photometry was not as contaminated with emission from heated dust in the circumstellar material, making it a better measure for just photospheric emission than the *NIR* photometry. The dominating factor of emission from circumstellar material in the optical is the Hα-emission line. But, relative to the total flux that is measured in the r' band, the Hα-emission line is dominated by continuum emission. This means the $r'/(r'-i')$ diagram gives a better indication of the age and mass of the stars relative to evolutionary lines. The optical photometry suffers more extinction than the near-infrared results, but all of the cluster members, except for those with excess *NIR*-emission, were identified from optical results.

6.1.5 The excess emission colour-colour diagrams

The last tool that was used for the analysis of the multi-wavelength data is a hybrid excess emission diagram using optical and *NIR* colours as a $(r'-H\alpha)/(H-K_s)$ colour-colour diagram. It exclusively serves as a measure of how much excess emission is there for each cluster member. It shows: (1) How much excess emission is given off by the heated dust in the accretion disk in the $(H-K_s)$ colour. (2) The $(r'-H\alpha)$ colour is a narrow-band measurement which tests for an Hα-emission line. The Hα-emission line shows how much heated gas is around these young stars. It arises from heated gas free-falling from the accretion disk to the young star's surface. It can also be emitted by both infalling material and heated outflows as shown in Figures 5.33-5.34 from the model by Hamilton *et al* (2012). The introduction of this colour-colour diagram gives a unique way of determining at what stage of evolution a young star is; the youngest stars shown on this diagram — CTTs younger than 3 Myr — show strong excess emission in both colours. The amount of excess emission shown in each colour will gradually decreases for older PMS stars which are closer to the main sequence. The Hα-emission originates from radiative-transfer processes which are given off by gas in the accretion disk and stellar wind outflows; the processes are described by Kurosawa *et al* (2005). The Hα-line profile is affected by various factors, such as the inclination angle, outflows, or other sources that contribute to the Hα-emission. The excess emission in the $(r'-H\alpha)$ colour is affected by the profile of the Hα-line. Thus, if a star's Hα-emission line profile is influenced by some of these factors the excess $(H-K_s)$ emission may show more than the optical colour. WTTs show some excess emission in the $(r'-H\alpha)$ colour, but does not have much excess $(H-K_s)$ emission, because the accretion disk will have dissipated to a small size. The excess emission colour-colour diagram indicates a star's evolutionary status from two independent colours, more than just the optical or *NIR* colour-colour diagrams in Chapter 3 and 4 show. It is complimentary to the $(r'-H\alpha)/(r'-i')$ and $(J-H)/(H-K_s)$ colour-colour diagrams, because they also give other information.

6.1.6 The mass and age distributions

The same sources that were used in the optical colour-colour diagrams are shown on the $r'/(r'-i')$ colour-magnitude diagrams for RCW 34 and NGC 2626. From these colour-magnitude diagrams, the evolutionary models from Siess *et al* (2000) were used to derive ages and masses for the stars in the combined datasets. The $r'/(r'-i')$ colour-magnitude diagrams were used rather than the $K_s/(H-K_s)$ diagrams because there was not so much excess emission in the $(r'-i')$ colour from heated dust as in the $(H-K_s)$ colour. The isochrones and evolutionary lines from the models by Siess *et al* (2000) were used to determine the masses and ages for the stars which lie between the different classifications. Not all of the sources in RCW 34 or NGC 2626 can be classified in this manner, but this classification scheme gives a rough indication of the age and mass distributions of each cluster. Uncertainties were

introduced when the sources were dereddened using the *NIR NICEST LinES* extinction maps and some sources also have excess emission contributed by circumstellar material. The uncertainties and the excess emission make a definite impact on the colour and magnitudes which had to be taken into account when compared to the discrete classification of the models. For example, the extra contributing emission from circumstellar material may cause the stars to have slightly brighter magnitudes than just the photospheric emission. This implies that the mass and age distributions that are derived from the colour-magnitude diagrams have to be viewed as a rough indicator of the mass and age distributions for each cluster, rather than an indicative distribution. The properties for the individual stars assumed to be cluster members were used as a rough estimate for the star-formation history of both RCW 34 and NGC 2626. These rough histories are compared to one another and discussed relative to other high-mass star-forming regions.

6.2 RCW 34

In Chapter 1 a literary background was given on RCW 34. A thorough description was given of the molecular cloud to the north of the O8.5V star, and the bubble clearing with excited gas being transported away by a champagne effect towards the south of the O-star, VdBH 25a. In Chapter 3 low-mass, young embedded stars were identified in RCW 34 from the *IRSF* data which present excess emission characteristic to CTTs. In Chapter 4 *VPHAS+* data was used to identify stars with an Hα-emission line using excess emission in the $(r' - H\alpha)$ colour. The spatial distribution of both the stars that were identified in the optical and *NIR* datasets extended further than the literature had shown. In this section, all of these stars that were identified as PMS stars using the optical and *NIR* datasets, as well as the *SALT* sources in RCW 34 are compared to each other.

6.2.1 Near-infrared colour-colour diagram

The first — and most important — tool is the colour-colour diagram that was used in Chapter 3 for identifying sources with excess *NIR*-emission. Lada *et al* (1993) explained that PMS sources which have heated circumstellar material present excess emission on the colour-colour diagram. Meyer *et al* (1997) showed that there is an empirical indicator for CTTs on a colour-colour diagram called the CTT locus. A CTT will lie on the locus, and the amount of excess emission is proportional to the amount of circumstellar material. It is important that the stars that show excess Hα- or u'-emission in the optical and amongst the *SALT* candidates be compared to the excess *NIR*-emission sources on the same *NIR* colour-colour diagram. Figure 6.1 shows all of the presumed cluster members plotted together, yet it is a very busy diagram. To better understand the explanation each group is plotted separately on the same diagram in Figures 6.2-6.5 and described in paragraphs **(a)-(f)** respectively.

(a) Uncertainties in the dereddened colours: Figure 6.1 shows the dereddened colours for all the stars that comply with the assumption that they are cluster members. All of these stars were dereddened using the extinction that was read from each corresponding position on the *NICEST LinES* extinction map. In section 3.3.2 a detailed description was given about the construction of the extinction map. The large uncertainties in the dereddened colours are a consequence to the random position to where a field star was dereddened between the two legs of the main sequence. The same large uncertainties are a consequence to the random position where stars that were assumed to be CTTs are dereddened to between the upper and lower limits of the T Tauri locus. The uncertainties in the extinction map at the position of the assumed cluster members are propagated through to the error on each star's extinction. A result of the large uncertainties is that Figure 6.1 indicates how the colours for the cluster members of RCW 34 looks, and none of these should be taken as exact values. The typical error on each colour in Figure 6.1 is $\delta(J - H) = 0.11$ and $\delta(H - K_s) = 0.09$.

(b) The excess *NIR*-emission sources relative to the Herbig Ae/Be region: In Figure 6.2 a Herbig Ae/Be locus from the paper by Lee *et al* (2005) is plotted as a dashed black line and is used to determine which of the cluster members are Herbig stars. Between the Herbig Ae/Be locus, and the main sequence, is a region marked by a yellow rectangle that Hernández *et al* (2005) showed as a region where stars, that are probably Herbig Ae/Be stars, are found. Lee & Chen (2009) showed that

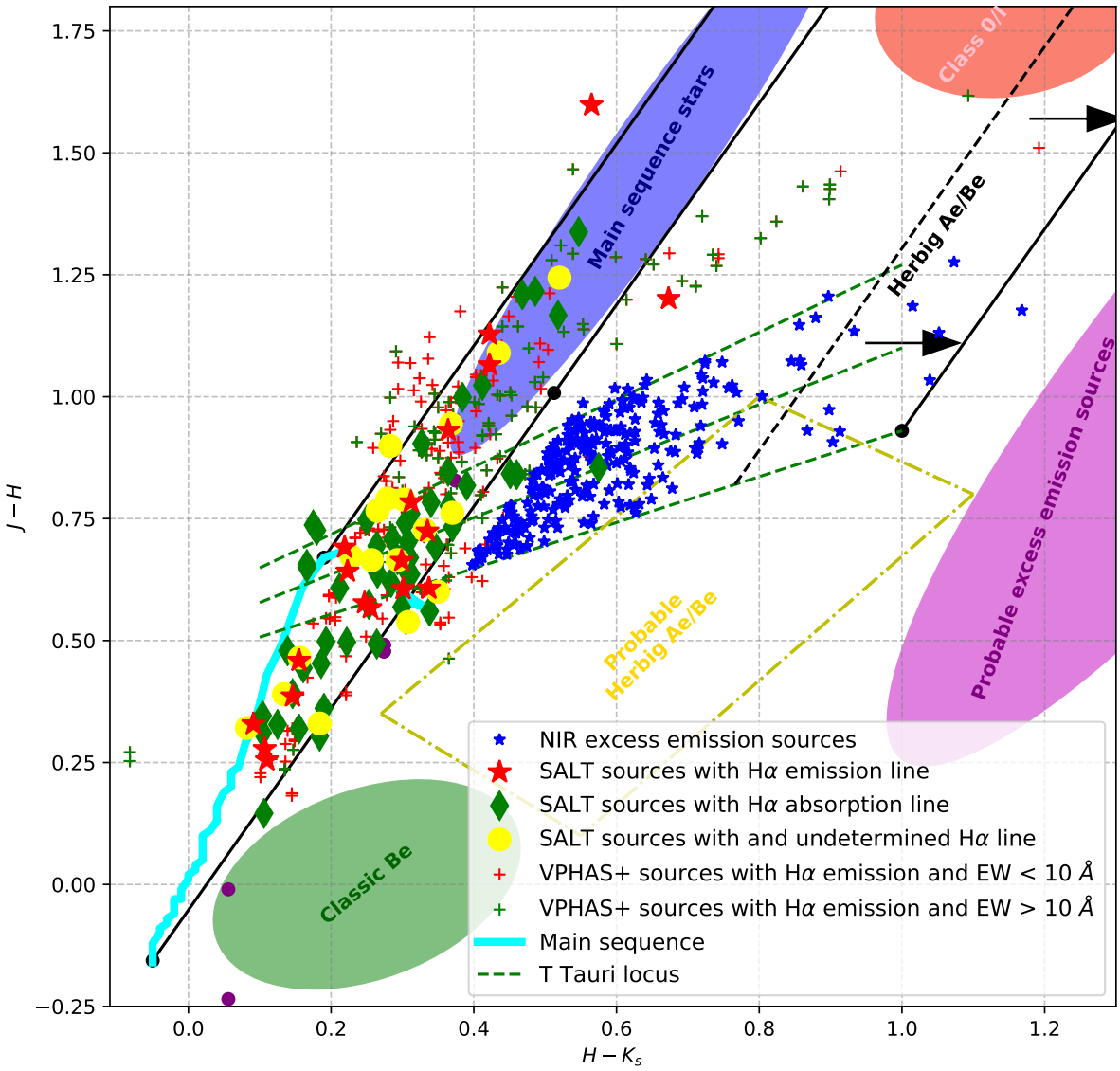

Figure 6.1: $(J-H)/(H-K_s)$ diagram for all of the presumed cluster members in RCW 34.

the region between the yellow rectangle and the main sequence are mainly filled with classic Be stars (it is between the two indication arrows on the figure). There are 19 sources with excess *NIR*-emission that lie past the Herbig Ae/Be excess line, implying they are Herbig Ae/Be stars (see Figure 6.2). There are 21 stars that lie in the yellow rectangle, but also between the limits of the CTT locus, without knowing their spectral class it is not possible to determine what type of PMS stars they are. A single star with excess Hα-emission lies in the yellow rectangle; it may be a Herbig Ae/Be-star. There is just one star with excess u'-emission in the region of the classic Be stars. The vast majority of the cluster members do not feature in the regions where Herbig Ae/Be stars are found, suggesting that most of the excess emission sources in RCW 34 may be CTTs. The uncertainty on each colour makes the exact separation between the CTTs and Herbig Ae/Be stars difficult.

(c) The excess Hα-emission sources: Various sources from the WTTs, CTTs, and a *SALT* source with Hα-emission exhibit strong excess *NIR*-emission and are located past the high-mass reddening line that extends from the main sequence and above the CTT locus (Group A in Figure 6.3). Lada *et al* (1993) explained that sources which present these colours are usually class 0/I infrared sources which are also subject to high extinction. Most of the remainder of sources which were photometrically

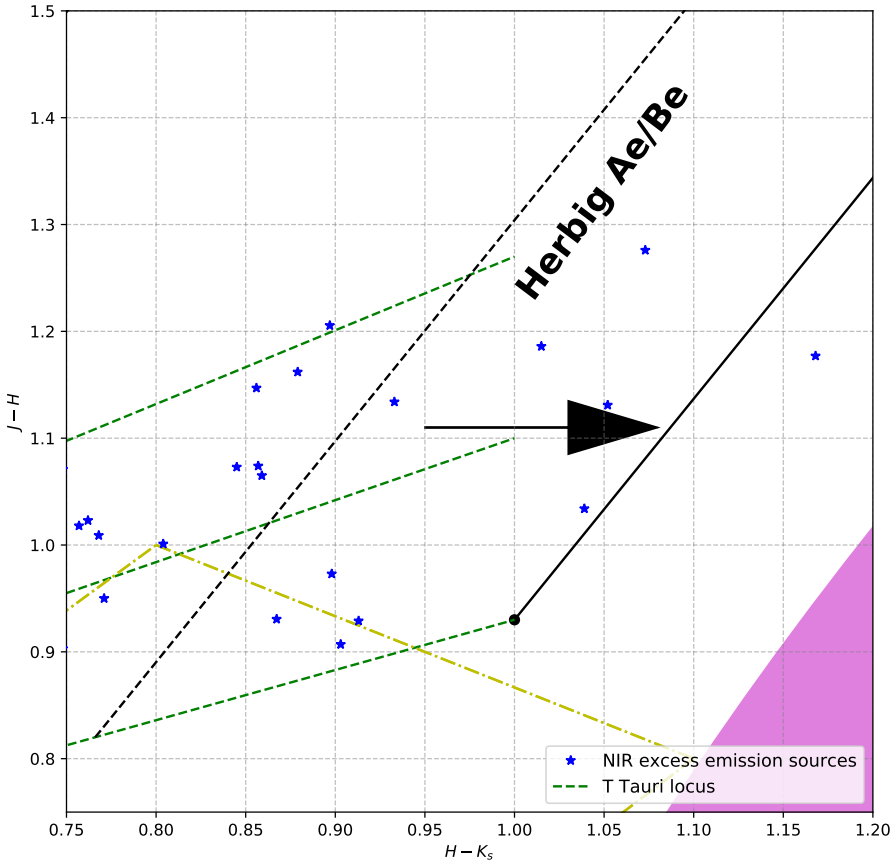

Figure 6.2: The excess *NIR* sources relative to the Herbig Ae/Be seperation line.

identified as Hα-emission stars are distributed between the limits of the CTT locus. The stars that presented photometrically that they have EW $>$ 10 Å, and are between the upper and lower limits of the CTT locus, are considered to be CTTs. The red and green crosses that lie between the lower limit of the CTT locus and the main sequence are most likely WTTs (Group B in Figure 6.3). They are located in the same region of the colour-colour diagram where Strom *et al* (1989) showed a large abundance of WTTs. It is not possible to determine if these stars are main sequence stars which were dereddened with a significant large uncertainty, or PMS stars with some excess emission. The green and red crosses, and the *SALT* Hα-emission source that was dereddened to above the upper limit of the CTTs —and past the high-mass reddening vector — have so much excess emission that they are probably class 0/I *NIR* sources.

(d) The *SALT* candidates and cluster members that lie between the high- and low-mass reddening vectors: For the *SALT* Hα-emission sources in Figure 6.3, there are six with dereddened colours between the upper and lower limits of the CTT locus, meaning they are most probably CTTs (Group A in Figure 6.3). Except for these six, and another one which is amongst the class 0/I (Group B in Figure 6.3) *NIR* sources, the rest are between the high and low-mass reddening vectors of the main sequence. Many of the other green and red crosses are also between the reddening vectors and even though Corradi *et al* (2008) showed that many reddened CTTs have colours in the region, it is not possible to distinguish between CTTs and main sequence stars. There are five *SALT* Hα-emission sources and numerous green and red crosses between the lower limit of the CTT locus and the main sequence (Group C in Figure 6.3). These sources show Hα-emission, but they do not lie on the CTT locus. It is possible that they may be WTTs — Gras-Velázquez & Ray (2005) showed that some WTTs do have some excess *NIR*-emission, but not as much as CTTs. Littlefair *et al* (2004) explains that sources with Hα-emission lines may not show so much excess *NIR*-emission, which may be a

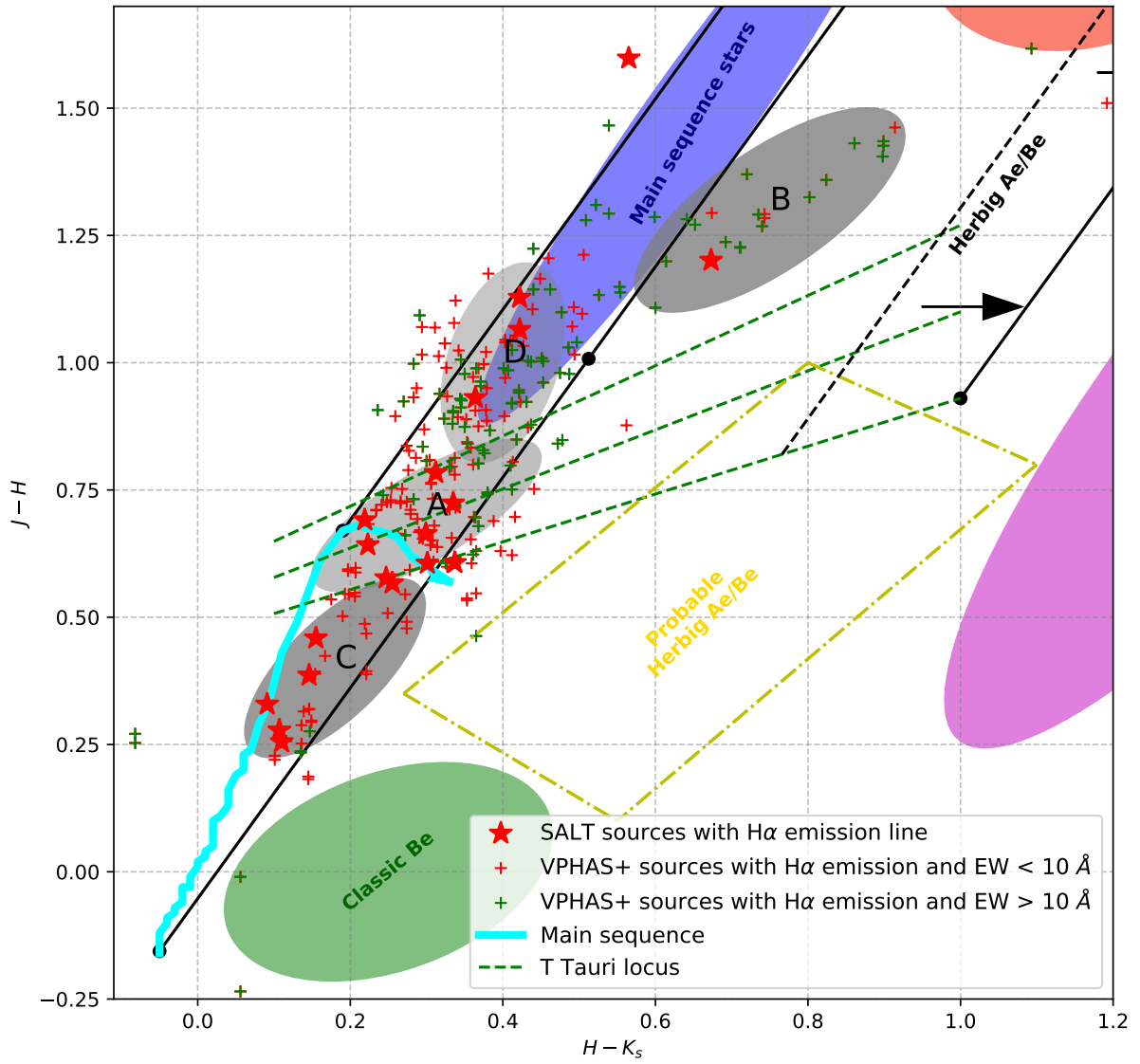

Figure 6.3: The *VPHAS+* Hα-emission sources.

result of variability in the *NIR* colour. A possible physical description for the colour excess shown by sources between the main sequence and the CTT locus, is caused by holes in the circumstellar material giving partial exposure of the photosphere to the observer (shown in SEDs by Gras-Velázquez & Ray 2005). The three *SALT* Hα-emission line sources, and the green and red crosses that group around the low-mass reddening vector resemble a distribution of stars in the Orion nebula cluster (Group D in Figure 6.3). Carpenter *et al* (2002) showed that they are very young cluster members who have *NIR* excess, show variability, and lie in the same region of the low-mass reddening vector.

(e) The *SALT* Hα-absorption line stars: There is one *SALT* source with an Hα-absorption line which lies past the high-mass reddening vector of the main sequence (A in Figure 6.4). This may be due to a systematic error, or a large uncertainty in the dereddened colour, because this star is very unlikely to present excess *NIR*-emission. The other Hα-absorption star population may either be cluster members or field stars; it is not possible to say. They were most likely selected because they had the highest p-selection criteria in a specific region so they were selected by their spatial distribution, which was subject to the maximum number of candidates. The stars with an undetermined Hα-line profile can either be very faint cluster members, WTTs, or faint field stars. It is not practical to determine

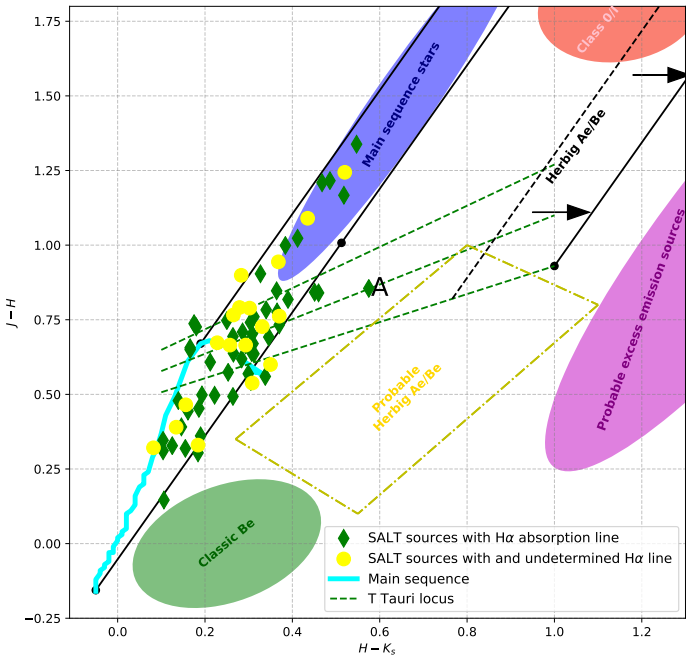

Figure 6.4: The *SALT* sources with an Hα-absorption line.

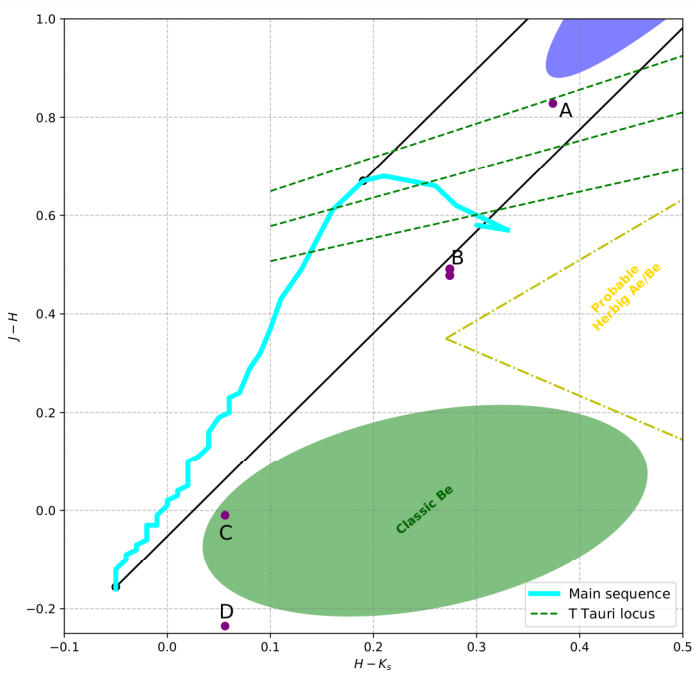

Figure 6.5: The sources with excess u'-emission.

if these stars are indeed cluster members of RCW 34.

(f) The excess u'-emission sources: There are five sources with excess u'-emission of which one has *NIR* colours placing it on the CTT locus (A in Figure 6.5). Two sources lie below the lower limit of the CTT locus — they practically lie on top of each other (B in Figure 6.5). These sources may be slowly accreting T Tauri stars which are described by Ingleby *et al* (2011). The excess ultra-violet emission comes from the inner-disk emission and they are at the final stages of disk evolution. There are two other excess u'-emission sources that lie under the high-mass reddening vector (C and D in Figure 6.5). They may be classic Be stars, or their colours may be a result of systematic errors.

6.2.2 Near-infrared colour-magnitude diagrams

The same sources that are shown in Figure 6.1 are shown in the following colour-magnitude diagram. On a colour-magnitude diagram, the age and mass of a star can be determined when its position is compared to evolutionary models, as shown in Figure 6.6. A distinction can be made between CTTs and Herbig Ae/Be stars based on their magnitudes, similar to the amount of excess emission from a Herbig Ae/Be star on a colour-colour diagram. A Herbig Ae/Be star will have a magnitude brighter than an A9 star and show colour excess, as shown in the colour-magnitude diagrams in Chapter 3. The difference between the previous *NIR* colour-magnitudes in Chapter 3 and Figure 6.6 is that the previous diagrams showed the full population, where as this one only shows the suspected cluster members.

In Figure 6.6 the sources with excess *NIR*-emission are shown as the blue stars, the optical sources with $(r' - H\alpha)$ colour excess similar to an Hα-emission line with EW $<$ 10 Å as red crosses, and those with EW $>$ 10 Å as green crosses. The *SALT* sources with a Hα-emission, absorption, and undetermined line profile are shown as red stars, green diamonds, and yellow dots, respectively. All of the sources have been corrected for a distance modulus at 2.5 kpc and have been dereddened using the *NICEST LinES* extinction map. When compared to colour-magnitude diagrams of the Chameleon nebula by Carpenter *et al* (2002), the ONC by Carpenter *et al* (2001), RCW 38 by Mužić *et al* (2017), and NGC 2264 by Dahm & Simon (2005), the main sequence is placed at the same distance as each star-forming region. In this study the absolute magnitudes are used, meaning the measured magni-

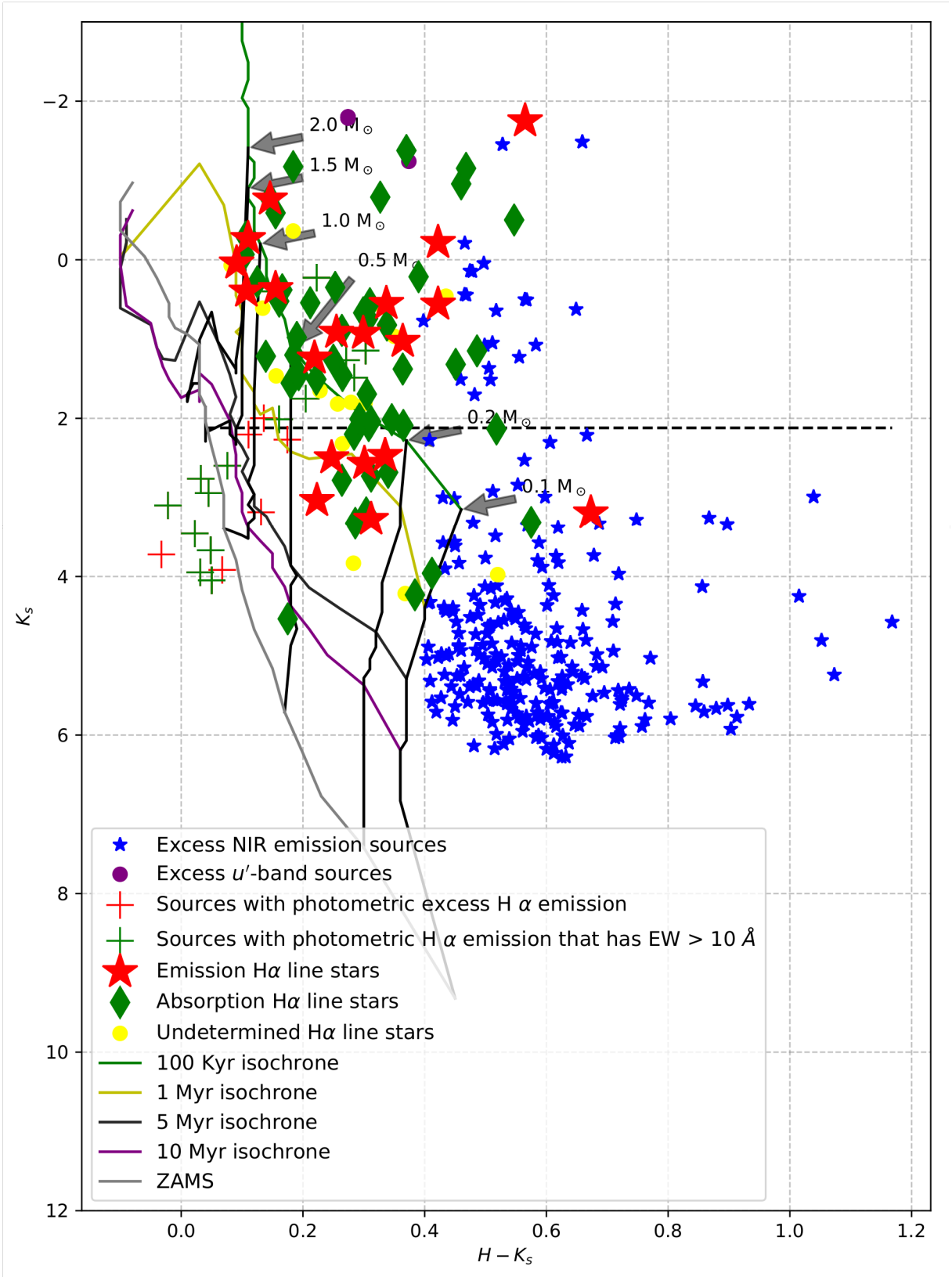

Figure 6.6: $K_s/(H - K_s)$ diagram for all of the presumed cluster members in RCW 34.

tudes are corrected for distance and extinction, and are comparable to evolutionary models and the main sequence without any alteration. Any of these sources may be either foreground or background

stars, even though they do show properties characteristic to PMS stars. If a star is either a foreground or background star the distance modulus for the specific source can not be calculated, and it cannot be compared with the main sequence of evolutionary lines. It has to be assumed that all of the sources on the colour-magnitude diagram are cluster members, especially if a source presented excess emission characteristic to PMS star. Most of the foreground stars have been filtered out during the construction of the extinction map. In Chapter 3 it was explained that the extinction to individual sources were calculated on a colour-colour diagram. It was also explained that those that have a measured extinction less than the average extinction in the Galactic Plane in the direction of both RCW 34 and NGC 2626, were removed from the respective population.

To use the colour-magnitude diagrams to determine ages and masses for the dereddened stars the models from Siess *et al* (2000) were used. In order to use the models an input parameter for the metallicity of the evolutionary lines was required. The metallicities that were measured with PyHammer from the optical spectra in Chapter 5 can be used as an indicator of the metallicity value that should be used for the evolutionary models. The average metallicity measured from most of the *SALT* sources is similar to the Sun $\log_{10}\left(\frac{Z_*}{Z_\odot}\right) = 0. \Rightarrow \frac{Z_*}{Z_\odot} = 1$, see tables 5.7-5.10. The input metallicity that was chosen for the Siess *et al* (2000) models is similar to the Sun, or $Z_* = 0.02$.

All of the optical sources (*VPHAS+* and *SALT*) have an absolute magnitude brighter than $K_s = 4.5$ and do not exhibit more colour excess emission than $(H - K_s) = 0.7$. Compared to the excess *NIR*-emission sources there are a few sources in common between the two groups, because the optical observations were not sensitive enough to detect the majority of the excess *NIR*-emission sources.

None of the dereddened colours and magnitudes of the *SALT* sources lie on the main sequence, suggesting that they may have circumstellar material which would contribute to more excess *NIR*-emission. The dereddened colours of stars with Hα-absorption suggest that they may be WTTs, or they may be field stars. If they are field stars, then the extinction and distance modulus for the star is incorrect, and it can not be compared to the rest of the cluster members. The large group of stars with Hα-absorption lines and $K < 2$ cannot be cluster members, because there are no other high-mass stars in the cluster other then VdBH 25a and its closely associated two B stars. If any of the Hα-absorption line stars are WTTs, they will show less excess emission than CTTs. Gras-Velázquez & Ray (2005) showed a decrease in excess emission in the SEDs of WTTs, when compared to those of CTTs. The physical cause for a Hα-absorption line is a reduced amount of circumstellar material and holes in the accretion disk, giving mainly emission from the photosphere.

Most of the *SALT* sources with Hα-emission which lie below the isochrones (the group with $4 \leq K \leq 2$ and $0.2 \leq (H - K_s) \leq 0.4$) are younger than 2 Myr. Yet most of the *SALT* Hα-emission sources lie above and along the 100 kyr evolutionary line, and not amongst the *VPHAS+* or excess *NIR*-emission sources. This leaves the possibility that the excess emission is from the circumstellar material. Ojha *et al* (2004) showed that many young class II *NIR* sources are some of the brightest sources in NGC 7358. This may also be the case for the *SALT* Hα-emission sources. If a young star has Hα-emission and excess *NIR*-emission in its colours, it is accompanied by an accretion disc. The median wavelength throughput of the K_s-band is around 2 μm, and Bertout *et al* (1988) showed that the heated dust in the accretion disk makes a strong contribution to the excess emission. The results from Hayashi *et al* (2017), which point to the collision between the two molecular clouds as the triggering mechanism for star formation in RCW 34 about 200 kyr ago, make the distribution of the sources above the 100 kyr isochrone believable.

The distribution of the stars with excess $(r' - H\alpha)$ (red and green crosses on the figure) lie amongst the bright *SALT* sources, and the distribution runs along the evolutionary line for stars with a mass of 0.5 $M_\odot < M_* < 1$ $M_\odot$. Some of the green crosses in Figure 6.6 lie along all of the isochrones on an evolutionary line of stars with a mass of 1 $M_\odot$, from above the 100 kyr isochrone up to the main sequence. If the distribution is correct, it shows an ongoing formation of stars within the mass

range of 0.5 $M_{\odot} < M_{*} < 1$ $M_{\odot}$. It is similar to a distribution of Hα-emission stars on a $H/(H-K_s)$ diagram of the ONC in the paper by Szegedi-Elek *et al* (2013). Most of the stars in the distribution by Szegedi-Elek *et al* (2013) are M stars with Hα-emission which are grouped together between the 1 Myr isochrone and the ZAMS. If the distribution of green crosses is correct, it suggests that there is an ongoing process of low-mass star formation in RCW 34, similar to the ONC. However, if the distribution of green crosses are incorrect, then there may be systematic errors in the measured colour and magnitudes, implying that no conclusion can be formed on the nature of these sources. The red crosses are distributed between the green crosses, which implies that there is a population of WTTs and CTTs that have the same ages. This is impossible, because WTTs are, per definition, more matured than CTTs. There has to be an explanation for this — it may be that the stars with Hα-emission have variable emission which implies that the amount of $(r'-H\alpha)$ colour excess and the Hα-emission line's EW changes with time (see Appenzeller *et al* 1986 and Hartmann 1982). If this is the case, then the sources that were observed with *SALT* two years after the *VPHAS+* data was obtained may explain why the *SALT* sources do not show $(r'-H\alpha)$ colour excess. The sources that were identified on the basis of the amount of $(r'-H\alpha)$ colour excess may show Hα-emission, but it is possible that the threshold that was used by Drew *et al* (2005) may differ for the case of RCW 34 or NGC 2626. This means that a colour excess of $(r'-H\alpha)=0.1$ could be used to identify CTTs from the *VPHAS+* data. Sources that showed a $(r'-H\alpha)\leq 0.1$ colour excess may either be WTTs or main sequence stars. The uncertainties induced in the $(r'-H\alpha)$ colour by dereddening makes it impossible to correctly distinguish between WTTs and main sequence stars. A higher threshold for the $(r'-H\alpha)$ colour excess may be used to identify stars which actually show Hα-emission, followed by an even higher threshold for CTTs. The two sources with excess u'-emission are the brightest sources in the field and have *NIR* magnitudes and colours that can not be compared to the isochrones/evolutionary lines. The sources are so bright in the K_s that they are most likely not associated with RCW 34, because they would be high-mass stars.

There are two different groups of stars in Figure 6.6 — those with excess *NIR*-emission and those with excess Hα-emission. Most of the sources with excess *NIR*-emission are fainter than any of those detected in the optical. Altough the optical sources present magnitudes much brighter than the evolutionary models. The distribution of the excess Hα-emission sources suggests that there may be systematic errors in their measurements, and the bright magnitudes of the *SALT* sources may have the same errors. An alternative explanation to systematic errors is that the sources with Hα-emission are the youngest cluster members and were formed during the collision of the two molecular clouds, as stated in Hayashi *et al* (2017). This outcome is most likely not correct, because Galli *et al* (2015) showed that CTTs and WTTs cannot have the same age in the case of the Lupus association — which is also the general case for star-forming regions. It is not possible to see if the errors are only on the *NIR* colour-magnitude diagram, however, closer inspection of the optical colour-magnitude diagram may show correct colours and magnitudes for the excess Hα-emission sources.

6.2.3 Optical colour-magnitude diagram

Figure 6.6 is used to show the absolute magnitudes and dereddened colours of the stars that show results characteristic to young PMS stars. The K_s-band magnitudes were dereddened directly from the extinction map that was constructed in Chapter 3, minimizing the uncertainties by not using an extinction law to calculate the extinction for a different magnitude. One problem with the K_s-band is that a lot of heated dust from circumstellar material contributes to the measured flux from the young star (see Furlan *et al* 2005 and Suh & Kwon 2011). The other problem is the colours and magnitudes of the optical sources which all suffered from systematic errors. An implication of colours and magnitudes which suffered some form of systematic error, is that the interpretation of the results is biased. For example, suppose that 50% of the sources that showed excess Hα-emission similar to WTTs in their $(r'-H\alpha)$ colours are field stars which are incorrectly classified as young cluster members. The age estimate of these incorrectly classified WTTs will influence the age measurement of the cluster because the biased sources will incorrectly be measured relative to isochrones and evolutionary lines and relative to the distance of the cluster. An advantage of using an optical colour-magnitude diagram, specifically a $r'/(r'-i')$ diagram above a *NIR* diagram is it will not be so strongly influenced

by emission from the circumstellar material. Using a $r'/(r'-i')$ diagram will give a better comparison to evolutionary models for excess Hα-sources than Figure 6.6.

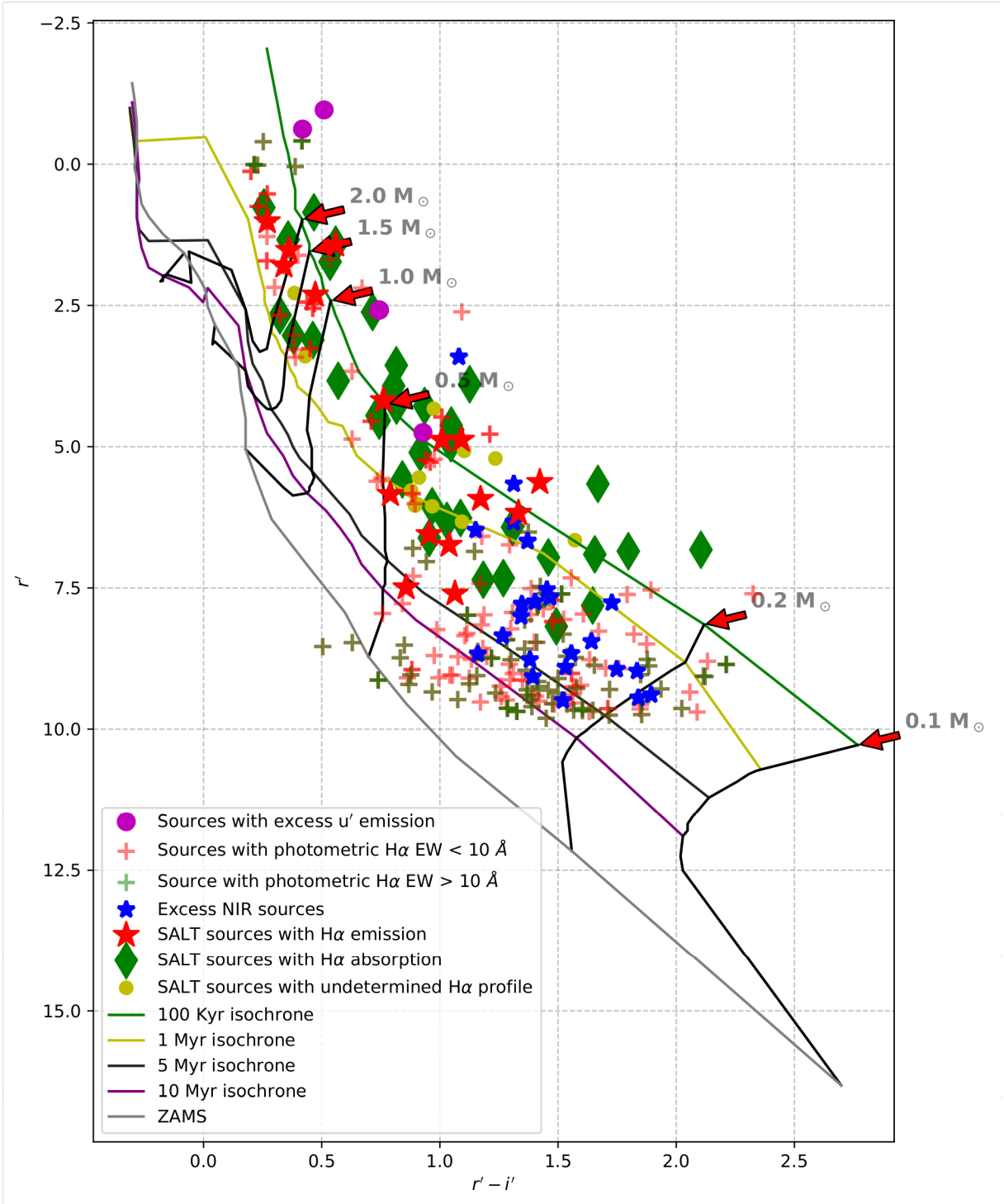

Figure 6.7: $r'/(r'-i')$ diagram for all of the presumed cluster members in RCW 34.

Figure 6.7 shows the dereddened $(r'-i')$ colour and r'-magnitude for the assumed cluster members of RCW 34. In Chapter 4 the recent formation of stars with masses higher than 0.5 $M_\odot$ were shown from the stars with excess Hα-emission. Both groups of the green and red crosses show continuous star formation in the mass $M_* < 0.5$ $M_\odot$ range from the 100 kyr isochrone up to the main sequence.

This would imply that there are WTTs and CTTs in the same cluster that have ages from 100 kyr, right up to the main sequence. Closer inspection of the groups in Figure 6.8 shows there are more WTTs that are younger than the CTTs, which is not possible. This is the same result that the *NIR* colour-magnitude diagram showed, and both of these results point to the same conclusion, namely, that the sources with excess Hα-emission, or at least some of them can not be PMS cluster members of RCW 34. The uncertainties introduced in the $(r' - H\alpha)$ colours by dereddening from the *NIR* extinction map does imply that the strong classification of sources as either WTTs or CTTs — based on the colour excess of $(r' - H\alpha) > 0.1$ — more than the main sequence can not be taken as absolute. This implies that there may be field stars which show excess $(r' - H\alpha)$ caused by the uncertainties from dereddening, and may explain why there are more WTTs which are younger than the CTTs. The ramification of this is that the sources classified as WTTs or CTTs based on the $(r' - H\alpha)$ excess can not be taken as accurate, and are kept in the diagram for illustrative reasons only. They are not considered as members of the cluster in RCW 34. In Chapter 4 and the previous sub-section, it was mentioned that the sources which were identified as Hα-emission sources from their *VPHAS+* colours may be variable sources. This may also explain why the *SALT* sources that showed Hα-emission do not present $(r' - H\alpha)$ excess. The uncertainties in the $(r' - H\alpha)$ colours also imply that this statement is nothing more than a speculation on why there are so few *SALT* sources with $(r' - H\alpha)$ excess.

All of the stars that showed $(r' - H\alpha)$ colour excess and an Hα-emission in their *SALT* spectra is shown in Figure 6.8 for a better comprison with each other, and with the evolutionary lines. The stars with excess *NIR*-emission all have masses $M_* < 0.5$ M$_\odot$, which is better illustrated on an optical colour-magnitude diagram relative to the evolutionary lines, rather than on the *NIR* colour-magnitude diagram. The majority of the stars with strong excess *NIR*-emission were not detected in the r' and i' bands. This may be because of the short exposure times that were used in the *VPHAS+* survey. This is expected, because the SED for the majority of CTTs and WTTs peak only in the *NIR*, and the short exposure times that were used in the *VPHAS+* survey are much shorter than the $\sim$3 hours of exposure time for the *NIR* photometry. With the shorter exposure time of the optical observations and the stronger influence of the extinction in the optical, it is not surprising that only 22 sources with excess *NIR*-emission — or 5% of the 399 stars with excess *NIR*-emission — were detected. Relative to the evolutionary models, these sources are mainly older than 1 Myr, but younger than 10 Myr which suggests that there was continuous star formation in RCW 34 during the past 10 Myr. If the distribution is correct, an implication would be that low-mass star formation in RCW 34 occurred over a longer period than the cloud-cloud collision that was suggested by Hayashi *et al* (2017). The four stars with excess u'-emission which lie above the 100 kyr isochrone may be very young sources. The physical cause for the excess u'-emission that is in most cases it is caused by accretion matter shocking onto the young star's surface (see Hartmann 1998). The excess u'-emission sources were identified using a different set of colour-colour diagrams than the excess Hα-emission colour-colour diagram. Thus, they may not have the same error as the green and red crosses. The bright r'-magnitudes are similar to the results from a study by Szegedi-Elek *et al* (2013) where very young sources showed bright r'-magnitude on a $r'/(r' - i')$ diagram, caused by continuum emission from an accretion disk.

The *SALT* sources and the Hα-emission line sources are all younger than the Siess *et al* (2000) evolutionary line for 10 Myr old stars. Three *SALT* emission line sources have masses $M_* > 1$ M$_\odot$ and are grouped with the other Hα-emission sources between the 100 kyr and 1 Myr isochrones. These three sources might have formed during the interaction between the two molecular clouds which led to the formation of VdBH 25a. With the uncertainties on the dereddened colour and magnitudes, it is not possible to put a definite age on any of these young sources. For the other sources with Hα-emission and a mass $M_* < 0.5$ M$_\odot$, there are five which are older than 1 Myr. If the *VPHAS+* Hα-emission line stars are taken just as an indicator for PMS stars in RCW 34, and the error with regard to the CTTs and WTTs are ignored: They lie together with the excess *NIR*-emission stars and four *SALT* Hα-emission stars on the diagram where $M_* \leq 0.5$ M$_\odot$ are older than 1 Myr. They also suggest that there was low-mass star formation in RCW 34 before the supposed collision of two molecular clouds which triggered the formation of the higher-mass stars.

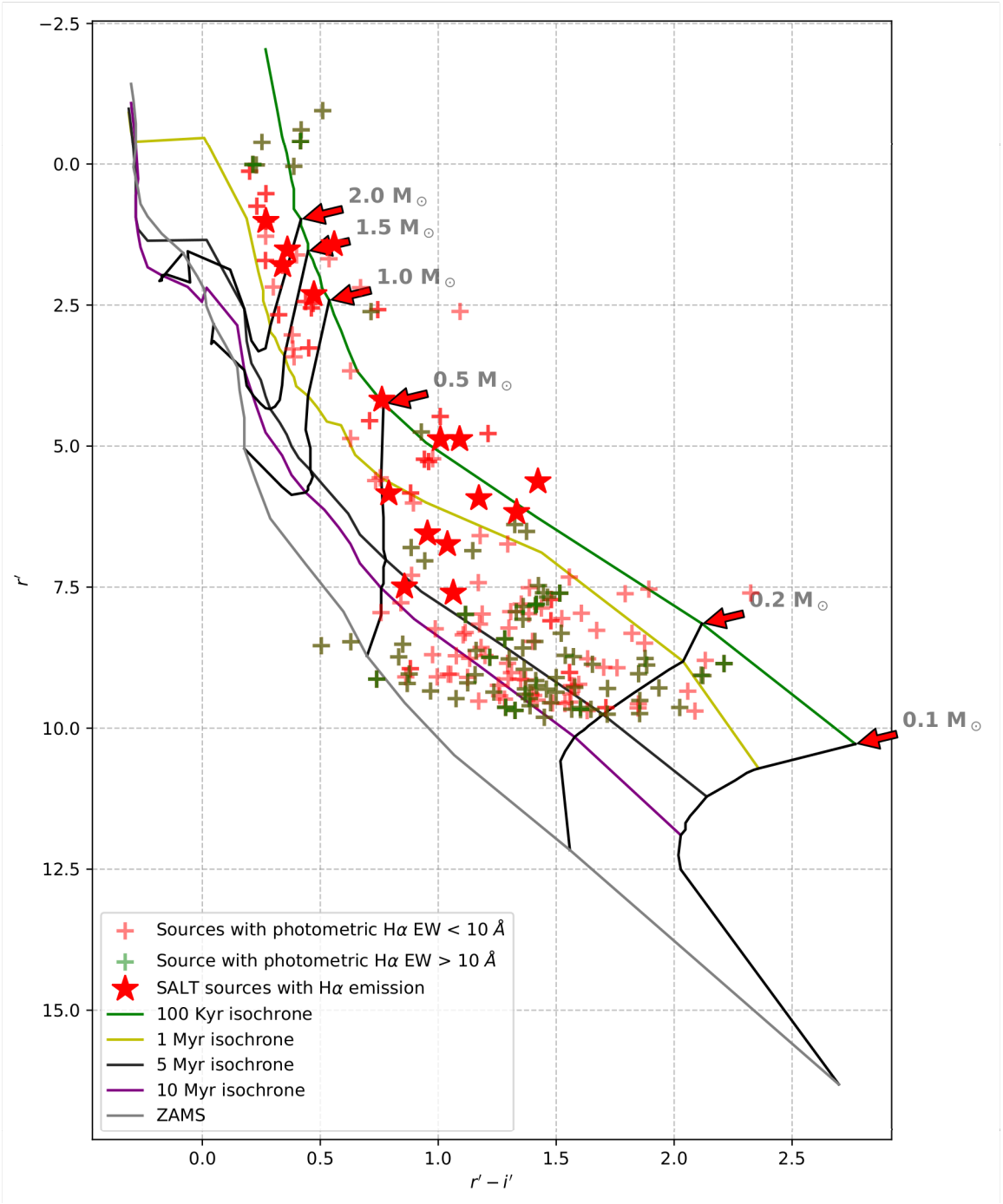

Figure 6.8: The sources that showed excess Hα-emission in their *VPHAS+* $(r' - H\alpha)$ colours.

No definite explanation can be given for the *SALT* sources with Hα-absorption lines. They can either be field stars or cluster members. There is no certain way to determine if the stars with Hα-absorption lines are definite cluster members from the observational data from this study. It is not possible to determine if the stars with an undetermined Hα-line profile are cluster members or not. They may be faint, deeply embedded PMS cluster members, or they may be faint field stars of which the S/N is too weakto resolve a spectrum. The only *SALT* sources that can be confirmed as cluster members are those with a Hα-emission line.

6.2.4 Optical colour-colour diagram

In Chapter 4 sources which presented Hα-emission were identified using the excess emission in their $(r' - H\alpha)$ colour. The classification scheme from Drew *et al* (2005) was used to classify stars as either CTTs or WTTs. From the age distributions of the stars with supposed Hα-emission on both the optical and *NIR* colour-magnitude diagrams, this classification scheme could not be used for RCW 34. The uncertainties in the dereddened colours did not make it possible to classify a star with definite certainty as either a CTT, WTT, or a main sequence star. One major concern that lead to this statement is that there were more WTTs which have ages younger than the CTTs. This concern led to the conclusion that this whole group of excess Hα-emission stars are considered to have been incorrectly identified. This also implies that no properties can be determined for the sources or be compared with the evolutionary models, irrespective of the properties for the models. These sources have been included for reference, and are compared to the *SALT* Hα-emission sources, to investigate if the excess of $(r' - H\alpha) = 0.1$ more than the main sequence can be used for the classification of CTTs.

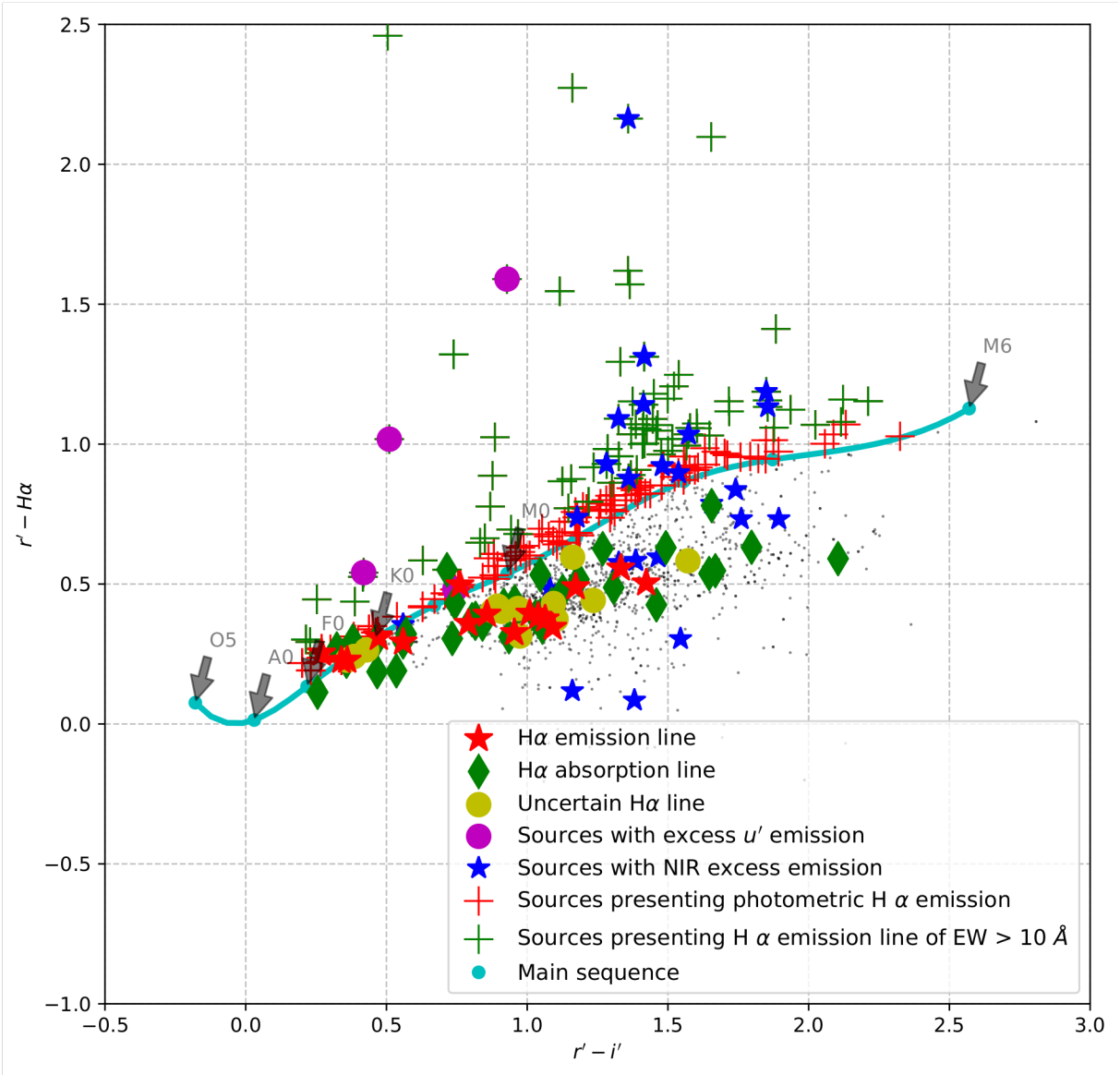

Figure 6.9: $(r' - H\alpha)/(r' - i')$ colour-colour diagram for all of the presumed cluster members in RCW 34.

Figure 6.9 shows the dereddened colours for the cluster members and *SALT* candidates in RCW 34. As in Chapter 4, the $(r' - i')$ colours have been used to estimate the spectral type of each star on the colour-colour diagram, and the $(r' - H\alpha)$ colour to indicate how much excess Hα-emission each star shows. The main sequence was taken from Drew *et al* (2005), where synthetic spectroscopic models for main sequence stars were used to calculate the flux for each spectral type in the respective filters. The main sequence is plotted as a cyan line. All of the *VPHAS+* sources that have a $(r' - H\alpha)$ colour excess are plotted as red crosses for those with an excess smaller than an EW < 10 Å and those with an EW > 10 Å are plotted as green crosses. The 30 sources that showed excess *NIR*-emission, which were detectable in the $r'-$, $i'-$, and Hα-bands, are plotted as blue star symbols.

There are eight excess *NIR*-emission sources that had a corresponding Hα-excess similar to an EW $>$ 10 Å and four with an EW < 10 Å, when compared to the main sequence and the EW classification by Drew *et al* (2014). The other sources with excess *NIR*-emission had various amounts of Hα-emission. The sources that showed excess *NIR*-emission and excess Hα-emission were all part of the large majority of M stars that showed a strong excess in Hα-emission. Some of the excess *NIR*-emission sources had a lot of $(r' - H\alpha)$ excess, while others showed very little excess. This suggests the same error of classifying CTTs and WTTs based on the amount of $(r' - H\alpha)$ excess. The three sources with excess u'-emission present strong Hα-emission in the $(r' - H\alpha)$ colours which is characteristic to CTTs (see Ingleby *et al* 2011 and Walker 1972).

Barentsen *et al* (2013) did a similar study to this one and added a Bayesian statistical analysis which gave an anticipated EW to the measured $(r' - H\alpha)$ excess. As previously stated a similar Bayesian study is outside the scope of this study, but a similar relation to what Barentsen *et al* (2013) established, cloud be established for the stars in RCW 34. Even though the spectra from *SALT* are not flux calibrated, it would be expected that if they have a Hα-emission line, there would be some amount of $(r' - H\alpha)$ excess. The *SALT* sources with Hα-emission and a $(r' - H\alpha)$ colour excess, showed a different result than the cluster studied by Barentsen *et al* (2013) (see Figure 6.10), because they group together with the main sequence stars in the region where Barentsen *et al* (2013) only found main sequence stars with Hα-absorption. The positions of all the *SALT* sources with Hα-emission, absorption, and undetermined Hα-profiles are distributed amongst main sequence field stars. Barentsen *et al* (2011) and Drew *et al* (2005) showed that only main sequence stars should feature in this region. It is not just the CTTs and WTTs on the colour-magnitude diagram which are at the incorrect positions relative to the main sequence. The *SALT* Hα-emission stars on the $(r' - i')/(r' - H\alpha)$ also do not show Hα-emission as $(r' - H\alpha)$ colour excess, relative to the main sequence. RCW 34 is not the only case where Hα-emission stars have $(r' - H\alpha)$ colours amongst the main sequence stars; There are some sources in Figure 5 of Vink *et al* (2008) which show a Hα-emission line in spectra, which have no $(r' - H\alpha)$ excess relative to the main sequence. Vink *et al* (2008) clearly showed that Hα-emission stars' colours which are distributed amongst main sequence stars have very narrow Hα-emission line profiles, similar to the spectrum shown in Figures 5.37a, 5.37c, 5.37d, 5.37e, and 5.37g. From the *SALT* stars with Hα-emission, no relation could be established between the measured EW and the excess in the $(r' - H\alpha)$ colour.

Eighteen sources with excess *NIR*-emission have no excess emission in their $(r' - H\alpha)$ colours. The eighteen *NIR*-excess emission stars with photometric Hα-absorption lie amongst many *SALT* sources that have colours similar to a second branch. This second branch is explained in Drew *et al* (2005) as the main sequence, at a different extinction law. In this secondary branch of the main sequence it is not possible to distinguish between stars which have Hα-absorption and those with emission lines. It is not uncommon to find varying extinction laws in star-forming regions. For example Ascenso *et al* (2012) showed that there are varying extinction laws in different star-forming regions, and a custom *NIR* extinction law was derived for RCW 34 in Chapter 3. It is not clear how such a custom extinction law will affect the broadband r' and narrow band Hα-magnitudes, and if a star with a Hα-emission line will show $(r' - H\alpha)$ excess in RCW 34.

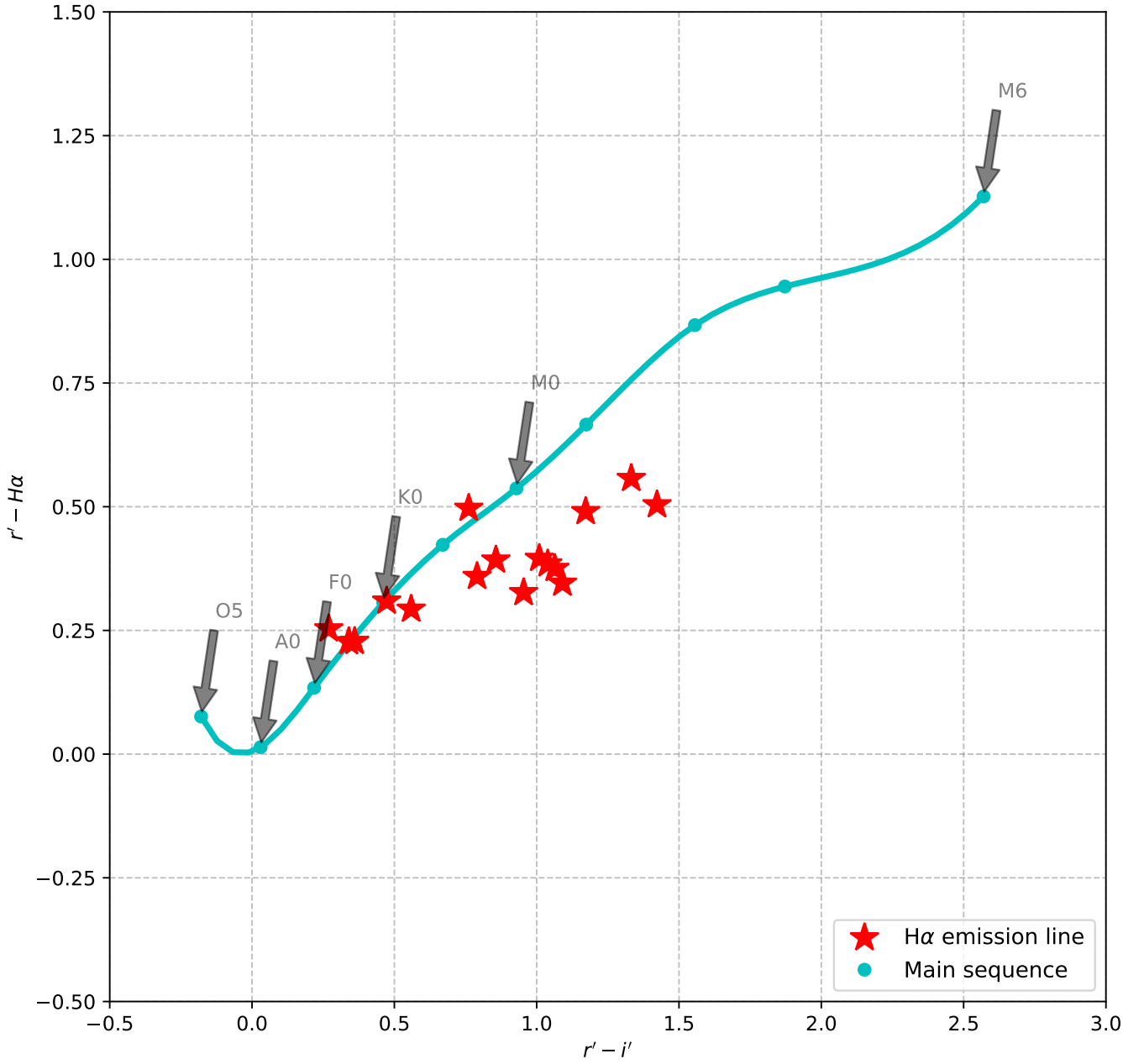

Figure 6.10: $(r' - H\alpha)/(r' - i')$ colour-colour diagram for stars that were observed with *SALT* surrounding RCW 34.

The presence of the *SALT* sources with a Hα-emission line amongst the other *SALT* sources with Hα-absorption also suggests that there is no direct relation between the observed Hα-line profile and the $(r' - H\alpha)$ colour for the sources observed with *SALT*. The distribution of the stars in the field of RCW 34 which lie between the main sequence with an extinction law of $R_V = 3.1$, and the one with a steeper extinction law, shows that the Galactic average extinction law does not apply in the direction of RCW 34. Drew *et al* (2005) distinctly explains that distinguishing between dwarf M emission stars and stars with Hα-absorption is not possible if the emission stars are subject to an extinction law different from the Galactic plane's average. The *SALT* Hα-emission stars have $(r' - H\alpha)$ colours similar to stars with clear Hα-absorption lines. If the extinction law affects the $(r' - H\alpha)$ colours of stars with Hα-emission so much, then using the $(R_s - H\alpha)$ *SuperCOSMOS* colour was not an effective method of selecting Hα-emission candidates. This suggests that colours for the *SALT* sources in

Figure 6.9 cannot be used to derive a relation between the $(r' - H\alpha)$ colour and the observed EW of the Hα-emission line. Interpreting the colours for the *SALT* sources on Figure 6.9 is very difficult, because the stars with Hα-emission, absorption, and undetermined profiles all group together along an apparent locus. For the stars on this secondary locus the $(r' - H\alpha)$ colours are not smaller for the stars with an absorption line than for those with an emission line. The custom extinction law for RCW 34 affects all of the stars in this colour-colour diagram in such a way that the stars that are classified as CTTs and WTTs, according to the scheme from Drew *et al* (2005), may also be incorrect. This cast some doubt on the results and conclusions that were made from the sources with excess Hα-emission in Chapter 4.

6.2.5 $(r' - H\alpha)/(H - K_s)$ excess emission diagram

The $(J - H)/(H - K_s)$ diagram was used to identify stars with excess *NIR*-emission, and the $(r' - i')/(r' - H\alpha)$ diagram to identify stars with Hα-emission. By combining the $(H - K_s)$ and $(r' - H\alpha)$ colours, the amount of excess emission from the accretion disk can be measured from two different excess emission processes. The star's position relative to the main sequence on the colour-colour diagram is an indication of the star's age. The youngest stars have the most excess emission in both colours, as the star matures the excess emission will decrease, and its colours will come closer to the main sequence.

Figure 6.11 shows the excess emission colour-colour diagram for the dereddened cluster members and *SALT* candidates in RCW 34. One colour shows excess emission from heated dust in the circumstellar material, while the other colour shows excess emission if the star has a Hα-emission line. With the new introduction of this colour-colour diagram, the only indication of a star's spectral type is the main sequence; there is no evolutionary indication if a star has excess emission, or what its age or spectral type might be. There is also a degeneracy for the $(r' - H\alpha)$ colour of K-M stars. If a star of this type has Hα-emission it does not show excess $(r' - H\alpha)$ emission, implying that stars with Hα-emission and absorption may have the same colours. This influences the $(r' - H\alpha)$ colour of each K-M star, but does not influence the excess *NIR*-emission from these young stars. Figure 6.9 does not only show this degeneracy for RCW 34, but it also shows that there is no relation between the $(r' - H\alpha)$ excess and an Hα-emission line. In the literature the degeneracy does not exist for some of the other star-forming regions, which means the general rule is that the relation between $(r' - H\alpha)$ excess and an Hα EW differs between star-forming regions (see Barentsen *et al* 2011, Barentsen *et al* 2013, Vink *et al* 2008, and Corradi *et al* 2008). The excess *NIR*-emission sources show some of the largest variety in $(r' - H\alpha)$ excess. This large variety of the $(r' - H\alpha)$ emission for the excess *NIR*-emission is a direct consequence of the lack of a relation between the observed Hα EW and any $(r' - H\alpha)$ excess. The exact reason for this lack of relation between the Hα EW and $(r' - H\alpha)$ is not clear, however, it can be a result of extinction. Some sources may have a clearing in the line of sight so that the Hα-emission from the accretion disk can be observed, while the emission from others with similar colours are completely absorbed by the dust in the circumstellar material. The two sources with excess u'-emission have strong excess *NIR*-emission, and one also shows strong $(r' - H\alpha)$ excess. These two stars are assumed to be CTTs.

All the *SALT* sources show the same grouping as in the $(r' - H\alpha)/(r' - i')$ diagram. The sources with Hα-absorption and emission line profiles lie together, not showing any effects of the amount of excess $(r' - H\alpha)$ or $(H - K_s)$. Similarly to the $(r' - H\alpha)/(r' - i')$ diagrams, this may be the effect of using a different extinction law than the Galactic plane's average, $R_V = 3.1$. It is interesting that the *SALT* sources with Hα-absorption lines have some of the strongest *NIR*-excess emission, while those with Hα-emission lines lie closer to the main sequence. No interpretation can be made from the $(r' - H\alpha)$ colours of the *SALT* sources, due to the uncommon effects of the extinction law on the $(r' - H\alpha)$ colours.

The sources that presented excess emission in their $(r' - H\alpha)$ colour, relative to the main sequence on a $(r' - H\alpha)/(r' - i')$ colour-colour diagram, were identified as Hα-emission sources using the criteria from Drew *et al* (2005). From the two colour-magnitude and two colour-colour diagrams, these sources have been disregarded from analysis on this excess emission diagram.

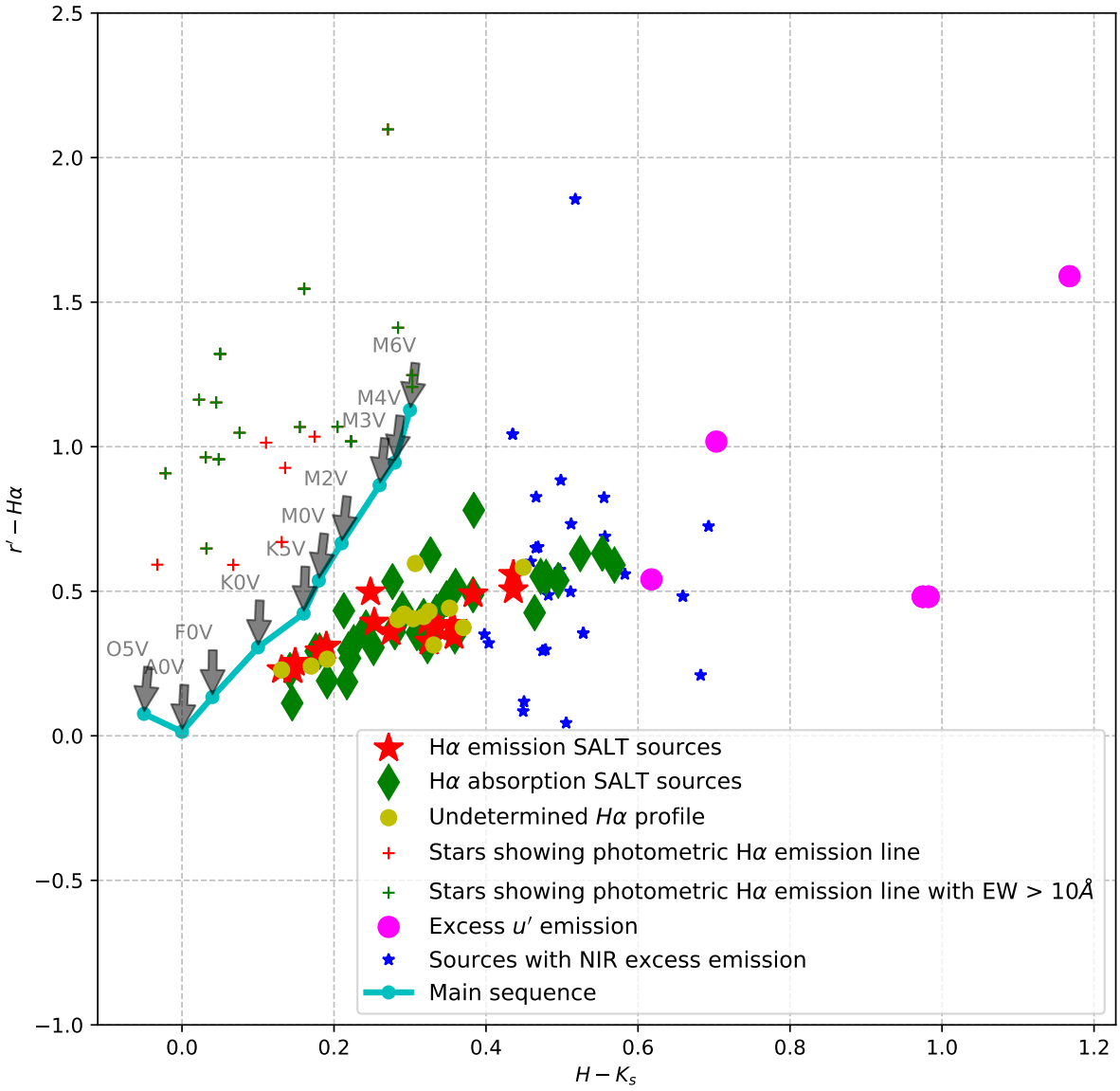

Figure 6.11: $(r' - H\alpha)/(H - K_s)$ excess colour-colour diagram for all of the cluster members in RCW 34.

The excess emission diagram does not serve its intended purpose, specifically for the case of RCW 34. This is because none of the *SALT* Hα-emission line sources, or the excess Hα-emission sources showed strong excess emission in both colours. Only speculation can be given for this negative result, but the custom extinction law for RCW 34 may not affect the $(H - K_s)$ only, but also the $(r' - H\alpha)$ colour.

6.2.6 Mass distribution

The mass distributions were derived from the optical colour-magnitude diagrams for the stars that lay between the 100 kyr and ZAMS isochrones, laying between the 0.1 $M_\odot$ and 2.0 $M_\odot$ evolutionary lines. In this section a mass distribution is analysed for the nine *SALT* sources with Hα-emission, excess *NIR*- and u'-emission.

The binning was done in intervals of 0.1 $M_\odot$ over the mass range under which young PMS stars are classified as CTTs ($M_* < 2$ $M_\odot$). The majority of the sources have a stellar mass of $M_* < 0.5$ $M_\odot$, which is contributed by the population of low-mass stars shown in Figure 6.7. The number of cluster

members is very low — it would be significantly larger if optical photometry could be used to identify sources with excess Hα-emission. The distribution of groups of supposed CTTs and WTTs were identified using $(r' - H\alpha)$ excess, which showed that the classification was incorrect and is thus not used here. Using a low number of sources may not give an accurate indication of the mass distribution, but the distributions are tested against two theoretical IMFs.

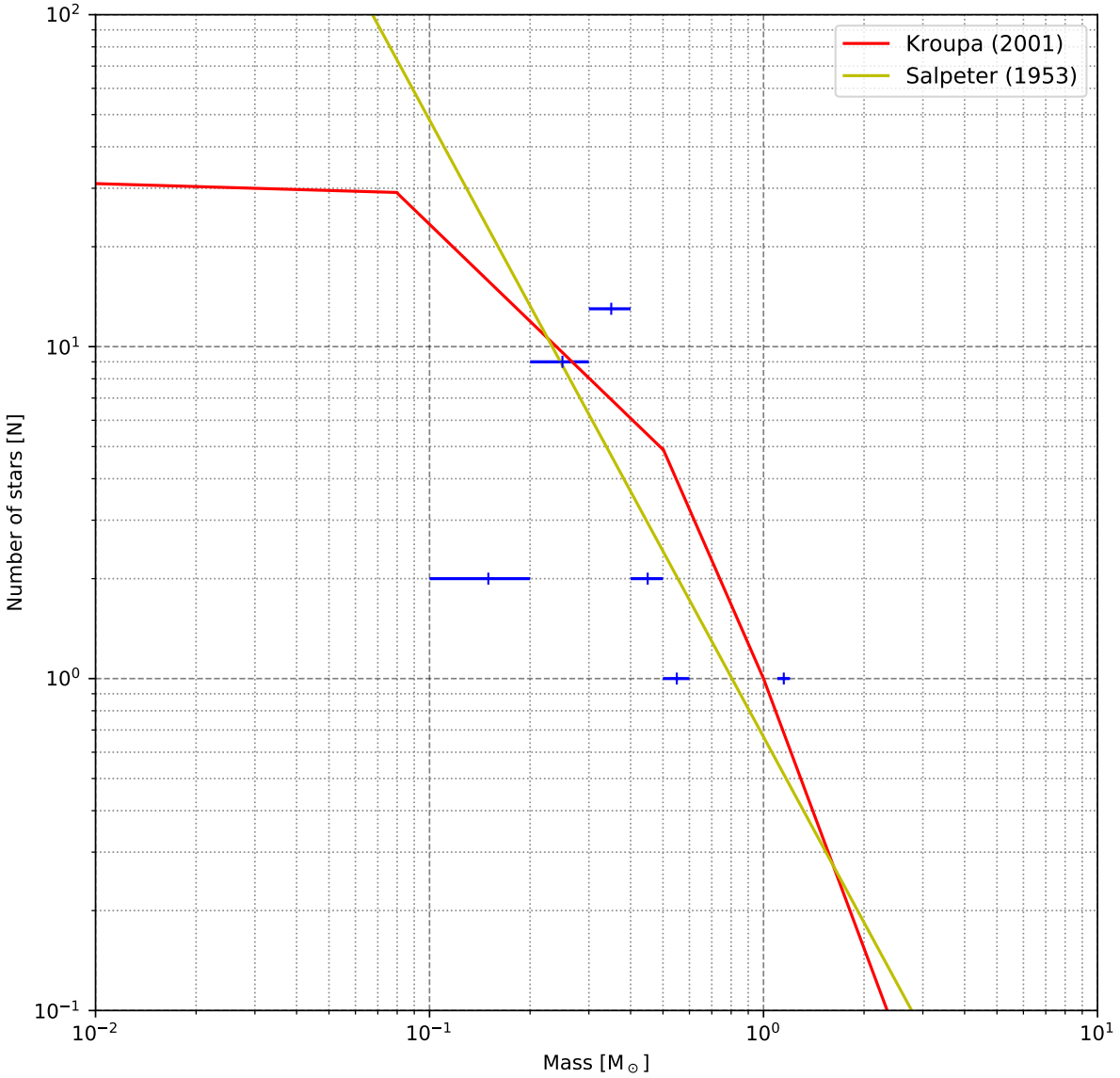

Figure 6.12: The mass distribution for all of the cluster members observed in RCW 34.

Figure 6.12 shows all of the sources binned in each mass interval that are counted together. The mass distribution for the cluster members were tested against the well-known IMF's from Salpeter (1955) and Kroupa (2001). There were only 33 sources in the total distribution, which made the comparison with the theoretical power-laws impractical. Barentsen *et al* (2013) also had a limited number of sources, but established what power-law fit their data over a specific mass range. The same fit could not be done for this data, because of the low number of sources; it can either be a Salpeter or Kroupa power-law.

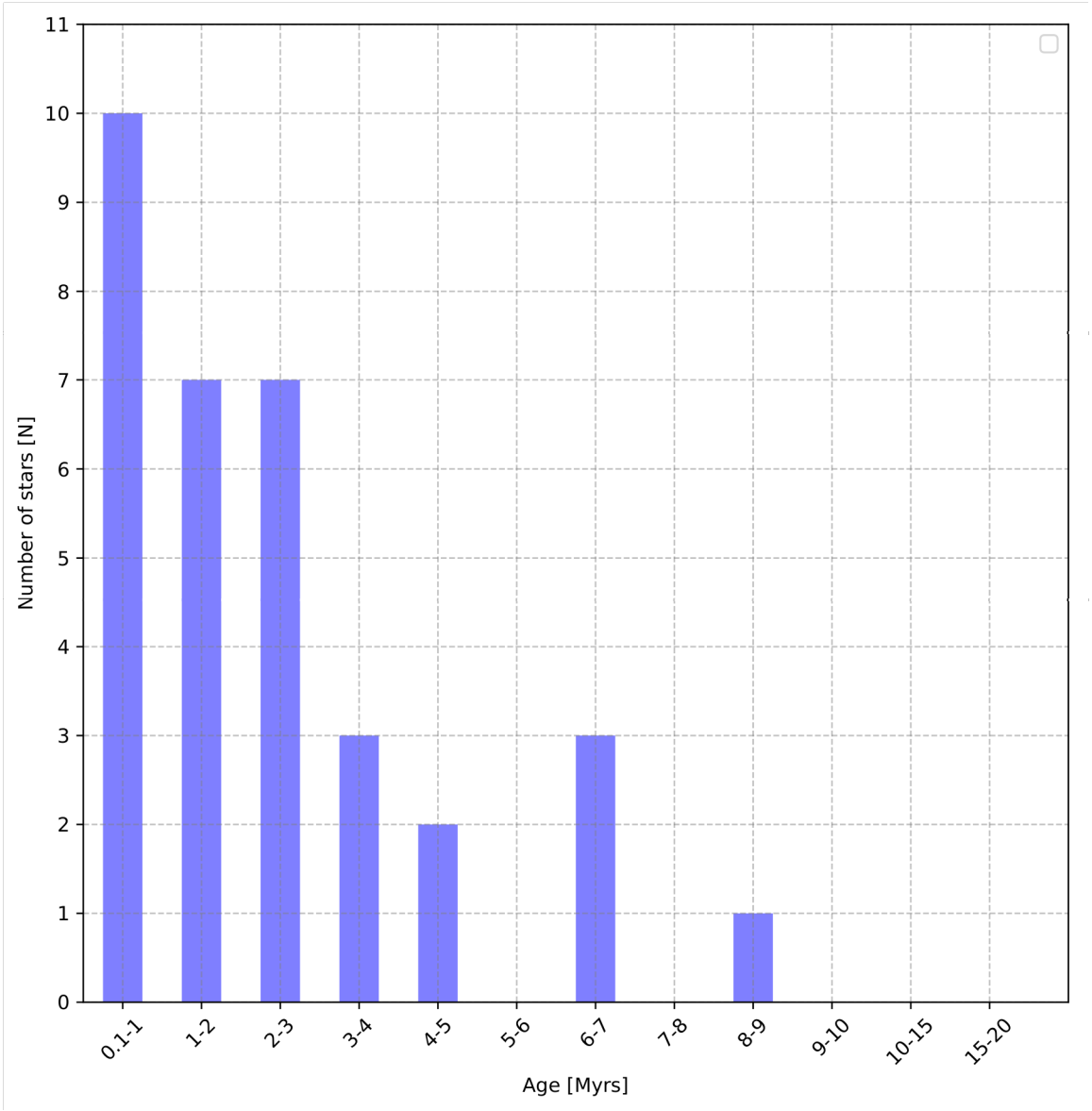

Figure 6.13: The age distribution for all of the cluster members in RCW 34.

6.2.7 Age distribution

Figure 6.13 shows the distribution of the 33 sources which are considered as cluster members in RCW 34. If the distribution is correct, then it shows that a significant number of sources are younger than 3 Myr. The formation of the younger sources was most likely triggered by the same mechanism that formed VdBH 25a — most likely the cloud-cloud collision that was suggested by Hayashi *et al* (2017). Bik *et al* (2010) put an upper limit of 2 ± 1 Myr on the population of the stars that were studied in the bubble region, but mentions that there are younger low-mass members shown by the presence of class 0/I infrared sources. With all of the previous studies and the cluster members in Figure 6.13 showing that most of the stars formed within the last 1-3 Myr, the probability that the triggering mechanism for star formation in RCW 34 was the cloud-cloud collision suggested by Hayashi *et al* (2017) is quite high.

The age distribution in Figure 6.13 is consistent with the age of the cluster given by Bik *et al* (2010). The precision of the ages is not high enough to compare it with the age of 200 kyr old objects, as was found by Hayashi *et al* (2017). These results will be compared to the matching sets for NGC 2626 that are shown in the next section, and will be discussed in the final Chapter, Chapter 7.

6.3 NGC 2626

In Chapter 1, a literary background for NGC 2626 reported that the Hα-emission stars discovered by Mueller & Graham (2000) span far from the bright rim cloud: In the center of the field, embedded in a molecular cloud (SFO 54 called by Sharma *et al* 2016) there is a maser source which can be associated with a closely positioned Herbig-Haro source, HH-132. Sharma *et al* (2016) also showed that there is a continuous process of star formation occurring in NGC 2626; Because there are both class 0/I and class II *NIR* sources, as well as low-mass cluster members close to the main sequence in the molecular cloud. Even though Sharma *et al* (2016) did a study on a larger field, detailed attention was not given to Hα-emission sources. This left some room for a study that looked at young low-mass cluster members in both the optical and the *NIR*. It is important to compare the sources that showed excess *NIR*- and u'-emission with each other, and the stars observed with *SALT*.

6.3.1 Near-infrared colour-colour diagram

The *NIR* colour-colour diagram is shown first, similar to the section on RCW 34, because it is the most direct way of showing which sources have excess emission. It is the primary source used in Chapter 3 to identify young PMS stars and it played an important role in this study and is used to determine how much excess *NIR*-emission the other suspected cluster members show.

Figure 6.14 shows the dereddened cluster members and *SALT* candidates observed in NGC 2626. As mentioned in the case of Figure 6.1, the colours were dereddened using the extinction maps built in Chapter 3. This implies that a significant uncertainty exists for the colours shown in Figure 6.14. There are fewer field stars behind the cluster that were used for the construction of the extinction map for NGC 2626 than for RCW 34. This implies that the dereddened colours for NGC 2626 in Figure 6.14 have larger uncertainties than those for RCW 34. However, it is necessary to compare these dereddened colours of the young stars with the CTT locus (see Meyer *et al* 1997), the Herbig Ae/Be locus (see Lee *et al* 2005), and the region occupied by stars with a probability of being Herbig Ae/Be stars (see Lee & Chen 2009).

The sources with excess *NIR*-emission are shown as blue stars in Figure 6.15. As discussed in Chapter 3 the sources between the upper and lower limits of the CTT locus, are considered to be CTTs. There are seven *NIR*-excess sources and a *SALT* Hα-emission line source that lie on the upper limit of the CTT locus (Group A). This grouping, the excess *NIR*-emission sources between the limits of the CTT locus, and the three *SALT* Hα-emission sources that lie at the lower limit of the CTT locus, are considered CTTs. The three *SALT* Hα-emission line sources between the high-mass reddening vector and the Herbig Ae/Be locus above the upper limit of the CTT locus, are most likely class 0/I sources (Group B). Together with these three *SALT* sources there are four excess *NIR*-emission sources which are also considered to be class 0/I *NIR* sources. There are four *SALT* Hα-emission sources which are not included in the CTTs or class 0/I *NIR* source classification. Two of these *SALT* Hα-emission line sources lie on the main sequence; this location on the diagram is where Strom *et al* (1989) found many WTTs. These sources are most likely WTTs (Group C). The last two *SALT* Hα-emission line stars lie above the upper limit of the CTT locus between high-mass and low-mass reddening vectors of the main sequence. The first of these does not lie unreasonably far above the upper limit of the CTT locus so it can be considered a CTTs. The last *SALT* Hα-emission line star lies along the high-mass reddening vector of the main sequence. This star can be dereddened to the CTT locus if the errors on the magnitude and the extinction map are taken into account.

There are three *SALT* sources with undetermined Hα-line profiles, one in the upper limit of the CTT locus, which may be a reddened field star. Two other undetermined Hα-line profiles with strong excess emission, more than HH-132, lie in the region of the diagram where class 0/I infrared sources are present. Of the eight *SALT* sources with a Hα-absorption line, six lie in a region of the colour-colour diagram where they can be dereddened to the main sequence. One lies right next to the high-mass reddening vector, which may also be dereddened to the main sequence, and the last one is HH-132. There are five *NIR* sources which have excess more than the Herbig Ae/Be locus, of which one lies

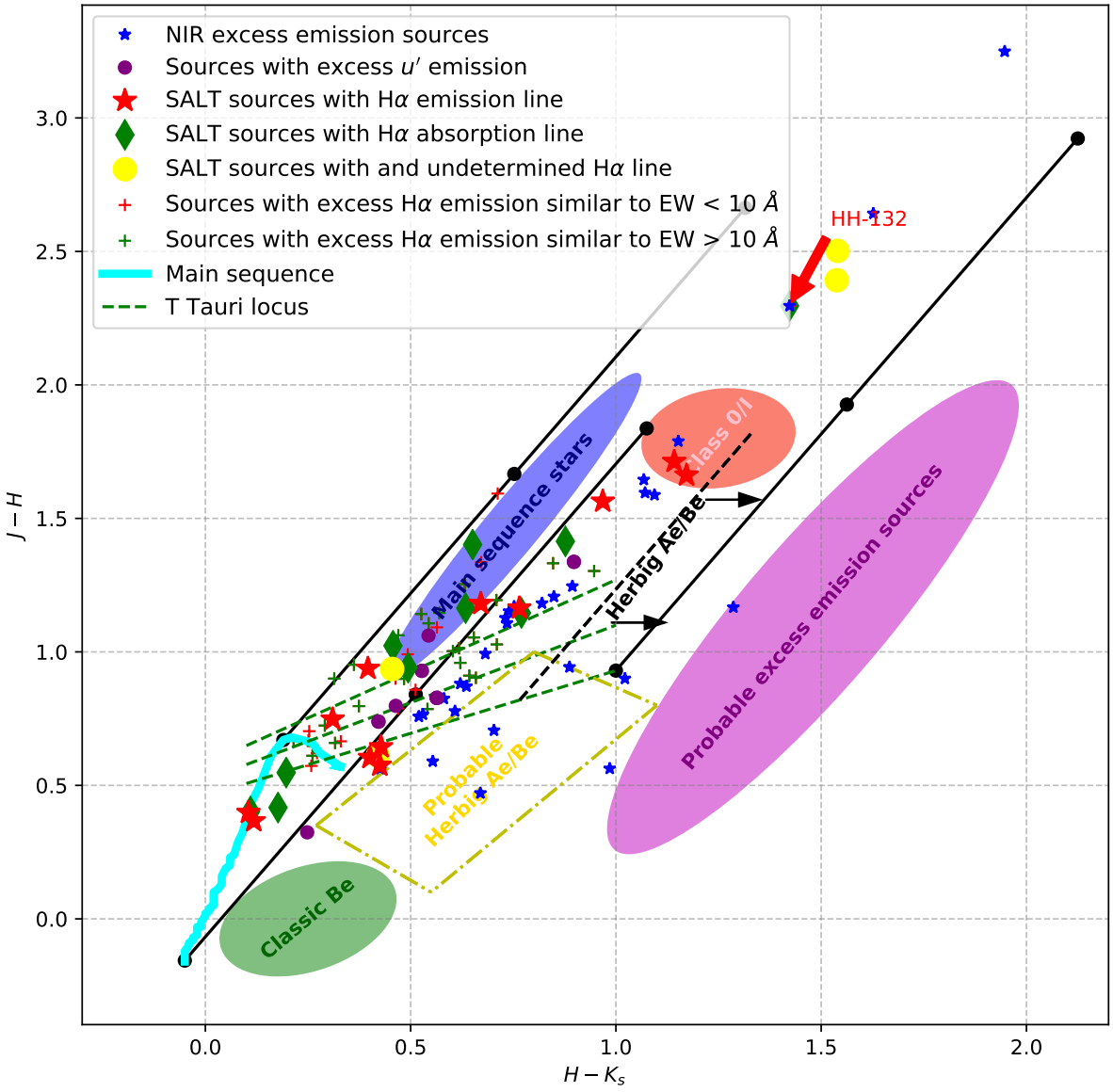

Figure 6.14: $(J-H)/(H-K_s)$ diagram for all of the suspected cluster members in NGC 2626.

within the limits of the CTT locus. Three of these lie in the region where stars have high likelihood of being Herbig Ae/Be stars, and one that is not past the Herbig Ae/Be locus. The three that have excess more than the locus, and are in the yellow rectangle, have to be Herbig Ae/Be stars. In Chapter 3 there were four sources with excess *NIR*-emission on the $K_s/(H-K_s)$ colour-magnitude diagram shown in Figure 3.43 which were brighter than an A-type line, which included the driving star for HH-132. A possible reason why the star driving HH-132 does not appear past the excess Herbig Ae/Be locus may be the emission from the Herbig Haro object, that was included in the photometric measurements from the star, resulting in the strong $(J-H)$ excess.

The *NIR* colours for four of the seven stars with excess u'-emission lie between the limits of the CTT locus. With both excess u'-emission and *NIR*-emission on the CTT locus, these stars are most likely CTTs. Two stars with excess u'-emission have colours above the upper limit of the CTT locus, they are close to the upper limit of the CTT locus. If the uncertainties on the dereddened colours are taken into account, they may be considered to be on the CTT locus. The last star with excess u'-emission lies far below the CTT locus, and it is not uncommon to find WTTs below the CTT locus. They can

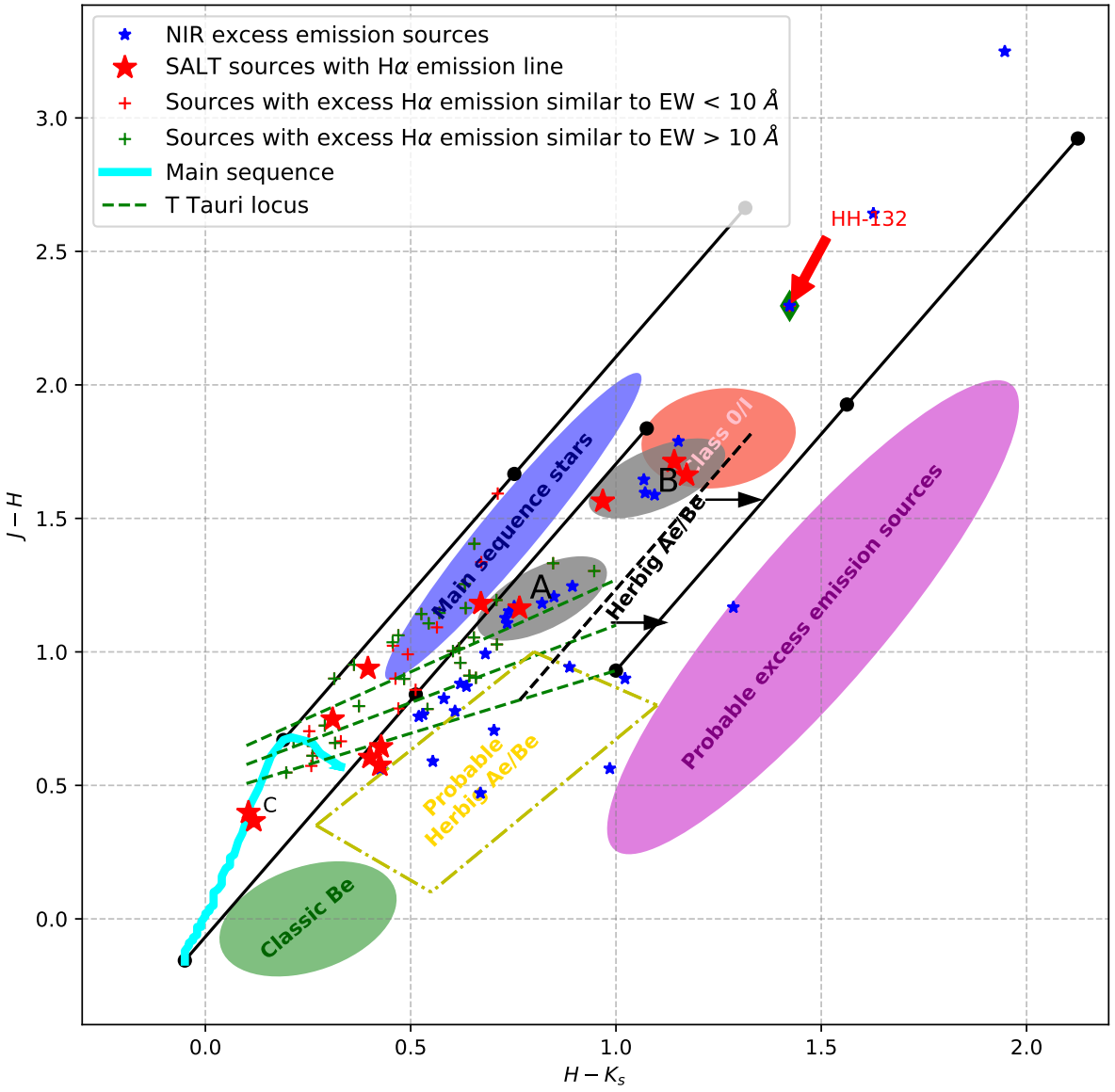

Figure 6.15: All of the sources that showed Hα-emission and excess *NIR*-emission in NGC 2626.

show excess u'-emission as was shown by Ingleby *et al* (2011).

The sources that were identified with the *VPHAS+* photometry as Hα-emission line stars are plotted as green and red crosses, representing the stars with excess more than the main sequence for $(r' - H\alpha) > 0.1$ and $(r' - H\alpha) < 0.1$, respectively. The uncertainties introduced into the dereddened $(r' - H\alpha)$ colours from the *NIR* extinction map implies that none of the stars which are classified as Hα-emission sources according to their *VPHAS+* colours can be seen as correct. The most likely cause was the custom extinction law in RCW 34, but NGC 2626 had the same general extinction law as the Galactic Plane, which might imply that $(r' - H\alpha)$ excess indicates Hα-emission. The majority of these sources lie between the upper and lower limits of the CTT locus — with apparent excess Hα-emission and excess *NIR*-emission characteristic to CTTs, these sources may be CTTs. Others lie above the upper limit of the CTT locus, between the low-mass reddening vector of the main sequence, and the Herbig Ae/Be separation line. It is not clear if these sources may be PMS stars, but with excess Hα-emission and some excess *NIR*-emission, they might be.

6.3.2 Near-infrared colour-magnitude diagrams

The *NIR* colour-magnitude diagrams shown in Chapter 3 and for RCW 34 in the previous section showed magnitudes of the suspected cluster members that were too bright to compare with the evolutionary models from Siess *et al* (2000). It is not just that the models from Siess *et al* (2000) which do not include the excess emission from an accretion disk or the outflows associated with a T Tauri system, which makes it impractical to compare the measurements with the evolutionary models. However, with all other models only the evolutionary stages of photospheric emission are included (see Paxton *et al* 2015, Pietrinferni *et al* 2004, Yi *et al* 2001). The main purpose of theoretical evolutionary models is to describe a star's evolutionary progress during the main sequence. The only theoretical models which describe the evolution of a star-and-disk system during the PMS phase are the models from Lodato *et al* (2017) on a $\dot{M}/M_d$ (change in a mass against the mass of the disk) diagram.

The colour-magnitude diagrams are important because they show young cluster members which have strong emission from circumstellar material that contributes to the measured emission from the sources. This makes it difficult to determine an age and mass for these suspected cluster members, but shows the extra emission from the heated gas in the circumstellar material.

Figure 6.16 shows the sources in NGC 2626 and uses the same colour and symbol annotation for the *VPHAS+*, *IRSF*, and *SALT* sources as in Figure 6.6. All of the sources have been dereddened using the *NICEST LinES* extinction map from Chapter 3. The sources with excess *NIR*-emission are the faintest sources and have excess emission from circumstellar material which causes them not to be comparable with the evolutionary models from Siess *et al* (2000). Three sources with excess *NIR*-emission also showed Hα-emission similar to an EW $>$ 10 Å. They are indicated with green crosses over blue stars.

The sources with excess Hα-emission show $(H - K_s)$ colour excess and have magnitudes brighter than the evolutionary models. Comparing the populations of supposed WTTs and CTTs to each other, there is no clear distinction between the groups of the red and green crosses, respectively. At least the WTTs should be comparable to the models, and have less $(H - K_s)$ than the CTTs. These results imply the same as the colour-magnitude diagrams for RCW 34 in Figure 6.6 and 6.7, namely that the stars which showed excess $(r' - H\alpha)$ can not be considered as young cluster members and do not indicate CTTs and WTTs.

The distribution of sources with excess *NIR*-emission agree with the distribution of the $K_s/(H - K_s)$ colour-magnitude diagram in Figure 7 of Sharma *et al* (2016). Sharma *et al* (2016) distinguishes between class 0/I, and II infrared and confirmed CTTs on a colour-magnitude diagram and compares them with theoretical models. For comparison with this colour-magnitude diagram it has to be noted that Sharma *et al* (2016) placed the main sequence and evolutionary lines at the same distance as NGC 2626, but did not deredden their colours and magnitudes. In this study, the absolute magnitudes and dereddened colours are used in this colour-magnitude diagram, as well as for RCW 34. Most of the sources in Figure 6.16 with strong excess *NIR*-emission are in the same region as the class 0/I infrared sources. The bright sources with excess u'-emission have $(H - K_s)$ excess compared to the evolutionary models, which implies that they have circumstellar material and may be CTTs.

Four *SALT* Hα-emission sources can be compared to the evolutionary models — three are younger than 5 Myr and have a mass in the range 0.5 $M_\odot < M_* <$ 1 $M_\odot$, and one is younger than 1 Myr and has a mass of 0.2 $M_\odot < M_* <$ 0.5 $M_\odot$. The other three sources lie outside of the evolutionary models, suggesting that these sources are young PMS sources. The two *SALT* Hα-absorption line stars cannot be distinguished as either field stars or cluster members. The driving star for HH-132 is the only *SALT* source with strong $(H - K_s)$ excess emission and an Hα-absorption line. It is very unusual that this source has Hα-absorption and so much excess *NIR*-emission. Piche *et al* (1995) also observed strong excess $(H - K_s)$ emission from HH-124. The colour excess emission in HH-132 is from a *NIR* reflective nebula and the heated gas of the Herbig Haro outflows. HH-132 has an outflow

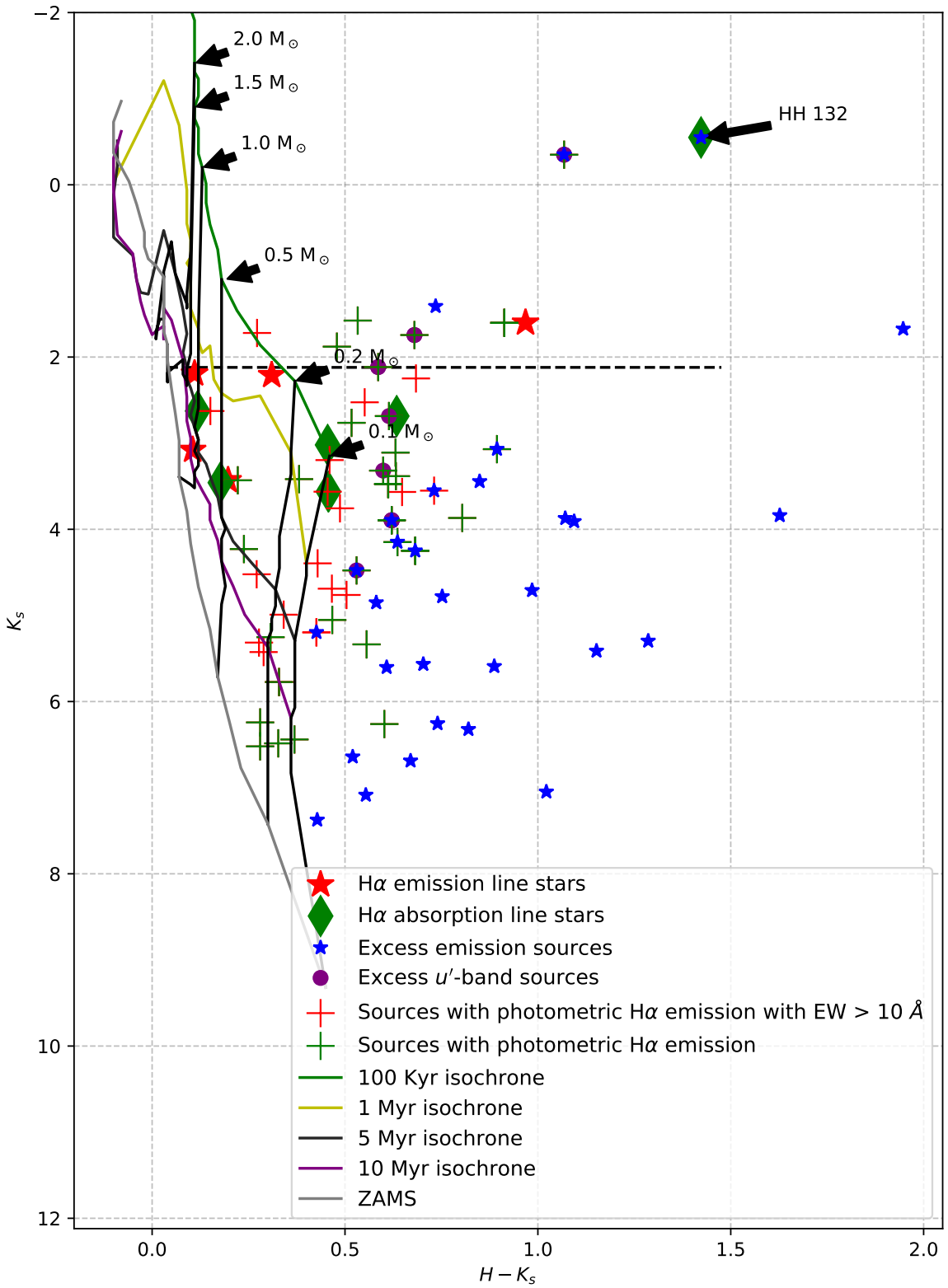

Figure 6.16: $K_s/(H - K_s)$ diagram for all of the red *VPHAS+* and *SALT* sources around NGC 2626.

extending from the driving star outwards; the excess emission has to come from the outflow, and not the star. The emission from the gas in the outflow had to be measured together with the emission from the star during the photometric measurements.

6.3.3 Optical colour-magnitude diagram

The optical colour-magnitude diagrams do not show as much excess emission from circumstellar material as the *NIR* colour-magnitude diagram shows. In Chapter 4 the optical colour-magnitude diagrams were used to gauge the cluster members' ages and spectral class, because there is not so much excess emission from circumstellar material in the optical r' and i' bands than in the *NIR*. It is important to see how the same technique is applied to the presumed cluster members of NGC 2626. This classification is also used to build a mass and age distribution for NGC 2626, similar to RCW 34.

Figure 6.17 shows the dereddened colours and magnitudes for the cluster members of NGC 2626. In Chapter 4 it was stated that the sources with excess Hα-emission and those with excess u'-emission indicated an ongoing process of star formation in NGC 2626. The red and green crosses which represent the WTTs and CTTs are distributed between the 100 kyr isochrone and the ZAMS with no distinction between the older and younger population members. The WTTs all appear to be younger than 10 Myr and the CTTs are distributed up to the ZAMS, which is not possible. With the same problem of identifying Hα-emission sources using *VPHAS+* data in RCW 34 and NGC 2626, the *VPHAS+* Hα-emission sources have to be disregarded in both datasets.

The *SALT* stars with Hα-absorption lines are possibly either young stars that are close to the main sequence or field stars. It is not possible to determine if they are either, but Hillenbrand *et al* (2013) showed that there are many young cluster members in the ONC which have Hα-absorption lines. Of the *SALT* Hα-emission sources, three are excess *NIR*-emission sources that were also detected in the *VPHAS+* data. All of the excess *NIR*-emission sources have ages from 1 Myr up to the main sequence, and a stellar mass less than 0.5 $M_{\odot}$, meaning that they are M stars, which may have formed at different periods. The two *SALT* Hα-sources that lie past the 0.1 $M_{\odot}$ evolutionary line — and the one source on the same line — can not be classified with the evolutionary models.

The driving star for HH-132 also has excess *NIR*-emission, but the spectroscopic classification done in Chapter 5 shows that this is either a late O or early B star. The spectra for the driving star show that it is already on the main sequence. This is supported by Keto (2003) who shows that high-mass proto-stars are already on the main sequence on a HR-diagram. It is the brightest source in the population, and its magnitude is close to the high-mass end of the evolutionary models. It lies close to the 2 $M_{\odot}$ evolutionary line, yet its spectra resembles that of a late O/early B main sequence star. The large uncertainties introduced by dereddening from the extinction map in Chapter 3 may have influenced the exact position to where the source lies in Figure 6.17. There was no extra emission in the r' for the driving star of HH-132 so the excess *NIR*-emission observed for this star must originate from the gas in the jets, which were included in the *NIR* PSF photometry.

6.3.4 Optical colour-colour diagram

The Hα-emission sources that were identified on the $(r' - i')/(r' - H\alpha)$ colour-colour diagram in Chapter 4 were not correct and these Hα-emission sources are disregarded for further analyses on this diagram. This diagram will only be used to analyse if the *SALT* Hα-emission line sources, and the excess *NIR*-emission sources show $(r' - H\alpha)$ colour excess.

Figure 6.18 shows the $(r' - i')/(r' - H\alpha)$ colour distribution for the stars shown in Figure 6.17. There are twelve sources with excess *NIR*-emission that were detectable in the optical bands and are plotted as blue stars. Nine of the twelve excess *NIR*-emission stars showed excess photometric Hα-emission — more than the main sequence from Drew *et al* (2014). There are eight sources with excess u'-emission, and all also show excess $(r' - H\alpha)$ emission relative to the main sequence, implying that they have Hα-emission. Three of the excess u'-emission sources also showed excess *NIR*-emission and excess $(r' - H\alpha)$ emission; these sources have to be CTTs.

Of the ten *SALT* Hα-emission sources, there are only two with excess $(r' - H\alpha)$ emission more than the main sequence. The inconsistency between the $(r' - H\alpha)$ colour and the detection of a Hα-emission

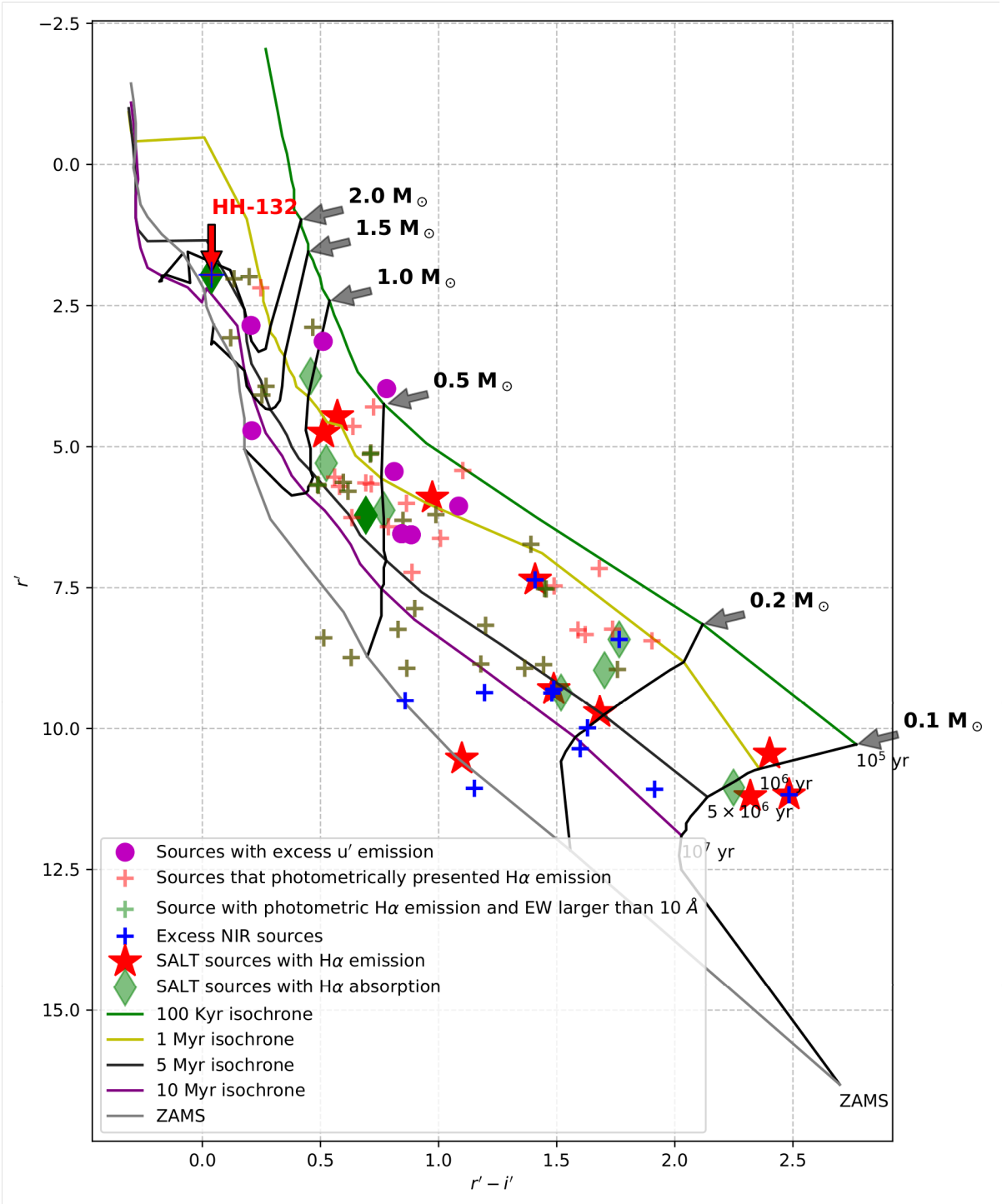

Figure 6.17: $r'/(r'-i')$ diagram for all of the stars showing properties characteristic to PMS stars in NGC 2626.

line with *SALT* shows the same result for RCW 34, namely, that there is no relation between stars that have a Hα-emission line and excess $(r'-H\alpha)$. The *SALT* Hα-emission sources were all observed during the same instance with the RSS, which means that their spectra would be comparable to each other because the spectra were subject to the same observation conditions. If there existed a relation between a $(r'-H\alpha)$ colour excess and the EW, it would be apparent in a diagram such as Figure 6.19. A possible explanation for the lack of relation between the Hα-emission line and excess $(r'-H\alpha)$, is that the spectroscopic and photometric observations were performed two years from each other. It is

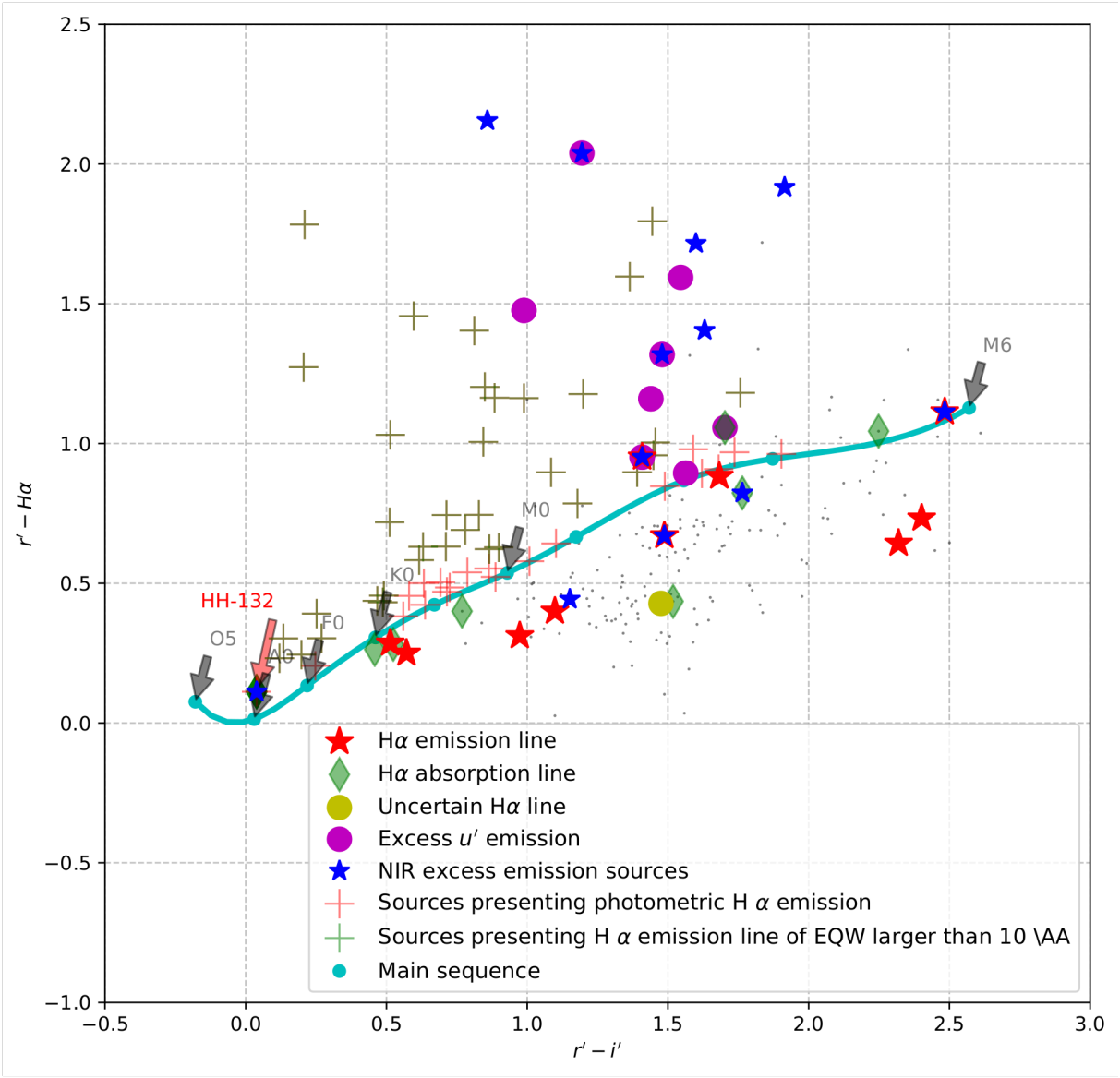

Figure 6.18: $(r' - H\alpha)/(r' - i')$ colour-colour diagram for stars that were observed with *SALT*, and showed excess *NIR*-emission in NGC 2626.

possible that the sources that were observed with *SALT* may have a time-dependent Hα-line profile. It is common for violently variable CTTs to have a time-dependent Hα-emission line (see Hamilton *et al* 2012).

Eight *SALT* sources showed an Hα-absorption line, which include the driving star of HH-132, and a star with excess u'-emission that lie just above the main sequence in Figure 6.18. For the driving star of HH-132, the colours correspond to an early A/B star, even though its spectra resembles that of a late O/early B star. This difference between the spectral classes in the $(r' - i')$ colour may be caused by the small space taken up by the high-mass end on the main sequence.

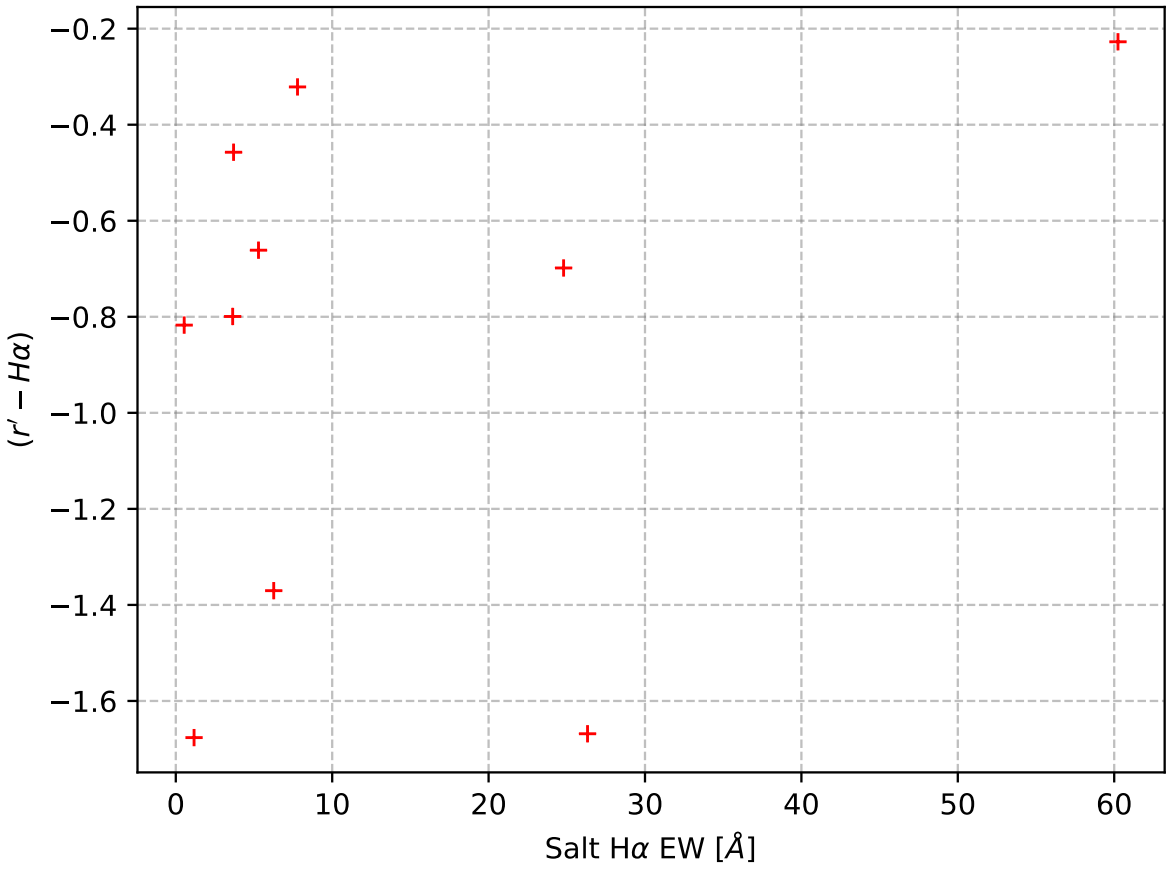

Figure 6.19: The equivalent width of the Hα-emission line measured from the *SALT* spectra against the difference of the star's $(r' - H\alpha)$ colour relative to the main sequence.

6.3.5 $(r' - H\alpha)/(H - K_s)$ excess emission diagram

Figure 6.20 shows the excess emission diagram for the cluster members and the *SALT* candidates in NGC 2626. The sources with excess Hα-emission are shown as green and red crosses. The *SALT* sources with Hα-absorption are included just for reference and not for analysis. The reason is that the green and red crosses do not correctly represent stars with Hα-emission, and the Hα-absorption line sources are most likely field stars. All of the sources in excess u'-emission have both excess emission in the $(H - K_s)$ and $(r' - H\alpha)$ colours, and they are located at a position where the youngest stars should be. There is a lot of excess relative to the main sequence in both the colours. They are the sources in NGC 2626 with the strongest Hα-emission and are located in a region of the excess emission diagram where the youngest CTTs lie. This shows that the sources with the most excess emission are most probably some of the youngest sources in the cluster, these excess u'-emission sources all have the characteristics of CTTs younger than 3 Myr (see McClure *et al* 2013 and Sousa *et al* 2016).

The *SALT* Hα-emission line sources all show excess $(H - K_s)$ emission more than the main sequence, but do not show excess $(r' - H\alpha)$, as was shown in Figure 6.18. The *SALT* Hα-absorption line sources have the same amount of excess $(H - K_s)$ emission as the *SALT* Hα-emission line sources. Both groups have much more excess $(H - K_s)$ emission than the main sequence and little to no excess $(r' - H\alpha)$ relative to the main sequence.

For the driving star of HH-132, the strong Hα-absorption line is consistent with the $(r' - H\alpha)$ colour. Very little excess emission is expected from a source which is already on the main sequence. The $(r' - H\alpha)$ colour of the star driving HH-132 is consistent with a high-mass star; both are ~ 0. The $(H - K_s)$ colour excess is so much, that the only possible source for this amount of emission would be

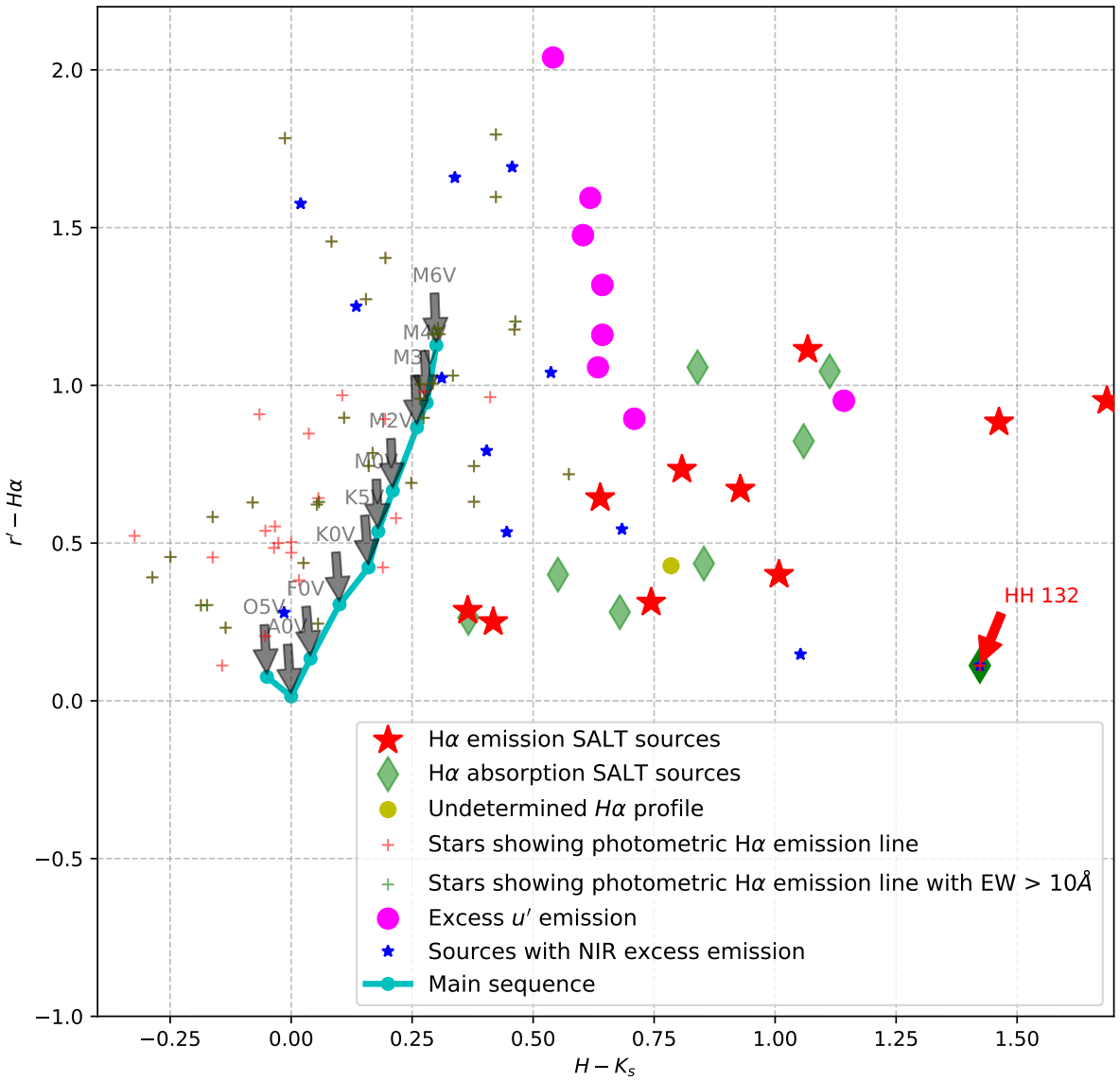

Figure 6.20: $(r' - H\alpha)/(H - K_s)$ excess colour-colour diagram for all of the *SALT* sources, and excess u', *NIR*-emission sources in NGC 2626.

from the outflow that was included when the *NIR*-photometry was performed.

The stars with excess *NIR*-emission show various values for their $(H - K_s)$ colours, ranging from 0.0-1.75. They have various values in their $(r' - H\alpha)$ colours. There is no apparent relation between the amount of excess *NIR*-emission and $(r' - H\alpha)$ colour excess. The sources are not grouped together in Figure 6.20. The sources with excess *NIR*-emission in RCW 34 are grouped together in Figure 6.11, possibly because many of these sources formed during the same star-forming epoch. The differences in the $(H - K_s)$ colour excess for sources in NGC 2626 strongly suggest that they formed over a longer time span than those in RCW 34. This is consistent with the results from the study by Sharma *et al* (2016) when PMS stars at various stages of formation occurred, for example, there were class 0/I, II, and III *NIR* sources in NGC 2626, inside and around SFO 54.

6.3.6 Mass distribution

The mass distribution is shown for all of the *SALT* Hα-emission sources, the *VPHAS+*, and the sources with excess *NIR*-emission which are comparable with an evolutionary model. The evolutionary lines from Siess *et al* (2000) were used to bin the stars in mass divisions of 0.1 $M_\odot$ for stars within the mass range of 0.1 $M_\odot < M_* < 2\ M_\odot$ on the colour-magnitude diagram in Figure 6.17. The mass distribution is plotted together with the IMF of Salpeter (1955) and Kroupa (2001). Each Salpeter IMF was normalised so that the power-law intersects the mass distribution. The Kroupa IMF was normalised that each part of the broken power-law is continuous and close enough to the mass distribution for comparison.

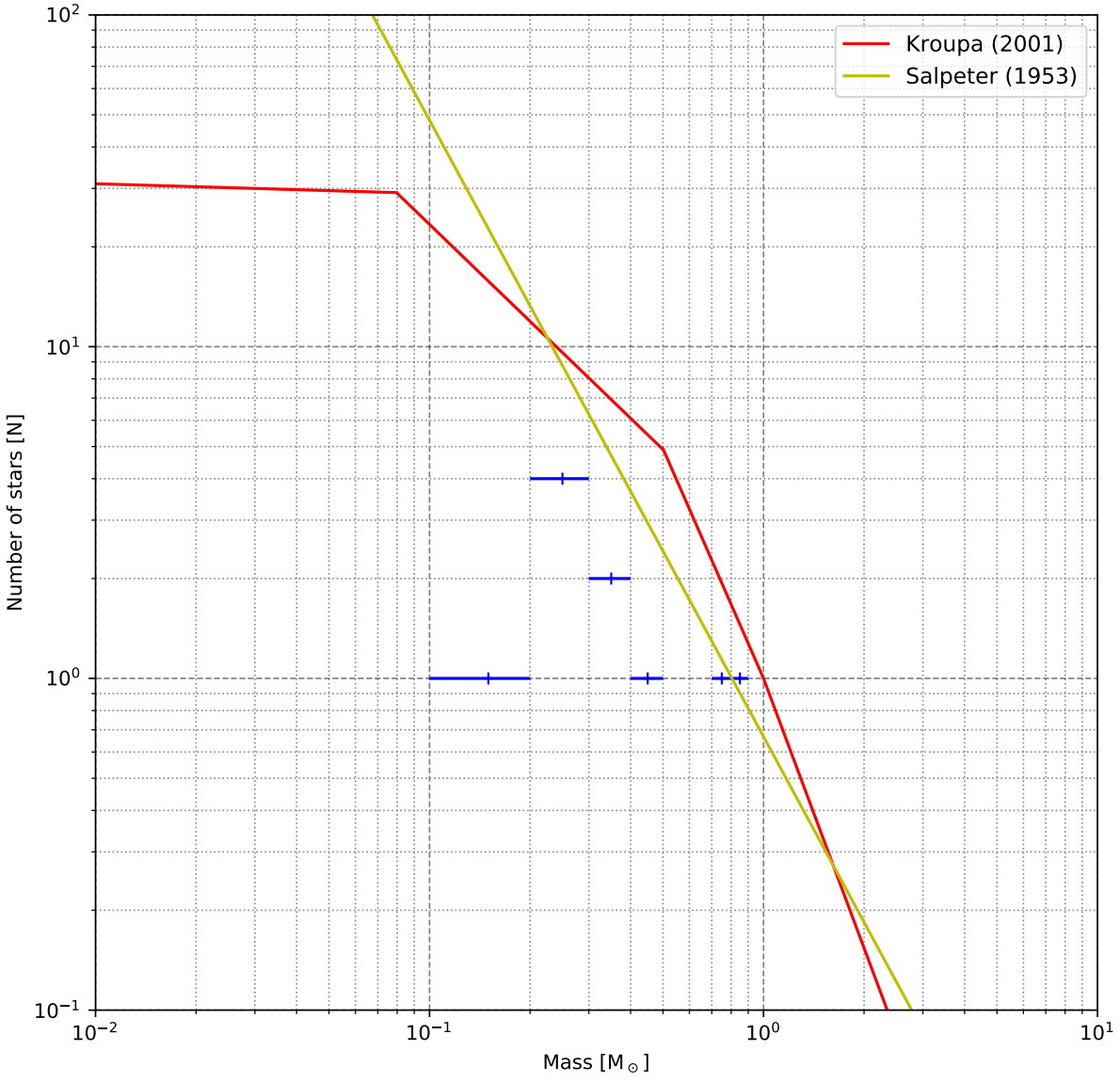

Figure 6.21: The mass distribution for all of the cluster members in NGC 2626.

There are only ten stars that are considered to be cluster members in NGC 2626 which make up the mass distribution in Figure 6.21. This number of stars is far too small to indicate how the mass distribution for NGC 2626 looks. The mass distribution is shown just for reference reasons, and it may either be a Salpeter or Kroupa power-law.

6.3.7 Age distribution

The ages for the *SALT* Hα-emission stars and excess *NIR*-emission stars were determined from the theoretical models from Siess *et al* (2000) in Figure 6.17. The ages were binned in 1 Myr intervals, except for the first age interval which was from 0.1-1 Myr. The upper limit for the age of T Tauri stars was given as 10 Myr by Hartmann (1998). Thus, any star older than 10 Myr should be close to the main sequence and could not be considered to be a T Tauri.

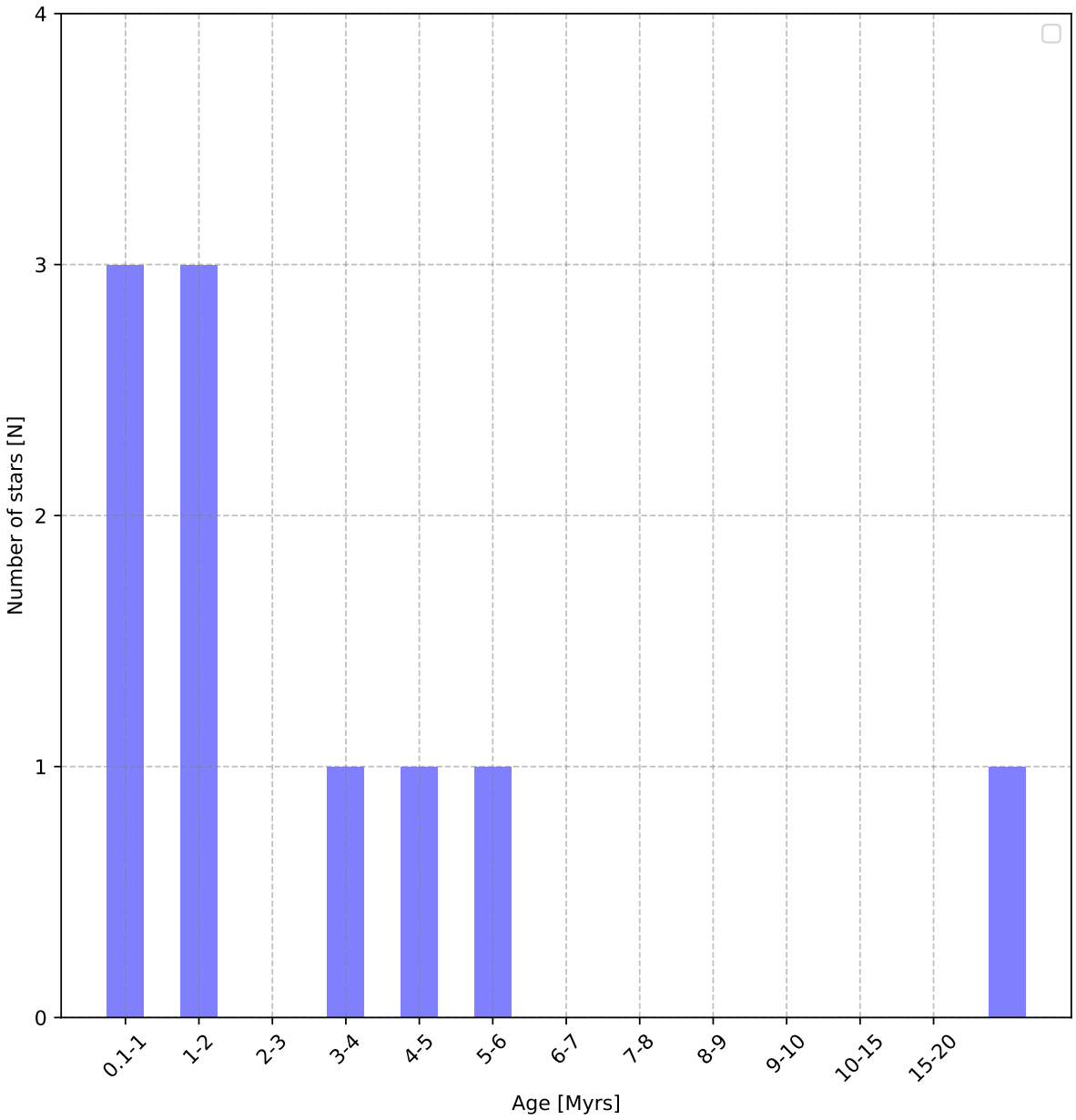

Figure 6.22: The age distribution for all of the cluster members in NGC 2626.

Figure 6.22 shows the same 10 cluster members as the mass distribution in Figure 6.21. This population is far too small to give an accurate indication of the cluster's age. The distribution shows that there are six stars younger than 3 Myr, but the population that was classified by Sharma *et al* (2016) is considered to be a much better representation of the population's age.

CHAPTER 7: FINAL DISCUSSION, SUMMARY AND CONCLUSION

7.1 Introduction

In this final Chapter, all of the results that were obtained in Chapters 3, 4, 5, and 6 are discussed, the final conclusion is presented, and future work is proposed. A review of the previous results is given to show the reasoning for the final discussion. In Chapter 1, the rationale for this thesis was given, followed by a literature review of both RCW 34 and NGC 2626. Chapter 2 gave a theoretical description of the physics involved in star formation and the photometric tools that were used to characterise the young stellar populations. In Chapter 3 *IRSF* images were stacked to perform deep *NIR* photometry. The photometry was used to identify stars with excess *NIR*-emission, and the reddened colours from field stars behind the star-forming regions were used to build extinction maps with the *NICEST LinES* algorithm. In Chapter 4 optical photometry from the *VPHAS+* survey data was used to identify sources with Hα-emission using narrow band imaging. In Chapter 5 optical spectroscopy was performed on candidates from *SALT*, which were selected on the basis of their spatial distribution, excess *NIR*- and Hα-emission. In Chapter 6 the multi-wavelength results from the most likely cluster members were combined and compared to each other.

7.2 Discussion: A comparison between RCW 34, NGC 2626, and other star-forming regions

7.2.1 The properties for RCW 34

7.2.1.1 *The NIR photometry and extinction maps*

The *NIR* photometry was used to derive a custom extinction law for RCW 34 according to the *LinES* algorithm which was outlined by Ascenso *et al* (2013). Using the custom extinction law, a total of 399 sources with excess *NIR*-emission, which is characteristic to young PMS stars, were identified in Chapter 3 (see Lada *et al* 1993). Field stars behind RCW 34 which could be dereddened onto the main sequence, and excess emission stars that could be dereddened to between the upper and lower limits of the CTT locus, created a grid of extinction points. The extinction of each dereddened star was used to construct an extinction map of the molecular cloud in RCW 34, using the *NICEST* interpolation method developed by Lombardi *et al* (2011). The extinction map was used to deredden all of the sources on the colour-magnitude and colour-colour diagram.

From the extinction maps dense structures were identified across the $15.9' \times 15.9'$ field. Where the *NICEST LinES* extinction map and the CO maps from Pagani *et al* (1993) overlapped each other, the dense structures agreed. The spatial distribution of the sources with excess emission showed that the cluster is significantly larger than the study by Bik *et al* (2010) discovered. The temperature and measurements from Pagani *et al* (1993) were used to show that the densest regions (A-G given in Table 3.2 and shown in Figure 3.23) on the extinction map would collapse under the Jeans criteria. Clumps A and D-G hold the highest potential for future star formation.

In Chapter 3 the colour-colour and colour-magnitude diagrams showed the dereddened colours and magnitudes for stars in RCW 34 in Figures 3.33 and 3.41, respectively. On the colour-magnitude diagrams, the dereddened colours and magnitudes showed that sources with excess emission lie past the evolutionary models of Siess *et al* (2000), which only shows photospheric evolution. Even though the isochrones/evolutionary models were not used, they are included for reference as to how the photospheric evolution of a PMS star would occur, and to emphasise the contributing emission from the

accretion disk to the system.

The spatial distribution of the young stars in RCW 34 indicates that the cluster is as big as the study by van der Walt *et al* (2012) suggested. The only documented trigger for star formation in RCW 34 was the cloud-cloud collision 0.2 Myr ago, described by Hayashi *et al* (2017). The mass for the two molecular clouds were measured by Hayashi *et al* (2017) as $\sim 2.7 \times 10^4$ $M_\odot$ (cloud 1) and $\sim 10^3$ $M_\odot$ (cloud 2), which are respectively represented by regions A-D and F-G in Table 3.2 and Figure 3.23. The total mass for regions F-G is 758.54 ± 27.65 $M_\odot$ and regions A-D is 1409.19 ± 47.79 $M_\odot$. Compared to the results from Hayashi *et al* (2017) the mass of cloud 2 is roughly the same, but cloud 1 has a factor ∼19 difference. This large factor difference suggests that for low-density structures such as cloud 2, the results from the *NICEST LinES* study is the same as for CO observations. However, for denser structures, the method vastly underrepresents the amount of matter. A possible reason for this may be that many background stars were not included in the construction of the extinction map. Another possibility is contamination in the magnitudes measured from the field stars behind RCW 34, due to emission from the HII region. Without enough field stars behind most of the dense region, specifically clump A, the amount of material in cloud 1 was underestimated during the construction of the extinction map. This may also explain why the *NIR* counterpart for the maser, which is located at the core of clump A, was not detected — because there is so much dense material that the field stars behind this clump could not be detected. The structures shown in the extinction map of RCW 34 show more detailed structures than the CO maps, even with an underestimate of the amount of material, just as the other observations from Lombardi (2008) showed for the pipe nebula.

The *NIR*-based extinction map shows more structure than the CO maps, suggesting there is a more dense structure in the region than what Hayashi *et al* (2017) showed. Moreover, the distribution of the excess *NIR*-emission sources across the whole field also show that star formation occurred over a much larger scale than Heydari-Malayeri (1988), Bik *et al* (2010), or Hayashi *et al* (2017) showed. The age distribution in Figure 6.13 suggests that the number of stars that formed in RCW 34 increased over time, but that the age distribution far underrepresents the population, thus, it does not give the whole picture for the star-formation history. The stars with excess *NIR*-emission across the entire $15.9' \times 15.9'$ field may have formed in each molecular cloud, before their collisions. The collision triggered a cascade formation of new stars in the remnants of the molecular clouds.

7.2.1.2 *Optical photometry and identification of excess Hα-emission sources*

The optical *VPHAS+* imaging from Chapter 4 showed 216 sources with Hα-emission in Figure 4.11. According to the classification scheme from Drew *et al* (2014), 88 have a photometric Hα-excess similar to an Hα EW $>$ 10Å, and the other 128 have excess similar to an Hα EW $<$ 10Å. The optical and *NIR* colour-magnitude diagrams in Chapter 6 showed that this classification scheme is not applicable to RCW 34. The reason for this was that the sources with high amounts of $(r' - H\alpha)$ colour excess did not show that they are younger than the sources which barely have $(r' - H\alpha)$ excess. All of the stars that were identified as Hα-emission sources from their $(r' - H\alpha)$ excess were disregarded from the rest of the study. Five sources with excess u'-emission were also identified from the *VPHAS+* data.

7.2.1.3 *Spectroscopic results*

In Chapter 5 spectroscopic observations were performed on sources which were selected according to their $(R_s - H\alpha)$ colour excess from the *SuperCOSMOS* survey, the $(H - K_s)$ colour excess, and their spatial distribution. The sources were selected in such a manner that the maximum number of slits could be fit onto a MOS slitmask. The selection of the candidates was done with the slitmask tool in the *pySALT* software package, where the position of each slit on the mask was selected using the criteria of fitting the maximum number of sources on the mask. This implied that the sources with the highest probability of being PMS sources were not always selected. This explains why the *SALT* sources with Hα-emission do not necessarily show strong excess $(r' - H\alpha)$ or $(H - K_s)$ emission.

In RCW 34 there were 18 out of the 92 stars that showed Hα-emission line profiles, meaning the candidate selection process had a bias towards fitting the most sources on the slitmask, rather than the amount of colour excess that each source presented. The whole point of selecting the *SALT* candidates was to obtain spectra for T Tauris in RCW 34, so that the properties of the T Tauris could be determined and used as a gauge for the properties of the star-forming regions. The chosen set of candidates are a mix of different stars — some have a Hα-emission line, some a Hα-absorption line, and others Hα-profiles that can not be determined. The spectral class and metallicity were determined for each spectral candidate using the PyHammer software package, if the spectra were precise enough. The metallicity measurement for each star in RCW 34 was used to calculate the average for the cluster as solar-like. The cluster's metallicity was used in the calculation of evolutionary models used in the optical colour-diagrams in Chapter 6 to derive the age and spectral class of cluster members.

7.2.2 The properties for NGC 2626

7.2.2.1 *The NIR photometry and extinction maps*

For NGC 2626 a set of images that were centred on the Herbig Haro object, HH-132 were combined to roughly the same exposure time as for RCW 34. The observational data was not over an area as big as the study by Sharma *et al* (2016), but it does probe deeper, and the photometric errors are smaller than the other study. To test whether the *IRSF* results are compatible with the results from Sharma *et al* (2016) an extinction map was built using their field star data from the same *NICEST LinES* algorithm which was used in Chapter 3.

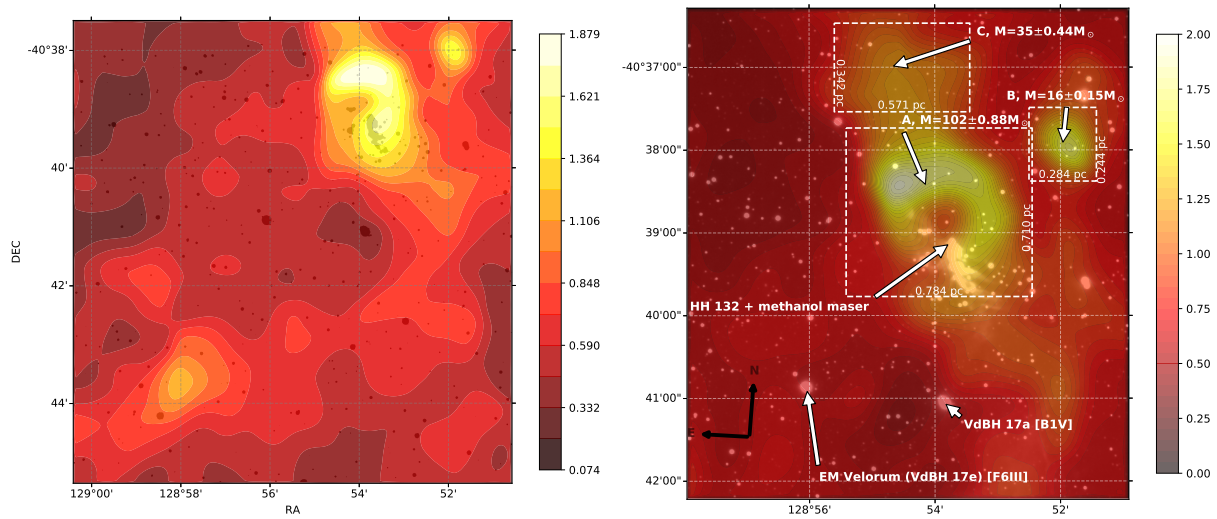

Figure 7.1: The first extinction map shown here was built with the *NICEST LinES* algorithm from the observational data in the study by Sharma *et al* (2016). The second image is the same extinction map that was shown in Chapter 3.

The extinction map that was built using the data from Sharma *et al* (2016) shows the same dense structures in the molecular cloud as the *IRSF* data. The agreement between the two extinction maps and the CO map from Sharma *et al* (2016) (also shown in Figure 1.8) affirms again that the *NIR* data and the extinction map used for NGC 2626 is correct. Both sets of the extinction maps show that the molecular cloud, called SFO 54 in Sharma *et al* (2016), has a hole that has been cleared away by the driving star of HH-132.

The *LinES* algorithm showed that the extinction law for NGC 2626 is similar to the extinction law from Rieke & Lebofsky (1985), and was used for the rest of the photometric data. There were 29 sources in NGC 2626 with excess *NIR*-emission characteristic to PMS stars, which are shown in Figure 3.37. There were so few sources above the upper limit of the CTT locus that they were not used in the construction of the extinction map, but the extinction for each star was taken from the map. From the dereddened colours some showed colours characteristic to class 0/I *NIR* sources, while the majority

were class II sources. The driving star for HH-132 showed very strong excess *NIR*-emission, while there was low extinction according to the extinction map. In Chapter 3 it was emphasized that the driving star for HH-132 is very young and most likely the driving source for the maser at the same coordinates.

7.2.2.2 *Optical photometry and identification of excess Hα-emission sources*

In Chapter 4 the optical *VPHAS+* survey data for NGC 2626 was used to identify sources with excess u' emission and $(r' - H\alpha)$ colour excess. Figure 4.13 shows 30 out of the 180 sources that exhibited $(r' - H\alpha)$ colour excess. Of the 30 sources which showed $(r' - H\alpha)$ excess, 8 also showed excess u'-emission. Similar to RCW 34, the amount of $(r' - H\alpha)$ colour excess measured does not show a relation to the EW measured from the star's spectra in NGC 2626. The same reason applies, namely, that the sources with a lot of $(r' - H\alpha)$ colour excess (CTTs) should present colours and magnitudes of very young sources relative to the evolutionary models, but these sources are distributed between the other Hα-emission sources (WTTs). It is not possible that CTTs and WTTs have the same ages, thus these sources were also disregarded for the rest of the study.

The same problem is seen in Figure 6.18; all of the *SALT* sources lie on or below the main sequence, and just two sources with an Hα-emission line lie marginally above the main sequence. If there was a relation between the amount of $(r' - H\alpha)$ colour excess and the EW of an Hα-emission line, the *SALT* Hα-emission line sources would lie above the main sequence according to the relation. Even though there are excess *NIR*- and u'-emission sources that show excess $(r' - H\alpha)$ emission, the *SALT* Hα-emission line sources do not show $(r' - H\alpha)$ colour excess.

7.2.2.3 *Spectroscopic results*

The spectroscopic results for the *SALT* candidates that were observed in NGC 2626 are shown in Chapter 5, and not all of these candidates had Hα-emission line profiles as was expected. There were 11 stars with Hα-emission lines and 8 with Hα-absorption lines. Due to the closer proximity of NGC 2626 than RCW 34, there were no cluster members of which the Hα-line could not be resolved. The metallicity for each star was also used to determine an average metallicity for the cluster, which was used in the modelling of the Siess *et al* (2000) evolutionary models. An interesting find was that the driving star of HH-132 does have a Hα-absorption line profile, implying that this young star is already on the main sequence.

7.2.2.4 *The driving star for HH-132*

With the presence of a Hα-absorption line for the driving star of HH-132, the spectra showed only photospheric emission. The low extinction that was derived from the extinction map for this star explains why blue optical spectra could be obtained for this source. The spectra resembled a late O or early B star. The 6.7-GHz methanol maser is situated at the same coordinates as the driving star of HH-132. Thus, it has to be the same star that is causing the maser and HH-132. It has not been previously discovered in the literature, and may be the first instance where optical spectra have been observed for the driving star of a maser. This is profound because similar sources suffer so much extinction, which makes detecting them in the optical very difficult.

It is common to find mid-infrared, or even near-infrared counterparts for methanol masers, see respectively the studies by Pandian & Goldsmith (2007) and Goedhart *et al* (2000). Pandian & Goldsmith (2007) explain that young HII regions are optically thick, and the optical depth decreases with time. Methanol masers have an upper age limit in the range of $(2.5 - 4.5) \times 10^4$ yr according to van der Walt (2005). Thus, if the star driving HH-132 is also causing the methanol maser, it has to be very young, somewhere in the region of 150 kyr. The optical spectroscopy gives a unique view into the system of a young star which is causing the methanol maser. The spectra are shown in Figures 5.45-5.50 and it clearly shows only a Hα-absorption line. This means that the spectra appears to be from photospheric emission, and is not subject to emission from circumstellar material. The spectra

do not have significant differences from a late O to early B star found in the Pickles (1998) library, yet it can not be determined how the extinction of the embedding material affects this observed spectra.

7.2.3 Comparison between RCW 34 and NGC 2626

The young clusters in RCW 34 and NGC 2626 have been studied by carefully analysing multi-wavelength data for individual stars. The difference in the distance to each cluster would present a significant challenge to detect the faintest members in RCW 34, due to the distance and extra extinction suffered by the light propagating through the Galactic plane. However, RCW 34 lies at a Galactic latitude of $b = +1.46$, meaning that the light does not suffer as much extinction as light from NGC 2626, which lies directly in the Galactic plane. Making it possible to compare similar spectral types with each other.

7.2.3.1 *The mass distributions*

The difference in the mass distributions shown in Figures 6.12 and 6.21 show very little information for either RCW 34 or NGC 2626. Each distribution has a few stars which can be confirmed as cluster members, but neither distribution is large enough that it can be compared to the power-law of the IMF of Salpeter (1955) or Kroupa (2001). In each distribution the largest number of sources have a mass in the range of 0.2-0.4 $M_{\odot}$.

7.2.3.2 *The age distributions*

The age distributions for RCW 34 and NGC 2626 are shown in Figures 6.13 and 6.22, respectively. For each distribution, there are too few sources in the population to construct a detailed star-formation history of each region. The distribution for RCW 34 and NGC 2626 each show that the majority of the sources are younger than 3 Myr.

7.2.3.3 *The high-mass stars*

RCW 34 has the O8.5V and two B stars which excite the gas in the HII region. Hayashi *et al* (2017) showed that the cause for the high-mass star formation in RCW 34 was most likely the collision between two molecular clouds. Similar collisions between molecular clouds have been the cause for high-mass star formation in RCW 120, RCW 38, NGC 2024, and M42 as stated by Torii *et al* (2015), Fukui *et al* (2016), Ohama *et al* (2017), and Fukui *et al* (2017), respectively. This shows that RCW 34 is part of a larger group of high-mass star-forming regions where two molecular clouds collided and served as the triggering mechanism for star formation. The criteria given by Fukui *et al* (2017) for high-mass star formation to occur in a molecular cloud is that the column density should be $\sim 10^{22}$ cm^{-2}, and that for multiple high-mass stars to form, the density should be $\sim 10^{23}$ cm^{-2}. Moreover, the *NANTEN2* CO observations in Hayashi *et al* (2017) showed that the densest part of the molecular cloud north of VdBH 25a had a column density of 2.2×10^{22} cm^{-2}; This is the same location where the methanol maser is located. At the distance of RCW 34, the methanol maser can be placed together with VdBH 25a, which is most likely the source of the maser. Breen *et al* (2013) shows that class II methanol masers are exclusively associated with very young high-mass stars. If there were any other young high-mass stars which are associated with the maser, then they would have been detected in the deep *NIR* photometry. If the collision between the two molecular clouds occurred about 200 kyr ago, as Hayashi *et al* (2017) stated, and it triggered the formation of VdBH 25a, then that event places an upper limit on the star's age. A methanol maser has a typical lifetime of (1-4.5)$\times 10^4$ yr, and an OH maser has a lifetime of (3-4.7)$\times 10^4$ yr, according to Breen (2010). Both methanol and OH masers occur quite early in the lifetime of a high-mass star. Putting an exact period on this is very difficult, but it constrains the age of VdBH 25a to nothing more than a few 100 kyr (see Battersby *et al* 2017 about the early stages/cycle of young high-mass stars). The criteria for high-mass star formation by Fukui *et al* (2017) are satisfied by the measured CO density, meaning that it is higher than 10^{22} cm^{-2}, and another high-mass star may still form in the densest regions. The *NICEST LinES* extinction map gives a visual extinction at the densest location as $A_V = 17$. The extinction was converted to the same column density (using the relation given on page 154 of Tielens 2005) as the measurements

by Hayashi *et al* (2017), which gave a density of $17A_V = 17 \times \frac{1.2\times10^{22}\ \mathrm{cm}^{-2}}{0.6} = 3.4 \times 10^{22}\ \mathrm{cm}^{-2}$. The *NICEST LinES* extinction map thus shows an extinction higher than the CO maps from Hayashi *et al* (2017), which further implies that high-mass star formation is possible. The only alternative to the maser being associated with VdBH 25a is that there is a very young high-mass star embedded in cloud A which was not detected with the *NIR* photometry. The location of cloud A does agree with the position of the maser. Moreover, the under representation of the cloud's mass from the *NICEST LinES* extinction map implies that the photometry was not sensitive enough to look through this part of the molecular cloud. This could explain why a potential source responsible for the maser could not be detected with the deep *NIR*-photometry.

NGC 2626 has the central high-mass star which created the clearing in the molecular cloud, drives the Herbig-Haro object HH-132, and causes the 6.7-GHz methanol maser. The extinction maps in Figure 7.1 show that this high-mass star has cleared away some of the surrounding material in the molecular cloud, SFO 54. In the densest parts of SFO 54, the column density that was measured in the *NICEST LinES* extinction map showed a visual extinction $A_V \sim 30$. This extinction translates to a column density of $3.57\times10^{23}\ \mathrm{cm}^{-2}$, and leaves the possibility that more high-mass star formation can occur. The Herbig-Haro outflow had just one jet that was observed, suggesting that the opposite outflow is blowing towards the molecular cloud. The outflow facing into the molecular cloud may be the trigger for further star formation in the densest part of the molecular cloud, which is also near the star causing the Herbig-Haro outflow. It is unique that the optical spectra could be obtained for this star, and it may be due to the low extinction in the line of sight towards the star. The maser implies the same age constraints on the star driving it as the maser associated with VdBH 25a does. If the paper by Battersby *et al* (2017) can be taken as an indication for an upper limit of the age of a methanol maser, then the star cannot be older than a few 100 kyr. This may have been a very rare occurrence where optical spectra were observed for a star which is causing a maser, especially for such a young source. It shows that after just a few 100 kyr the high-mass star is already on the main sequence.

7.2.3.4 *The molecular clouds*

The molecular clouds from which the young cluster in RCW 34 formed are shown in the *NICEST LinES* extinction map in Chapter 3. It shows the same structures as the CO maps shown by Pagani *et al* (1993) and Hayashi *et al* (2017). They also show similar structure to the molecular clouds associated with other high-mass star-forming regions, as in RCW 120, RCW 38, M42, and NGC 2024 (see Figueira *et al* 2017, Fukui *et al* 2016, Mužić *et al* 2017, Fukui *et al* 2016, and Ohama *et al* 2017). Bik *et al* (2010) stated that the bubble region was cleared out by the population of young stars, without knowing that the cluster extended out much further than just the clearing. This bubble region is situated at a position between the two molecular clouds, so the gas may not just have been displaced by the high-mass and young PMS stars. The remaining material that is moving in two separate directions — leaving the cavity between the two molecular clouds in the shape of the bubble — also contributed to the clearing. Figure 2 of Hayashi *et al* (2017) shows the two molecular clouds moving away from each other at a relative velocity of $\sim 5\ \mathrm{km.s}^{-1}$.

The molecular cloud associated with NGC 2626 is shown in Figure 7.1. In the light of the papers by Torii *et al* (2015) and Fukui *et al* (2017), where a cloud-cloud collision is regarded as a trigger for high-mass star formation, the same trigger has to be considered in NGC 2626. The *NICEST LinES* map in Figure 7.1, which was built from the data provided by Sharma *et al* (2016), shows two dense regions other than the molecular cloud, SFO 54. The larger field also shows the same bubble shape as the extinction map of RCW 34 and other high-mass star-forming regions after the recent collision of two molecular clouds. The densest region of the bubble-shaped molecular cloud is also right next to the high-mass star, similar to the dense region A, next to VdBH 25a in RCW 34. Sharma *et al* (2016) did not build extinction maps from reddened field stars using their *NIR* data, and the CO maps were not detailed enough to reveal these dense structures. There is also no velocity data available for the gas to investigate if there is a molecular cloud that is red or blue shifted relative to each other. However, it is possible that the two dense clumps seen in the extinction map may be two molecular

clouds that collided and resulted in the formation of the star driving HH-132.

Both the high-mass star-forming regions RCW 34 and NGC 2626 are closely associated with two dense molecular clouds which have collided, leaving a bubble-shaped dense molecular cloud. Both high-mass star-forming regions are located on the inner, low-density part of a bubble-shaped region. Each region also has low-mass cluster members spatially distributed so that they are not just near the high-mass star, but as extensive as the outer brim of the molecular clouds. Both are dispersing the excited gas in the direction of the bubble clearing. Zychova & Ehlerova (2017) showed that bubble-shaped regions are an indication specifically for high-mass star formation. Thus the extinction maps of RCW 34 and NGC 2626 do add to the collection of high-mass star-formation regions, found in bubble-shaped regions.

7.2.3.5 *The excess emission sources and the extent of the clusters*

In RCW 34 the spatial distribution of the stars with excess *NIR*-emission is shown in Figure 3.44. As previously mentioned this distribution shows that the cluster is substantially larger than the previous study on the low-mass cluster members by Bik *et al* (2010) showed. The distribution of these excess emission sources is across the whole field where the collision of the two molecular clouds occurred, as shown in the study by Hayashi *et al* (2017). Szegedi-Elek *et al* (2013) showed that Hα-emission extends a significant distance from the HII region in the ONC, similar to the far-reaching distribution of the excess emission stars. Even though the excess Hα-emission stars in RCW 34 can not be identified, due to the complications with the *VPHAS+* Hα-data, the excess *NIR*-emission source showed how large the cluster is.

In both the cases of RCW 34 and NGC 2626, the *VPHAS+* results should have shown where stars with Hα-emission in each cluster are. There was a problem that those with a lot of $(r' - H\alpha)$ excess (or even the maximum amount), and those with slightly more $(r' - H\alpha)$ excess than the main sequence were indistinguishable from each other on a colour-magnitude diagram. Drew *et al* (2014) and Barentsen *et al* (2011) made a distinction between CTTs and WTTs: The CTTs have $(r' - H\alpha) > 0.1$ emission more that the main sequence, while WTTs have an excess of $(r' - H\alpha) \leq 0.1$ more than the main sequence. On a colour-magnitude diagram the groups, if they formed at the same time, should also be distinguishable with age, so that the CTTs are younger than 3 Myr, and the WTTs have ages from 3-10 Myr. In all of the optical and *NIR* colour-magnitude diagrams, the two groups are indistinguishable from each other. Even though Kalari *et al* (2015) showed the same results in $r'/(r' - i')$ colour-magnitude diagrams as RCW 34 and NGC 2626, where CTTs candidates showed ages from 0.01-10 Myr; The conservative route was chosen when interpreting the results of RCW 34 and NGC 2626. Thus, all of the candidate Hα-emission line stars were disregarded for further analysis, because of this discrepancy. Another motivation for disregarding these sources was the amount of $(r' - H\alpha)$ excess shown by the *SALT* sources with Hα-alpha emission lines. Figure 6.19 showed that many of these sources had $(r' - H\alpha)$ emission less than the main sequence. To determine what the exact reason for this discrepancy is, is very complex. For example, it may be that the extinction law in each region differs and affects the amount of $(r' - H\alpha)$. Another reason may be that the *VPHAS+* and *SALT* data were observed at different dates. Young CTTs are very variable — if they showed Hα-emission in 2013, they might not show as much in 2015. It is not clear what the exact reason is, this is why the conservative decision was taken, and these sources were disregarded from further analysis.

The tidal radius cannot be determined for RCW 34 using a technique similar to Danilov & Loktin (2015), however it is assumed that the location of the excess emission sources shows the extent of the cluster. This assumption means that the cluster is $\sim$11.5 pc in diameter, which implies that the cluster is 9 pc larger in a norther-southern and eastern-western direction than the $\sim$2.4 pc bubble region where Bik *et al* (2010) studied the PMS stars. According to Alves & Bouy (2012), the ONC region comprises various sub-clusters — which were all triggered at separate star-formation epochs, and extend over a region of $\sim 3.5 \times 20$ pc. The ONC is physically larger than RCW 34, and it also presented more epochs of star formation. Close to the ONC — also in the Orion star-forming complex

— is the flame nebula (NGC 2024) where Ohama *et al* (2017) showed that high-mass star formation was also triggered by a cloud-cloud collision. The well studied Orion star-forming complex has been subject to various triggers of star formation, and serves as a template of how star formation looks in a region where cloud-cloud collision occurred. Alves & Bouy (2012) suggested that the triggering mechanism for star formation in NGC 1981 — a group of young stars in front of the ONC — was a cascading effect of triggered star formation caused by the displacement of gas by the HII regions. The different mechanical triggers, namely HII gas expansion due to photo-ionization in NGC 1981, and the collision of two molecular clouds for NGC 2024 and RWC 34, makes a difference in the way that the stars formed. When an OB star ionizes the embedding material around it, the perturbations in the material is a trigger for the formation of new stars as a localized event, see Chen (2010) for a detailed description.

The collision of two molecular clouds results in the formation of new stars in the wake of the colliding material, specifically the formation of high-mass stars (see Torii *et al* 2015 and Balfour *et al* 2015). Ohama *et al* (2017) mentions that high-mass star formation in RCW 38 also formed through cloud-cloud collision. Thus, the results for RCW 34 can be compared to those from Mužić *et al* (2017). Mužić *et al* (2017) had a larger sample of 476 cluster members which had numerous more sources for a large variety of mass range, not like the 33 sources in RCW 34. The distance towards RCW 34 and the lack of relation between a $(r' - H\alpha)$ excess and a Hα EW is a hindrance for observing any of the low-mass stars which are used to construct an IMF. The excess *NIR*-emission sources showed the extent of the cluster, and they may have formed across the whole intersection of the two colliding clouds. Alternatively their formation may have been triggered by cascading star formation — it is not possible to test either possibility with the available data. In RCW 38, M42 and NGC 2024 (see Mužić *et al* 2017, Fukui *et al* 2017, and Torii *et al* 2015) the formation of the high-mass stars were triggered by cloud-cloud collision. In each of these instances, low-mass star formation occurred in the wake of material across the whole field.

One question that is still open for investigation is how the distribution of these accompanying low-mass stars are affected by the collisional path. A reason for this is that the excess emission sources and numerous O stars in RCW 38 are concentrated in a 0.5 pc $\times$ 0.5 pc region, while the excess emission sources in RCW 34 are distributed across the whole $\sim$11.5 pc $\times$ 11.5 pc field. Hayashi *et al* (2017) gives a good comparison between RCW 34 and the results by Fukui *et al* (2016) for RCW 38. To start, both have relatively the same velocity difference between the molecular clouds, both the collisions occurred at roughly 0.2 Myr and resulted in the formation of O stars. In RCW 38 about 20 O stars formed and many low-mass sources with excess NIR- and Hα-emission are concentrated in a 0.5 pc $\times$ 0.5 pc region. In RCW 34 only a single O and a set of 2 B stars formed, which have many excess *NIR*-emission sources scattered across a $\sim$11.5 pc $\times$ 11.5 pc region. The difference between the low-mass populations in RCW 34 and RCW 38 cannot be properly investigated without accurate radial velocity measurements or knowing which stars present excess Hα-emission in RCW 34. What the results of this study show are that the stars with excess Hα-emission are distributed over an area larger than the bubble region studied by Bik *et al* (2010), or the molecular clouds studied by Hayashi *et al* (2017).

For NGC 2626 the 29 excess sources that were detected with the *IRSF* are fewer than the 97 that were discovered by Sharma *et al* (2016). This is because (1) The *IRSF* 1.4-m telescope is not as sensitive as opposing the 4.0-m Blanco telescope; (2) The angular size of the deep-stacked image of NGC 2626 of this study is $6.779' \times 7.198'$. This study essentially concentrated on the bright rim nebulosity, whereas the field that was studied by Sharma *et al* (2016) is $10' \times 10'$ which includes more cluster members. The excess emission sources that were discovered in this study do not reveal more about the cluster in NGC 2626 than Sharma *et al* (2016) showed. However, this study revealed that the driving star for HH-132 has excess emission characteristic to a very young star. This is even after dereddening the strong excess emission seen in the colours from the star, which are most likely from the nebulous gas of the Herbig-Haro outflow.

To compare the low-mass members of RCW 34 and NGC 2626 with each other, the extent of the cluster first needs to be taken into account. The low-mass members in RCW 34 have a spatial extent of ∼11.5 pc × 11.5 pc, while the population of NGC 2626 stretches across ∼2.8 pc × 2.8 pc. Both star-forming regions have a young single late O star, which is the activating source for a 6.7-GHz maser. Each is near a molecular cloud and have low-mass members scattered across the whole field that was studied. Which means they only differ regarding their physical extent and the number of high-mass stars that have formed in the densest part of the molecular cloud.

7.3 Summary and conclusion

The focus of this thesis was the low-mass PMS stars that are associated with the two high-mass star-forming regions RCW 34 and NGC 2626. From the results obtained in this multi-wavelength study the final thoughts are:

- The infrared extinction law used in the field surrounding RCW 34 differs from the general extinction law derived by Rieke & Lebofsky (1985), which is used in the rest of the Milky Way's Galactic plane. This custom extinction law showed many sources with excess *NIR*-emission which are spatially distributed across a field larger than any previous study on the cluster associated with RCW 34. The wide spatial distribution of the excess *NIR*-emission sources means the cluster is distributed across an area of about ∼11.5 pc × 11.5 pc.

- Even though it is shown that the spatial density of stars decreases as a function of radial distance from VdBH 25a in Chapter 3, the number of stars with excess *NIR*-emission still span across the whole field. The exact trigger for the widely distributed excess emission stars could not be determined; it may have been the perturbation of the collision of the molecular clouds. The low-mass stars on the outside of the bubble region may also have formed in the wake of the material of the two colliding molecular clouds. The high density of low-mass stars in the immediate region around VdBH 25a may have been induced by the high-mass stars perturbing the embedding gas, forming the HII region (see Elmegreen & Lada 1977).

- The high-mass star associated with NGC 2626 is both the source of the Herbig Haro object HH-132 and the 6.7-GHz maser. In this study, the first optical spectra were obtained at both the blue and red ends of the spectra for a high-mass star, that is the driving source of a methanol maser. This is a remarkably rare occurrence because the spectra seem to be the purely photospheric emission of an early B- or late O star, which presents strong hydrogen absorption lines.

- From the small number of stars in the age distributions of RCW 34 and NGC 2626 the majority of the sources seem to be younger than 3 Myr.

7.3.1 Where do RCW 34 and NGC 2626 fit into the larger picture of star-formation theory?

In section 1.1.1 the biggest questions in star-formation theory were listed, and as part of the concluding ideas surrounding these questions, results obtained for RCW 34 and NGC 2626 fit into the questions as follow:

What is the relation between the formation of low-mass and high-mass star formation? Where does this relation fit into competitive star formation? In the scheme of star formation the order in which either the high-mass or low-mass stars form is still an open question. To answer this question, observational studies like this one are a way of directly determining the properties of high-mass star-forming regions. Zinnecker (1982) and Bonnell *et al* (1998) have proposed models where the accretion of mass comes down to a competitive process, and the question is which of the following occurs: (1) Do high-mass stars induce the formation of low-mass stars? (2) Do low-mass stars group together and form a high-mass star, or (3) Does a high-mass star initiate the grouping of embedding material in its vicinity and low-mass stars form in the denser clumped matter around the high-mass star. It is difficult to give a definite answer to this question, but the stellar density in RCW 34 around VdBH 25a in Figure 3.45, and the spatial distribution in Figure 3.44 give an indication of the star

formation in RCW 34. It can be speculated that the high density of low-mass stars around the O and B stars may have been triggered by the presence of the high-mass stars. The formation of low-mass stars further than a radial distance of ∼2.5 pc from VdBH 25a may have been triggered by another event. For NGC 2626 a more detailed analysis was done by Sharma *et al* (2016) using a nearest neighbour analysis, where clustering between neighbouring stars was analysed. Sharma showed that most of the young sources are concentrated in the dense molecular cloud next to the driving star of HH-132. The formation of these young stars may have been induced by a massive star. It is only possible to speculate about the exact relation between the formation of high-mass and low-mass stars, but more multi-wavelength studies should be conducted on high-mass star formation regions. For example, using GAIA survey data the distances to many sources will be known, making the distinction between cluster members and field stars much clearer. If a cluster's members are definitely distinguished from field stars, a mass distribution for the cluster can easily be constructed.

How do the mass distributions of the clusters compare to theoretical models of the IMF? To answer this question a definite distinction should be made between which stars in the science field are either foreground stars, background stars, or cluster members. This requires precise radial velocity measurements and photometry of all the stars in the field. In this study no radial velocity data was available, thus only the few stars with characteristics of young PMS stars could be considered as cluster members. This approach left out the majority of the cluster. The 33 stars for RCW 34, and the 10 stars for NGC 2626 were not enough to construct a mass and age distribution for either cluster. No IMF of Kroupa or Salpeter could be fit to the few sources to get a rough indication of the power-law that best describes the mass distribution for each cluster. If a larger population were used then an IMF could be fit to the mass distribution.

Many studies from the literature cited in this study do not provide clear answers to the larger, still unanswered, questions of star-formation theory. The question around the IMF could not be addressed in this study due to a lack of data on cluster members. However, the increasing amount of observational data brings us closer to answering these fundamental questions. Studying star formation in the Milky Way remains a fundamental part of astrophysical research; Because, it is monumentally important to understand how the essential building blocks of a galaxy, the stars, and gas in the Galactic plane are related to each other through the stellar life cycle. By better understanding the relationship of how dense molecular gas forms stars, and stars chemically enrich galaxies, the evolution of galaxies is better understood, and cosmological questions can be better answered.

7.3.2 Future work

This study showed that there was more to learn from the low-mass stellar populations of RCW 34 and NGC 2626. And as previously mentioned, more studies like this one are needed to better understand high-mass star formation and their immediate environments. Future work needs to be conducted on both RCW 34 and NGC 2626. The papers that are continuing to be published on high-mass star-forming regions show that more of these regions are being understood with more sensitive equipment, and a better underlying theoretical description. Future work on RCW 34 and NGC 2626 may include:

- A follow-up optical spectroscopic study on the driving star for HH-132. The blue and red spectra of this star shown in Chapter 5 may be the first optical spectroscopy that has been observed from a star that is the driving source of a maser, and requires further investigation.

- Using the *NIR* observations that were performed on various dates on RCW 34, a study can be performed to identify variable sources. The standard star data for the observation periods are available to calibrate the observed magnitudes and colours to a standard system, where variable sources can be identified by comparing the data for specific sources on different dates. Variability is an intrinsic property of T Tauri stars, where the youngest T Tauri sources show the most variable activity. With this extra information, a better distinction can be made between the younger and older cluster members.

- Doing a follow-up X-ray survey of the suspected young cluster members. Young CTTs are known as active X-ray sources; if observations could be conducted with Chandra or a similar X-ray observatory, then the youngest sources could be identified. If the spatial distribution of the youngest sources were known, then the star-formation history for these star-forming regions could be better investigated.

- Performing a Bayesian statistical analysis on all of the multi-wavelength data, similar to the study that was performed by Barentsen *et al* (2011). In a Bayesian model, all of the multi-wavelength data is combined to best determine properties for single stellar cluster members. These properties include the visual extinction, accretion rate, age, metallicity, stellar mass, stellar radius, and radial velocity. This analysis was initially planned as a final part of this specific project but was not done due to time constraints. Further, the project would be too large for a PhD thesis. The results from such an analysis would give more distinct and accurate quantities for the age, mass, radius, and possible accretion rates for individual cluster members. Such a follow-up project could result in a paper from the multi-wavelength data given in this study.

- Expanding similar multi-wavelength studies to other star-forming regions. To better understand star-formation theory more studies on high-mass star-forming regions have to be performed, specifically those which are visible in the optical. With infrared observations, the extinction caused by the embedding gas is overcome, yet in the excess optical, emission from young stellar members can be tested for excess Hα- and ultraviolet-emission.

- Performing a similar study on NGC 2626 as Drass *et al* (2016) performed on the ONC. Drass *et al* (2016) used CO mapping, radial velocities, HAWK-I *NIR* imaging, and spectroscopic data to distinguish between cluster members and field stars. The combined data was used to probe the lower-limit of the mass distribution, down to objects 20 times Jupiter's mass. NGC 2626 is less than 1 kpc away, which implies that with an instrument sensitive enough, the lower limit of the mass distribution can be tested.

Bibliography

Adams, F. C., Lada, C. J., & Shu, F. H. 1987, ApJ, 312, 788

Akritas, M. G., & Bershady, M. A. 1996, ApJ, 470, 706

Alencar, S. H. P., Basri, G., Hartmann, L., & Calvet, N. 2005, AAP, 440, 595

Alves, J., & Bouy, H. 2012, AAP, 547, A97

Alves, J., Lombardi, M., & Lada, C. J. 2008, The Pipe Nebula: A Young Molecular Cloud Complex (Astronomical Society of the Pacific Monograph Publications), 415

Anandarao, B. G., Raman, V. V., Ghosh, S. K., Ojha, D. K., & Kumar, M. S. N. 2008, MNRAS, 390, 1185

André, P. 1994, in The Cold Universe, ed. T. Montmerle, C. J. Lada, I. F. Mirabel, & J. Tran Thanh Van, 179

André, P., Di Francesco, J., Ward-Thompson, D., *et al.* 2014, Protostars and Planets VI, 27

Andre, P., & Montmerle, T. 1994, ApJ, 420, 837

Appenzeller, I., Jankovics, I., & Jetter, R. 1986, AAPS, 64, 65

Appenzeller, I., & Wagner, S. 1989, A&A, 225, 432

Ascenso, J., Lada, C. J., Alves, J., Román-Zúñiga, C. G., & Lombardi, M. 2013, A&A, 549, A135

Ascenso, J., Lombardi, M., Lada, C. J., & Alves, J. 2012, A&A, 540, A139

Asplund, M., Grevesse, N., Sauval, A. J., & Scott, P. 2009, ARAA, 47, 481

Balfour, S. K., Whitworth, A. P., Hubber, D. A., & Jaffa, S. E. 2015, MNRAS, 453, 2472

Bally, J. 2002, Irradiated Jets and Proto-Planetary Disks in the Outer Orion Nebula, HST Proposal

Bally, J., & Zinnecker, H. 2005, AJ, 129, 2281

Barentsen, G., Vink, J. S., Drew, J. E., & Sale, S. E. 2013, MNRAS, 429, 1981

Barentsen, G., Vink, J. S., Drew, J. E., *et al.* 2011, Science And Technology, 20, 1

Battersby, C., Bally, J., & Svoboda, B. 2017, ApJ, 835, 263

Beltran, M. T., & de Wit, W. J. 2015, AJ, 71

Bertout, C., Basri, G., & Bouvier, J. 1988, ApJ, 330, 350

Bertout, C., Bouvier, J., Duschl, W. J., & Tscharnuter, W. M. 1993, A&A, 275, 236

Bessell, M. S., & Brett, J. M. 1989, in Lecture Notes in Physics, Berlin Springer Verlag, Vol. 341, Infrared Extinction and Standardization, ed. E. F. Milone, 61

Bik, a., Puga, E., Waters, L. B. F. M., *et al.* 2010, ApJ, 713, 883

Bilir, S., Karaali, S., & Tunçel, S. 2005, Astronomische Nachrichten, 326, 321

Bodenheimer , P. H. 2011, Principles of Star Formation (Springer-Verlag Berlin Heidelberg)

Bonnell, I. A., Bate, M. R., & Zinnecker, H. 1998, MNRAS, 298, 93

Bowler, B. P., Waller, W. H., Megeath, S. T., Patten, B. M., & Tamura, M. 2009, AJ, 137, 3685

Breen, S. L. 2010, PhD thesis, University of Tasmania

Breen, S. L., Ellingsen, S. P., Contreras, Y., *et al.* 2013, MNRAS, 435, 524

Burgh, E. B., Nordsieck, K. H., Kobulnicky, H. A., *et al.* 2003, in Instrument Design and Performance for Optical/Infrared Ground-based Telescopes, ed. M. Iye & A. F. M. Moorwood, Vol. 4841, 1463–1471

Calvet, N., & Hartmann, L. 1992, ApJ, 386, 239

Cardelli, J. A., Clayton, G. C., & Mathis, J. S. 1988, ApJl, 329, L33

Cardelli, J. A., Clayton, G. C., & Mathis, J. S. 1989, ApJ, 345, 245

Carpenter, J. M., Hillenbrand, L. A., & Krutskie, M. F. 2001, ApJ, 3160

Carpenter, J. M., Hillenbrand, L. A., Meyer, M. R., *et al.* 2002, AJ, 124, 1001

Carroll, B. W., & Ostlie, D. A. 2006, An introduction to modern astrophysics and cosmology (Pearson International)

Cesaroni, R. 2005, in Cores to Clusters: Star Formation with Next Generation Telescopes, ed. M. S. N. Kumar, M. Tafalla, & P. Caselli, 131

Chapman, N. L., Mundy, L. G., & Lai, S.-p. 2009, AJ, 496

Chapman, S., Pongracic, H., Disney, M., *et al.* 1992, Nature, 359, 207

Chen, L., Hou, J. L., & Wang, J. J. 2003, AJ, 125, 1397

Chen, W. P. 2010, in Astronomical Society of India Conference Series, Vol. 1, Astronomical Society of India Conference Series

Chiu, I., Desai, S., & Liu, J. 2016, Astronomy and Computing, 16, 79

Cieslinski, D., Jablonski, F. J., & Steiner, J. E. 1997, AAPs, 124, 55

Collins, G. W. 2003, The Fundamentals of Stellar Astrophysics, 2nd edn. (Book News Inc.)

Corradi, R. L. M., Rodríguez-Flores, E. R., Mampaso, A., *et al.* 2008, AAP, 480, 409

Covey, K. R., Ivezić, v., Schlegel, D., *et al.* 2007, AJ, 134, 2398

Czanik, R. J. 2013, Msc thesis, North-West University

Dahm, S. E., & Simon, T. 2005, AJ, 129, 829

Danilov, V. M., & Loktin, A. V. 2015, Astrophysical Bulletin, 70, 414

Davenport, J. R. A., Ivezić, Ž., Becker, A. C., *et al.* 2014, MNRAS, 440, 3430

De Marchi, G., Paresce, F., & Portegies Zwart, S. 2010, AJ, 718, 105

de Villiers, H. M. 2009, Msc thesis, North-West University

De Vries, C. H., Narayanan, G., & Snell, R. L. 2002, ApJ, 577, 798

Deharveng, L., Zavagno, A., & Caplan, J. 2005, AAP, 433, 565

Devorkin, D. H. 1977, in IAU Symposium, Vol. 80, IAU Symposium, 61

Di Cecco, A., Faustini, F., Paresce, F., Correnti, M., & Calzoletti, L. 2014, Herschel Far IR observations of the giant HII region NGC 3603

Dib, S. 2014, MNRAS, 26, 1

Dib, S., Schmeja, S., & Parker, R. J. 2017, ArXiv e-prints

Dokkum, P. G. 2001, in PASP, ed. J. Rhoades, Vol. 113, 1420–1427

Drass, H., Haas, M., Chini, R., *et al.* 2016, MNRAS, 11, 1

Drew, J. E., Greimel, R., Irwin, M. J., *et al.* 2005, MNRAS, 362, 753

Drew, J. E., Gonzalez-Solares, E., Greimel, R., *et al.* 2014, MNRAS, 440, 2036

Edwards, S., Cabrit, S., Strom, S. E., *et al.* 1987, ApJ, 321, 473

Ellsworth-Bowers, T. P., Glenn, J., Riley, A., *et al.* 2015, ApJ, 805, 157

Elmegreen, B. G., & Lada, C. J. 1977, ApJ, 214, 725

Faustini, F., Molinari, S., Testi, L., & Brand, J. 2009, AAP, 503, 801

Feigelson, E. D., Jackson, J. M., Mathieu, R. D., Myers, P. C., & Walter, F. M. 1987, AJ, 94, 1251

Field, G. B., Blackman, E. G., & Keto, E. 2006, ArXiv Astrophysics e-prints

Figueira, M., Zavagno, A., Deharveng, L., *et al.* 2017, AAP, 600, A93

Flaherty, K. M., Pipher, J. L., Megeath, S. T., *et al.* 2007, AJ, 4

Frew, D. J., Boji i, I. S., Parker, Q. A., *et al.* 2014, MNRAS, 440, 1080

Fujii, M. S., & Portegies Zwart, S. 2016, ApJ, 817, 4

Fukui, Y., Torii, K., Ohama, A., *et al.* 2016, ApJ, 820, 26

Fukui, Y., Torii, K., Hattori, Y., *et al.* 2017, ArXiv e-prints

Furlan, E., Calvet, N., D'Alessio, P., *et al.* 2005, ApJ, 628, L65

Gahm, G. F., & Malmort, A. M. 1980, AAP, 82, 295

Gahm, G. F., Walter, F. M., Stempels, H. C., Petrov, P. P., & Herczeg, G. J. 2008, A&A, 38, 35

Galli, P. A. B., Bertout, C., Teixeira, R., & Ducourant, C. 2015, A&A, 11

García-Vargas, M. L., Mollá, M., & Martín-Manjón, M. L. 2013, MNRAS, 432, 2746

Goedhart, S., van der Walt, D. J., & Schutte, A. J. 2000, MNRAS, 315, 316

Goodwin, S. P., Nutter, D., Kroupa, P., Ward-Thompson, D., & Whitworth, A. P. 2008, AAP, 477, 823

Gras-Velázquez, À., & Ray, T. P. 2005, AAP, 443, 541

Grinin, V. P., Kozlova, O. V., Natta, A., *et al.* 2001, AAP, 379, 482

Hambly, N. C., Davenhall, A. C., Irwin, M. J., & MacGillivray, H. T. 2001a, MNRAS, 326, 1315

Hambly, N. C., Irwin, M. J., & MacGillivray, H. T. 2001b, MNRAS, 326, 1295

Hambly, N. C., MacGillivray, H. T., Read, M. A., *et al.* 2001c, MNRAS, 326, 1279

Hamilton, C. M., Johns-Krull, C. M., Mundt, R., Herbst, W., & Winn, J. N. 2012, ApJ, 751, 147

Hansen, C. J., Kawaler, S. D., & Trimble, V. 2004, Stellar interiors : physical principles, structure, and evolution (Springer-Verlag New York)

Hartmann, L. 1982, ApJs, 48, 109

Hartmann, L. 1994, in ASPCS, Vol. 65, Clouds, Cores, and Low Mass Stars, ed. D. P. Clemens & R. Barvainis, 315

—. 1998, Accretion Processes in Star Formation (Cambridge Astrophysics Series)

Hayashi, C. 1961, Publications of the Astronomical Society of Japan, 13

Hayashi, E., & Matsuda, T. 2001, Progress of Theoretical Physics, 105, 531

Hayashi, K., Sano, H., Enokiya, R., *et al.* 2017, ArXiv e-prints

Heiter, U., Soubiran, C., Netopil, M., & Paunzen, E. 2014, AAP, 561, A93

Henderson, C. B., Gaudi, B. S., Han, C., *et al.* 2014, ApJ, 794, 52

Henyey, L. G., Lelevier, R., & Levée, R. D. 1955, PASP, 67, 154

Herczeg, G. J., & Hillenbrand, L. A. 2014, ApJ, 786, 97

Hernández, J., Calvet, N., Hartmann, L., *et al.* 2005, AJ, 129, 856

Heydari-Malayeri, M. 1988, Astronomy and Astrophysics (ISSN 0004-6361), 202, 240

Hillenbrand, L. A., & Carpenter, J. M. 2000, ApJ, 540, 236

Hillenbrand, L. A., Hoffer, A. S., & Herczeg, G. J. 2013, AJ, 146, 85

Howarth, I. D. 1983, MNRAS, 203, 301

Indebetouw, R., Mathis, J. S., Babler, B. L., *et al.* 2005, ApJ, 619, 931

Ingleby, L., Calvet, N., Bergin, E., *et al.* 2011, ApJ, 743, 105

Ingraham, A. D. R. 2012, PhD thesis, University of Toronto

Israelian, G., & de Groot, M. 1999, SSR, 90, 493

Jacoby, G. H., Hunter, D. A., & Christian, C. A. 1984, ApJs, 56, 257

Jester, S., Schneider, D. P., Richards, G. T., *et al.* 2005, AJ, 130, 873

Johnson, H. L. 1968, Interstellar Extinction (the University of Chicago Press), 167

Jordi, K., Grebel, E. K., & Ammon, K. 2006, AAP, 460, 339

Joshi, G. C. 2016, pre-print

Juvela, M., & Montillaud, J. 2015, A&A, 585, 1

Kalari, V. M., & Vink, J. S. 2015, ApJ, 800, 113

Kalari, V. M., Vink, J. S., Drew, J. E., *et al.* 2015, MNRAS, 453, 1026

Karaali, S., Bilir, S., & Tunçel, S. 2005, PASA, 22, 24

Kato, D. 2007, PhD thesis, Department of Astrophysics at Nagoya University

Kenyon, S. J., Gomez, M., & Whitney, B. A. 2008, Handbook of Star Forming Regions, I, 54

Kenyon, S. J., & Hartmann, L. 1987, ApJ, 323, 714

Kesseli, A. Y., West, A. A., Veyette, M., *et al.* 2017, ApJs, 230, 16

Keto, E. 2003, ApJ, 599, 1196

Kharchenko, N. V., Piskunov, A. E., Schilbach, E., Röser, S., & Scholz, R.-D. 2012, AAP, 543, A156

—. 2013, AAP, 558, A53

Kim, S.-L., Cha, S.-M., Lee, C.-U., *et al.* 2016, Publication of Korean Astronomical Society, 31, 35

Kippenhahn, R., Weigert, A., & Weiss, A. 2012, Stellar Structure and Evolution (Springer)

Kobulnicky, H. A., Nordsieck, K. H., Burgh, E. B., *et al.* 2003, in Instrument Design and Performance for Optical/Infrared Ground-based Telescopes, ed. M. Iye & A. F. M. Moorwood, Vol. 4841, 1634–1644

Koerner, D. W., Sargent, A. I., & Beckwith, S. V. W. 1993, Icarus, 106, 2

Kong, S., Lada, C. J., Lada, E. A., *et al.* 2015, ApJ, 805, 58

Koornneef, J. 1983, A&ASS, 51, 489

Kraus, A. L., & Hillenbrand, L. A. 2008, ApJ, 686, L111

Kroupa, P. 2001, MNRAS, 322, 231

Krumholz, M. R. 2014, Physics Reports, 91

Kurosawa, R., Harries, T. J., & Symington, N. H. 2005, in Protostars and Planets V Posters, Vol. 1286, 8412

Lada, C. J. 2005, Progress of Theoretical Physics Supplement, 158, 1

Lada, C. J., & Adams, F. C. 1992, ApJ, 393, 278

Lada, C. J., Alves, J., & Lada, E. A. 1996, AJ, 111, 1964

Lada, C. J., Alves, J. F., & Lombardi, M. 2007, Protostars and Planets V, 3

Lada, C. J., & Lada, E. A. 2003, ARAA, 41, 57

Lada, C. J., Lada, E. A., Clemens, D. P., & Bally, J. 1993, Bulletin of the American Astronomical Society, 25, 1333

Lada, E. A. 1998, in ASPCS, Vol. 148, Origins, ed. C. E. Woodward, J. M. Shull, & J. H. A. Thronson, 198

Lago, M. T. V. T., Gameiro, J. F., Costa, V. M., Machado, L., & Pedrosa, A. 1998, APSS, 261, 107

Lee, C. D., & Chen, W. P. 2009, in ASPCS, Vol. 404, The Eighth Pacific Rim Conference on Stellar Astrophysics: A Tribute to Kam-Ching Leung, ed. S. J. Murphy & M. S. Bessell, 302

Lee, H.-T., Chen, W. P., Zhang, Z.-W., & Hu, J.-Y. 2005, ApJ, 624, 808

Li, W., Evans II, N. J., & Lada, E. A. 1997, ApJ, 488, 277

Littlefair, S. P., Naylor, T., Harries, T. J., Retter, A., & O'Toole, S. 2004, MNRAS, 347, 937

Lodato, G., Scardoni, C. E., Manara, C. F., & Testi, L. 2017, MNRAS, 472, 4700

Lombardi, M. 2008, A&A, 493, 13

Lombardi, M., Alves, J., & Lada, C. 2011, A&A, 13

Lombardi, M., Alves, J., & Lada, C. J. 2006, Astronomy and Astrophysics, 796, 781

Luhman, K. L., Rieke, G. H., Lada, C. J., & Lada, E. A. 1998, ApJ, 508, 347

Lynden-Bell, D., & Pringle, J. E. 1974, MNRAS, 168, 603

Magazzu, A., Rebolo, R., & Pavlenko, I. V. 1992, ApJ, 392, 159

Marsh, K. A., Kirk, J. M., Andre, P., *et al.* 2017, VizieR Online Data Catalog, 745

Maschberger, T. 2013, MNRAS, 429, 1725

McClure, M. K., Calvet, N., Espaillat, C., *et al.* 2013, ApJ, 769, 73

Menten, K. M. 1991, ApJl, 380, L75

Meyer, M. R., Calvet, N., & Hillenbrand, L. A. 1997, AJ, 114, 288

Morgan, W. W., Keenan, P. C., & Kellman, E. 1943, An atlas of stellar spectra, with an outline of spectral classification (Astrophysical Monographs by AJ)

Mowat, C., Hatchell, J., Rumble, D., *et al.* 2017, MNRAS, 467, 812

Mueller, K. E., & Graham, J. A. 2000, PASP, 112, 1426

Murray, N. 2011, ApJ, 729, 133

Mužić, K., Schödel, R., Scholz, A., *et al.* 2017, MNRAS, 471, 3699

Muzerolle, J., Calvet, N., & Hartmann, L. 2001, ApJ, 550, 944

Nakano, T. 1989, MNRAS, 241, 495

Nandy, K., Thompson, G. I., Jamar, C., Monfils, A., & Wilson, R. 1976, A&A, 51, 63

Netopil, M., Paunzen, E., Heiter, U., & Soubiran, C. 2016, AAP, 585, A150

Ohama, A., Tsutsumi, D., Sano, H., *et al.* 2017, ArXiv e-prints

Ojha, D. K., Tamura, M., Nakajima, Y., *et al.* 2004, ApJ, 616, 1042

Pagani, L., Heydari-Malayeri, M., & Castets, A. 1993, A&A

Palla, F., & Prusti, T. 1993, AAP, 272, 249

Palla, F., Testi, L., Hunter, T. R., *et al.* 1995, AAP, 293, 521

Pandian, J. D., & Goldsmith, P. F. 2007, ApJ, 669, 435

Parravano, A., McKee, C. F., & Hollenbach, D. J. 2011, AJ, 726, 27

Pattle, K., Ward-Thompson, D., Kirk, J. M., *et al.* 2017, MNRAS, 464, 4255

Paunzen, E., Heiter, U., Netopil, M., & Soubiran, C. 2010, AAP, 517, A32

Paxton, B., Marchant, P., Schwab, J., *et al.* 2015, ApJs, 220, 15

Pecaut, M. J., & Mamajek, E. E. 2013, ApJs, 208, 9

Pecaut, M. J., Mamajek, E. E., & Bubar, E. J. 2012, ApJ, 746, 154

Persson, S. E., Murphy, D. C., Krzeminski, W., Roth, M., & Rieke, M. J. 1998, AJ, 116, 2475

Petrenz, P., & Puls, J. 1996, AAP, 312, 195

Phelps, R. L. 1997, ApJ, 483, 826

Piche, F., Howard, E. M., & Pipher, J. L. 1995, MNRAS, 275, 711

Pickles, A. J. 1998, PASP, 110, 863

Pietrinferni, A., Cassisi, S., Salaris, M., & Castelli, F. 2004, ApJ, 612, 168

Pineda, J. E., Goodman, A. A., Arce, H. G., *et al.* 2011, ApJl, 739, L2

Pinheiro, M. C., Copetti, M. V. F., & Oliveira, V. A. 2010, AAP, 521, A26

Reed, B. C. 2003, AJ, 125, 2531

Reipurth, B., Pedrosa, A., & Lago, M. T. V. T. 1996, AAPs, 120, 229

Rieke, G. H., & Lebofsky, M. J. 1985, ApJ, 288, 618

Rivera-Ingraham, A., Martin, P. G., Polychroni, D., & Moore, T. J. T. 2011, ApJ, 3

Rodgers, C. T., Canterna, R., Smith, J. A., Pierce, M. J., & Tucker, D. L. 2006, AJ, 132, 989

Román-Zúñiga, C. G., Alves, J. F., Lada, C. J., & Lombardi, M. 2010, ApJ, 725, 2232

Russell, H. N. 1913, The Observatory, 36, 324

Rykoff, E. S., Rozo, E., & Keisler, R. 2015, ArXiv e-prints

Salpeter, E. 1955, ApJ, 121, 161

Sandage, A. 1956, PASP, 68, 498

Schmeja, S. 2010, in Astronomical Society of India Conference Series, Vol. 1, Astronomical Society of India Conference Series

Schmeja, S., Kharchenko, N. V., Piskunov, A. E., *et al.* 2014, AAP, 568, A51

Schultz, G. V., & Wiemer, W. 1975, A&A, 43, 133

Sharma, S., Pandey, A. K., Borissova, J., *et al.* 2016, AJ, 151, 126

Shepherd, D. S., & Churchwell, E. 1996, ApJ, 457, 267

Shu, F. H., Lizano, S., & Adams, F. C. 1987, in IAU Symposium, Vol. 115, Star Forming Regions, ed. M. Peimbert & J. Jugaku, 417–433

Siess, L., Dufour, E., & Forestini, M. 2000, Astronomy and Astrophysics, 358, 593

Sousa, A. P., Alencar, S. H. P., Bouvier, J., *et al.* 2016, A&A, 586, A47

Stahler, S. W. 1983, AJ, 274, 822

Stahler, S. W., & Palla, F. 2005, The Formation of Stars (Wiley-VCH), 865

Stead, J. J., & Hoare, M. G. 2009, MNRAS, 400, 731

Straižys, V., & Lazauskaitė, R. 2009, Baltic Astronomy, 18, 19

Strom, K. M., Wilkin, F. P., Strom, S. E., & Seaman, R. L. 1989, AJ, 98, 1444

Strom, S. E. 1993, Nature, 364, 99

Stuewe, J. A., & Schultz, R. 1994, Astronomische Nachrichten, 315, 427

Suh, K.-W., & Kwon, Y.-J. 2011, Journal of Astronomy and Space Sciences, 28

Szegedi-Elek, E., Kun, M., Reipurth, B., *et al.* 2013, ApJs, 208, 28

Tayler, R. J. 1994, Science, 266, 666

Teixeira, P. S., Fernandes, S. R., Alves, J. F., *et al.* 2004, A&A, 413, L1

Teixeira, P. S., Lada, C. J., Marengo, M., & Lada, E. A. 2012, A&A, 540, A83

Tielens, A. G. G. M. 2005, The Physics and Chemistry of the Interstellar Medium (Cambridge Astrophysical Series)

Torii, K., Hasegawa, K., Hattori, Y., *et al.* 2015, ApJ, 806, 7

Trumpler, R. J. 1934, PASP, 46, 208

Uchida, Y., & Shibata, K. 1984, PASJ, 36, 105

Urquhart, J. S., Morgan, L. K., & Thompson, M. a. 2009, A&A, 497, 789

van den Bergh, S., & Herbst, W. 1975, AJ, 80, 208

van der Walt, D. J., de Villiers, H. M., & Czanik, R. J. 2012, AJ, 144, 13

van der Walt, J. 2005, MNRAS, 360, 153

Venuti, L., Bouvier, J., Flaccomio, E., *et al.* 2014, A&A, 82, 24

Vink, J. S., Drew, J. E., Steeghs, D., *et al.* 2008, MNRAS, 387, 308

Vittone, A. A., de Martino, D., Giovannelli, F., & Rossi, C. 1987, A&A, 179, 157

Walker, M. 1972, ApJ, 175, 89

Walsh, A. J., Burton, M. G., Hyland, A. R., & Robinson, G. 1999, MNRAS, 309, 905

Walter, F. M. 1986, PASP, 98, 1100

Ward-Thompson, D., & Whitworth, A. P. 2011, An Introduction to Star Formation (Cambridge Astrophysical Series)

Weingartner, J. C., & Draine, B. T. 2001, ApJ, 548, 296

West, A. A., Walkowicz, L. M., & Hawley, S. L. 2005, PASP, 117, 706

Whitford, A. E. 1958, AJ, 63, 201

Whittet, D. C. B. 1992, JBAA, 102, 230

Whittet, D.C.B.; Gerakines, P. 2001, ApJ, 547, 872

Yi, S., Demarque, P., Kim, Y.-C., *et al.* 2001, ApJs, 136, 417

Yorke, H. W. 2002, in ASPCS, Vol. 267, Hot Star Workshop III: The Earliest Phases of Massive Star Birth, ed. P. Crowther, 165

Zinnecker, H. 1982, Annals of the New York Academy of Sciences, 395, 226

Zychova, L., & Ehlerova, S. 2017, in Star Formation from Cores to Clusters, 66

APPENDIX A: MATHEMATICAL DERIVATION FOR THE STATISTICAL MODEL FOR *LINES*

Let the variables of interest be denoted as (X_{1i}, X_{2i}) and the observed data be denoted by:

$$(Y_{1i}, Y_{2i}, \mathbf{V}_i) \text{ where } i = 1, ..., n, \tag{A.1}$$

where for each $i, \mathbf{V}_i$ is a 2×2 matrix with elements denoted by $V_{11,i}, V_{22,i}$, and $V_{12,i}$, for the diagonal and the common off-diagonal elements, respectively. The observed data are related to the unobserved variables of interest by

$$Y_{1i} = X_{1i} + \epsilon_{1i} \text{ and } Y_{2i} = X_{2i} + \epsilon_{2i}, \tag{A.2}$$

where the errors $(\epsilon_{1i}, \epsilon_{2i})$ have a joint bi-variant distribution with zero mean and covariance matrix $\mathbf{V}_i$ for all i. In this model, we allow $\mathbf{V}_i$ to depend on (Y_{1i}, Y_{2i}) and therefore, implicitly on (X_{1i}, X_{2i}). Thus, we do not require $(\epsilon_{1i}, \epsilon_{2i})$ to be independent of (X_{1i}, X_{2i}). However, we assume that $\mathbf{V}_i$ is the only aspect of the distribution of $(\epsilon_{1i}, \epsilon_{2i})$ that depends on (Y_{1i}, Y_{2i}). In the other words, we assume that, given $\mathbf{V}_i$, $(\epsilon_{1i}, \epsilon_{2i})$ in independent of (X_{1i}, X_{2i}).

The intuitive meaning of the technical assumption that " given $\mathbf{V}_i$, $(\epsilon_{1i}, \epsilon_{2i})$ is independent of (X_{1i}, X_{2i}) " is that ϵ_{1i}, for example, is equally likely to be positive or negative for any value of X_{1i}, and the size of its absolute value is governed (in addition to the type of the measurement error distribution) by the magnitude of $V_{11,i}$, which is given. All astronomical datasets that we are aware of comply to this assumption.

In most cases, the measurement errors for the two variables are independent (so that $V_{1\ 2,i} = 0$ for all i), and the observed data is of the form

$$(Y_{1i}, Y_{2i}, V_{11,i}, V_{22,i}), \tag{A.3}$$

with $V_{kk,i}$ denoting the variance of $\epsilon_{ki}, k = 1, 2$. It is assumed that the variables of interest follow the usual simple regression model

$$X_{2i} = \alpha_1 + \beta_1 X_{1i} + \epsilon_i \tag{A.4}$$

where ϵ_i is assumed to have zero mean and finite variance. The terminology "intrinsic scatter" is commonly used to indicate the variance or standard deviation of ϵ_1. We want to estimate the regression coefficients α_1, β_1 and the uncertainties of these estimators using the data in equation A.1.

The **b**ivariate **c**orrelation **e**rrors and intrinsic **s**catter (BCES$(X_2|X_1)$) estimator that will be used is an extension of the **o**rdinary **l**east **s**quare (Ordinary least squares (OLS)$(X_2|X_1)$) estimator, which is valid for all data sets that fit the measurement error model specified above. The estimator is based on the fact that the parameters of equation A.4 are related to the moments of the bivariate distribution of (X_{1i}, X_{2i}). In particular,

$$\beta_1 = \frac{\text{Cov}(X_{1i}, X_{2i})}{\text{Var}(X_{1i})} \text{ and } \alpha = E(X_{2i}) - \beta_1 E(X_{1i}) \tag{A.5}$$

where $\text{Cov}(X_{1i}, X_{2i})$ denotes the covariance of $X_{1i}, X2i, \text{Var}(X_{1i})$ the variance of X_{1i}, and $E(X_{1i}), E(X_{2i})$ the expected values for X_{1i} and X_{2i}.

APPENDIX B: SPECTROSCOPIC PROFILES FOR THE STARS OBSERVED WITH *SALT* IN RCW 34

The red spectra were observed with *SALT* and the grey spectra were closest match made with PyHammer to each specific case.

Hα-emission line stars

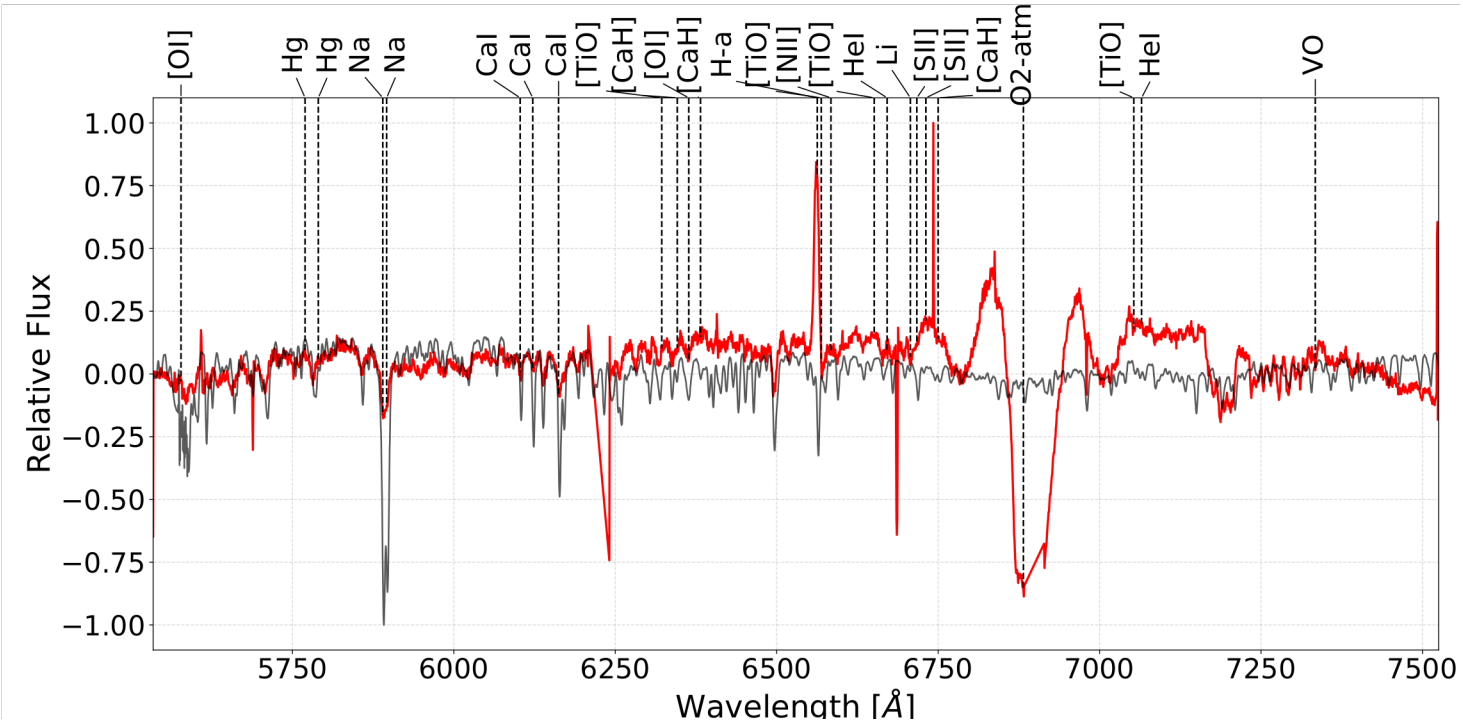

Figure B.1: Slit 1 for the NE field of RCW 34

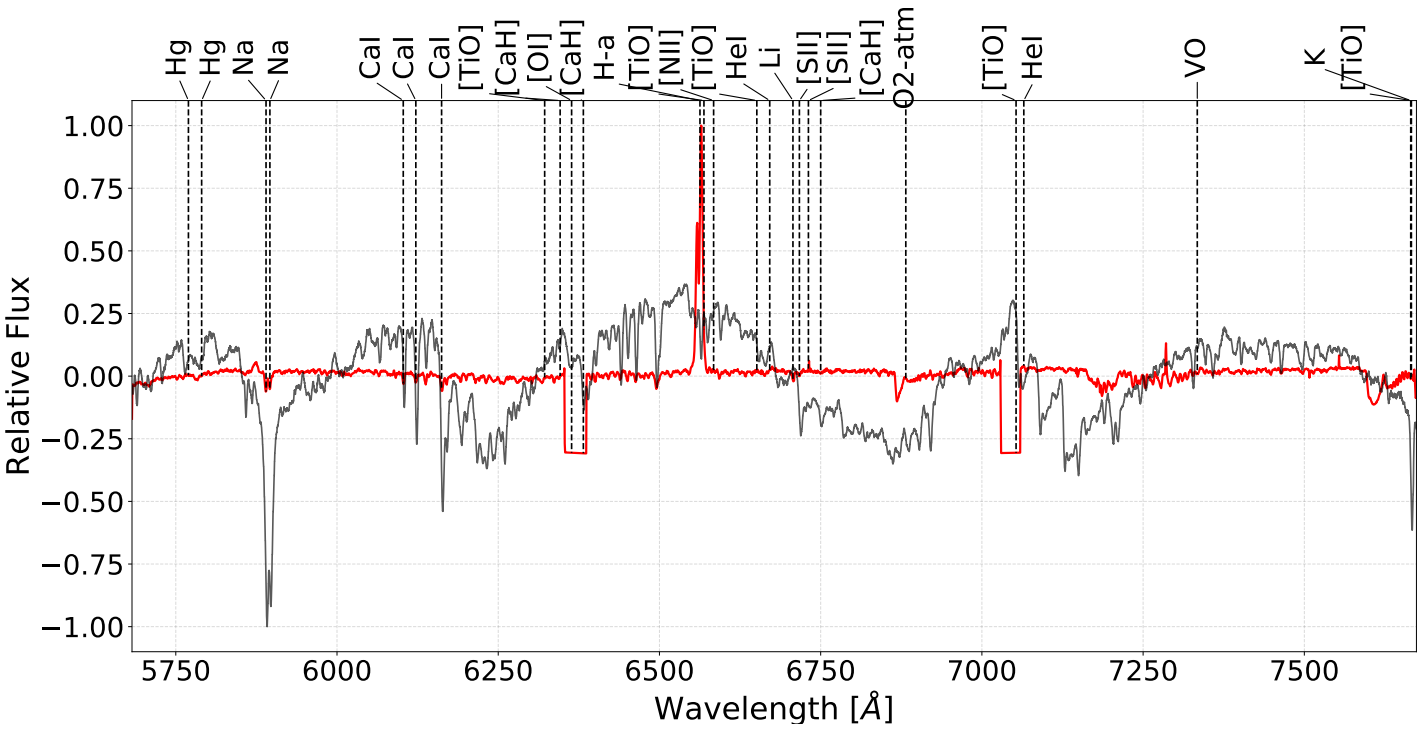

Figure B.2: Slit 2 for the NE field of RCW 34

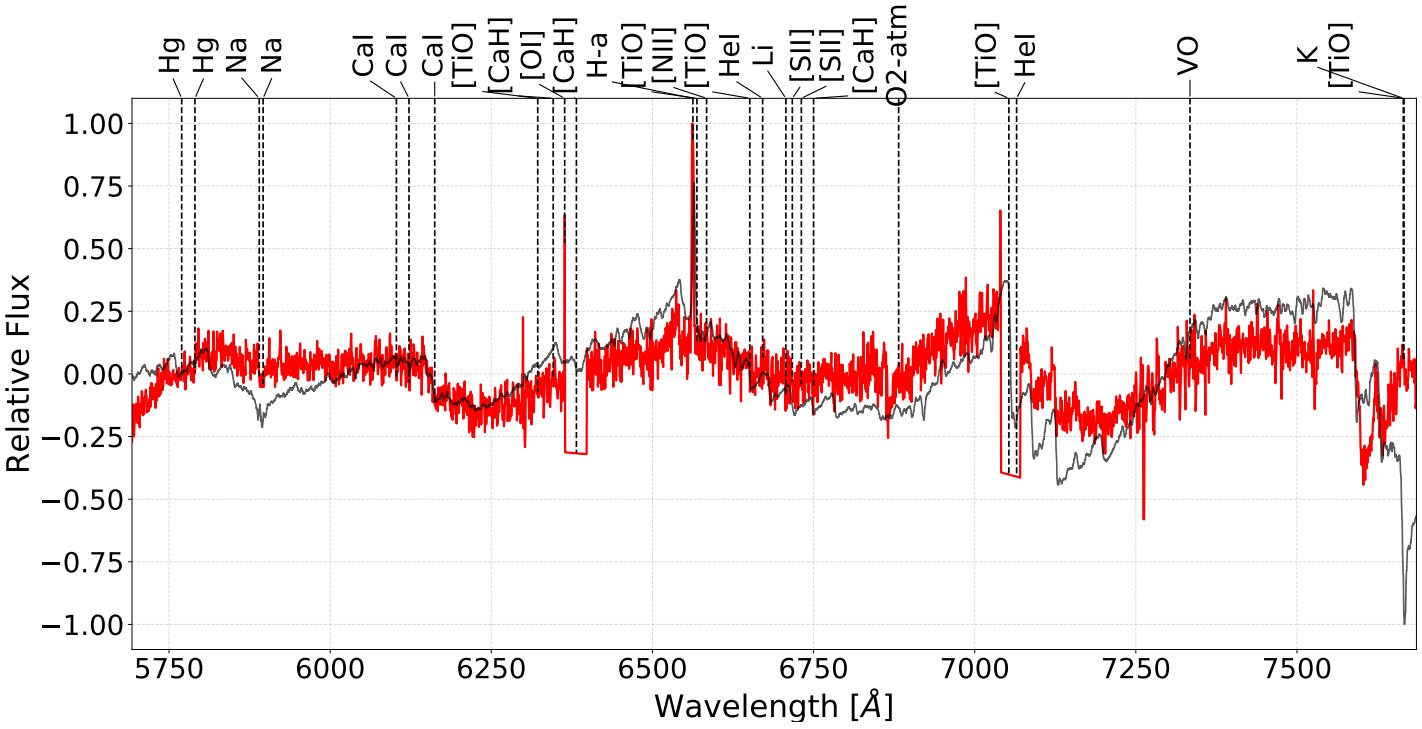

Figure B.3: Slit 4 for the NE field of RCW 34

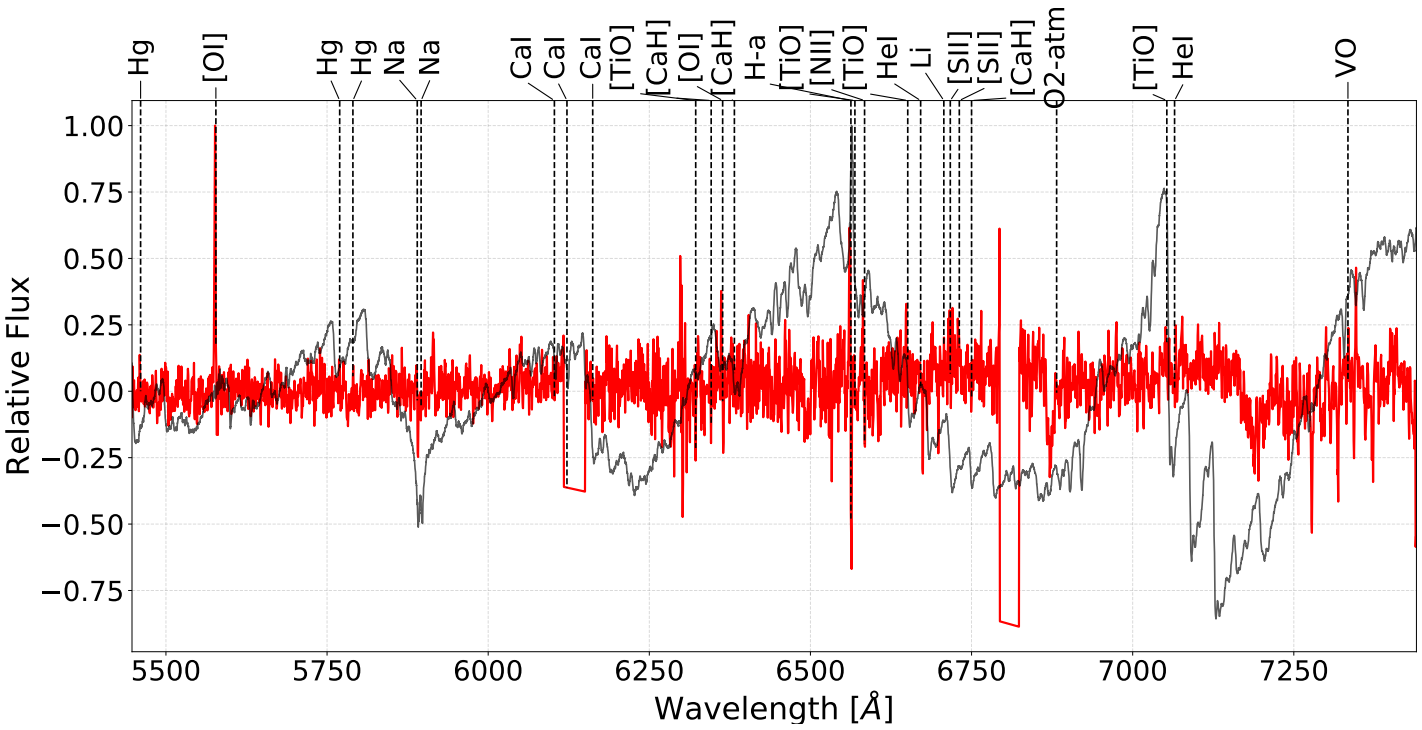

Figure B.4: Slit 5 for the NE field of RCW 34

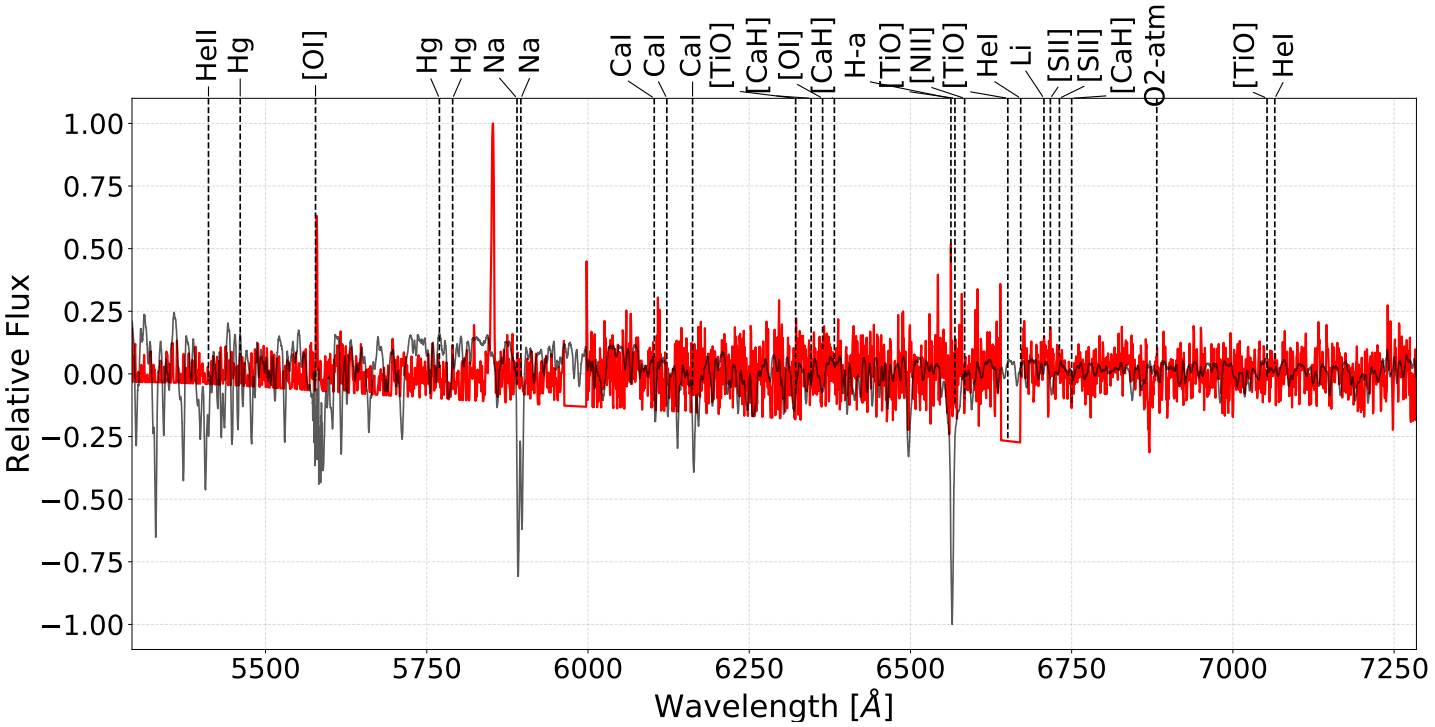

Figure B.5: Slit 21 for the NE field of RCW 34

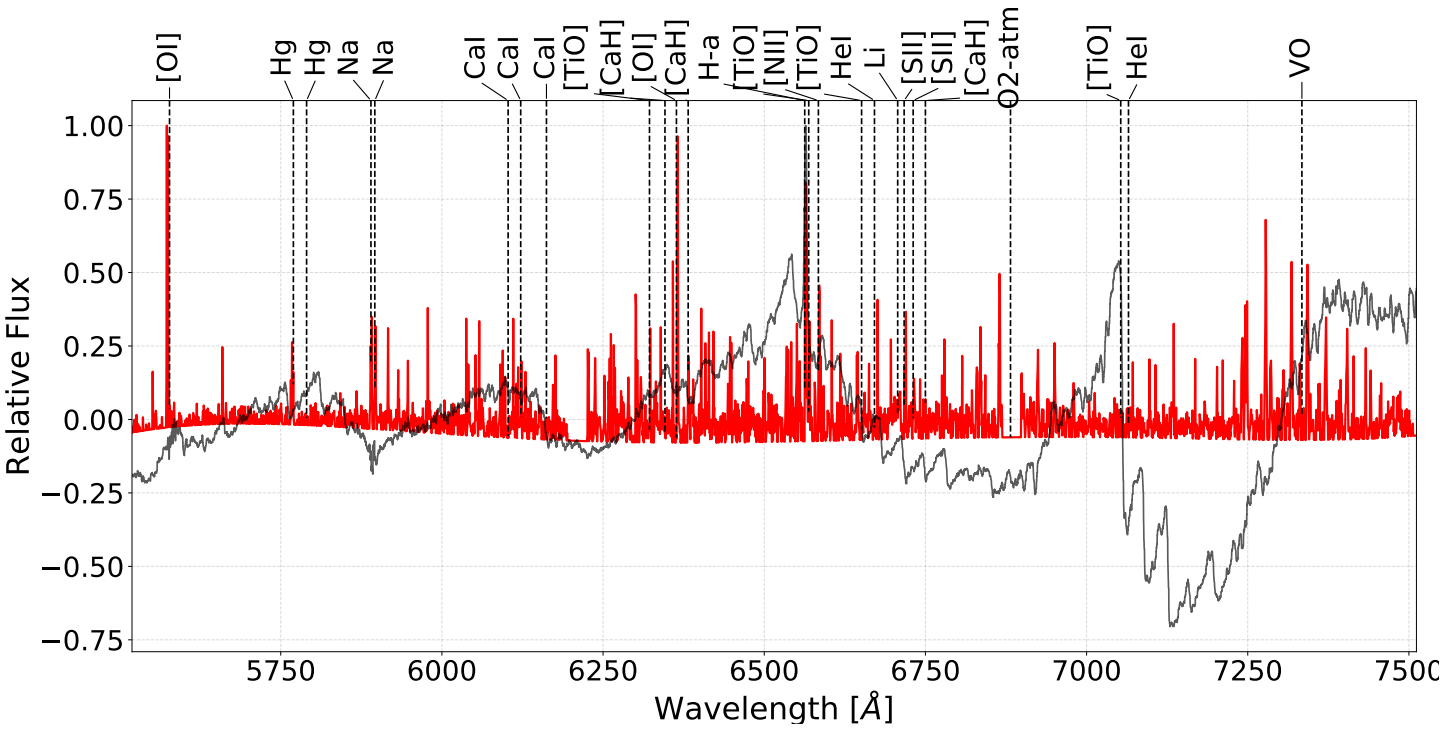

Figure B.6: Slit 1 for the NW field of RCW 34

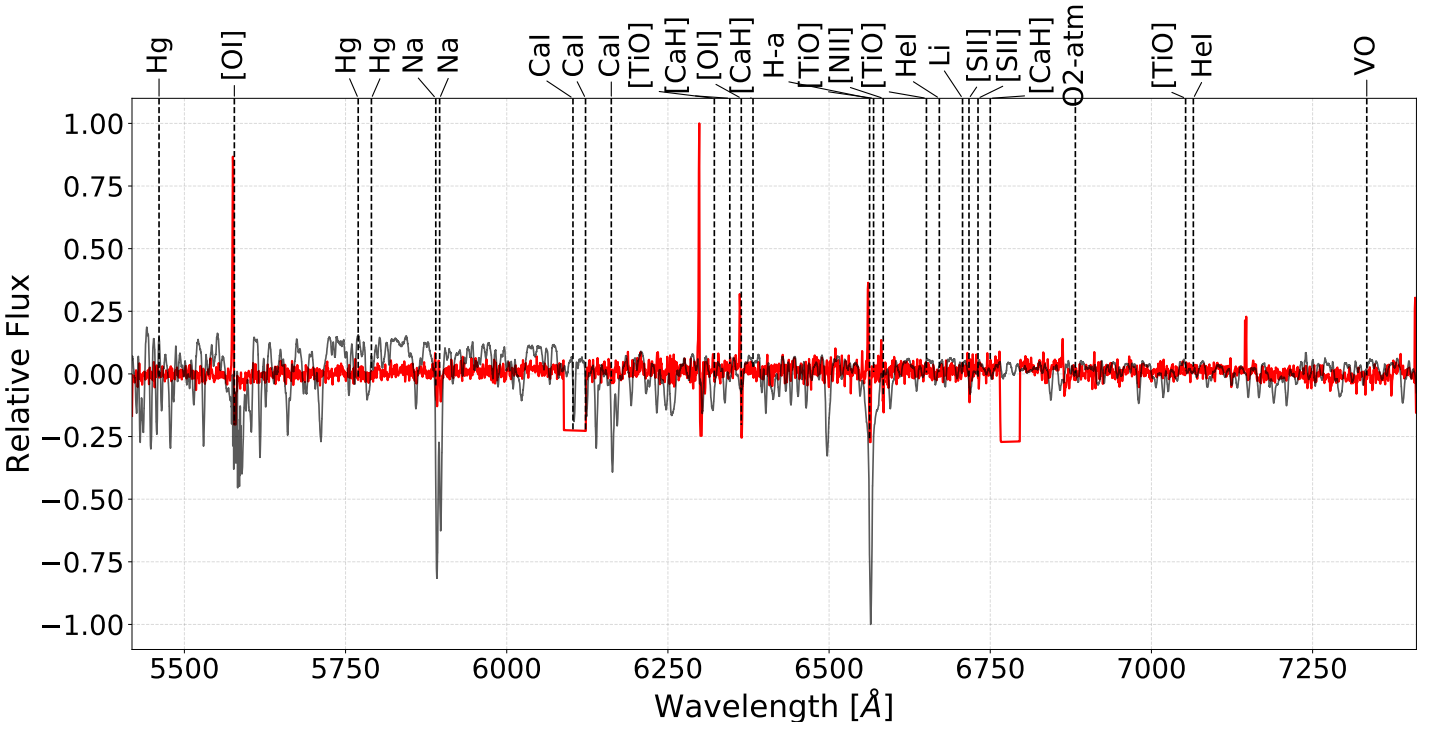

Figure B.7: Slit 2 for the NW field of RCW 34

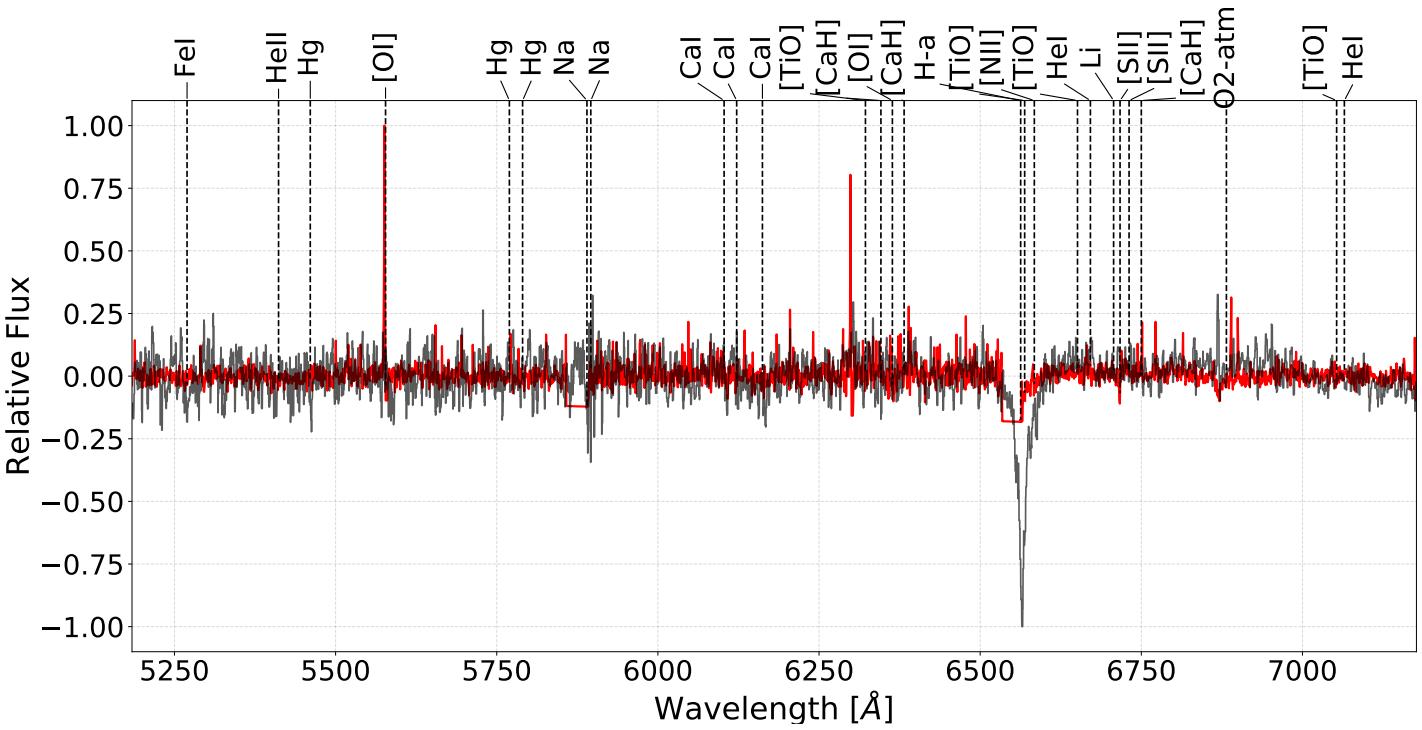

Figure B.8: Slit 5 for the NW field of RCW 34

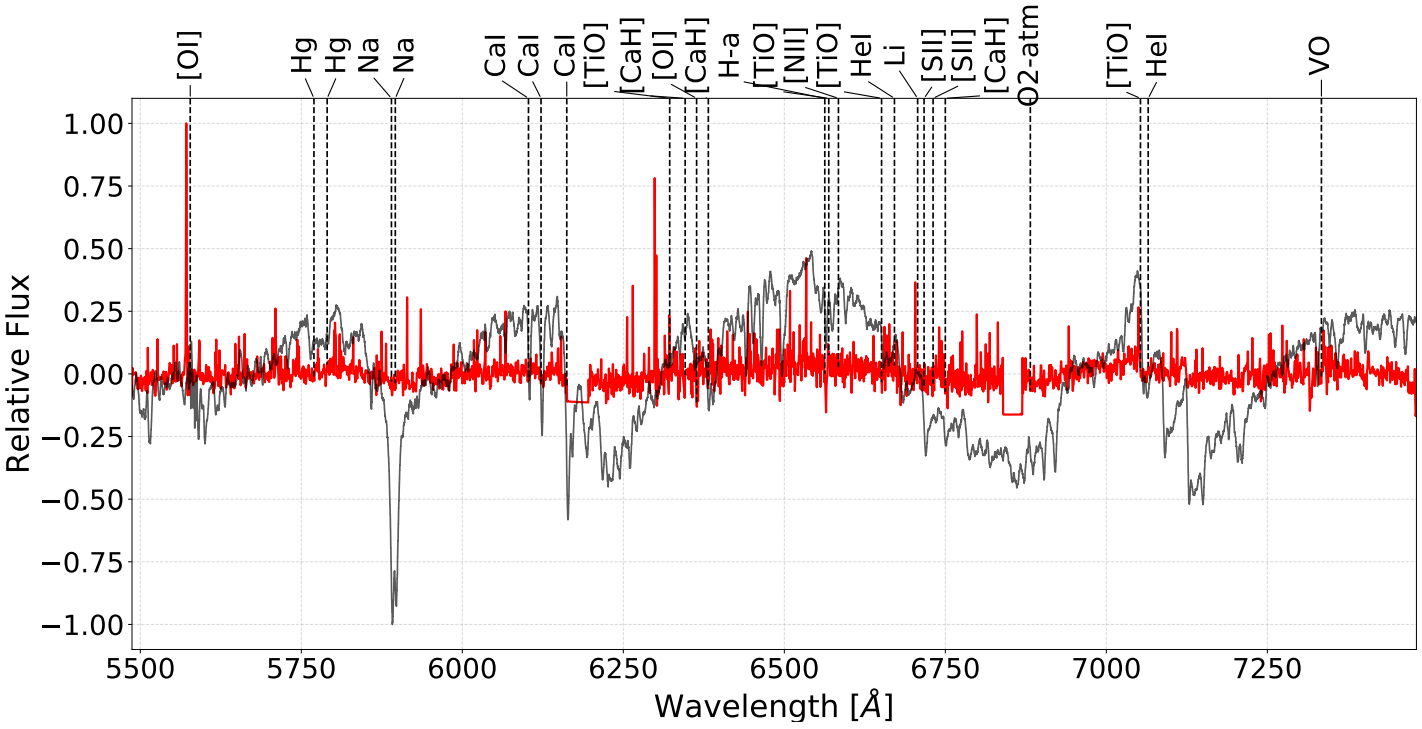

Figure B.9: Slit 6 for the NW field of RCW 34

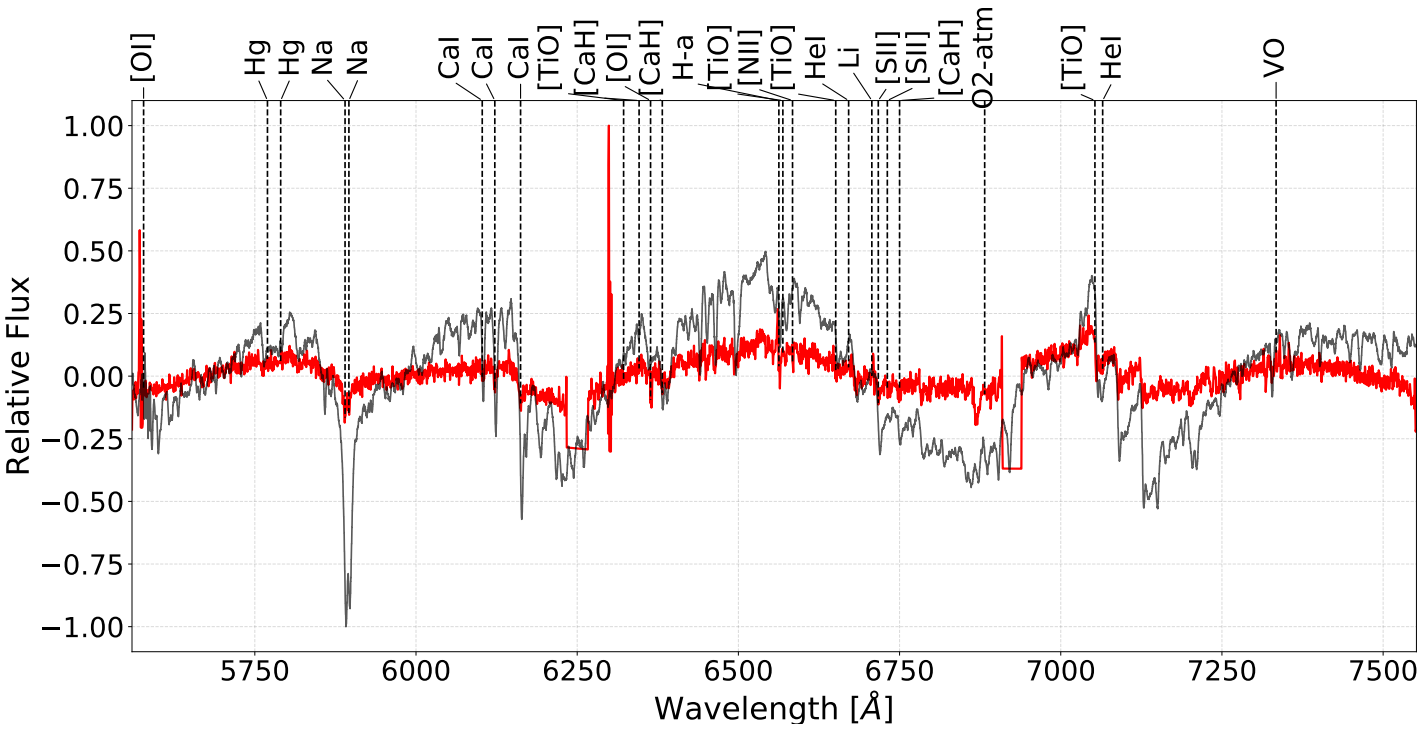

Figure B.10: Slit 1 for the SE field of RCW 34

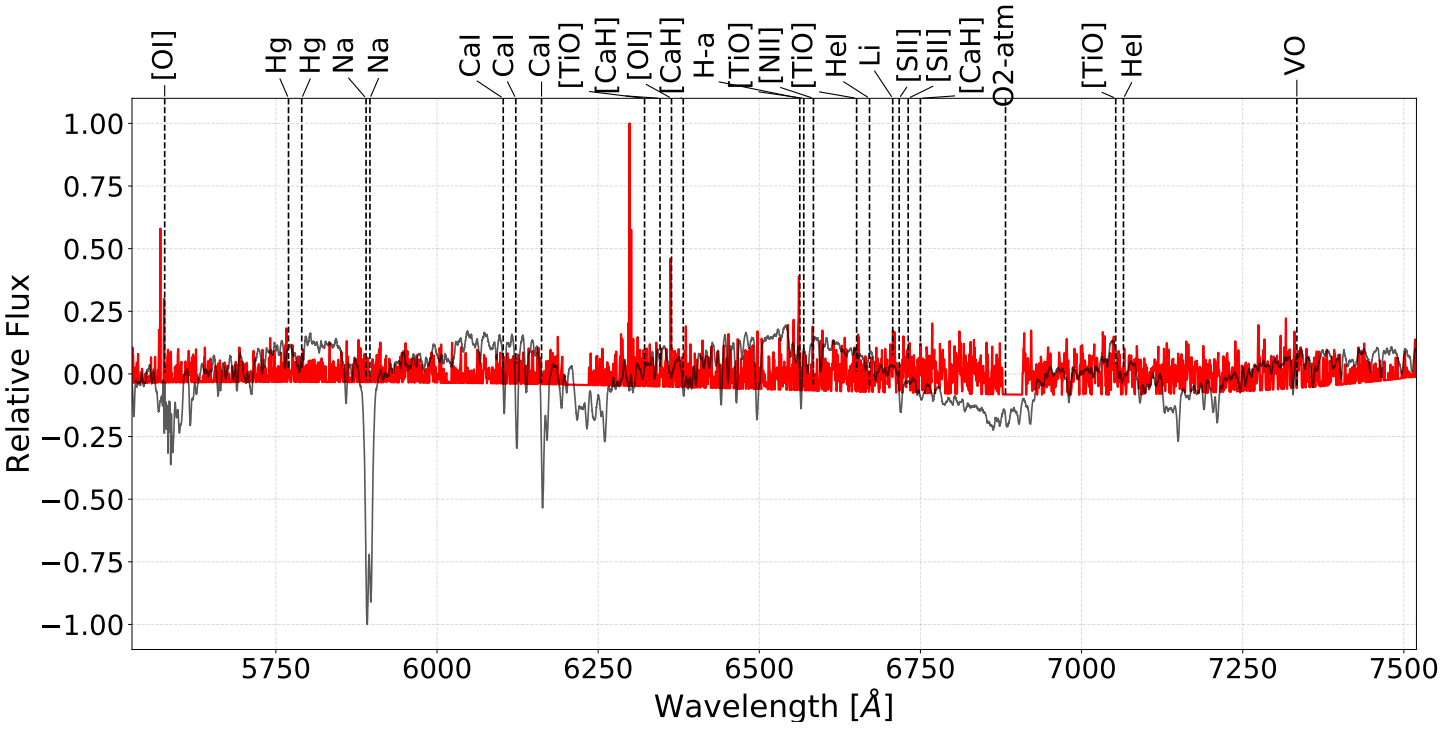

Figure B.11: Slit 3 for the SE field of RCW 34

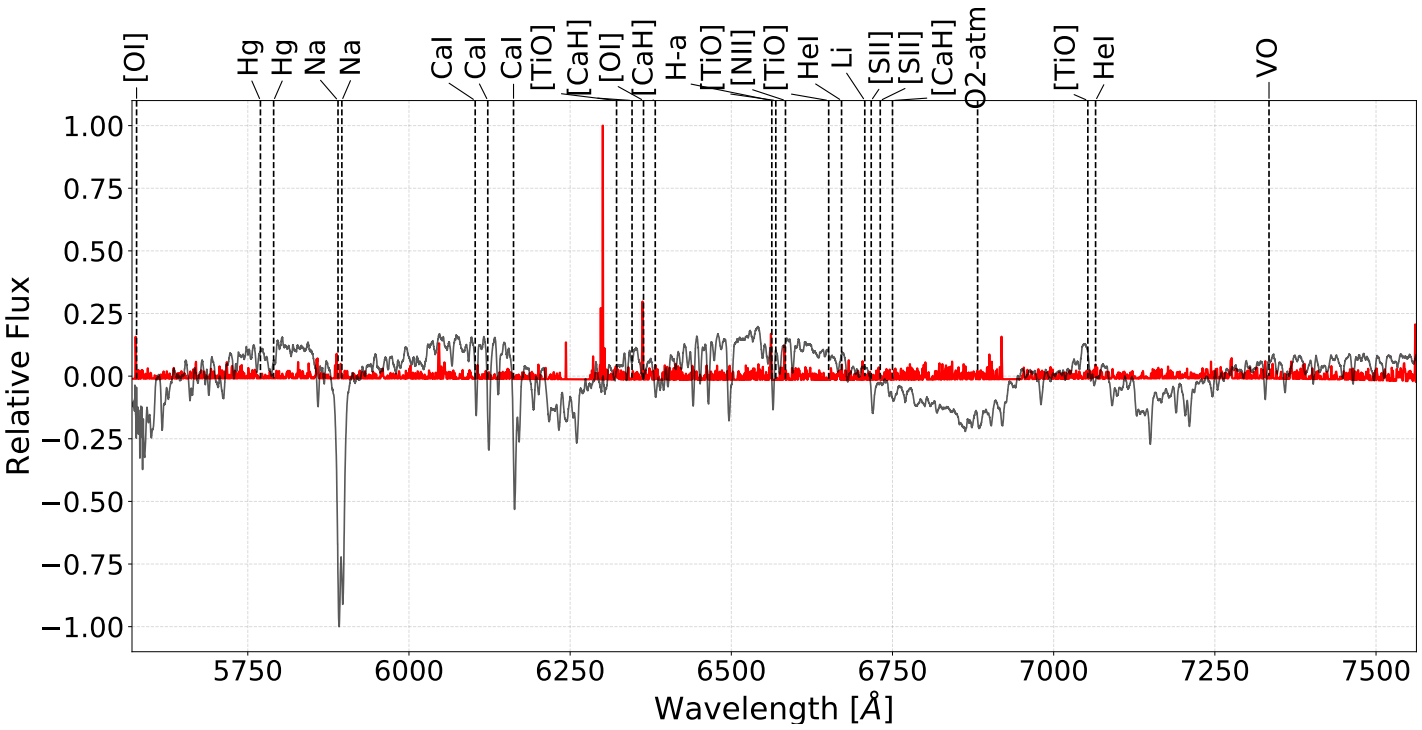

Figure B.12: Slit 4 for the SE field of RCW 34

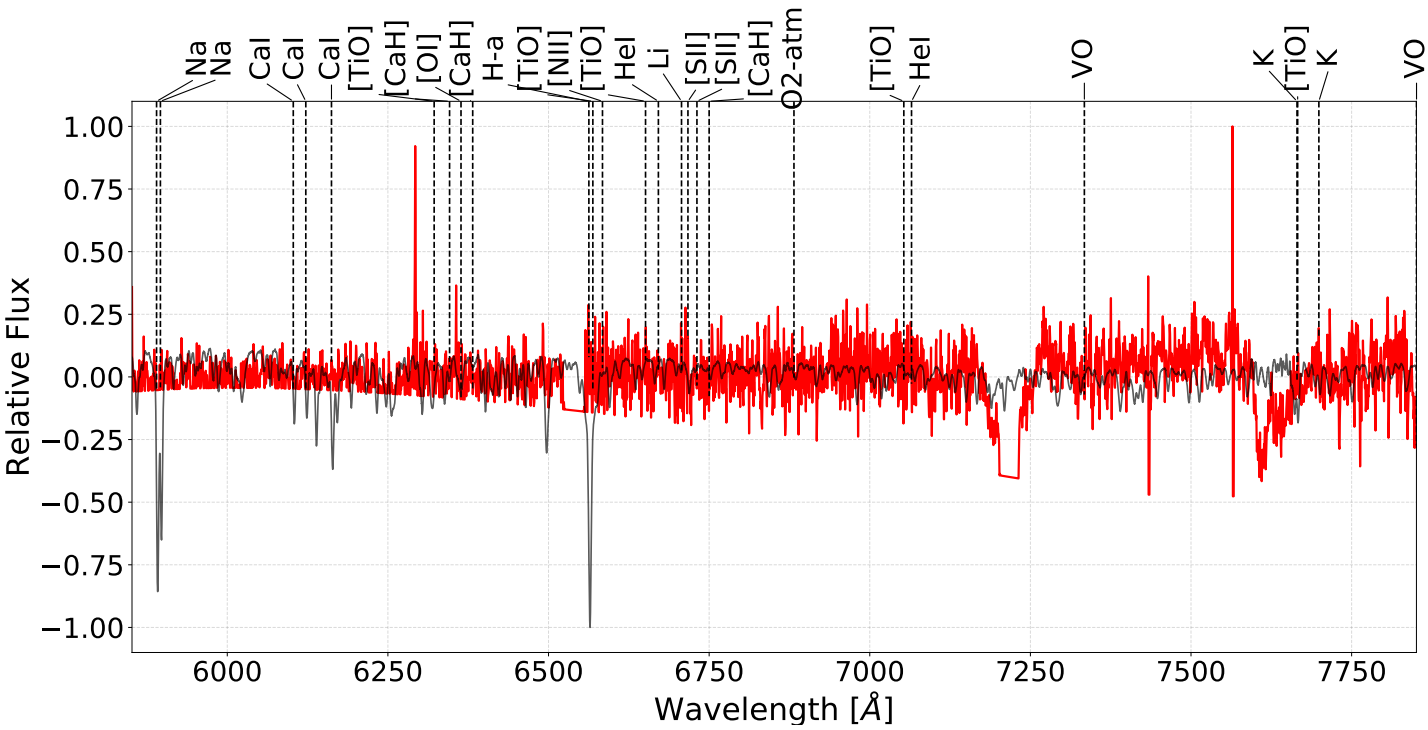

Figure B.13: Slit 7 for the SE field of RCW 34

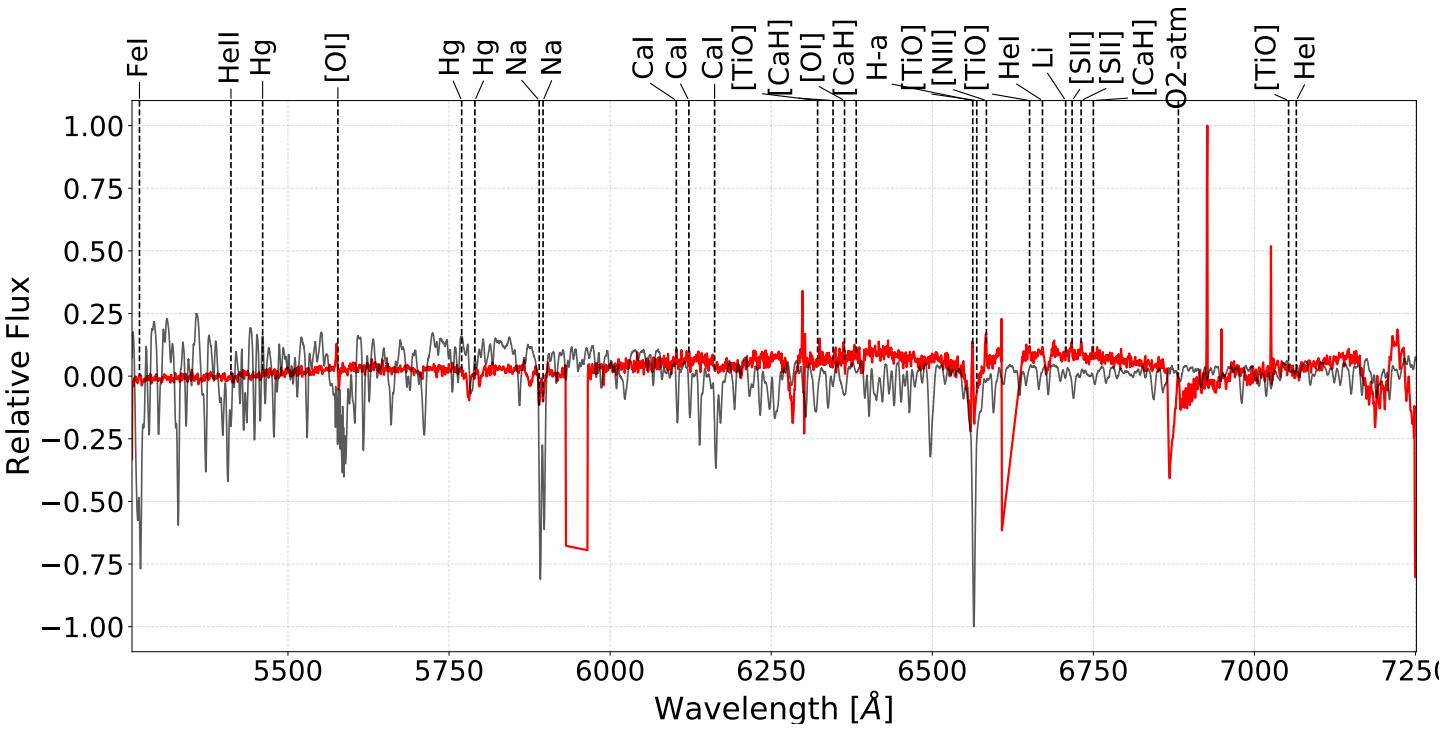

Figure B.14: Slit 12 for the SE field of RCW 34

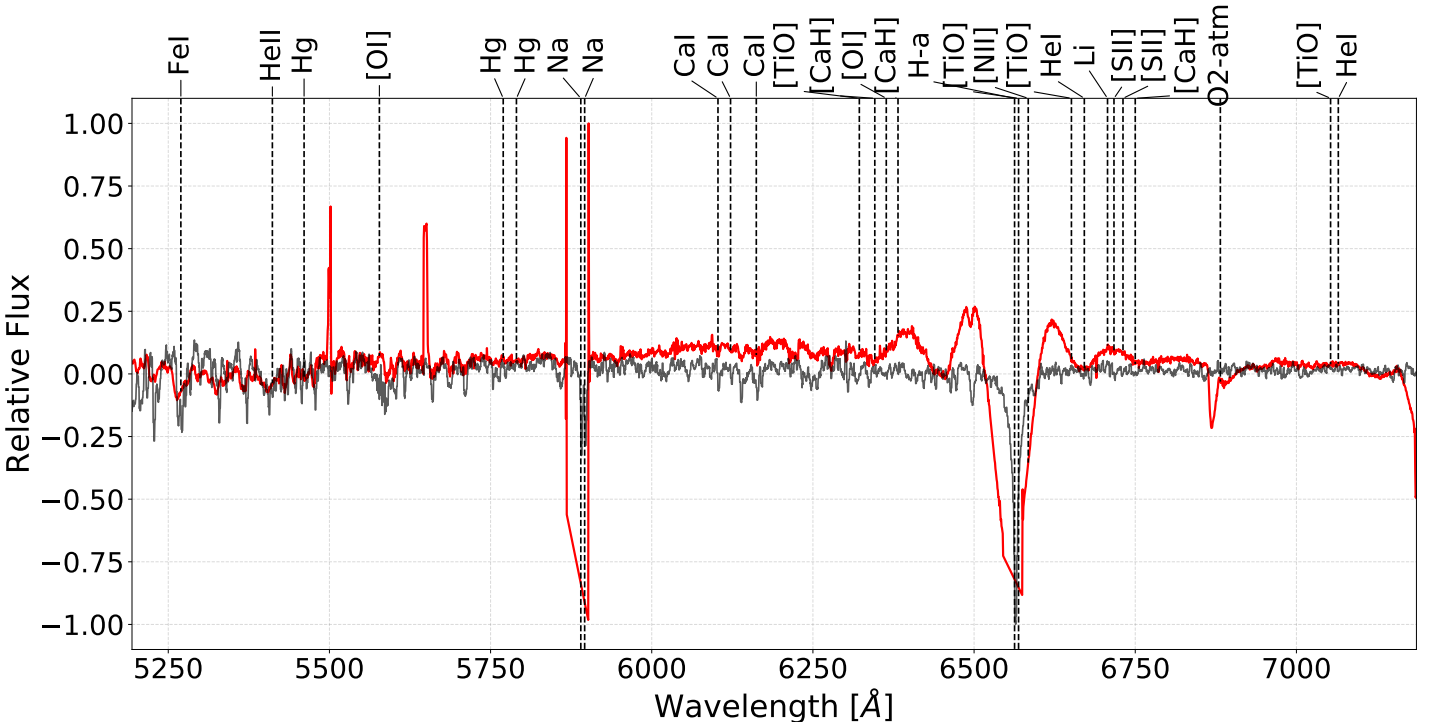

Figure B.15: Slit 16 for the SE field of RCW 34

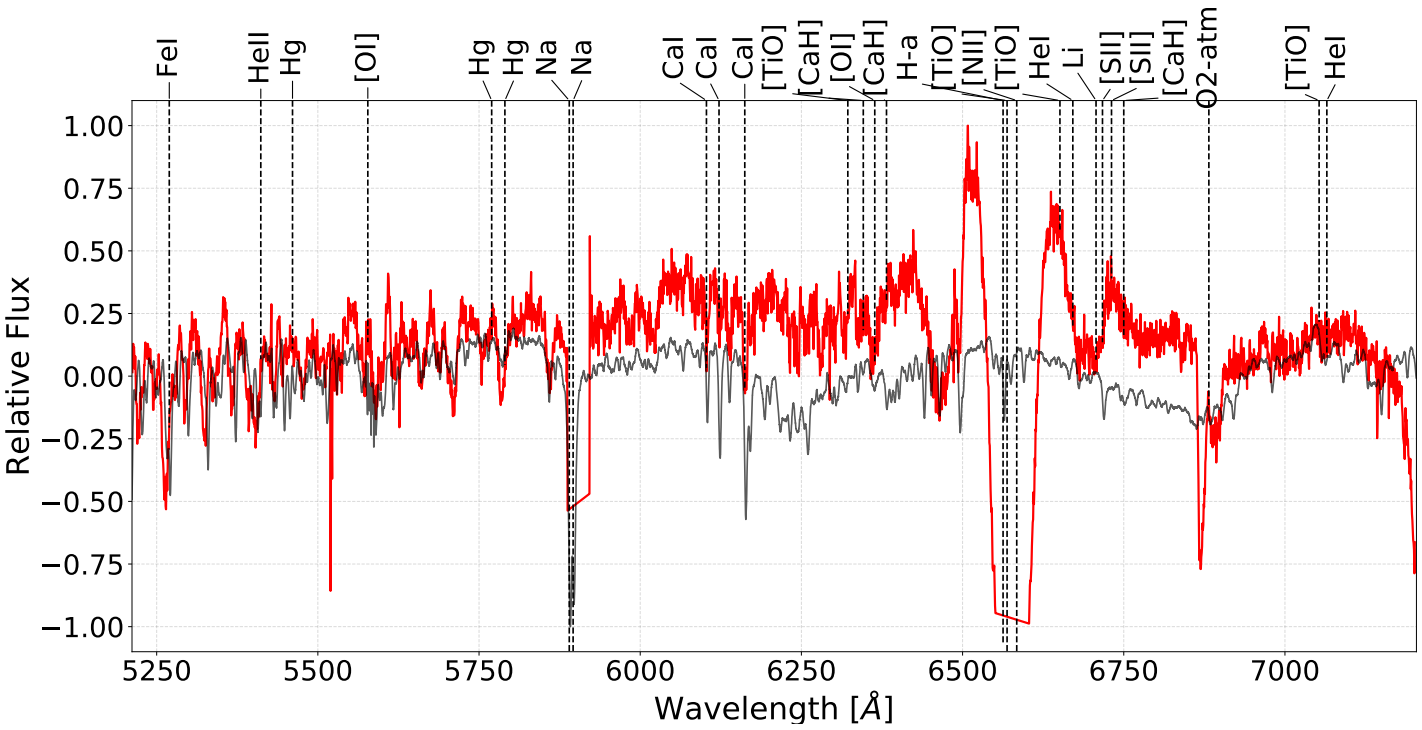

Figure B.16: Slit 20 for the SE field of RCW 34

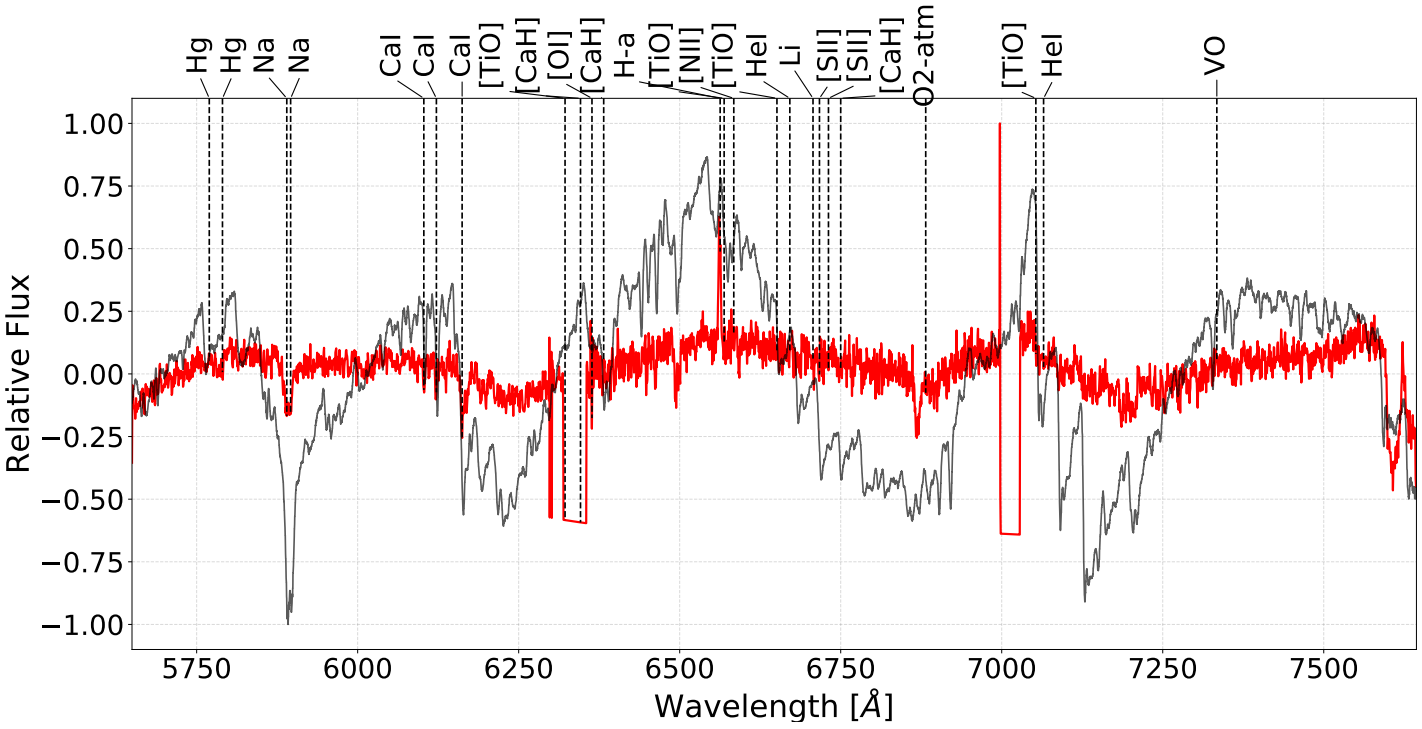

Figure B.17: Slit 22 for the SE field of RCW 34

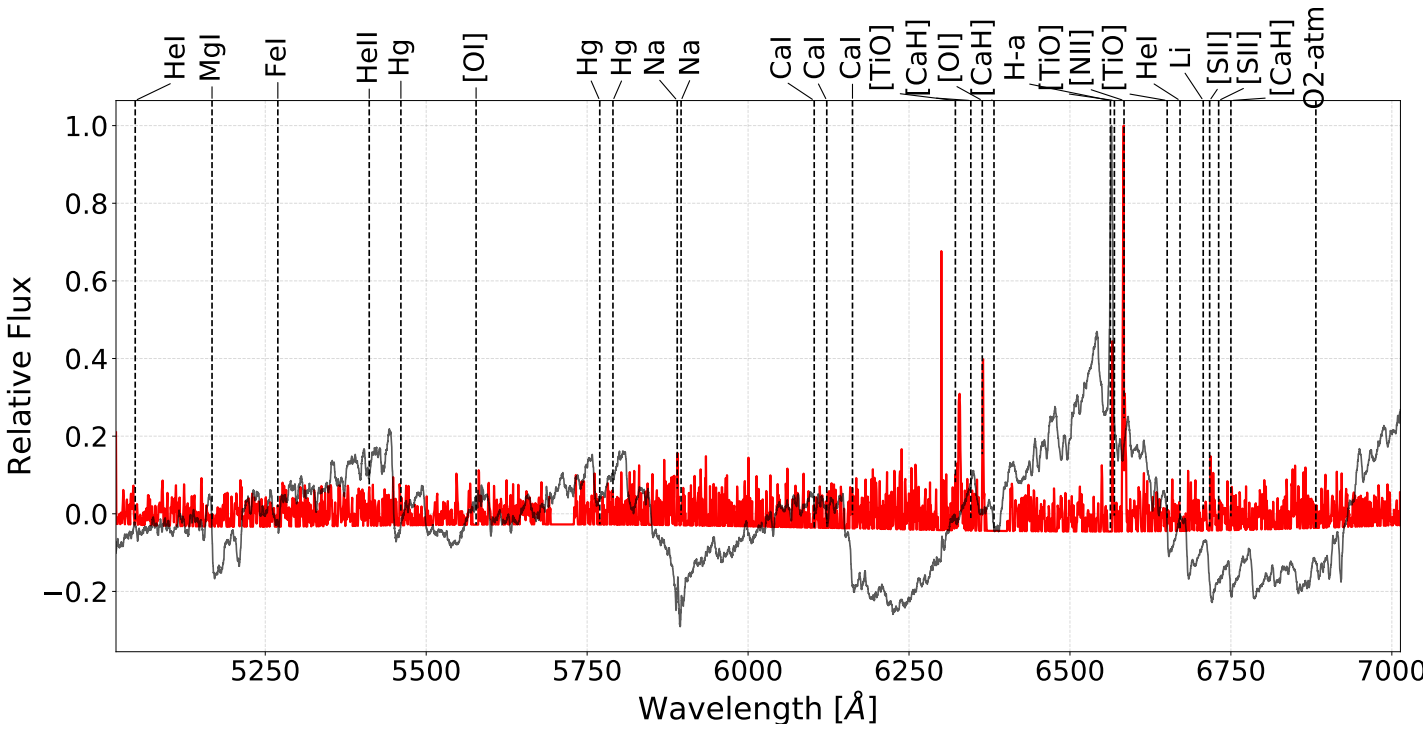

Figure B.18: Slit 25 for the SE field of RCW 34

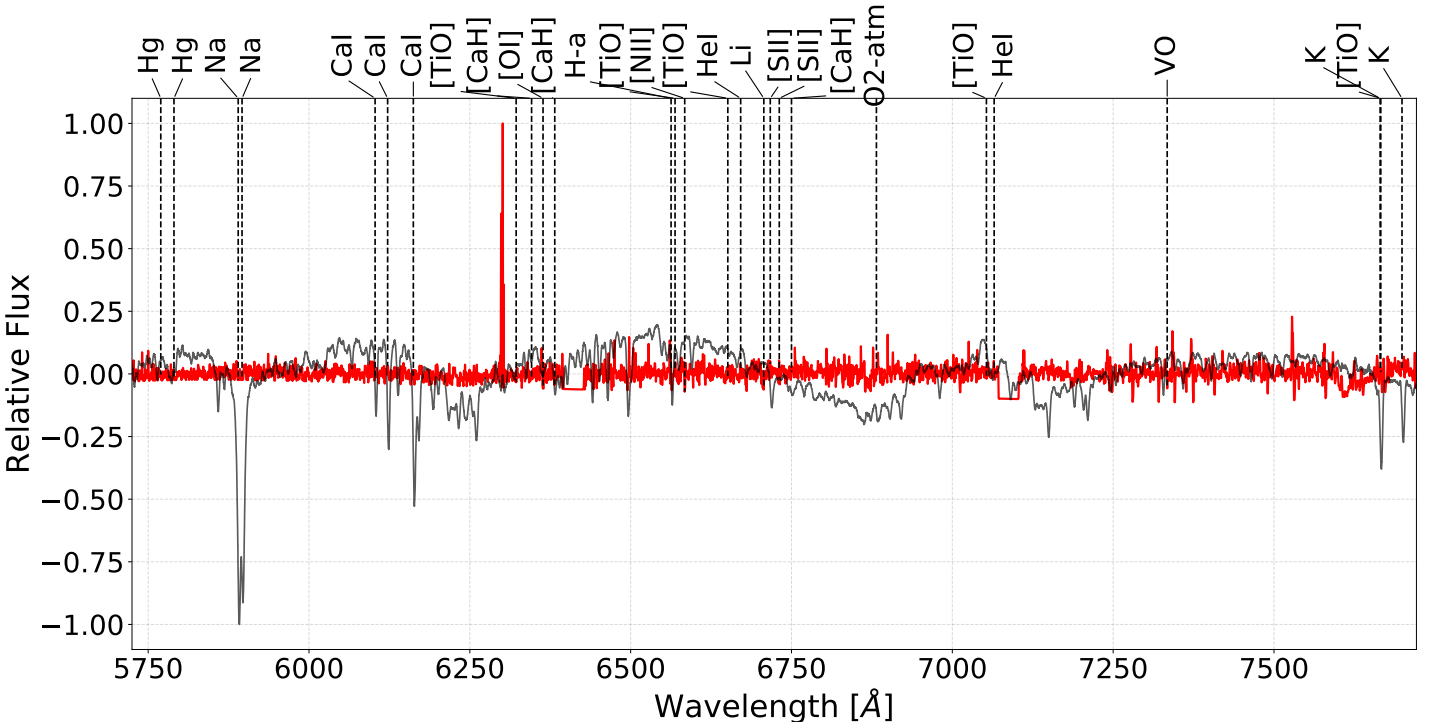

Figure B.19: Slit 3 for the SW field of RCW 34

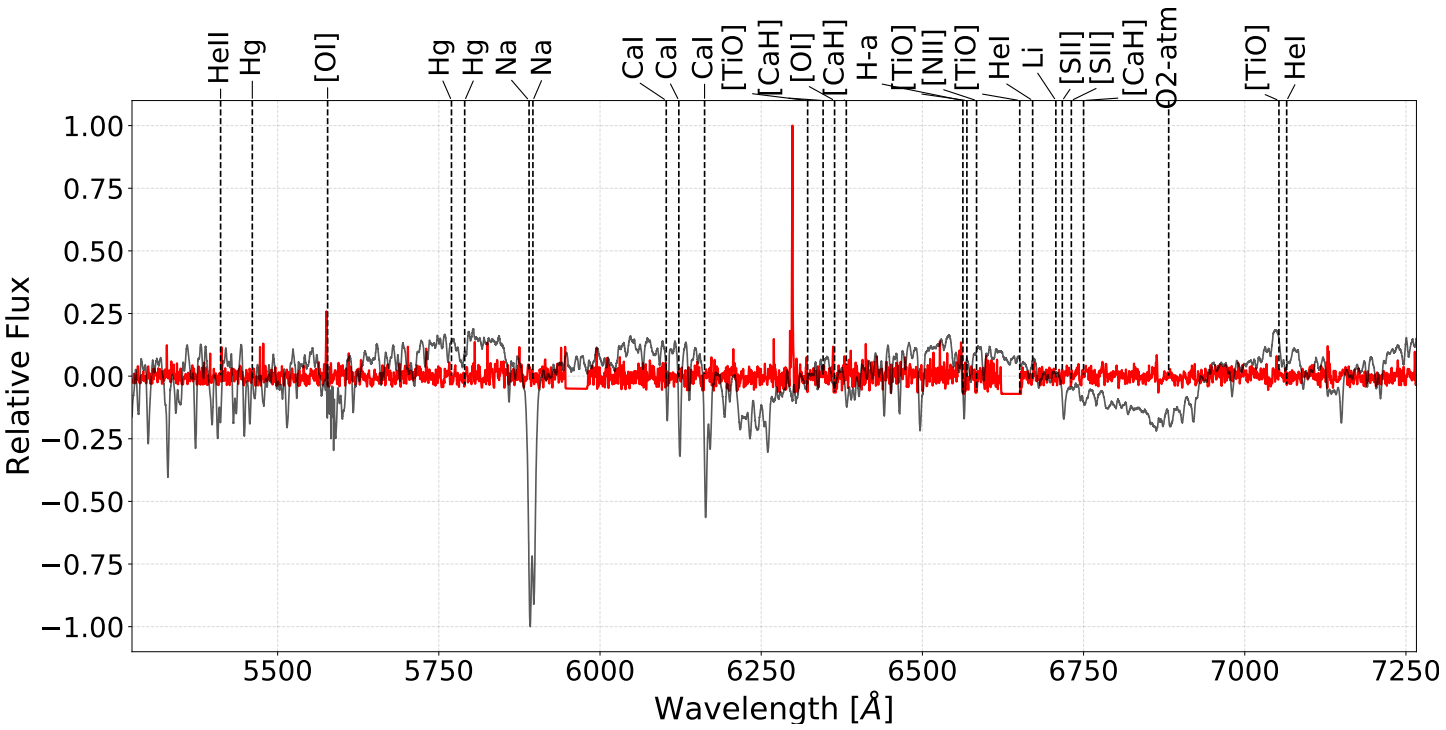

Figure B.20: Slit 6 for the SW field of RCW 34

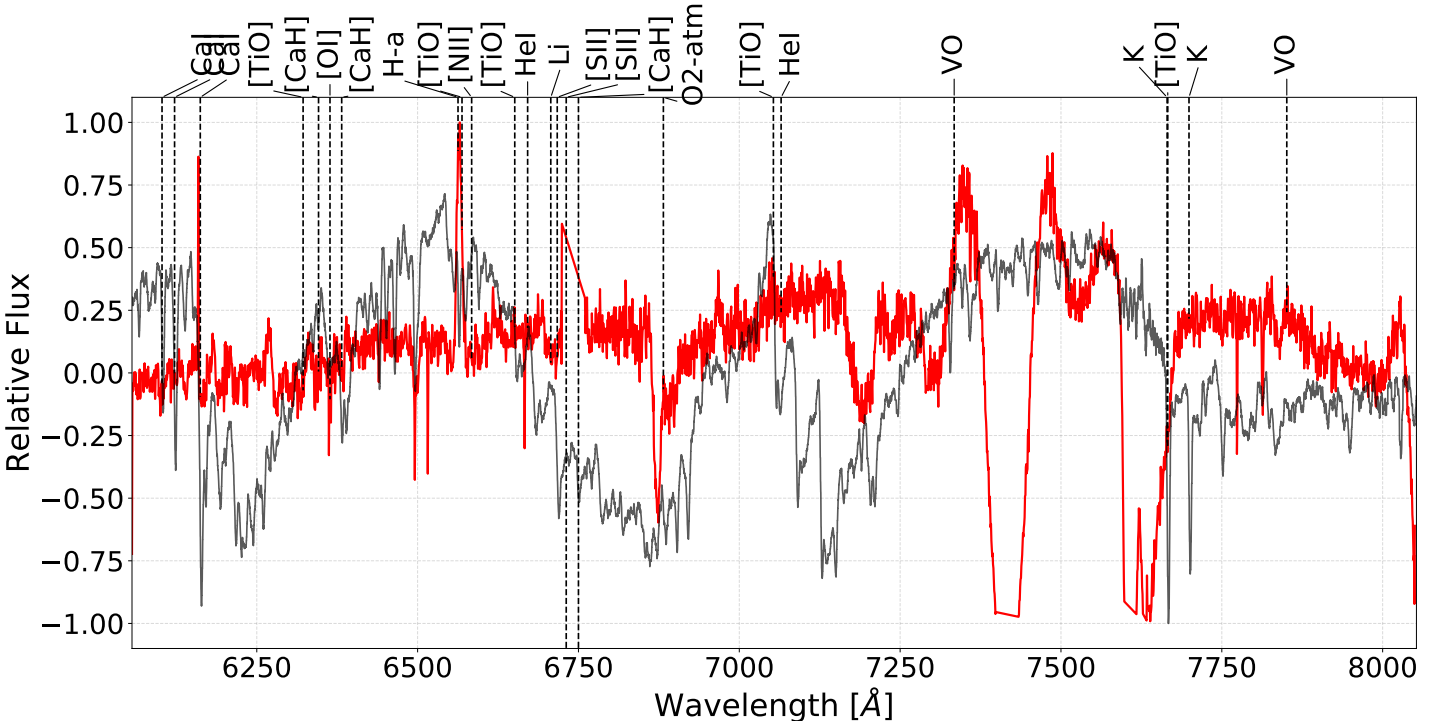

Figure B.21: Slit 22 for the SW field of RCW 34

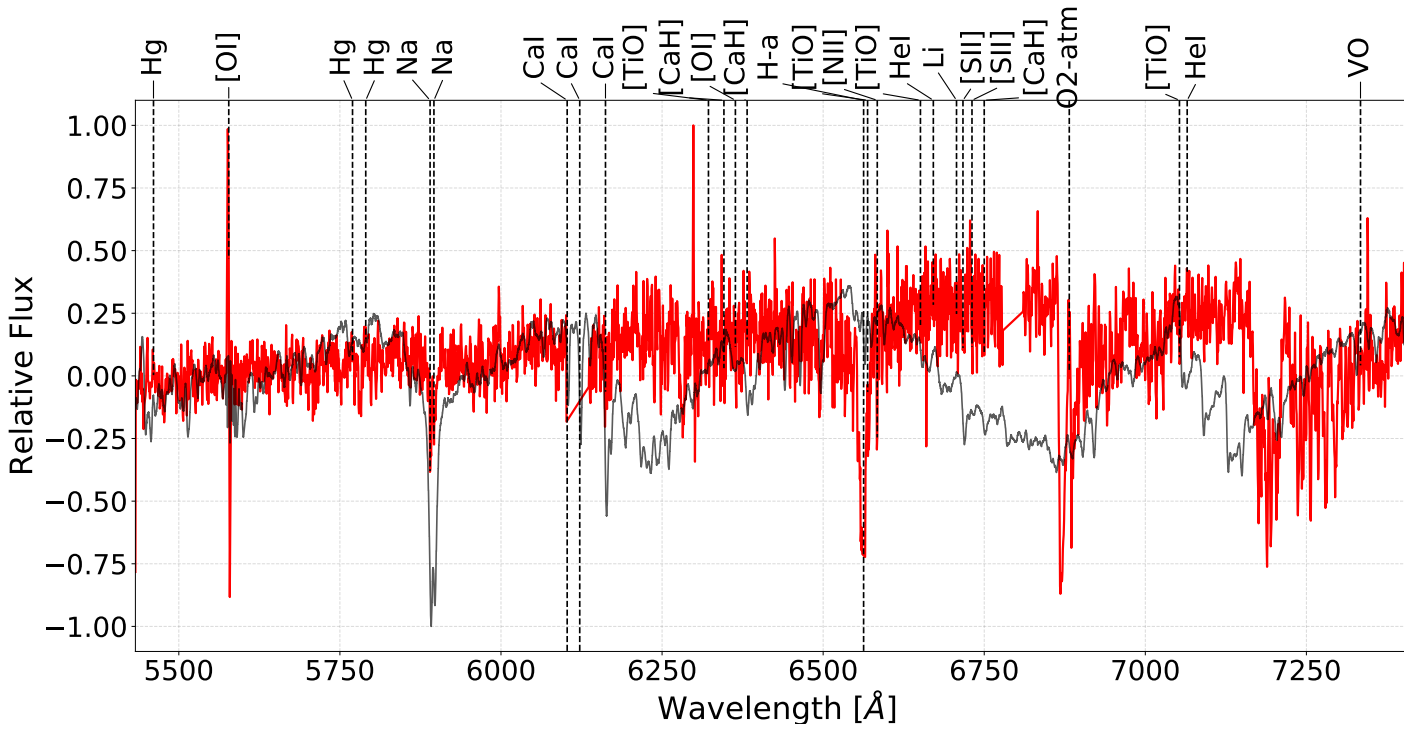

Figure B.22: Slit 6 for the NE field of RCW 34

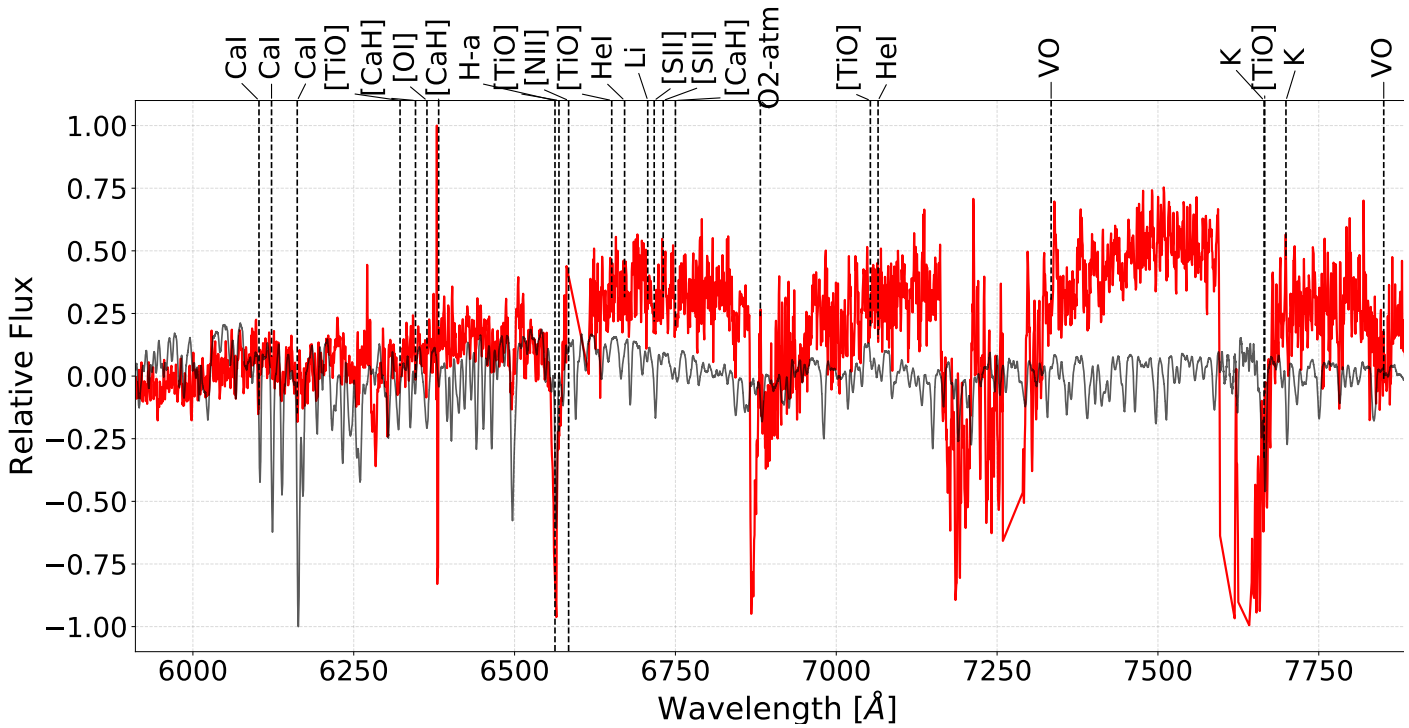

Figure B.23: Slit 7 for the NE field of RCW 34

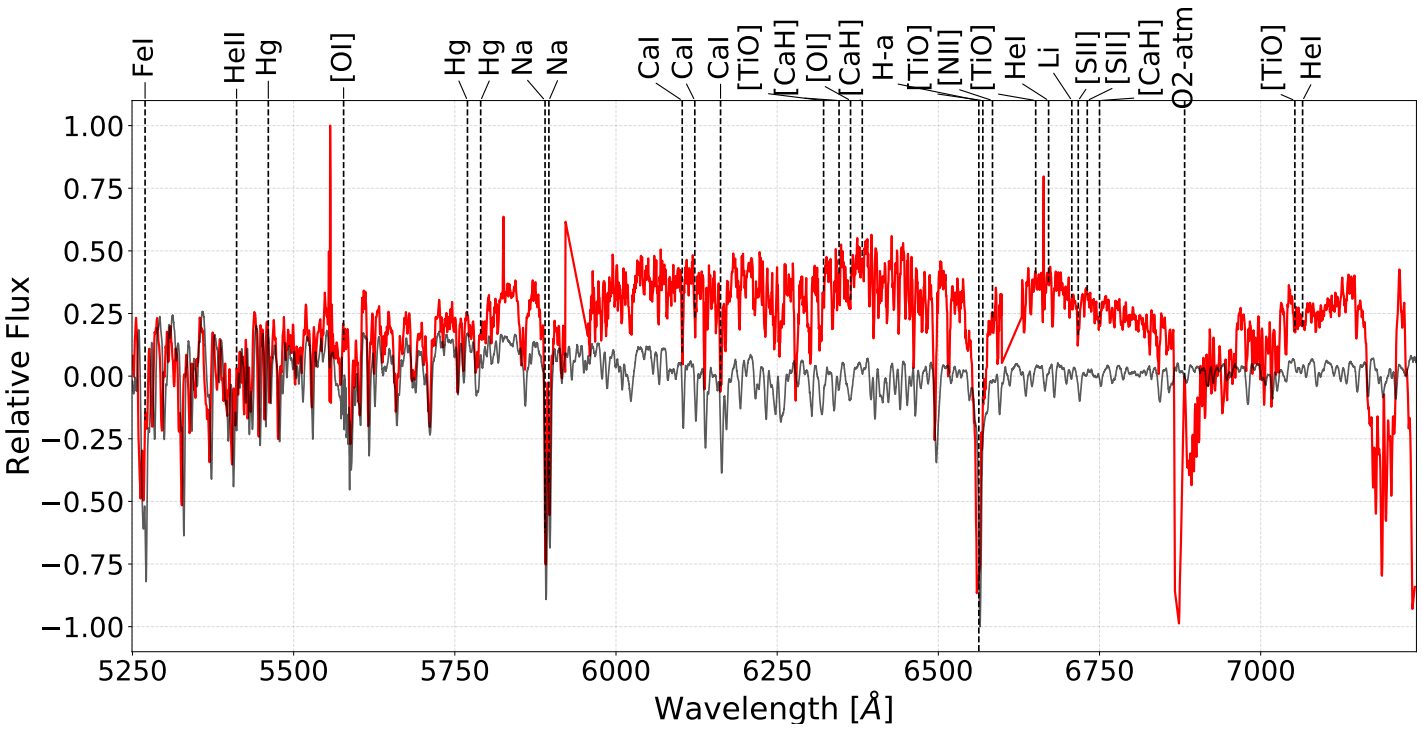

Figure B.24: Slit 8 for the NE field of RCW 34

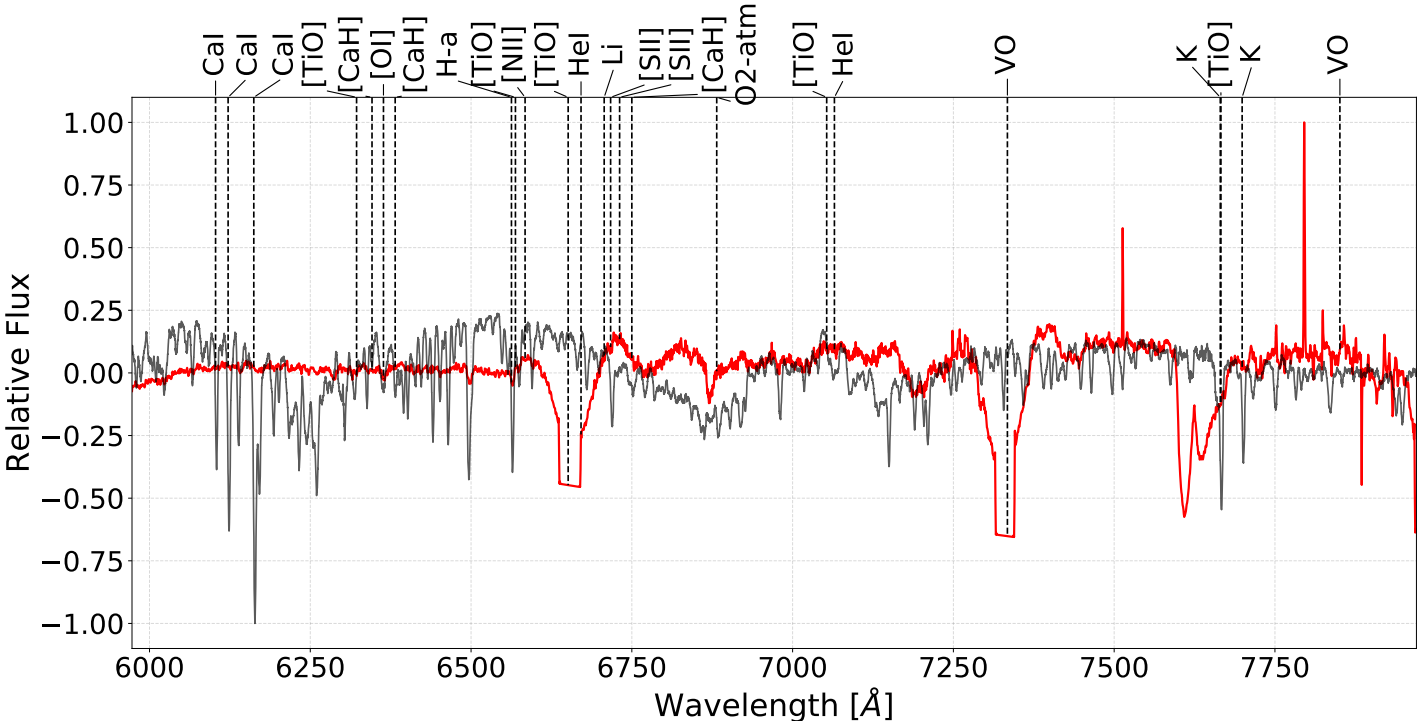

Figure B.25: Slit 9 for the NE field of RCW 34

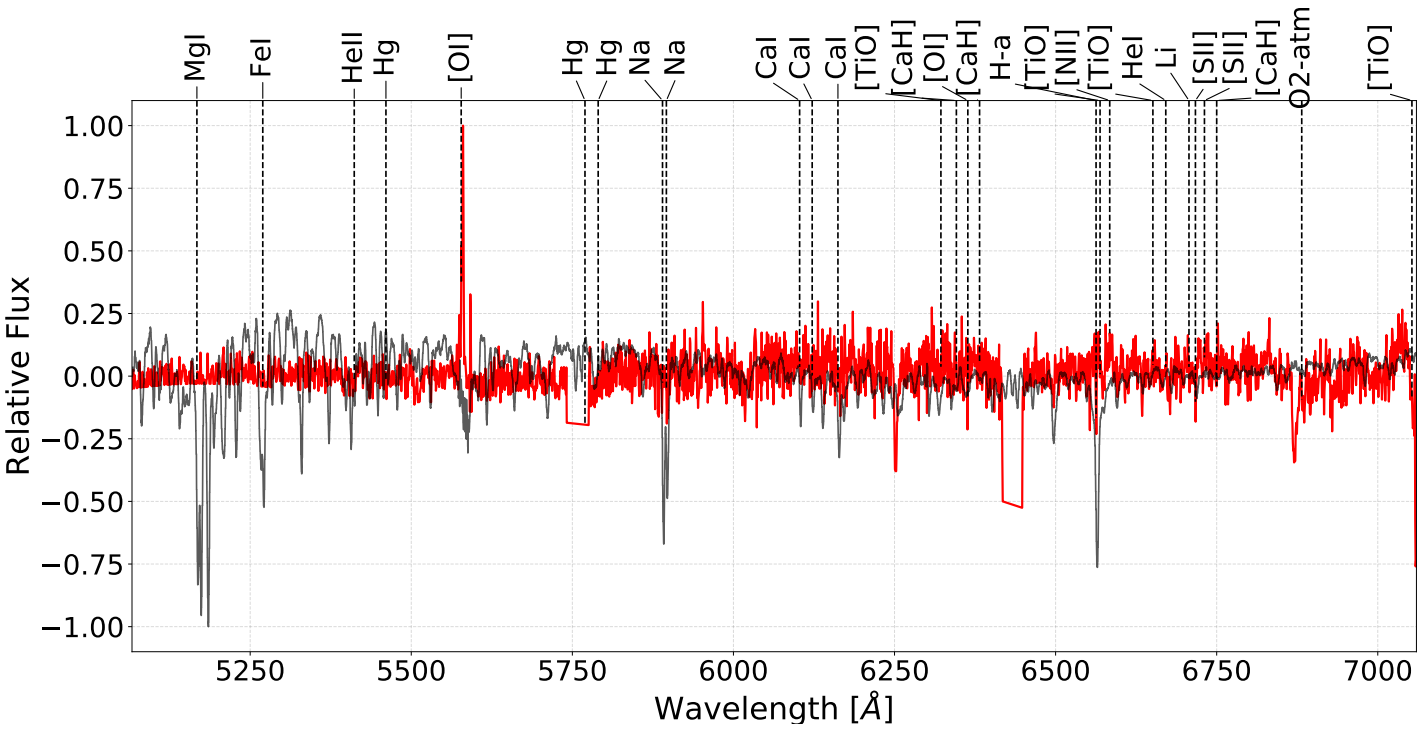

Figure B.26: Slit 10 for the NE field of RCW 34

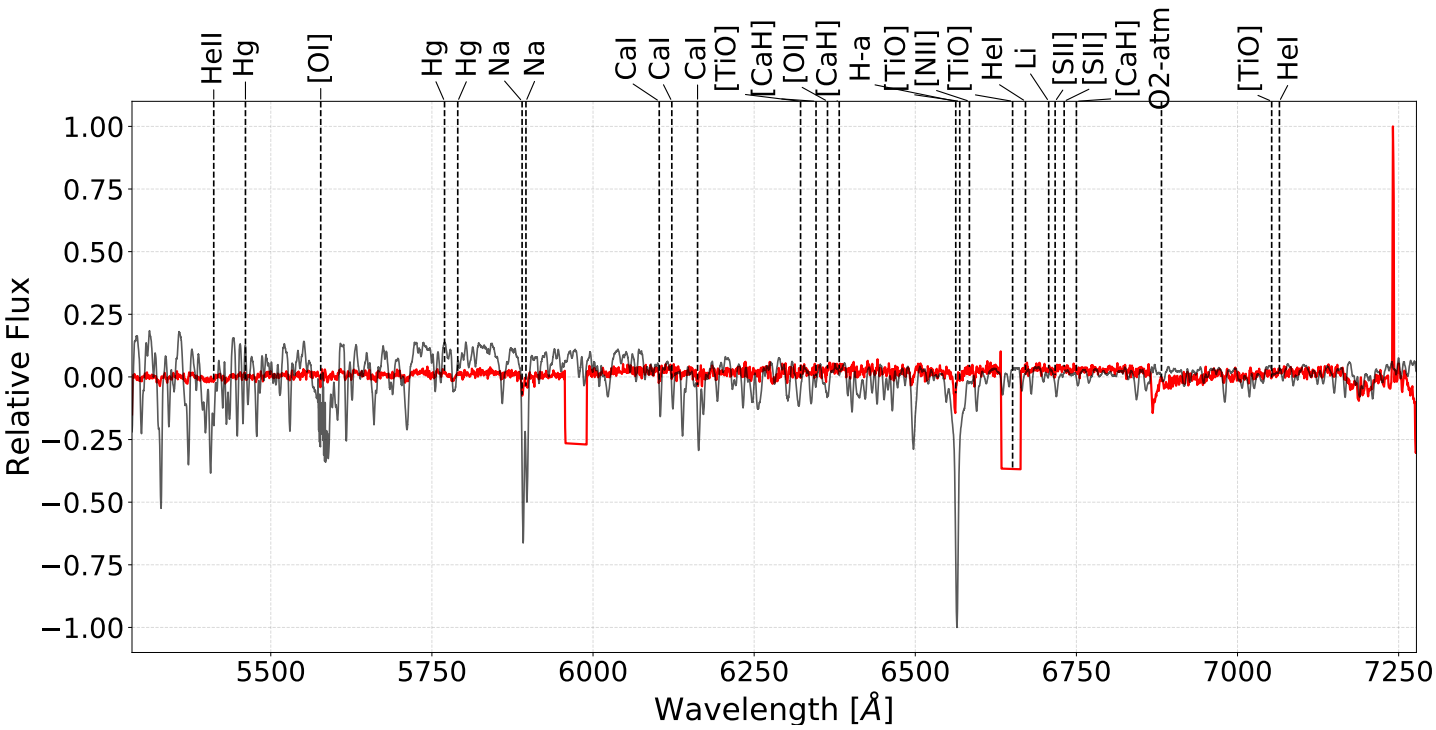

Figure B.27: Slit 11 for the NE field of RCW 34

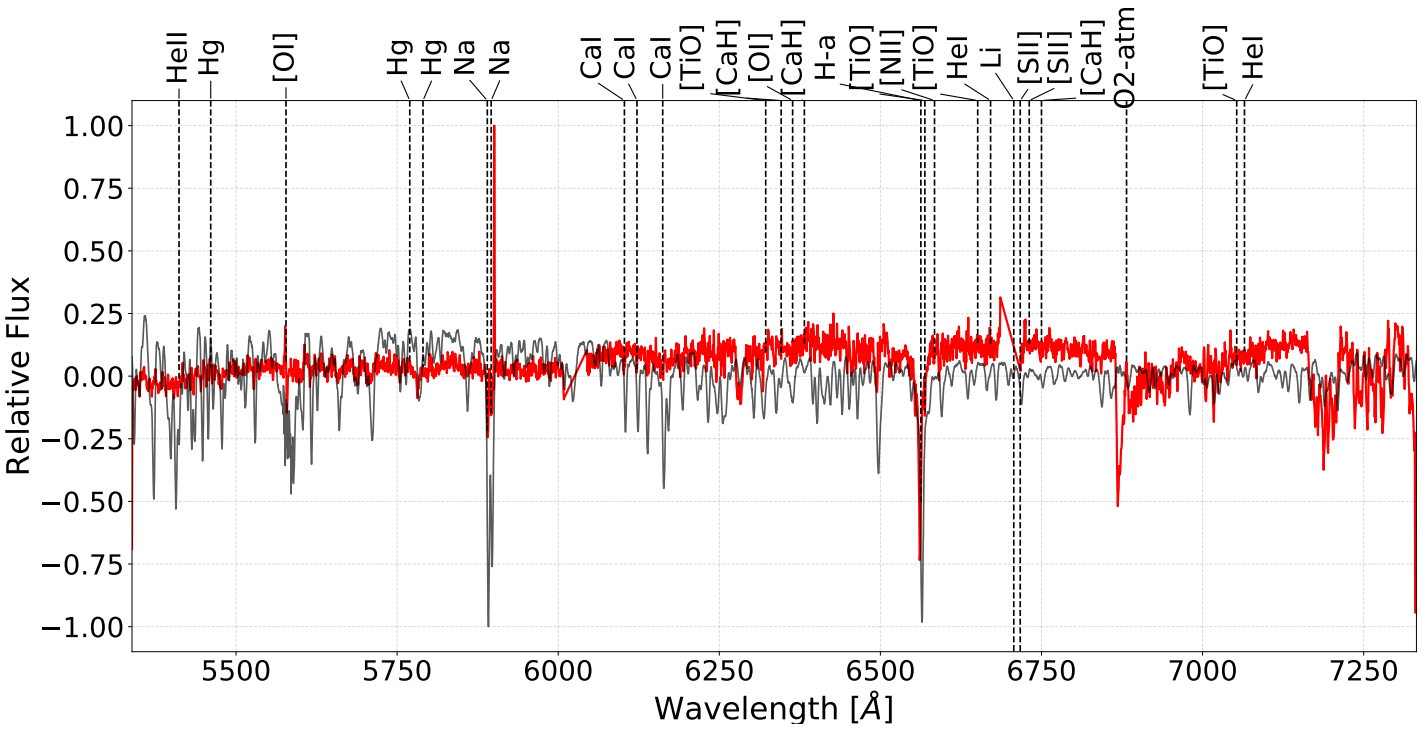

Figure B.28: Slit 12 for the NE field of RCW 34

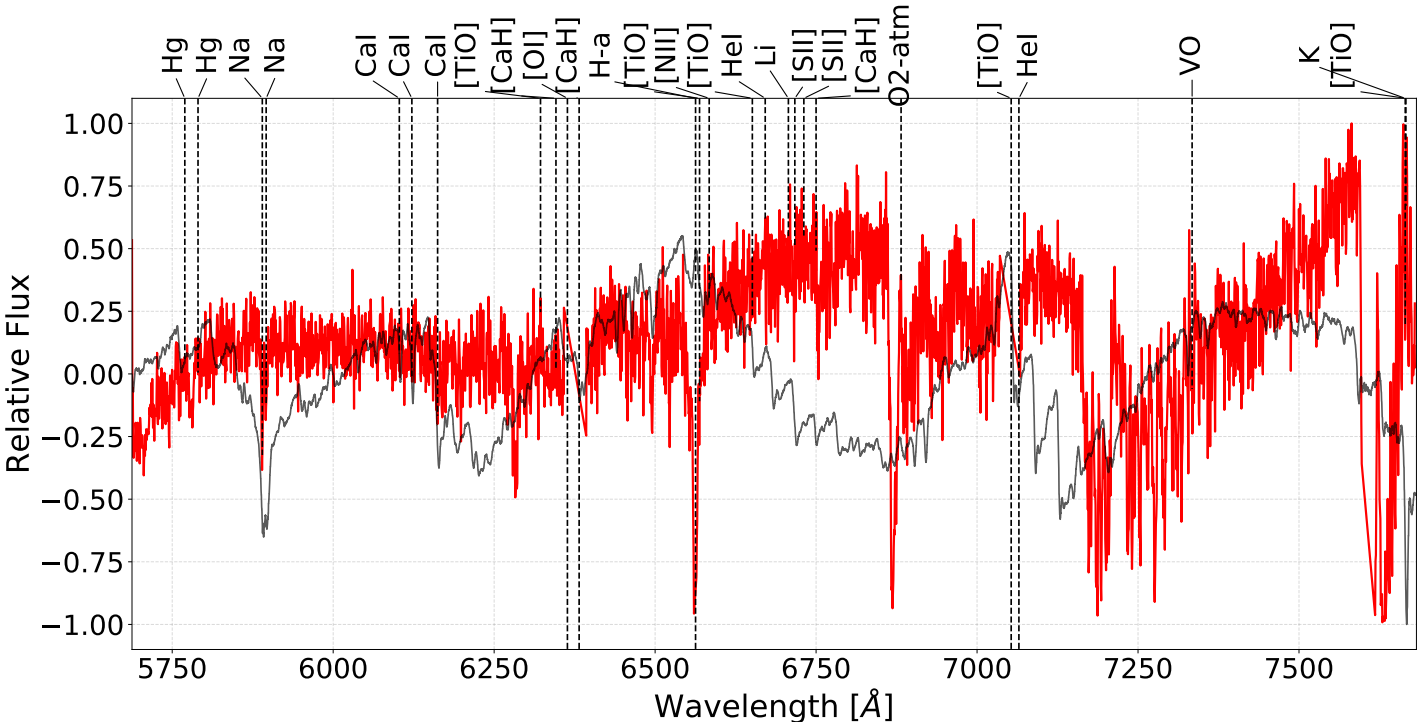

Figure B.29: Slit 13 for the NE field of RCW 34

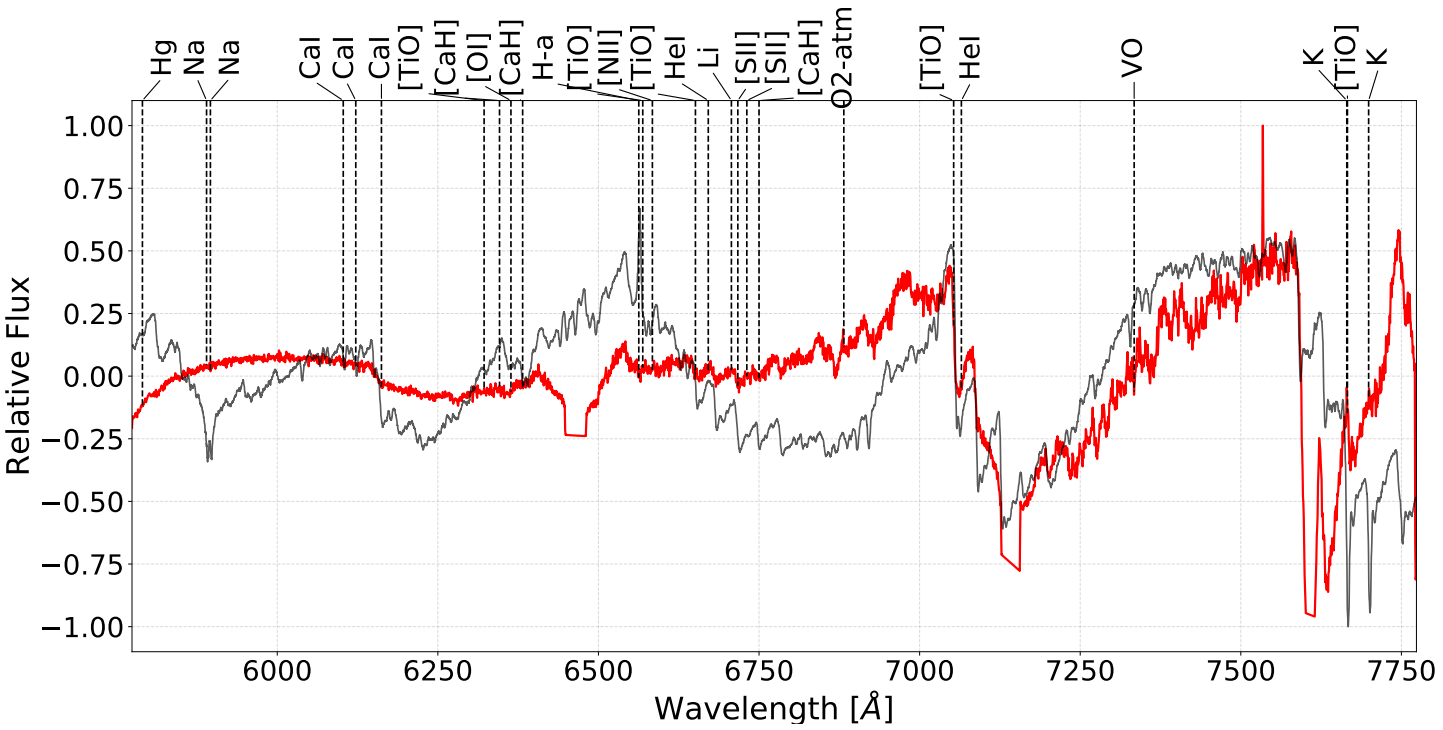

Figure B.30: Slit 14 for the NE field of RCW 34

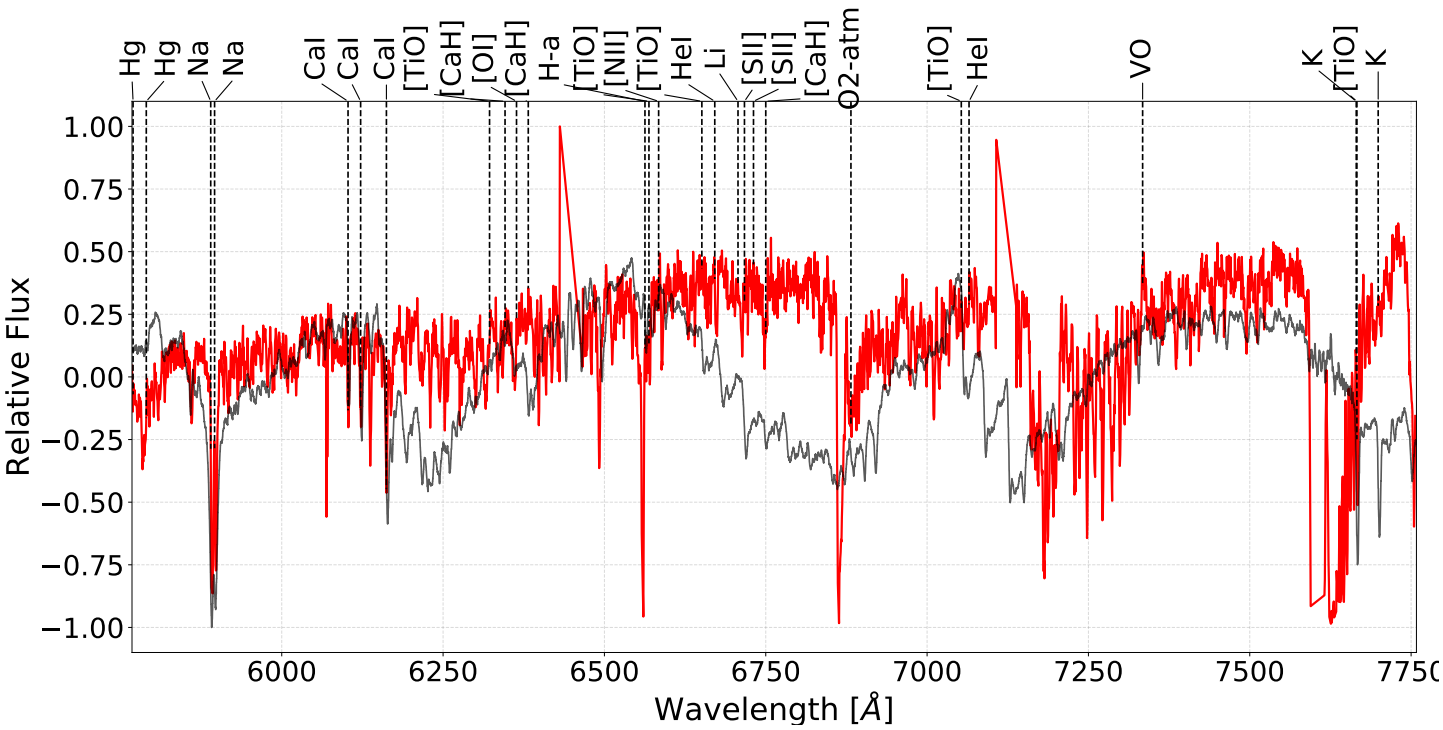

Figure B.31: Slit 15 for the NE field of RCW 34

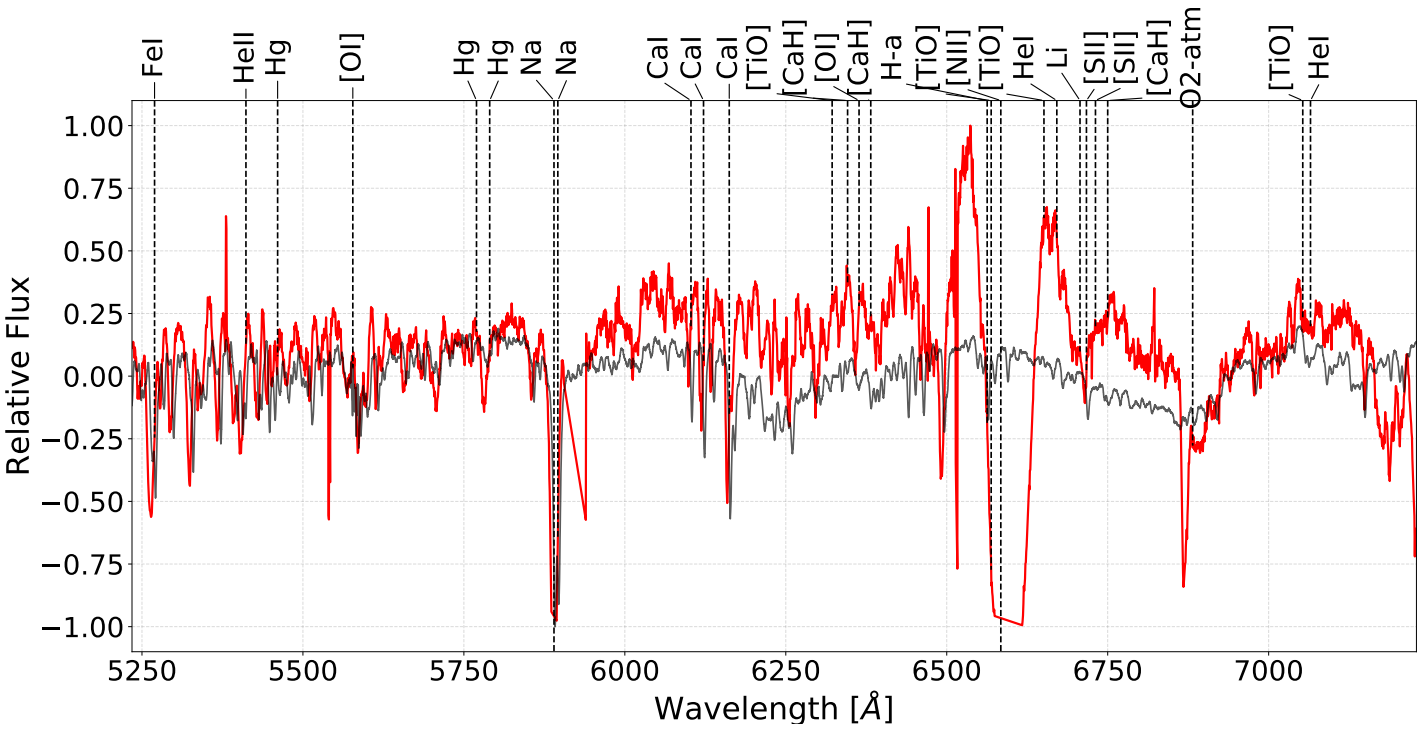

Figure B.32: Slit 16 for the NE field of RCW 34

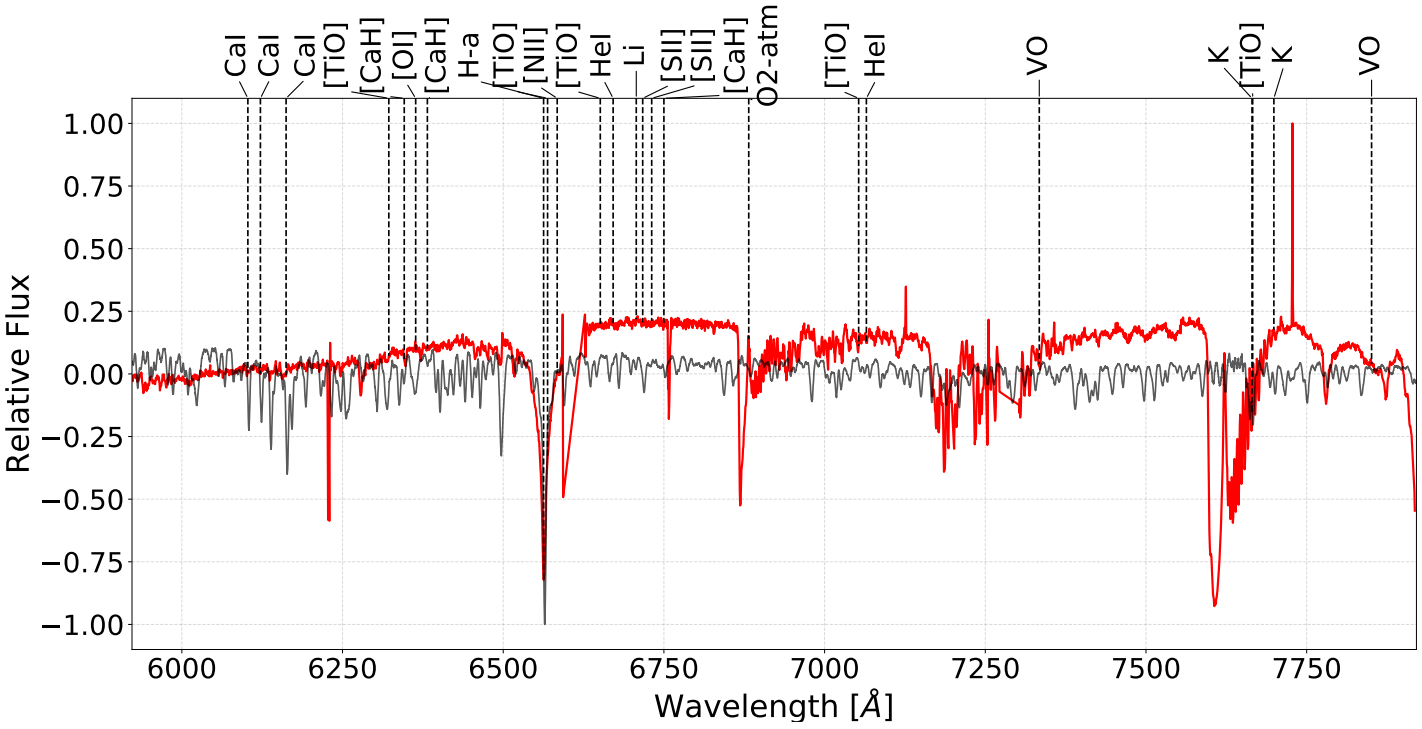

Figure B.33: Slit 17 for the NE field of RCW 34

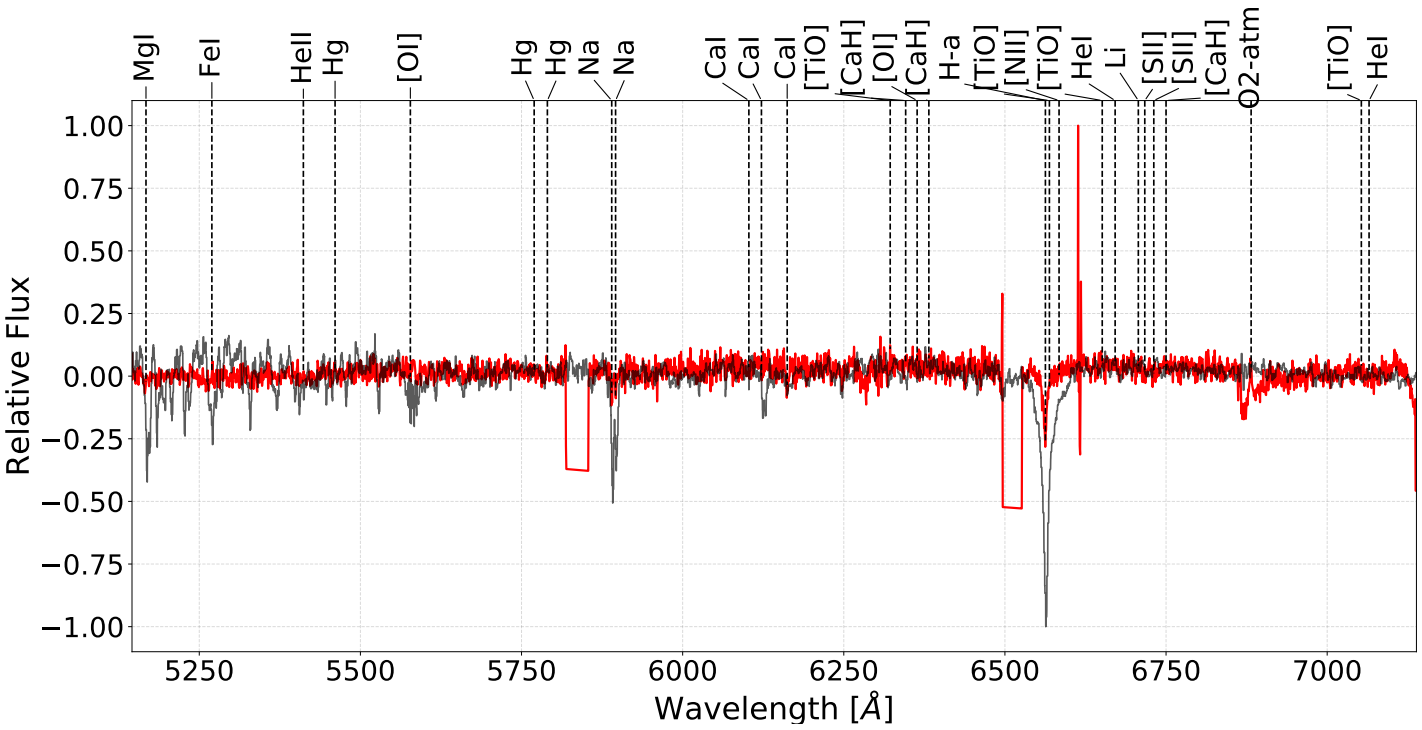

Figure B.34: Slit 18 for the NE field of RCW 34

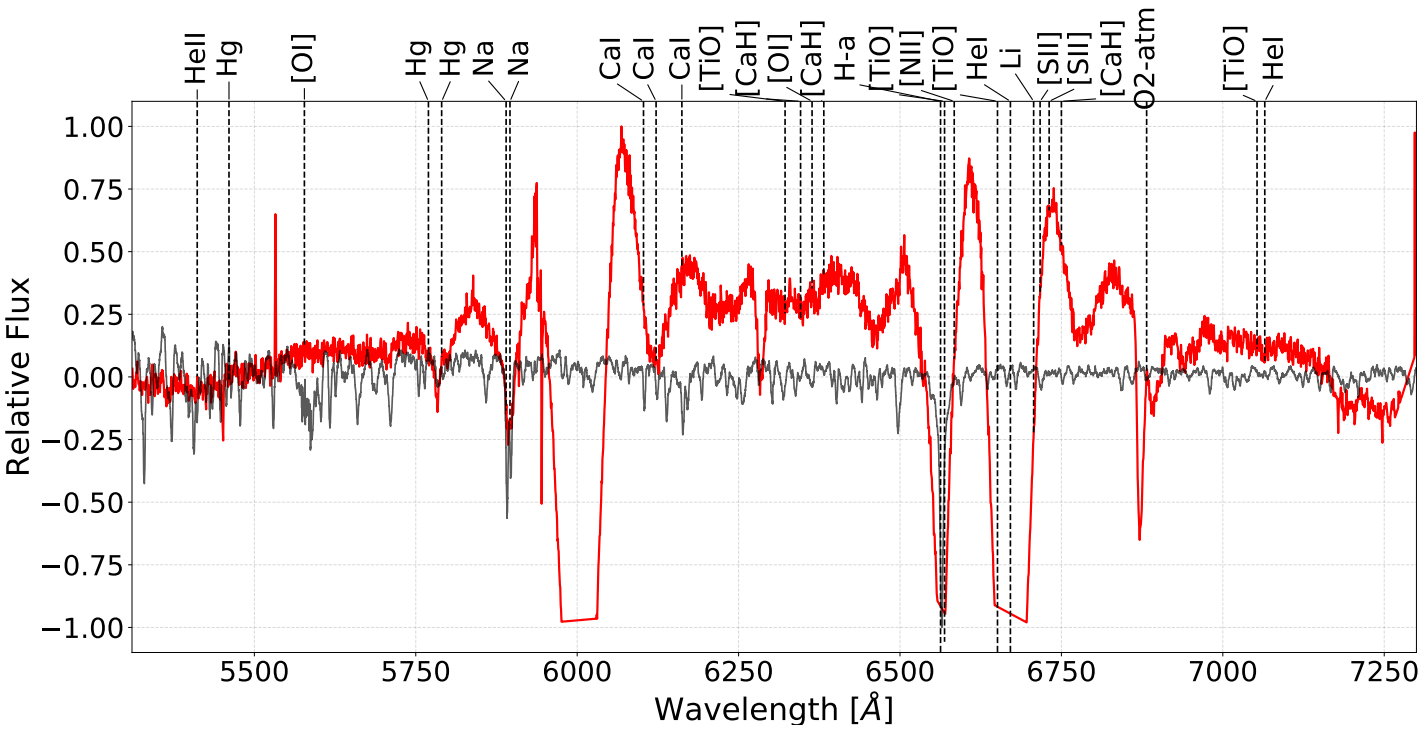

Figure B.35: Slit 3 for the NW field of RCW 34

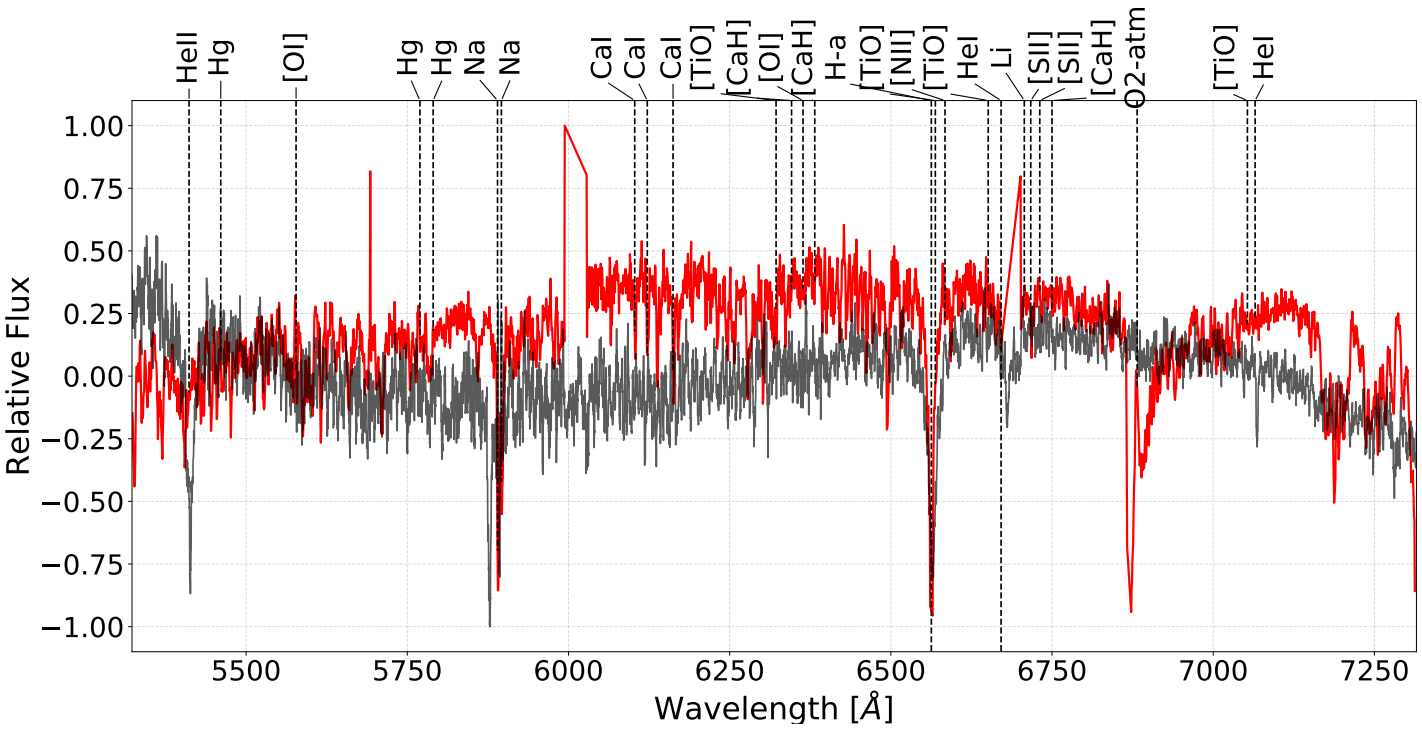

Figure B.36: Slit 4 for the NW field of RCW 34

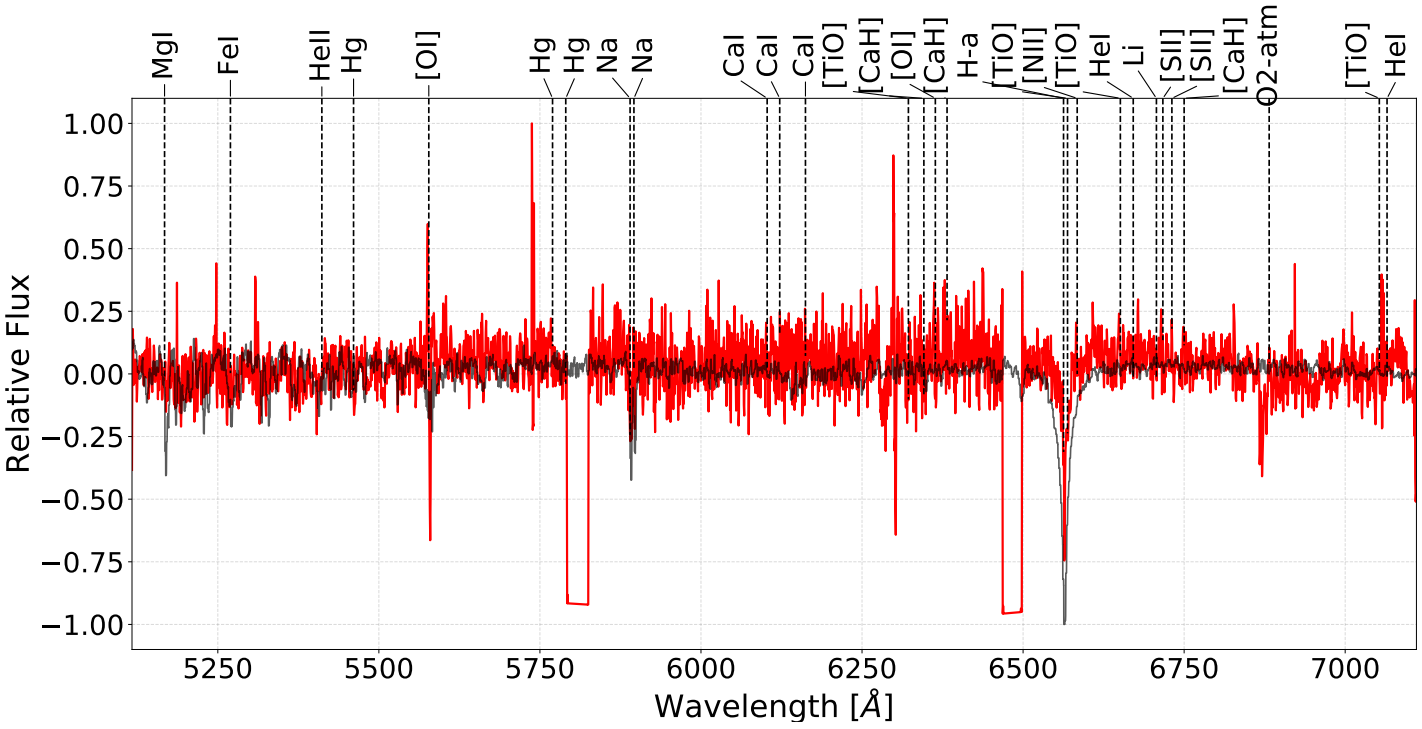

Figure B.37: Slit 7 for the NW field of RCW 34

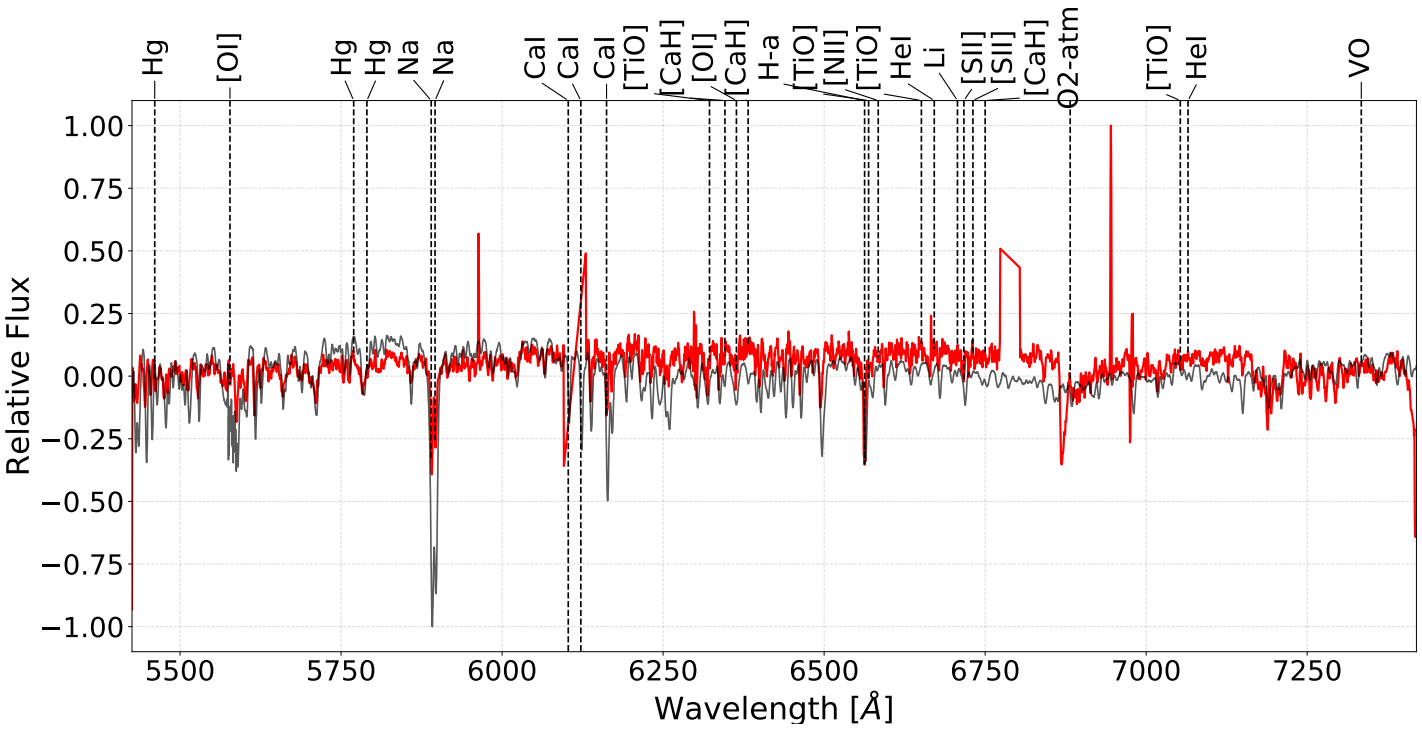

Figure B.38: Slit 8 for the NW field of RCW 34

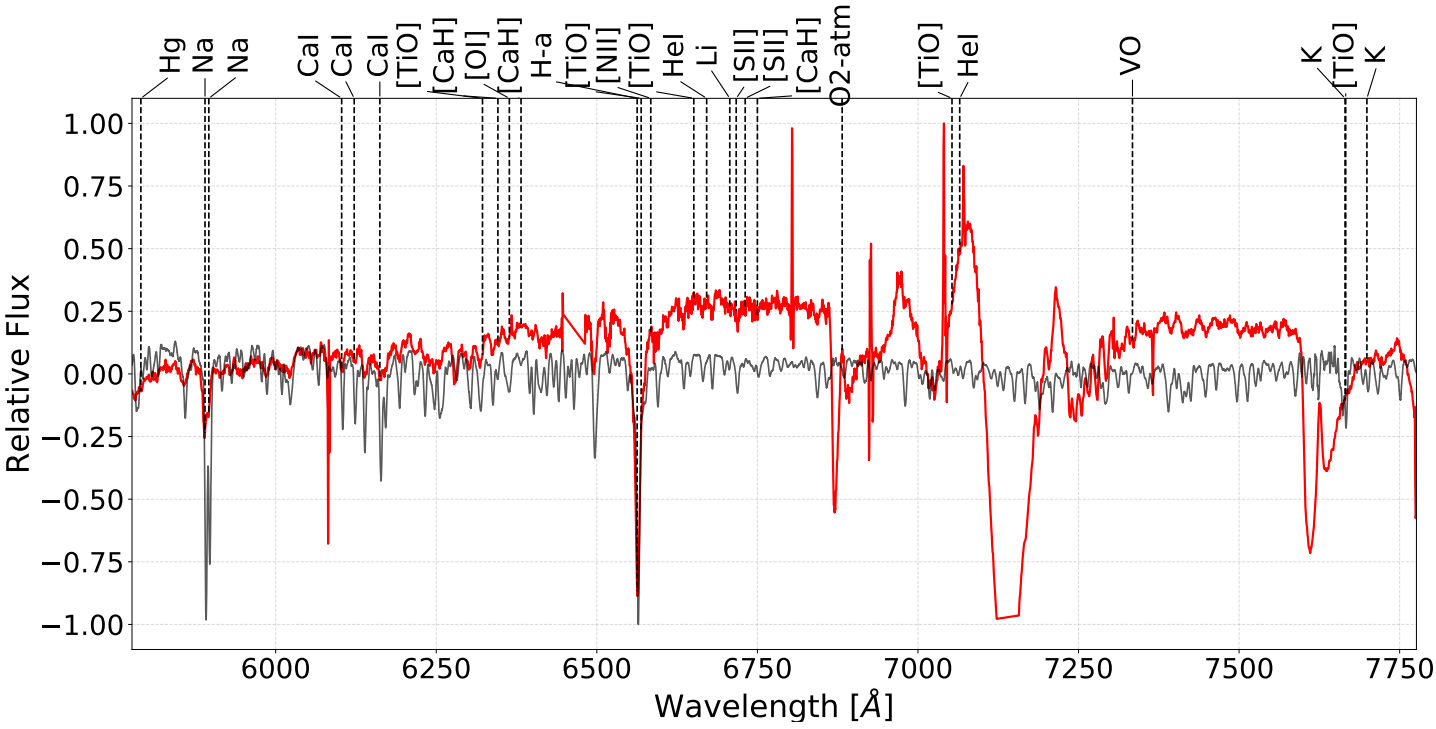

Figure B.39: Slit 9 for the NW field of RCW 34

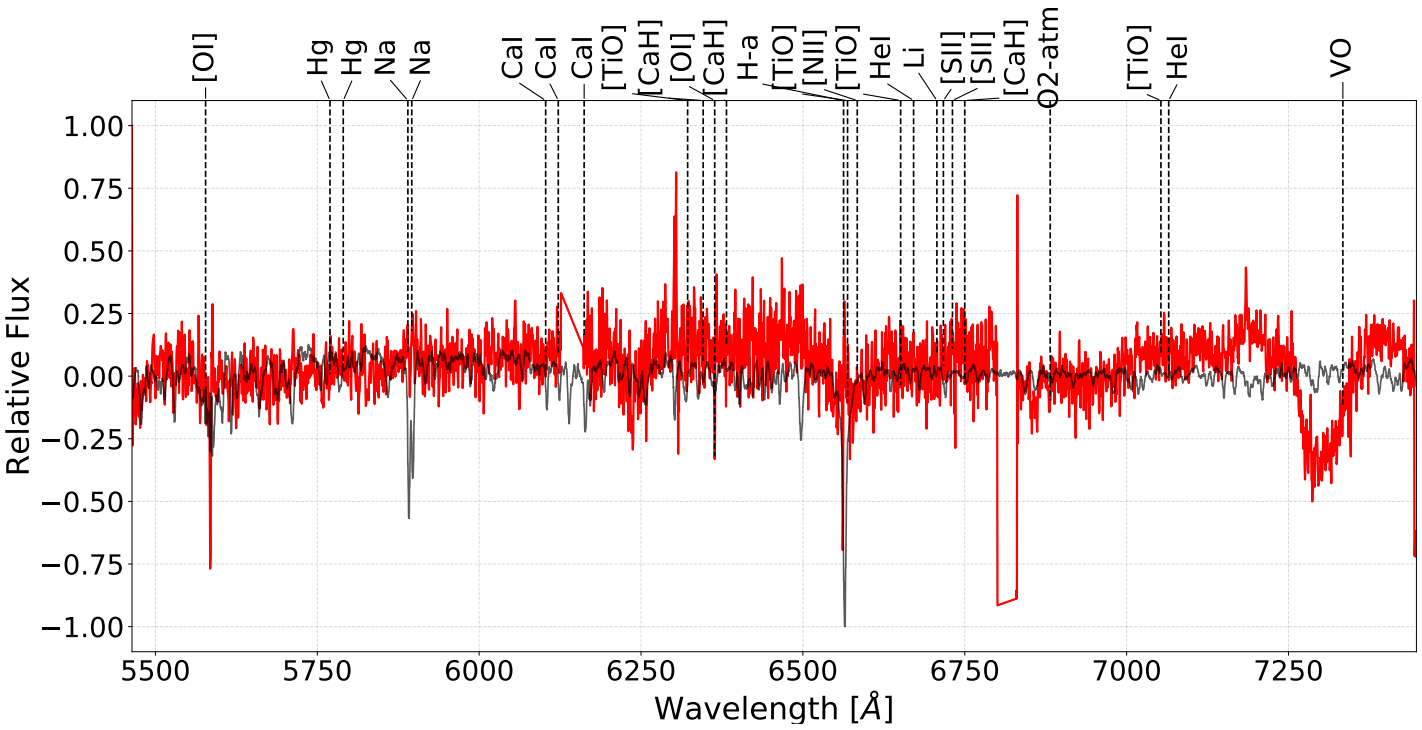

Figure B.40: Slit 10 for the NW field of RCW 34

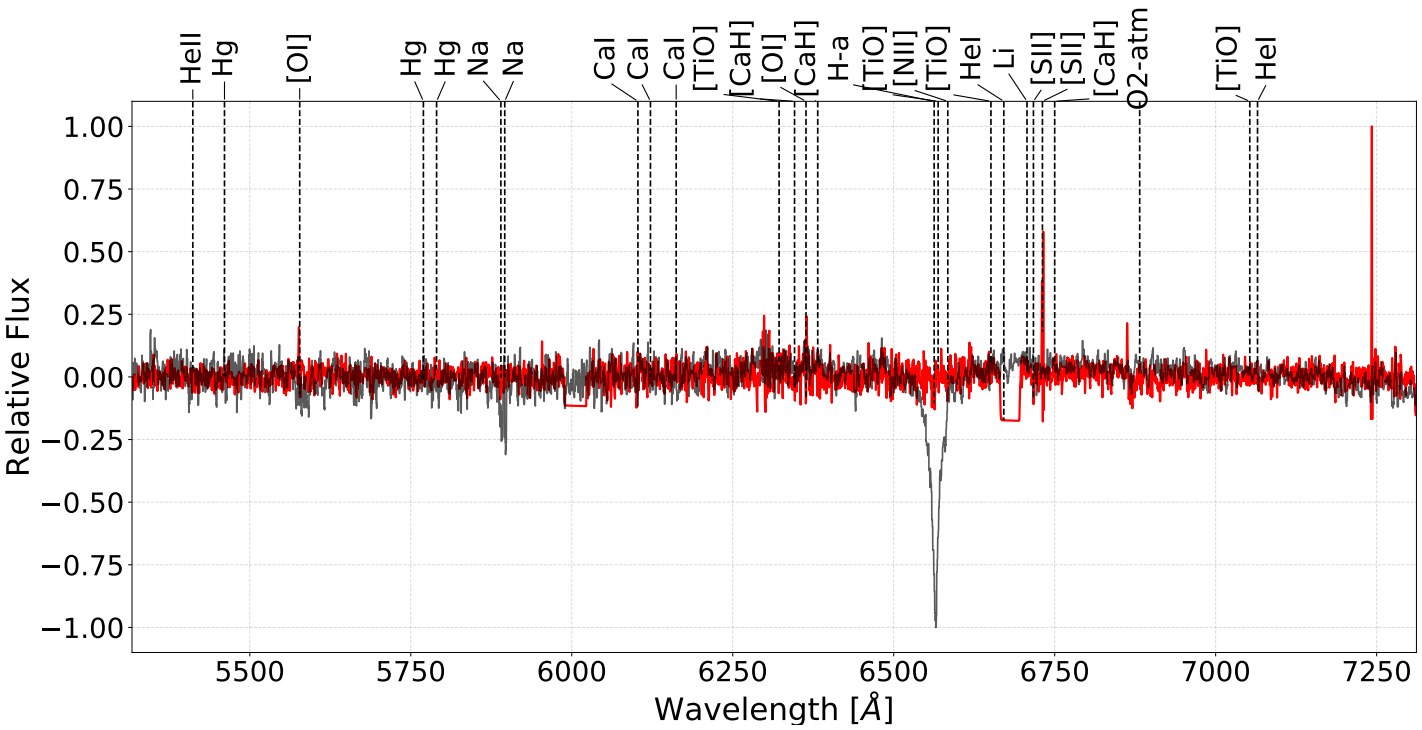

Figure B.41: Slit 13 for the NW field of RCW 34

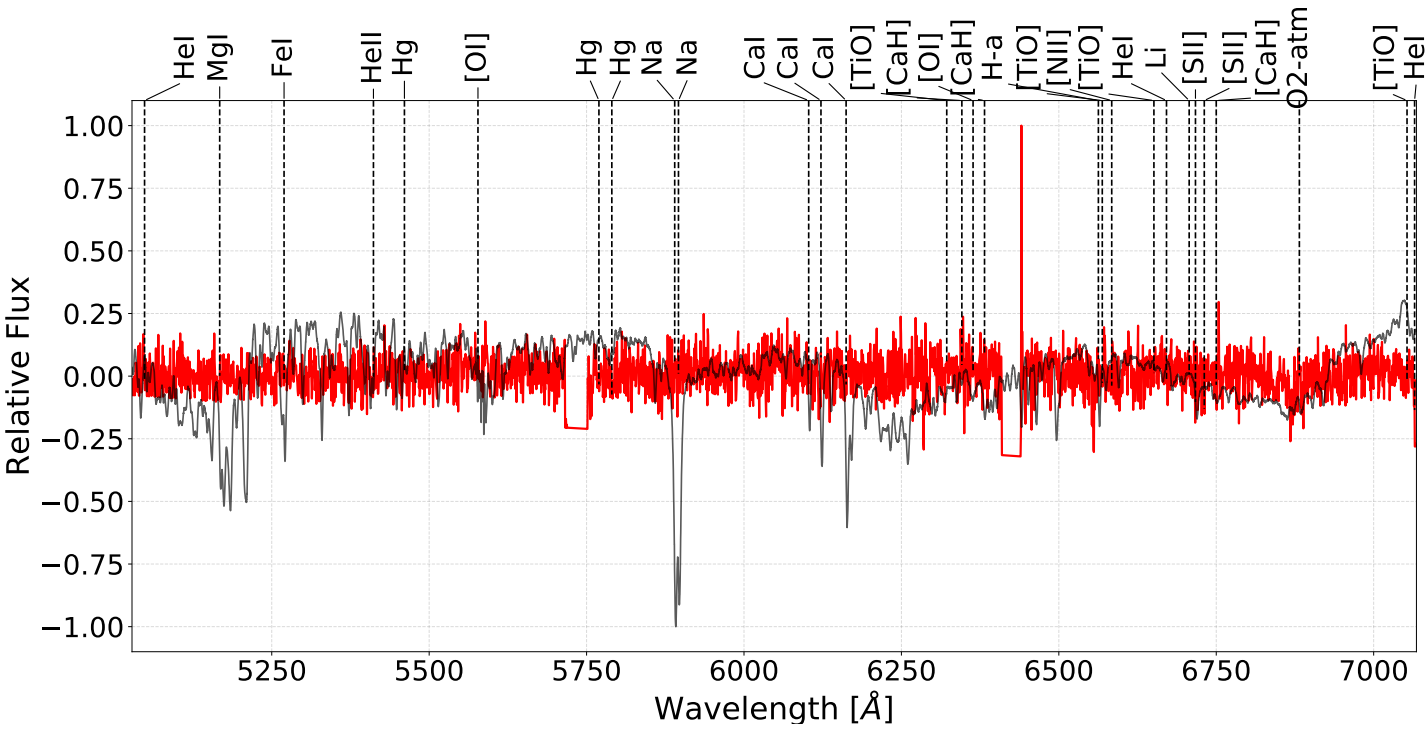

Figure B.42: Slit 15 for the NW field of RCW 34

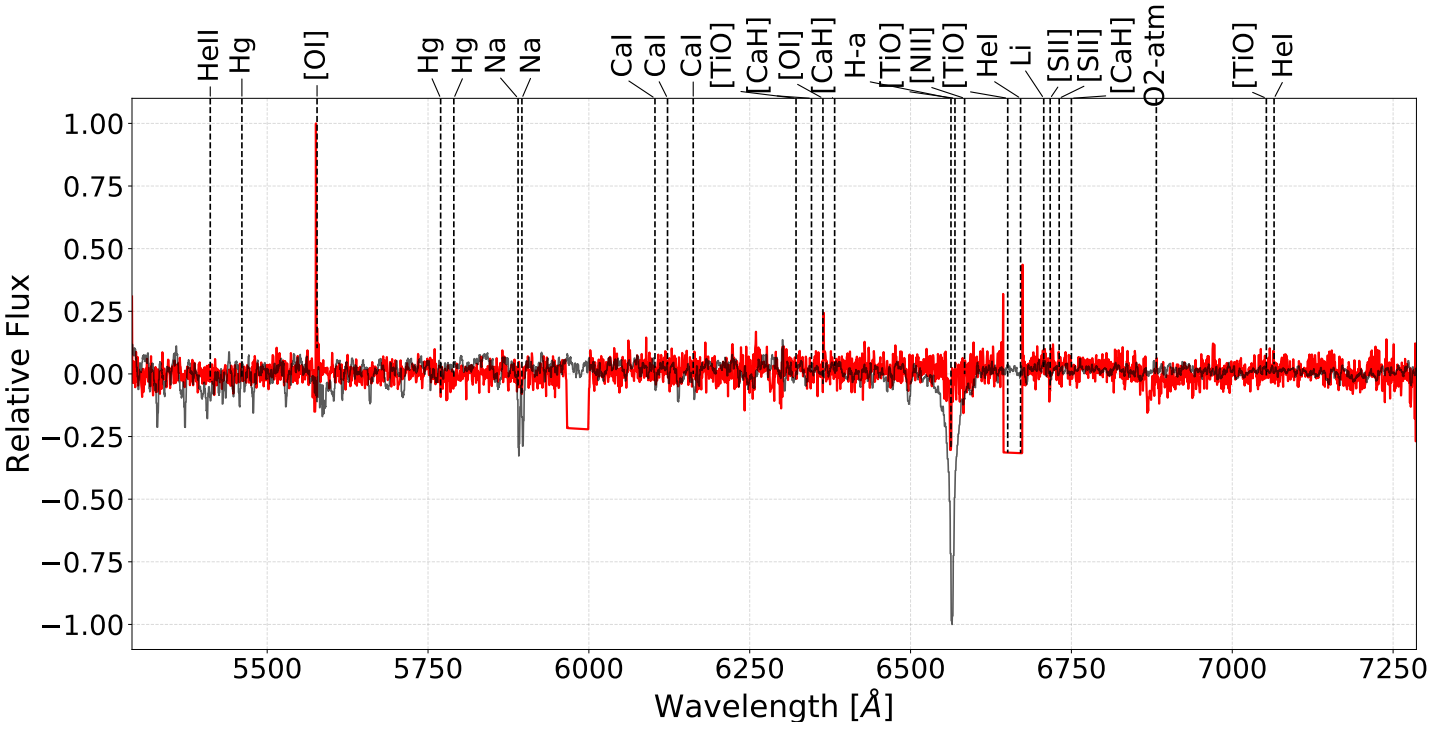

Figure B.43: Slit 16 for the NW field of RCW 34

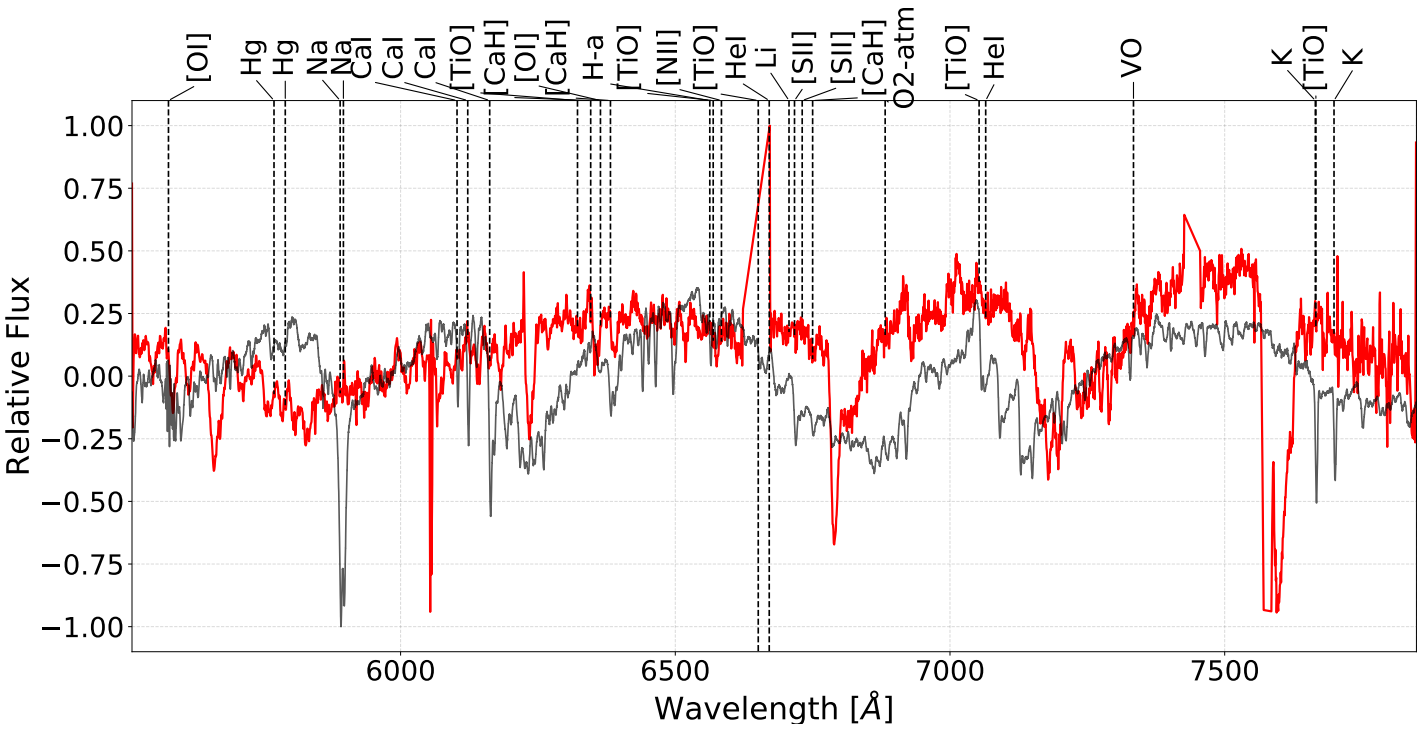

Figure B.44: Slit 17 for the NW field of RCW 34

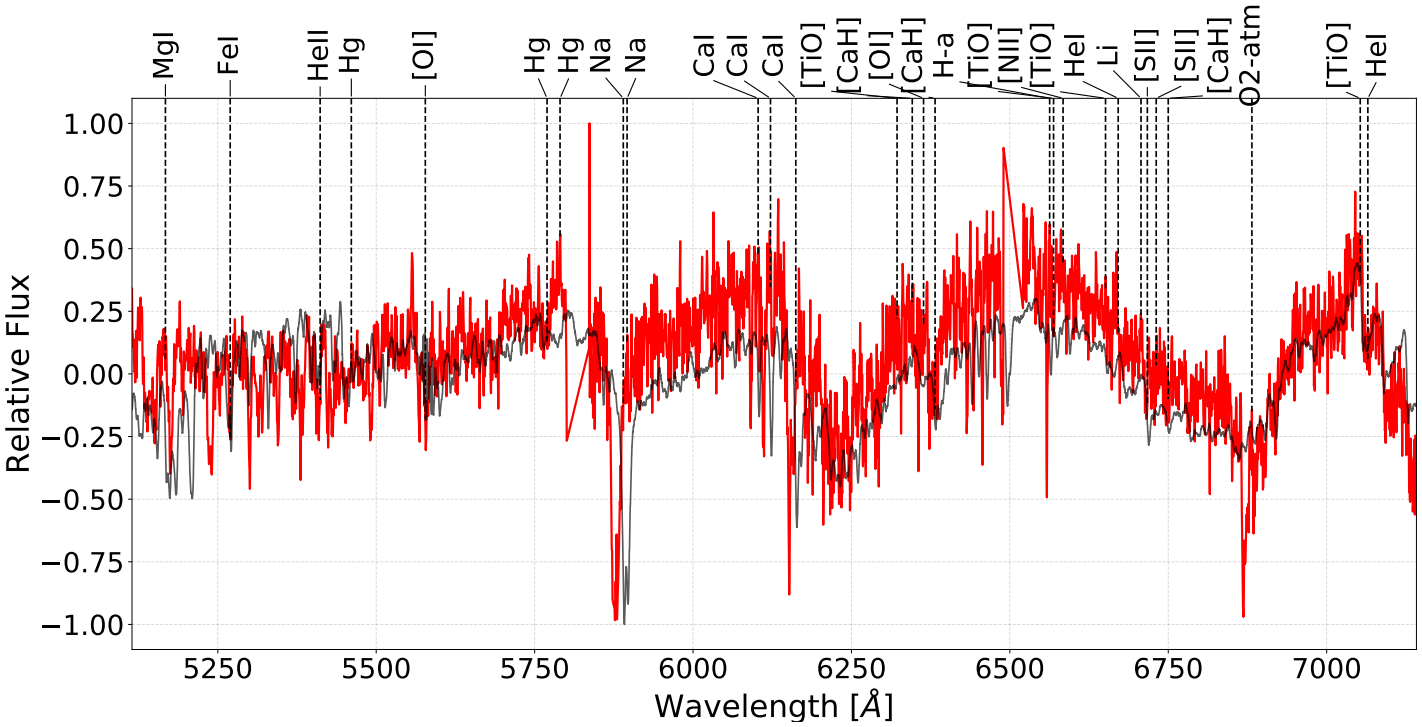

Figure B.45: Slit 18 for the NW field of RCW 34

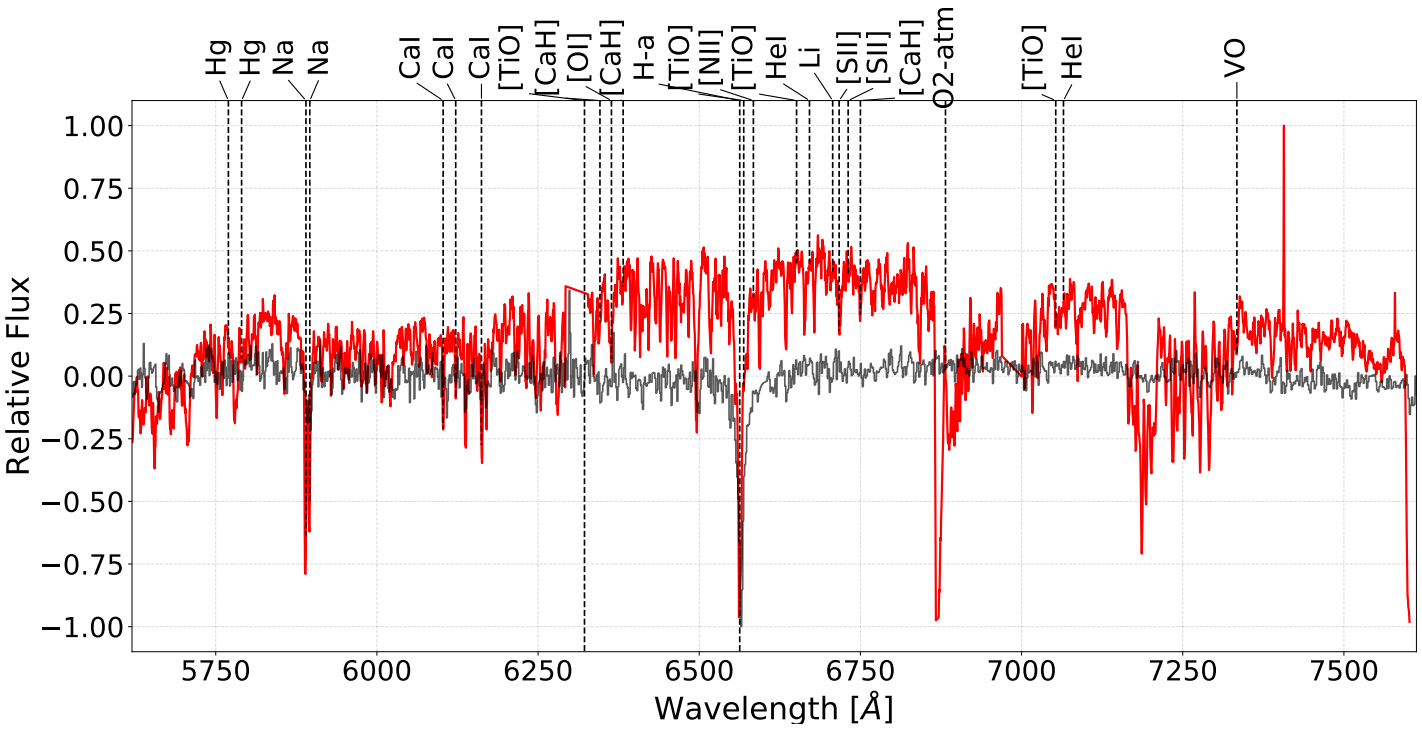

Figure B.46: Slit 2 for the SE field of RCW 34

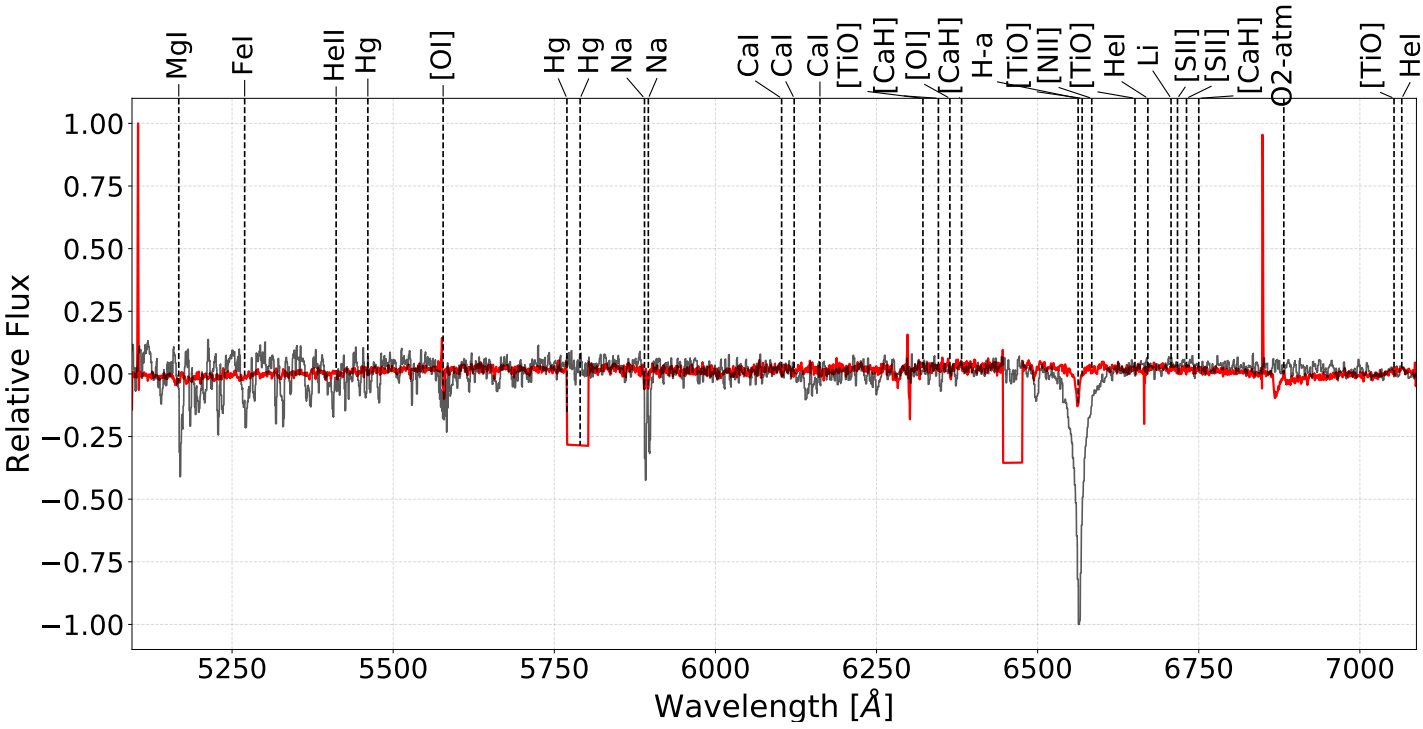

Figure B.47: Slit 5 for the SE field of RCW 34

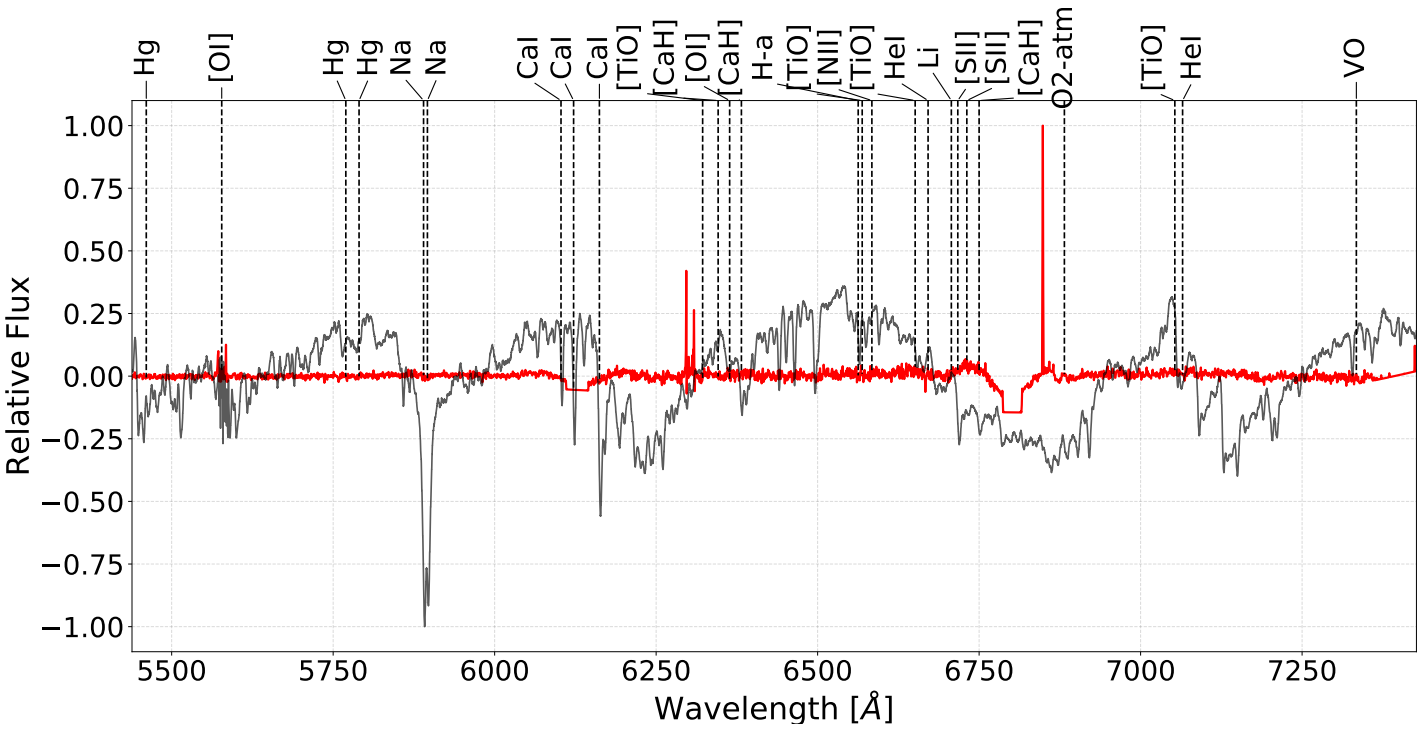

Figure B.48: Slit 6 for the SE field of RCW 34

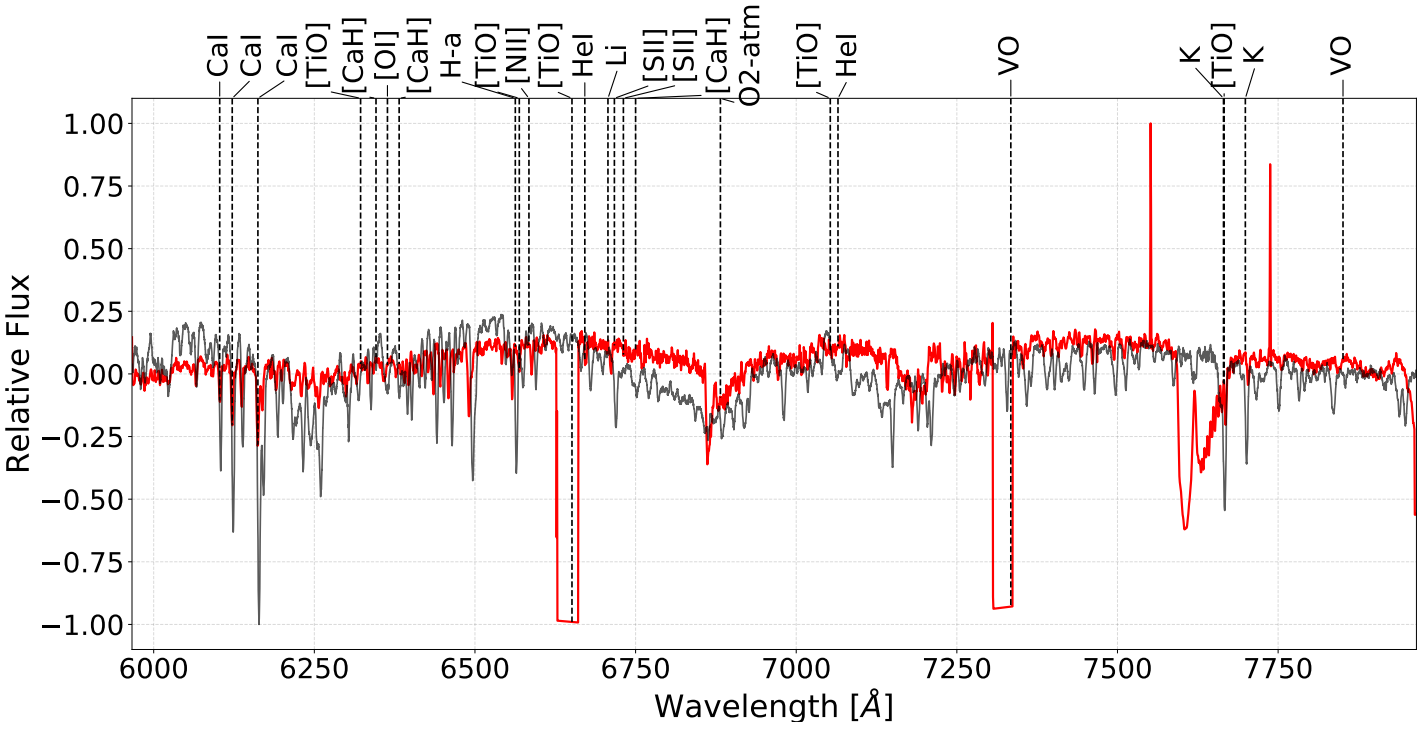

Figure B.49: Slit 8 for the SE field of RCW 34

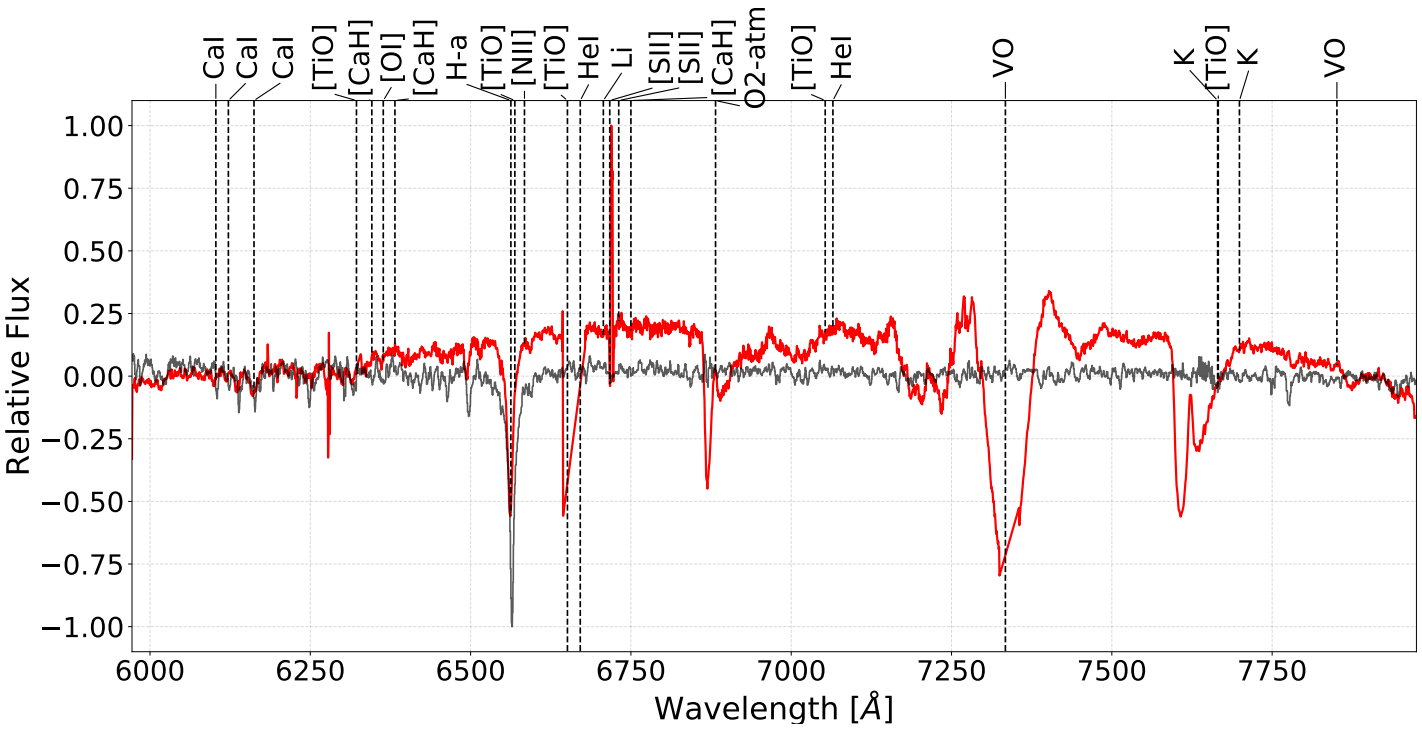

Figure B.50: Slit 9 for the SE field of RCW 34

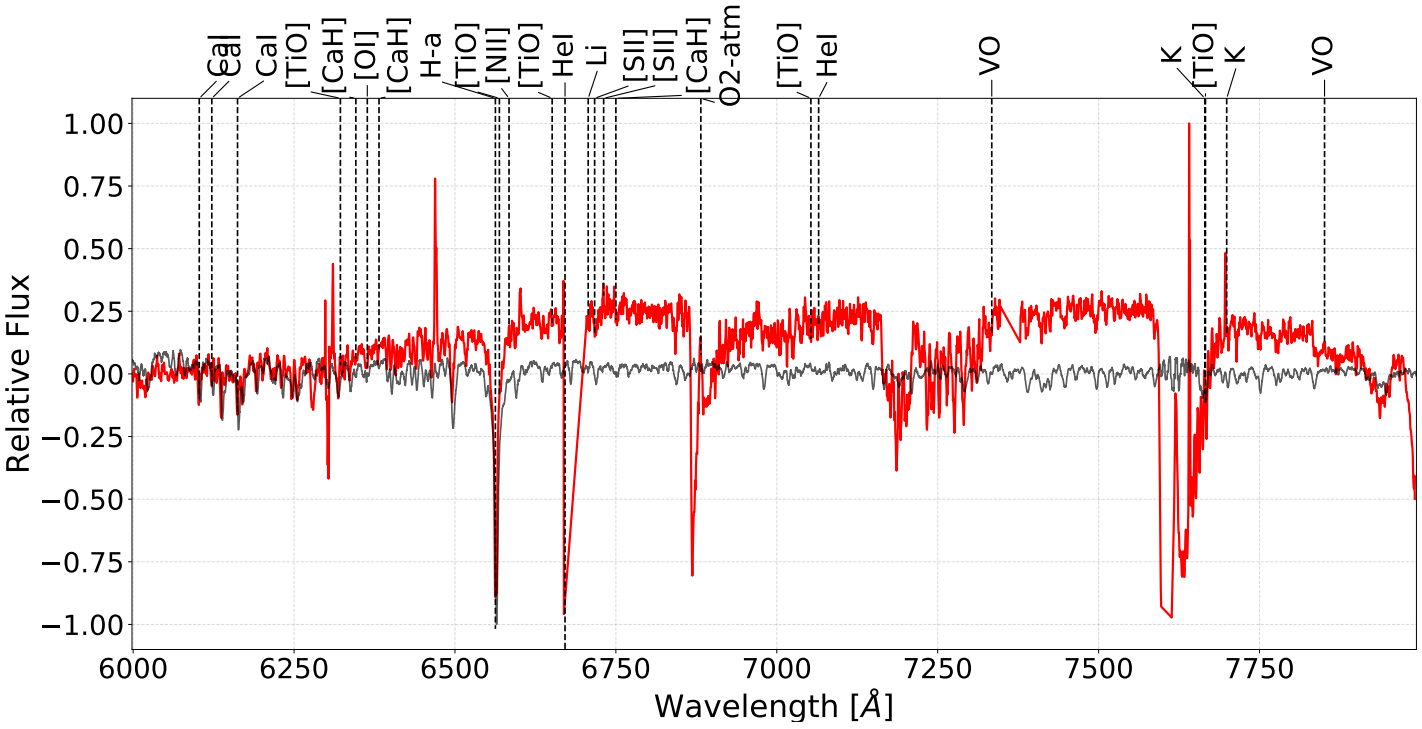

Figure B.51: Slit 11 for the SE field of RCW 34

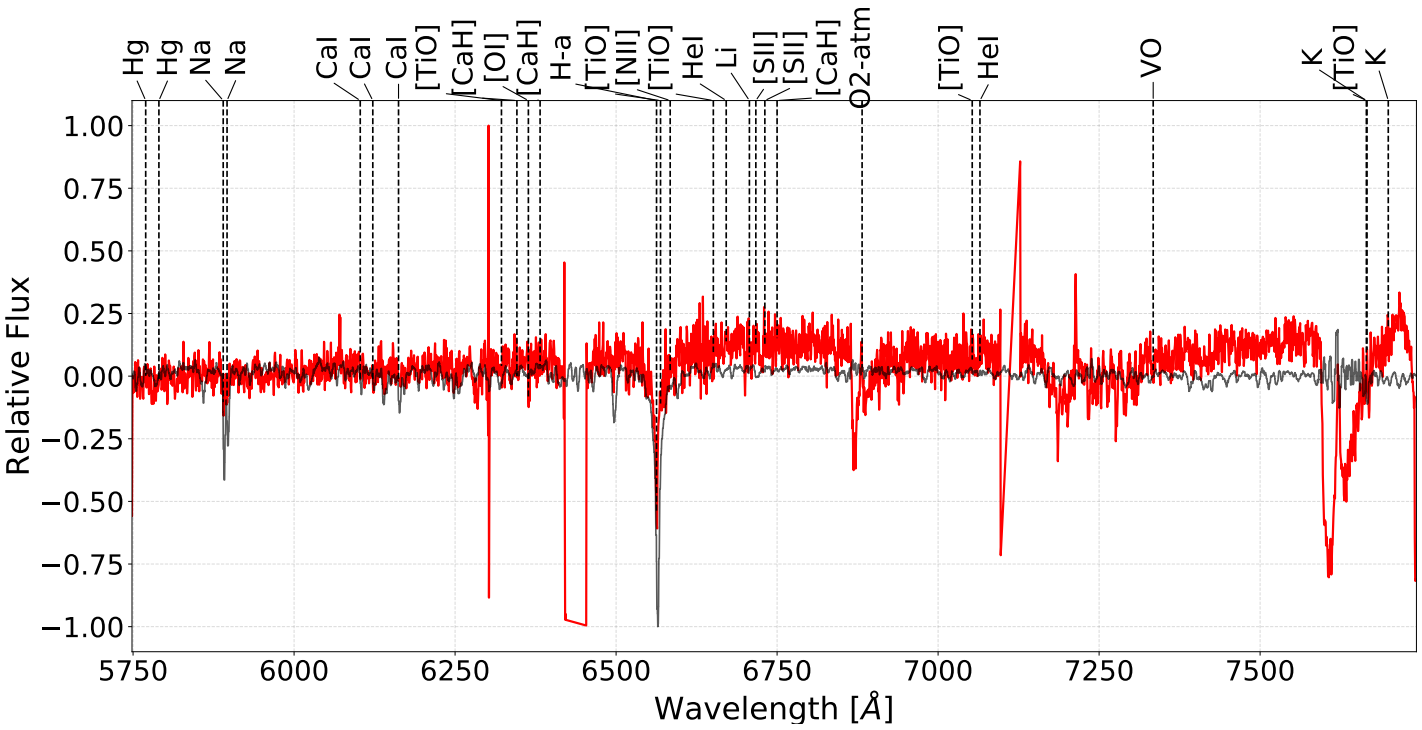

Figure B.52: Slit 14 for the SE field of RCW 34

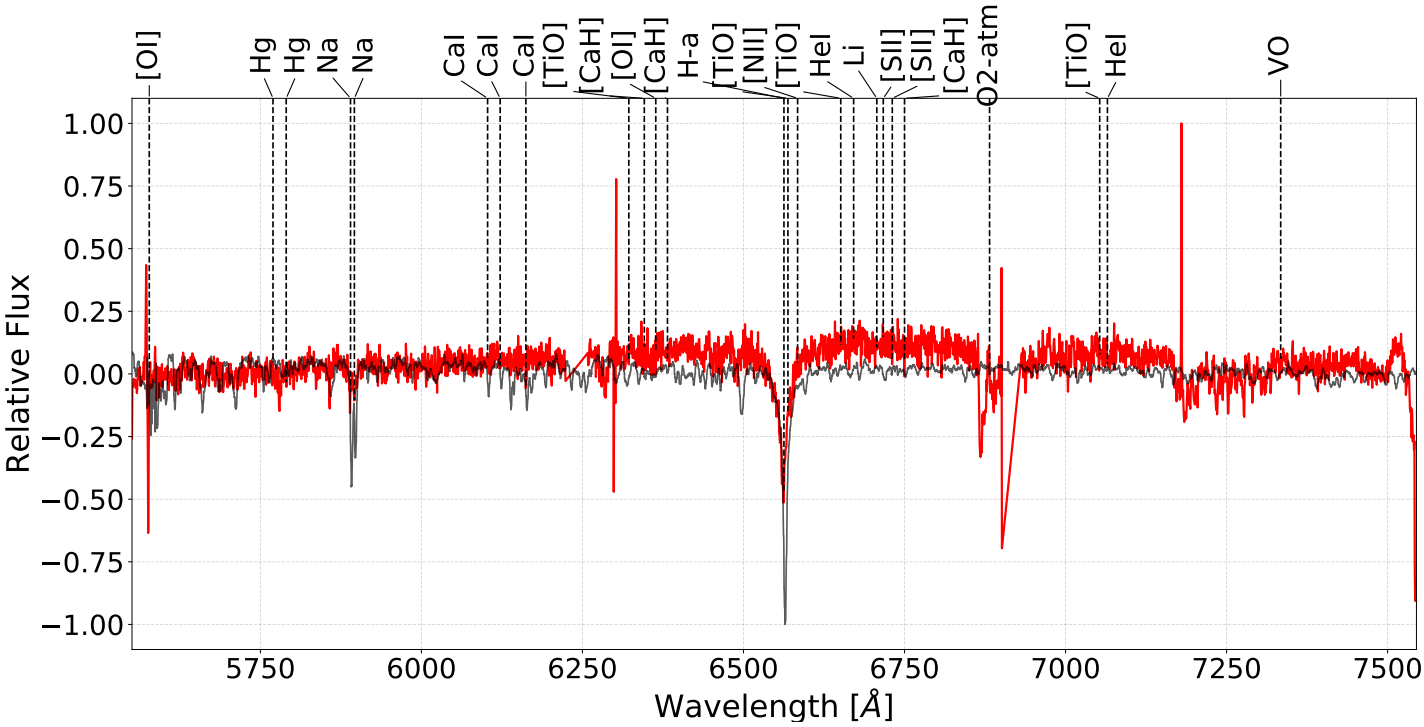

Figure B.53: Slit 15 for the SE field of RCW 34

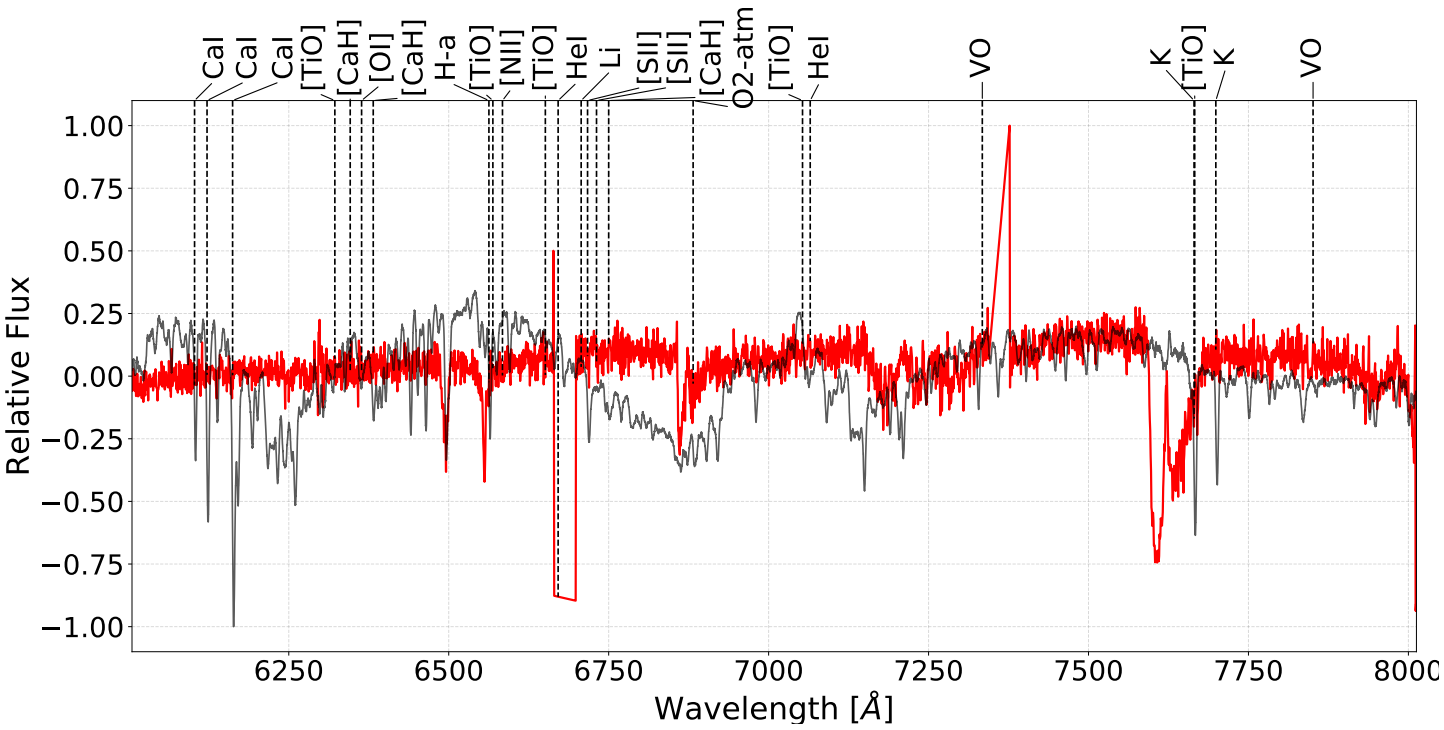

Figure B.54: Slit 18 for the SE field of RCW 34

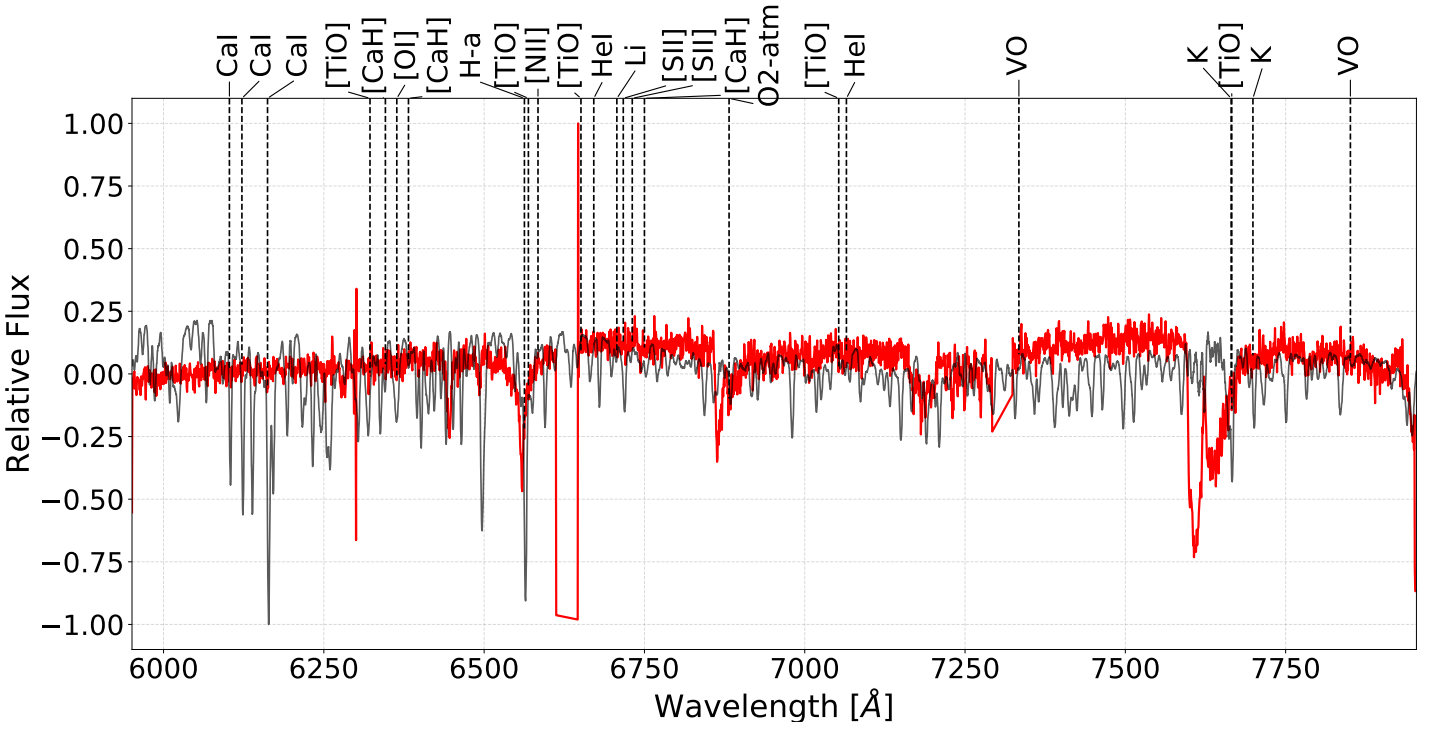

Figure B.55: Slit 19 for the SE field of RCW 34

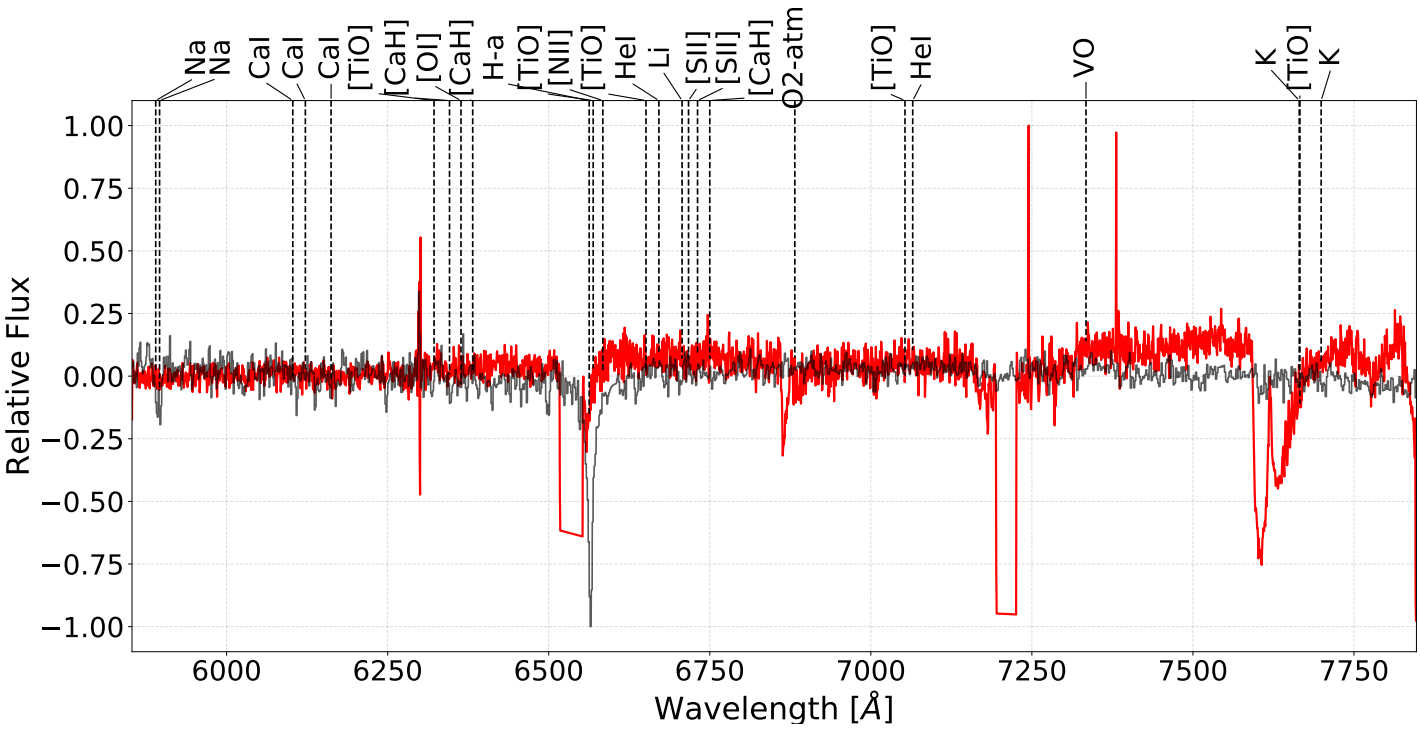

Figure B.56: Slit 23 for the SE field of RCW 34

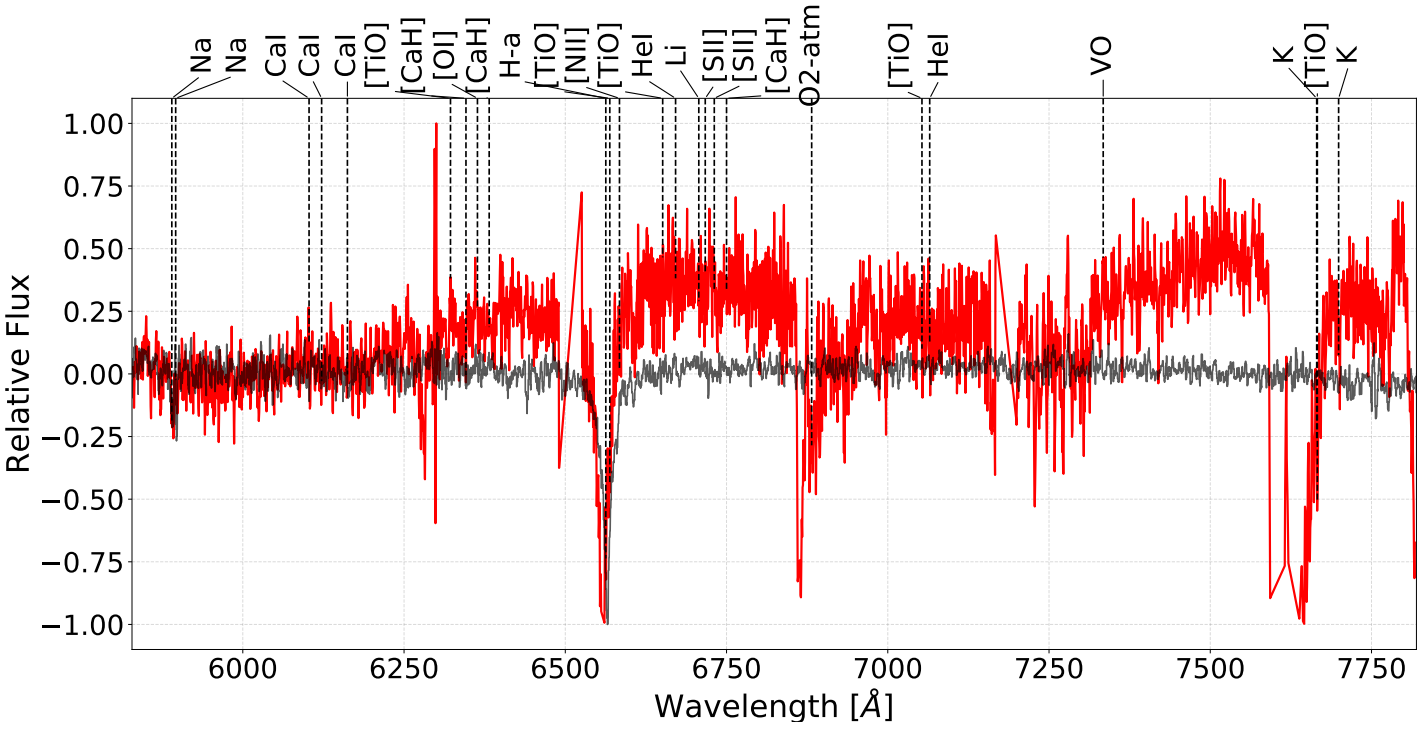

Figure B.57: Slit 24 for the SE field of RCW 34

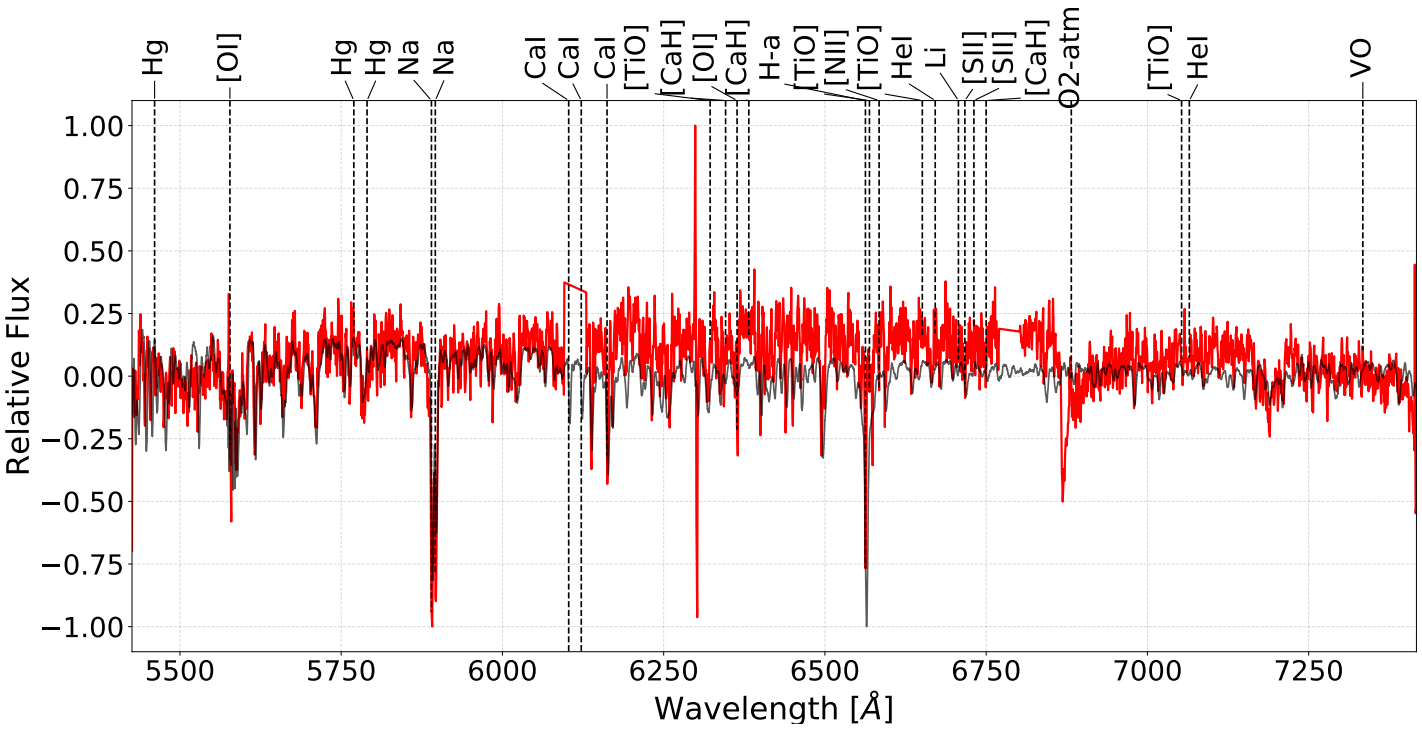

Figure B.58: Slit 1 for the SW field of RCW 34

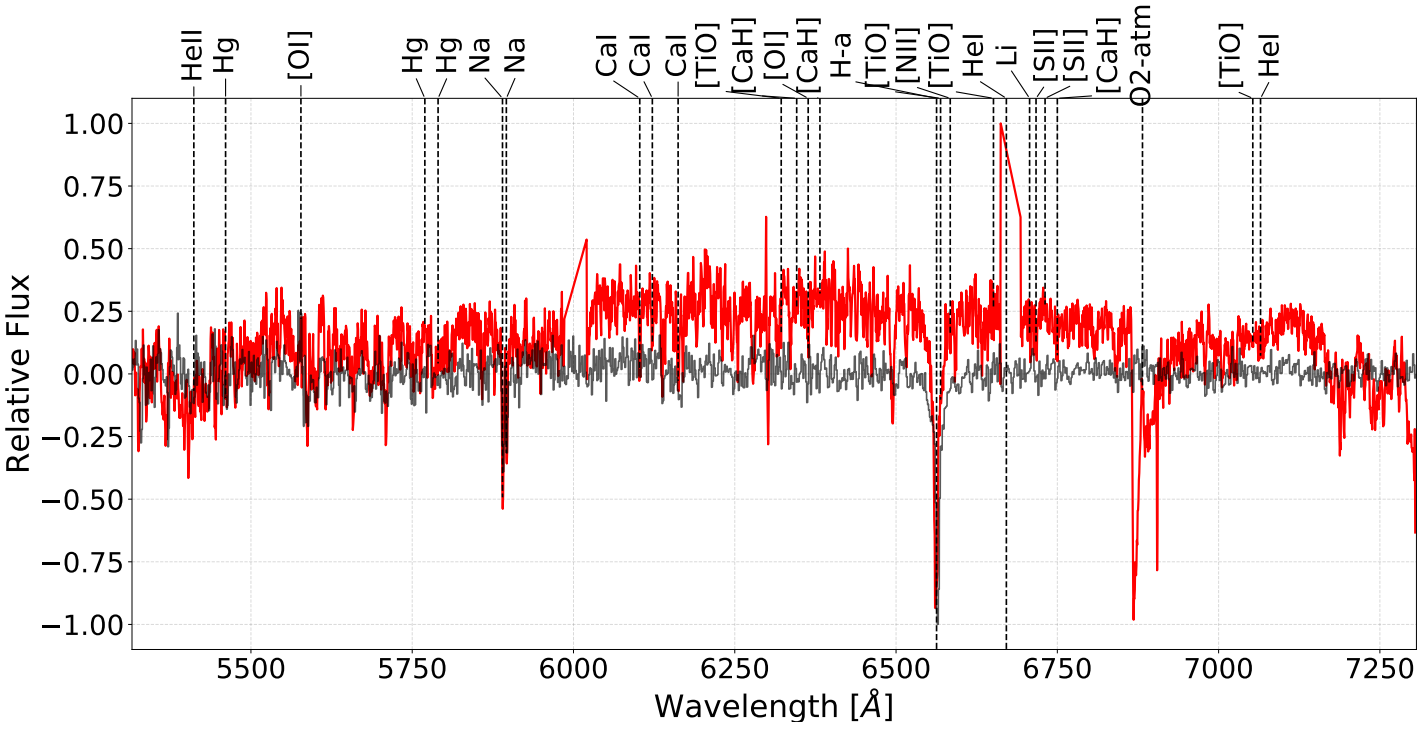

Figure B.59: Slit 2 for the SW field of RCW 34

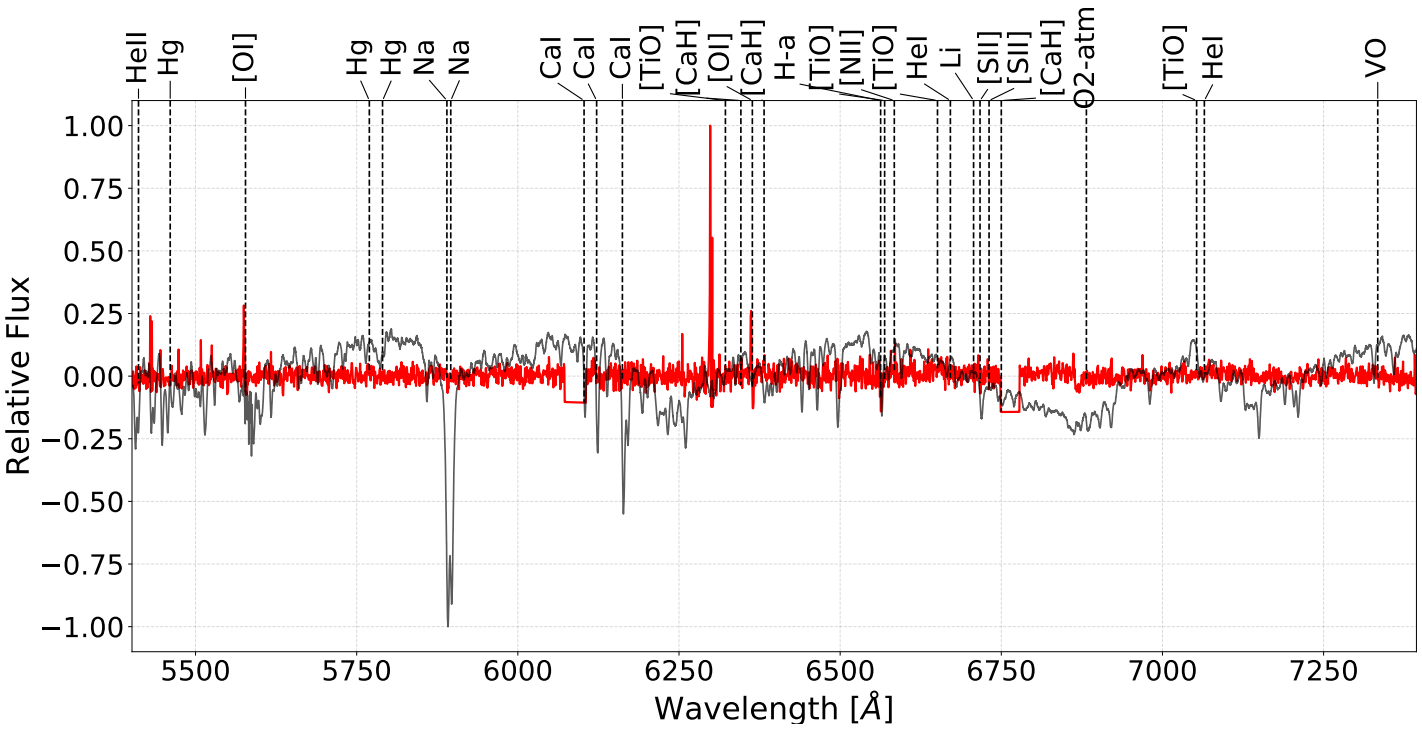

Figure B.60: Slit 5 for the SW field of RCW 34

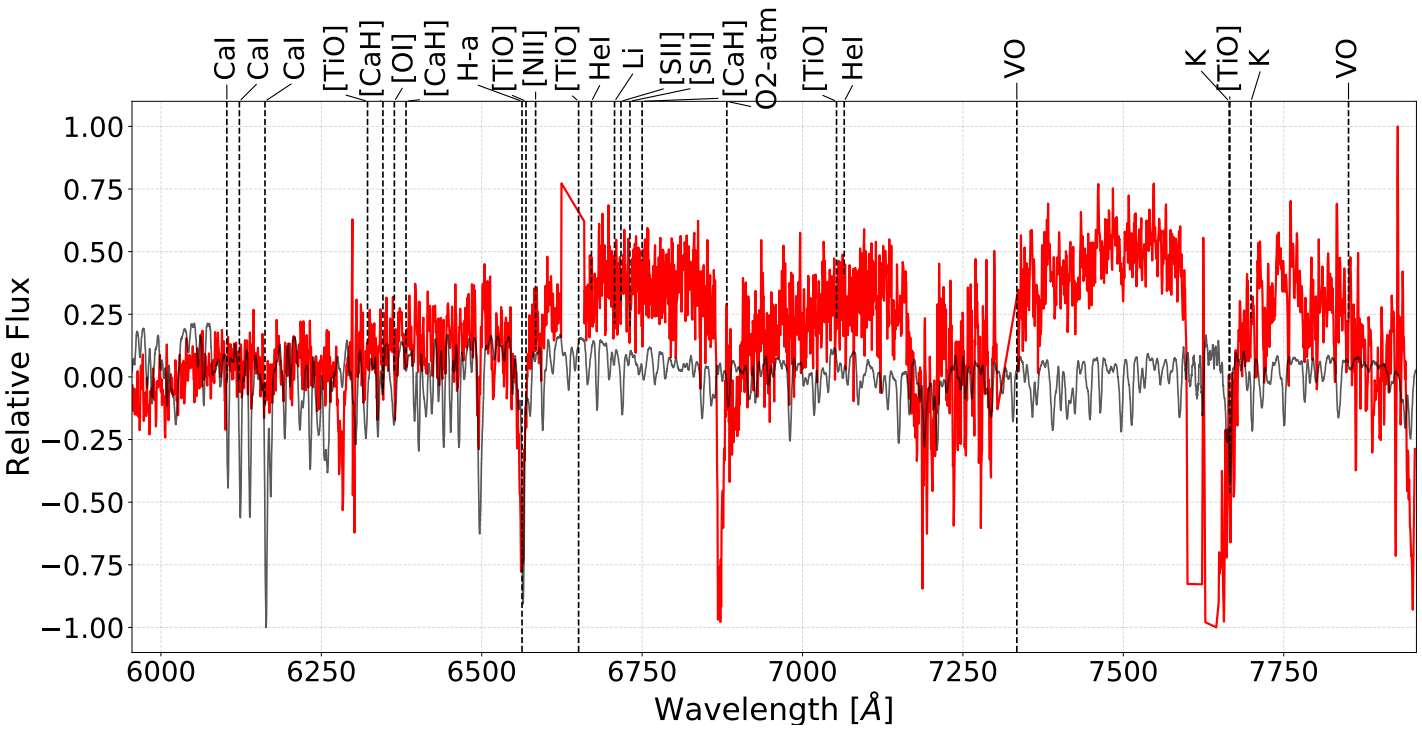

Figure B.61: Slit 7 for the SW field of RCW 34

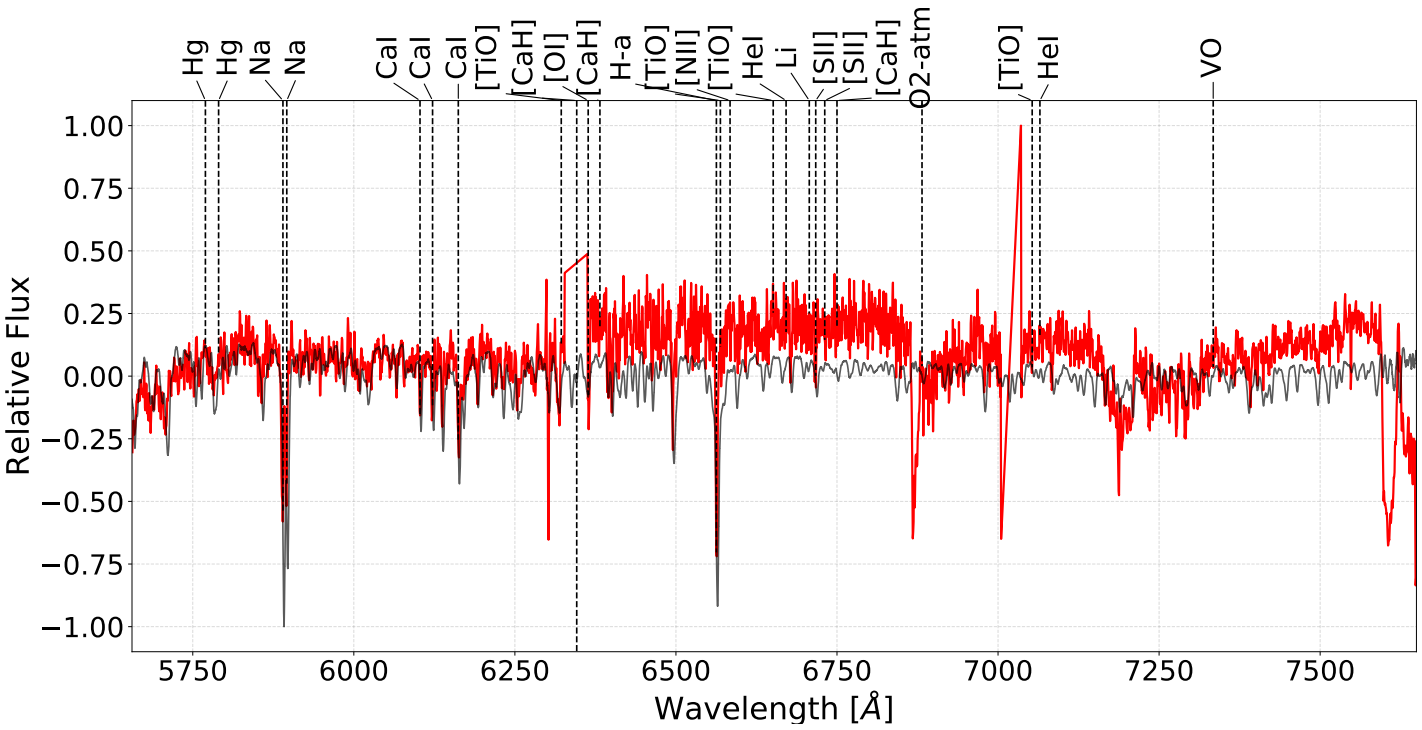

Figure B.62: Slit 8 for the SW field of RCW 34

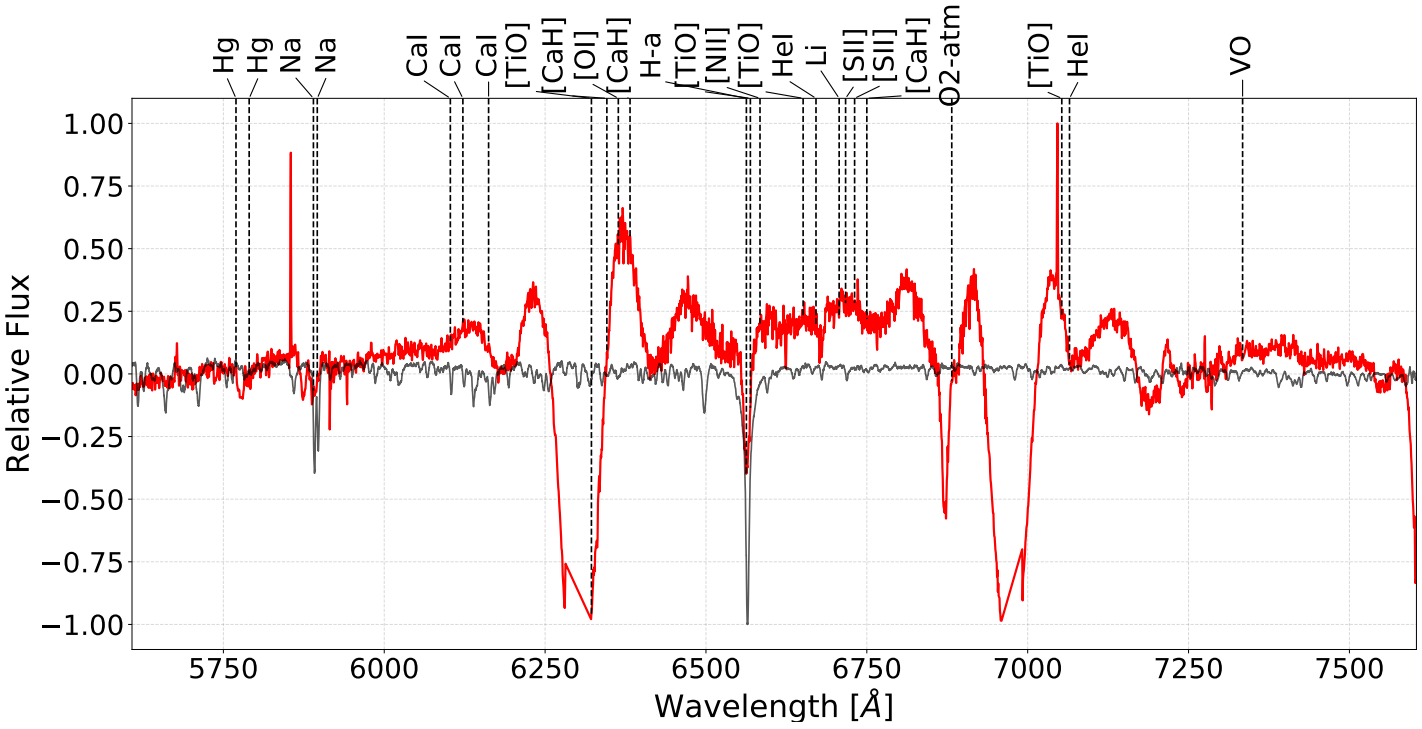

Figure B.63: Slit 9 for the SW field of RCW 34

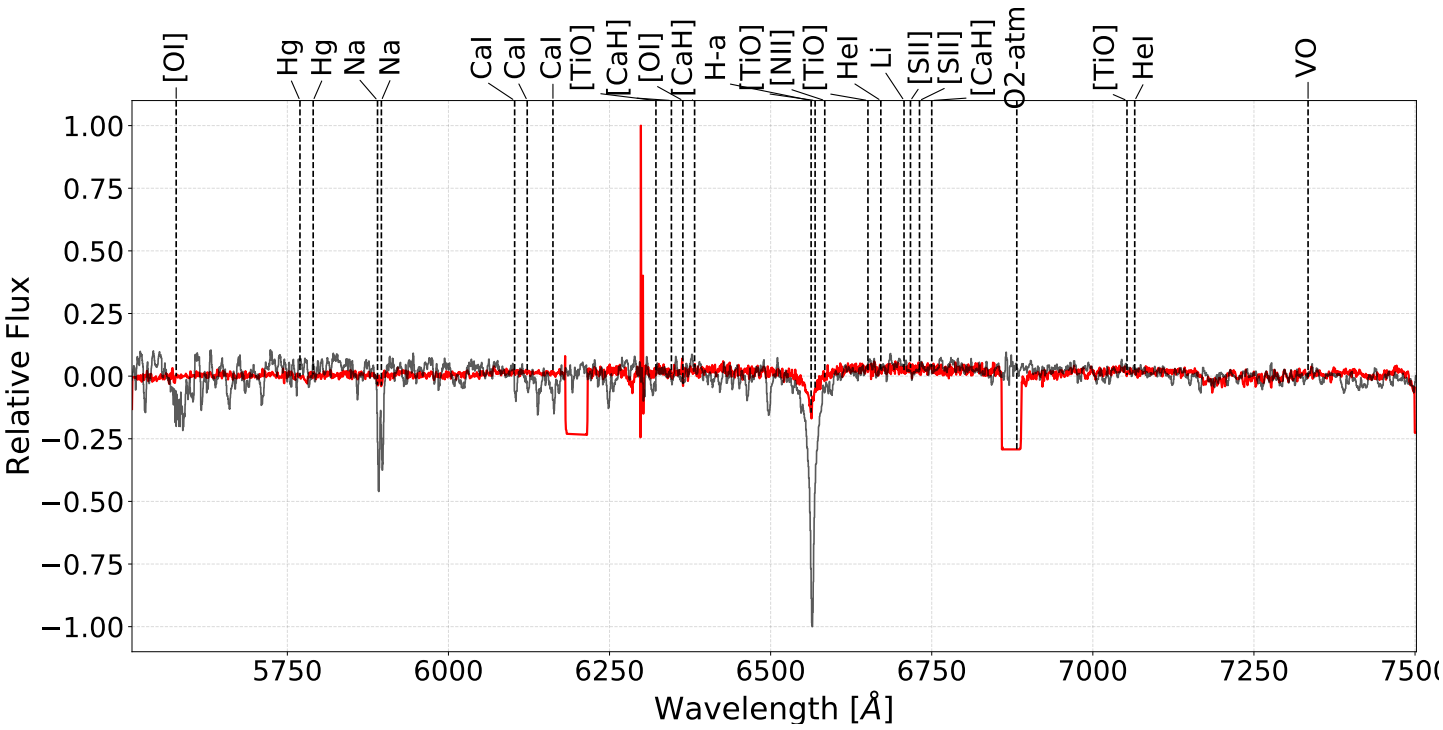

Figure B.64: Slit 10 for the SW field of RCW 34

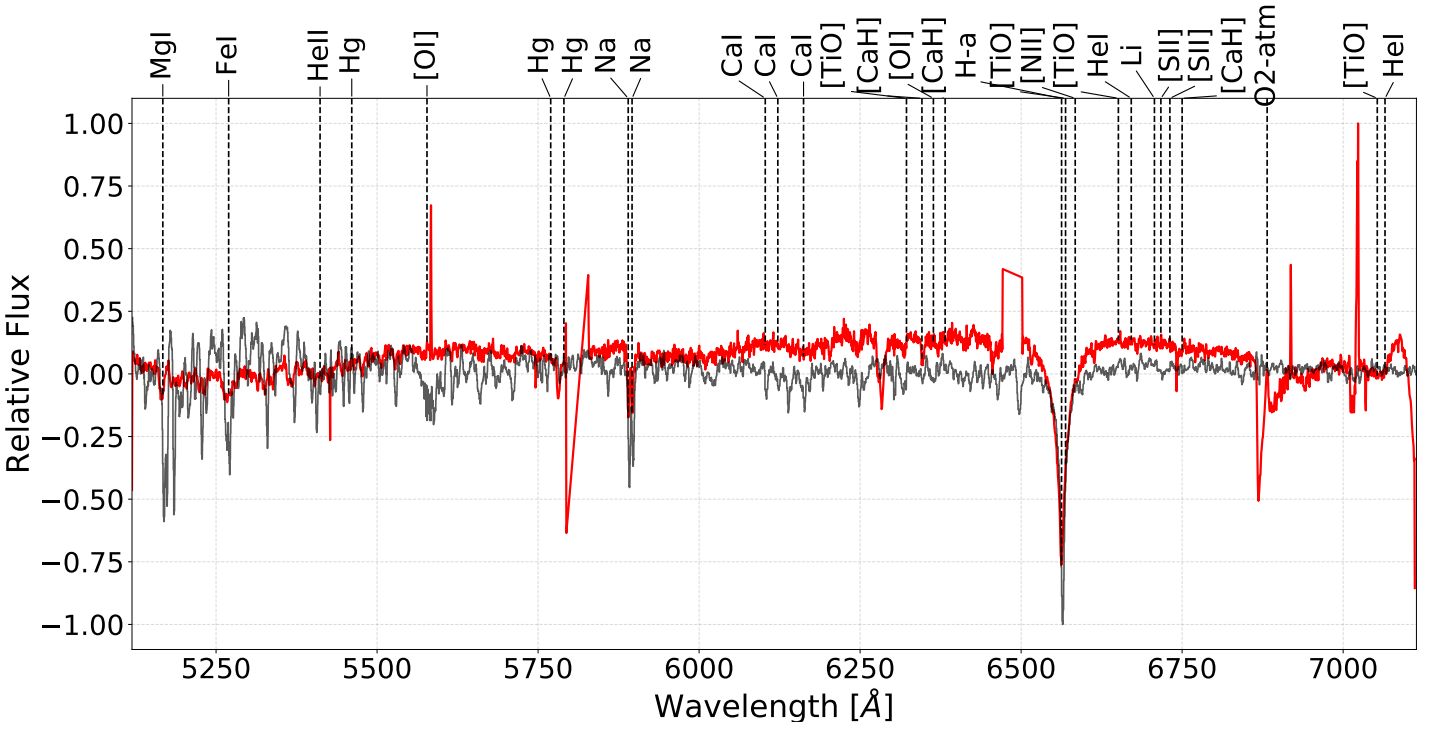

Figure B.65: Slit 13 for the SW field of RCW 34

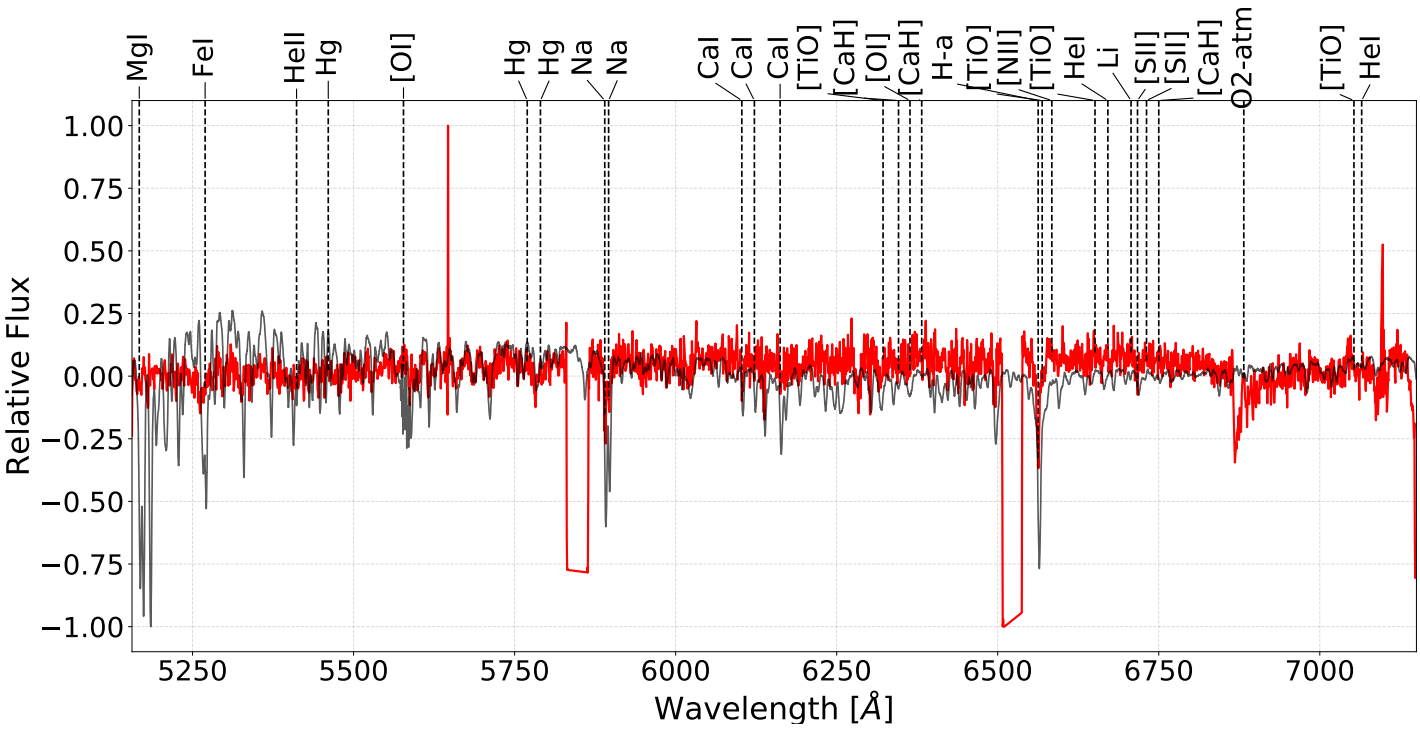

Figure B.66: Slit 14 for the SW field of RCW 34

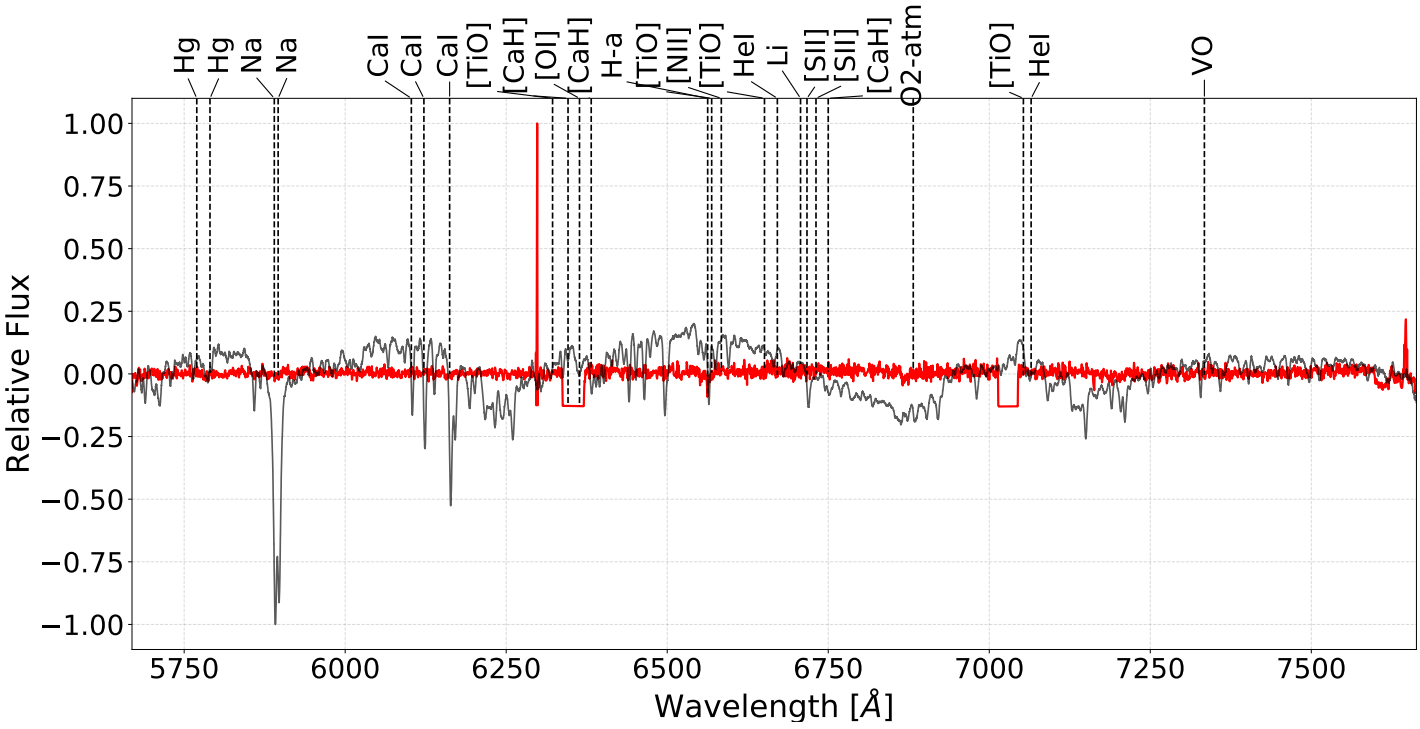

Figure B.67: Slit 15 for the SW field of RCW 34

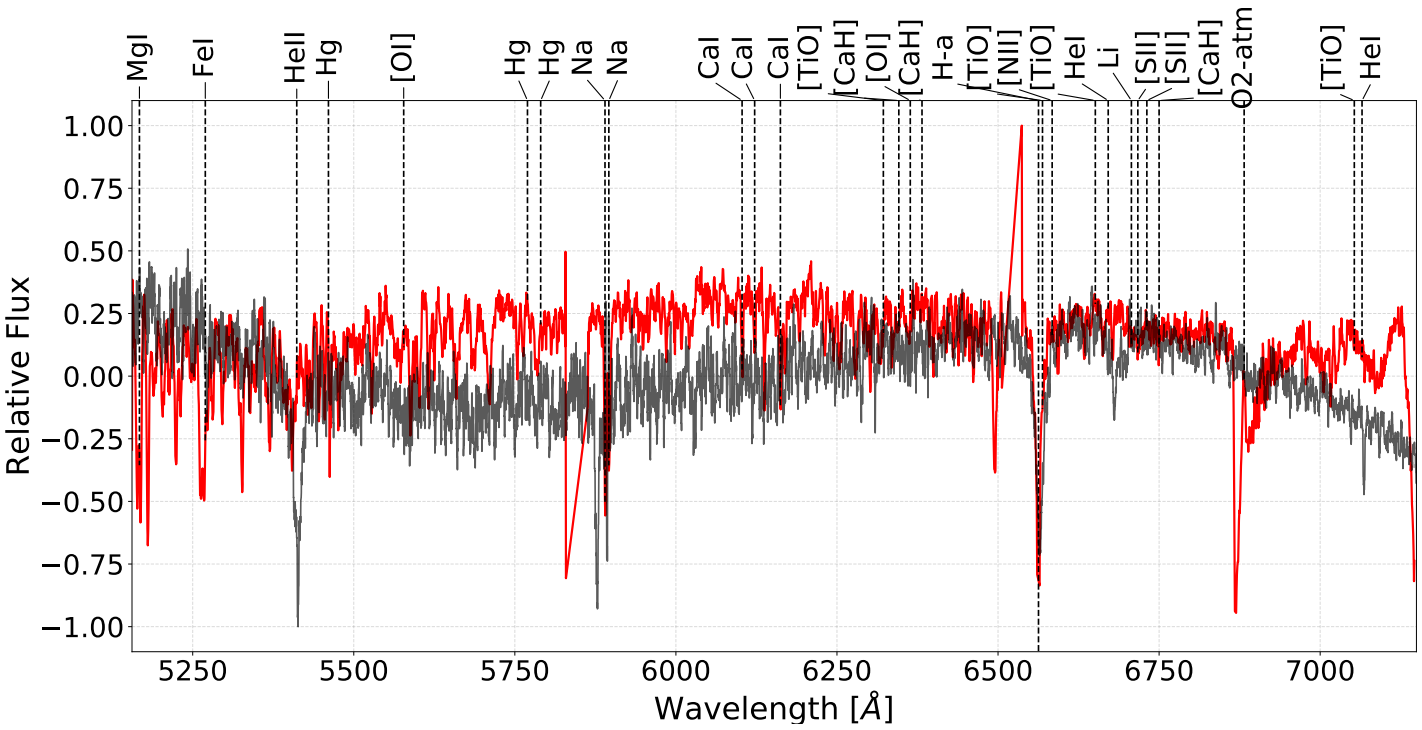

Figure B.68: Slit 17 for the SW field of RCW 34

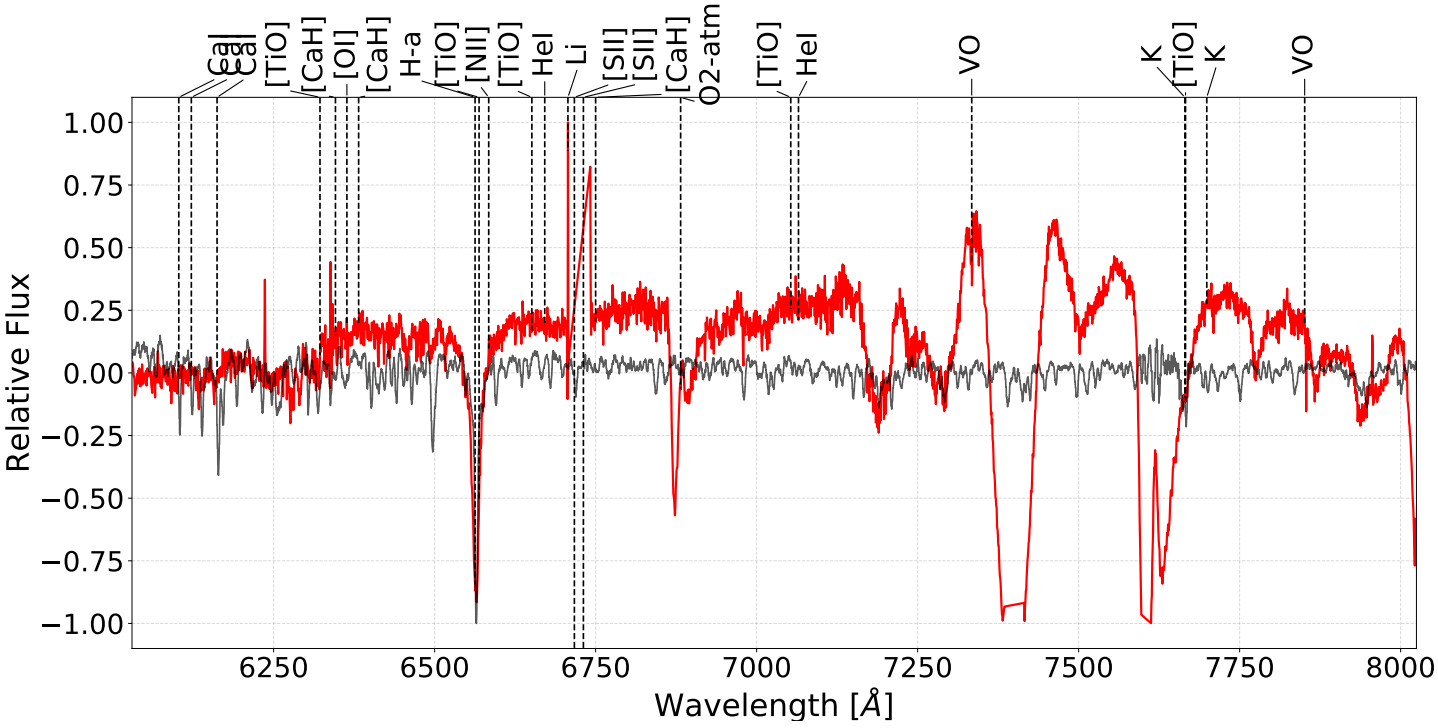

Figure B.69: Slit 18 for the SW field of RCW 34

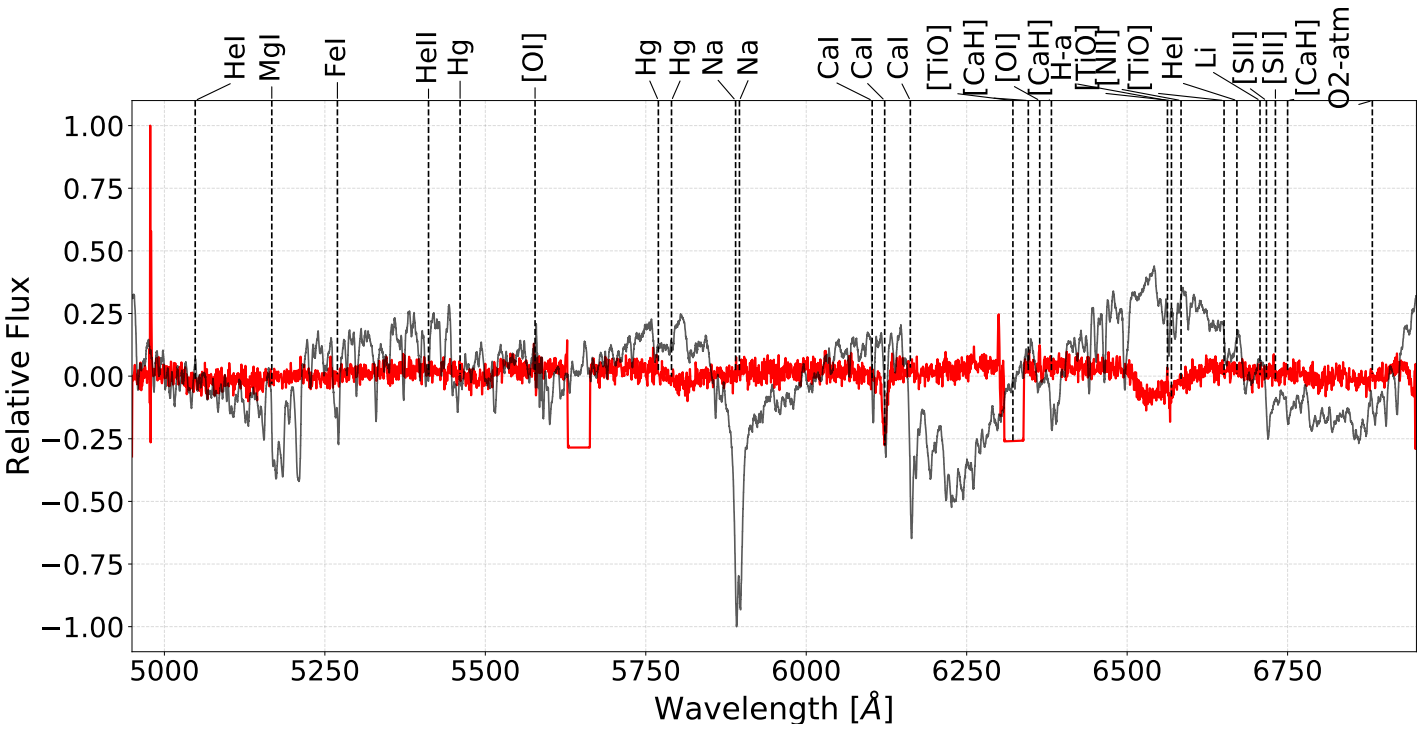

Figure B.70: Slit 19 for the SW field of RCW 34

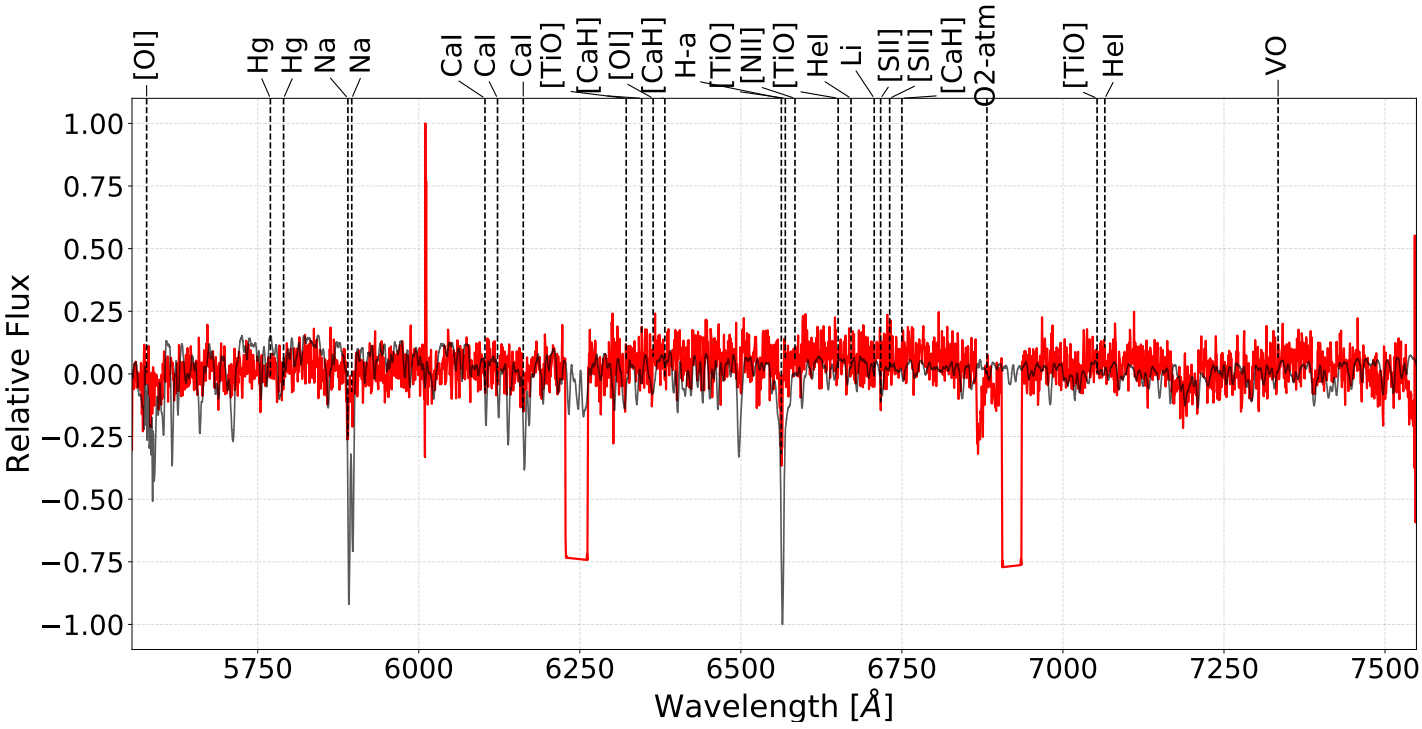

Figure B.71: Slit 20 for the SW field of RCW 34

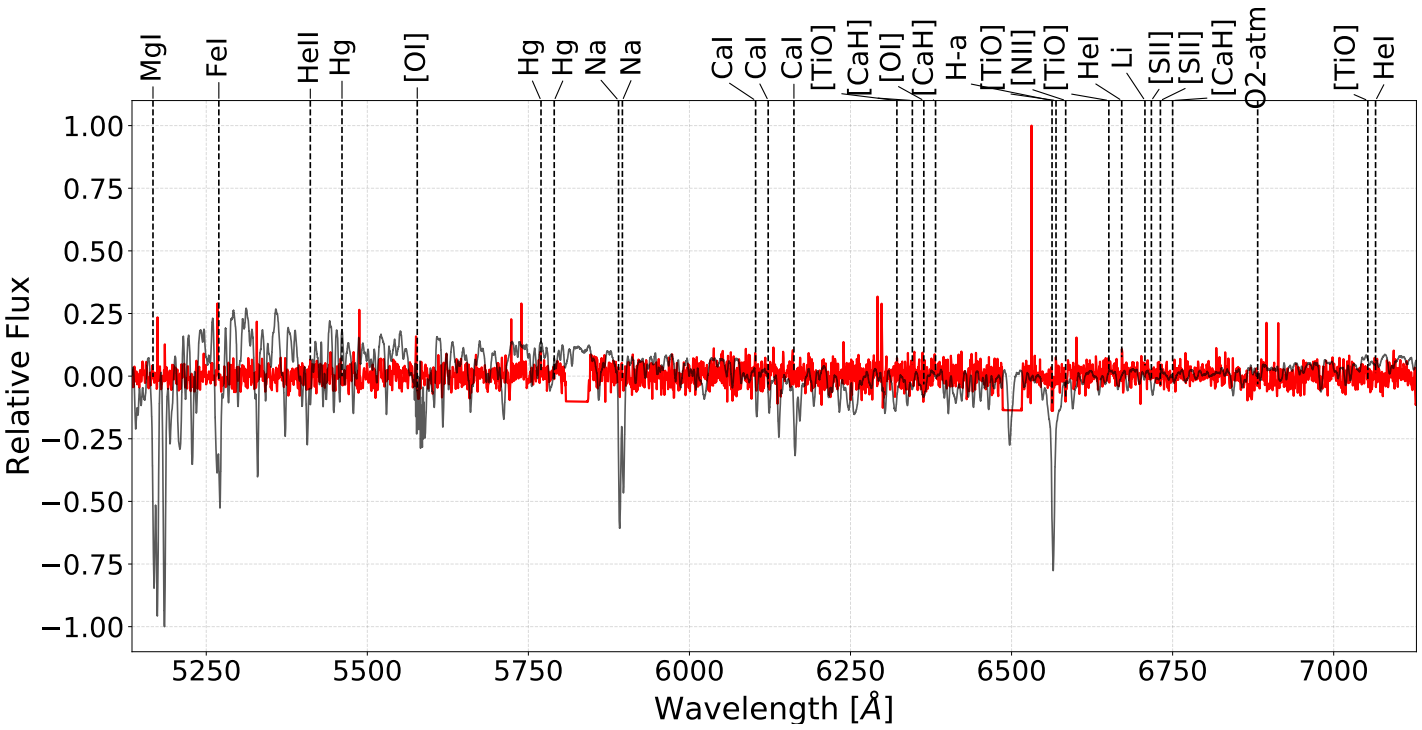

Figure B.72: Slit 21 for the SW field of RCW 34

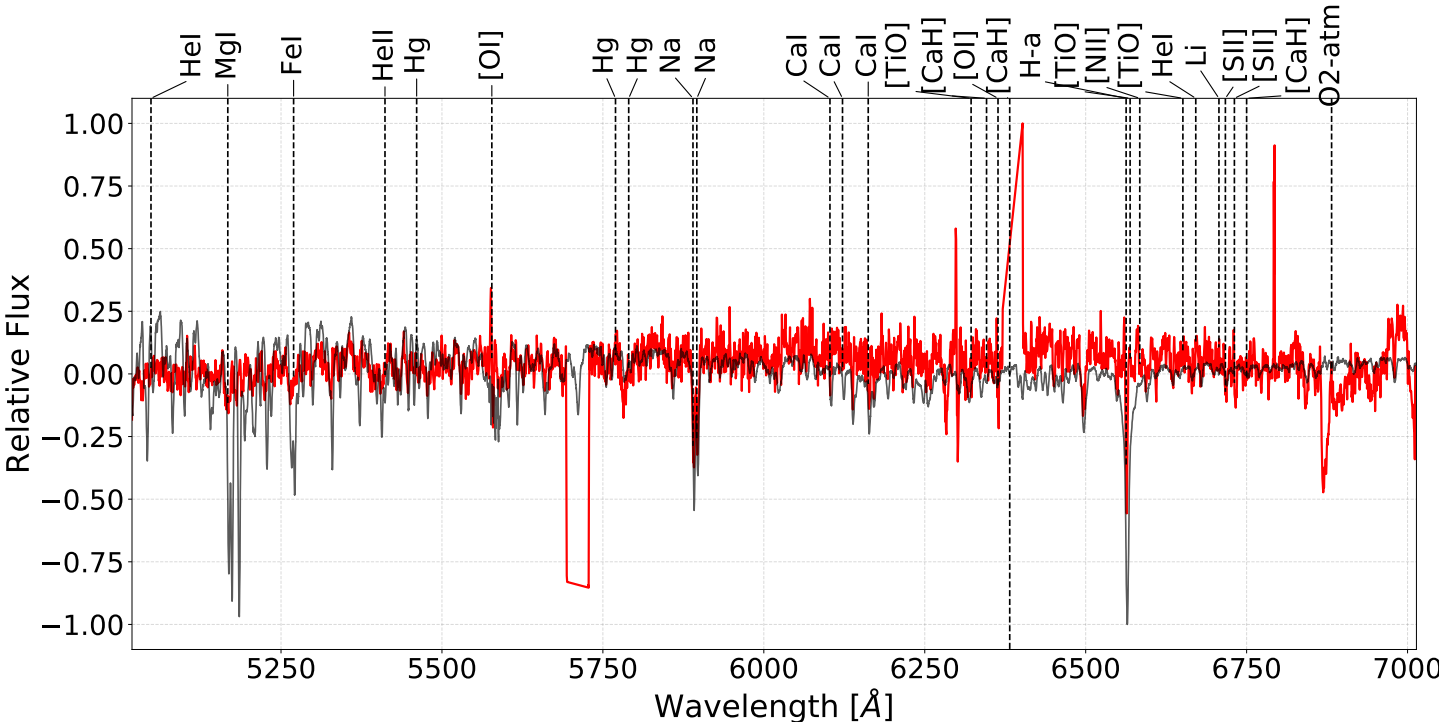

Figure B.73: Slit 23 for the SW field of RCW 34

Stars with an undetermined Hα line

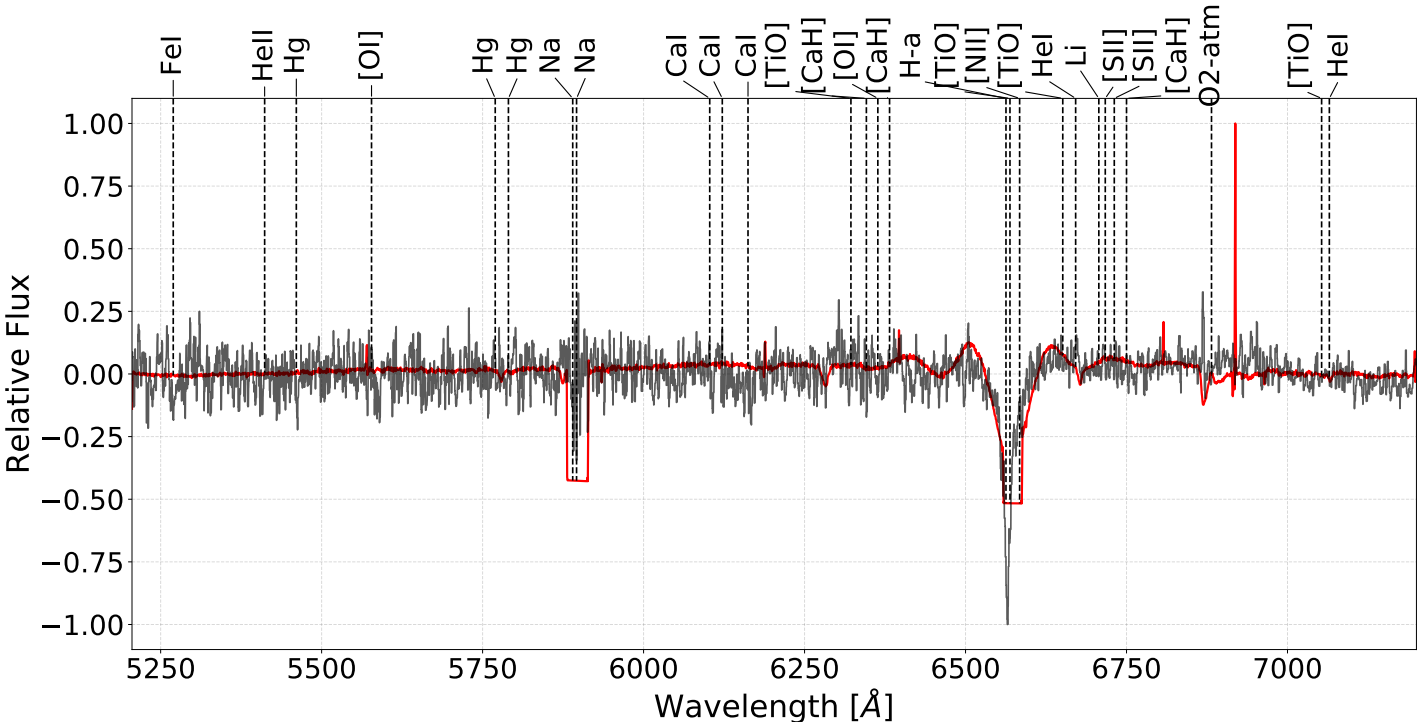

Figure B.75: Slit 3 for the NE field of RCW 34

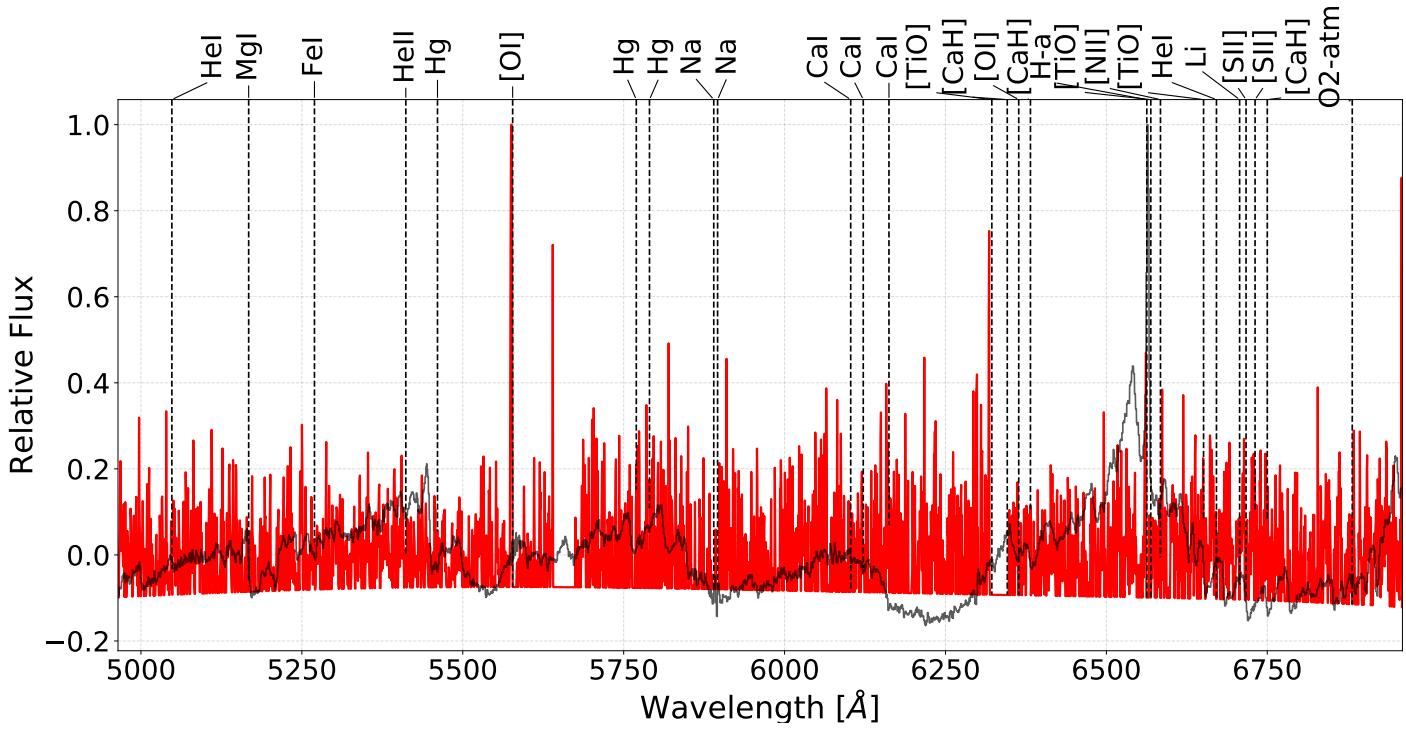

Figure B.76: Slit 19 for the NE field of RCW 34

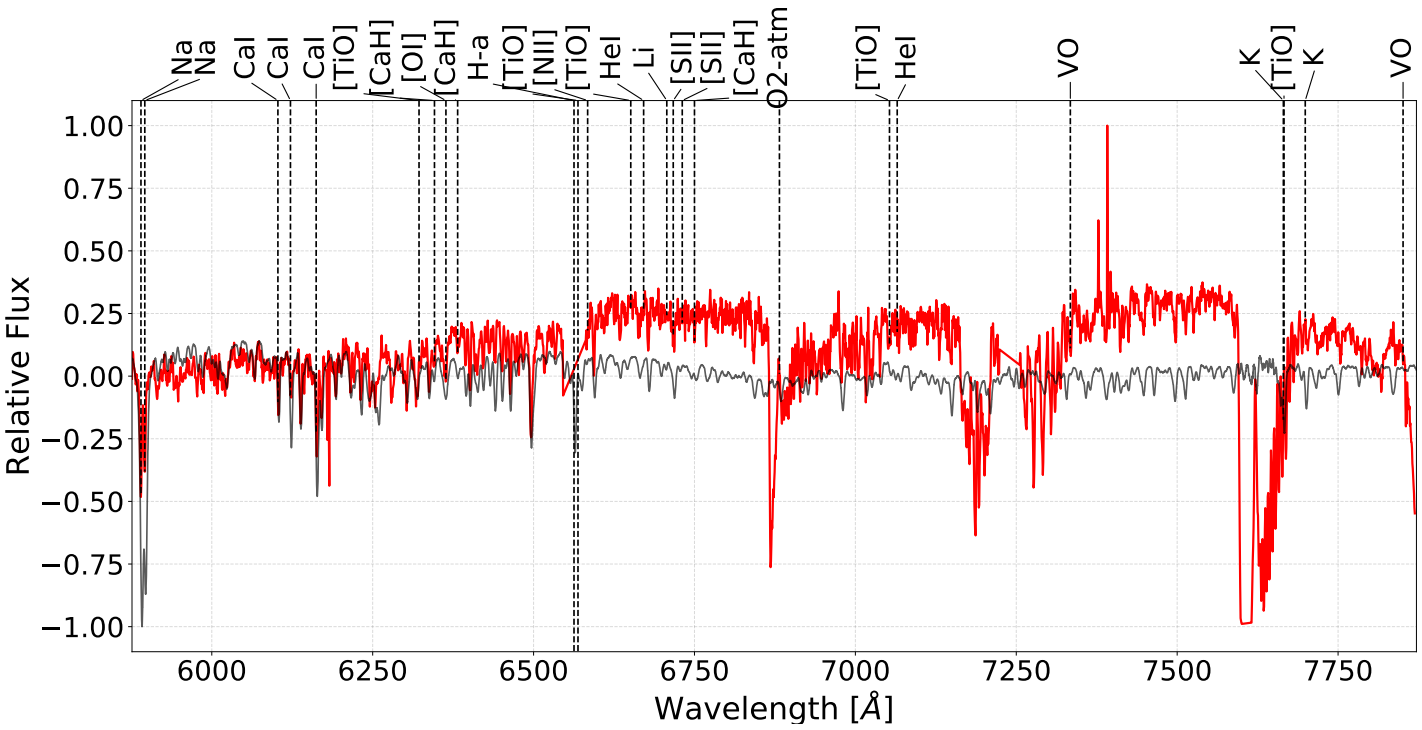

Figure B.77: Slit 20 for the NE field of RCW 34

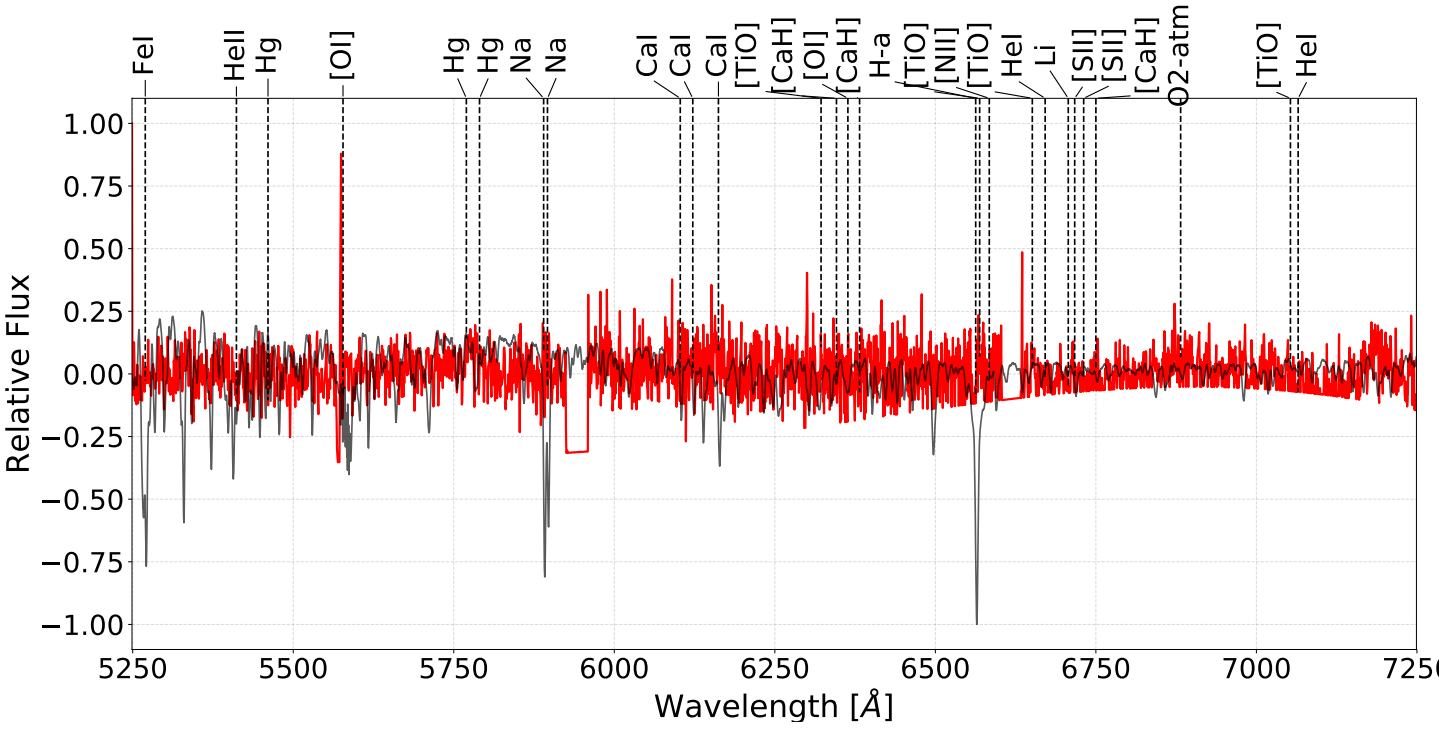

Figure B.78: Slit 11 for the NW field of RCW 34

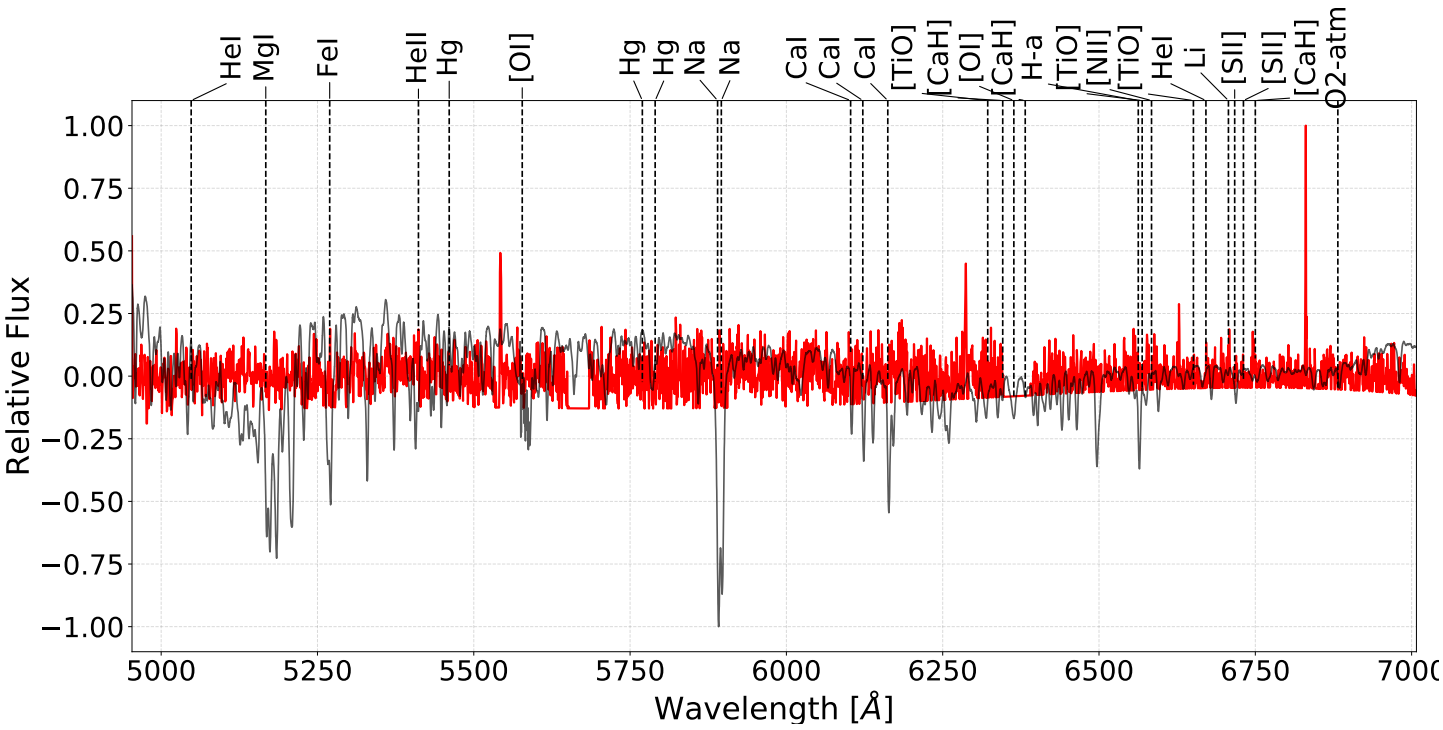

Figure B.79: Slit 12 for the NW field of RCW 34

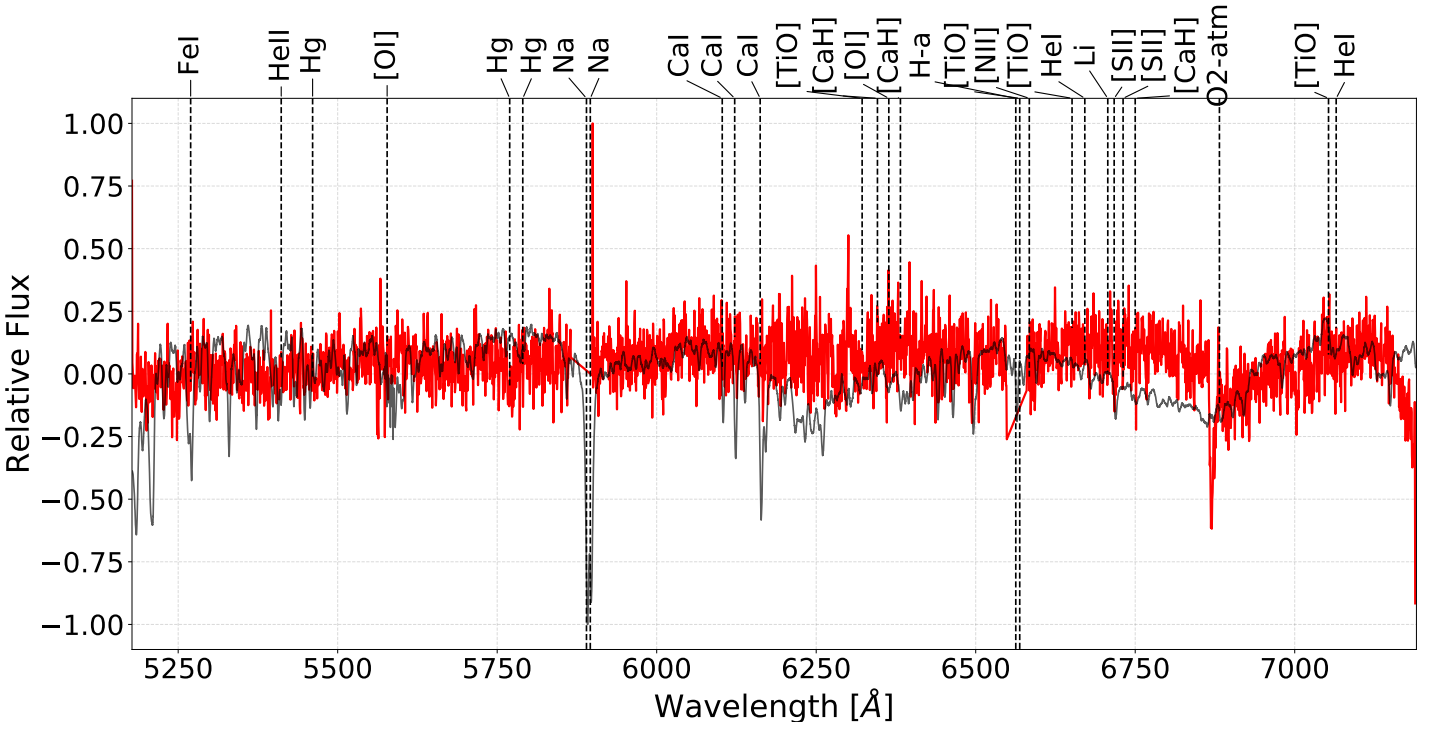

Figure B.80: Slit 14 for the NW field of RCW 34

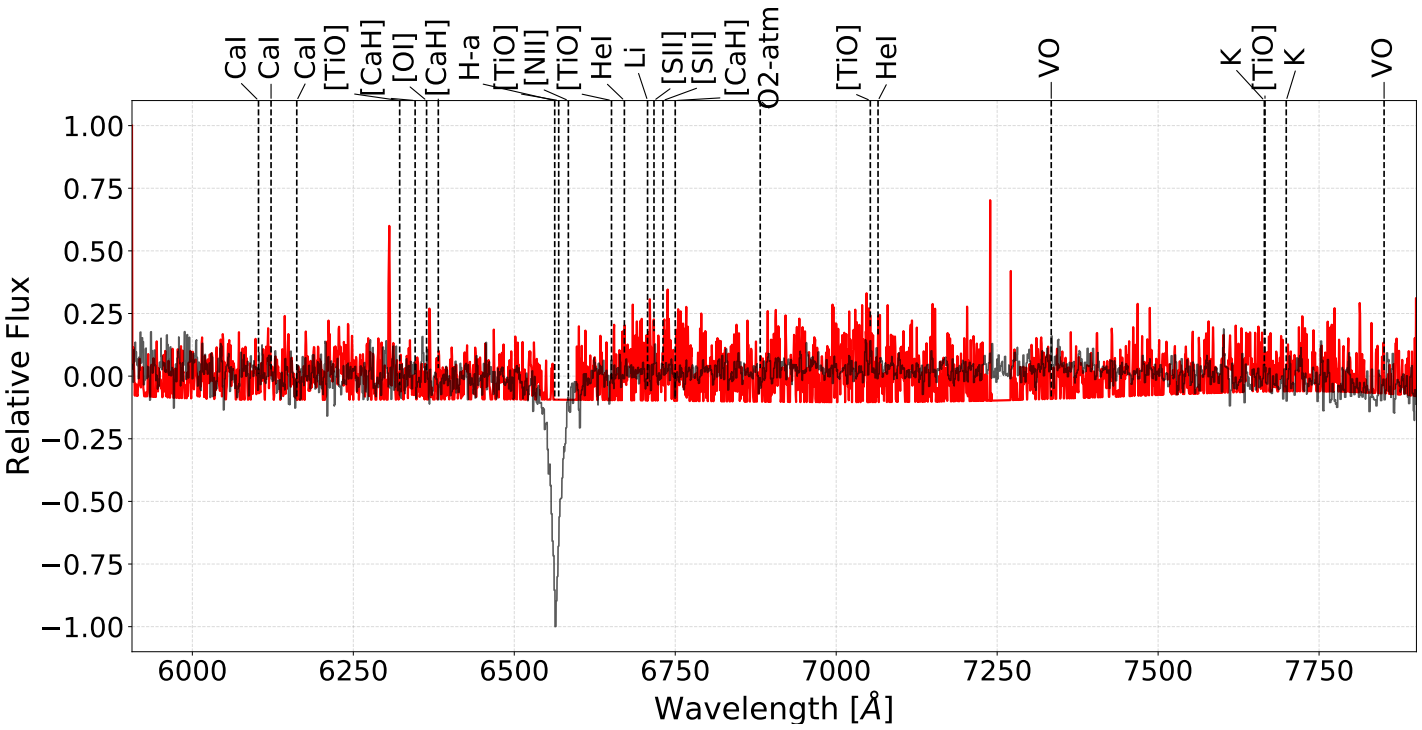

Figure B.81: Slit 20 for the NW field of RCW 34

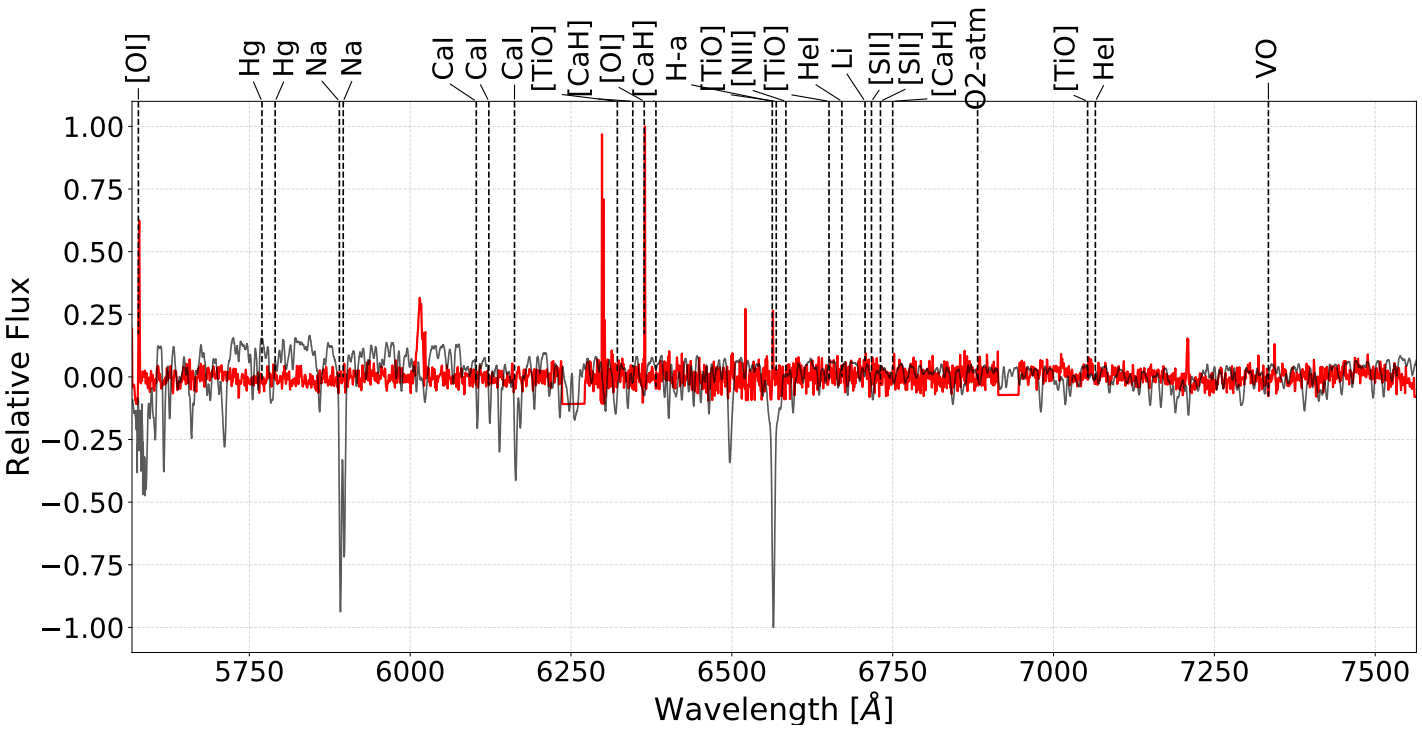

Figure B.82: Slit 10 for the SE field of RCW 34

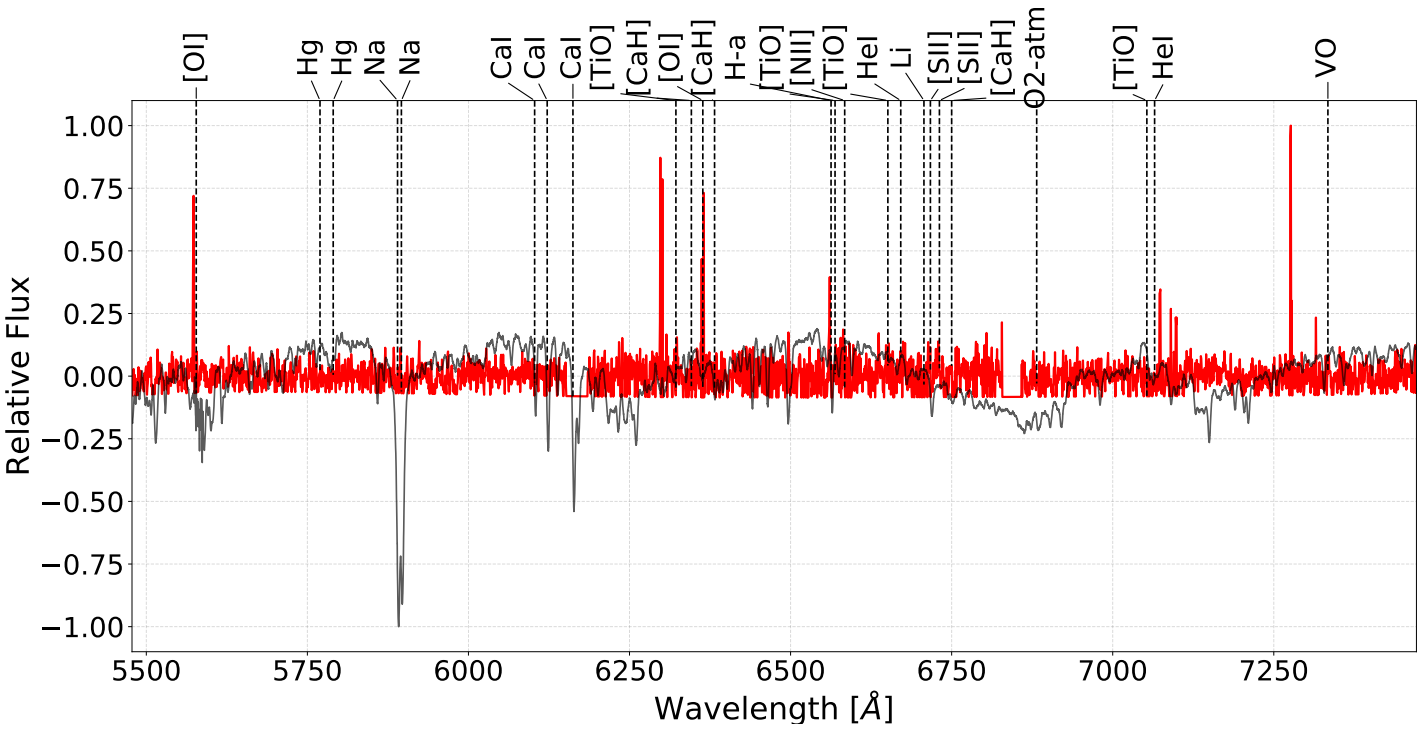

Figure B.83: Slit 13 for the SE field of RCW 34

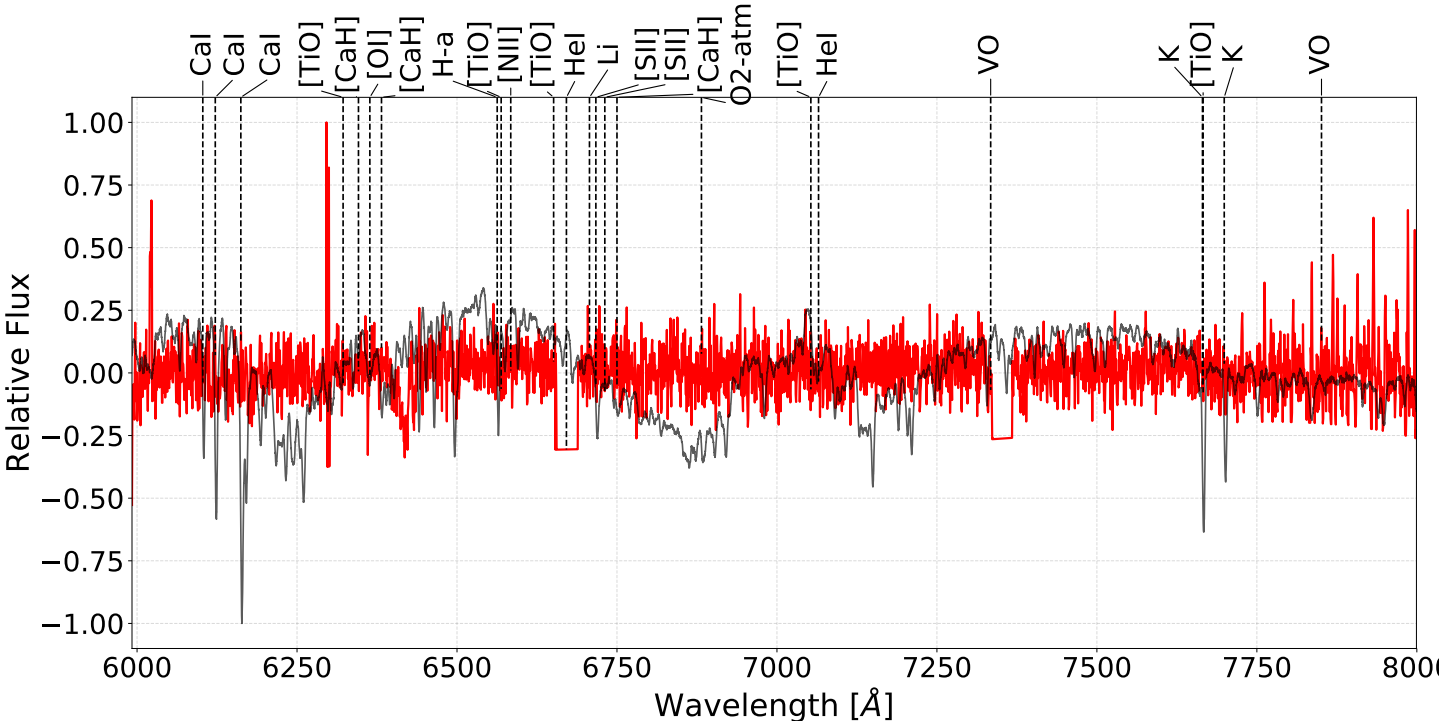

Figure B.84: Slit 17 for the SE field of RCW 34

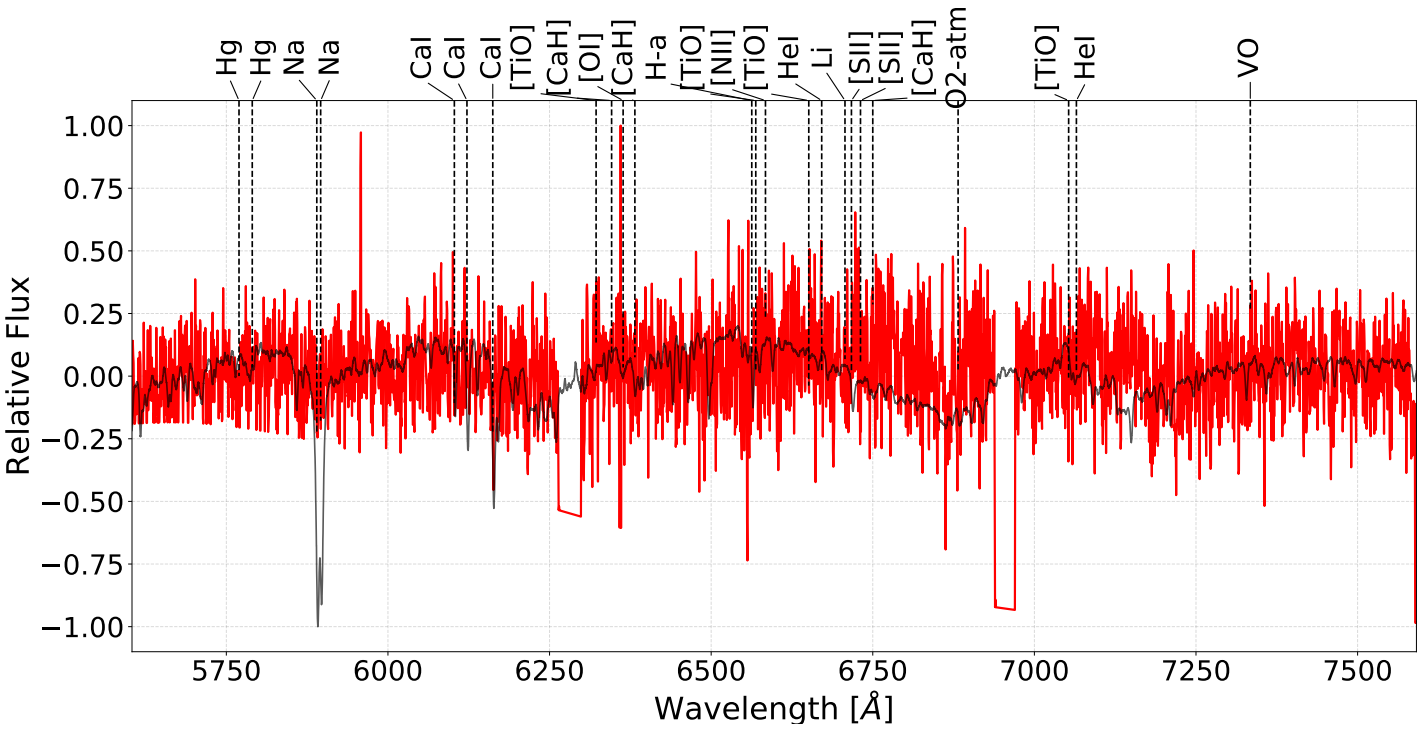

Figure B.85: Slit 21 for the SE field of RCW 34

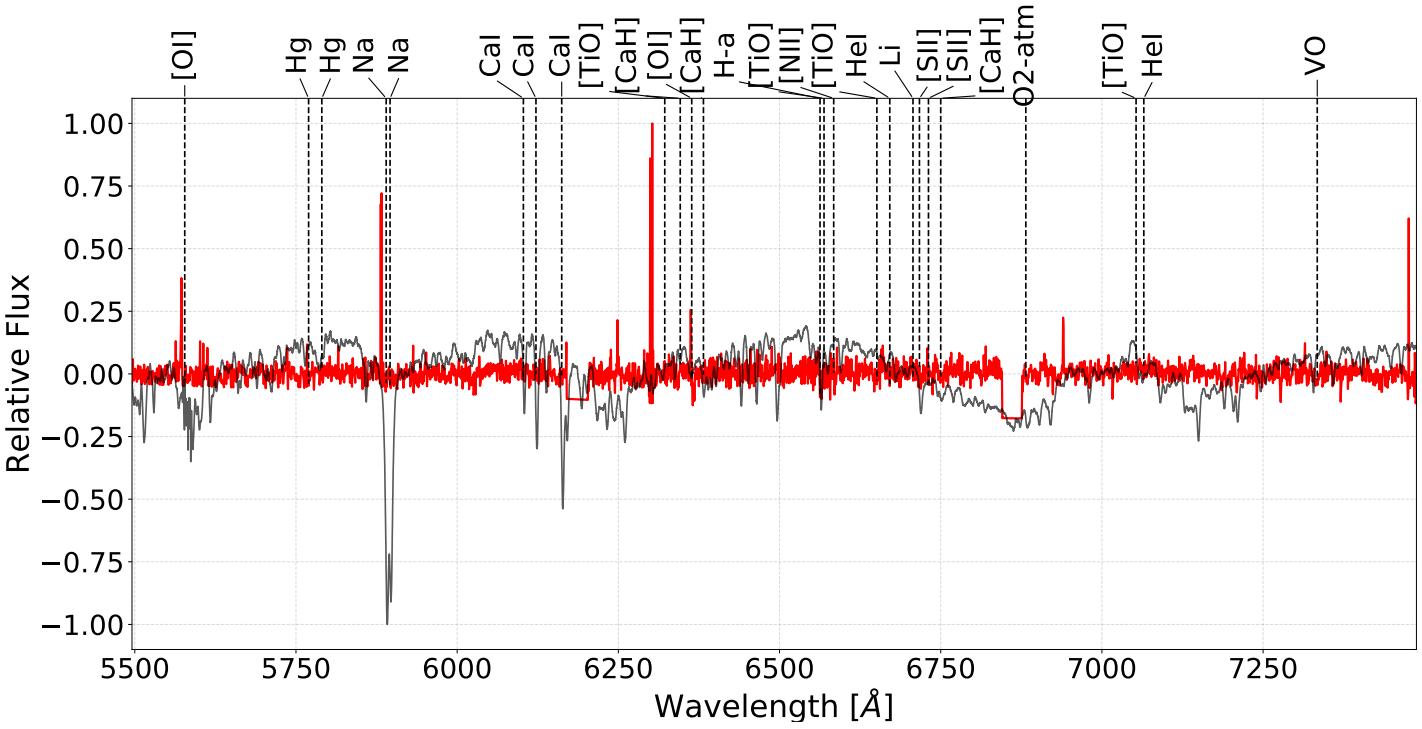

Figure B.86: Slit 4 for the SW field of RCW 34

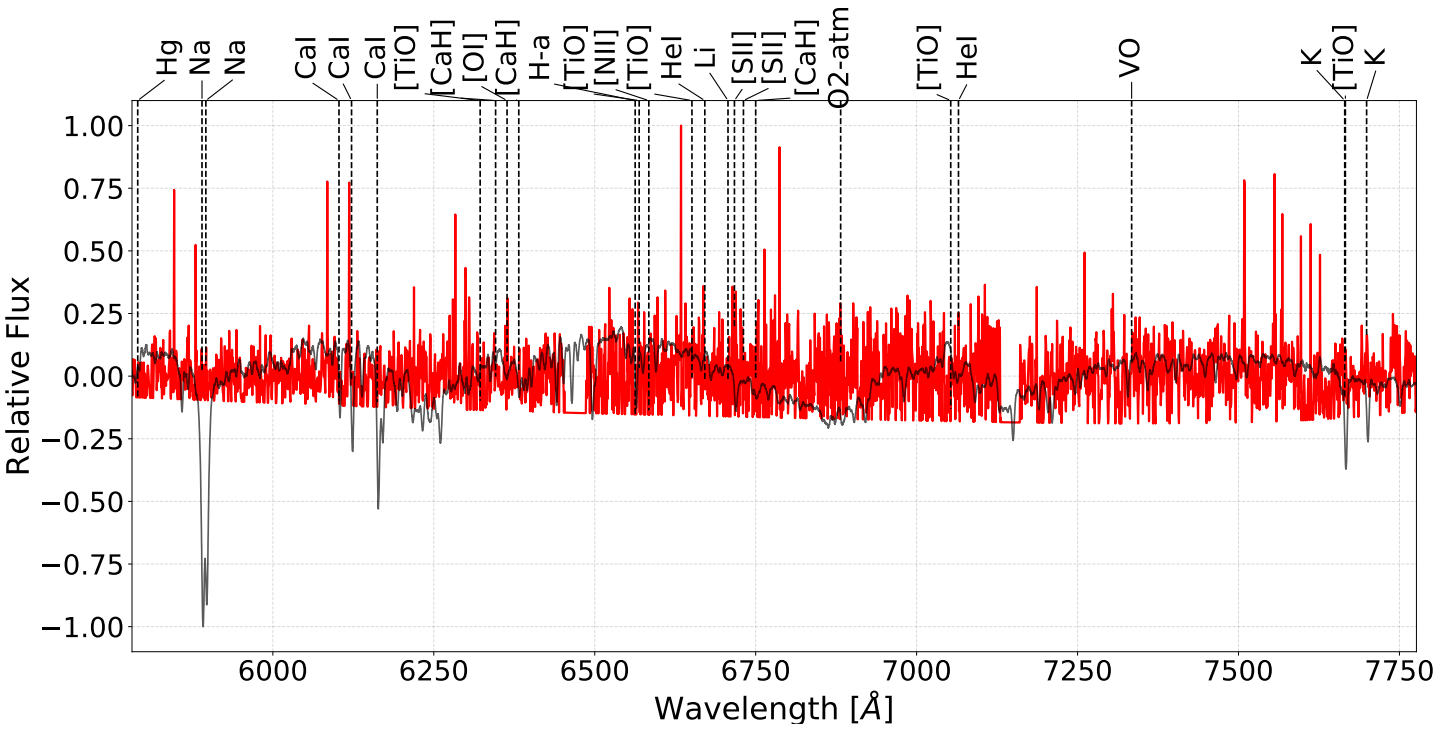

Figure B.87: Slit 11 for the SW field of RCW 34

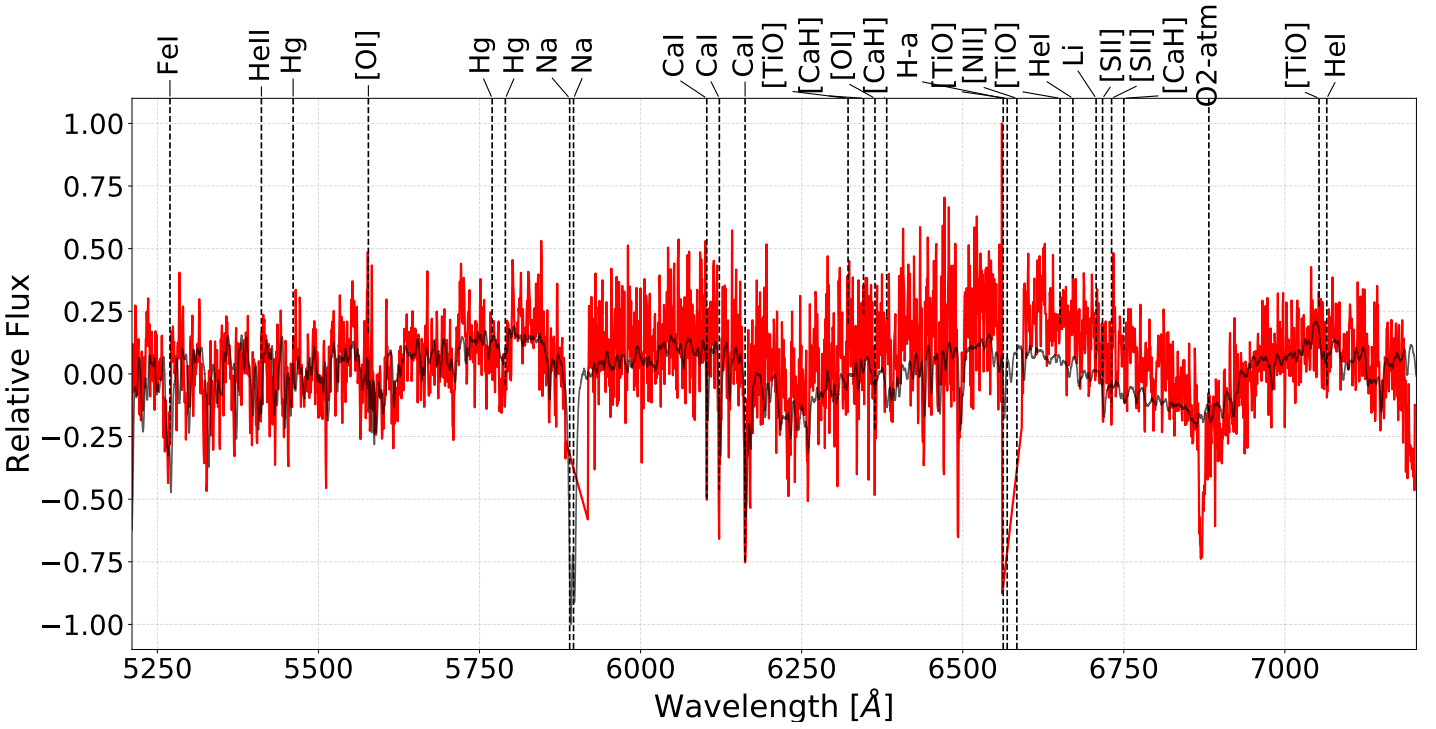

Figure B.88: Slit 12 for the SW field of RCW 34

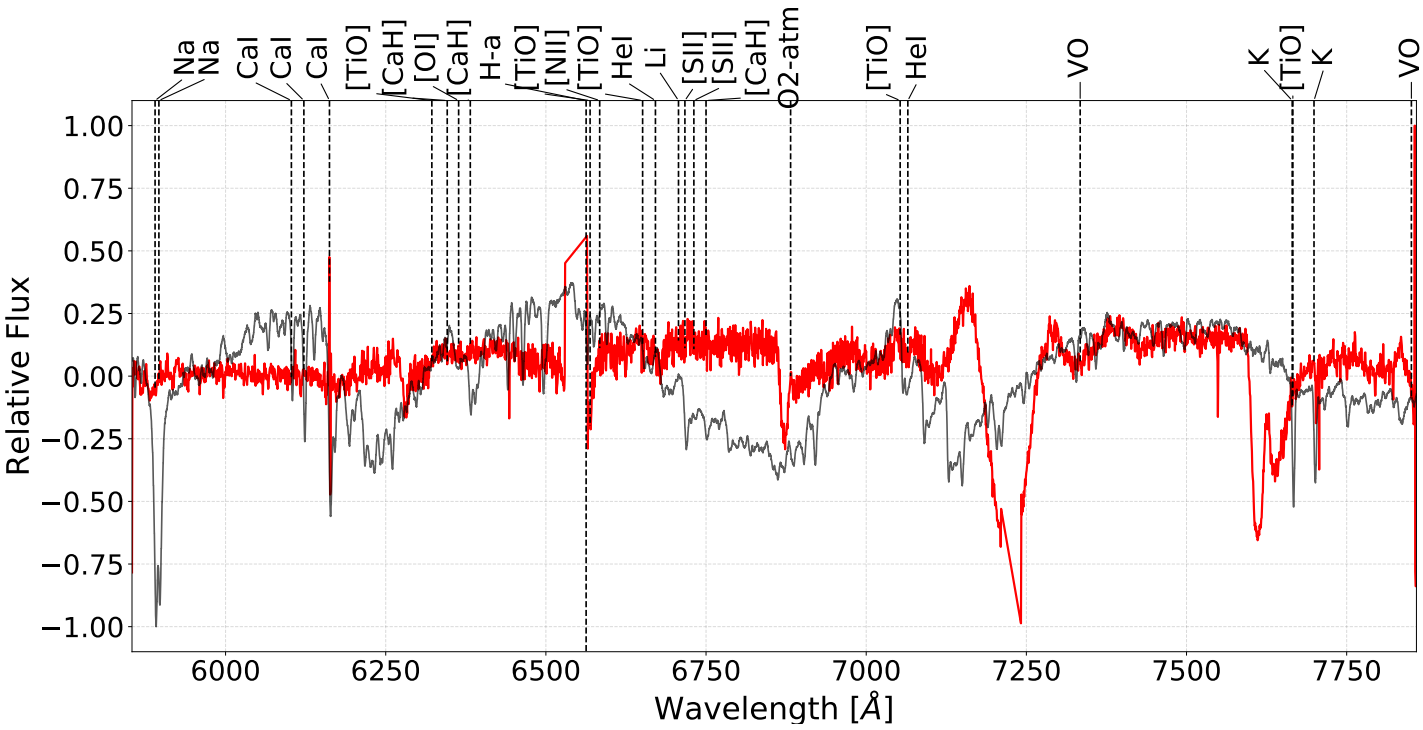

Figure B.89: Slit 16 for the SW field of RCW 34

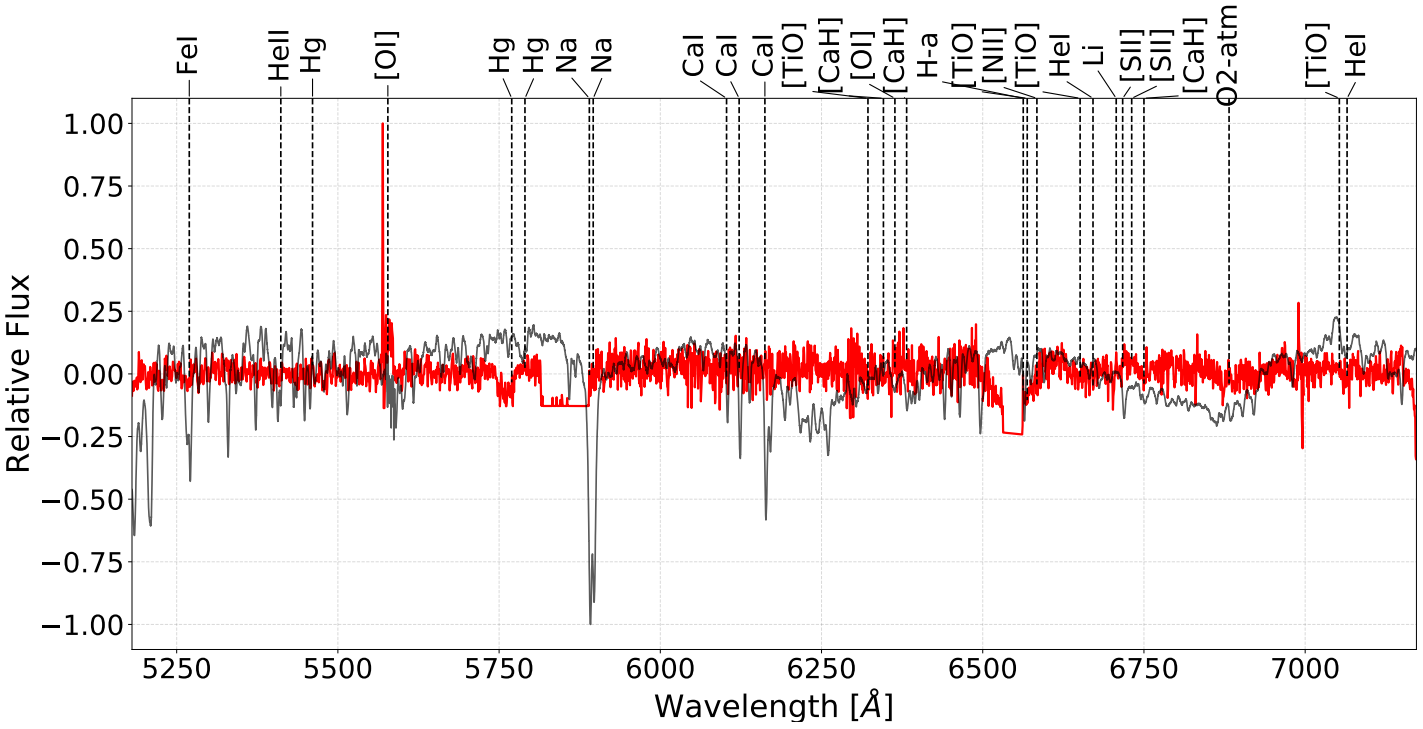

Figure B.90: Slit 24 for the SW field of RCW 34

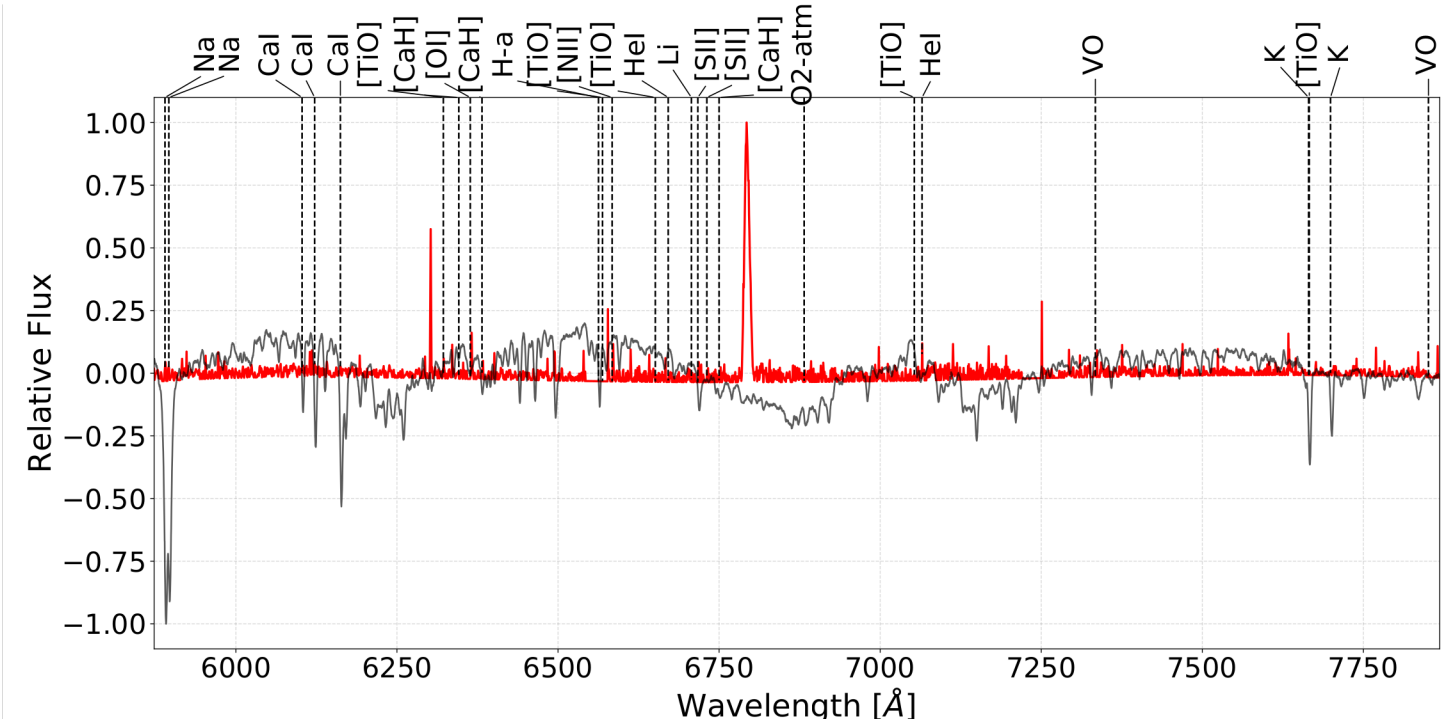

Figure B.91: Slit 25 for the SW field of RCW 34

APPENDIX C: SPECTROSCOPIC PROFILES FOR THE STARS OBSERVED WITH IN NGC 2626

The red or blue spectra were observed with *SALT* and the grey spectra were closest match made with PyHammer to each specific case.

Hα-emission line stars

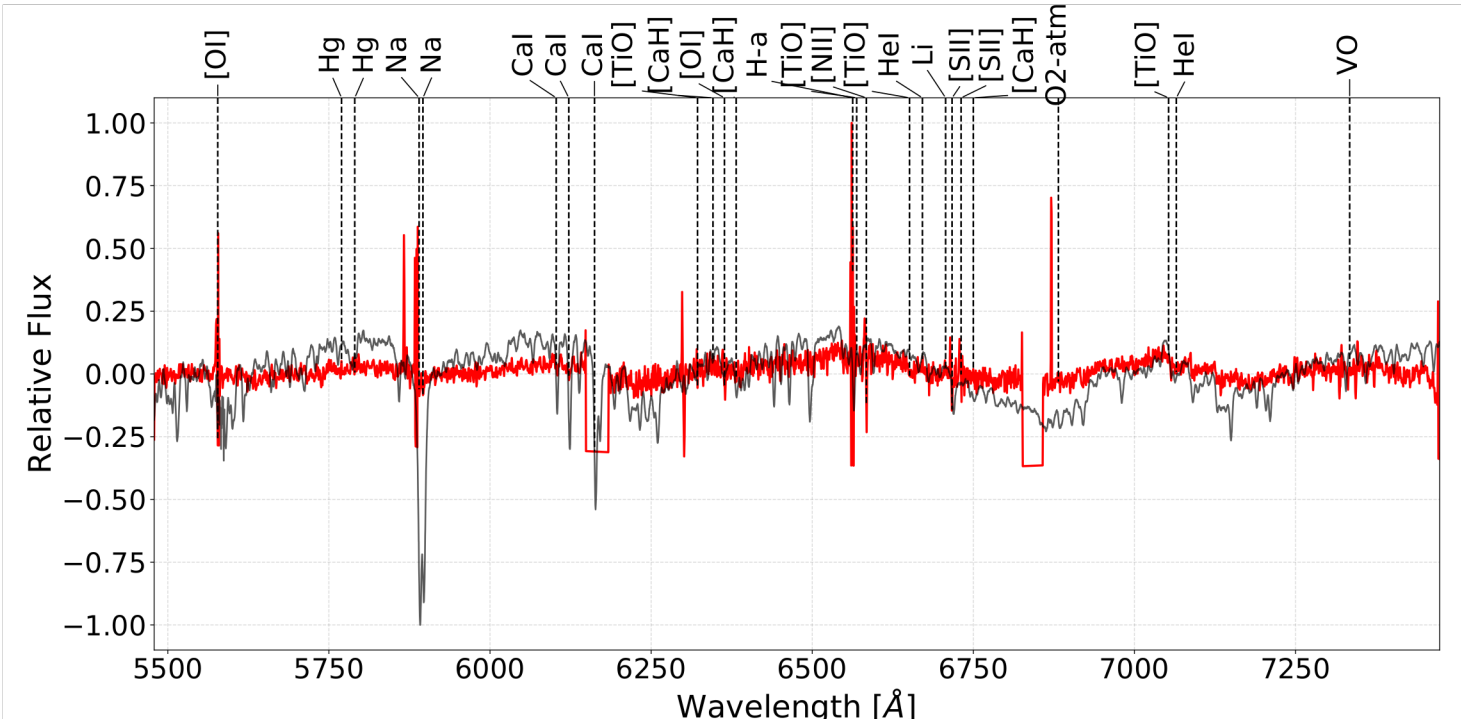

Figure C.1: Slit 5 for in NGC 2626

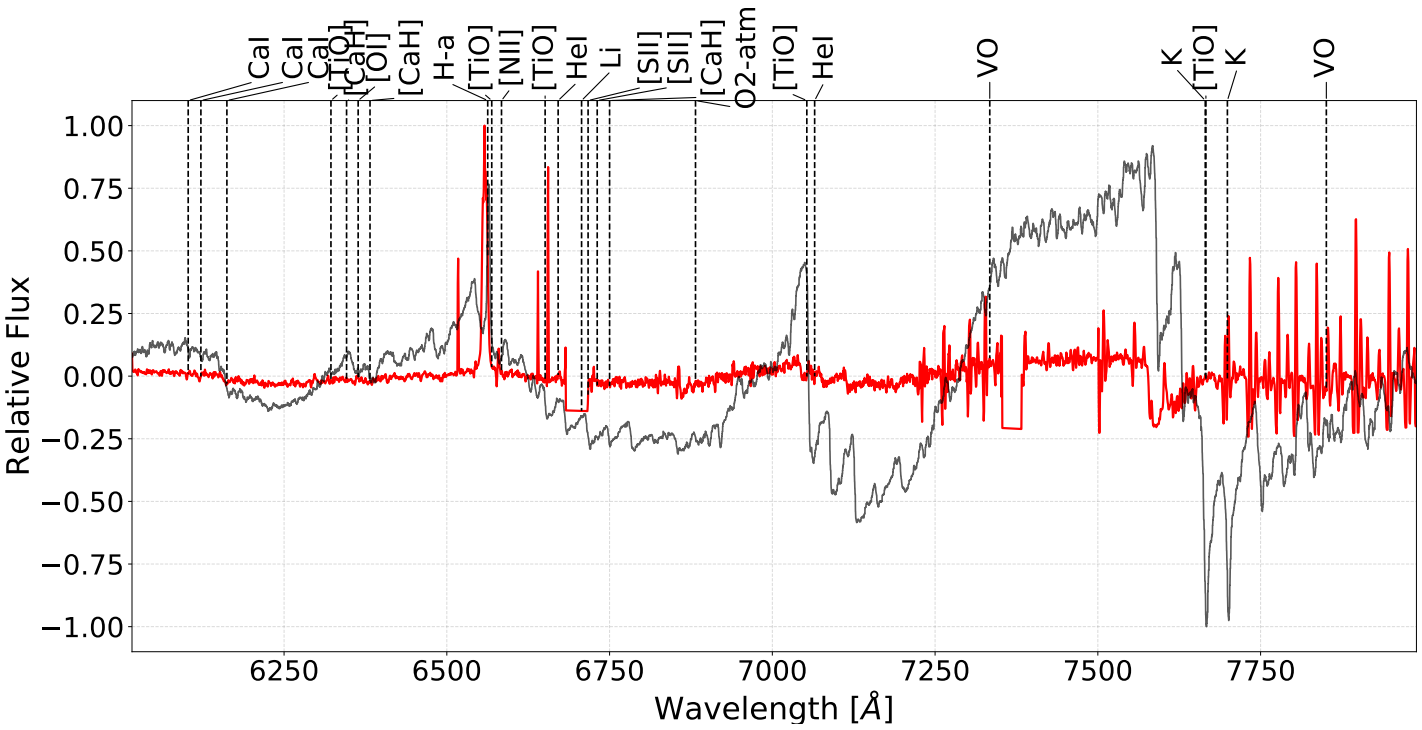

Figure C.2: Slit 7 for in NGC 2626

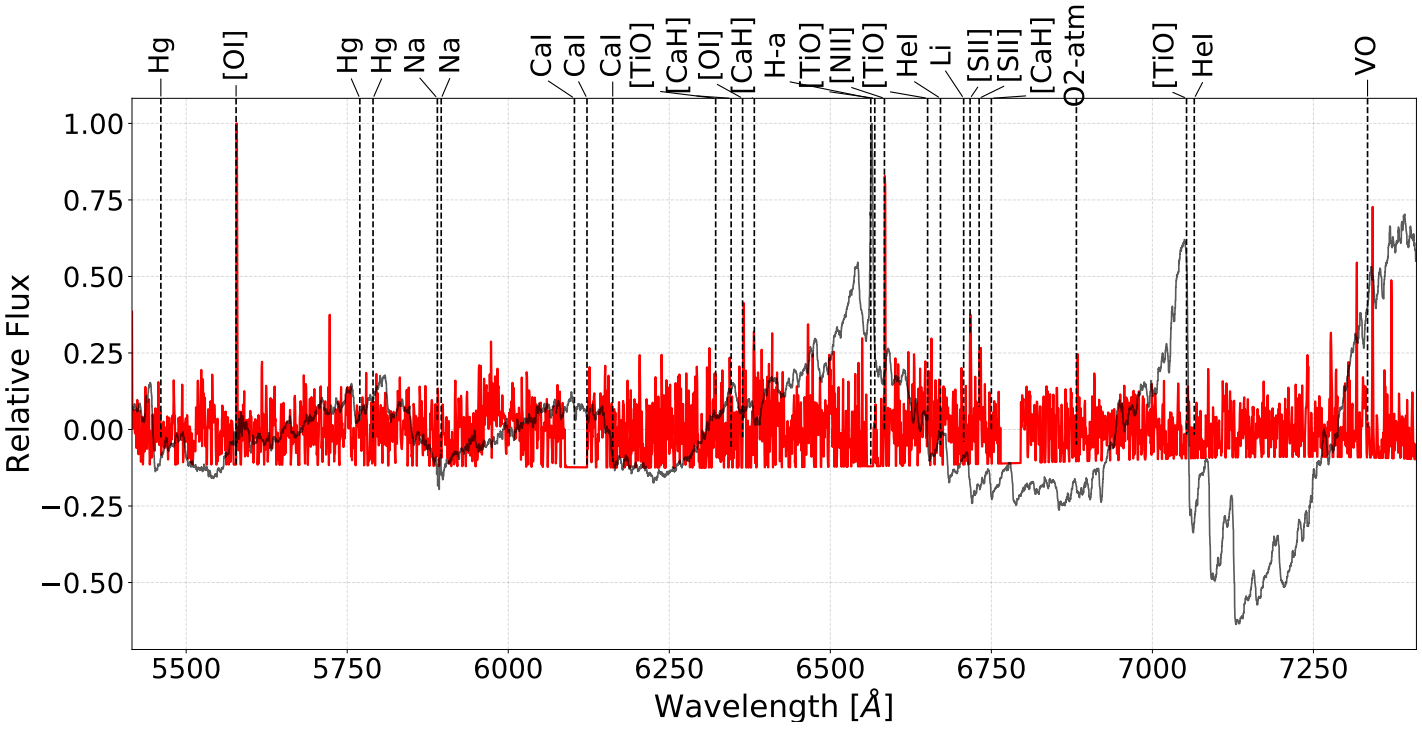

Figure C.3: Slit 9 for in NGC 2626

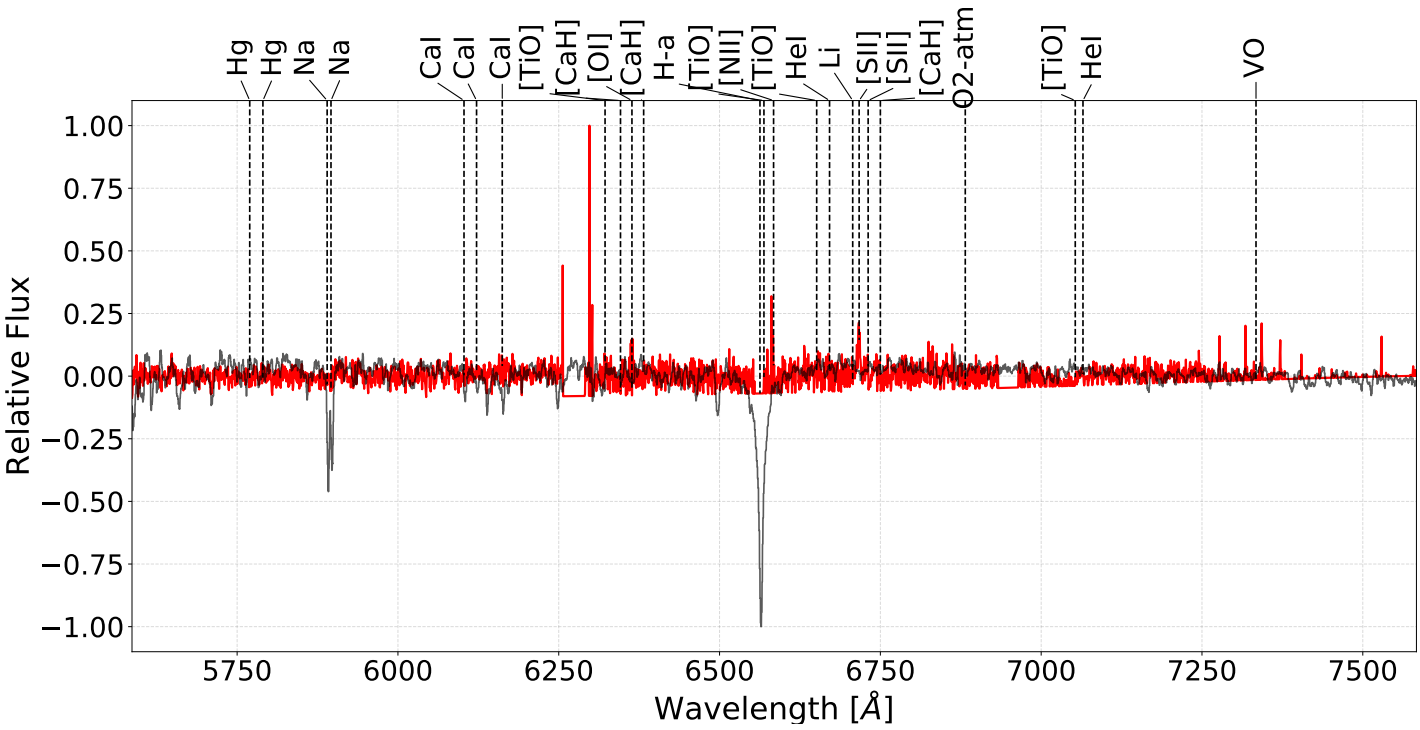

Figure C.4: Slit 11 for in NGC 2626

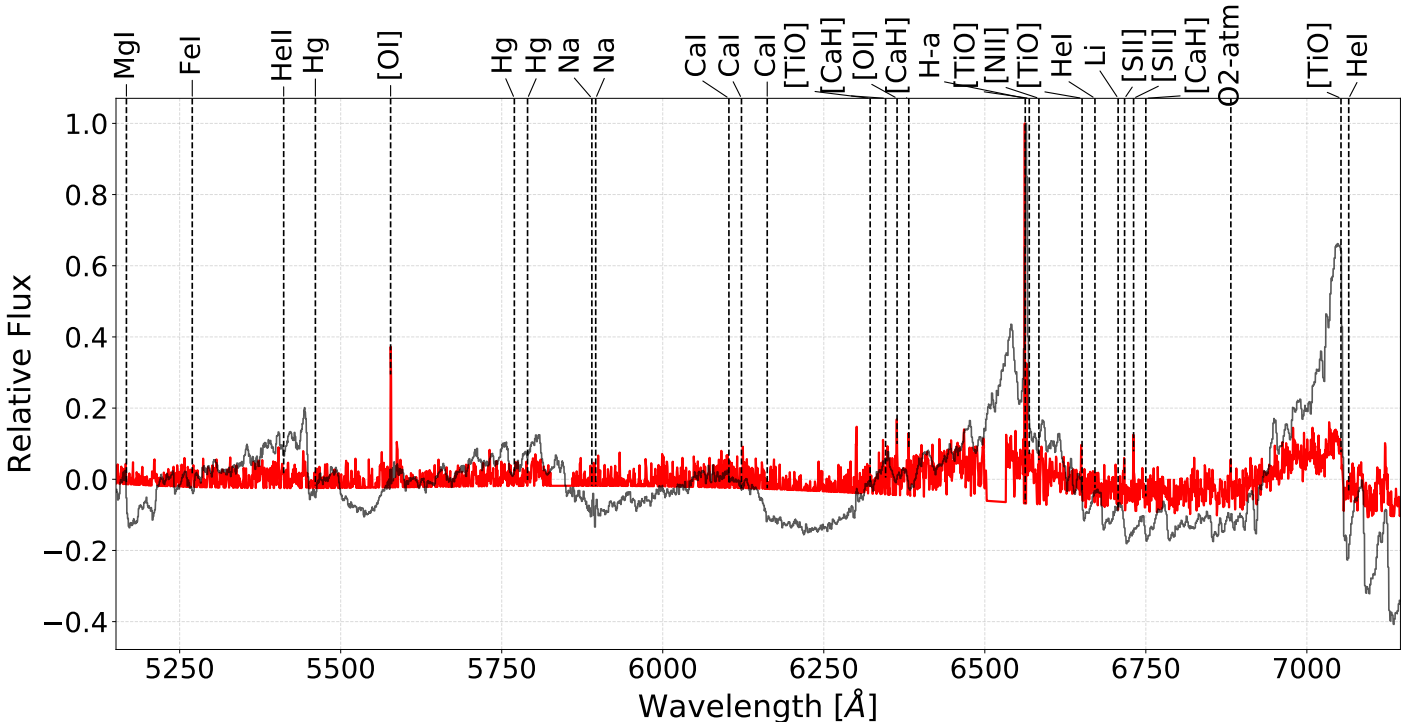

Figure C.5: Slit 12 for in NGC 2626

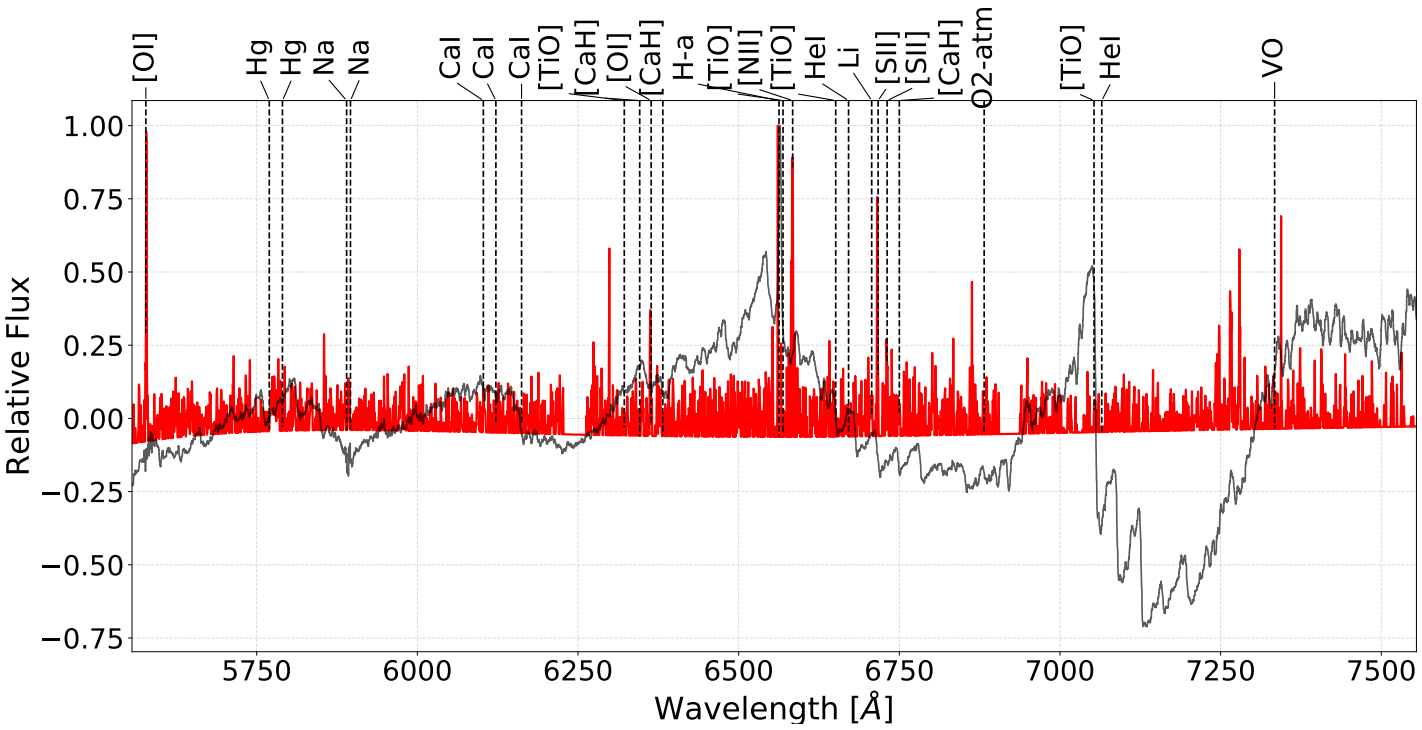

Figure C.6: Slit 13 for in NGC 2626

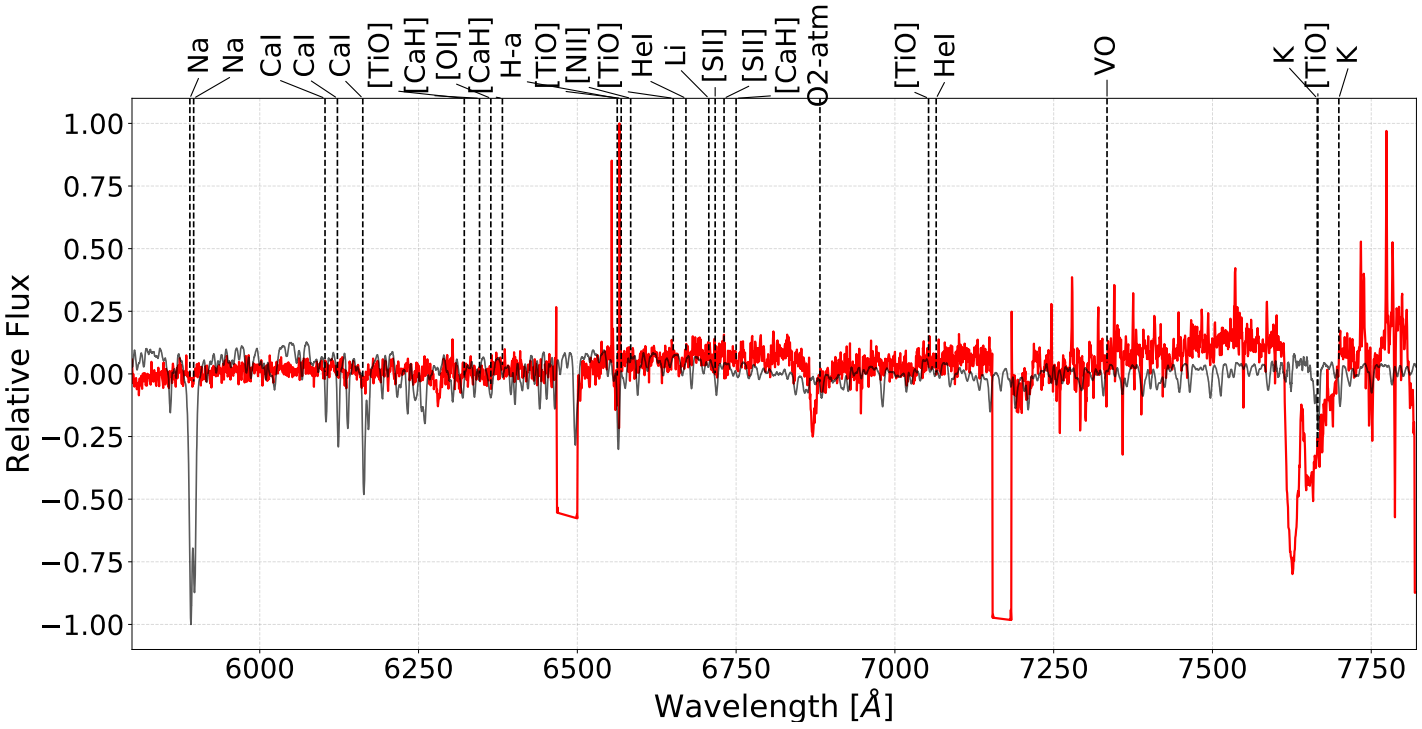

Figure C.7: Slit 14 for in NGC 2626

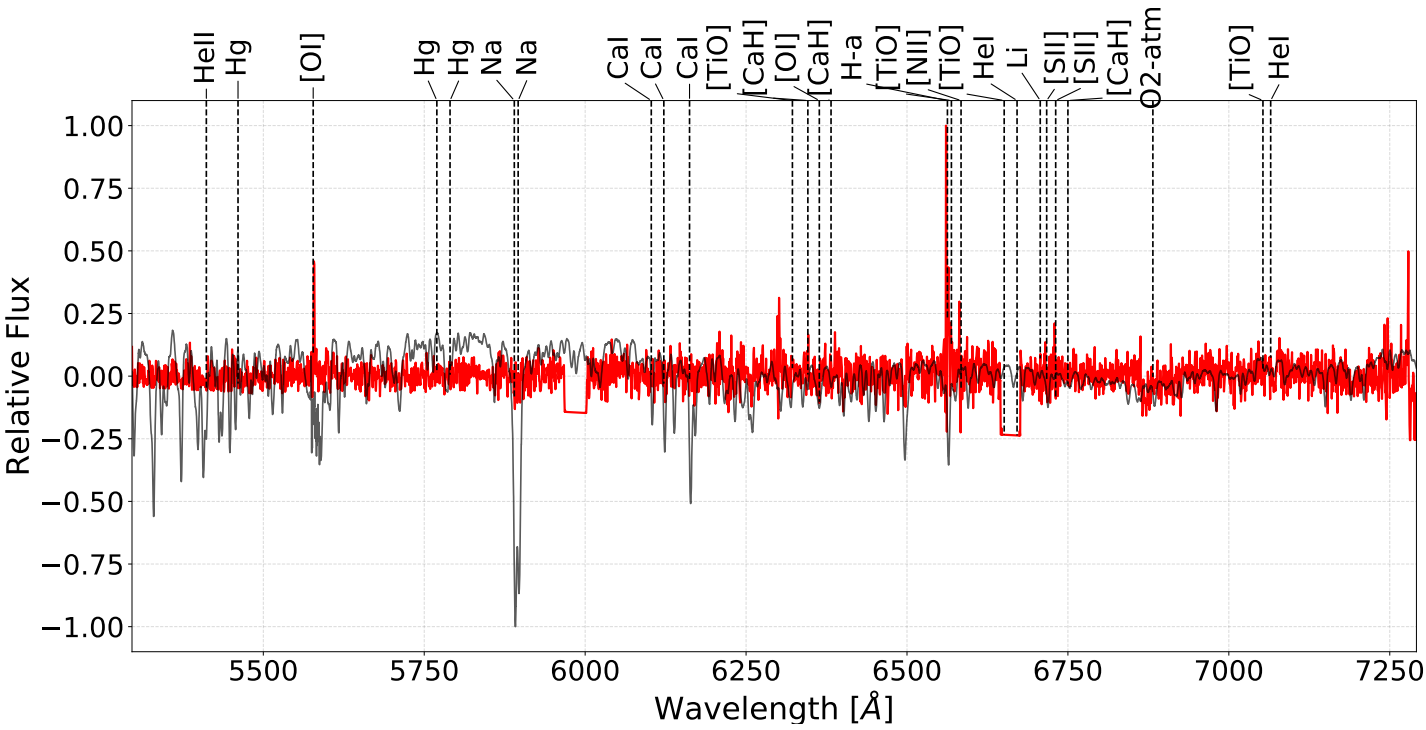

Figure C.8: Slit 16 for in NGC 2626

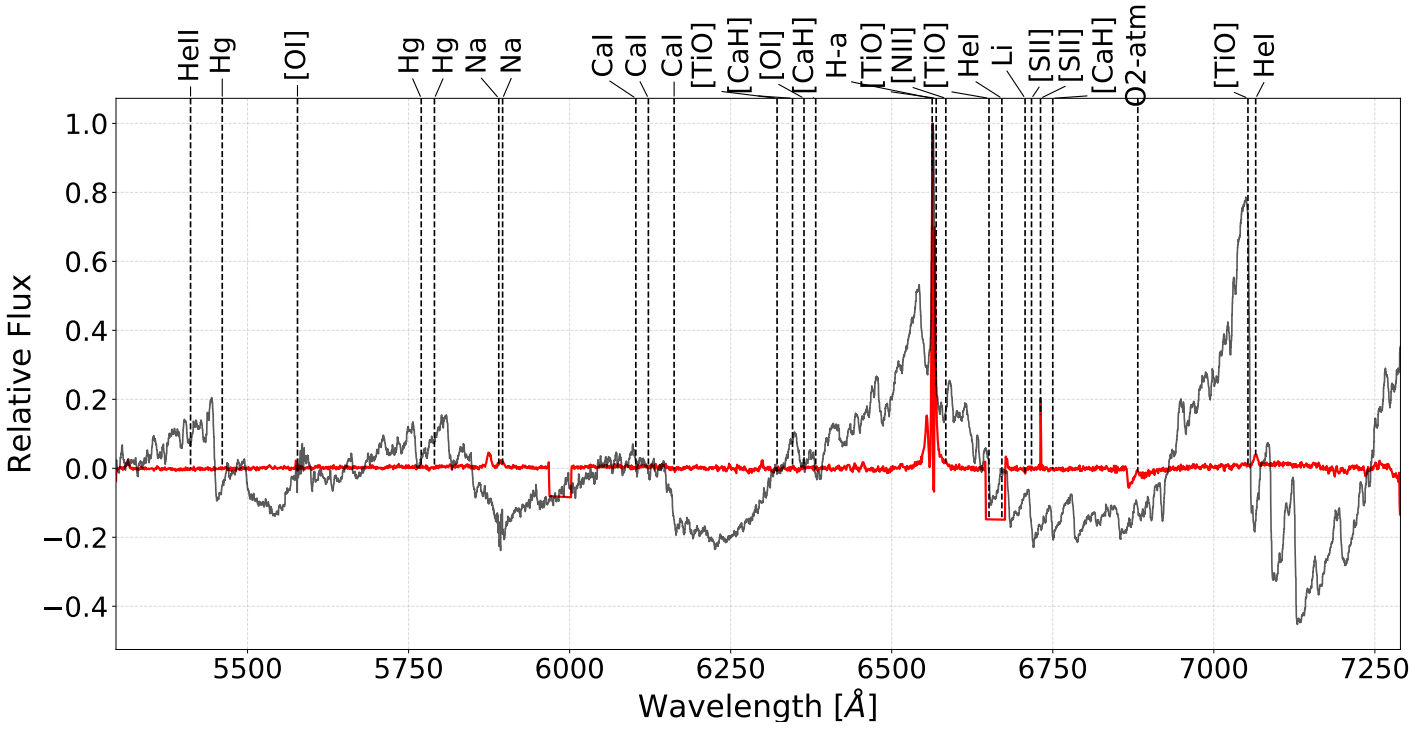

Figure C.9: Slit 17 for in NGC 2626

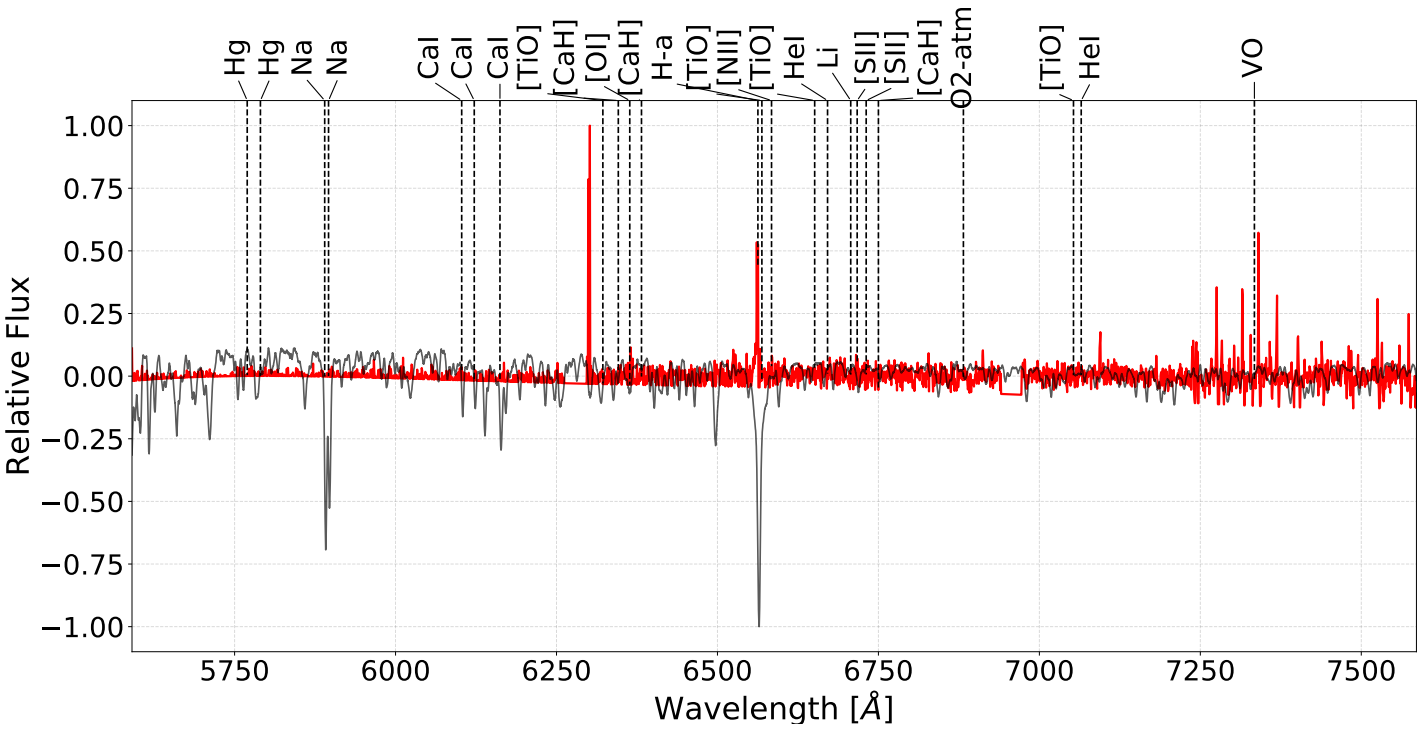

Figure C.10: Slit 18 for in NGC 2626

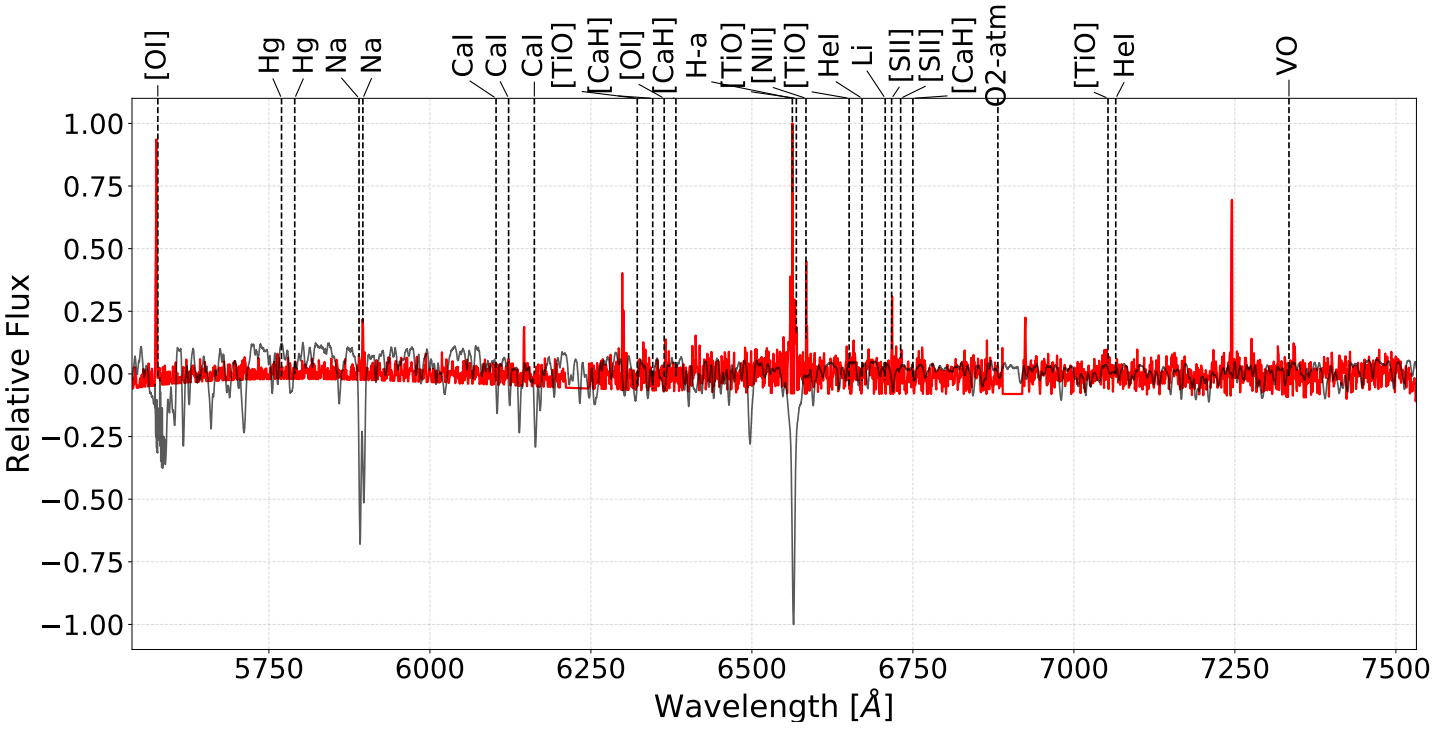

Figure C.11: Slit 19 for in NGC 2626

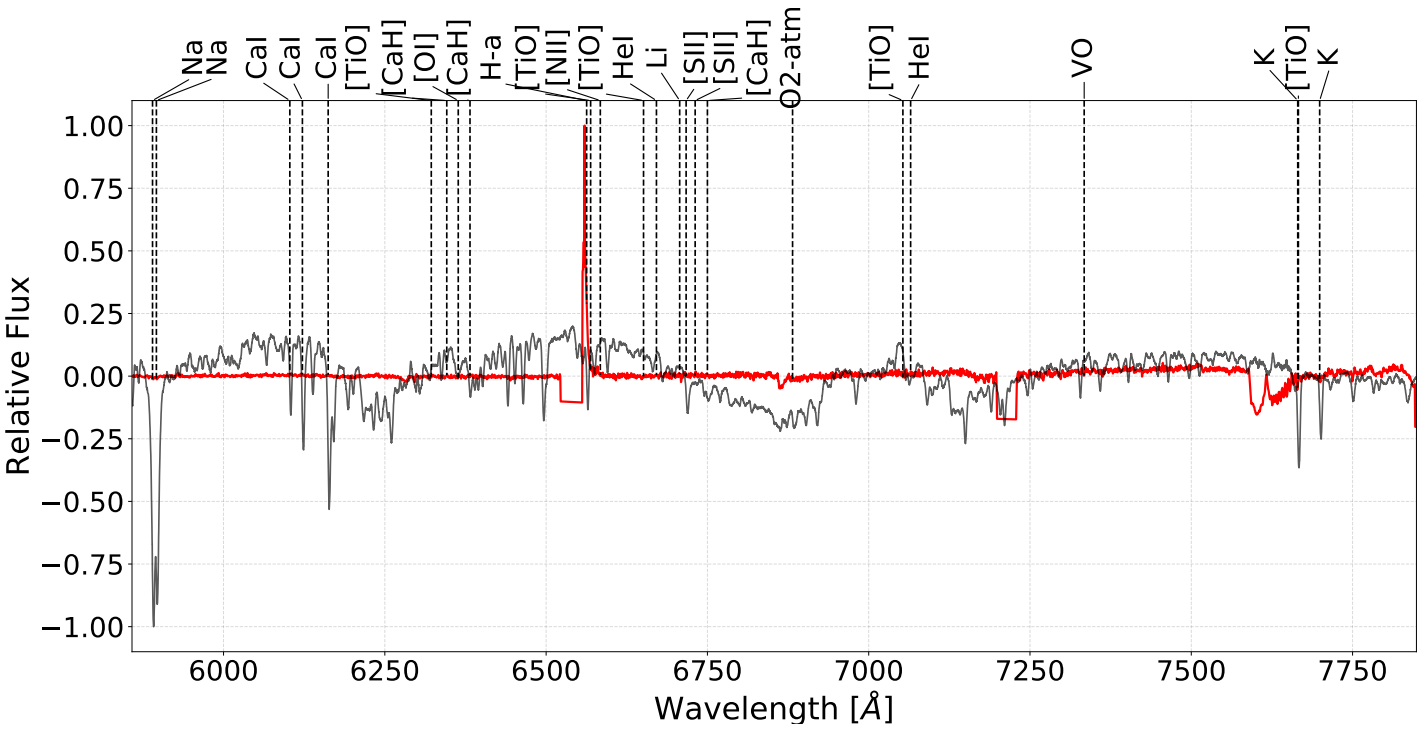

Figure C.12: Slit 20 for in NGC 2626

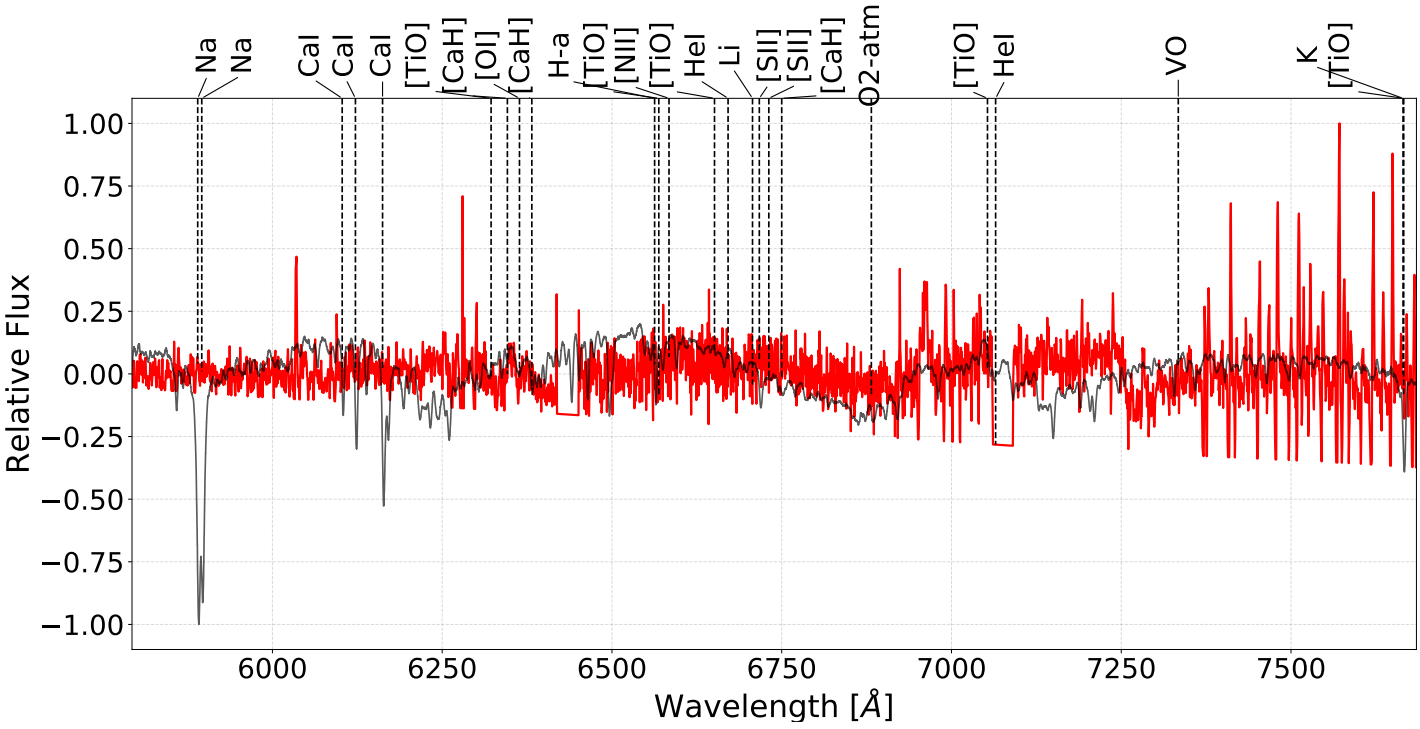

Figure C.13: Slit 22 for in NGC 2626

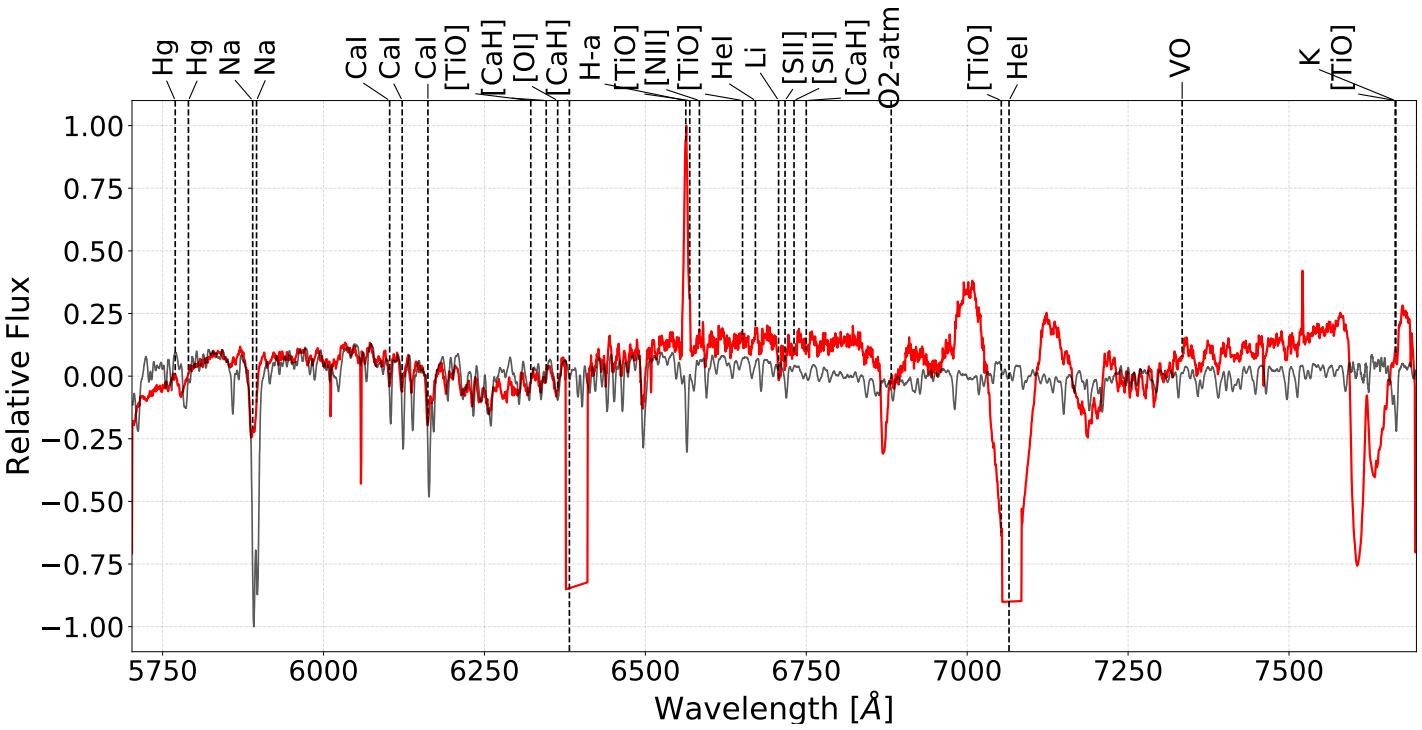

Figure C.14: Slit 23 for in NGC 2626

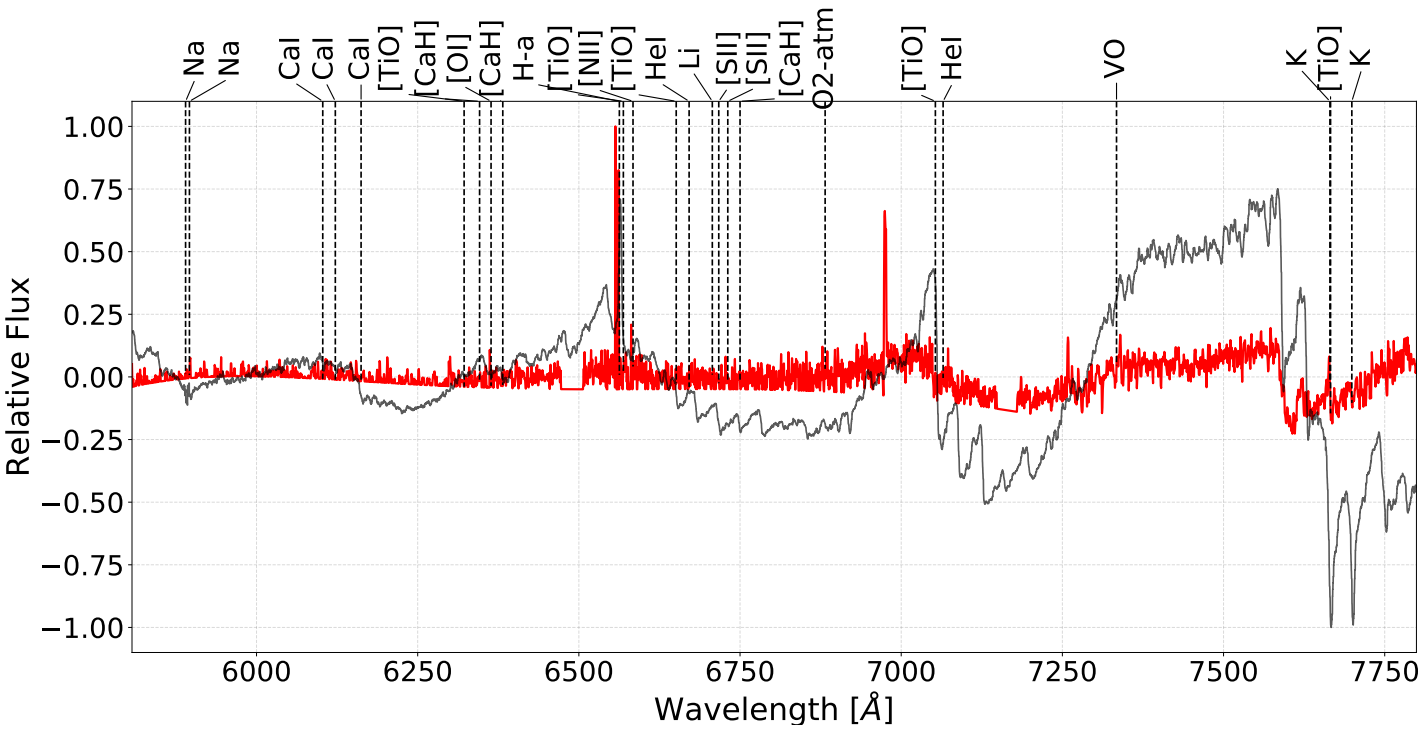

Figure C.15: Slit 24 for in NGC 2626

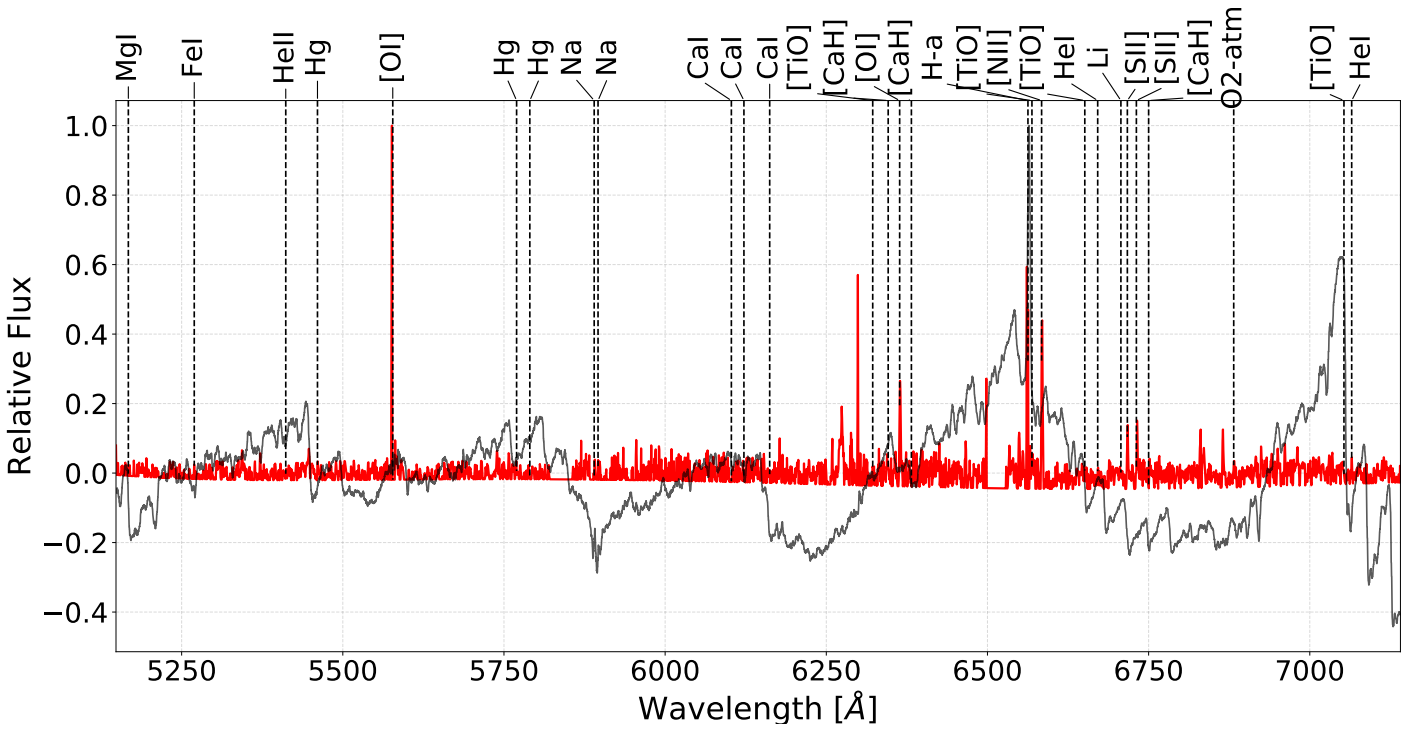

Figure C.16: Slit 25 for in NGC 2626

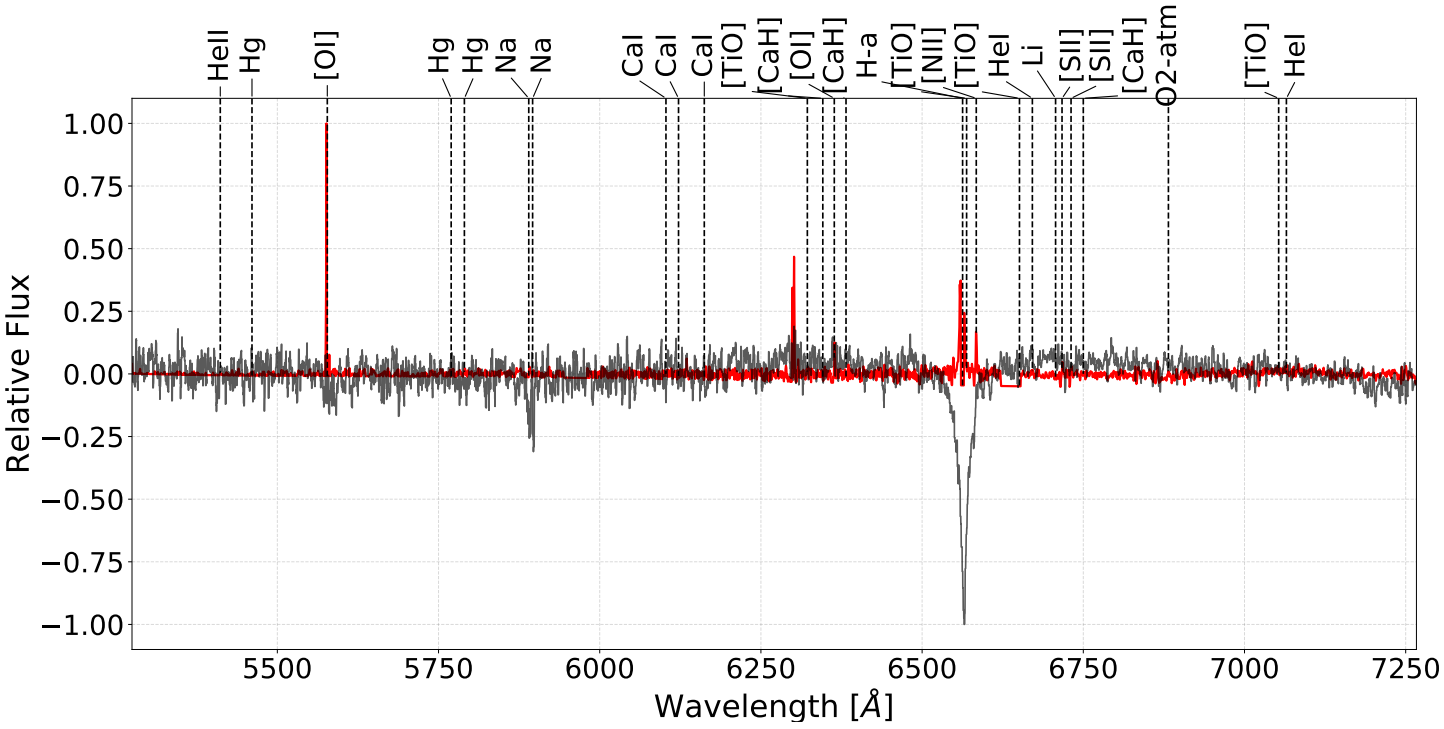

Figure C.17: Slit 26 for in NGC 2626

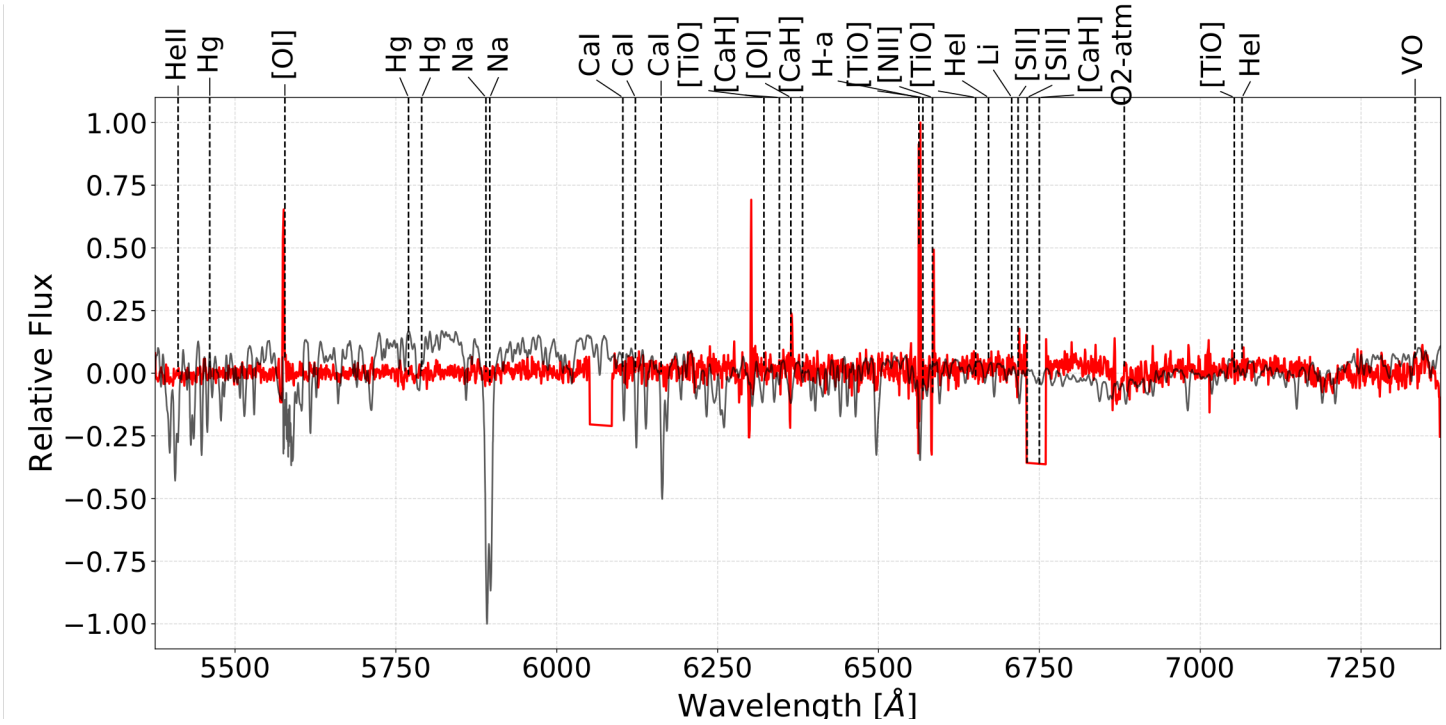

Figure C.18: Slit 27 for in NGC 2626

Hα-absorption line stars

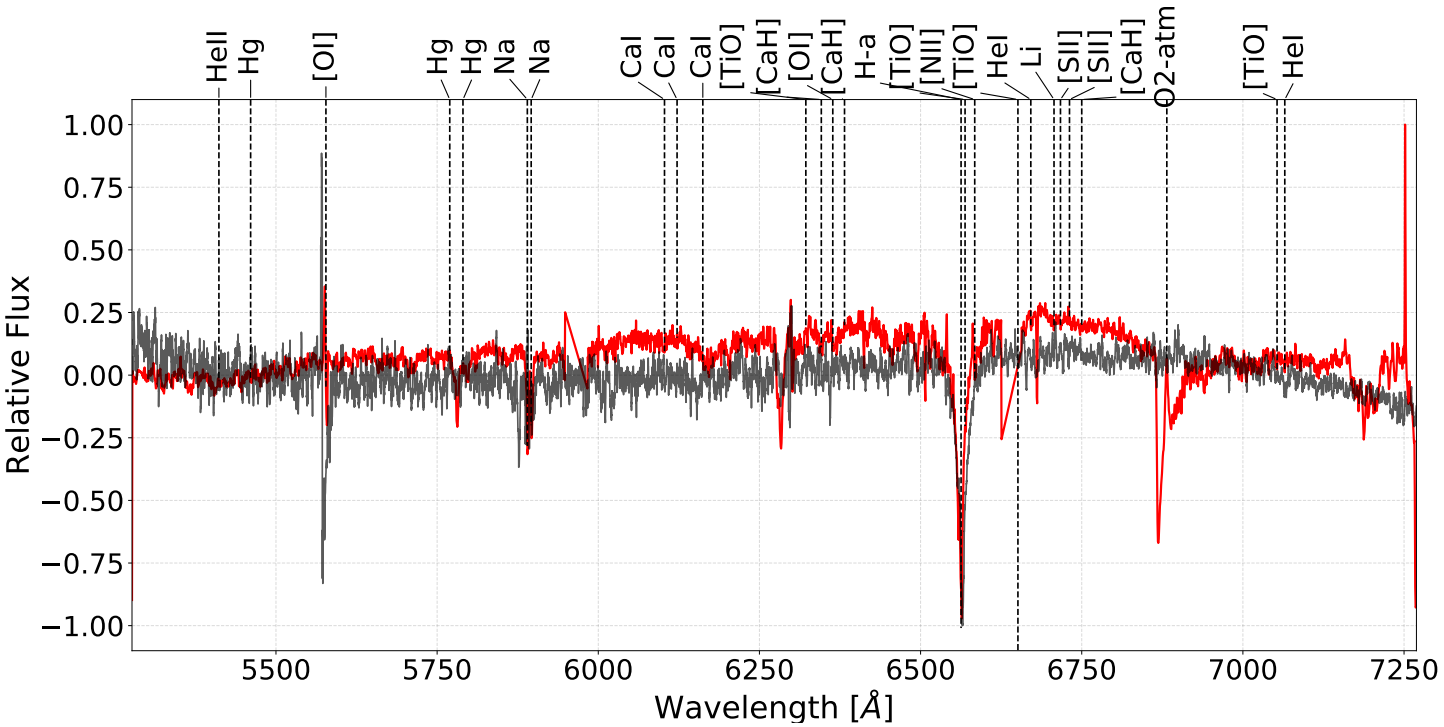

Figure C.19: Slit 1 for in NGC 2626

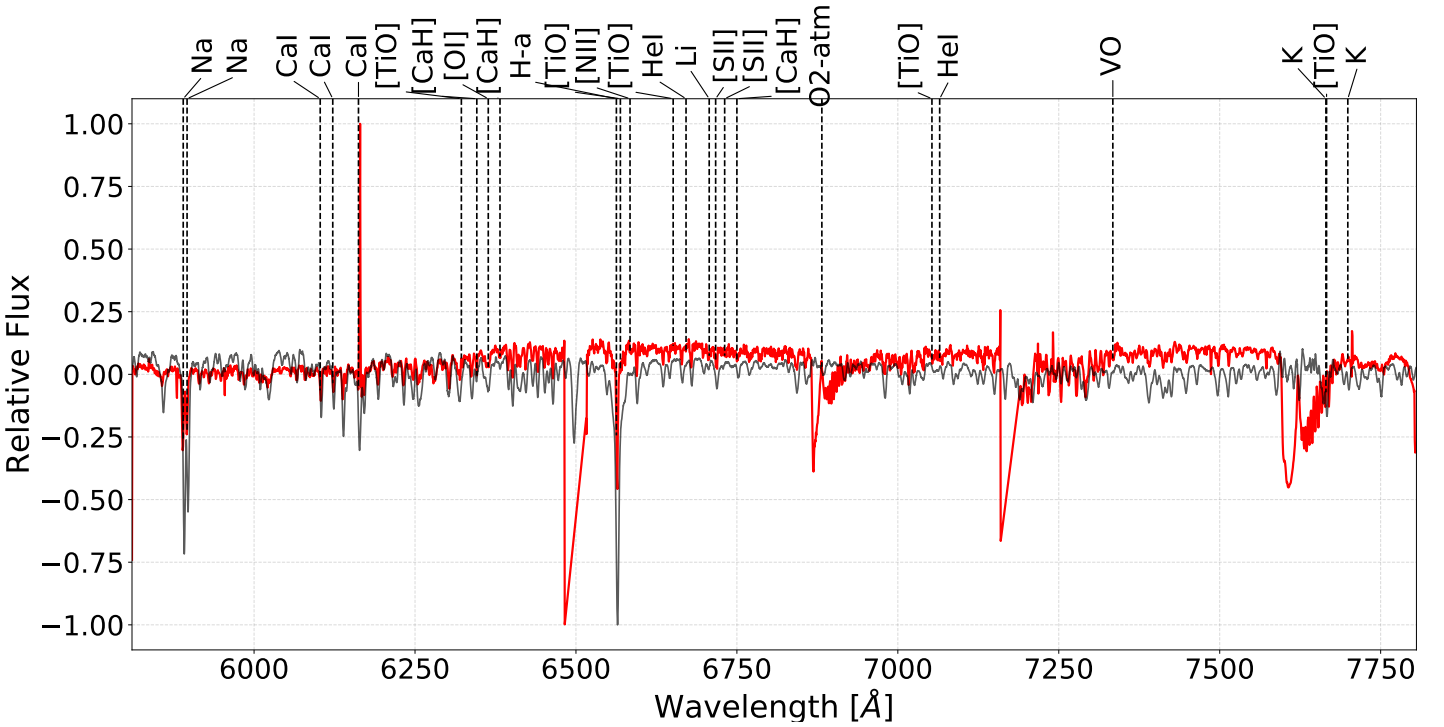

Figure C.20: Slit 2 for in NGC 2626

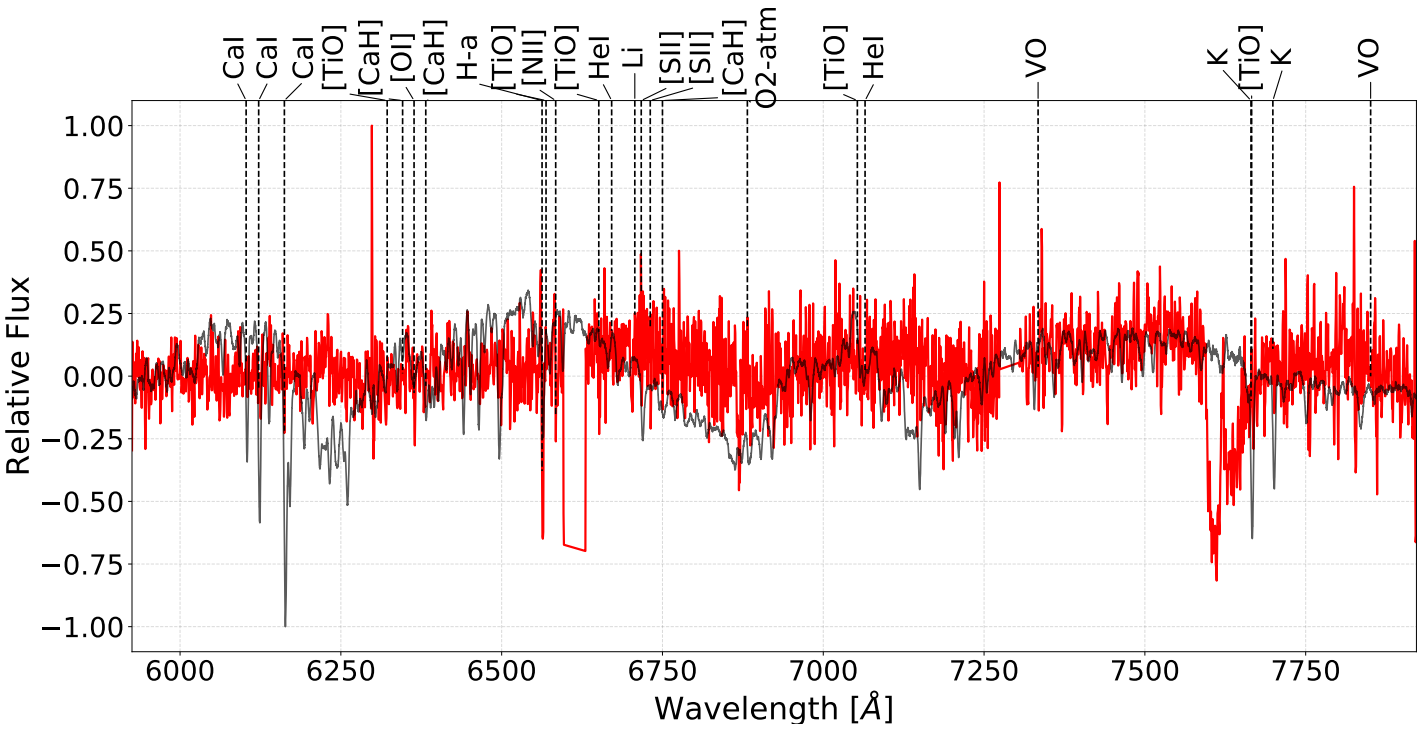

Figure C.21: Slit 4 for in NGC 2626

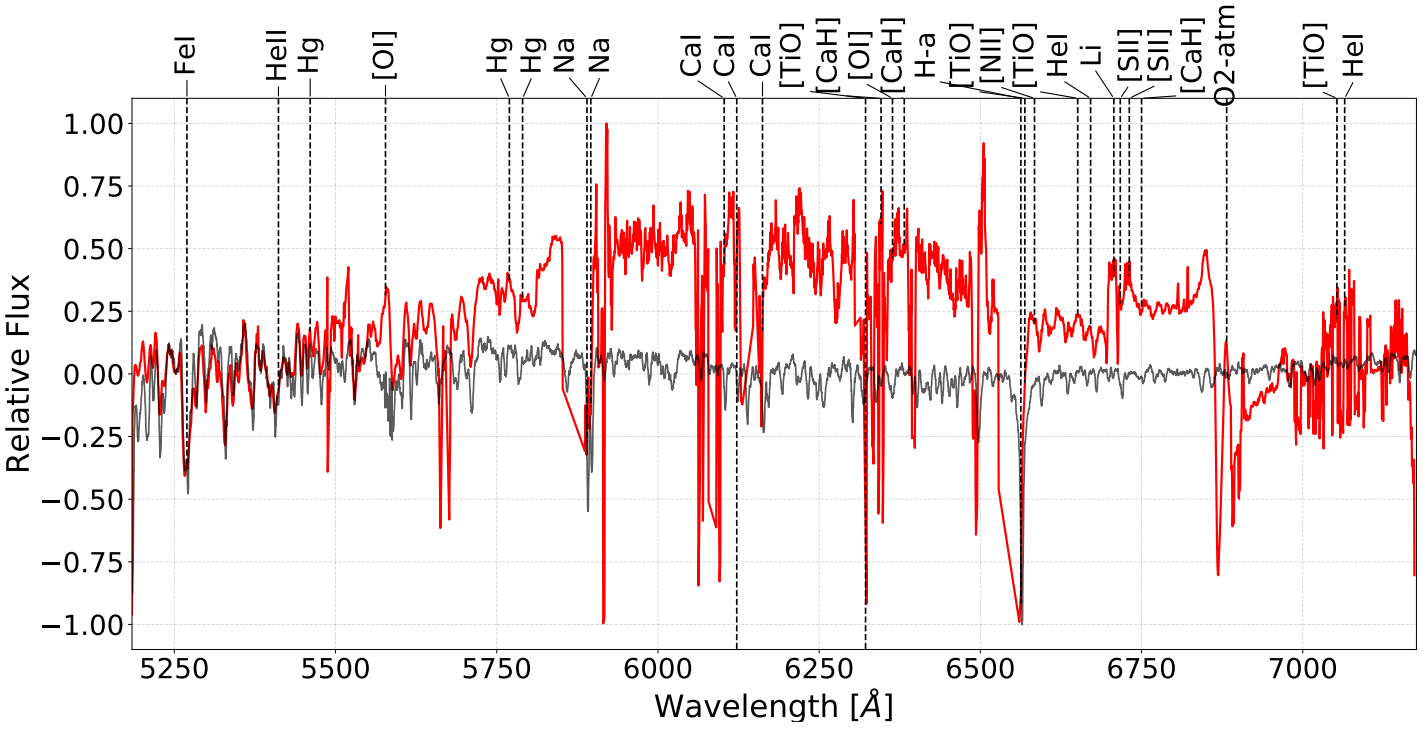

Figure C.22: Slit 6 for in NGC 2626

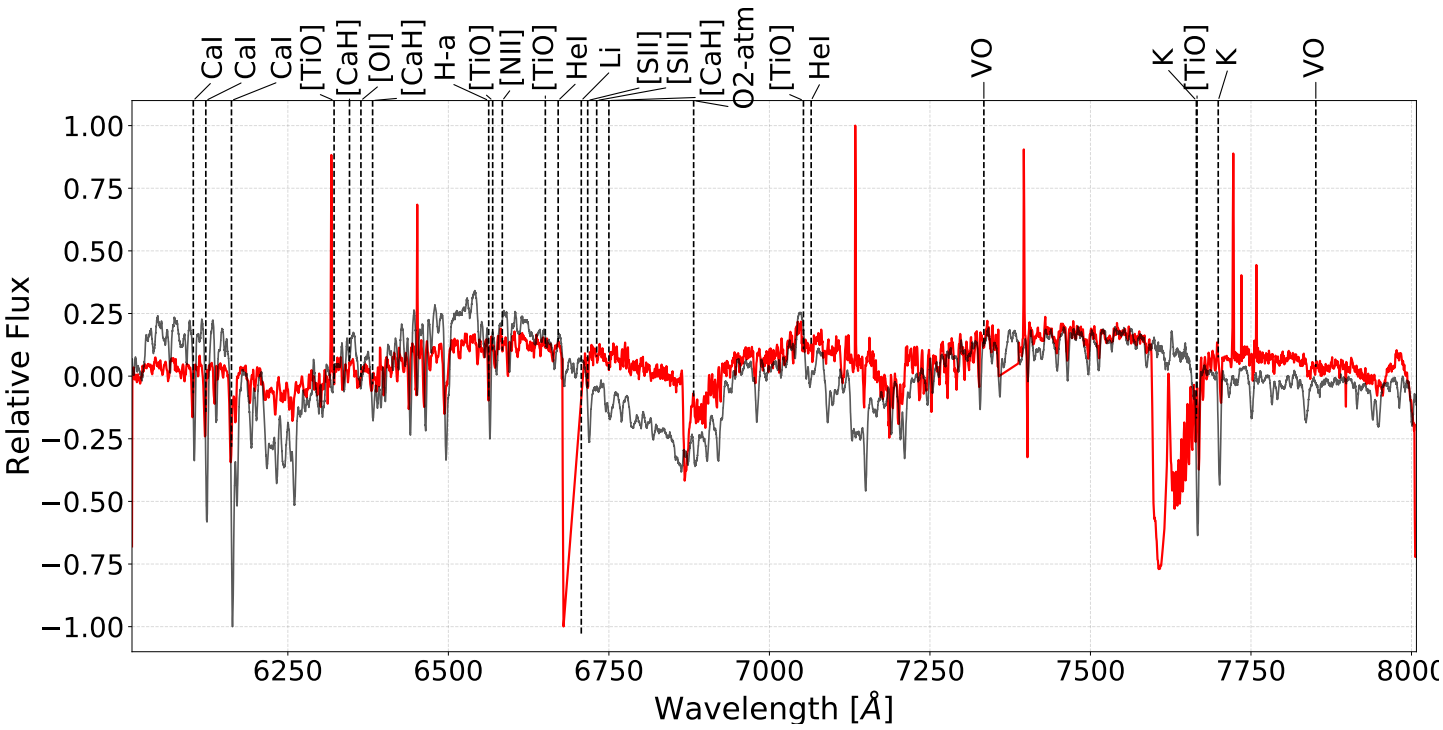

Figure C.23: Slit 8 for in NGC 2626

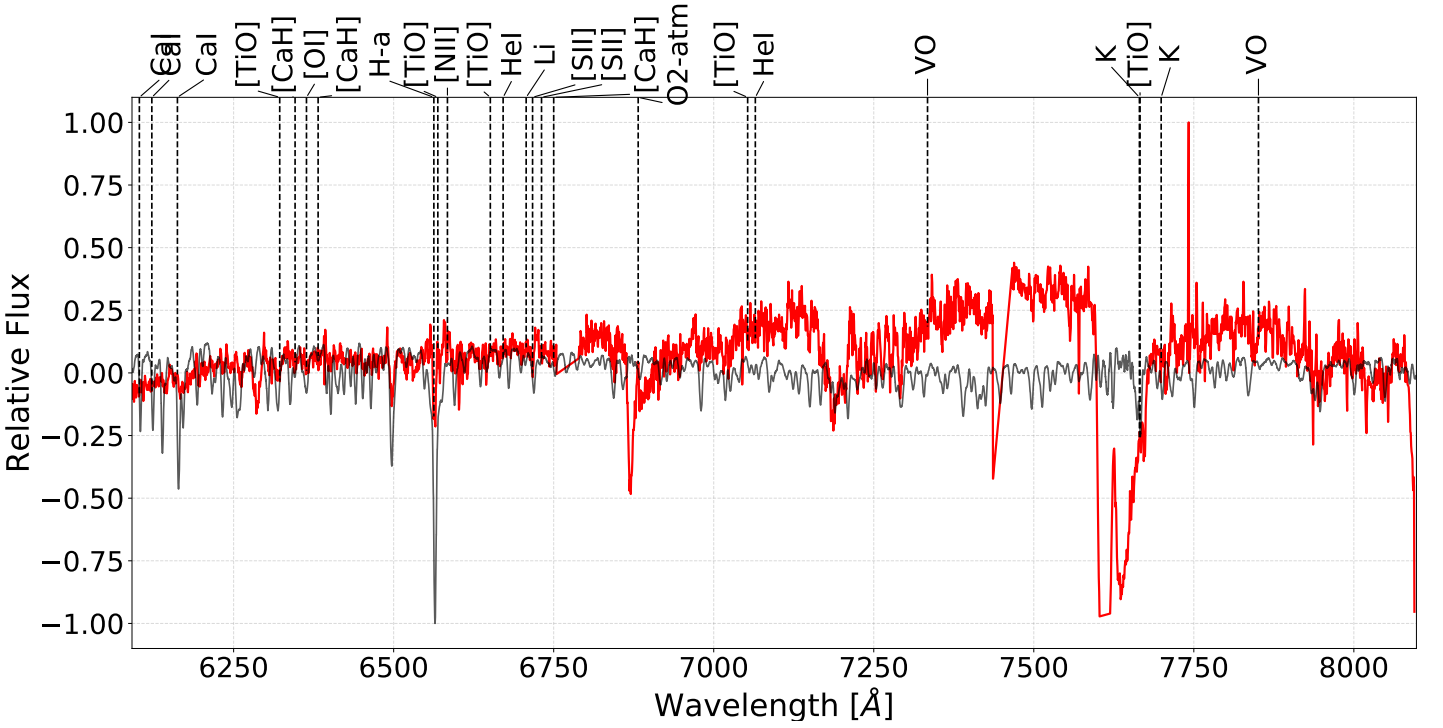

Figure C.24: Slit 10 for in NGC 2626

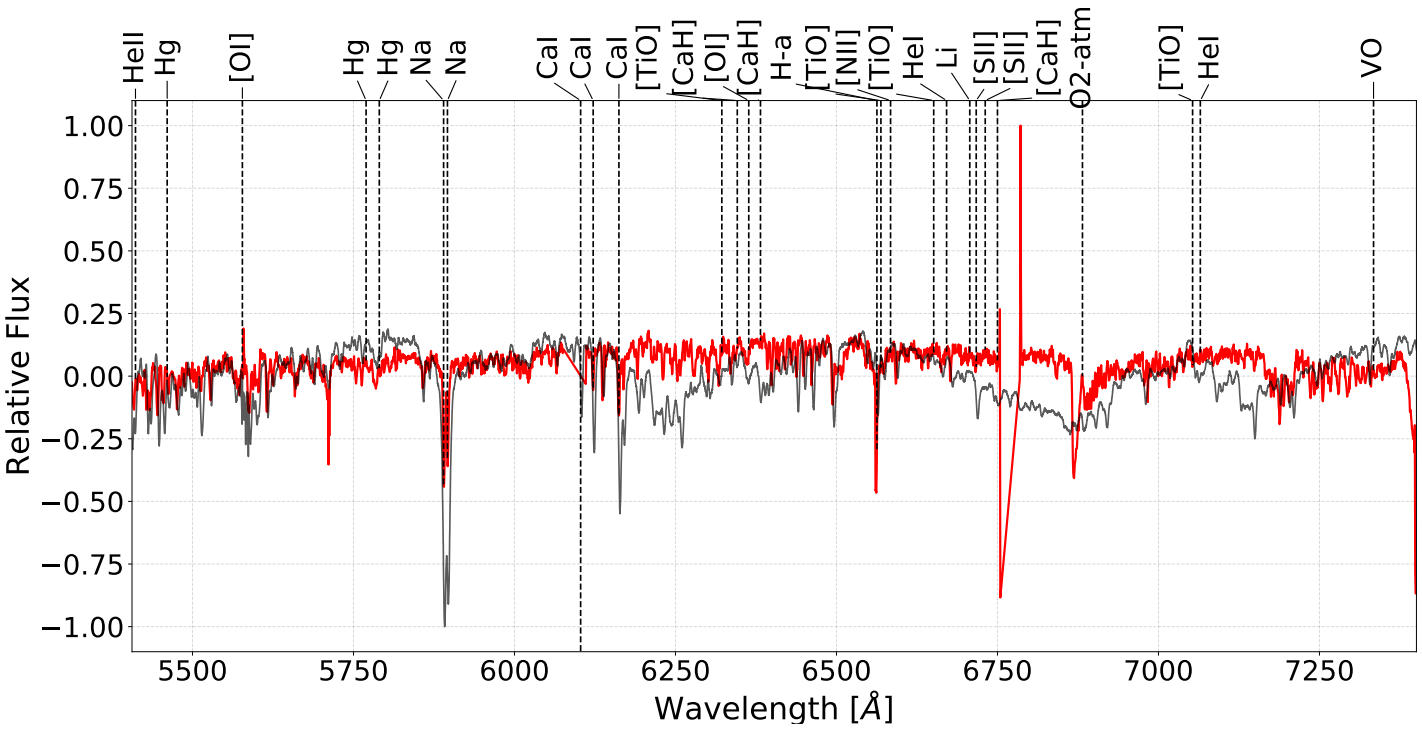

Figure C.25: Slit 15 for in NGC 2626

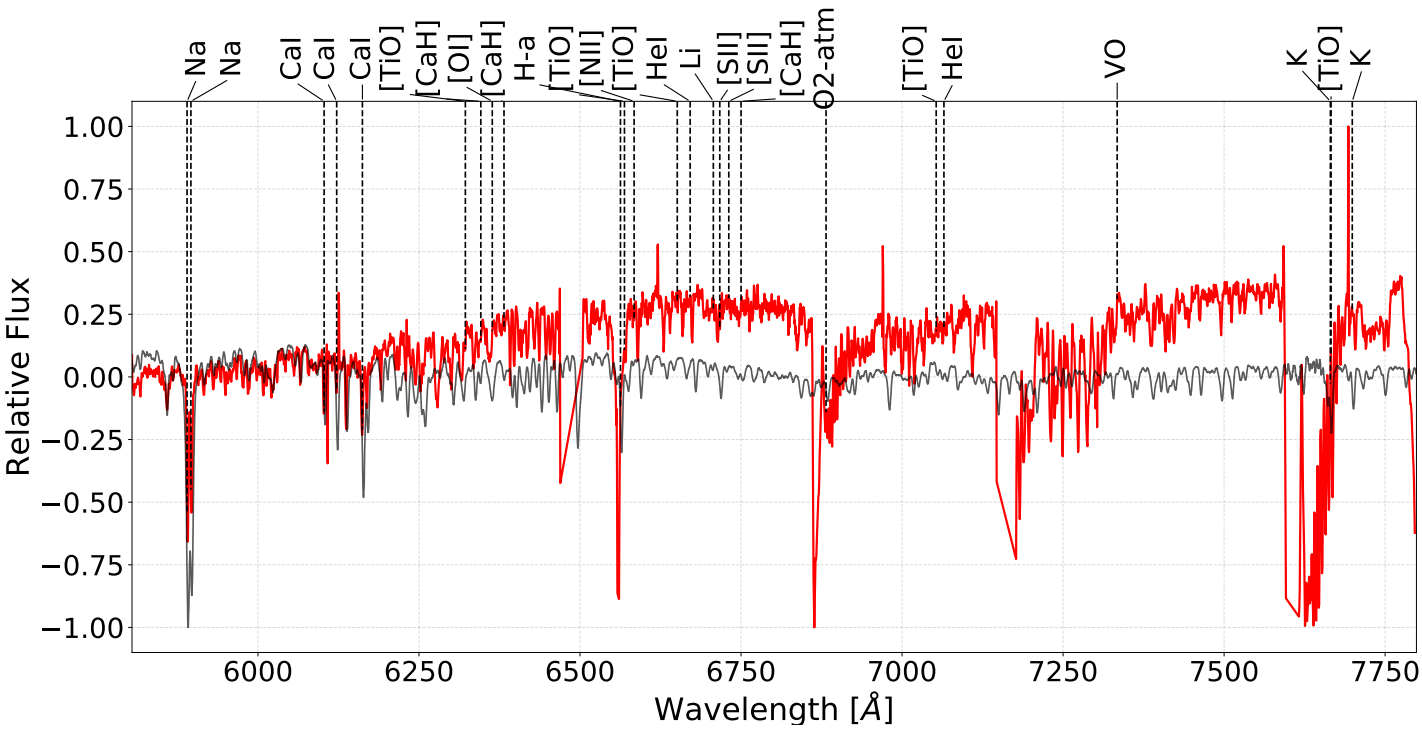

Figure C.26: Slit 21 for in NGC 2626

Stars with an undetermined Hα line

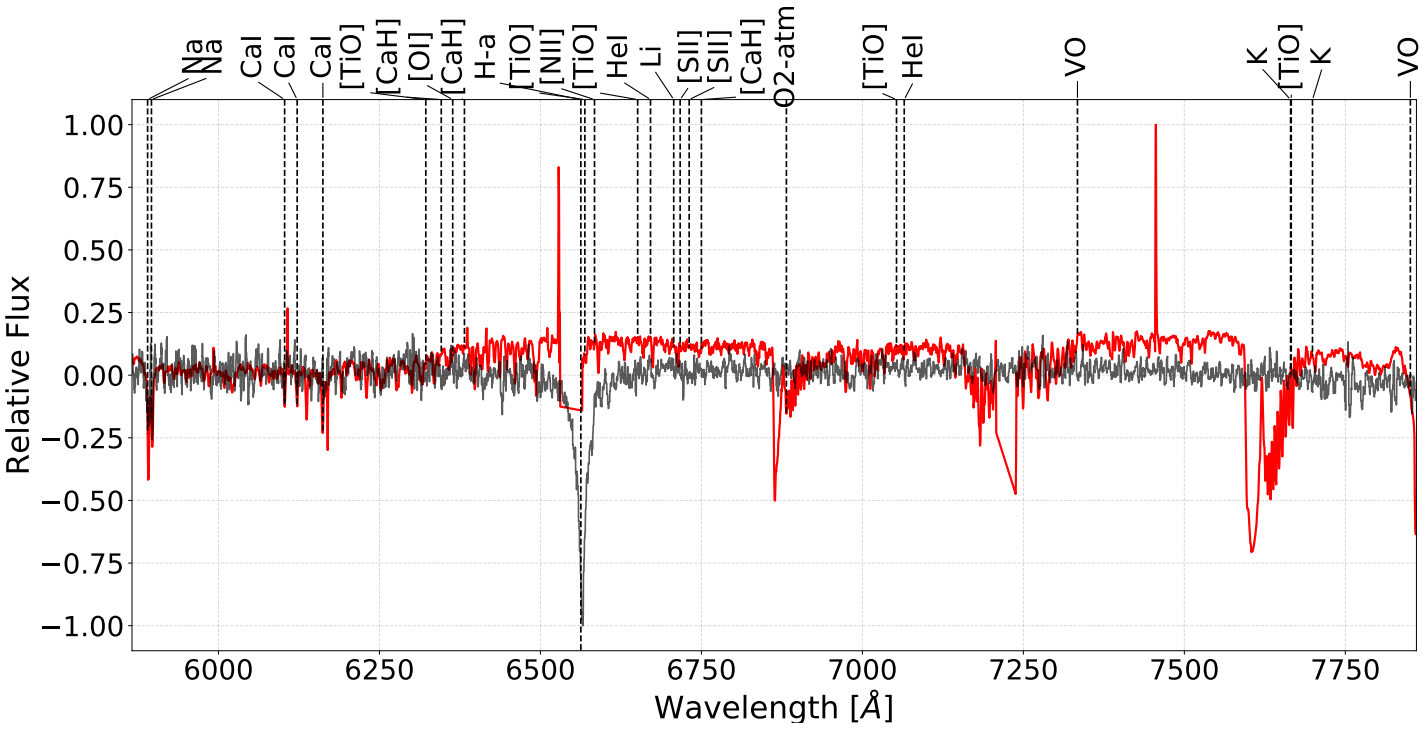

Figure C.27: Slit 3 for in NGC 2626

Blue spectrum of stars

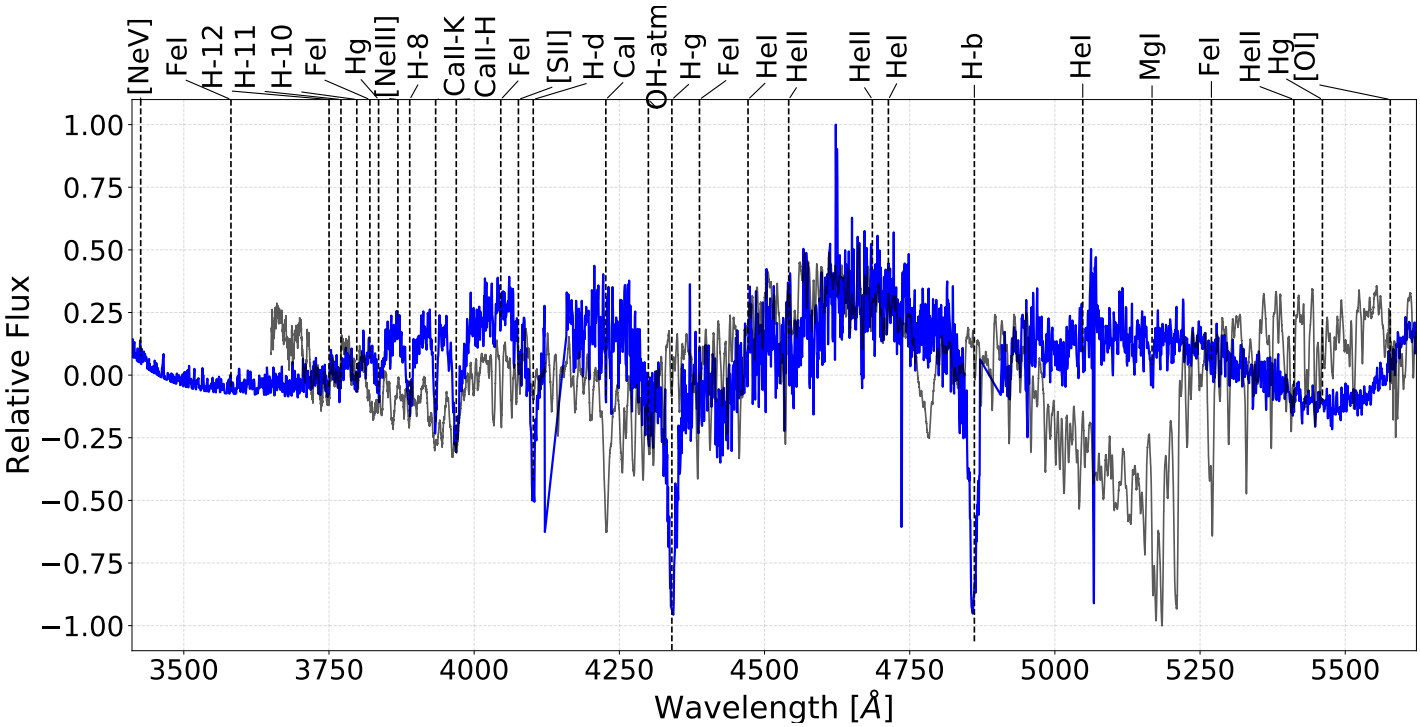

Figure C.28: Slit 1 for in NGC 2626

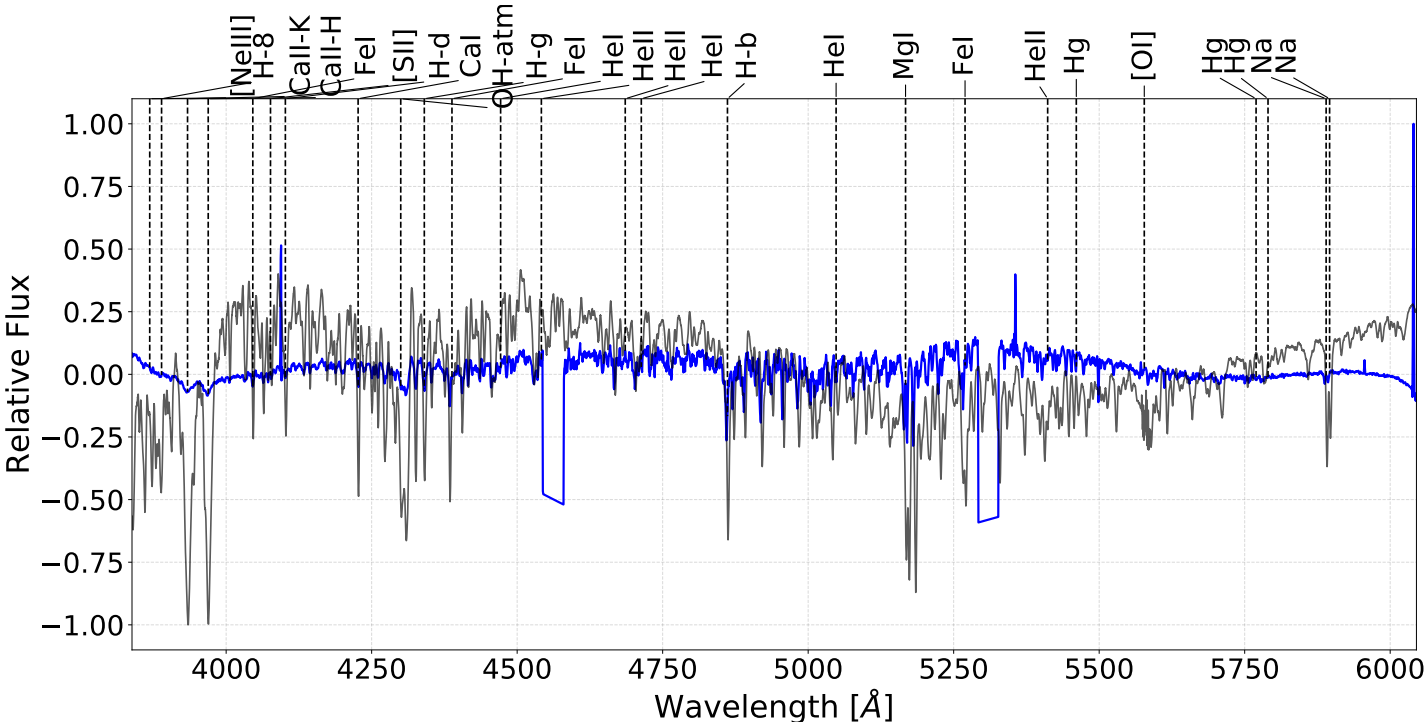

Figure C.29: Slit 2 for in NGC 2626

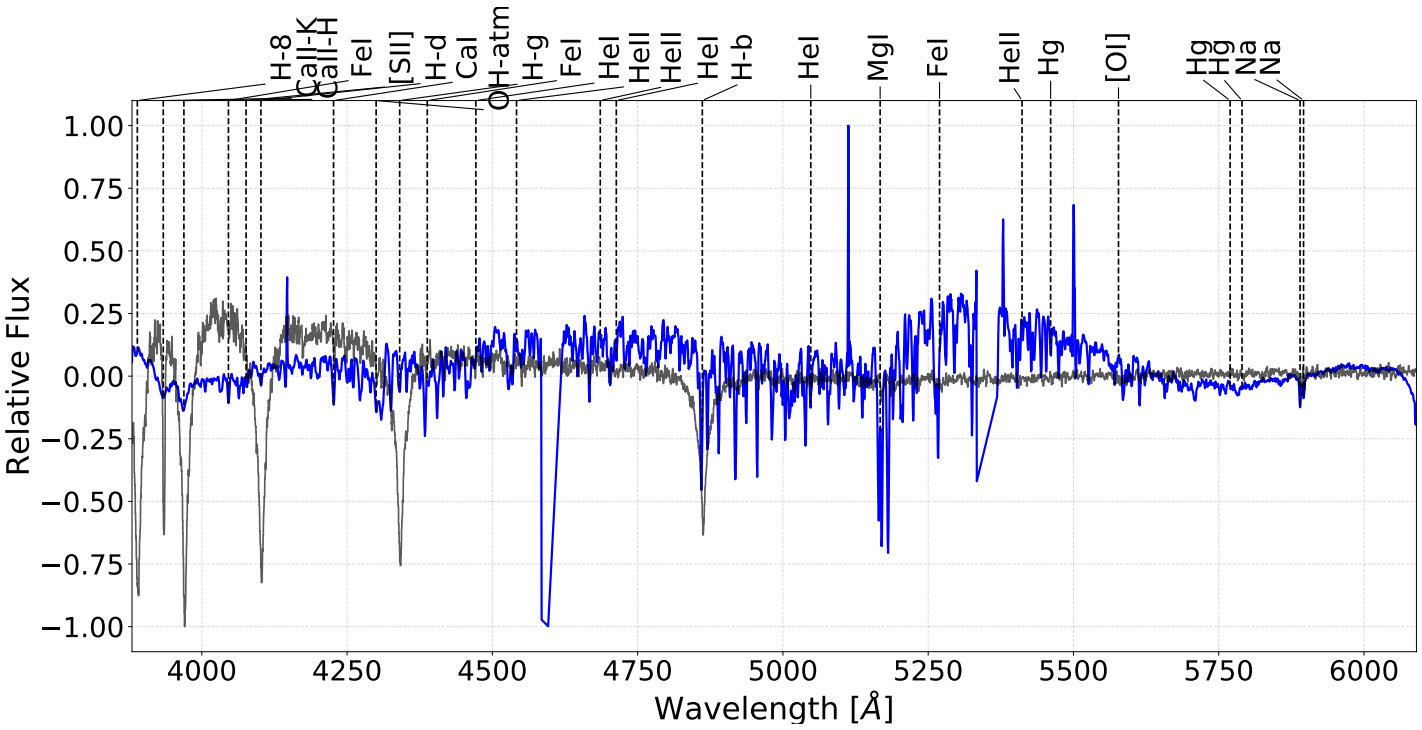

Figure C.30: Slit 3 for in NGC 2626

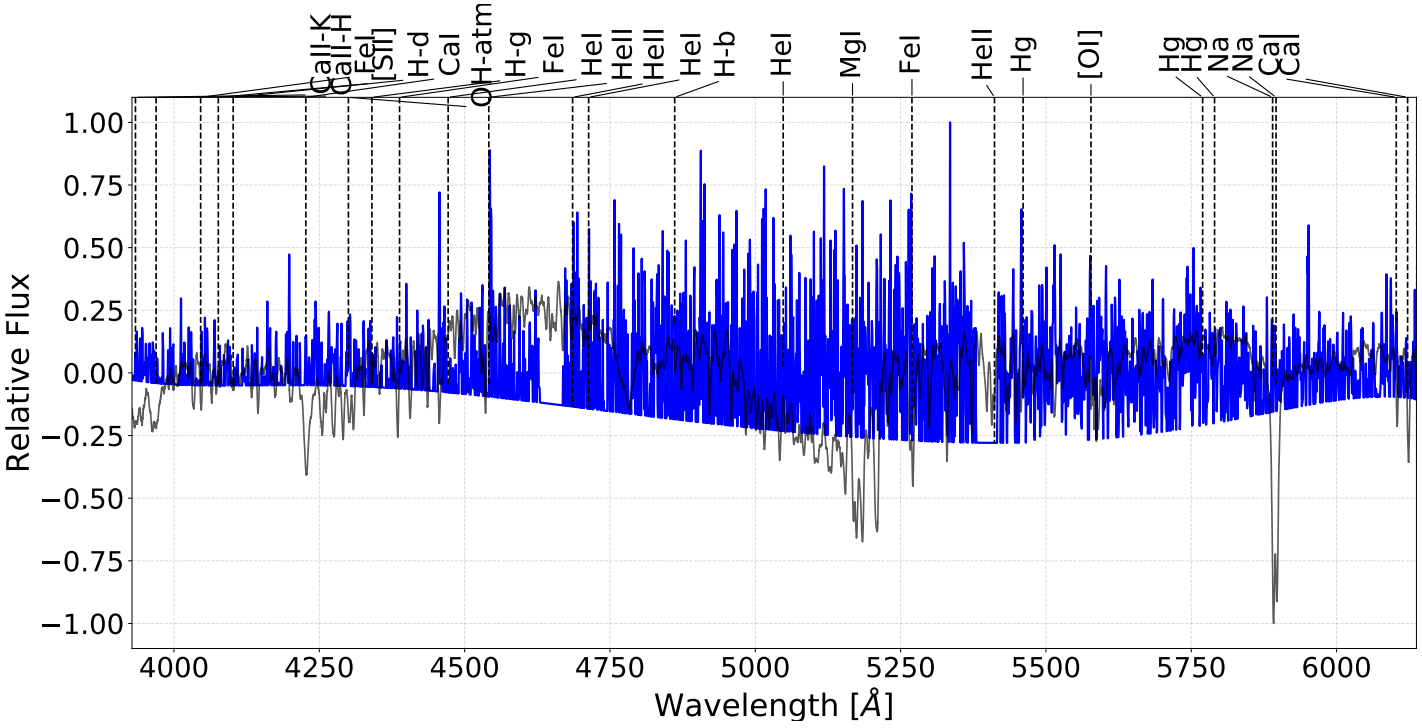

Figure C.31: Slit 4 for in NGC 2626

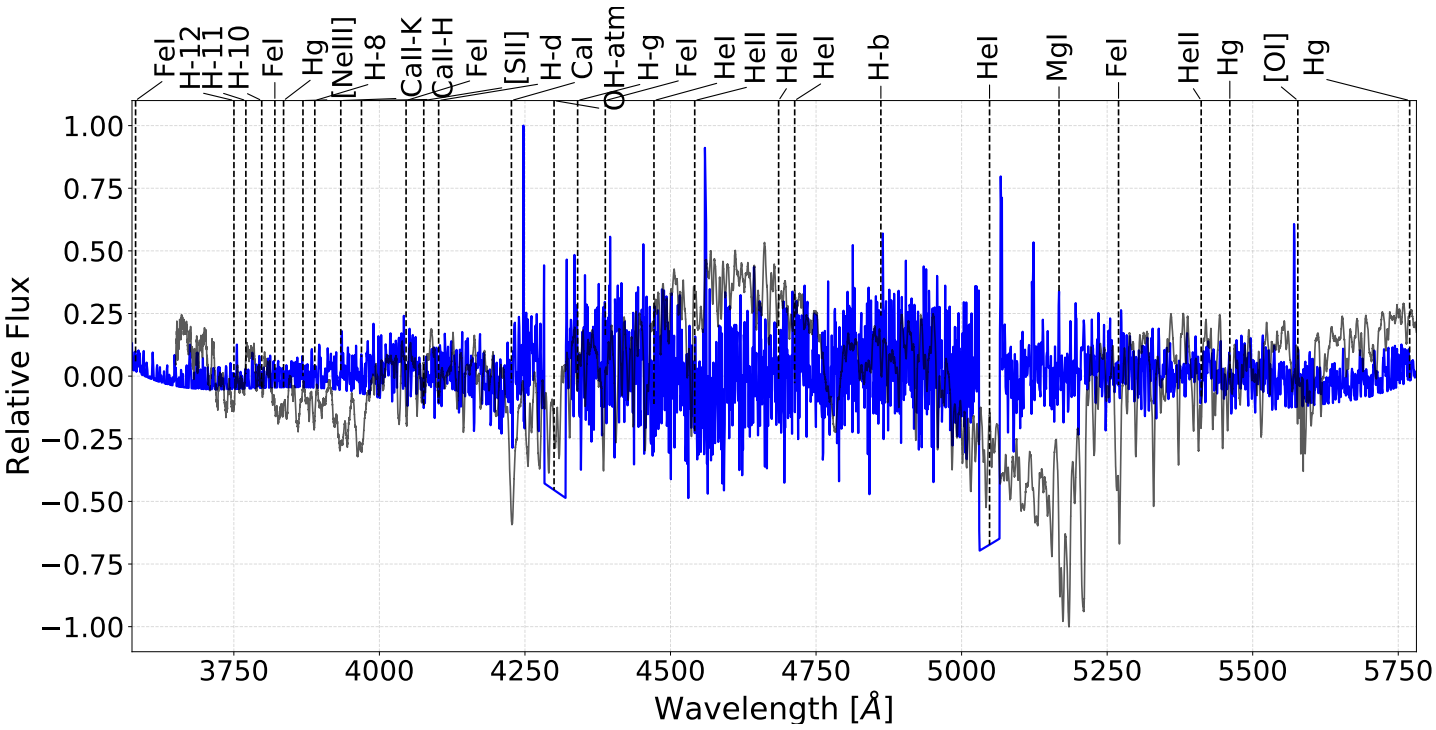

Figure C.32: Slit 5 for in NGC 2626

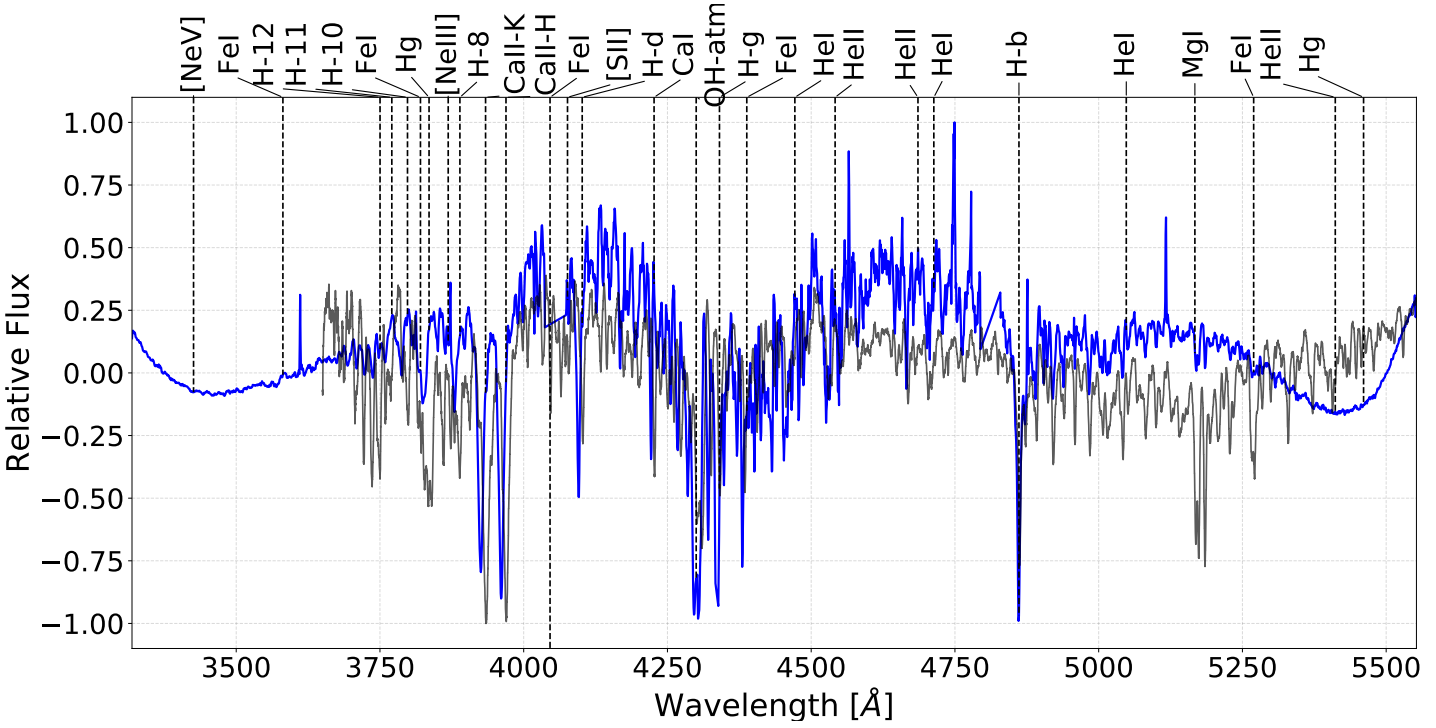

Figure C.33: Slit 6 for in NGC 2626

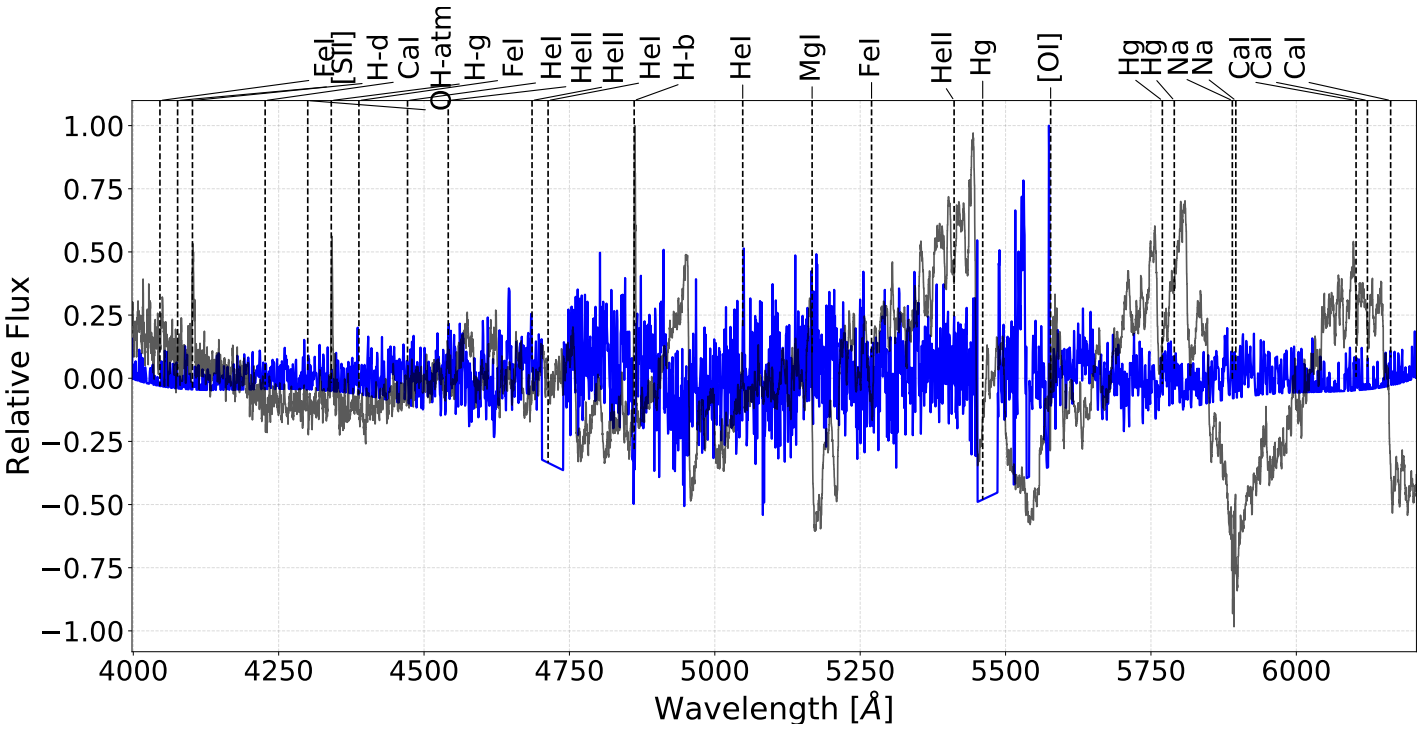

Figure C.34: Slit 7 for in NGC 2626

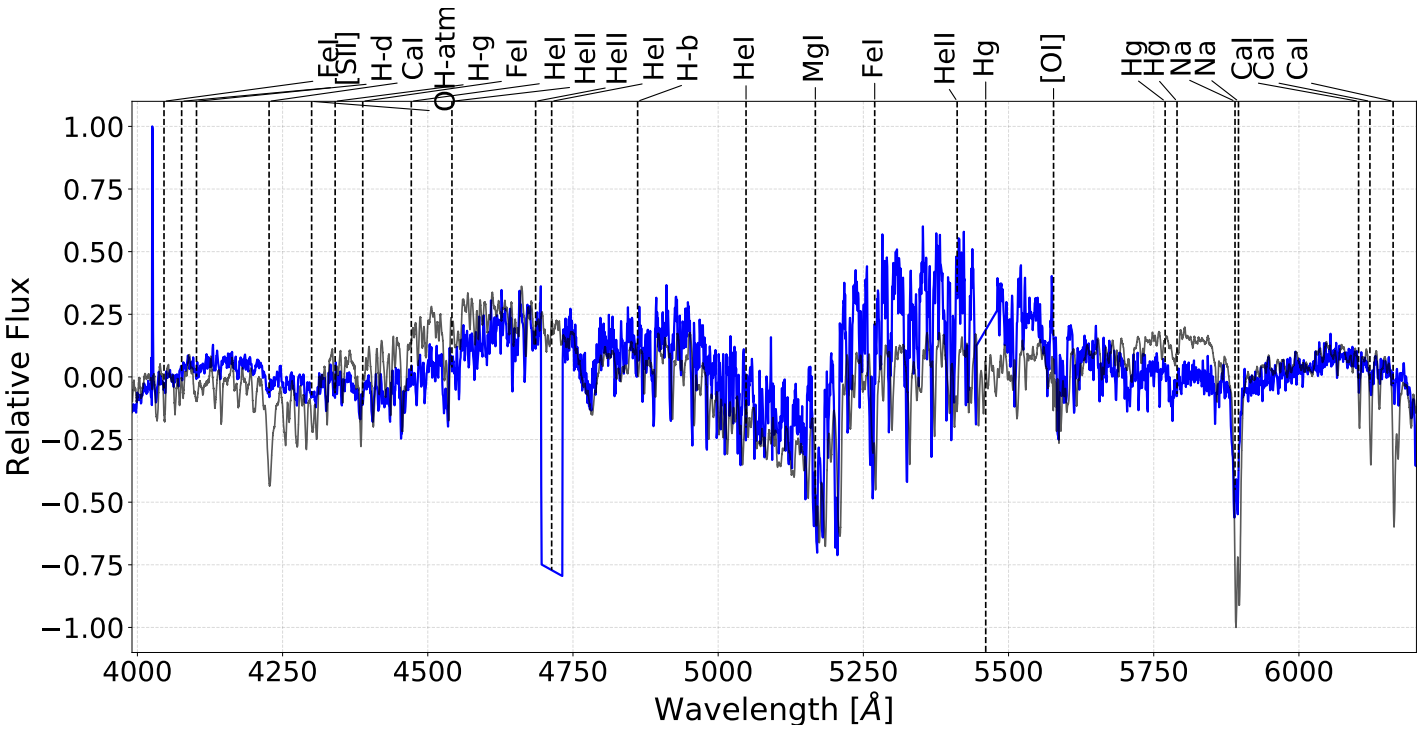

Figure C.35: Slit 8 for in NGC 2626

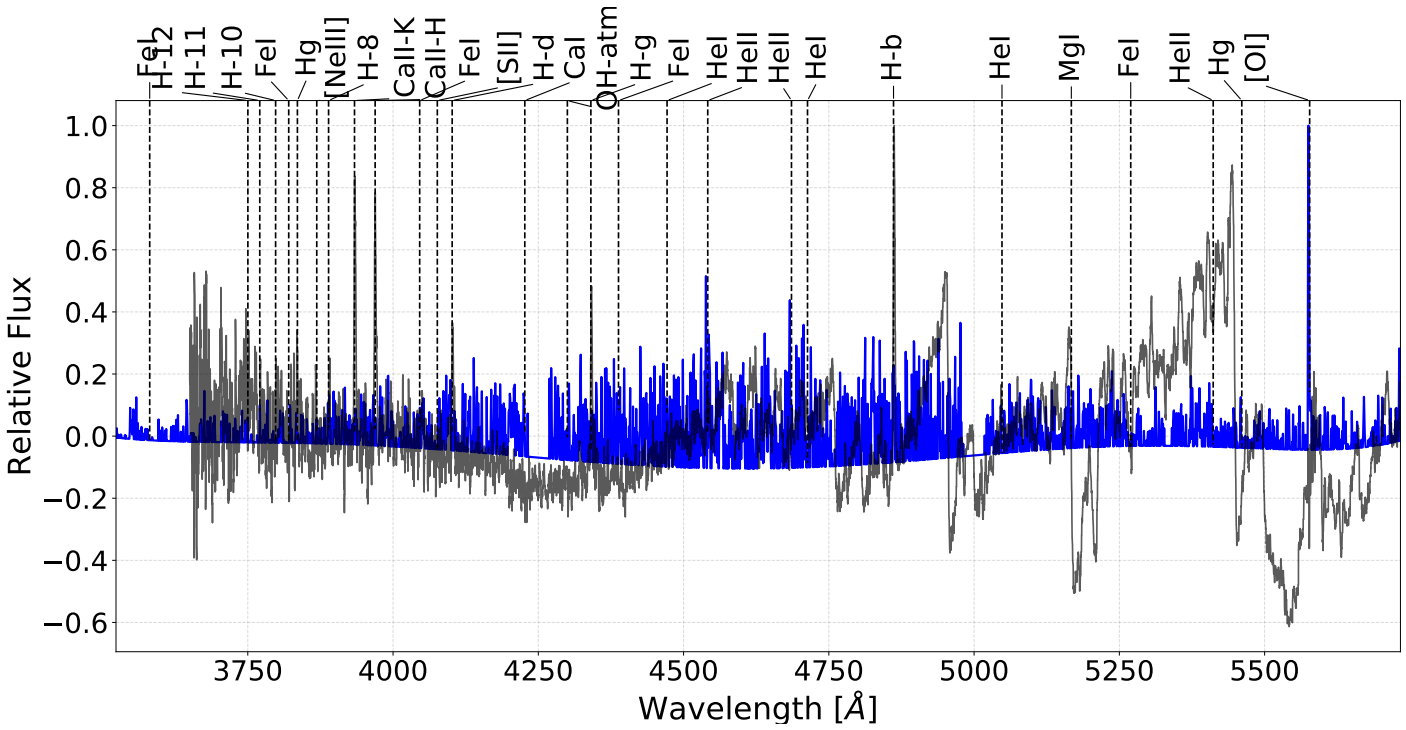

Figure C.36: Slit 9 for in NGC 2626

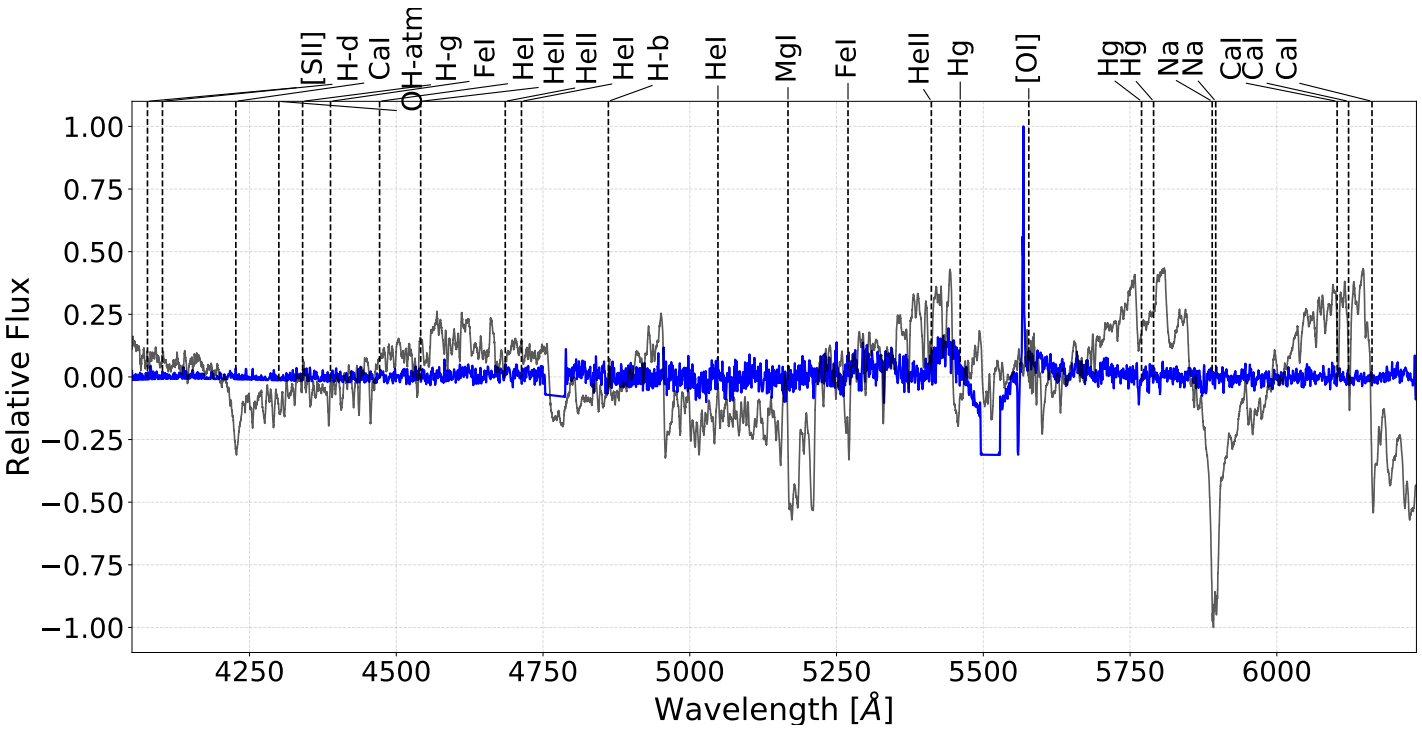

Figure C.37: Slit 10 for in NGC 2626

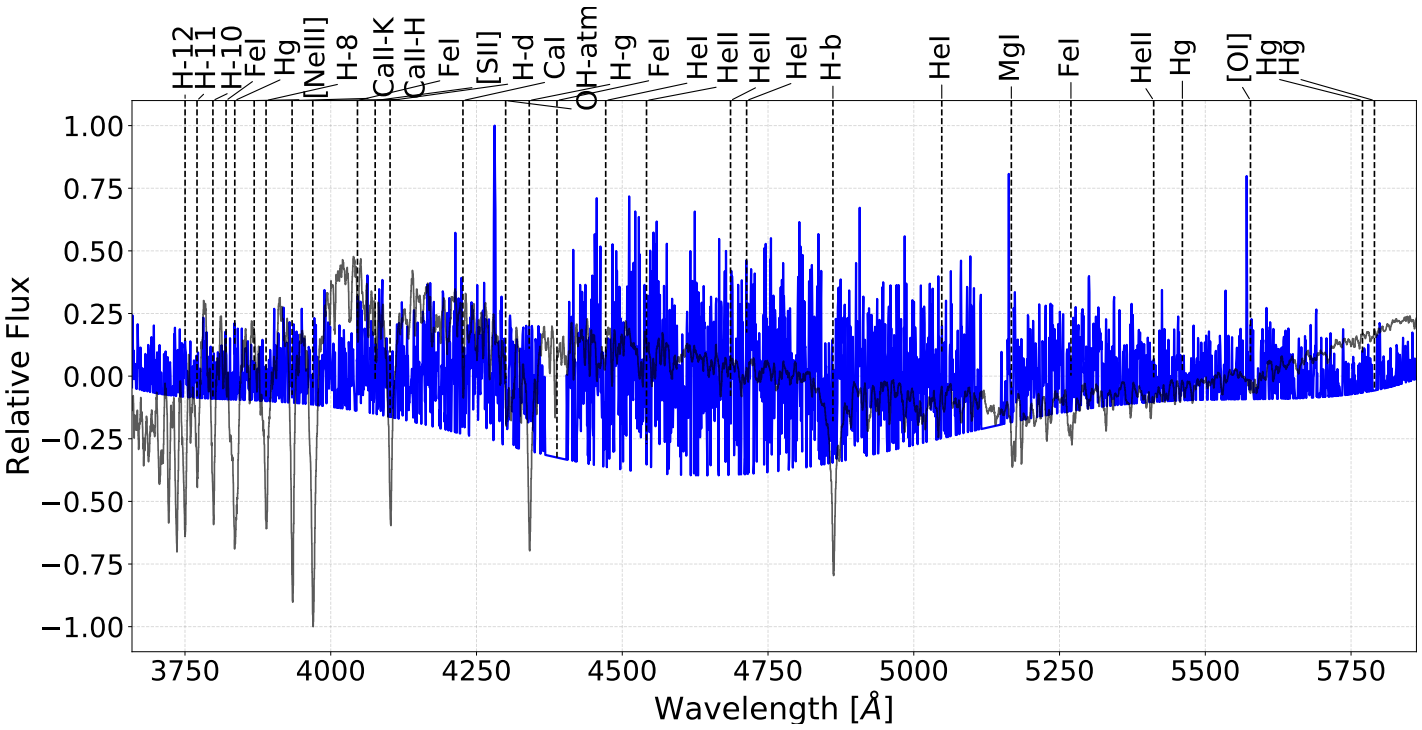

Figure C.38: Slit 11 for in NGC 2626

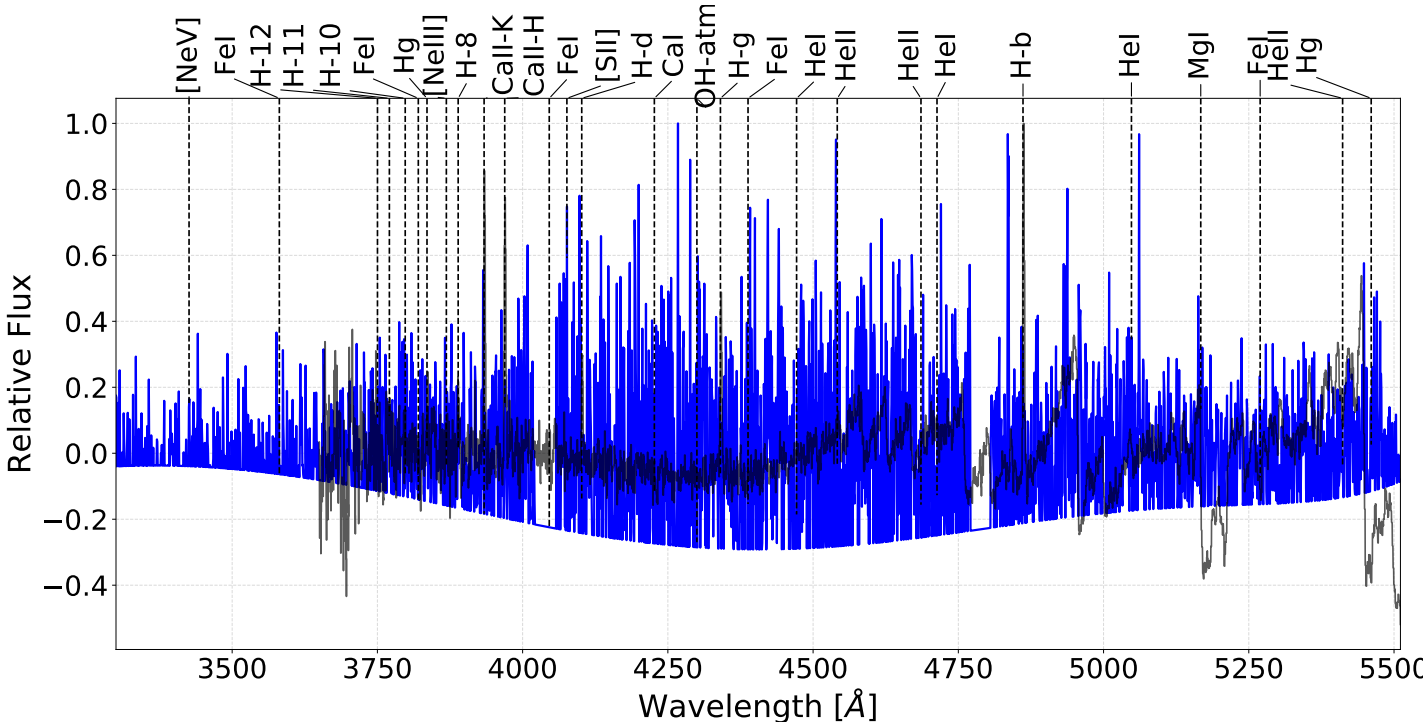

Figure C.39: Slit 12 for in NGC 2626

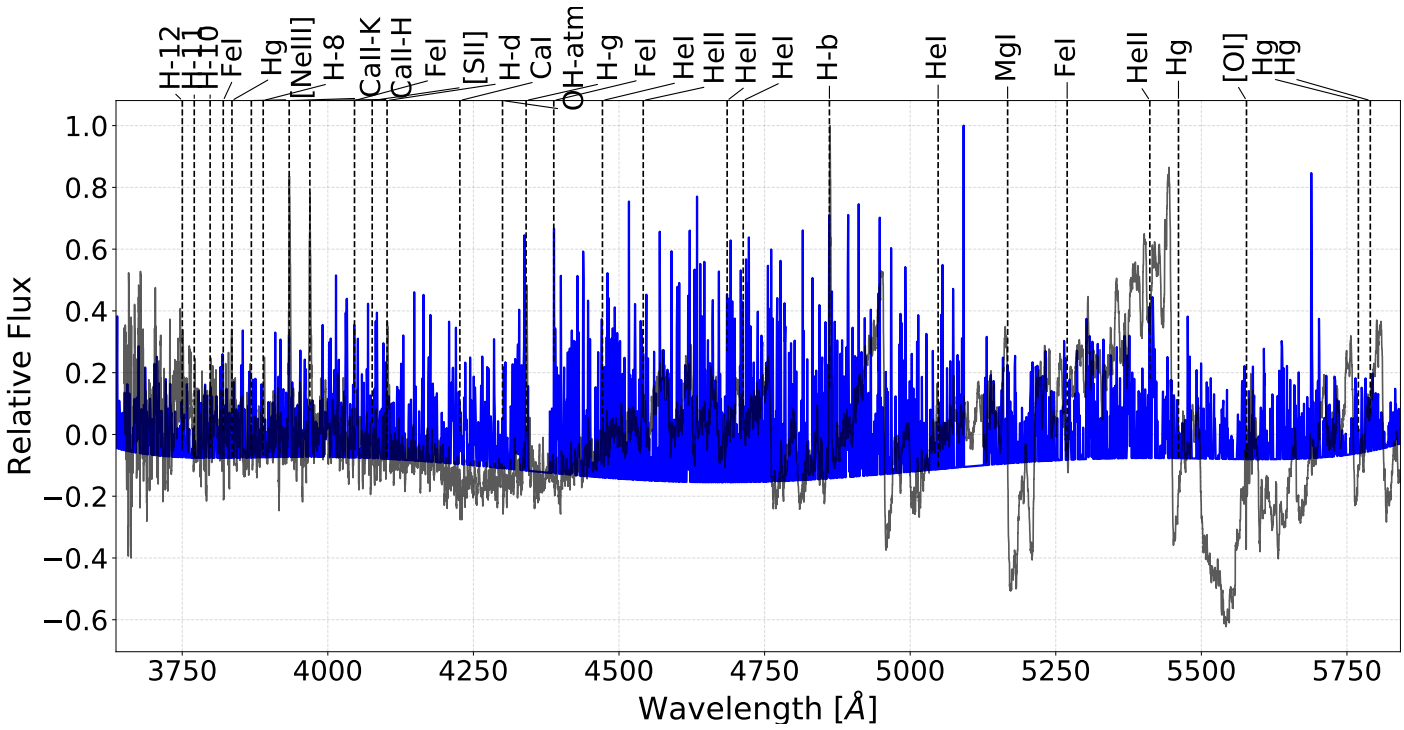

Figure C.40: Slit 13 for in NGC 2626

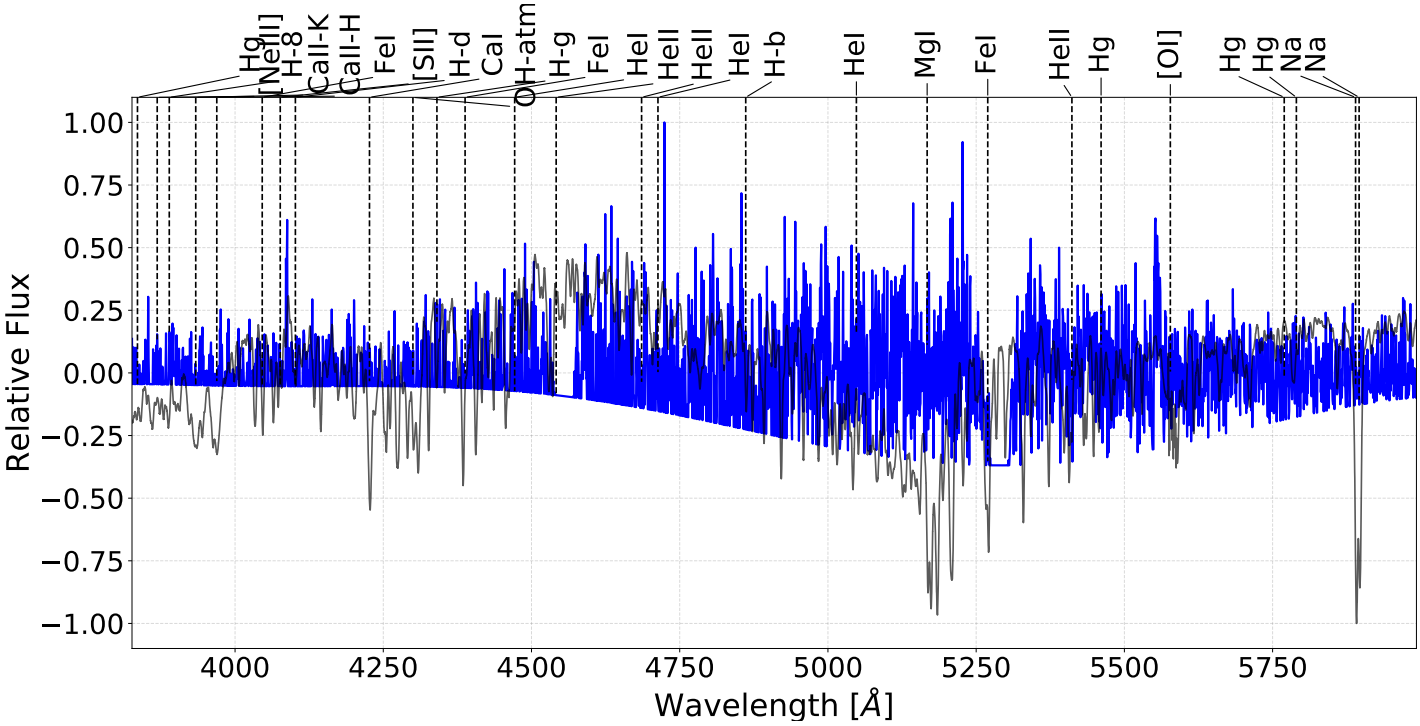

Figure C.41: Slit 14 for in NGC 2626

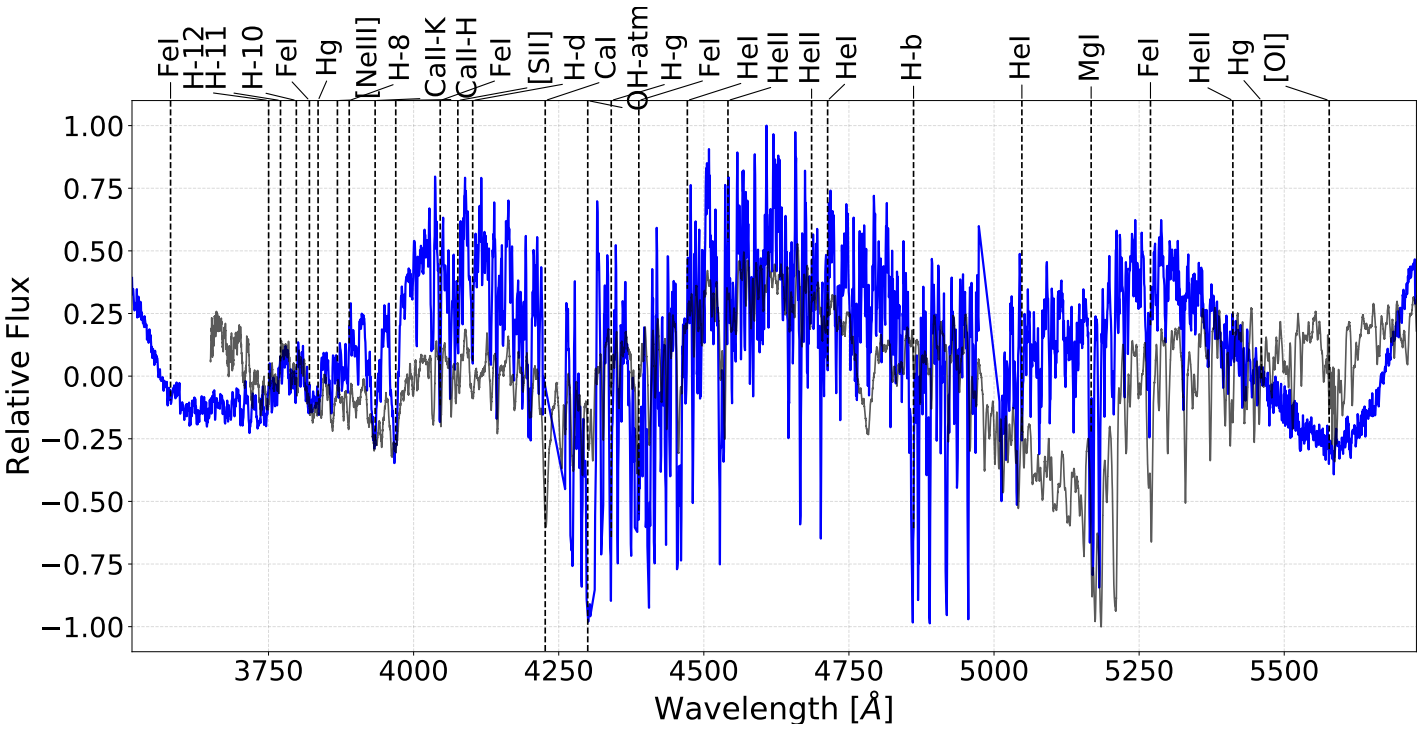

Figure C.42: Slit 15 for in NGC 2626

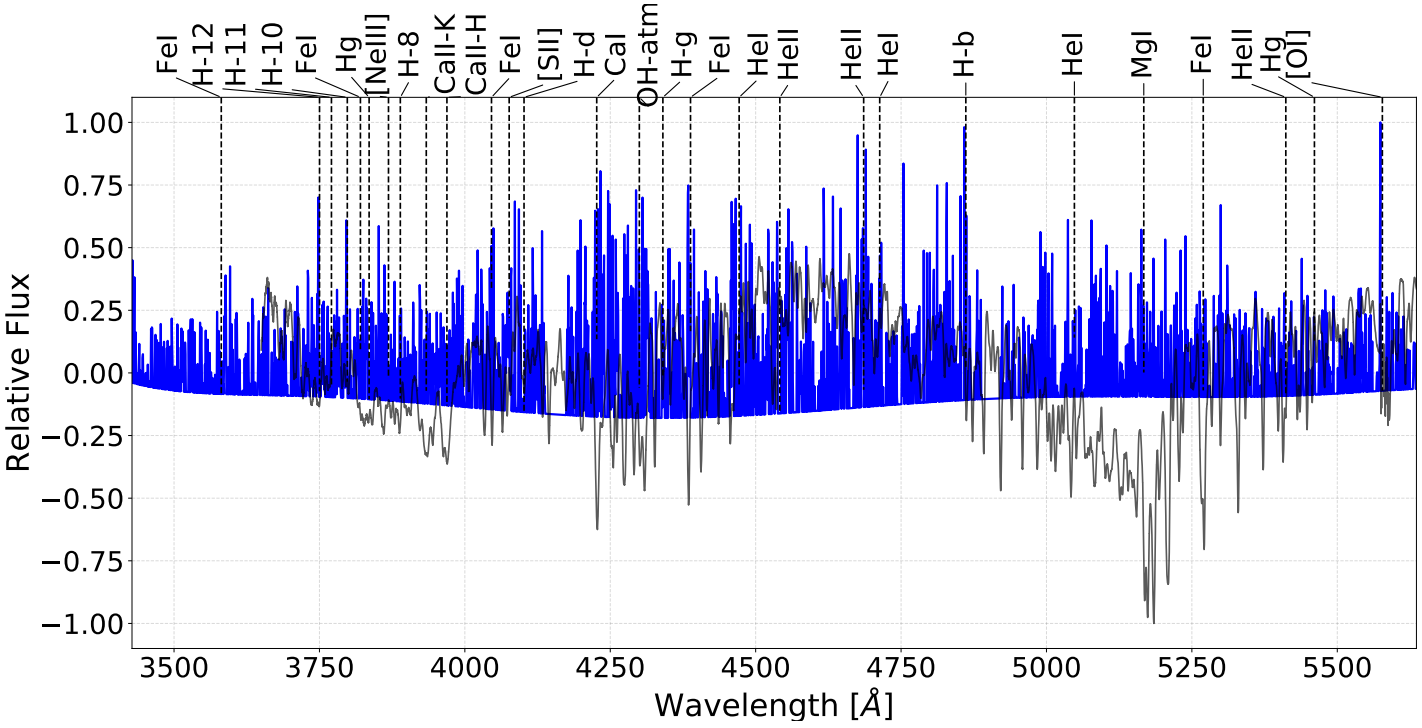

Figure C.43: Slit 16 for in NGC 2626

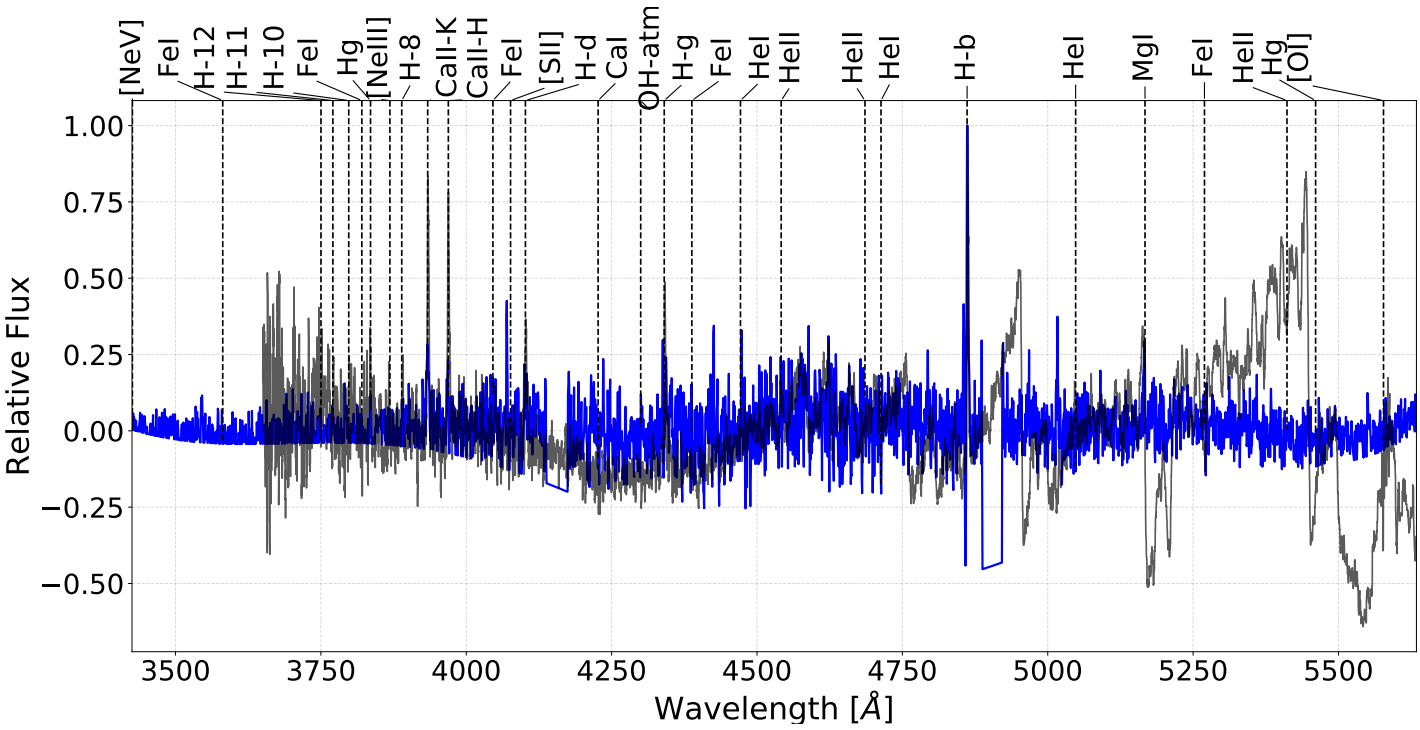

Figure C.44: Slit 17 for in NGC 2626

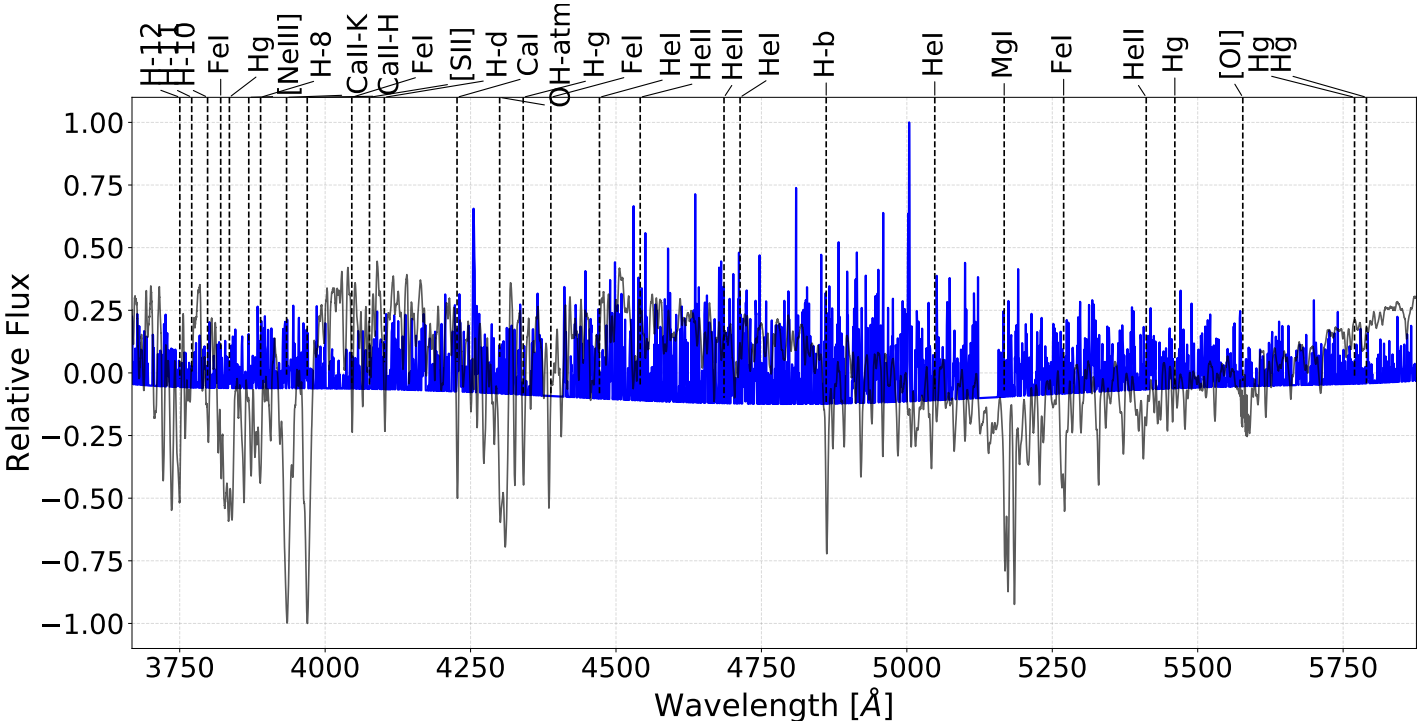

Figure C.45: Slit 18 for in NGC 2626

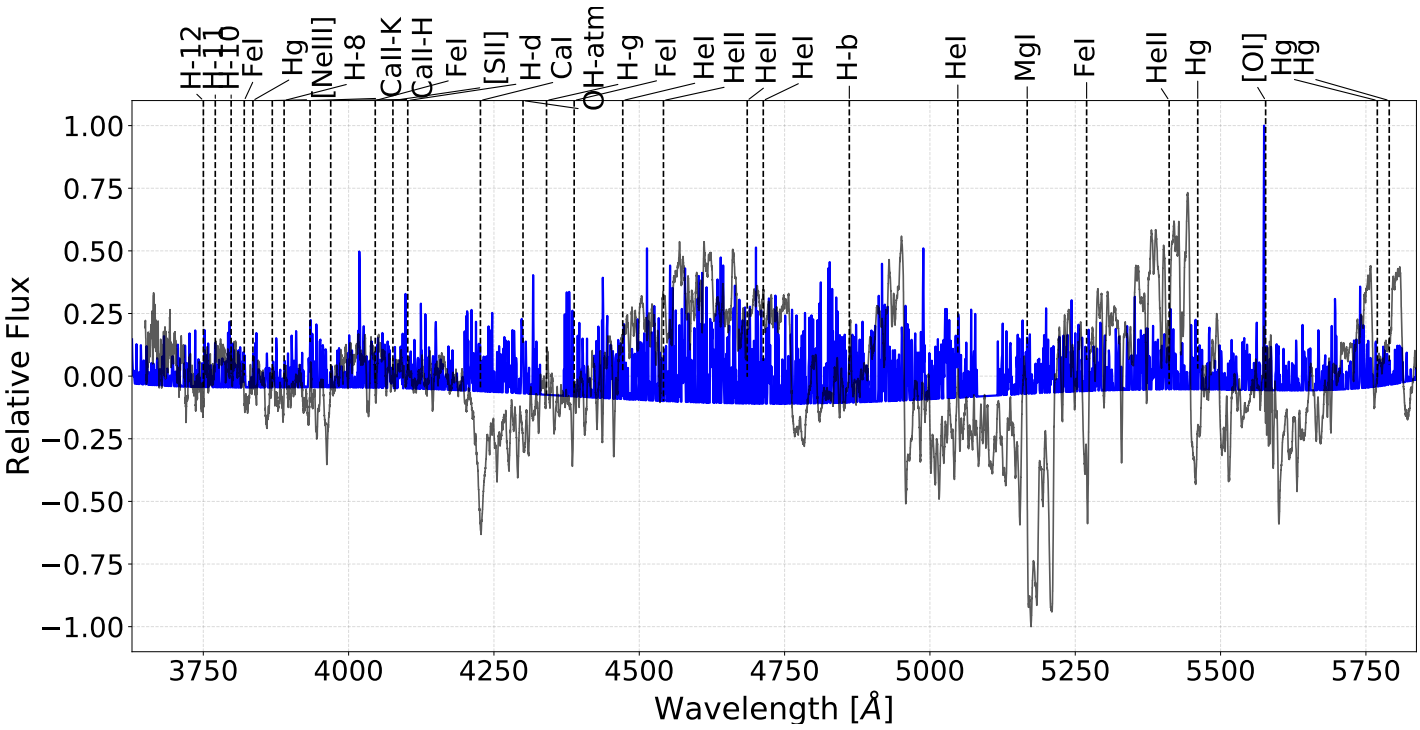

Figure C.46: Slit 19 for in NGC 2626

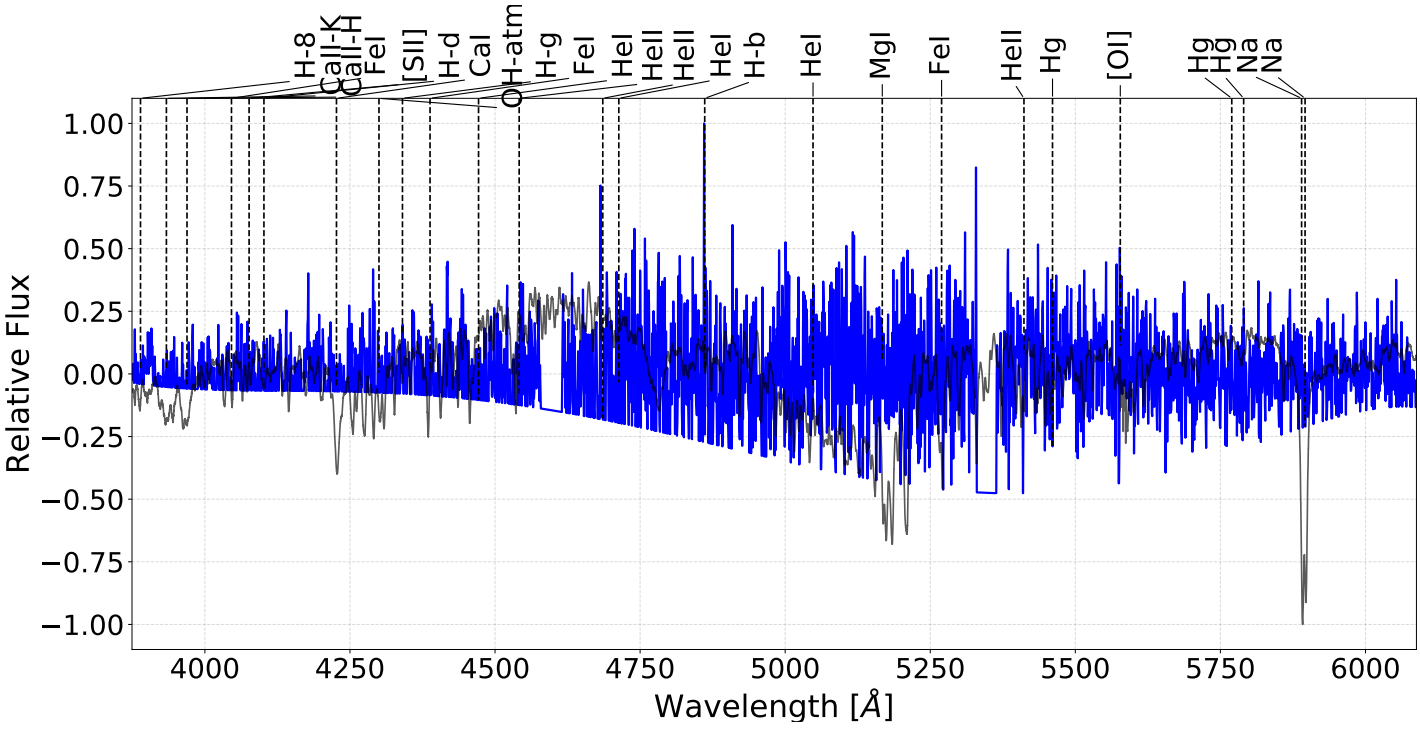

Figure C.47: Slit 20 for in NGC 2626

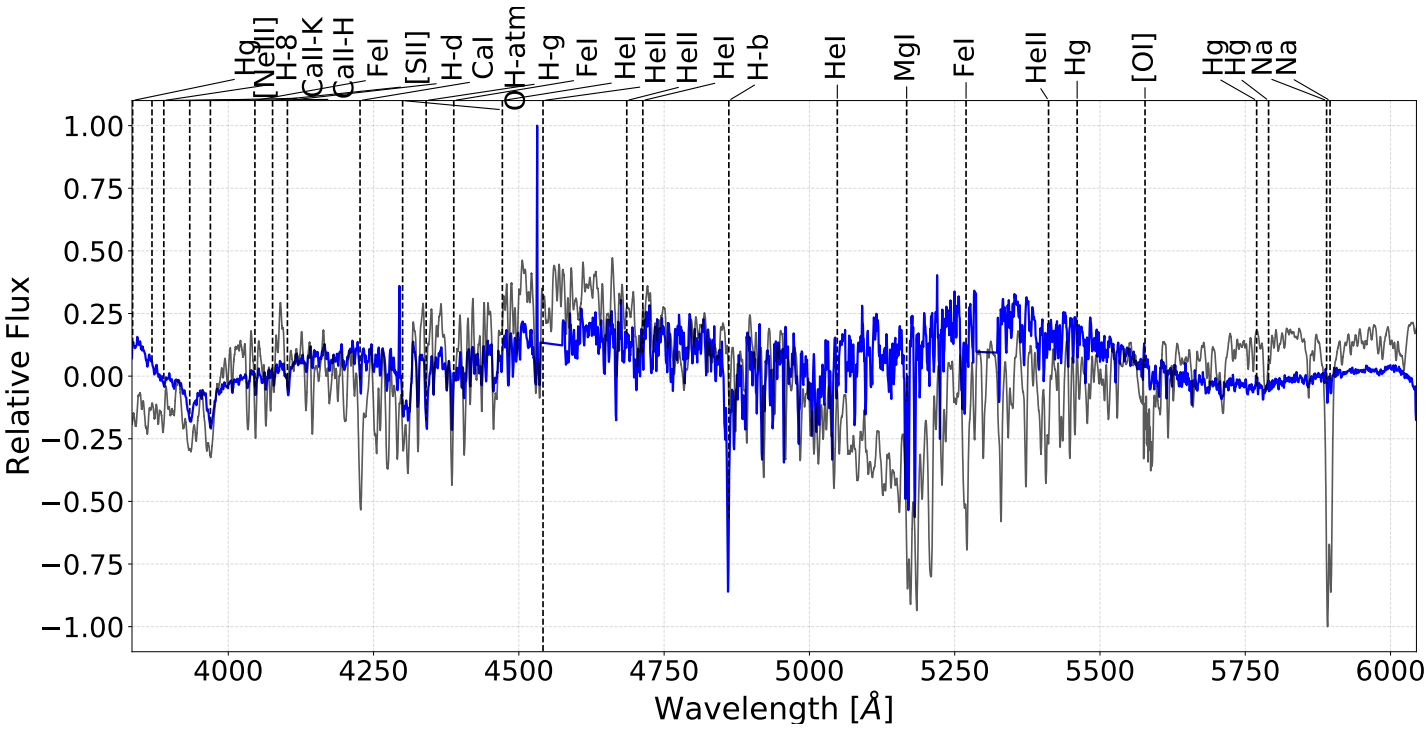

Figure C.48: Slit 21 for in NGC 2626

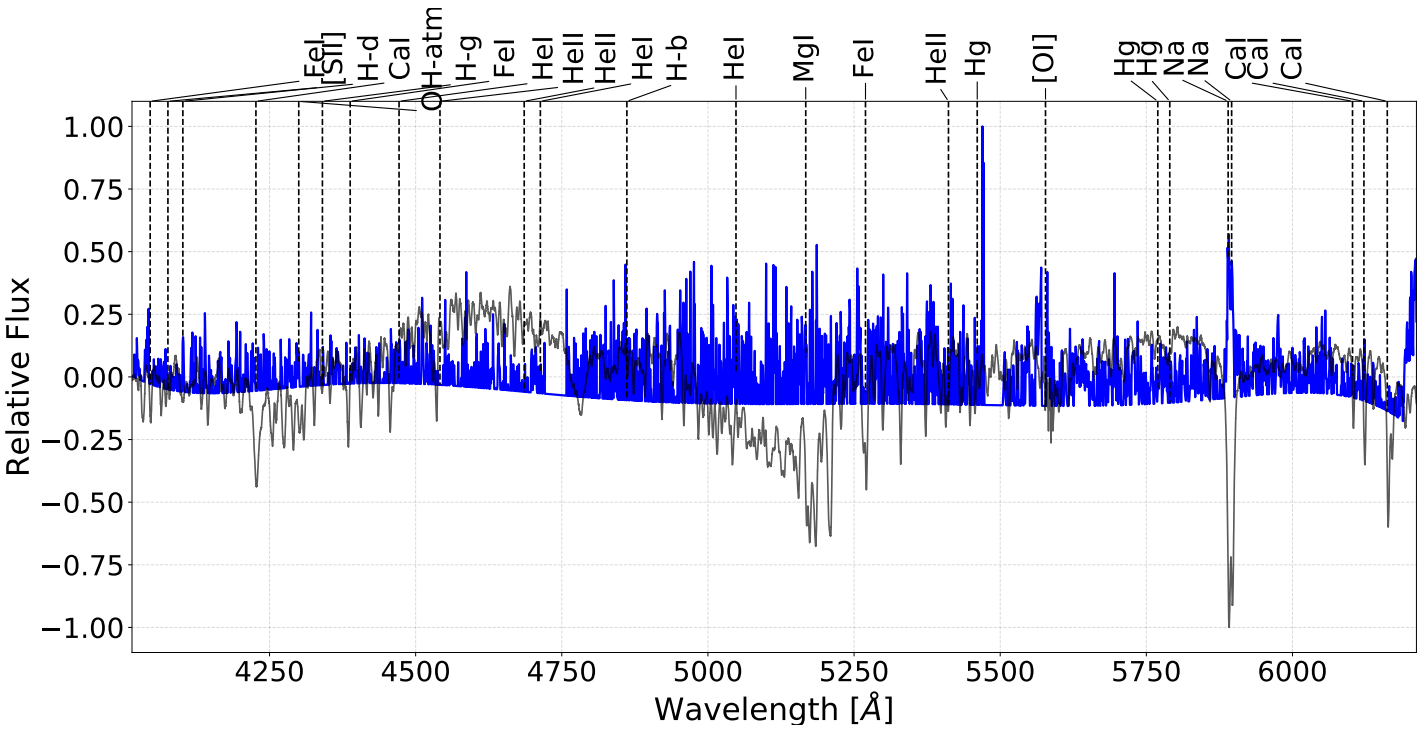

Figure C.49: Slit 22 for in NGC 2626

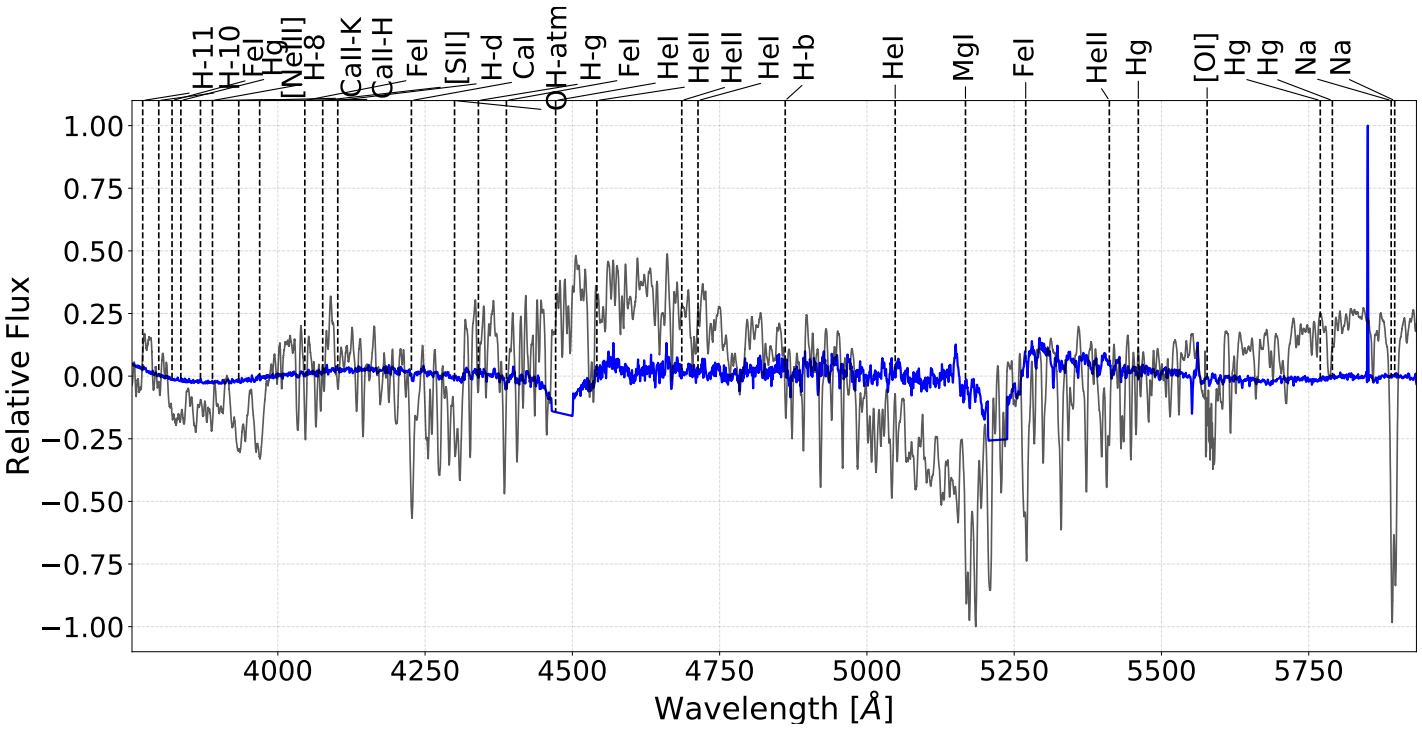

Figure C.50: Slit 23 for in NGC 2626

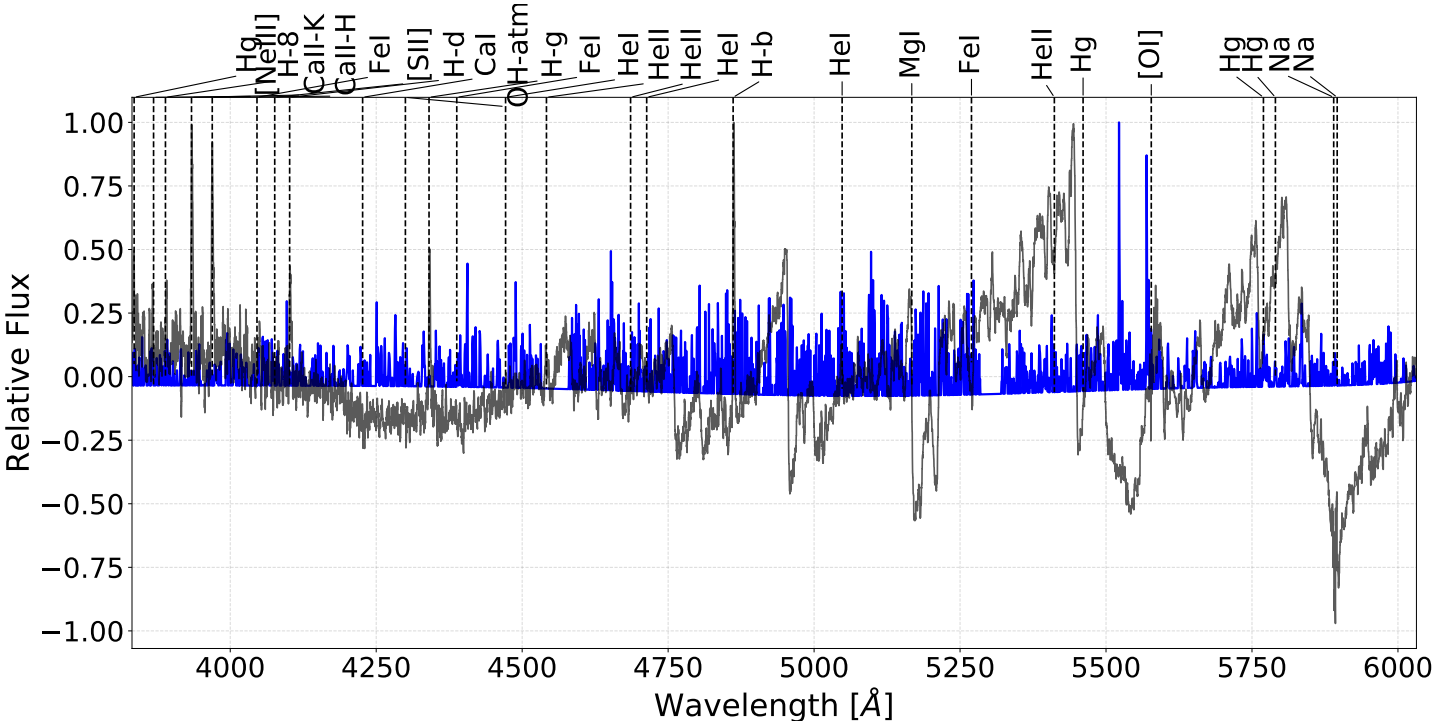

Figure C.51: Slit 24 for in NGC 2626

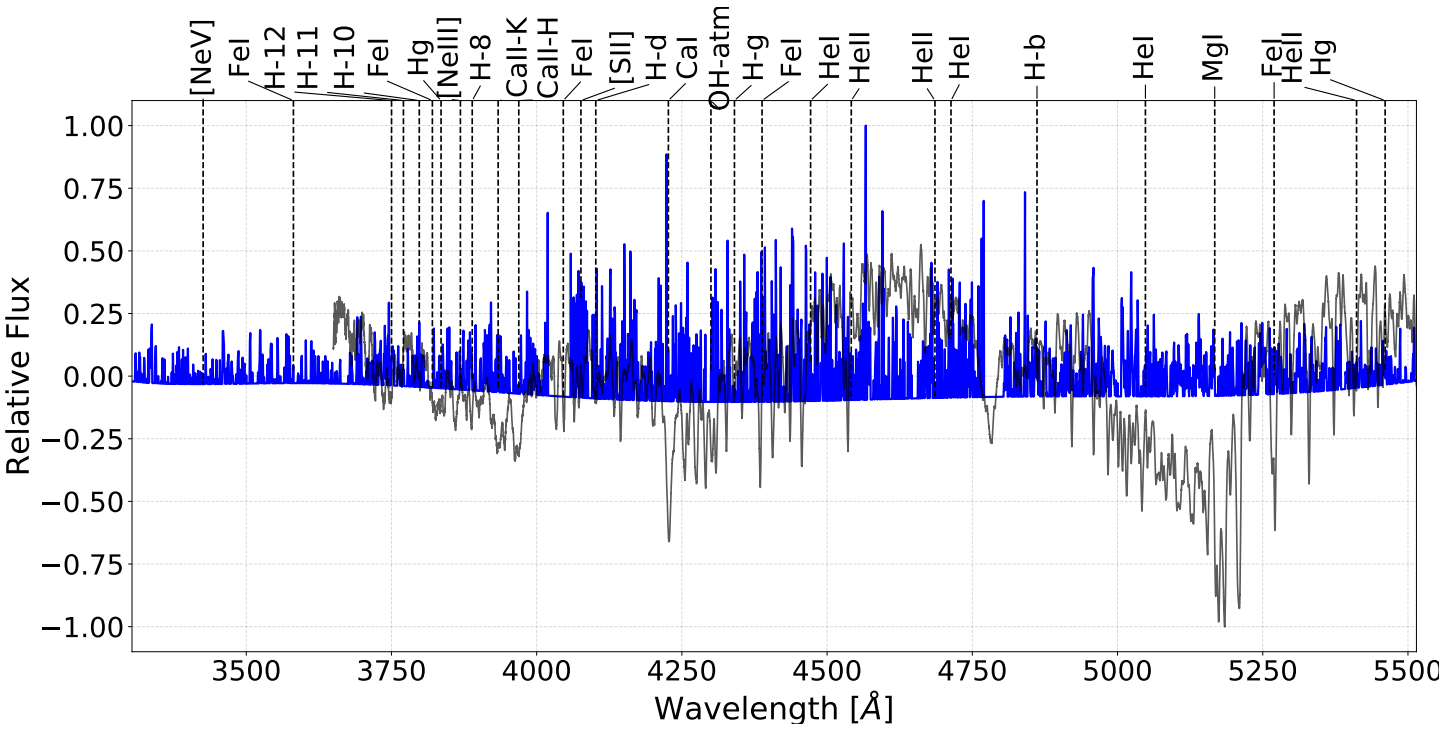

Figure C.52: Slit 25 for in NGC 2626

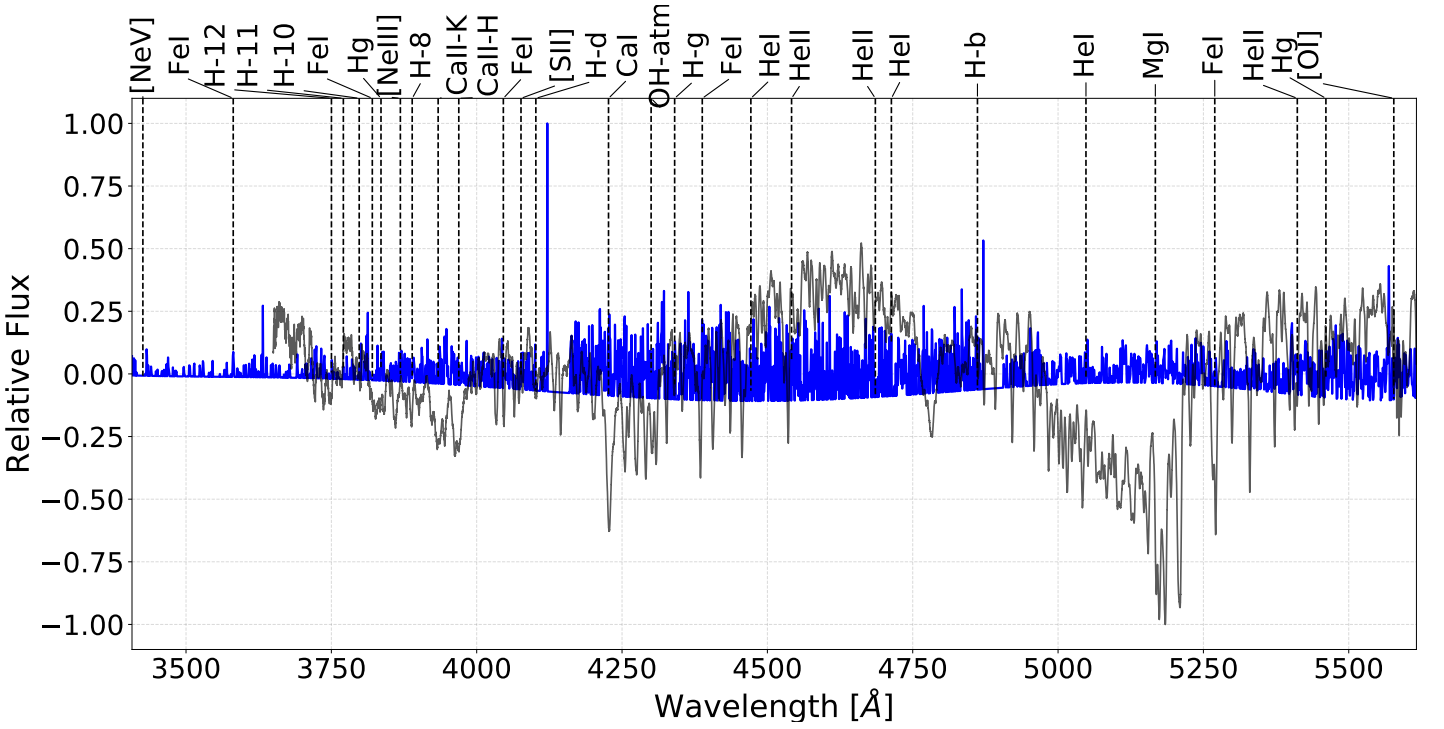

Figure C.53: Slit 26 for in NGC 2626

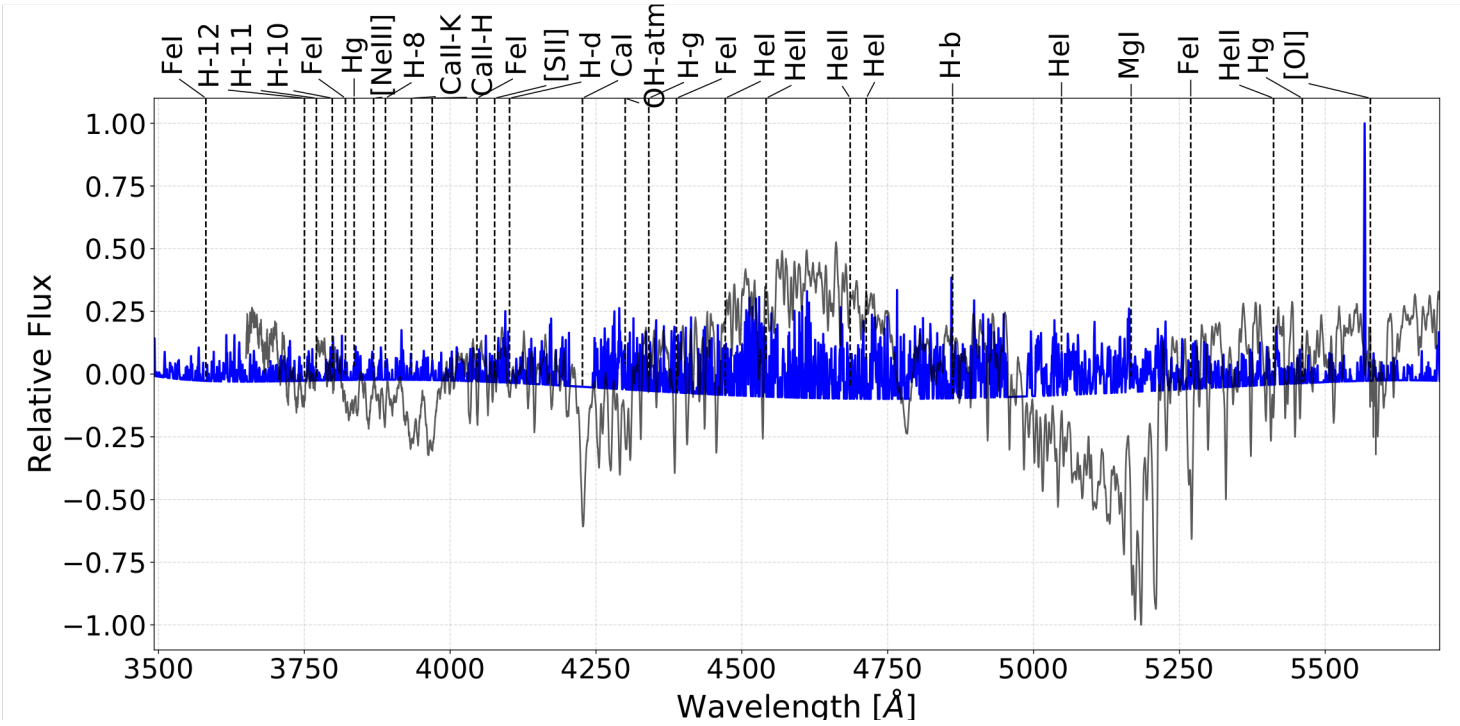

Figure C.54: Slit 27 for in NGC 2626

APPENDIX D: FULL PAGE SPECTRA OF THE STAR DRIVING HH-132

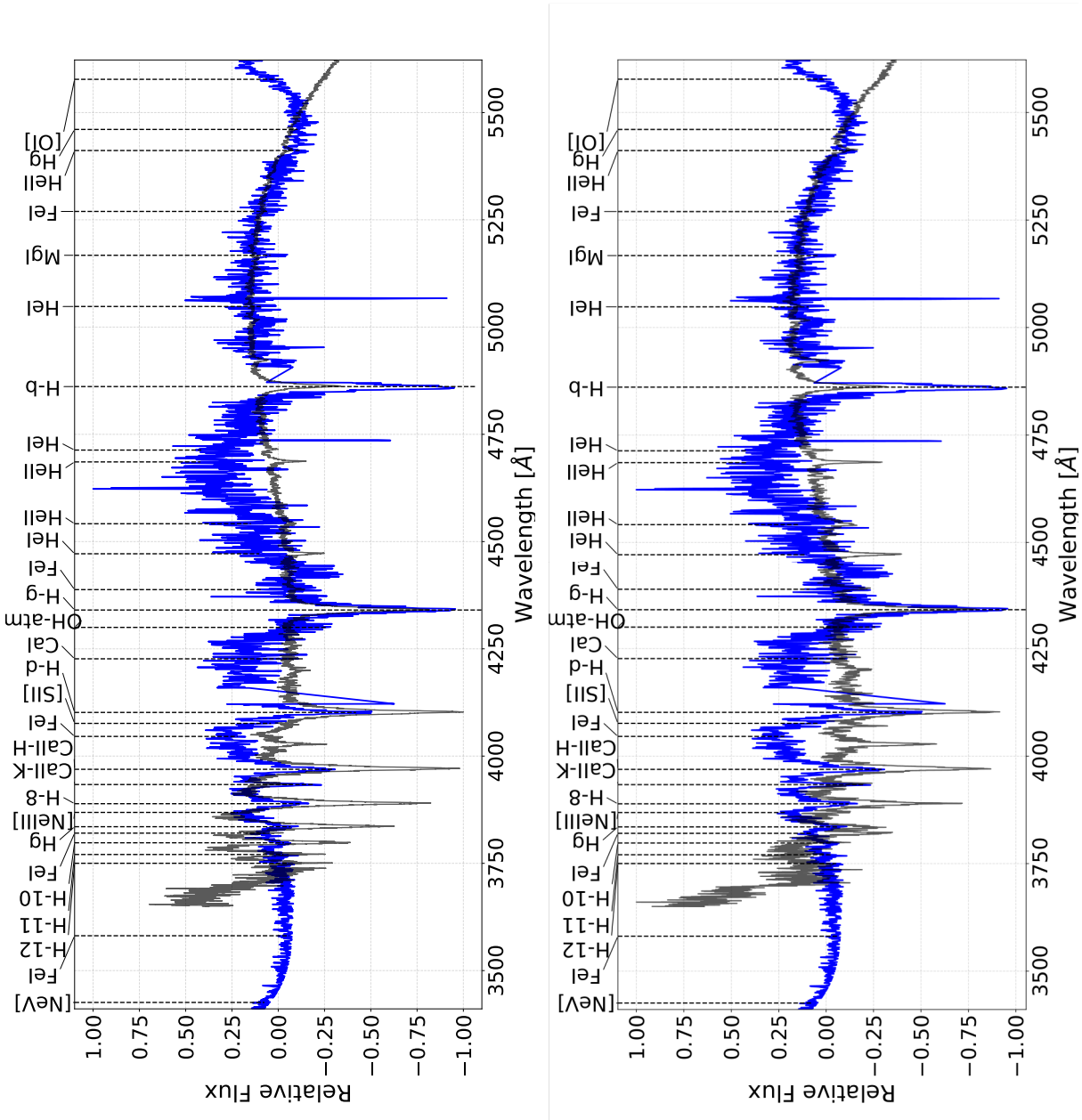

Figure D.1: The spectrum for the star associated with HH-132 plotted against the spectra of a O5 and O9 star from a standard spectral library in the left and right panels respectively spanning over the wavelength range from 3500Å to 5750Å.

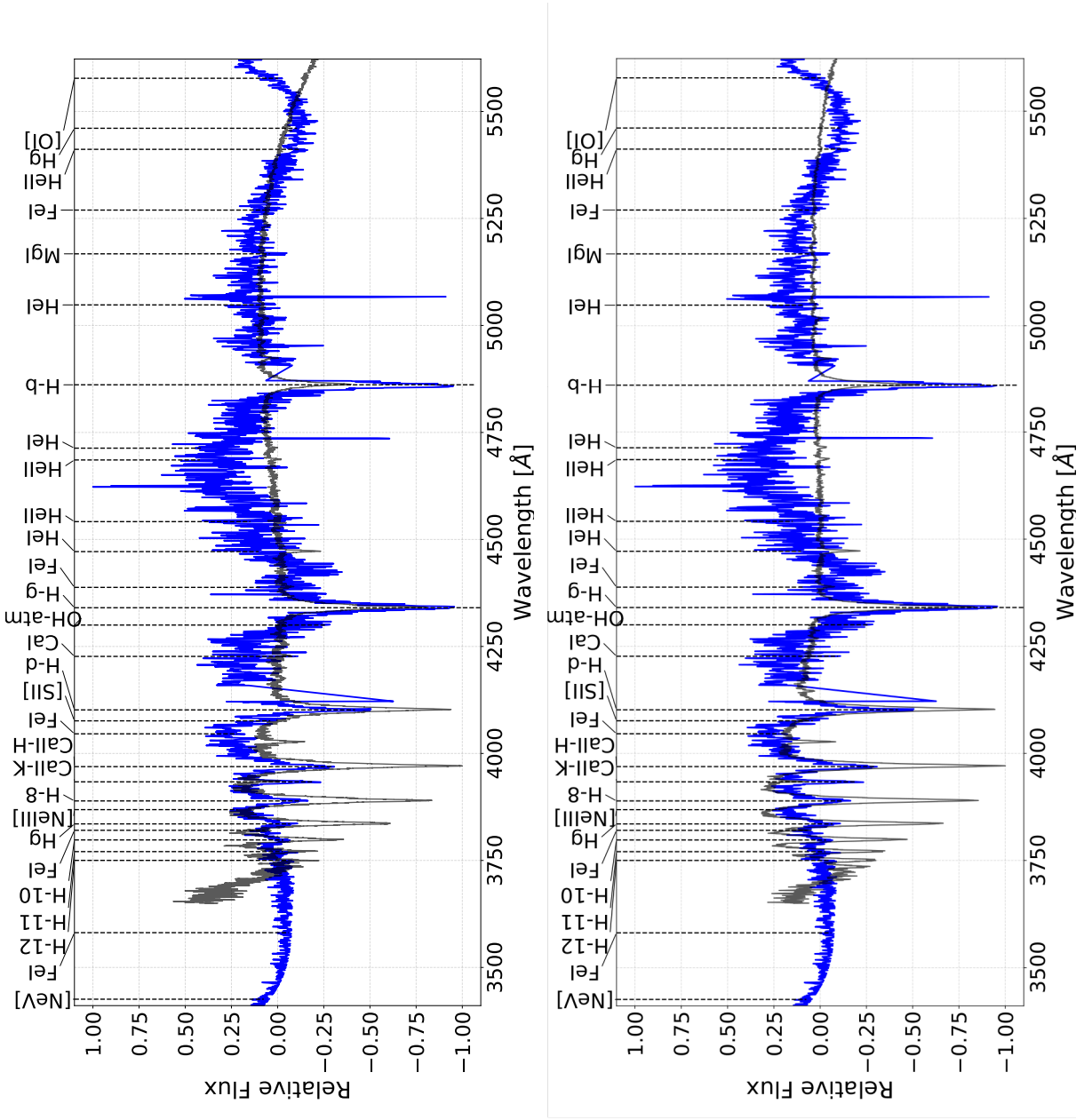

Figure D.2: The spectrum for the star associated with HH-132 plotted against the spectra of a B0 and B2 star from a standard spectral library in the left and right panels respectively spanning over the wavelength range from 3500Å to 5750Å.

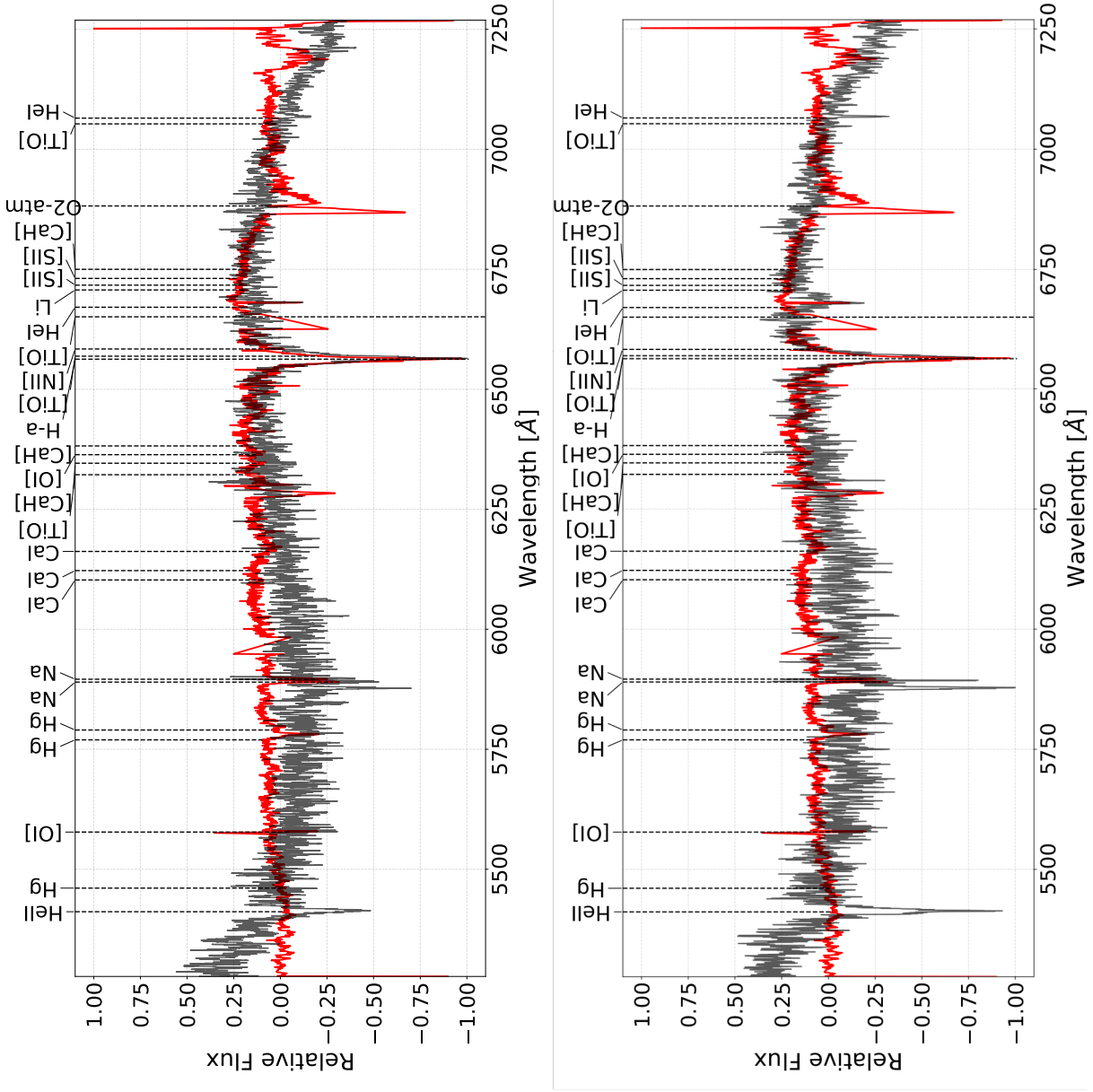

Figure D.3: The spectrum for the star associated with HH-132 plotted against the spectra of a O5 and O9 star from a standard spectral library in the left and right panels respectively spanning over the wavelength range from 4750Å to 7250Å.

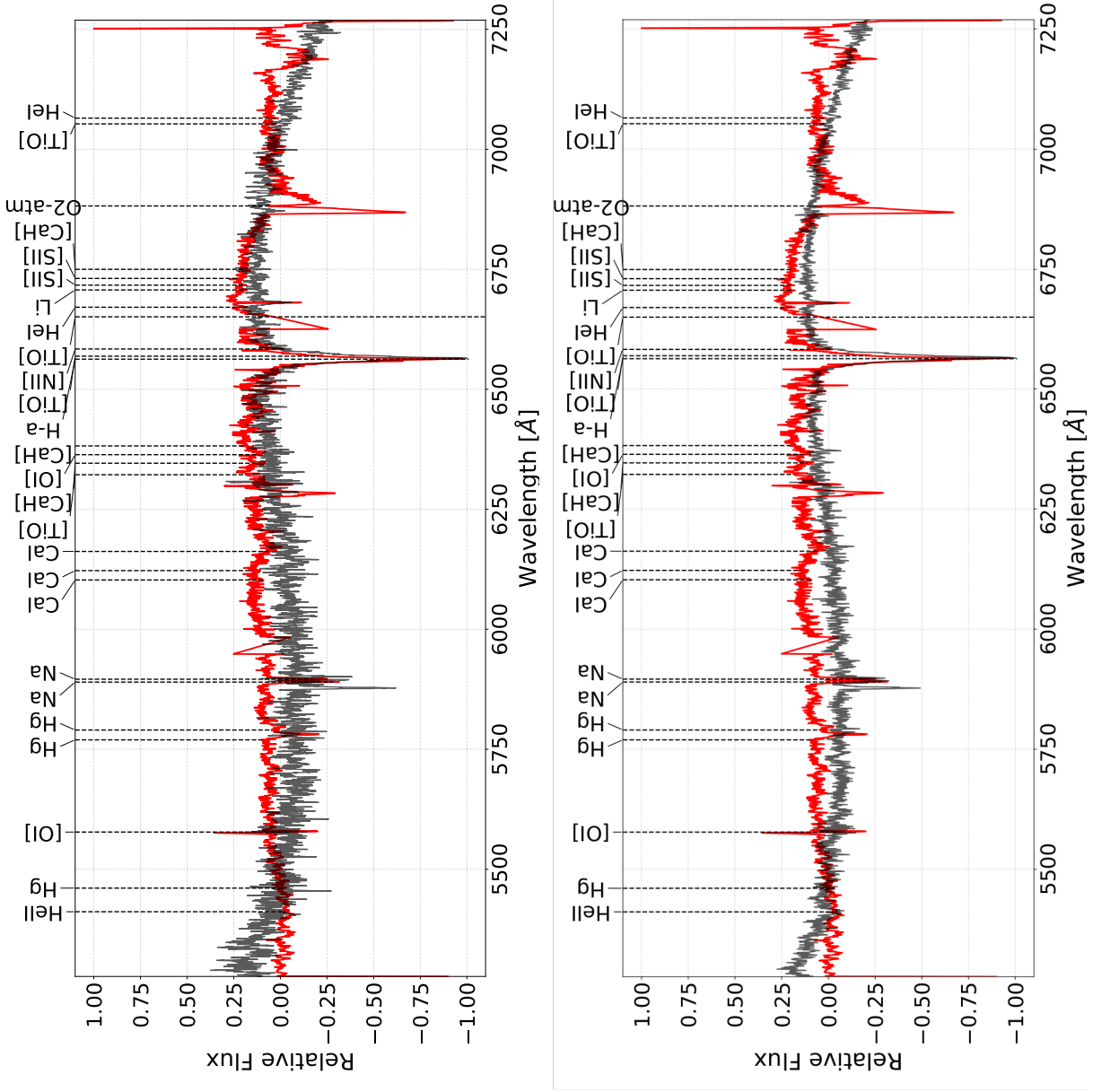

Figure D.4: The spectrum for the star associated with HH-132 plotted against the spectra of a B0 and B2 star from a standard spectral library in the left and right panels respectively spanning over the wavelength range from 4750 Å to 7250 Å.

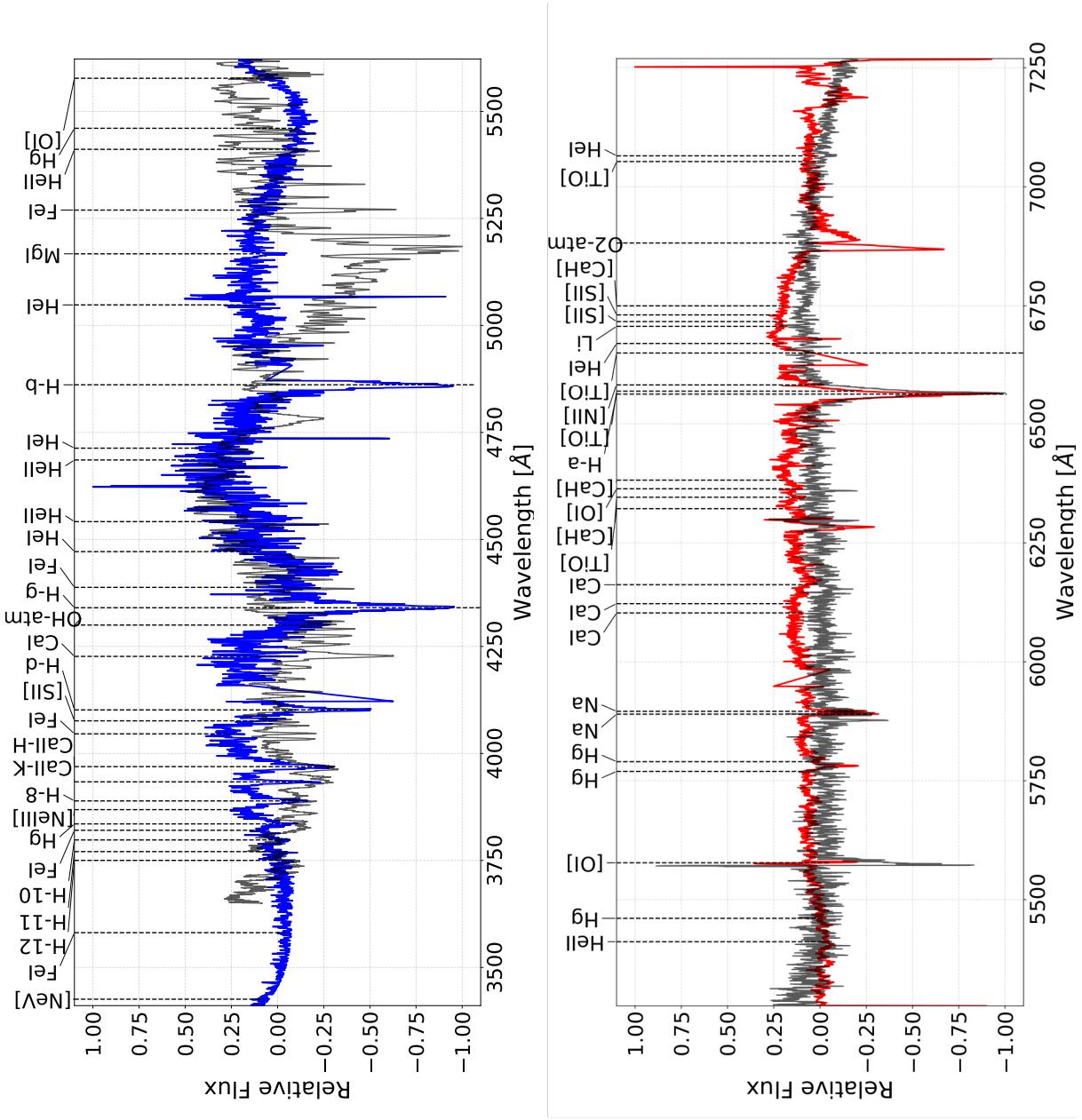

Figure D.5: The blue and red spectrum for the star associated with HH-132 plotted against the spectra of a B5 star from a standard spectral library spanning over the wavelength range from 3500Å to 5750Å in the left and 4750Å to 7250Å in the right panels respectively .